

Mapping Voids, Debonding, Delaminations, Moisture, and Other Defects Behind or Within Tunnel Linings

DETAILS

32 pages | | PAPERBACK

ISBN 978-0-309-27291-9 | DOI 10.17226/22609

AUTHORS

Wimsatt, Andrew; White, Joshua; Leung, Chin; Scullion, Tom; Hurlebaus, Stefan; Zollinger, Dan; Grasley Zachary; Nazarian, Sohei; Azari, Hoda; Yuan, Deren; Shokouhi, Parisa; Saarenketo, Timo; Oy, Roadscanners; and Tonon, Fulvio

BUY THIS BOOK

FIND RELATED TITLES

Visit the National Academies Press at NAP.edu and login or register to get:

- Access to free PDF downloads of thousands of scientific reports
- 10% off the price of print titles
- Email or social media notifications of new titles related to your interests
- Special offers and discounts



Distribution, posting, or copying of this PDF is strictly prohibited without written permission of the National Academies Press. (Request Permission) Unless otherwise indicated, all materials in this PDF are copyrighted by the National Academy of Sciences.

The Second
S T R A T E G I C H I G H W A Y R E S E A R C H P R O G R A M

 **SHRP 2 REPORT S2-R06G-RR-1**

Mapping Voids, Debonding, Delaminations, Moisture, and Other Defects Behind or Within Tunnel Linings

ANDREW WIMSATT, JOSHUA WHITE, CHIN LEUNG, AND TOM SCULLION
Texas A&M Transportation Institute

STEFAN HURLEBAUS, DAN ZOLLINGER, AND ZACHARY GRASLEY
Texas A&M University

SOHEL NAZARIAN, HODA AZARI, AND DEREN YUAN
The University of Texas at El Paso

PARISA SHOKOUHI
The German Federal Institute for Materials Research and Testing

TIMO SAARENKETO
Roadscanners Oy

FULVIO TONON
The University of Texas at Austin

TRANSPORTATION RESEARCH BOARD

WASHINGTON, D.C.
2014
www.TRB.org

Subscriber Categories

Bridges and Other Structures

Construction

Highways

The Second Strategic Highway Research Program

America's highway system is critical to meeting the mobility and economic needs of local communities, regions, and the nation. Developments in research and technology—such as advanced materials, communications technology, new data collection technologies, and human factors science—offer a new opportunity to improve the safety and reliability of this important national resource. Breakthrough resolution of significant transportation problems, however, requires concentrated resources over a short time frame. Reflecting this need, the second Strategic Highway Research Program (SHRP 2) has an intense, large-scale focus, integrates multiple fields of research and technology, and is fundamentally different from the broad, mission-oriented, discipline-based research programs that have been the mainstay of the highway research industry for half a century.

The need for SHRP 2 was identified in *TRB Special Report 260: Strategic Highway Research: Saving Lives, Reducing Congestion, Improving Quality of Life*, published in 2001 and based on a study sponsored by Congress through the Transportation Equity Act for the 21st Century (TEA-21). SHRP 2, modeled after the first Strategic Highway Research Program, is a focused, time-constrained, management-driven program designed to complement existing highway research programs. SHRP 2 focuses on applied research in four areas: Safety, to prevent or reduce the severity of highway crashes by understanding driver behavior; Renewal, to address the aging infrastructure through rapid design and construction methods that cause minimal disruptions and produce lasting facilities; Reliability, to reduce congestion through incident reduction, management, response, and mitigation; and Capacity, to integrate mobility, economic, environmental, and community needs in the planning and designing of new transportation capacity.

SHRP 2 was authorized in August 2005 as part of the Safe, Accountable, Flexible, Efficient Transportation Equity Act: A Legacy for Users (SAFETEA-LU). The program is managed by the Transportation Research Board (TRB) on behalf of the National Research Council (NRC). SHRP 2 is conducted under a memorandum of understanding among the American Association of State Highway and Transportation Officials (AASHTO), the Federal Highway Administration (FHWA), and the National Academy of Sciences, parent organization of TRB and NRC. The program provides for competitive, merit-based selection of research contractors; independent research project oversight; and dissemination of research results.

SHRP 2 Report S2-R06G-RR-1

ISBN: 978-0-309-27291-9

Library of Congress Control Number: 2014937961

© 2014 National Academy of Sciences. All rights reserved.

Copyright Information

Authors herein are responsible for the authenticity of their materials and for obtaining written permissions from publishers or persons who own the copyright to any previously published or copyrighted material used herein.

The second Strategic Highway Research Program grants permission to reproduce material in this publication for classroom and not-for-profit purposes. Permission is given with the understanding that none of the material will be used to imply TRB, AASHTO, or FHWA endorsement of a particular product, method, or practice. It is expected that those reproducing material in this document for educational and not-for-profit purposes will give appropriate acknowledgment of the source of any reprinted or reproduced material. For other uses of the material, request permission from SHRP 2.

Note: SHRP 2 report numbers convey the program, focus area, project number, and publication format. Report numbers ending in “w” are published as web documents only.

Notice

The project that is the subject of this report was a part of the second Strategic Highway Research Program, conducted by the Transportation Research Board with the approval of the Governing Board of the National Research Council.

The members of the technical committee selected to monitor this project and review this report were chosen for their special competencies and with regard for appropriate balance. The report was reviewed by the technical committee and accepted for publication according to procedures established and overseen by the Transportation Research Board and approved by the Governing Board of the National Research Council.

The opinions and conclusions expressed or implied in this report are those of the researchers who performed the research and are not necessarily those of the Transportation Research Board, the National Research Council, or the program sponsors.

The Transportation Research Board of the National Academies, the National Research Council, and the sponsors of the second Strategic Highway Research Program do not endorse products or manufacturers. Trade or manufacturers' names appear herein solely because they are considered essential to the object of the report.



SHRP 2 Reports

Available by subscription and through the TRB online bookstore:
www.TRB.org/bookstore

Contact the TRB Business Office:
 202-334-3213

More information about SHRP 2:
www.TRB.org/SHRP2

THE NATIONAL ACADEMIES

Advisers to the Nation on Science, Engineering, and Medicine

The **National Academy of Sciences** is a private, nonprofit, self-perpetuating society of distinguished scholars engaged in scientific and engineering research, dedicated to the furtherance of science and technology and to their use for the general welfare. On the authority of the charter granted to it by Congress in 1863, the Academy has a mandate that requires it to advise the federal government on scientific and technical matters. Dr. Ralph J. Cicerone is president of the National Academy of Sciences.

The **National Academy of Engineering** was established in 1964, under the charter of the National Academy of Sciences, as a parallel organization of outstanding engineers. It is autonomous in its administration and in the selection of its members, sharing with the National Academy of Sciences the responsibility for advising the federal government. The National Academy of Engineering also sponsors engineering programs aimed at meeting national needs, encourages education and research, and recognizes the superior achievements of engineers. Dr. C. D. (Dan) Mote, Jr., is president of the National Academy of Engineering.

The **Institute of Medicine** was established in 1970 by the National Academy of Sciences to secure the services of eminent members of appropriate professions in the examination of policy matters pertaining to the health of the public. The Institute acts under the responsibility given to the National Academy of Sciences by its congressional charter to be an adviser to the federal government and, on its own initiative, to identify issues of medical care, research, and education. Dr. Victor J. Dzau is president of the Institute of Medicine.

The **National Research Council** was organized by the National Academy of Sciences in 1916 to associate the broad community of science and technology with the Academy's purposes of furthering knowledge and advising the federal government. Functioning in accordance with general policies determined by the Academy, the Council has become the principal operating agency of both the National Academy of Sciences and the National Academy of Engineering in providing services to the government, the public, and the scientific and engineering communities. The Council is administered jointly by both Academies and the Institute of Medicine. Dr. Ralph J. Cicerone and Dr. C. D. (Dan) Mote, Jr., are chair and vice chair, respectively, of the National Research Council.

The **Transportation Research Board** is one of six major divisions of the National Research Council. The mission of the Transportation Research Board is to provide leadership in transportation innovation and progress through research and information exchange, conducted within a setting that is objective, interdisciplinary, and multimodal. The Board's varied activities annually engage about 7,000 engineers, scientists, and other transportation researchers and practitioners from the public and private sectors and academia, all of whom contribute their expertise in the public interest. The program is supported by state transportation departments, federal agencies including the component administrations of the U.S. Department of Transportation, and other organizations and individuals interested in the development of transportation. www.TRB.org

www.national-academies.org

SHRP 2 STAFF

Ann M. Brach, *Director*

Stephen J. Andrie, *Deputy Director*

Neil J. Pedersen, *Deputy Director, Implementation and Communications*

Cynthia Allen, *Editor*

Kenneth Campbell, *Chief Program Officer, Safety*

JoAnn Coleman, *Senior Program Assistant, Capacity and Reliability*

Eduardo Cusicanqui, *Financial Officer*

Richard Deering, *Special Consultant, Safety Data Phase 1 Planning*

Shantia Douglas, *Senior Financial Assistant*

Charles Fay, *Senior Program Officer, Safety*

Carol Ford, *Senior Program Assistant, Renewal and Safety*

Jo Allen Gause, *Senior Program Officer, Capacity*

James Hedlund, *Special Consultant, Safety Coordination*

Alyssa Hernandez, *Reports Coordinator*

Ralph Hessian, *Special Consultant, Capacity and Reliability*

Andy Horosko, *Special Consultant, Safety Field Data Collection*

William Hyman, *Senior Program Officer, Reliability*

Linda Mason, *Communications Officer*

Reena Mathews, *Senior Program Officer, Capacity and Reliability*

Matthew Miller, *Program Officer, Capacity and Reliability*

Michael Miller, *Senior Program Assistant, Capacity and Reliability*

David Plazak, *Senior Program Officer, Capacity and Reliability*

Rachel Taylor, *Senior Editorial Assistant*

Dean Trackman, *Managing Editor*

Connie Woldu, *Administrative Coordinator*

ACKNOWLEDGMENTS

This work was sponsored by the Federal Highway Administration in cooperation with the American Association of State Highway and Transportation Officials. It was conducted in the second Strategic Highway Research Program, which is administered by the Transportation Research Board of the National Academies. The project was managed by Dr. Monica A. Starnes, Senior Program Officer for SHRP 2 Renewal.

The research documented in this report was performed under Strategic Highway Research Program (SHRP 2) Project R06G by the Texas A&M Transportation Institute (TTI) in College Station, Texas. TTI was the contractor for this study, and the Research Foundation of Texas A&M University served as fiscal administrator.

Andrew J. Wimsatt, P.E., Research Engineer with TTI, was the project director and principal investigator. The other authors of this report are Joshua White, Tom Scullion, and Chin Leung, graduate students at Texas A&M University; Stefan Hurlbaas, P.E., Associate Professor, Zachary Grasley, Associate Professor, and Dan Zollinger, P.E., Professor, Department of Civil Engineering at Texas A&M University; Soheil Nazarian, P.E., Professor, Department of Civil Engineering at The University of Texas at El Paso; Deren Yuan, Researcher, The University of Texas at El Paso; Ms. Hoda Azari,

graduate student at The University of Texas at El Paso; Parisa Shokouhi, Alexander von Humboldt Research Fellow at the German Federal Institute for Materials Research and Testing; Timo Saarenketo, Managing Director of Roadscanners Oy; and Fulvio Tonon at The University of Texas at Austin.

The project team thanks Robert Johnson and Eddie Black of the Chesapeake Bay Bridge-Tunnel, Mike Salamon and Stephen Quick of the Colorado Department of Transportation, and Ms. Gail Miller of Harris County, Colorado, for allowing the team to test in their tunnel facilities and for their assistance.

The team also thanks the expert panel for this project. The panel members were Helmut Ernst, P.E., former Chief Engineer, Massachusetts Turnpike Authority; Bernard Yostpille, P.E., Assistant Chief Structural Engineer, Port Authority of New York and New Jersey; Blake D. Rothfuss, P.E., D.WRE, Jacobs Associates; Robert E. Johnson, Director of Maintenance, Chesapeake Bay Bridge-Tunnel District; Michael J. Abrahams, P.E., Senior Vice President, Parsons Brinckerhoff Quade & Douglas, Inc.; Mike Salamon, Colorado Department of Transportation Superintendent for the Eisenhower Memorial Tunnel; John S. Popovics, Associate Professor, University of Illinois; and Frank Jalinoos, Federal Highway Administration.

FOREWORD

Monica A. Starnes, PhD, *SHRP 2 Senior Program Officer, Renewal*

The Big Dig ceiling collapse in Boston in 2006 and the 2012 collapse event in Japan's Sasago Tunnel, where numerous people lost their lives, illustrate that timely detection and remediation of problems within tunnel linings are central to ensuring road user safety. Periodic monitoring of tunnel conditions and deterioration rates is the answer to determining the appropriate schedule of maintenance or rehabilitation activities to remedy structural problems that could lead to rapid deterioration and unexpected tunnel failures. The aggressive environmental conditions in which tunnels exist, as well as the need to keep tunnels open to traffic, make their inspection a challenge. Nondestructive testing (NDT) methods that are automated, quantitative, and rapid, and that provide complete coverage compared with conventional visual inspections, could solve this dilemma.

This report presents the findings of SHRP 2 Renewal Project R06G—High-Speed Non-destructive Testing Methods for Mapping Voids, Debonding, Delaminations, Moisture, and Other Defects Behind or Within Tunnel Linings. The study was divided into two phases to (1) establish testing criteria and prioritize the techniques to be developed and evaluated under the project on the basis of tunnel operators' requirements and (2) conduct the necessary technology development for those techniques recommended.

This project benefited from the expertise of numerous NDT and tunnel experts from the United States, Germany, and Finland, starting with the members of the research team. The list of experts directly involved with the research team also included the DOT and NDT experts who volunteered to be part of the advisory expert panel.

In addition to conducting technology development, the project was charged with performing proof-of-concept and field testing. The Finnish Transport Agency, the Colorado Department of Transportation, the Chesapeake Bay Bridge-Tunnel, and Harris County in Colorado graciously provided access to the tunnels and additional help during the field testing stages of the project.

Beyond this report, the deliverables for this project include two products that will be published separately:

1. A user's manual, which provides information on three NDT technologies for inspection of tunnels; and
2. A brief manual to the analysis software Tunnelcheck, which was developed under this project.

The Tunnelcheck software is available for download here: <http://www.trb.org/Main/Blurbs/168768.aspx>.

CONTENTS

1	Executive Summary
3	CHAPTER 1 Background
3	SHRP 2 Background
3	Problem Statement
3	Research Objectives
4	CHAPTER 2 Research Approach
4	Introduction
4	Research and Development Plan
5	Test Specimens
8	Tunnels Tested in the Study
11	NDT Devices and Techniques Used in the Study
18	CHAPTER 3 Findings and Applications
18	An Investigation for Detecting Delaminations, Voids, and Water Intrusion
20	Field Validation Testing of NDT Devices by Using Actual Tunnels
27	An Investigation for Detecting Loose Tiles and Moisture Underneath Tiles
28	Developing NDT for Measuring Concrete Permeability
30	CHAPTER 4 Conclusions and Recommended Research
33	Appendix A. Air-Coupled Ground-Penetrating Radar Testing Criteria
35	Appendix B. Ground-Coupled Ground-Penetrating Radar Testing Criteria
36	Appendix C. Handheld Thermal Camera Testing Criteria
38	Appendix D. Ultrasonic Tomography Testing Criteria
41	Appendix E. Ultrasonic Echo Testing Criteria
43	Appendix F. Ultrasonic Surface Waves and Impact Echo Testing Criteria
47	Appendix G. Field Testing with Acoustic Sounding
52	Appendix H. Vehicle-Mounted Thermal Camera Testing Criteria
53	Appendix I. Survey of the Chesapeake Bay Bridge-Tunnel
66	Appendix J. Tunnel Tests in Finland 2010–2011
91	Appendix K. Air-Coupled Ground-Penetrating Radar Field Tests
98	Appendix L. Evaluation of Texas A&M Transportation Institute Test Specimens with the Handheld Infrared Camera
109	Appendix M. Ultrasonic Tomography Field Tests in the United States
146	Appendix N. Ultrasonic Tomography Test Summaries

205	Appendix O. Evaluation of Tiled Tunnel Linings by Using Acoustic Sounding
209	Appendix P. Portable Seismic Property Analyzer Field Tests in the United States
238	Appendix Q. BAM Testing in U.S. Tunnels
290	Appendix R. Estimated Depths to Defects from Nondestructive Testing
293	Appendix S. Concrete Permeability Laboratory Study
312	Appendix T. Radar Specifications for Air-Coupled Ground-Penetrating Radar Antennae
315	Appendix U. Portable Seismic Property Analyzer Slab Tests
358	Appendix V. Analysis of SPACETEC Data
379	Appendix W. Findings and Applications of the BAM
387	Appendix X. Digital Photogrammetry

Executive Summary

This report documents the work conducted under Phase 2 of Strategic Highway Research Program (SHRP 2) Renewal Project R06G. Renewal Project R06G seeks dependable nondestructive testing (NDT) techniques that minimize disruption to traffic. The objectives of the proposed research are as follows:

- Identify NDT technologies for evaluating the condition (e.g., moisture, voids, and corrosion) of various types of tunnel linings (e.g., unreinforced concrete, reinforced concrete, shotcrete, and steel) and tunnel lining finishes such as tile. The techniques must be capable of analyzing conditions within the tunnel lining and the surrounding substrate.
- Evaluate the applicability, accuracy, precision, repeatability, ease of use, capacity to minimize disruption to vehicular traffic, and implementation and production costs of the identified technologies.
- Within the time limitations of this project, develop the hardware or software for those techniques that show potential for technological improvement.
- Prove the validity of the selected technologies/techniques to detect flaws within or verify conditions of the targeted tunnel components.
- Recommend test procedures and protocols to successfully implement those techniques.

Chapter 2 reports the advisory expert panel's findings on performance criteria. According to the results reported in Chapter 3, the following techniques meet the necessary criteria to be candidate solutions:

- Air-coupled ground-penetrating radar (GPR);
- Thermography (handheld thermal camera);
- SPACETEC scanner;
- Ground-coupled GPR;
- Ultrasonic tomography (UST);
- Ultrasonic echo; and
- Portable seismic property analyzer (PSPA) ultrasonic surface waves (USW) and impact echo (IE).

Each technique should be considered useful for implementation. Table ES.1 summarizes aspects of these technologies. All of these devices will require a combination of classroom and hands-on training for collecting and analyzing data. But each technology also has limitations that need to be assessed. Limitations are outlined in individual appendices. Chapter 4 presents conclusions and recommendations.

Table ES.1. Summary of Nondestructive Testing (NDT) Devices

Device	Accuracy	Detection Depth	Deterioration Mechanisms Detected	Tunnel Lining Type	Other Information
Air-coupled GPR	Locates defect within 1 ft of its actual location	Does not measure depth, but indicates areas of high moisture or low density (high air voids). Such areas may represent problems within or behind the tunnel lining.	Tile debonding, delaminations, air-filled voids, water-filled voids, moisture intrusion	Concrete, tile-lined concrete, and shotcrete	This is a scanning tool that can indicate where to conduct testing with in-depth devices.
Thermography (handheld thermal camera)	Locates defect within 1 ft of its actual location	Does not measure depth, but can indicate tile debonding, delaminations up to 1 in., and voids up to 3 in.	Tile debonding, delaminations, air-filled voids, water-filled voids, moisture intrusion	Concrete, tile-lined concrete, and shotcrete	This is a scanning tool that can indicate where to conduct testing with in-depth devices.
SPACETEC scanner	Locates defect within 1 ft of its actual location	Does not measure depth, but can indicate tile debonding, possibly delaminations up to 1 in., and possibly voids up to 3 in.	Tile debonding, delaminations, air-filled voids, water-filled voids, moisture intrusion	Concrete, tile-lined concrete, and shotcrete	This is a scanning tool that can indicate where to conduct testing with in-depth devices. Testing can only be conducted through a service contract.
Ground-coupled GPR	Can determine defect depth within 10% of the actual depth without reference cores—5% if cores are available	Can possibly detect defects at any depth within or immediately behind tunnel linings. However, specimen testing indicates it cannot locate 1-sq-ft voids in steel plates behind tunnel linings.	Delaminations, air-filled voids, water-filled voids, moisture intrusion	Concrete, tile-lined concrete, and shotcrete	Experienced personnel are needed to interpret defect locations and depths from the GPR scans. Specimen testing indicates it cannot locate 1-sq-ft voids in steel plates behind tunnel linings.
Ultrasonic tomography	In concrete, can detect voids within 0.5 in., shallow delaminations within 0.75 in. In shotcrete, can detect air-filled voids within 0.7 in., water-filled voids within 1.21 in., shallow delaminations within 1.88 in.	Can detect defects up to 8 in. deep according to specimen tests. Tunnel tests indicate it can detect possible defects up to 20 in. deep.	Delaminations and voids	Concrete, tile-lined concrete, and shotcrete	This device may not be effective for measuring defects that are 2 in. or less from the lining surface. It may not be accurate enough for measuring defect depths in shotcrete.
Ultrasonic echo	Comparable to the ultrasonic tomography system according to tunnel testing with both devices. Can measure tunnel lining thickness within 3% of the actual thickness	Comparable to the ultrasonic tomography system according to tunnel testing with both devices	Delaminations and voids	Concrete and shotcrete	This device may not be effective for measuring defects that are 2 in. or less from the lining surface. It may not be accurate enough for measuring defect depths in shotcrete. Tunnel tests indicate problems with using this device on tiles.
Portable seismic property analyzer (PSPA) ultrasonic surface waves and impact echo	Ultrasonic surface waves: about 15% of the actual depth for defects up to 6 in. deep Impact echo: 10% for deep delaminations greater than 6 in. deep	Ultrasonic surface waves: up to 6 in. deep Impact echo: up to 18 in. deep	Delaminations and voids	Concrete, tile-lined concrete, and shotcrete	Quantifying the depth of defects that are shallow or extensive may be difficult with this device. It may not get good results when testing on very rough concrete surfaces, oily surfaces, and severely curved surfaces.

CHAPTER 1

Background

SHRP 2 Background

To address the challenges of moving people and goods efficiently and safely on the nation's highways, Congress has created the second Strategic Highway Research Program (SHRP 2). Under current legislative provisions, the SHRP 2 program will receive approximately \$232 million over 9 years.

The U.S. highway system is aging and must be rebuilt while drivers are driving on it and living next to it. Research in the SHRP 2 Renewal focus area addresses the need to develop a consistent, systematic approach to completing highway projects quickly, with minimal disruption to the community, and producing facilities that are long lasting. Identifying new technologies for locating underground utilities; developing procedures to speed the evaluation of designs and the inspection of construction; and applying new methods and materials for preserving, rehabilitating, and reconstructing roadways and bridges are among the goals for this focus area. Alternative strategies for contracting, financing and managing projects and for mitigating institutional barriers also are part of the emphasis on rapid renewal. The renewal scope applies to all classes of roads.

Problem Statement

Periodic inspection of highway tunnels to assess changes in structural condition over time is critical to timely detection and remediation of problems to ensure road user safety. Some tunnel structural problems are considered widespread and potentially serious: tunnel leaks, concrete cracking, concrete spalling, concrete delamination, debonding, steel corrosion, and improper drainage. Monitoring tunnel conditions and deterioration rates is key to determining the appropriate schedule of maintenance and/or rehabilitation activities needed to remedy structural and safety problems. Failure to do so could lead to accelerated deterioration and sudden tunnel failures, which in turn could cause serious injuries and even fatalities.

Tunnel inspection is challenging. Tunnels typically service high-volume traffic and operate in aggressive environments.

Keeping tunnels open during inspection and minimizing tunnel closures and user delays must be carefully balanced with the need to conduct detailed inspections that ultimately ensure the safety of drivers. Consequently, nondestructive testing (NDT) methods that are automated, quantitative, and rapid and that provide more complete coverage than conventional visual inspections need to be identified and evaluated. At this point, no high-speed NDT method for assessing the condition of tunnel linings that would minimize the disruption of ongoing traffic has been found.

Research Objectives

The objectives of the proposed research are to

- Identify NDT technologies for evaluating the condition (e.g., moisture, voids, and corrosion) of various types of tunnel linings (e.g., unreinforced concrete, reinforced concrete, shotcrete, and steel) and tunnel lining finishes such as tile. The techniques must be capable of analyzing conditions within the tunnel lining and the surrounding substrate.
- Evaluate the applicability, accuracy, precision, repeatability, ease of use, capacity to minimize disruption to vehicular traffic, and implementation and production costs of the identified technologies.
- Within the time limitations of this project, develop the hardware or software for those techniques that show potential for technological improvement.
- Prove the validity of the selected technologies/techniques to detect flaws within or verify conditions of the targeted tunnel components.
- Recommend test procedures and protocols to successfully implement these techniques.

In the context of this project, *evaluation* is defined as both a rapid screening of the testing area and an in-depth, although slower, assessment of an area deemed problematic during screening. In both cases, and based on SHRP 2 priorities, Renewal Project R06G seeks dependable NDT techniques that minimize disruption to traffic.

CHAPTER 2

Research Approach

Introduction

According to data provided by the Federal Highway Administration, the vast majority of tunnel linings in the United States use cast-in-place (CIP) reinforced concrete, with a significant number using CIP unreinforced concrete, steel/iron liner plate, or shotcrete. In addition, a significant number of tunnels use CIP concrete and a steel/iron liner plate behind the concrete.

According to the advisory expert panel for this project, NDT methods are needed to assess the extent of several major problems with tunnel linings:

- Water leakage;
- Delaminations and spalling of concrete liners due to reinforcing steel corrosion;
- Voids behind and within tunnel linings;
- Concrete permeability;
- Tiles separating from the tunnel liner;
- The integrity of steel liners underneath concrete linings; and
- Problems with the integrity of ceiling systems and connections to the tunnel lining.

The advisory expert panel indicated that NDT should be able to detect any defect within or immediately behind the tunnel linings that have a minimum surface area of 1 sq ft, and any defect needs to be located within 1 ft of the actual location on the tunnel lining. The panel also indicated that NDT should be able to identify delaminated areas and voids up to 4 in. deep as measured from the lining surface with an accuracy within 0.25 in.

The advisory expert panel stated that NDT hardware developed for in-depth assessment of tunnel linings should be a simple screening tool—a handheld device—that inspectors can easily use to rapidly detect, locate, and report tunnel lining defects. The panel noted that NDT should facilitate the process of locating and calculating quantities for areas to be repaired.

Research and Development Plan

Based on the findings indicated above, the team produced a research and development plan as follows:

- An investigation for detecting delaminations, voids, and water intrusion with NDT. The investigation involved concrete, shotcrete, and steel test specimens constructed at the Texas A&M Transportation Institute (TTI) Riverside Annex. It employed the NDT techniques of ultrasonic tomography, IE, ultrasonic surface waves, air-coupled GPR, ground-coupled GPR, and thermography. And it used 11 concrete and 13 shotcrete specimens; each slab was 6 ft by 6 ft. To simulate delaminations, the team placed plastic sheets in the concrete specimens and thin cloth sheets in the shotcrete specimens. To simulate air voids, the team placed 1-in.-thick Styrofoam wrapped in plastic in the specimens. To simulate water-filled voids, the team placed water-filled plastic bags approximately 1-in. thick in the specimens. The first set of specimens included six intact concrete slabs with thicknesses of 12 in., 15 in., 18 in., and 24 in., and three defective 15-in.-thick slabs with 1-ft by 1-ft delaminated zones embedded in the center of the slabs. The three defective slabs contained defects at depths of 1 in., 2 in., and 3 in. from the top surface. Two additional concrete slabs in this set were 15 in. thick with embedded air voids and water voids at a depth of 8 in. The second set of slabs used shotcrete and included four intact slabs with thicknesses of 4 in., 6 in., 8 in., and 12 in., and five 12-in.-thick delaminated slabs. The 1-ft by 1-ft delaminated areas were embedded at the center of each slab at depths of 1 in., 2 in., 3 in., 4 in., and 8 in. from the top surface. Four additional shotcrete slabs contained air voids and water voids of different sizes at different depths. The team also used specimens containing clay lumps constructed under another TTI study, a concrete bridge deck constructed by the University of Texas at El Paso (UTEP) for another SHRP 2 study, a continuously reinforced concrete pavement

section on I-20 in Fort Worth, and an airport runway section at the George Bush Intercontinental Airport.

- Field validation testing of NDT devices using actual tunnels. A pilot project for the SPACETEC equipment was conducted for the Chesapeake Channel Tunnel in April 2011. In addition, initial tests with air-coupled GPR and thermal cameras were conducted using two tunnels in Helsinki, Finland. Finally, the team conducted tunnel testing in Colorado, Texas, and Virginia.
- An investigation for detecting loose tiles and moisture underneath tiles using NDT. The NDT techniques used in this investigation are air-coupled GPR, thermal cameras, and sounding. The team is using a tiled surface in an actual tunnel for this ongoing investigation.
- Development of NDT for measuring concrete permeability. This step involved a laboratory study to correlate NDT measurements with concrete specimens that have different permeabilities, and field verification using existing concrete tunnel linings. The NDT techniques used in this investigation were the dielectric probe, air-coupled GPR, resistivity, and ultrasonic surface waves. As described in this report, concrete permeability cannot be measured directly in the field using air-coupled GPR; however, the team did generate recommendations that relate potential for corrosion to GPR dielectric measurements. In addition, the report indicates

how permeability could be estimated if future NDT can measure certain properties.

Test Specimens

Concrete and Shotcrete Specimens with Simulated Delaminations and Voids

Eleven normal-weight concrete slabs and 13 shotcrete slabs were constructed to simulate various defects. The concrete slabs were used to mimic typical concrete tunnel linings with and without reinforcing steel. The shotcrete slabs were constructed to mimic applications in which shotcrete is sprayed on as a finished layer, as typically found in tunnel linings. A specially designed lattice girder, also typical in tunnel wall construction, was used as reinforcement in the shotcrete slabs (Figure 2.1, bottom right).

The simulated delaminations in the slabs were constructed from three types of material. Delaminations were imitated by using 0.05-mm (0.002-in.) plastic square sheets and 0.25-mm (0.01-in.) cloth squares (Figure 2.1, top right). Air-filled voids (Figure 2.1, top left) were constructed by inserting foam squares 13 mm (0.5 in.) thick in vacuum-sealed plastic bags. Water-filled voids (Figure 2.1, bottom left) were constructed in a similar manner by placing water-filled Ziploc bags within vacuum-sealed plastic bags and carefully padding the defect



Figure 2.1. Construction of slabs with simulated defects.

Table 2.1. Summary of Concrete and Shotcrete Slab Specimens with Simulated Defects

Specimen Name	Specimen Depth (mm)	Material	Reinforced Detail	Defect	True Depth of Defect (mm)
Alpha	305	Concrete	None	None	NA
Beta	457	Concrete	$d = 127 \text{ mm}^a$	Natural crack	NA
Gamma	305	Concrete	$d = 127 \text{ mm}^a$	None	NA
Delta	610	Concrete	None	None	NA
Epsilon	610	Concrete	$d = 127 \text{ mm}^a$	None	NA
Zeta	381	Concrete	$d = 127 \text{ mm}^a$	None	NA
Eta	381	Concrete	$d = 127 \text{ mm}^a$	0.05-mm thin plastic	51 from top
Theta	381	Concrete	$d = 127 \text{ mm}^a$	0.05-mm thin plastic	76 from top
Iota	381	Concrete	$d = 127 \text{ mm}^a$	0.05-mm thin plastic	25 from top
Kappa	381	Concrete	$d = 127 \text{ mm}^a$	Air-filled void (13-mm Styrofoam)	203 from top
Lambda	381	Concrete	$d = 127 \text{ mm}^a$	Water-filled void (Ziploc bag)	203 from top
A	102	Shotcrete	None	None	NA
B	152	Shotcrete	None	None	NA
C	203	Shotcrete	None	None	NA
D	305	Shotcrete	One lattice girder in center of slab, sitting on bottom form	Air-filled void (13-mm Styrofoam)	193 from top
E	305	Shotcrete	One lattice girder in center of slab, sitting on bottom form	Water-filled void (Ziploc bag)	191 from top
F	305	Shotcrete	One lattice girder in center of slab, sitting on bottom form	Air-filled void (13-mm Styrofoam)	76 from top
G	305	Shotcrete	One lattice girder in center of slab, sitting on bottom form	Water-filled void (Ziploc bag)	76 from top
H	305	Shotcrete	One lattice girder in center of slab, sitting on bottom form	0.25-mm thin cloth	203 from top
I	305	Shotcrete	One lattice girder in center of slab, sitting on bottom form	0.25-mm thin cloth	102 from top
J	305	Shotcrete	One lattice girder in center of slab, sitting on bottom form	0.25-mm thin cloth	76 from top
K	305	Shotcrete	One lattice girder in center of slab, sitting on bottom form	0.25-mm thin cloth	51 from top
L	305	Shotcrete	One lattice girder in center of slab, sitting on bottom form	0.25-mm thin cloth	25 from top
M	305	Shotcrete	One lattice girder in center of slab, sitting on bottom form	None	NA

Note: All slab specimens are nominally 1.83 m by 1.83 m. NA = not available.

^a Two mats of No. 5 rebar, at depth d from top and bottom, 203 mm on center.

with concrete/shotcrete during construction so as not to puncture the plastic. Table 2.1 provides a summary of the specimen details.

Concrete Specimens with Simulated Clay Lumps

In addition to the concrete and shotcrete slabs, six concrete slabs were tested that TTI had constructed in the 1990s as part of a

previous research project. These slabs contain manufactured clay lumps of different diameters. The clay lumps are a high-plasticity clay, classified as Bureson Clay CH (AASHTO A-7-6) with a plasticity index (PI) range of 35 to 45. The slabs and lumps are shown in Figure 2.2 and are summarized in Table 2.2 (Specimens A2 through F2). These six specimens consist of two sets of three slabs: one set with steel reinforcement and one set without. In each set, one slab was designated as the control with no clay lump contaminations. The remaining two had various



Figure 2.2. Clay lump slab construction.

levels of lumps of documented sizes corresponding to three regions of interest: (1) lumps below the reinforcement that represent typical lumps dense enough not to be quickly displaced toward the surface via vibration, (2) lumps that are caught in the reinforcing steel layer on their path toward the surface, and (3) lumps that are dispersed between the reinforcement and the top surface. The depth of the slabs is nominally 305 mm (12 in.), but all measurements are taken as approximate since neither ground truth data were retrieved nor any accurate pictures were taken to confidently support documented placement.

Concrete Bridge Deck with Simulated Defects

In addition to the above-mentioned slabs, a bridge deck constructed by UTEP was available for blind testing. The bridge deck was constructed with known artificial delaminations, cracks, and corroded reinforcement. Several parameters were considered in the construction of the artificial delaminations. These included stacked delaminations and delaminations of various thicknesses, ranging from 0.3 mm (0.01 in.) to 2.0 mm

(0.08 in.); sizes ranging from 305 mm by 305 mm to 610 mm by 1220 mm (12 in. by 12 in. to 24 in. by 48 in.); and depths above reinforcing steel at 64 mm (2.5 in.) below the surface and below two layers of reinforcing steel at 152 mm (6 in.), with some located above prestressed girders supporting the slab. The deck, as shown in Figures 2.3 and 2.4, measures 2.4 m by 6.1 m by 0.2 m (8 ft by 20 ft by 8.75 in.) and rests on three prestressed concrete girders. Simulated defects constructed in the deck consist of nine artificial delaminations, five cracks, and two corroded reinforcement mats, all of which are summarized in Table 2.3.

In constructing the deck, 27.6 MPa (4,000 psi) concrete was used, and two layers of No. 5 longitudinal and transverse steel were placed at 254 mm and 203 mm (10 in. and 8 in.) on center, respectively, at centroid depths of 83 mm and 184 mm (3.25 in. and 7.25 in.) from the surface. The 28-day strength and modulus exceeded 34.5 MPa (5,000 psi) and 27.6 MPa (4,000 psi), respectively. A 0.25-mm (0.01-in.) polyester fabric was used to mimic an ultrathin horizontal delamination. The vertical cracks were constructed from both thick and thin cardboard

Table 2.2. Summary of Concrete Specimens with Simulated Clay Lumps

Specimen Name	Specimen Depth (mm)	Material	Reinforced Detail (mm)	Defect	True Depth of Defect (mm)
A2	305	Concrete	$d = 152^a$	None	NA
B2	305	Concrete	$d = 152^a$	Large (152-mm \varnothing) clay lumps	152 from top
C2	305	Concrete	$d = 152^a$	Medium (102-mm \varnothing) clay lumps	76, 152, and 229 from top
D2	305	Concrete	$d = 152^a$	None	NA
E2	305	Concrete	$d = 152^a$	Large (152-mm \varnothing) clay lumps	152 from top
F2	305	Concrete	$d = 152^a$	Medium (102-mm \varnothing) clay lumps	76, 152, and 229 from top

Note: NA = not available.

^a Two mats of No. 5 rebar, at depth d from top and bottom, 203 mm on center.



Figure 2.3. Simulated bridge deck at UTEP in El Paso, Texas.

sheets. The No. 5 corroded steel mats were electrically merged and attached to the normal reinforcement. The corrosion depth was measured to be 1–2 mm (0.04–0.08 in.) before pouring the concrete.

Tunnels Tested in the Study

Chesapeake Channel Tunnel, Virginia

The Chesapeake Channel Tunnel (Figure 2.5) is one of two tunnels that make up the Chesapeake Bay Bridge-Tunnel system, joining southeastern Virginia to the Delmarva Peninsula. Hailed worldwide as a modern engineering wonder, the 37-km (23-mi) long system includes 3.2 km (2 mi) of causeway, four manmade islands, 8.9 km (5.5 mi) of approach roads, 19.3 km (12 mi) of low-level trestle, two 1.6-km (1-mi) steel tunnels, and two bridges. The Chesapeake Channel Tunnel (during construction and briefly afterward it was called the Baltimore

Channel Tunnel) was constructed using a cut-and-cover method. Precast steel tubes, fabricated and assembled in Orange, Texas, were floated to a shipyard in Norfolk, Virginia, where the reinforced concrete linings and roadway were constructed. The sections were floated to the site before being sunk into a trench. Each steel tube, 90 m (300 ft) in length and 11 m (37 ft) in diameter, was joined to the other, sealed, and connected to its adjoining section. As each steel section was welded together, patches between the 90-m (300-ft) sections had to be formed with concrete to make an overlapping seal.

Eisenhower Memorial Tunnel, Colorado

The Eisenhower Memorial Tunnel, located approximately 97 km (60 mi) west of Denver, Colorado, is one segment of a 2.7-km (1.7-mi) dual bore project started in 1968. Shown in Figure 2.6, the Eisenhower Memorial Tunnel, which carries I-70 west, is paired with the Edwin C. Johnson Memorial Tunnel, which carries eastbound I-70. Although the eastbound bore was not completed until almost 1980, construction on the Eisenhower bore was completed by 1973. Built using drill and blast methods through a mountain with a maximum overburden of 448 m (1,470 ft), the average tunnel dimensions are 14.6 m in height (48 ft) and 12.2 m (40 ft) in width. In 2011, the average daily traffic was 28,155 vehicles. All areas of interest evaluated within the tunnel were tested from inside the plenum (above the traffic, Figure 2.7).

Hanging Lake Tunnel, Colorado

Completed in 1992 with a maximum length of 1,219 m (4,000 ft) through the southern wall of Glenwood Canyon, Hanging Lake Tunnel (Figure 2.8) was the last link in the

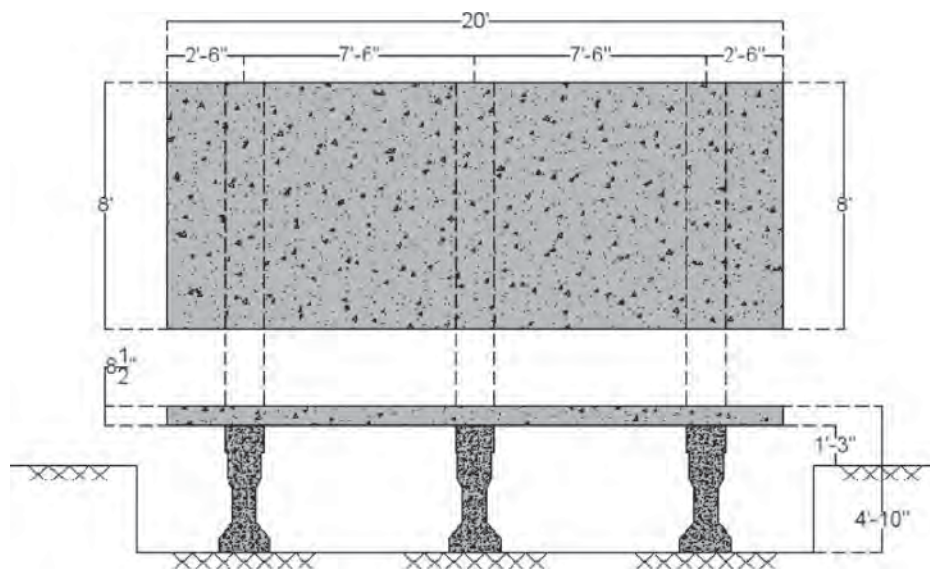


Figure 2.4. Layout of constructed bridge deck.

Table 2.3. Summary of Simulated Defects in Concrete Bridge Deck

Simulated Defect	Defect Material	Actual Dimension (mm)	Actual Depth (mm)
Delamination (DL 1)	Soft, high-strength 1-mm Styrofoam	305 by 305	64
Delamination (DL 2)	Soft, high-strength 1-mm Styrofoam	610 by 610	64
Delamination (DL 3)	Soft, high-strength 1-mm Styrofoam	610 by 610	64
Delamination (DL 4)	Soft, high-strength 2-mm Styrofoam	305 by 305	64
Delamination (DL 5)	Soft, high-strength 2-mm Styrofoam	610 by 610	64
Delamination (DL 6)	Soft, high-strength 2-mm Styrofoam	610 by 610	64
Delamination (DL 7)	Soft, high-strength 1-mm Styrofoam	610 by 610	152
Delamination (DL 8)	Soft, high-strength 1-mm Styrofoam	610 by 1,219	152
Delamination (DL 9)	Soft, 0.25-mm polyester fabric	305 by 610	64
Vertical crack (CK 1)	Soft, thin cardboard	305 long	64
Vertical crack (CK 2)	Soft, thin cardboard	305 long	64
Vertical crack (CK 3)	Soft, thick cardboard	305 long	76
Vertical crack (CK 4)	Soft, thick cardboard	305 long	152
Vertical crack (CK 5)	Natural crack (observed after construction)	330 long	64
Corroded reinforcement (CR 1)	1–2 mm deep corrosion, No. 5 bars	762 by 762	76
Corroded reinforcement (CR 2)	1–2 mm deep corrosion, No. 5 bars	762 by 762	165

**Figure 2.5. Chesapeake Channel Tunnel: entrance (left) and interior view (right).**



Figure 2.6. Eisenhower Memorial Tunnel, Colorado.

Interstate highway system. Both bores of the tunnel were built using multiple-face drill and blast methods. Between the westbound and eastbound bores, a four-story control center monitors traffic along I-70, fully equipped with emergency response vehicles and trained staff.

No Name Tunnel, Colorado

The No Name Tunnel was constructed in 1965 and is located approximately 7.5 miles west of the Hanging Lake Tunnel. The team collected air-coupled GPR data and infrared images only in the westbound bore, which is approximately 1,000 ft long. The upper portion of the tunnel has a concrete surface; the sides are tiled. Figure 2.9 shows the TTI

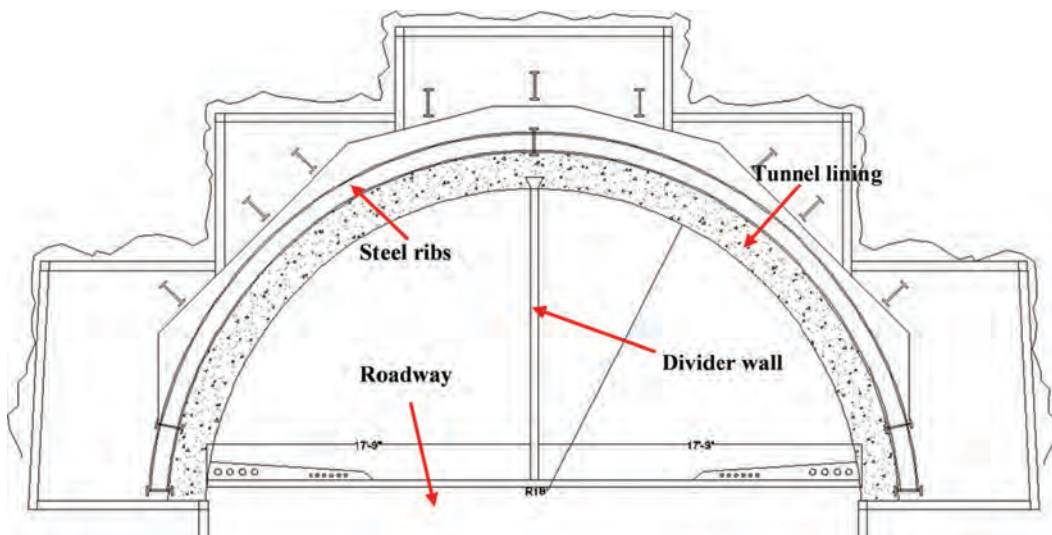


Figure 2.7. Eisenhower Memorial Tunnel plenum view.



Figure 2.8. Hanging Lake Tunnel: exterior (left) and interior plenum view (right).



Figure 2.9. TTI air-coupled GPR system collecting data in No Name Tunnel.

air-coupled GPR system collecting data in the tunnel. Plan sets were not available.

Washburn Tunnel, Texas

The Washburn Tunnel (Figure 2.10), the only underwater vehicle tunnel in operation in Texas, was completed in 1950 and carries a federal road beneath the Houston Ship Channel, joining two Houston suburbs. The tunnel was constructed using the immersed-tube method, with sections joined together in a prepared trench, 26 m (85 ft) below water. The entire inner wall is tiled with 110-mm by 110-mm (4.3-in. by 4.3-in.) ceramic tiles.

NDT Devices and Techniques Used in the Study

Air-Coupled Ground-Penetrating Radar

Ground-penetrating radar sends discrete electromagnetic pulses into a structure and then captures the reflections from

layer interfaces in the structure. Radar is an electromagnetic wave and therefore obeys the laws governing reflection and transmission of electromagnetic waves in layered media. At each interface within a structure, part of the incident energy is reflected, and part is transmitted. The amplitude of radar reflections and the time delay between reflections are used to calculate layer thicknesses and layer dielectrics. For purposes of this study, the surface layer dielectric is of most interest. This value is calculated as follows:

$$\epsilon_a = \left[\frac{1 + \left(\frac{A_1}{A_m} \right)}{1 - \left(\frac{A_1}{A_m} \right)} \right]^2$$

where

ϵ_a = dielectric of lining surface,

A_1 = amplitude of reflection from surface in volts, and

A_m = amplitude of reflection from a large metal plate in volts (this represents the 100% reflection case).

Because air-coupled systems (Figure 2.11) are not in contact with the structure, data collection can theoretically happen at full traffic speeds, although this is not practical for tunnel lining data collection. Air-coupled antenna systems are manufactured by GSSI, Penetradar, Pulse Radar, and Wavebounce—all from the United States. Butterfly dipole systems are manufactured by Radarteam Sweden AB.

The system used by TTI to collect tunnel lining data includes a Wavebounce 1-GHz central frequency GPR antenna with distance measuring indicator equipment. The system uses data collection software developed by TTI. Researchers used the Pavecheck and Colormap programs, also developed by TTI, to analyze the data. The researchers slightly modified Pavecheck and renamed it Tunnelcheck. (This software is available for free



Figure 2.10. Washburn Tunnel: entrance (left) and interior view (right).

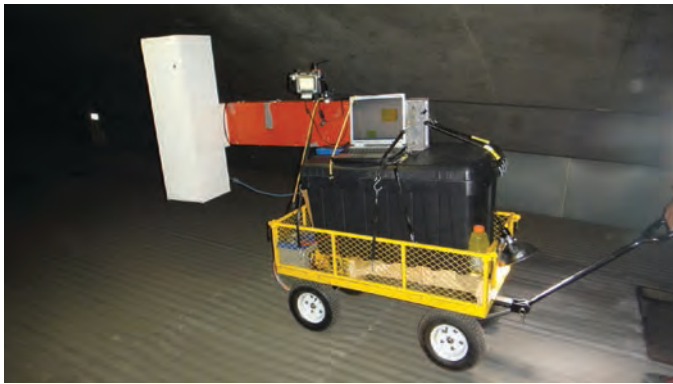


Figure 2.11. TTI air-coupled GPR system collecting tunnel roof lining data in Colorado.

download; the user's manual is provided in a separate publication.) The researchers also mounted a FLIR T300 camera on the GPR boom and the TTI data collection system collected images from this camera along with the GPR data.

The penetration depth of air-coupled GPR is usually around 24 in. for a 1-GHz system. Although air-coupled GPR can detect reinforcing steel, it cannot detect defects in concrete unless the defects contain significant air pockets or significant moisture. Nonetheless, the research team believes that the surface dielectric can be used to determine where to conduct testing with in-depth NDT devices and techniques.

Appendix A contains the air-coupled GPR testing criteria. Appendix K contains data analysis results from the air-coupled GPR tunnel and specimen testing conducted under this study.

Ground-Coupled Ground-Penetrating Radar

Ground-coupled GPR needs to be either in contact with or close to the lining surface when collecting data (Figure 2.12). The operating principles are the same as air-coupled GPR: ground-coupled GPR cannot detect defects in concrete unless the defects contain significant air pockets or significant moisture. However, ground-coupled GPR can detect defects that



Figure 2.12. Ground-coupled GPR equipment.

air-coupled GPR cannot. Ground-coupled GPR can also detect reinforcing steel. Researchers used the GSSI 1.5-GHz central frequency GPR antenna during the tunnel tests because shallow defects were found during those tests; researchers used a 900-MHz central frequency GPR antenna during the TTI specimen tests because the researchers were trying to determine if ground-coupled GPR can detect deep defects.

Appendix B contains the ground-coupled GPR testing criteria. Appendix Q contains data analysis results from the ground-coupled GPR testing conducted under this study.

Handheld Thermal Camera

Handheld thermal cameras (Figure 2.13) have improved significantly over the past decade, with consistently higher image resolutions and improved temperature accuracy occurring over time. The research team used the FLIR T300 thermal camera. The researchers analyzed the images for changes in tunnel lining temperature, which could indicate possible defects within or behind the lining. The team believes that the images from such cameras can be used to determine where to conduct testing with in-depth NDT devices and techniques.

Appendix C contains the handheld infrared camera testing criteria. Appendix L contains selected images from tunnels and TTI test specimens.

Ultrasonic Tomography

The ultrasonic tomography (UST) system used in this study is a device with an array of ultrasonic transducers that transmit and receive acoustic stress waves for the inspection of concrete structures. The system used here, the A1040 MIRA, is produced by Acoustic Control Systems (Figure 2.14).



Figure 2.13. FLIR T300 thermal camera used in the study.



Figure 2.14. A1040 MIRA system (left) and transmission/reception of acoustic waves and corresponding echo intensity (right).

The tomograph, shown in Figure 2.14 (left), uses a 4-by-12 grid of mechanically isolated and dampened transducers that can fit the profile of a rough concrete testing surface with a variance of approximately 10 mm (0.4 in.). Each row of four transducers transmits stress waves sequentially while the remaining rows act as receivers. In this manner, there is a wide coverage of shear wave pulses that reflect at internal interfaces where the material impedance changes.

With the help of a digitally focused algorithm, a three-dimensional (3-D) volume is presented with each point of possible reflection in half-space represented by a color scheme, scaled according to reflecting power. This 3-D image can also be dissected into each of the three planes representing its volume: the B-scan, C-scan, and D-scan (Figure 2.15). The B-scan is an image slice showing the depth of the specimen on the vertical (or z) axis versus the width of scan on the horizontal (or x) axis. This slice is a plane perpendicular to the scanning surface and parallel to the length of the device. The C-scan is an image slice showing the plan view of the tested area, with the vertical (or y) axis of the scan depicting the width parallel to the scanning direction and the horizontal

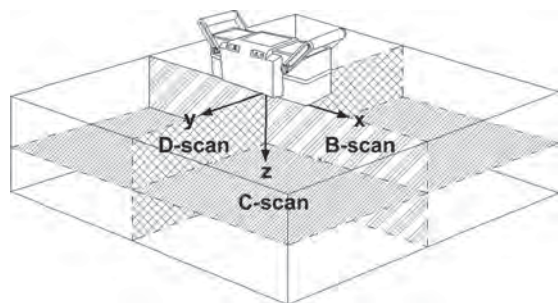


Figure 2.15. B-scan, C-scan, and D-scan relative to the tomograph.

(or x) axis of the scan representing the length perpendicular to the scanning direction. Note that the scanning direction is always defined as the y -axis as seen in Figure 2.15. The D-scan is like the B-scan in that it images a plane perpendicular to the testing surface, but it is oriented parallel to the scanning direction. On each of the scans, the various intensities reported by the returned waves are color-coded from light blue to deep red, representing low reflectivity (typically sound concrete) and high reflectivity (any type of impedance), respectively. With this intensity scaling, any discontinuities are readily apparent, with distinctly different wave speeds such as voids, delaminations, cracks, and other abnormalities. This UST system has had limited exposure to industrial applications but is quickly becoming recognized as a powerful NDT method.

Appendix D contains the ultrasonic tomography testing criteria. Appendices M and N contain the testing results from tunnel linings and test specimens, respectively.

Ultrasonic Echo

An ultrasonic transducer is used to generate and/or receive ultrasonic waves in/from a test medium. Ultrasonic echo technique involves sending and receiving ultrasonic pulses from the same side of the test object, by the same or two separate transducers. The ultrasonic pulse velocity is correlated to material strength or quality. The measurement of propagation time is used to localize cracks, voids, and delamination and/or to estimate the thickness of a structure. Structural boundaries and defects that are large enough (with respect to the ultrasonic wavelength) induce a high contrast in acoustic impedance and result in the reflection of ultrasonic waves. The reflected waves are detected in ultrasonic scans, and the two-way travel time is used to estimate the reflector location



Figure 2.16. Ultrasonic echo equipment A1220 Monolith by ACSYS.

(assuming or knowing the ultrasonic wave velocity in the test medium).

The handheld ultrasonic transducer used by the Federal Institute for Materials Research and Testing (BAM) in Germany for field testing together with the corresponding data acquisition/analyzer unit is shown in Figure 2.16. In tunnel testing applications, the ultrasonic echo technique can be used to estimate the thickness of the tunnel lining and to detect delamination and voids within the lining.

Appendix E contains the ultrasonic echo test criteria and Appendix Q contains data analysis results from the ultrasonic echo testing conducted under this study.

Ultrasonic Surface Waves and Impact Echo Methods with the Portable Seismic Property Analyzer

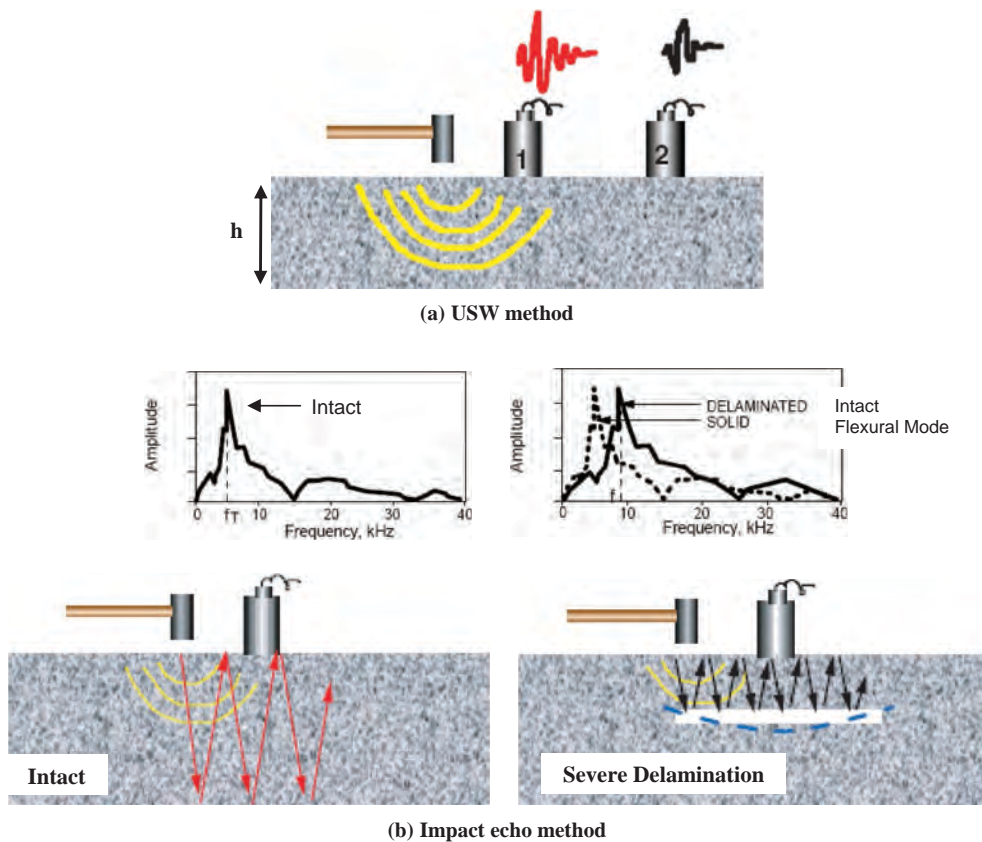
Ultrasonic Surface Wave Method

The ultrasonic surface wave (USW) method is used to estimate the average velocity of propagation of surface waves in a medium, based on the time at which different types of energy arrive at each sensor (Figure 2.17a). The velocity of propagation, V_R , is typically determined by dividing the distance between two receivers, ΔX , by the difference in the arrival time of a specific wave, Δt . Knowing the wave velocity, E , the modulus can be determined from shear modulus, G , through Poisson's ratio (ν) by using

$$E = 2(1 + \nu)G$$

Shear modulus can be determined from shear wave velocity, V_S , by using

$$G = \frac{\gamma}{g} V_S^2$$



Source: Gucunski and Maher 1998

Figure 2.17. Schematic illustration of test methods: (a) ultrasonic surface wave method and (b) IE method.

The modulus from surface wave velocity, V_R , first converted to shear wave velocity, can be determined by using

$$V_S = V_R(1.13 - 0.16v)$$

In the USW method, the variation in velocity with wavelength is measured to generate a dispersion curve. For a uniform or intact tunnel lining, the dispersion curve shows more or less a constant velocity within the wavelengths no greater than the thickness of the slab. When a delamination or void is present in a concrete slab or the concrete has deteriorated, the average surface wave velocity (or modulus) becomes less than the actual modulus because of interference from the defect. In this case, the velocity or modulus obtained may be called an apparent velocity or modulus.

Impact Echo Method

The IE method is one of the most commonly used NDT methods for detecting delamination in concrete. This method works by striking a plate-like object such as a tunnel lining with an impactor that generates stress waves at frequencies up to 20 kHz to 30 kHz and collecting signals with a receiver (see Figure 2.17b). By using a fast Fourier transform (FFT) algorithm, the recorded time domain signal is converted into a frequency domain function (amplitude spectrum), and the peak frequency is monitored. For an intact point on a slab, the thickness (h) is then determined from the compression wave velocity (V_p) and the return frequency (f):

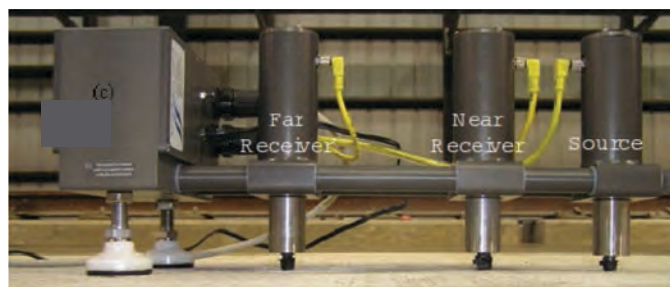
$$h = \alpha \frac{V_p}{2f}$$

where α is about 0.96 for concrete slabs.

For a deep and relatively small delaminated location in a tunnel lining, the return frequency may shift to a higher frequency corresponding to the depth of the delamination. As shown in Figure 2.17b, a shallow or a deep but extensive and severely delaminated area is usually manifested by a low peak frequency, indicating that little or no energy propagates toward the bottom of the deck, and a flexural mode dominates the frequency response. In this case, the equation is not applicable to measure the depth of delamination since it is influenced by several factors.

Description of the PSPA

USW and IE measurements can be performed with these two methods simultaneously with the PSPA shown in Figure 2.18. The traditional PSPA is a box containing a solenoid-type impact hammer and two high-frequency accelerometers (Figure 2.18a). All controls and data acquisition are in a computer connected to the box. The two receivers allow the calculation V_p using the USW method. The test at a single point is simple



(a) Traditional device



(b) New version

Figure 2.18. Portable seismic property analyzer (PSPA).

and takes less than 30 s. The impact duration (contact time) is about 60 μ s, and the data acquisition system has a sampling frequency of 390 kHz.

As shown in Figure 2.18b, the PSPA has been redesigned to make it more user friendly and compact for tunnel work. The new PSPA is self-contained and eliminates the need for an external computer to collect data. The waveforms collected in the field are stored in a removable flash memory. The new PSPA is also lighter compared with the traditional PSPA (8 lb versus 16 lb). Data collection with the new PSPA is a two-hand operation, which can accommodate the curvature within the tunnel more easily. Data acquisition with the new PSPA is on average two to three times faster than with the traditional one. The new PSPA is also equipped with three receivers to better optimize the data collection for the combined IE-USW methods. The power source for the device is six AAA batteries placed in a container that operators can carry on their belts. Typical signals collected with the PSPA are shown in Figure 2.19. These signals are used to develop USW dispersion curves and the IE amplitude spectra. The advantage of combining USW and IE methods in a single device is that once the test is performed, the variations in the modulus (an indication of the quality of concrete) and return resonance frequency (an indication of the full thickness or depth of delamination) of a slab can be assessed concurrently.

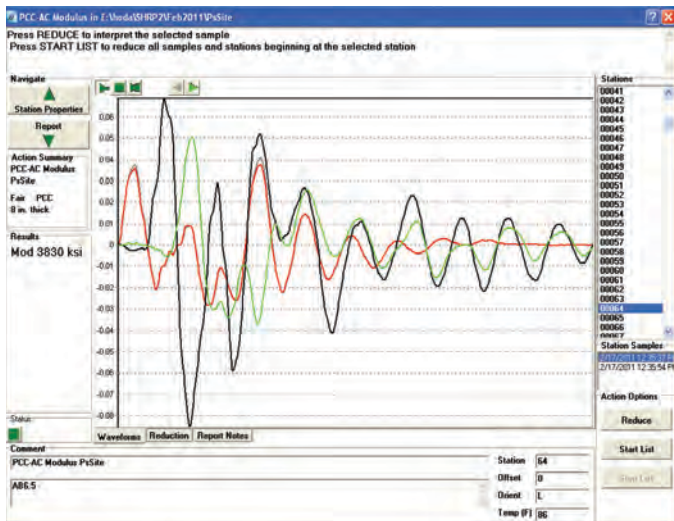


Figure 2.19. PSPA sample test results.

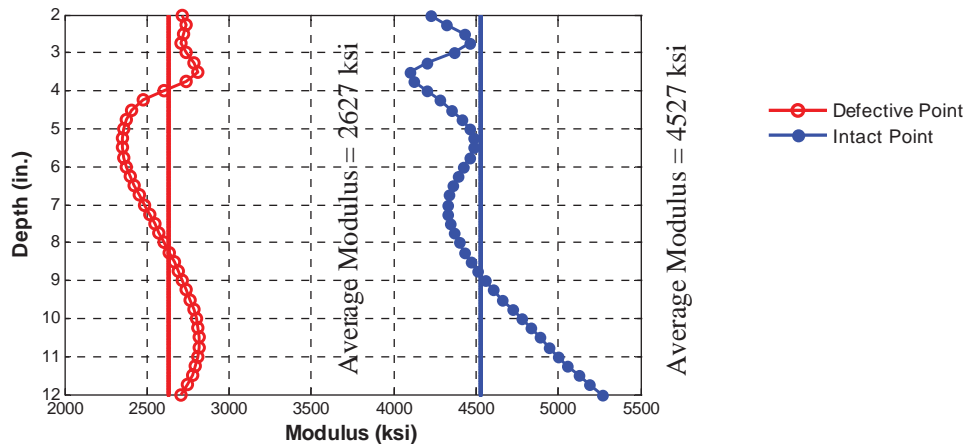


Figure 2.20. Typical dispersion curves for defective and intact points.

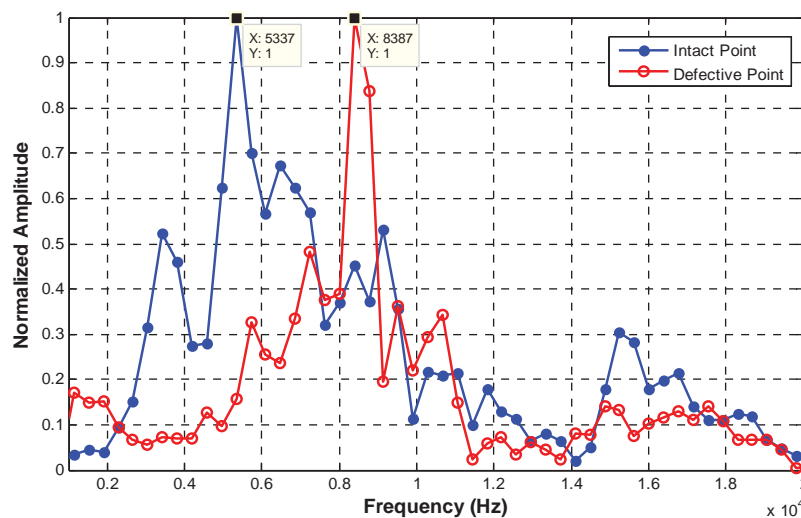


Figure 2.21. Typical amplitude spectra for intact and defective points. Appendix F contains the ultrasonic surface waves and impact echo testing criteria.

Figure 2.20 compares typical USW dispersion curves from an intact area and a defective area. The dispersion curve shifts to lower moduli in defective areas. The amplitude spectra for typical intact and defective points are shown in Figure 2.21. Based on an average compression wave velocity of about 14,000 ft/s measured for the concrete, the dominant frequency corresponding to the tunnel thickness (15 in.) is around 5.4 kHz. Compared with the intact point, higher peak frequencies mostly control the response at the defective points.

SPACETEC Scanner

The SPACETEC scanner (Figure 2.22) is a mature system developed specifically for the inspection of railway and roadway tunnels. Therefore, employing this technology for this project required no additional hardware and software development. The scanner system has been used to survey many miles



Figure 2.22. SPACETEC scanner in the Chesapeake Channel Tunnel.

of railway and roadway tunnels (mostly railway) in various countries but was never used in the United States before this project.

The SPACETEC TS3 scanner records three different measurements in a single pass:

- Survey of the cross-sectional tunnel profile;
- Full-surface visual recording of the tunnel lining; and
- Full-surface thermographic recording (thermal imaging) of the tunnel surface.

The scanner processes the measurements, which can then be viewed individually or together to detect and locate tunnel surface and near-surface anomalies. The high-resolution visual recording allows a thorough inspection of the tunnel surface and, combined with the profiling, the location of surface defects. The cold spots in the thermal images are usually indications of near-surface moisture. Superimposing the thermal images on the visual recordings allows such moist zones to be easily identified. Monitoring changes in the tunnel profile over time presents another potential application of this system.

Appendix I contains results of the SPACETEC testing in the Chesapeake Channel Tunnel.

Other NDT Devices and Techniques Used in the Study

The research team used resistivity and dielectric probe devices during this research. However, the devices were only useful in a laboratory environment and are not recommended for use in tunnel lining field tests. Appendix S contains the results of a laboratory study that attempted to correlate dielectric (or permittivity) measurements to concrete permeability. Researchers used resistivity and dielectric probe equipment during this laboratory study.

Researchers also attempted to develop an acoustic sounding technique for detecting delaminated tiles. Appendix O contains a description of the technique and the results obtained so far. This technique is still under development; thus, it is not ready for implementation.

The team did collect thermal data in Finnish and U.S. tunnels with the FLIR A325 vehicle-mounted thermal camera. This camera has the same thermal measurement specifications as the FLIR T300 handheld thermal camera. Roadscanners developed commercial software before this SHRP 2 study began that collects and helps analyze such data for the FLIR A325 camera. Although the results from the testing are promising, the team does not recommend implementation of the system at this time. Further software refinements are needed before this system can be implemented effectively. Appendix H contains the system's testing criteria and Appendix L contains images from the system.

As described later in this report, the research work in Finland also involved the use of laser scanning systems. Although the data analysis results and images from those systems did not apply directly to the goals of this project, the testing results in Finland indicated that laser scanning systems provide interesting and useful data relating to the shape (or profile) and the surface condition of tunnel linings. Appendix J offers more information about the results of testing with these systems.

Dr. Fulvio Tonon, one of the authors, conducted digital photogrammetry work in three tunnels during the course of this project. Although the data analysis results and images from this technique did not apply directly to the project, the results may be of interest to the reader. Appendix X contains a description of, and results from, this technique.

CHAPTER 3

Findings and Applications

An Investigation for Detecting Delaminations, Voids, and Water Intrusion

Introduction

As indicated in Chapter 2, this investigation used several NDT techniques—the ultrasonic linear array system, air-coupled GPR, ground-coupled GPR, thermal camera, and the portable seismic property analyzer—to detect defects in concrete, shotcrete, and steel test specimens.

Ultrasonic Tomography

The results of the ultrasonic tomography testing are contained in Appendices M and N. As indicated in Appendices D and M, the team concluded that the system is effective in detecting defects but with the following limitations:

- Speed of data acquisition is low (0.8 to 2.3 min/sq ft).
- The system provides no phase change information to infer defect type.
- No information deeper than initial air interfaces is discernible.
- The system has difficulty detecting reinforcement below two layers of reinforcement mesh.
- For a 50-kHz use, defects under 2 in. from the surface are not directly detected.
- For a 50-kHz use, reinforcement under No. 5 (0.625-in. diameter) is not typically detected.

Air-Coupled GPR

For this investigation, TTI personnel used the specimens described previously (see Tables 2.1 through 2.3). Details of the results are in Appendix K. The team used a 1-GHz central frequency device owned by TTI and determined that the equipment could detect only three simulated voids, all of

them located in the shotcrete sections. Those specimens are the following:

- Specimen D, air-filled void placed 7.625 in. from the surface;
- Specimen F, air-filled void placed 3 in. from the surface; and
- Specimen G, water-filled void placed 3 in. from the surface.

The equipment could not detect delaminations or voids in the other specimens. The delaminations in the specimens did not contain significant air pockets or moisture, so GPR would not be effective in any case.

The team estimated the depth to the defect using air-coupled GPR analysis software developed by TTI. For Specimen D, the estimated depth is 7.7 in. For Specimen F, the estimated depth is 2.6 in. For Specimen G, the estimated depth is 2.7 in.

The team also collected air-coupled GPR data on a 12-in.-thick plain concrete specimen placed on top of a steel plate with a 1-sq ft void in the center of the plate. The team determined that the equipment could not locate this defect. The team repeated the test with a 15-in.-thick specimen with two layers of reinforcement. Again, the team determined that the equipment could not locate the defect.

Although layer depth information, areas of moisture, and areas of low material density can possibly be measured with air-coupled GPR, the team recommends using surface dielectric measurements from this device to determine areas to test with other devices. Normal concrete has a dielectric value usually between 8 and 12. Values above this range indicate excessive moisture; values below this range indicate lower than normal material density (i.e., more air voids). Air has a dielectric value of 1; water has a dielectric value of 81.

Ground-Coupled GPR

The research team collected data by using a 900-MHz ground-coupled GPR on five reinforced concrete specimens. Three specimens had simulated 1-sq-ft delaminations, one specimen had a simulated 1-sq-ft air-filled void placed 8 in. from

the surface, and the final specimen had a 1-sq-ft water-filled void placed 8 in. from the surface. The team determined that the equipment could not locate the defects. The delaminations in the three specimens did not contain significant air pockets or moisture, so GPR would not be effective in any case. The voids in the other two specimens were located under a layer of reinforcement that consisted of No. 9 rebar placed at an 8 in. spacing in both directions. The ground-coupled GPR could not see through this layer of reinforcement. However, as documented in the literature, ground-coupled GPR is effective in detecting voids and significant delaminations in concrete, provided the correct device is used.

The team also collected ground-coupled GPR data on a 12-in.-thick plain concrete specimen placed on top of a steel plate with a 1-sq-ft void in the center of the plate. The team determined that the equipment could not locate this defect and repeated the test with a 15-in.-thick specimen with two layers of reinforcement. Again, the team determined that the equipment could not locate the defect. However, as described in Appendix Q, the ground-coupled GPR data showed defects in tunnel linings relatively near the tunnel lining surface.

Thermal Camera

In this investigation, the TTI team used a FLIR T300 infrared camera owned by TTI. The team collected infrared images on the specimens during the daytime and nighttime. Details of the results are in Appendix L.

The camera images indicated defects in three shotcrete specimens: (1) the 3-in.-deep air-filled void (Specimen F), (2) the 3-in.-deep water-filled void (Specimen G), and (3) the 1-in.-deep delamination (Specimen L). The image for Specimen F was the most distinct. The images did not indicate the defects in the other specimens. The team noted that surface texture influenced the surface temperature measured by the camera.

Portable Seismic Property Analyzer—Impact Echo and Ultrasonic Surface Waves

The IE and USW results on the TTI specimens are shown in Appendix U. As an example, a USW planar contour map and an IE spectral B-scan on selected intact concrete and shotcrete slabs are shown in Figure 3.1. In spite of the

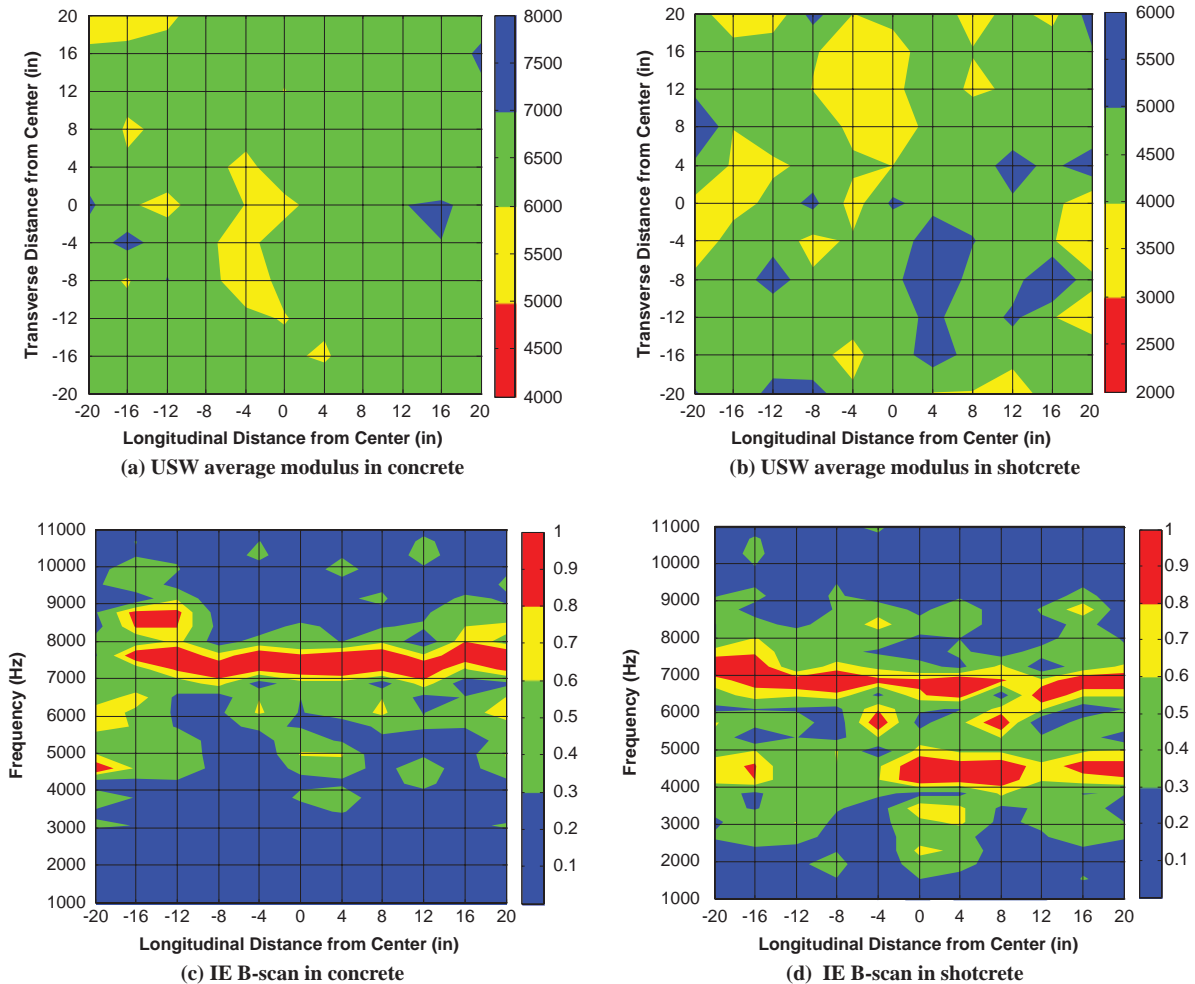


Figure 3.1. PSPA results on 12-in.-thick intact concrete and shotcrete slabs.

heterogeneity of the shotcrete slabs, the contour maps of the variations in average USW modulus and dominant IE frequency exhibited reasonable uniformity for intact slabs (both concrete and shotcrete). In most cases the variation in modulus with depth was quite small. The reported thicknesses from spectral B-scan agreed well with the actual slab thicknesses. However, the peak frequency along the centerline varies more significantly in the shotcrete slab than the concrete slab, mostly because of the heterogeneity of shotcrete. In spite of the effectiveness of the IE method in estimating the slab thickness, this method, as configured in the PSPA, cannot estimate the thickness of slabs that are thicker than 18 in. or thinner than 6 in.

The manifestations of shallow delaminated zones or voids were quite apparent on the time records collected by the device. USW and IE contour maps on selected defective concrete and shotcrete slabs are shown in Figure 3.2. Planar maps of both methods provided confirmed shallow (3-in.) defects. When defects were deeper, the USW average modulus became less sensitive to the presence of defects, while the thickness mode (as opposed to the flexural mode) of the IE method became more effective. This occurs because surface waves propagate along a cylindrical front and thus become less

sensitive to horizontal discontinuities with depth. Deep defects (deeper than 6 in.) were not readily detectable from the USW results. However, they could be readily identified through the IE results.

Because of the size of the specimens, reflections from the vertical boundaries sometimes affect the frequency content of the signal. The PSPA software contains appropriate filters to minimize the effect of these reflections as long as the slab is not very thick and the PSPA is located at an adequate distance from the boundary.

Field Validation Testing of NDT Devices by Using Actual Tunnels

Introduction

This section summarizes the results of the following:

- A pilot project for the SPACETEC equipment;
- Initial tests with air-coupled GPR and thermal cameras in Finland; and
- Tunnel testing in Texas, Virginia, and Colorado.

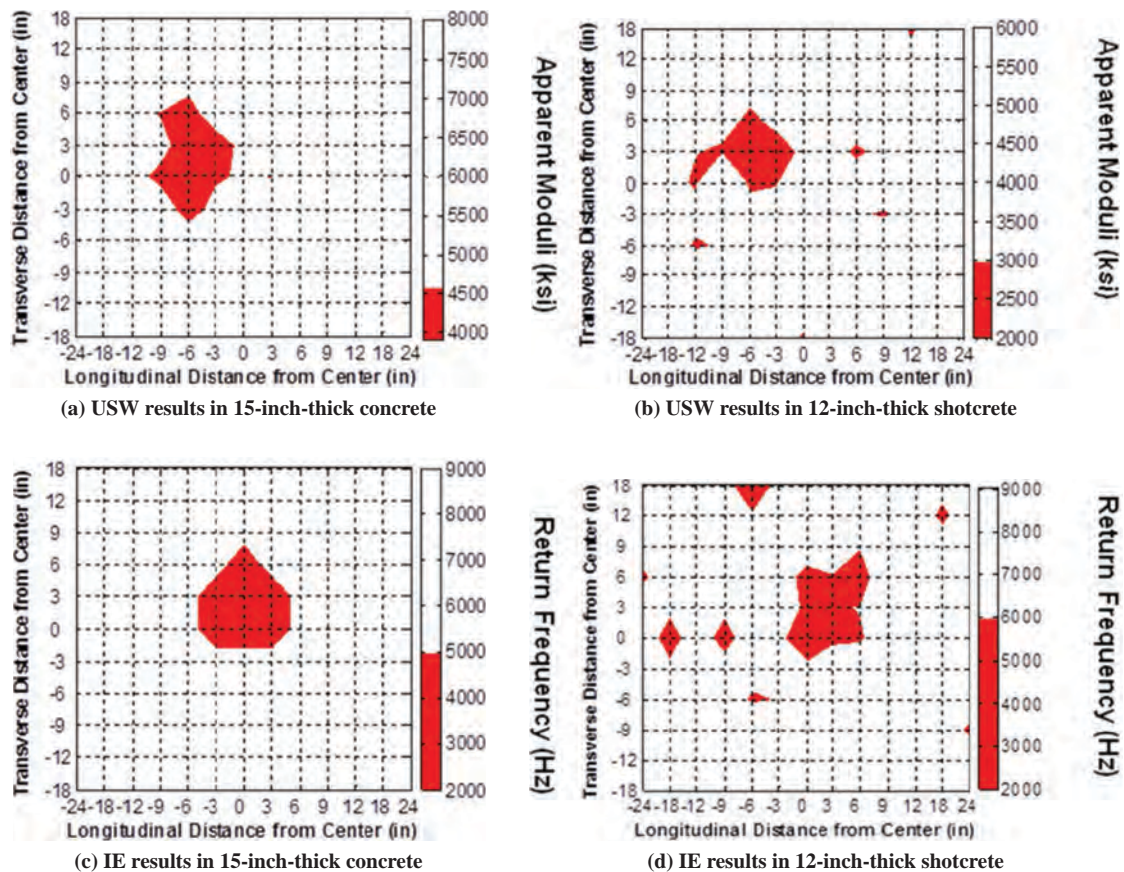


Figure 3.2. Contour maps of USW average modulus and IE dominant frequency in concrete and shotcrete slabs with embedded delamination 3 in. from top surface.

SPACETEC Pilot Project

The research team conducted the SPACETEC pilot project in the Chesapeake Channel Tunnel during the night of April 11–12, 2011. The TS3 scanner was installed on the roof at the rear of the inspection vehicle, providing an undisturbed 360° measurement. The highest resolution—10,000 pixels—was used for an appropriate imaging of fine-scale features.

A full traffic closure was not possible. Thus, the recording was performed twice: first in the north–south direction of the lane to Virginia Beach and second in the direction of the eastern shore of Virginia. Traffic could pass the inspection vehicle, as is visible in the recordings. Appendix I contains the results of this testing. SPACETEC personnel provided a copy of the TuView software that is used to analyze the data from this equipment and indicated areas of concern in the data files that the software displays. The research team was interested in the infrared images from this equipment, but this SHRP 2 study does not involve evaluating profile or visual images.

The team discussed the results of this testing with Chesapeake Bay Bridge-Tunnel (CBBT) personnel using the TuView software. CBBT personnel and the team compared the SPACETEC infrared images with CBBT construction plans for a tunnel tile replacement project. In addition, the SPACETEC equipment operator reviewed the infrared images immediately after collecting the data and noticed an area on the tunnel wall that appeared to have a defect. That image is shown in Figure 3.3.

The team evaluated this area using impact echo and determined that a problem did appear to be present in this area.

The team compared the SPACETEC thermal images with the hammer sounding results. Ninety-seven percent of areas covering more than 50 tiles could be detected, compared to 55% for areas covering less than 50 tiles. An additional

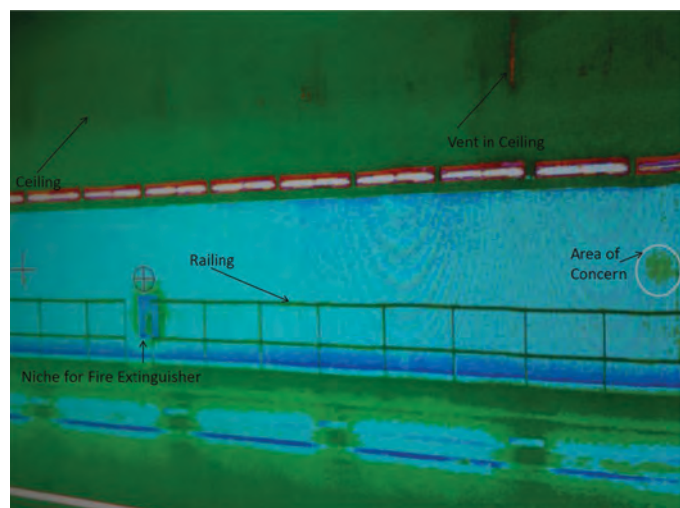


Figure 3.3. Infrared image from SPACETEC indicating area of concern.

analysis was performed to investigate why some of the debonded areas were not detected in the SPACETEC data. Small debonded areas covering less than 20 tiles were not reliably detectable in the thermal images obtained during this particular survey. When larger debonded areas were missed, the top two factors were found to be reflection of light from the surface of the tiles (at certain scanning angles) and interference with the temperature gradient in front of air vents. The great advantage of such scanning operations is the speed with which they can be performed: the SPACETEC survey took about 1 hour at 1.5 km/h (1 mph) compared with the tedious hammer sounding survey, which took one man-month. Appendix V contains the results of this analysis.

To summarize, the team's analysis suggests that a combination of thermal and visual imaging offers an alternative to the tedious practice of hammer sounding on individual tiles to determine tile debonding.

Initial Tests with Air-Coupled GPR, Thermal Cameras, and Laser Scanners in Finland

The tests in Finland concentrated on the technical feasibility of air-coupled GPR systems, thermal cameras, and laser scanners—as well as their integrated analysis—for monitoring tunnel lining conditions. The idea was to test whether these systems can provide reliable and repeatable data and to collect information on the potential sources of error in these techniques. Another goal for these tests was to provide basic information on the potential defects, such as moisture problems close to the surface of tunnel lining structures. The tests were carried out in two tunnels in the Helsinki area in Finland. One tunnel has a concrete lining, and the other tunnel lining is made of shotcrete.

The two tunnels were selected to determine whether air-coupled GPR can be used in different types of tunnel lining measurements. The research team used the same air-coupled GPR data collection settings as normally used in pavement thickness and quality control surveys. Preprocessing of the collected data was done using standard methods, including automatic air-coupled elevation and amplitude correction, background removal, and vertical time domain filtering. The standard GPR data analysis consisted of reflection amplitude and dielectric value calculations and their analysis.

The same two tunnels were also used to determine how well digital thermal cameras can detect thermal anomalies in tunnel linings, pointing out areas of moisture anomalies, voids, or cracks. The team tried different data collection and analysis techniques to find an optimal survey method.

The goal in the laser scanner tests was to determine whether the method could provide valuable information about the tunnel lining condition and shape. Although laser scanning is beyond the scope of this project, the results were of interest to the team.

The following findings are of particular interest for this study:

- GPR horn antenna data provided good quality structural information from the concrete tunnel but could not be used in the shotcrete tunnel where steel fibers were used in the shotcrete. The GPR data provided useful information on structures behind the tunnel linings.
- The optimum distance from the air-coupled GPR antenna to the tunnel lining surface is 0.5 m (19.7 in.).
- The thermal camera gave excellent results in the shotcrete tunnel. However, in the new concrete tunnel, hardly any anomalies could be detected. One reason for this may be a lack of problems close to the surface.
- The thermal camera results are repeatable, but tunnel wall surface temperature can change during the day, which could affect the results.
- Thermal anomalies can be seen in different ways when the surveys are conducted in summer, fall, and winter. The best time to survey is early summer. However, results, surprisingly, showed that moisture anomalies could always be seen as colder areas.
- The thermal camera is sensitive to the survey direction to the tunnel wall and roof, and focusing the camera on white tiles can be difficult. Also, the survey van can cause unwanted thermal reflections.
- Laser scanning systems provided useful data on the shape and condition of the tunnel linings. The results were excellent, especially in the shotcrete tunnel, but interesting and valuable information was also detected in the concrete tunnel.

Although layer depth information, areas of moisture, and areas of low material density can possibly be measured with air-coupled GPR, the researchers used surface dielectric measurements from this device to determine areas to test with in-depth devices. Normal concrete has a dielectric value usually between 8 and 12. Air has a dielectric value of 1; water has a dielectric value of 81. Values above this range indicate excessive moisture; values below this range indicate lower than normal material density (i.e., more air voids).

Appendix J reports the details of the tunnel testing in Finland.

Tunnel Testing in Texas, Virginia, and Colorado

The team conducted nondestructive testing in the following tunnels:

- Washburn Tunnel, located under the Ship Channel east of Houston, Texas: The TTI team collected air-coupled GPR,

ultrasonic tomography, and acoustic sounding data in this tunnel in September 2011.

- Chesapeake Channel Tunnel, located east of Norfolk, Virginia: The team collected NDT data in this tunnel in September and October 2011.
- Hanging Lake Tunnel, located on I-70 west of Denver, Colorado: The team collected NDT data in this tunnel in October 2011.
- No Name Tunnel, located on I-70 west of Denver, Colorado: The TTI team collected air-coupled GPR data in this tunnel in October 2011.

The following is a summary of the results from the tunnel testing.

Air-Coupled GPR

The team used the TTI 1-GHz air-coupled GPR system for collecting data in the tunnels listed above. In particular, the team collected data at 1-ft spacing in the plenums of the Chesapeake Channel, Eisenhower Memorial, and Hanging Lake tunnels; and along the tiled roadway sections in the Chesapeake Channel, Hanging Lake, and No Name tunnels. As mentioned earlier, the research team was most interested in the surface dielectric measurements from this device. The team mounted the equipment on a cart for testing in the plenums and on a vehicle with a crane for testing in the roadway.

Figure 3.4 shows results from testing on the Chesapeake Channel Tunnel roof. As shown in the figure, the surface dielectric varies, with significant peaks occurring in several areas. The research team was not able to test all areas because of time constraints. However, one high dielectric area selected for testing did contain a shallow delamination, though no visual distress was present. Researchers could only collect air-coupled GPR data along the top of the tunnel roof. The presence of cables and conduits on the sides of the tunnel roof made it impossible to collect GPR data in those areas.

Figure 3.5 shows results from testing on the Hanging Lake Tunnel roof. In this case, none of the surface dielectric values exceeded 11. However, peaks in the values occurred at several locations; these areas should be inspected more closely. This tunnel roof contained many cracks with moisture; however, the moisture usually was outside the GPR testing area. Again, the presence of cables and conduits on the sides of the tunnel roof made it impossible to collect GPR data in those areas.

To summarize, the team recommends that the surface dielectric measurements from air-coupled GPR be used for scanning purposes to determine where more in-depth inspection and testing may be useful. The team noted surface dielectric changes in both concrete and tile-lined tunnels. In general, the researchers recommend inspecting areas where the surface dielectric is greater than 11 or where significant

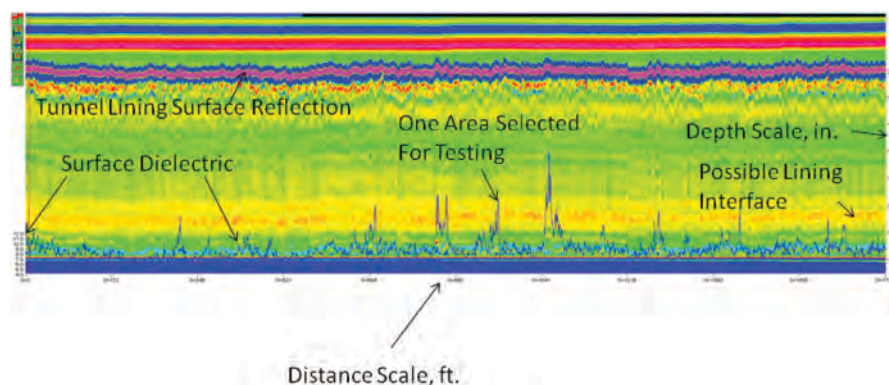


Figure 3.4. Air-coupled GPR data for Chesapeake Channel Tunnel roof.

peaks or troughs in the dielectric value are observed. The team noted that the data analysis could indicate lining interfaces and lining thickness estimates; however, actual defects within or behind the tunnel lining could not be readily determined from the analysis. In addition, more work is needed to keep the antenna at a relatively constant distance from the lining to calculate reasonable surface dielectric values. Ideally, this distance should not vary more than 4 in. from the recommended distance (usually 19.7 in.). Appendix K contains the data analysis of air-coupled GPR data collected in tunnels.

Thermal Cameras

The team collected thermal images using both handheld and vehicle-mounted thermal cameras in all of the tunnels tested in this project. Both cameras were able to detect significant thermal changes that indicated possible problems at those locations, on both concrete surfaces and tile-lined surfaces. Figure 3.6 shows a thermal camera image from the top of the Eisenhower Memorial Tunnel. Cracks and stalactites containing moisture are indicated in light blue. The team recommends that the handheld thermal camera be used for scanning purposes where more in-depth inspection and testing may be desired.

In particular, areas with images that contain significant thermal differences from the surrounding lining should be investigated. Appendix L contains more images from these devices.

Ultrasonic Tomography

Field evaluations of four public tunnels were conducted using the UST technique to evaluate natural structural defects within actual tunnel linings. The tunnels tested were the Eisenhower Memorial Tunnel, Hanging Lake Tunnel, Chesapeake Channel Tunnel, and Washburn Tunnel. Because the UST technique does not have a testing methodology that is field ready, the system was first evaluated on the basis of its ability to detect simulated defects in specimens as well as other available sites (e.g., pavements, airport runways, bridge decks) where ground truth validation was available. After that testing, the system was taken to the field to evaluate natural structural defects within actual tunnel linings. The conclusions of the tunnel testing are as follows:

- The UST system is exceptional at locating horizontal delaminations ranging in thickness from 0.05 mm to 2.0 mm (0.002 in. to 0.079 in.) and is able to differentiate between

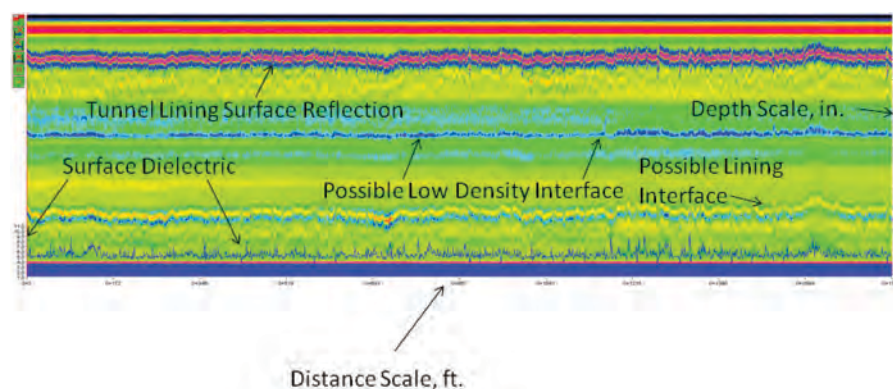


Figure 3.5. Air-coupled GPR data for Hanging Lake Tunnel roof.

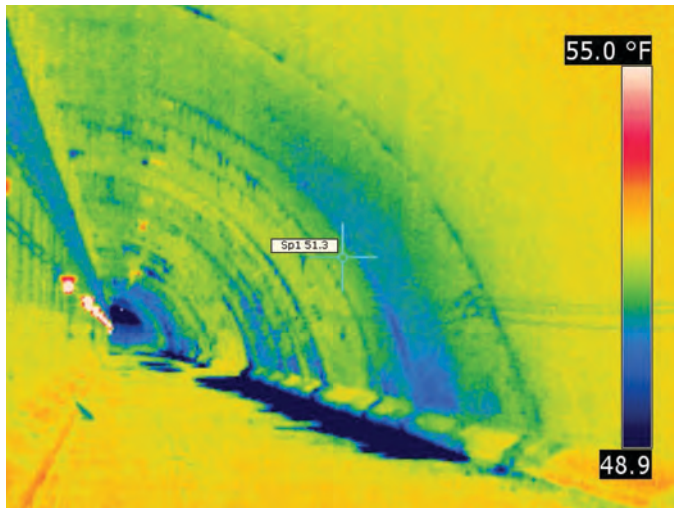


Figure 3.6. FLIR T300 infrared image of the top of Eisenhower Memorial Tunnel.

fully debonded and partially bonded areas within a single map based on the color distribution. It is not, however, able to measure the thickness of the delaminations directly.

- Cracks were only clearly characterized when they formed nonperpendicular to the testing surface; however, the presence of perpendicular cracks could be assumed by the omission of surface detail. Note that no crack depths were confirmed by ground truth validation, and that should be a focus of further research.
- Backwall surfaces up to a depth of 965 mm (38 in.) were successfully and accurately determined. Assuming the plan details were correct (no ground truth validation was available), the UST system predicted this depth within an accuracy of 5 mm (0.3 in.).
- Both air- and water-filled voids ranging from 76 mm to 203 mm (3 in. to 8 in.) in depth could be detected; but

differentiation between the two was difficult because shear waves are not supported by air or water, and almost all of the acoustic energy is reflected by these types of voids. Further study could be done to analyze the difference between phase changes involving these two types of voids.

- Reinforcement layout and depth was also successfully determined, as long as the device was polarized in the correct direction. The only exception was some shotcrete applications. When potentially porous materials such as the shotcrete specimens were evaluated, the presence of very small air voids made internal inspection difficult.
- With the exception of some medium-size clay lumps (with a diameter of approximately 102 mm, or 4 in.) surrounding reinforcement, clay lump testing was highly successful.
- The research team used two A1040 MIRA systems to compare the system's abilities to reproduce the same wave speed. For a test involving 16 specimens, a strong positive correlation existed (with a coefficient of determination of 0.952), with a standard error of approximately 33 m/s (108 ft/s).
- When detecting the depth of delaminations using the same device with the same testing procedures and input parameters (e.g., wave speed, frequency, gain selection), measurements typically varied by 1 mm to 3 mm (0.04 in. to 0.12 in.). That variation is more likely to be explained by user error or user interpretation than by device error. The same is true for water-filled and air-filled voids.
- The minimum area the MIRA system could test is tied to the size of the device: 370 mm by 170 mm (14.6 in. by 6.7 in.).

Figure 3.7 shows an example of a scan from the Hanging Lake Tunnel.

The researchers believe that the MIRA system is especially effective for mapping deeper defects and is recommended for situations where such deep defects are suspected. Results of

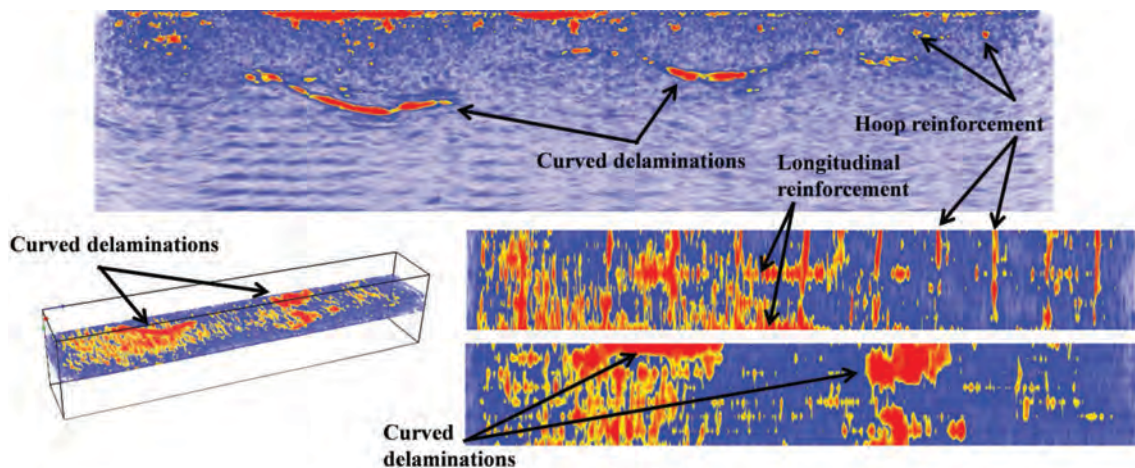


Figure 3.7. Ultrasonic tomography scan from Hanging Lake Tunnel.

tunnel testing using ultrasonic tomography are contained in Appendices M and N.

Portable Seismic Property Analyzer

The UTEP team used the PSPA, which can perform IE and USW tests simultaneously.

USW Method (PSPA). After testing each tunnel point by point with the PSPA, the cross sections of variation of modulus with wavelength (or depth) were obtained for each tested section. As shown in Figure 3.8a, intact areas exhibit more or less constant modulus with depth. The average modulus was around 4,500 ksi. Figure 3.9a shows an example of USW results in a defective area of one of the tested tunnels. In this figure, the problematic areas manifested themselves as areas with lower average moduli. The depth of delamination could be approximated through the B-scan in Figure 3.9a. In Figure 3.10a, the crack was recognized through high average moduli in the USW B-scan when the crack was between the source and the first receiver (because of the travel path of the wave). When the crack was between the two receivers, the reported USW modulus was lower than normal. The results for these points agreed well with the actual condition that was documented during visual inspection. The rest of the USW results for the tested tunnels are shown in Appendix P.

IE Method (PSPA). Similar to the USW method, the IE results, in the form of a spectral B-scan, were visualized in contour maps. As shown in Figures 3.8b and 3.9b, a thickness frequency (around 3 kHz) governed the response of intact test points. Other points in Figure 3.9b exhibit either a lower or higher dominant frequency. The low-frequency flexural mode results from a shallow or a deep but an extensive delamination.

Thus, its peak frequency does not correspond to any thickness measurement, and the depth of defect can be estimated from a USW B-scan (Figure 3.9a). Alternatively, the high frequency response is attributable to the onset of delamination. In that case, the depth of delamination can be estimated and confirmed with the USW B-scan. When a crack is present, data analysis is more complicated. As shown in Figure 3.10b, multiple frequencies were present in the response when a crack was between the source and receiver in an IE B-scan.

The remaining IE results are shown in Appendix P. In most cases, the calculated depth and location of delamination agreed well with the USW results. Some exceptions occurred. Where the IE and USW analyses were not consistent, the differences were attributed to the edge effect near a crack and placement of the PSPA sensor unit relative to the crack.

Ultrasonic Echo, Ground-Coupled GPR, and Impact Echo Testing

Field testing using three nondestructive testing techniques was carried out between October 3, 2011, and October 12, 2011, in three tunnels in the United States: two in Colorado (Eisenhower Memorial Tunnel and Hanging Lake Tunnel) and one in Virginia (Chesapeake Channel Tunnel). In each tunnel, selected areas were tested using three nondestructive testing (NDT) techniques: GPR, ultrasonic echo, and IE. The allocated testing time in each tunnel was limited. The number and location of the test areas were selected based on either previous analysis or the existence of visual distress. The on-site working conditions were also taken into account.

The different measurement techniques used by the Federal Institute for Materials Research and Testing (BAM) for this

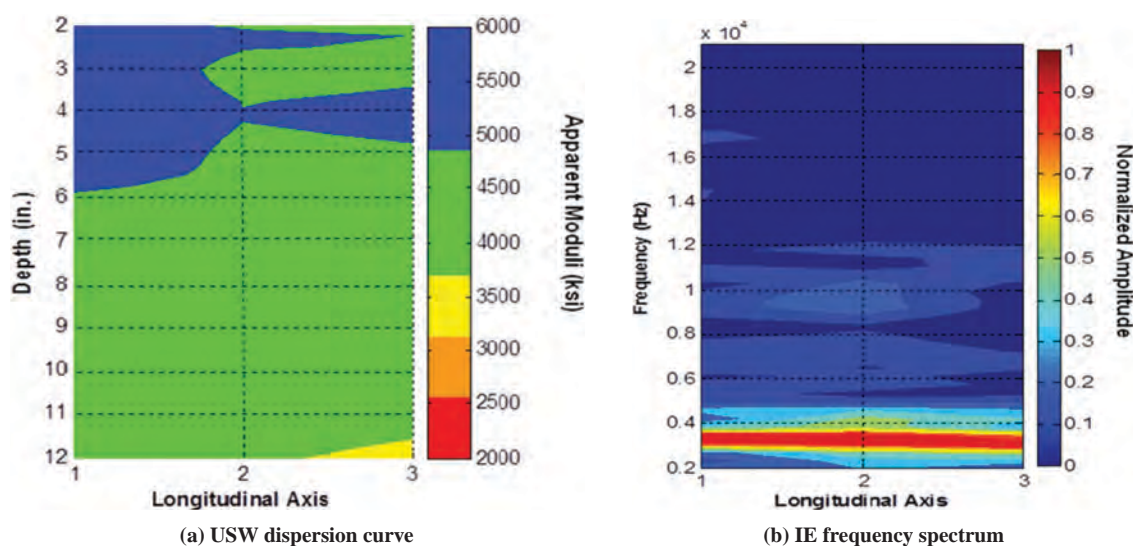


Figure 3.8. PSPA results on an intact area in the Chesapeake Channel Tunnel.

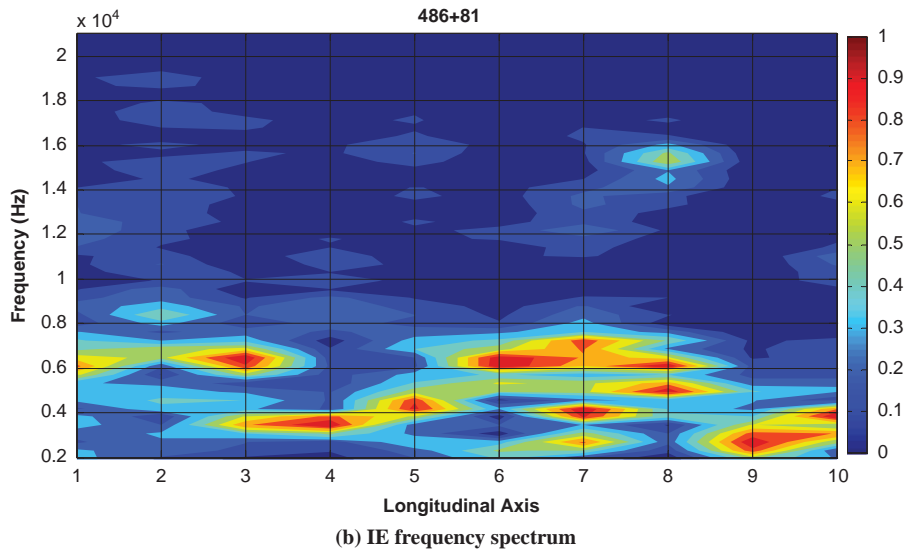
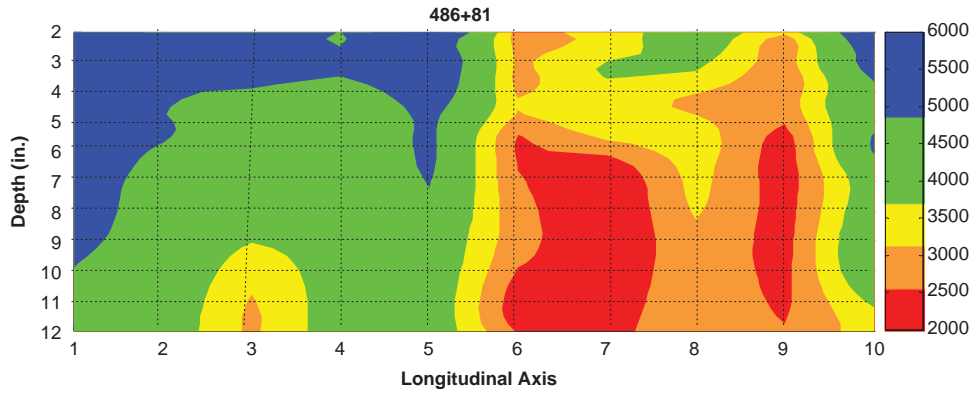


Figure 3.9. PSPA results on a defective area in the Chesapeake Channel Tunnel.

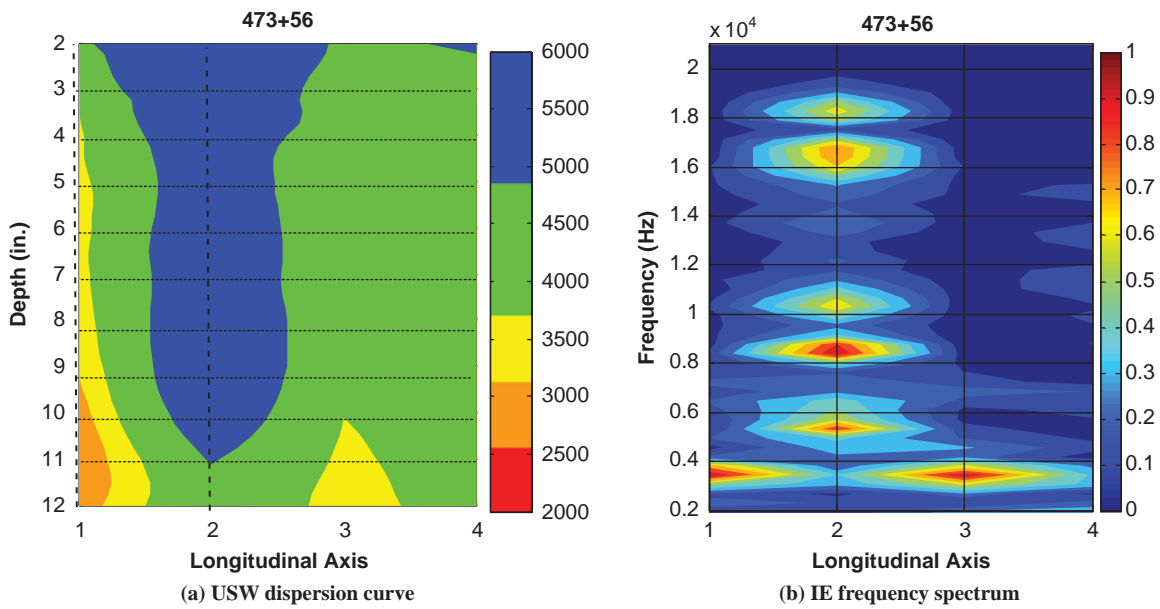


Figure 3.10. PSPA results on a cracked area in the Chesapeake Channel Tunnel.



Figure 3.11. BAM scanner with ultrasonic echo device.

project were mounted on an automated scanning device that BAM developed. Figure 3.11 shows the BAM scanner with the ultrasonic echo device. It can be carried in a relatively small, lightweight package. Its size allows the scanner to be transported in cars and carried through small openings to reach difficult-to-access areas such as the vents above tunnels. The equipment commonly used for NDT of structures—including GPR, ultrasonic echo, and IE devices—can be easily attached to the scanner for testing and detached after completing the measurements. The scanning and NDT data acquisition are controlled by a single notebook. This simplifies the control and reduces the amount of equipment and weight of the measurement system. Appendix W summarized the findings and applications of the Federal Institute for Materials Research and Testing (BAM).

For the Eisenhower Memorial tunnel plenum, the ground-coupled GPR proved to be the best tool for identifying and locating the reinforcement. However, the ultrasonic echo device was better at locating an anomaly of unknown origin than the ground-coupled GPR. A combination of the two result sets would provide the most detailed and reliable results. Both methods detected the reinforcement and an unknown anomaly. GPR was more effective in detecting the reinforcement, and ultrasonic echo was more effective in detecting the unknown anomaly. The backwall could not be seen with any of the employed techniques here. And the impact echo technique could not register either reinforcement or the anomaly detected by the other two techniques.

For the Hanging Lake tunnel plenum, the ground-coupled GPR was the only method able to identify the reinforcement mesh and the reinforcing elements. The fine measurement grid and 3-D data collection allowed detection of reinforcing elements overlapping each other in some views. The ultrasonic echo technique was able to detect a deeper anomaly and establish that the anomaly under the test area was located at different depths. No reliable information could be extracted from the impact echo data. Again, combining the results of the ground-coupled GPR and ultrasonic echo is desirable. Note that none of these NDT techniques were able to reliably identify the extent of the Hanging Lake tunnel lining.

For the Chesapeake Channel tunnel plenum, the ground-coupled GPR proved to be the most reliable NDT method for detecting and identifying reinforcement bars but could not detect a 15-in.-deep localized anomaly. The ultrasonic echo technique was not as clear in detecting the steel bars but did indicate the presence of an anomaly. Both ultrasonic echo and impact echo could detect the thickness of the tunnel lining. A clearer picture of the geometry and condition of the tunnel emerged using all three techniques.

For the section of the Chesapeake Channel Tunnel roadway that was lined with tiles, the ground-coupled GPR signals were not disturbed by the presence of the tiles and could image the reinforcement mesh behind the lining. The impact echo signals carried useful information about the bonding condition at the tile-concrete interface and occasionally about the lining itself. The ultrasonic echo device, however, provided no useful information about the condition of the lining. The ultrasonic echo transducer was too large (4 in. by 3 in.) compared with the size of the tiles (2 in. by 2 in.). The grid location and spacing had to be adjusted so that meaningful data could be obtained. However, testing was interrupted by an unforeseen weather condition, and no further measurements could be obtained with the ultrasonic echo device.

To summarize, the automated scanning device that BAM used was effective in collecting NDT data in the tunnels with the three techniques. The team recommends that data from both the ground-coupled GPR and the ultrasonic echo devices be collected when conducting in-depth evaluations directly on concrete surfaces. However, for tiled surfaces, data from the ground-coupled GPR and impact echo should be collected together—the ultrasonic echo device may not work on tiled surfaces because of the tile dimensions. These devices should be effective in collecting data on shotcrete linings as well. Appendix Q contains more information on the tunnel testing with these devices.

Other Information

Appendix R contains depth measurement estimates of apparent defects as indicated by the in-depth evaluation devices used in this portion of the research. The appendix also contains estimated depth measurements to reinforcing steel or the backwall of the tunnel lining if they were detected.

An Investigation for Detecting Loose Tiles and Moisture Underneath Tiles

As mentioned earlier, air-coupled GPR data on tiled linings in the Chesapeake Channel and Hanging Lake tunnels indicated high surface dielectric areas, greater than 11 (see Appendix K). Researchers tested some of those areas with ultrasonic tomography, impact echo, and hammer sounding. The researchers

found debonded tiles and delaminations in those areas. Thus, the team concluded that high surface dielectric measurements on tiled linings can indicate areas of debonded tiles or delaminations, as well as areas of high moisture behind tiles.

Also, as described earlier, the SPACETEC thermal imaging data can be useful for locating loose tiles. Thermal cameras can also indicate areas of loose tiles.

As indicated in Appendix G, the TTI team is developing an acoustic sounding test to detect loose tiles. However, this method is still under development and is not recommended for implementation at this time.

To summarize, the team suggests that air-coupled GPR, thermal cameras, and the SPACETEC system's thermal images can be effective scanning devices to locate loose tiles and moisture underneath tiles.

Developing NDT for Measuring Concrete Permeability

Appendix S contains the results of a laboratory study that attempted to correlate dielectric (or permittivity) measurements to concrete permeability. As indicated in the appendix, the team determined that the air-coupled GPR cannot measure permeability directly in the field. However, Appendix S does contain information that can be used for future NDT development. In addition, using the results in Appendix L, the TTI team developed Tables 3.1 and 3.2 for the real portion of the permittivity measurement for cement paste. These can be related to the dielectric measurements made with the air-coupled GPR. Table 3.1 is for a 1-GHz frequency. Table 3.2 is for a 2-GHz frequency.

The values in these tables can be used as a general guide. Although the measurements were made on cement paste, the team believes that the moisture content in the paste would have the greatest effect on dielectric readings with the GPR. Essentially, the tables suggest that air-coupled GPR dielectric

Table 3.1. Permittivity Values (Real Portion) for a 1-GHz Frequency

Water-to-Cement Ratio	Relative Humidity (%)				
	100	85	75	63	43
0.4	17	16	15.5	14.5	12.5
0.5	15	12.7	12	11.8	9.9
0.6	20	15	10.9	10	8.5

Table 3.2. Permittivity Values (Real Portion) for a 2-GHz Frequency

Water-to-Cement Ratio	Relative Humidity (%)				
	100	85	75	63	43
0.4	15.5	15	14.5	13.5	12
0.5	14.5	13.5	11.5	11	9
0.6	18	14.9	10.2	9.8	7.5

readings above 11 may indicate a potential problem, and readings above 15 may indicate excessive moisture in the concrete.

The team also attempted to measure resistivity on the concrete and shotcrete specimens. However, the measured values varied widely. The team concluded that the concrete resistivity device was suitable only for controlled laboratory testing purposes.

Based on the observed distress in the Chesapeake Channel Tunnel, the team developed the relationship in Figure 3.12 that relates surface dielectric values measured in the tunnel to surface distress that is assumed to be caused by excessive moisture, leading to reinforcing steel corrosion and further distress. Admittedly, significant scatter is apparent in the data shown in Figure 3.12. However, Figure 3.12 could be useful in interpreting surface dielectric data for concrete.

The surface rating is defined in Table 3.3.

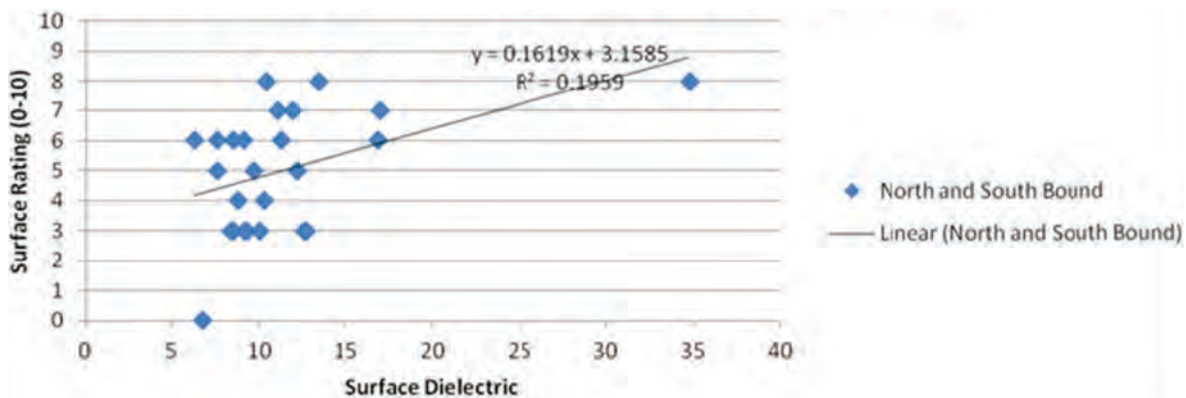


Figure 3.12. Surface dielectric versus surface rating (using Chesapeake Channel Tunnel results).

Table 3.3. Surface Rating Based on Distress Observed

Distress Observed	Surface Rating
Cracks, no staining	0
Cracks, light staining	1
Cracks, light staining, and light calcium carbonate deposits	2
Cracks, moderate calcium carbonate deposits and staining	3
Cracks, moderate calcium carbonate deposits and staining; potential spalling (<2 in.)	4
Cracks, moderate calcium carbonate deposits and staining; potential spalling (2–6 in.)	5
Cracks, moderate calcium carbonate deposits and staining; potential spalling (6–10 in.)	6
Cracks, moderate to heavy calcium carbonate deposits and staining; spalling (<2 in.)	7
Cracks, moderate to heavy calcium carbonate deposits and staining; spalling (2–6 in.)	8
Cracks, moderate to heavy calcium carbonate deposits and staining; spalling (6–10 in.)	9
Cracks, moderate to heavy calcium carbonate deposits and staining; spalling (>10 in.)	10

CHAPTER 4

Conclusions and Recommended Research

Chapter 2 reports the advisory expert panel's findings on performance criteria, which indicated that NDT should be able to detect any defect within or immediately behind tunnel linings that have a minimum surface area of 1 sq ft, and any defect needs to be located within 1 ft of the actual location on the tunnel lining. The panel also noted that NDT should identify delaminated areas and voids up to 4 in. deep as measured from the lining surface with an accuracy within 0.25 in.

According to the results reported in Chapter 3, the following techniques can detect defects with minimum surface areas of 1 sq ft up to 4 in. deep (and in some cases even deeper):

- Air-coupled ground-penetrating radar;
- Thermography (handheld thermal camera);
- SPACETEC scanner;
- Ground-coupled ground-penetrating radar;
- Ultrasonic tomography;
- Ultrasonic echo; and
- Portable seismic property analyzer ultrasonic surface waves and impact echo.

All these techniques appear to provide useful information for evaluating tunnel linings and should be considered for implementation; but the limitations of each technology need to be considered and are outlined in individual appendices. None of the devices are able to detect a 1-sq-ft void in a steel lining behind concrete. In addition, the 0.25-in. accuracy criterion for defects up to 4 in. deep can be problematic for the in-depth devices. A 0.5-in. accuracy appears to be more realistic. Table 4.1 summarizes the accuracy, detection depth, deterioration mechanisms detected, tunnel lining types, and other information for these technologies.

The following sequence of testing is suggested for evaluating tunnel linings based on the research conducted under this study:

- Collect thermal images and air-coupled GPR data on the tunnel lining. Air-coupled GPR data should be collected

every foot along the tunnel lining. Thermal images can be collected every foot as well; however, the equipment covered in this report can collect data at a spacing determined by the camera operator or tunnel inspector. Ideally, the data should be collected on the same day; however, they can be collected separately. The thermal images should be collected when the air temperature is rising or falling; areas of possible defects may show up better in the thermal images. The data from any of these devices can be obtained at a walking pace (around 1 mph, or 1.61 km/h). Air-coupled GPR data can be obtained at much higher speeds, but the geometry and features in tunnels may hinder operation of the equipment at speeds much greater than 1 mph.

- Analyze the data from the scanning devices listed in Table 4.1. Select areas for in-depth testing based on the GPR surface dielectric results, thermal images, and observed surface distresses that are of concern to tunnel inspectors.
- Conduct in-depth testing with the ground-coupled GPR and either the ultrasonic tomography, ultrasonic echo, or PSPA device. The choice of equipment can be based on the cost and the type of defect to be detected (tile debonding, delamination, or voids). The ultrasonic tomography and ultrasonic echo devices may be more appropriate for measuring and mapping defects greater than 2 in. from the tunnel lining surface. The ultrasonic tomography device is more expensive than the other two devices; however, it has the capability to provide more information in the field about such defects. The PSPA may be more appropriate for determining the limits of shallow defects.
- Evaluate the data collected from these devices.

The SPACETEC scanner is available only through a service provider. Service providers can also perform NDT by using the actual or similar devices or techniques described in this report. However, all but the SPACETEC equipment can be operated by tunnel owner personnel. The equipment and essential data processing software are commercially available. To implement

Table 4.1. Summary of Nondestructive Testing (NDT) Devices

Device	Accuracy	Detection Depth	Deterioration Mechanisms Detected	Tunnel Lining Types	Other Information
Air-coupled GPR	Locates defect within 1 foot of its actual location	Does not measure depth, but indicates areas of high moisture or low density (high air voids). Such areas may represent problems within or behind the tunnel lining.	Tile debonding, delaminations, air-filled voids, water-filled voids, moisture intrusion	Concrete, tile-lined concrete, and shotcrete	This is a scanning tool that can indicate where to conduct testing with in-depth devices.
Thermography (handheld thermal camera)	Locates defect within 1 ft of its actual location	Does not measure depth, but can indicate tile debonding, delaminations up to 1 in. and voids up to 3 in.	Tile debonding, delaminations, air-filled voids, water-filled voids, moisture intrusion	Concrete, tile-lined concrete, and shotcrete	This is a scanning tool that can indicate where to conduct testing with in-depth devices.
SPACETEC scanner	Locates defect within 1 ft of its actual location	Does not measure depth, but can indicate tile debonding, possibly delaminations up to 1 in. and possibly voids up to 3 in.	Tile debonding, delaminations, air-filled voids, water-filled voids, moisture intrusion	Concrete, tile-lined concrete, and shotcrete	This is a scanning tool that can indicate where to conduct testing with in-depth devices. Testing can only be conducted through a service contract.
Ground-coupled GPR	Can determine defect depth within 10% of the actual depth without reference cores—5% if cores are available	Can possibly detect defects at any depth within or immediately behind tunnel linings. However, specimen testing indicates it cannot locate 1-sq-ft voids in steel plates behind tunnel linings.	Delaminations, air-filled voids, water-filled voids, moisture intrusion	Concrete, tile-lined concrete, and shotcrete	Experienced personnel are needed to interpret defect locations and depths from the GPR scans. Specimen testing indicates it cannot locate 1-sq-ft voids in steel plates behind tunnel linings.
Ultrasonic tomography	In concrete, can detect voids within 0.5 in., shallow delaminations within 0.75 in. In shotcrete, can detect air-filled voids within 0.7 in., water-filled voids within 1.21 in., shallow delaminations within 1.88 in.	Can detect defects up to 8 in. deep according to specimen tests. Tunnel tests indicate it can detect possible defects up to 20 in. deep.	Delaminations and voids	Concrete, tile-lined concrete, and shotcrete	This device may not be effective for measuring defects that are 2 in. or less from the lining surface. It may not be accurate enough for measuring defect depths in shotcrete.
Ultrasonic echo	Comparable to the ultrasonic tomography system according to tunnel testing with both devices. Can measure tunnel lining thickness within 3% of the actual thickness	Comparable to the ultrasonic tomography system according to tunnel testing with both devices	Delaminations and voids	Concrete and shotcrete	This device may not be effective for measuring defects that are 2 in. or less from the lining surface. It may not be accurate enough for measuring defect depths in shotcrete. Tunnel tests indicate problems with using this device on tiles.
Portable seismic property analyzer (PSPA) ultrasonic surface waves and impact echo	Ultrasonic surface waves: about 15% of the actual depth for defects up to 6 in. deep Impact echo: 10% for deep delaminations greater than 6 in. deep	Ultrasonic surface waves: up to 6 in. deep Impact echo: up to 18-in. deep	Delaminations and voids	Concrete, tile-lined concrete, and shotcrete	Quantifying the depth of defects that are shallow or extensive may be difficult with this device. It may not get good results when testing on very rough concrete surfaces, oily surfaces, and severely curved surfaces.

each of these methods, however, the personnel in charge need to be sufficiently trained in data collection, reduction, and interpretation.

Of the devices tested under this study, the handheld thermal camera appears to be the easiest to use and can be effectively used by tunnel owner personnel. Data collection and analysis of the images can be conducted in the field. Conversely, the air-coupled and ground-coupled GPR equipment require considerably more training and experience for data collection and operation. These devices involve the use of integrated systems containing a data collection module, computer, antenna, and distance-measuring indicator. Data analysis of the air-coupled GPR data will generally be simpler than the ground-coupled GPR data. The researchers recommend that the surface dielectric data from the air-coupled GPR be used for determining where to conduct more in-depth tests; these data are easily generated by GPR analysis programs. The training and experience needed to effectively collect and analyze data by using the ultrasonic tomography, ultrasonic echo, and PSPA equipment are expected to be less than that for the GPR equipment.

For rapid scanning of tunnel linings, data from the SPACETEC scanner, the air-coupled GPR, and thermal camera images can indicate areas where further inspection by tunnel personnel may be warranted. All devices were able to detect problems within 1 ft of the actual location on the tunnel lining. However, the SPACETEC scanner is not for sale. Data collection and analysis are provided by SPACETEC through a service contract. The 1-GHz air-coupled GPR antennae, such as the one used in this study, are no longer for sale in the United States because of Federal Communications Commission regulations, though several service providers still own these antennae. Antennae available for sale in the United States should be effective for collecting data if they meet the radar specifications

contained in Appendix T. According to this study, thermal cameras have the ability to detect 1-sq-ft voids 3 in. deep when significant concrete thermal gradients exist, and the literature suggests they can detect even deeper voids. However, the research team believes that vehicle-mounted thermal camera systems are not quite ready for implementation; further software development is needed.

Ground-coupled GPR, ultrasonic tomography, ultrasonic echo, and the PSPA are all able to detect defects up to a depth of 4 in. However, for ground-coupled GPR, the defects can be detected only if they contain significant air pockets or significant moisture. Ultrasonic tomography can detect deeper defects but cannot directly detect defects if they are less than 2 in. from the surface.

All of these devices will require a combination of classroom and hands-on training for collecting and analyzing data. Although beyond the scope of this study, laser scanning and digital photogrammetry techniques can also provide information about tunnel lining profile and surface distress that may be useful to tunnel inspectors.

Finally, service providers can collect and analyze data for clients using the devices listed above. However, clients should consider the limitations for each device before selecting a service provider.

References

- Gucunski, N., and A. Maher. 1998. Bridge Deck Condition Monitoring by Impact Echo Method. *Proc., International Conference MATEST '98—Life Extension*, Brijuni, Croatia, pp. 39–45.
- Shokouhi, P., N. Gucunski, A. Maher, and S. Zaghoul, 2005. “Wavelet-Based Multiresolution Analysis of Pavement Profiles as a Diagnostic Tool,” *Transportation Research Record: Journal of the Transportation Research Board*, No. 1940, Transportation Research Board of the National Academies, Washington, D.C.

APPENDIX A

Air-Coupled Ground-Penetrating Radar Testing Criteria

Accuracy

The surface dielectric values calculated from the air-coupled ground-penetrating radar (GPR) data are used to determine where to test with in-depth nondestructive testing (NDT) devices. The surface dielectric is calculated as follows:

$$\epsilon_a = \left[\frac{1 + \left(\frac{A_1}{A_m} \right)}{1 - \left(\frac{A_1}{A_m} \right)} \right]^2$$

where

ϵ_a = dielectric of the lining surface,

A_1 = amplitude of reflection from the surface in volts, and

A_m = amplitude of reflection from a large metal plate in volts (this represents the 100% reflection case).

The accuracy of these amplitudes is critical in calculating the surface dielectric.

The Texas A&M Transportation Institute (TTI) developed an air-coupled GPR hardware specification that contains the requirements for such systems (see Appendix T for a discussion of this specification). The specification addresses the accuracy of the system. The distance measuring indicator (DMI) used with the air-coupled GPR system in this study is accurate within 1 ft.

Air-coupled GPR data should not be relied on for accurate measurements of the depths of defects in tunnel linings. The researchers believe that the surface dielectric value can indicate where such defects might be located. Testing conducted during this study indicated that the air-coupled GPR data could indicate 1-sq-ft air voids (1-in. thick) up to 3 in. from the lining surface for reinforced linings, and up to 7.625 in. from the lining surface for plain unreinforced linings. The calculated depths of the defects from the TTI air-coupled GPR data analysis software was 2.6 in. and 7.7 in., respectively. Therefore, the system was

accurate within 0.4 in. for the shallow void and approximately 0.1 in. for the deeper void.

The testing indicated that the air-coupled GPR data could indicate a 1-sq-ft water-filled void at 3 in. from the lining surface. The calculated depth of this defect from the TTI air-coupled GPR data analysis software was 2.7 in. Therefore, the system was accurate with 0.3 in. for this water-filled void.

Precision

The air-coupled GPR hardware specification also addresses the precision of the system to ensure that the surface dielectric measurement is precise. The measurement results of the DMI used with the TTI air-coupled GPR system are repeatable and reproducible within 1 ft.

Calibration Procedures

The air-coupled GPR hardware specification is also used for calibrating the system. The DMI should be calibrated every 3 months. This is done by traveling over a known distance (minimum 500 ft) and comparing the DMI measurement to the known distance measurement.

Testing Procedures

Air-coupled GPR antenna manufacturers have their own GPR-system-specific user manual that should be followed when collecting data. Before collecting data on a tunnel lining, personnel should collect at least 50 air-coupled GPR waveform traces over a minimum 16-sq-ft metal plate (4 ft long by 4 ft wide) at the operating height of the antenna (between 12 in. and 18 in.). These data will be used to calculate the surface dielectric. During data collection on the tunnel lining, the air-coupled GPR data should be collected at 1-ft intervals or less.

Cost

The price for a complete air-coupled GPR system with survey van and mounting is usually between \$180,000 and \$200,000.

Limitations

The air-coupled GPR surface dielectric is recommended for use in determining where to test tunnel linings with in-depth nondestructive testing devices.

At present, only one company manufactures Federal Communications Commission (FCC)–compliant air-coupled GPR systems for sale in the United States. However, several air-coupled GPR service providers in the United States provide data collection and interpretation services. They may use the FCC-compliant systems or grandfathered systems similar to the 1-GHz system used by TTI in this study.

Air-coupled GPR data should not be relied on to accurately measure the depths of defects in tunnel linings. Air-coupled GPR can detect 1-sq-ft defects up to a depth of 3 in. for reinforced linings and 7 in. for plain unreinforced linings if they contain a significant amount of air (such as a 1-in.-deep air gap) or a significant amount of moisture (such as a 1-in.-deep water-filled void).

External electromagnetic radiation such as cell phone antennae, radio antennae, and television station antennae

can cause signal degradation. Salts (either from deicing operations or from seawater) in the concrete may result in signal penetration problems. Also, steel fibers in shotcrete prevent air-coupled GPR signal penetration. Concrete containing steel slag can prevent air-coupled GPR signal penetration as well.

Data Management

Commercially available air-coupled GPR systems (such as the FCC-compliant system described at the webpage <http://www.geophysical.com/antennas.htm>) come with data collection and management software. Some air-coupled GPR service providers also have their own data management software.

Data Analysis and Interpretation

Data analysis software is provided by the manufacturer of such systems. Air-coupled GPR service providers may also provide data analysis and interpretation services.

The surface dielectric data are easy to calculate using available software. However, data interpretation for locating subsurface defects can only be done by experienced, trained users and usually demands engineering judgment.

APPENDIX B

Ground-Coupled Ground-Penetrating Radar Testing Criteria

Accuracy

Ground-coupled ground-penetrating radar (GPR) is used to detect the depth of defects in tunnel linings. The accuracy of determining depths to defects depends on the experience of the interpreter. But in general, the depth accuracy is $\pm 10\%$ without reference cores and 5% if cores are available.

Precision

The precision of ground-coupled GPR depends to some degree on the hardware, but in general all ground-coupled systems are precise enough for tunnel surveys (repeatable and reproducible) as long as no significant changes in moisture content or material properties occur in the area being measured. Such changes can have a complex effect on coupling and, thus, antenna performance. But typically, ground-coupled GPR does show anomalies on the same location.

Calibration Procedures

Ground-coupled GPR antennae require no special calibration. The important issue is to use a gain level that does not cause a signal clipping effect.

Testing Procedures

Ground-coupled GPR antenna manufacturers have their own GPR-system-specific user manual that should be followed when collecting data. For example, Geophysical Survey Systems, Inc. (GSSI) provides a handbook for concrete inspection on its website: <http://www.geophysical.com/Documentation/Manuals/MN72367D1%20Concrete%20Handbook.pdf>.

Cost

The price for a complete ground-coupled GPR system starts around \$50,000. Antennae with different central frequencies are available (usually from 100 MHz to 1.5 GHz).

The researchers used GSSI 900-MHz and 1.5-GHz antennae.

Limitations

Data collection can be slow because the antenna needs to be either in contact or close to the lining surface during data collection.

- Data interpretation requires educated and experienced personnel.
- External electromagnetic radiation such as cell phone antennae, radio antennae, and television station antennae could cause signal degradation, although that is not usually observed with these types of antennae.
- Salts (from either deicing operations or seawater) in the concrete may cause signal penetration problems.
- Steel fibers in shotcrete prevent ground-coupled GPR signal penetration. Concrete containing steel slag can also prevent signal penetration.

Data Management

Commercially available ground-coupled GPR systems (such as the systems described on the webpage <http://www.geophysical.com/antennas.htm>) come with data collection and management software. Ground-coupled GPR service providers may also have their own data management software.

Data Analysis and Interpretation

Data analysis software is provided by the manufacturer of such systems. Ground-coupled GPR service providers may also provide data analysis and interpretation services. However, data interpretation for locating subsurface defects can only be done by experienced, trained users and usually demands engineering judgment.

APPENDIX C

Handheld Thermal Camera Testing Criteria

Accuracy

A commercially available handheld thermal camera, the FLIR T300, was used in this study. The specifications for the camera can be found at http://support.flir.com/DsDownload/Assets/45305-0201_en_41.pdf. According to FLIR, the accuracy of the temperature readings is $\pm 3.6^\circ\text{F}$ or $\pm 2\%$ of the reading.

Images from this system do not indicate depths of defects. However, the images can indicate possible tile debonding, delaminations up to 1 in. deep with a minimum surface area of 1 sq ft, and voids up to 3 in. deep with a minimum surface area of 1 sq ft, based on specimen testing. Such defects can be pinpointed within 1 foot of their actual location.

Appendix L provides additional information on the FLIR T300 camera system used in this study, as well as selected images.

Precision

According to FLIR, the precision of the T300 system is less than 0.09°F (0.05°C). The areas of possible defects can be pinpointed within 1 foot of the actual defects as long as the thermal contrast of the area of interest has not changed and the system is properly calibrated.

Calibration Procedures

Each thermal camera manufacturer publishes its own calibration procedures (if needed). The user cannot make this calibration; the camera has to be sent to the manufacturer or authorized reseller for calibration.

Testing Procedures

The camera operator needs to ensure that the equipment is properly focused before beginning the data collection process. No other special testing procedures are needed.

The researchers used the following process when testing in tunnels:

1. Turn on the camera.
2. Aim the camera at a tunnel lining. Observe the temperature of the lining in the center of the display.
3. Manually set the temperature range to a range of around 5°F (e.g., 60°F to 65°F if the tunnel lining temperature at the center is 62°F).
4. Adjust the range so that a color spectrum appears on the camera display.
5. Aim the camera down the tunnel. With the laser pointer (mounted on the camera), point out areas to personnel where the temperature appears to be higher or lower than usual—according to the camera display.
6. Have the personnel inspect the area and determine if the area warrants further investigation by hammer tapping or visual observations of distress or moisture. Mark the area if further investigation is needed.

Cost

The FLIR T300 handheld thermal camera costs approximately \$9,000.

Limitations

The equipment is not accurate at temperatures below -4°F (-20°C) or above 248°F (120°C). (This is inferred from the FLIR A325 vehicle-mounted thermal camera default calibration.) The normal operating temperature is between 5°F (-15°C) and 122°F (50°C).

Data Management

Thermal cameras contain data collection and management software. The images are stored on a secure digital (SD) card with the image number and date. The SD card can be removed so the images can be transferred to a computer.

Data Analysis and Interpretation

Thermal camera manufacturers provide data analysis and interpretation software with which the images can be

further refined and inspected. For example, FLIR provides free software for data analysis and interpretation of images taken with its equipment. This software is described and can be downloaded at <http://www.flir.com/cs/emea/en/view/?id=42406>.

APPENDIX D

Ultrasonic Tomography Testing Criteria

Accuracy

The ultrasonic tomography (UST) system used in this study is a device with an array of ultrasonic transducers that transmit and receive acoustic stress waves for the inspection of concrete structures. The system used here, the A1040 MIRA, is produced by Acoustic Control Systems. The device's accuracy varies according to the material tested: concrete or shotcrete.

Concrete Slabs with Blind Calibration

When used for testing concrete slabs, UST typically relies on blind calibration in the field. Thus, the wave speed (the parameter that most affects the depth readings of anomalies) used in data collection is calculated by averaging wave speeds from eight initial calculations (see "Test Procedures" in Chapter 3 of the *Tunnel Nondestructive Testing Equipment User's Manual*). The resulting average may vary from location to location, giving an inaccurate depth reading. Even so, the UST system has been demonstrated to locate 8-in.-deep air-filled voids with 0.44-in. depth accuracy, 8-in.-deep water-filled voids with 0.50-in. depth accuracy, and 2-in.-deep to 3-in.-deep delaminations with 0.74-in. depth accuracy. Backwall reflections for specimens from 12 in. to 24 in. can be located with a 2.00-in. accuracy.

Shotcrete Slabs with Blind Calibration

In shotcrete slabs, the UST system has been demonstrated to locate 3-in.-deep to 8-in.-deep air-filled voids with a 0.70-in. accuracy, 3-in.-deep to 8-in.-deep water-filled voids with a 1.21-in. accuracy, and 2-in.-deep to 8-in.-deep delamination with a 1.88-in. accuracy. Backwall reflections for specimens as deep as 12 in. can be located with a 1.53-in. accuracy.

Note that under 2 in. (at 50 kHz), defects are typically seen only by the shadowing effect. Occasionally, the nature of the defect allows detection from 1 in. to 2 in. deep.

Precision

Three cases for precision are presented. They are *repeatability of one device*, in which the same device is used with the same settings on the same specimen; *reproducibility with the same settings*, in which two separate but identical devices are used with the same settings on the same specimens; and *reproducibility with blind testing*, in which two separate but identical devices are used to individually calculate wave speed but are used on the same specimens.

Repeatability of One Device

In repeatability tests using the same device with the same settings and parameters on the same day, air- and water-filled voids, delamination, and backwall reflections are detected with a precision of 0.16 in.

Reproducibility with the Same Settings

In reproducibility tests with two separate but identical systems compared side-by-side with the same settings and parameters on the same day, air- and water-filled voids, delamination, and backwall reflections are detected with a precision of 0.51 in.

Note that the two separate systems did not have the same version of firmware, and the system used for the comparison consistently predicted the anomalies 0.51 in. deeper than the Texas A&M Transportation Institute's system. The research team does not expect systems to differ this much when they use the same version of firmware.

Reproducibility with Blind Testing

The following are results from reproducibility tests using two systems that follow similar blind calibration procedures on the same day.

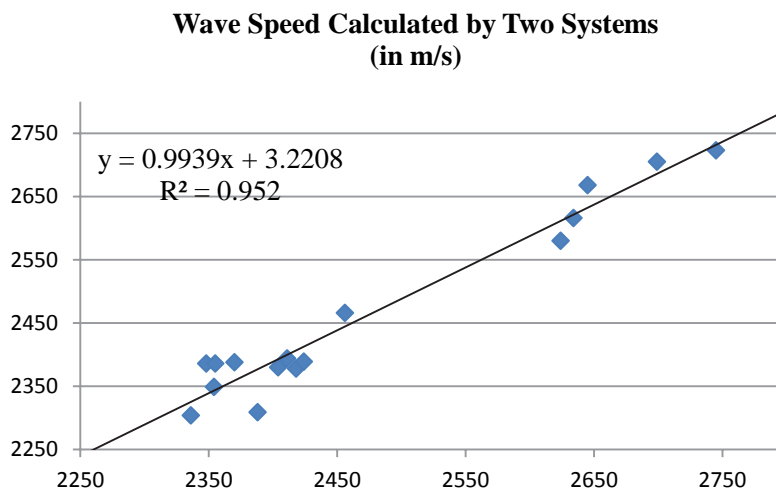


Figure D.1. R^2 for reproducibility of wave speed calculation (two separate MIRA systems).

Concrete Slabs with Blind Calibration

The two UST systems have been demonstrated to locate 8-in.-deep air- and water-filled voids with a 0.51-in. precision and 2-in.-deep to 3-in.-deep delamination with a 0.55-in. precision. Backwall reflections for specimens as deep as 12 in. to 24 in. can be located with a 0.70-in. precision.

Shotcrete Slabs with Blind Calibration

The two UST systems have been demonstrated to locate 3-in.-deep to 8-in.-deep air-filled voids with a 0.51-in. precision, 3-in.-deep to 8-in.-deep water-filled voids with a 0.70-in. precision, and 2-in.-deep to 8-in.-deep delamination with a 0.35-in. precision. Backwall reflections for specimens as deep as 12 in. can be located with a 0.70-in. precision.

Reproducibility of Wave Speed

Two MIRA UST systems were used to compare the system's abilities to reproduce the same wave speed. For a test involving 16 specimens, a strong positive correlation exists (with a coefficient of determination of 0.952), as shown in Figure D.1, with a standard error of approximately 33 m/s (108 ft/s).

Calibration Procedures

Blind Calibration Procedures

Blind calibration is performed when ground truth information is not available for the type of concrete under inspection. This is the typical field condition. The ultrasonic tomography system is calibrated using an average wave speed calculated

from eight randomly oriented collection points. Calibration procedures can be found in the *Tunnel Nondestructive Testing Equipment User's Manual* or Sections 1.3 and 1.4 in the manufacturer's user manual.

Ground Truth Calibration Procedures

When ground truth information is available to fine-tune the system, the wave speed should first be estimated by the procedure outlined in Chapter 1 of the *Tunnel Nondestructive Testing Equipment User's Manual*. If the determined wave speed does not accurately produce the same results as the ground truth information, the user should adjust the wave speed so that the displayed defect matches the ground truth information.

Testing Procedures

Testing procedures are given in "Test Procedures" of Chapter 1 in the *Tunnel Nondestructive Testing Equipment User's Manual* and in Section 2 in the manufacturer's user manual.

Cost

The cost of the A1040 MIRA UST system is approximately \$58,000, which includes the A1040 unit, a removable battery, analysis software on a laptop, a USB cable for data transfer, a user manual, and a transportation case.

Limitations

The limitations of the system are given in detail under "Limitations" in Chapter 1 of the *Tunnel Nondestructive*

Testing Equipment User's Manual. Limitations include the following:

- The speed of data acquisition is low (0.8 to 2.3 min/sq ft).
- No phase change information is available to infer defect type.
- No information deeper than initial air interfaces is discernible.
- The system has difficulty detecting reinforcement below two layers of reinforcement mesh.
- For a 50-kHz use, defects under 2 in. from the surface are not directly detected.
- For a 50-kHz use, reinforcements under No. 5 rebar (0.625-in. diameter) are not typically detected.

Data Management

Data files for typical grid spacing (50 mm to 200 mm by 50 mm to 200 mm) for comprehensive maps range from 12 kb/sq ft to 35 kb/sq ft. The research team recommends that all data be stored on a remote hard drive.

Data Analysis and Interpretation

Data reconstruction and imaging are performed automatically by the ultrasonic tomography system for two-dimensional review mode. Data reconstruction and imaging are performed automatically by the accompanying IDEalViewer software for three-dimensional map mode. Raw data files are generated as *.lbv, *.bin, *.bmp, and *.cfg files.

Data interpretation is manually performed by an experienced operator for both the map and review modes of operation. Interpretive guidelines are given under “Interpretation Guidelines” in Chapter 1 of the *Tunnel Nondestructive Testing Equipment User's Manual*.

Reference

White, J., S. Hurlbaas, S. Nazarian, and P. Shokouhi. 2014. *SHRP 2 R06G: Tunnel Nondestructive Testing Equipment User's Manual*. Transportation Research Board of the National Academies, Washington, D.C.

APPENDIX E

Ultrasonic Echo Testing Criteria

Accuracy

The ultrasonic echo equipment used in this research study is commercially available. It is the A1220 Monolith developed by Acoustic Control Systems, in cooperation with the Federal Institute for Materials Research and Testing (BAM) in Germany. The equipment's accuracy depends mainly on the data acquisition hardware; however, with the A1220, the tunnel thickness can be estimated within an accuracy of $\pm 3\%$ of the actual thickness. This system and the ultrasonic tomography testing system (discussed in Appendix D) measured comparable depths to defects in tunnel linings.

Precision

The A1220 measurements are highly reproducible (i.e., the precision is very good) when no coupling agent is used. Using a scanning system enhances the reproducibility of the measurements because the pressing pressure on the transducer and its location can be accurately controlled.

Calibration Procedures

No standard calibration procedures need to be performed before starting to take measurements.

Testing Procedures

When using dry-point contact probes, no coupling liquids need to be applied on the surface. However, the surface should be cleaned of dust and sand, and any materials that could prevent the penetration of low-frequency ultrasonic energy should be removed from the surface.

The location of the test site and its dimensions should be marked and noted to facilitate the reproduction of measurements if necessary and to locate the detected features. For scanner testing, the location of the scanner feet and the dimension

of the scanner aperture need to be carefully noted. Equally important, the orientation of the probe (i.e., its polarization) with respect to the test area or scanner opening should be recorded.

The technical passport of the hardware includes information about the center frequency of the probe, the delay time, and the voltage level. These constitute all the parameters to be set before starting the measurement process. The choice of parameters depends on the particular application, that is, the test material and the required penetration depth. For testing of concrete tunnel linings of up to 3 ft thick, a center frequency of 55 kHz could be used.

The number of test points and grid spacing depend on the required resolution (i.e., the minimum size of the defects being sought) and the time allocated for field investigations. For this project, the team chose a grid spacing of 1 in. in each direction, allowing the scanning operation at about 11 sq ft/h (or 1 sq m/h) for acoustic testing. Investigations revealed that doubling the grid spacing to 2 in. would not compromise the accuracy of the test results. Reconstruction algorithms used for postprocessing the data (e.g., synthetic aperture focusing technique) are most effective for grid spacing of 2 in. or less. To achieve the maximum accuracy, measurements might need to be performed with two polarizations.

Cost

A handheld unit with one transducer can be purchased for less than \$10,000. The cost of a scanning system with the control unit is about \$100,000.

Limitations

The main limitation of conventional ultrasonic techniques is that the sensors have to be in contact with the structure during the measurement process. This leads to several issues

such as poor repeatability and/or inconsistency of measurements, as well as delays from displacing and reinstalling the transducers. Mounting the ultrasonic device on a scanning system accelerates the measurement process and greatly enhances the repeatability and consistency of the results. However, compared with contact-free measurement systems, conventional ultrasonic testing (even with dry-contact transducers like A1220) is relatively slow. Therefore, it is suitable for the assessment of areas deemed problematic during screening. Other limitations of ultrasonic echo testing include the following:

- At or near block joints or other structural boundaries, the signals suffer great disturbance due to the reflection of surface waves. This makes the reliable evaluation of measurements difficult.
- The acoustic waves reflect partially at the interface between the inner shell concrete and roof gap backfill material. If these two materials are well bonded, the reflection is very small or may not be identified. However, a separation often occurs between these two materials. A gap of a few hundredths of a millimeter is sometimes enough to completely reflect the sound waves. In such cases, only the thickness of the inner shell is measured (excluding the backfill material).
- Even with the phase evaluation, the difference between certain types of defects (e.g., a flaw and an excessively thin cross section of lower acoustic impedance) cannot always be established.
- In the case of air-entrained concrete or fiber-reinforced concrete, the range of thickness measurements was reportedly reduced, or carrying out the measurements was more difficult.

Data Management

The collected data are downloaded from the ultrasonic hardware and saved on an external hard disk for safekeeping. Depending on the amount of data acquired, downloading might be necessary in between a measurement cycle; otherwise, an external hard disk can be connected to the instrument. Using the A1220 device on a 1-in. by 1-in. grid of size 48 in. by 24 in. (1,225 data points, 1,024 samples per signal, and a sampling frequency of 1 MHz) produces a 16-bit binary file of 2.39 MB. The analysis software delivered with the hardware is able to read the binary data format in which the information is saved. With other analysis software, the data might need to be transformed into a different file format.

Data Analysis and Interpretation

Basic data analysis software is provided by the manufacturer. Other standard data analysis software can be used for further postprocessing of the experimental data.

Interpretation depends on the mode of testing (one point [A-scan], linear [B-scan], or surface measurements [C- and D-scans]) and may be enhanced by using advanced analysis and visualization tools. For example, applying the synthetic aperture focusing technique to the data improves the signal-to-noise ratio. Phase analysis makes it possible to distinguish among features and anomalies of different constituents (e.g., steel or air void). Built-in plans or other information about the test area may greatly facilitate the interpretation of the results as well.

Data interpretation can be done by experienced trained users and usually demands engineering judgment.

APPENDIX F

Ultrasonic Surface Waves and Impact Echo Testing Criteria

Accuracy

The portable seismic property analyzer (PSPA) performs the ultrasonic surface wave and impact echo tests simultaneously. On the basis of the results obtained in SHRP 2 Renewal Project R06A, Nondestructive Testing to Identify Concrete Bridge Deck Deterioration, the measurement spacing should be equal to or less than the smallest delaminated area to be detected by either the ultrasonic surface waves (USW) or the impact echo (IE) method. To map the area of the delaminated area accurately, the measurement spacing should be half the desired smallest dimension of the area that is of practical value.

Figure F.1 represents the USW and IE results of the traditional PSPA, along with the approximate horizontal distribution of the defects from SHRP 2 Project R06A. According to an objective criterion defined by Azari et al. (2012), the accuracy of the USW and IE methods in detecting the defects was estimated at about 83% and 85% of the points tested, respectively. The detectability of the combined USW and IE results in locating the defects improved slightly, at 86%.

The new PSPA results are similar to the traditional PSPA results. The amplitude and dominant frequency spectra are shown in Figure F.2. The defective areas are indicated by high amplitude and low frequency.

The USW method is about 15% accurate in approximating the depth of defects. It becomes less effective when the delamination is deeper than 6 in. The IE method is more effective in locating deep delaminations. The accuracy of the IE method in estimating the depth of delamination is about 10%.

Precision

Precision was evaluated through statistical analyses of the three sets of data from the three runs of the USW and IE methods on the centerline of the specimen. The USW method's repeatability results from SHRP 2 Renewal Project R06A are

shown in Figure F.3a. The upper and lower bounds were calculated for each test by adding/subtracting one standard deviation μ of the three runs to/from the mean modulus of three runs. The coefficient of variation (cov), which was used as a measure of repeatability, was obtained by calculating μ of the three runs divided by their corresponding mean value μ ($\text{cov} = \sigma/\mu$). As shown in Figure F.3b, the average cov was about 12%. The repeatability of IE test results for estimating the thickness of the slabs was also evaluated. The main points contributing to the higher standard deviation are the severely deteriorated points—where slight spatial variation may cause differences in the values. Nazarian et al. (2006) have shown that for new construction, the average cov is less than 7%.

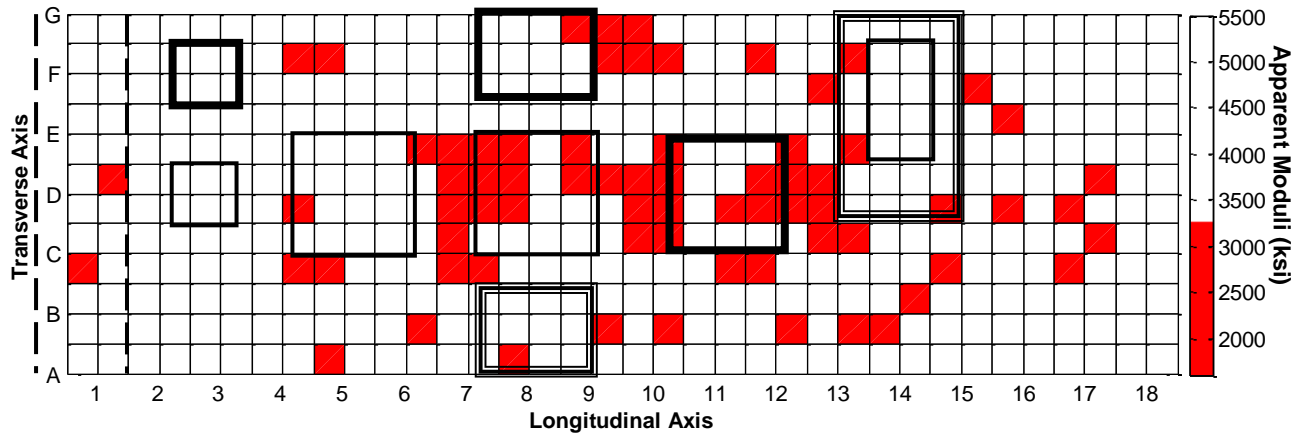
The thickness is calculated on basis of the dominant frequency and compression wave velocity of each slab. The average cov of thickness was about 6%. These values correspond well with the anticipated uncertainty of 5% to 10% reported in the literature for the IE method. As recommended by a number of researchers (Nazarian et al. 2006), the evaluative power of the thickness estimation with the IE method can be improved through a calibration process using one or two cores.

Calibration Procedures

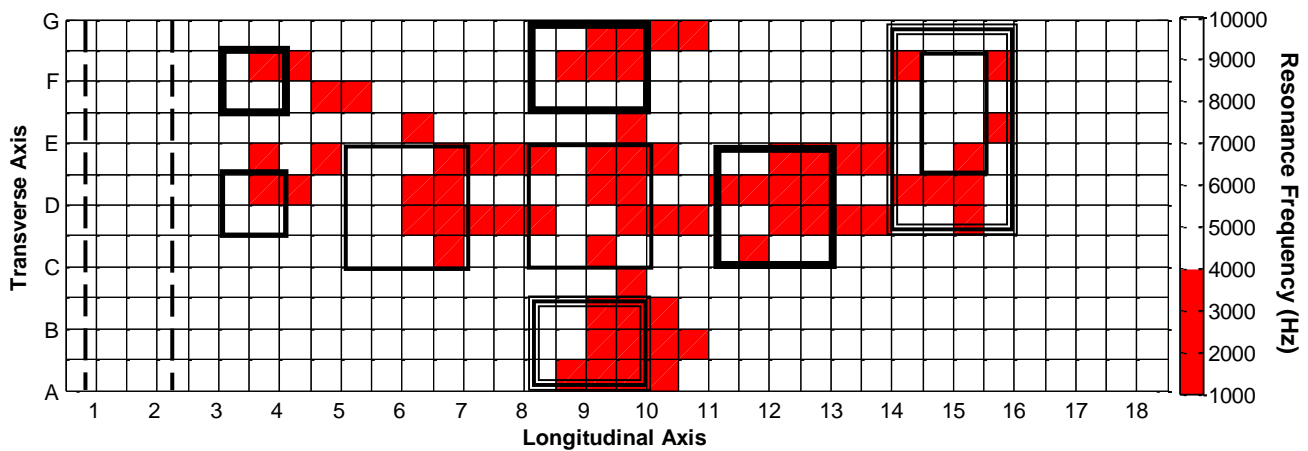
After initial calibration by the manufacturer, a rigorous calibration is not necessary unless the sensors are replaced.

Testing Procedures

Testing procedures are documented at <http://www.geomedia.us/>. To collect data with the PSPA, the user initiates the testing sequence through the computer. The high-frequency source is activated four to six times. The outputs of the two transducers from the last three impacts are saved and averaged (stacked). The other (prerecording) impacts are used to adjust the gains of the preamplifiers. The gains are set to optimize the dynamic range.



(a) Average apparent modulus obtained by USW method



(b) Dominant frequency obtained by IE method

Figure F.1. USW and IE contour maps.

Cost

The PSPA costs about \$25,000. The speed of data collection can also be considered in the cost category because of the cost of traffic control and losses associated with traffic interruptions. Although the PSPA collects data point-by-point, the PSPA is a relatively rapid testing device. The data collection speed of the PSPA is about 30 s/point.

Limitations

Although the USW and IE methods are shown to be successful in detecting internal defects, some apparent disadvantages should be considered. Both are localized testing methods, and testing a long tunnel may take a lot of resources and time. Although the IE method does have the ability to show the existence of a defect, the depth of defects that are shallow or extensive can be difficult to quantify. Inadequate contact will result in inaccurate and false measurements, especially for very rough concrete surfaces and oily and curved surfaces such as tunnel linings, which occasionally cause the device to

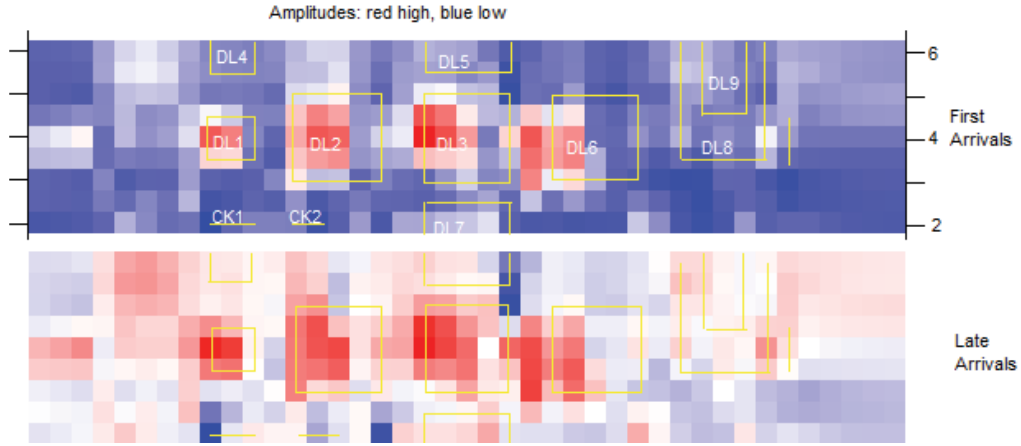
slip during testing. The new PSPA has resolved some of these issues.

Data Management

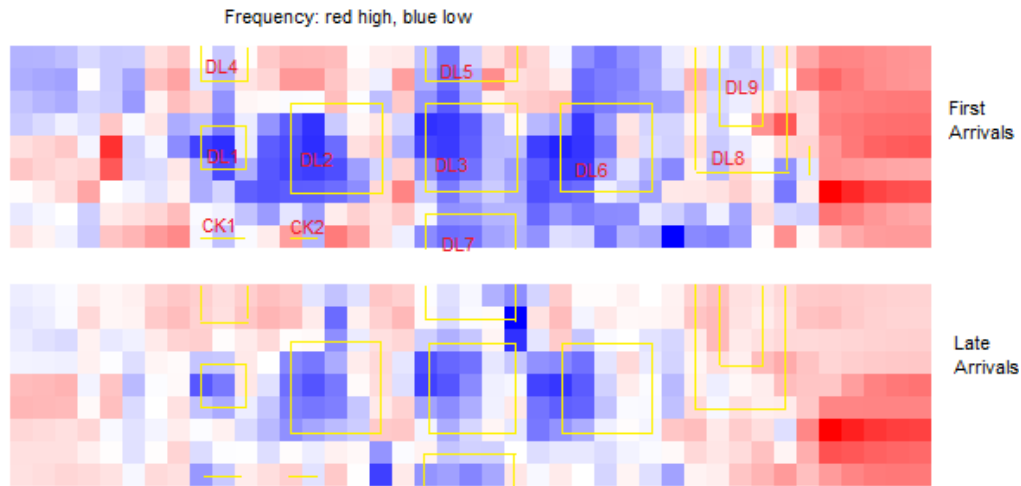
The PSPA saves the raw data from each test point with appropriate meta-data indicating the time and information about the test parameters. The collected data can be reanalyzed readily with new algorithms if necessary. At the start of a project, the user identifies the location where the data will be stored.

Data Analysis and Interpretation

The data analysis is defined as the processing of the raw data collected by the PSPA and includes preprocessing, data analysis and presentation, and data interpretation. In the preprocessing phase of the IE method, using a time window to remove the surface wave energy from the time records provides a more robust and accurate thickness measurement



(a) Planar contour map of amplitude of waveforms



(b) Planar contour map of dominant frequency

Figure F.2. New PSPA defect maps on the bridge deck.

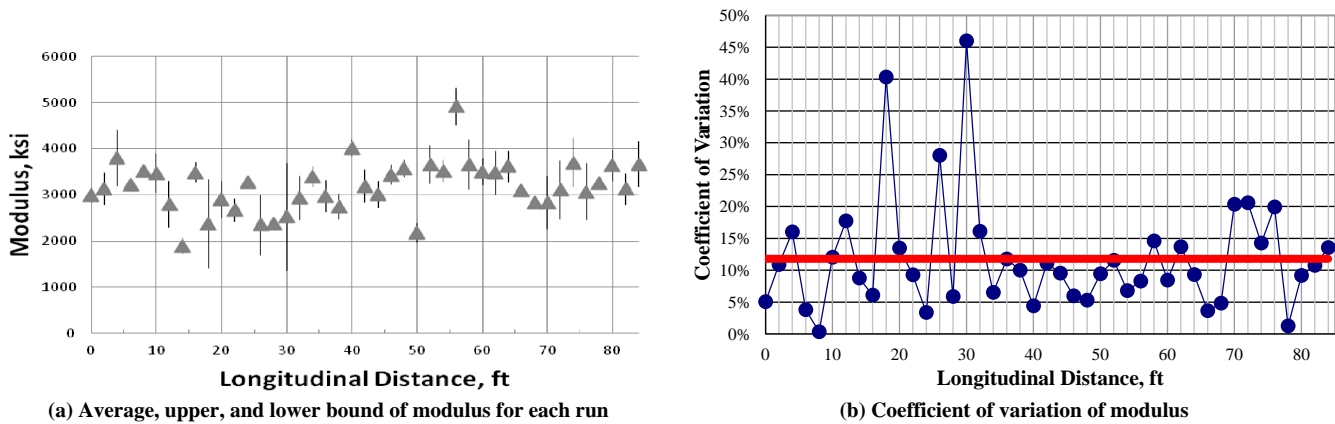


Figure F.3. Precision of the USW method.

than when the entire waveform is used. In the USW method, the surface wave energy should be reinforced by implementing proper filters to minimize the reflection and body wave energy.

The USW and IE results are graphically displayed in color contour maps, namely, traditional with unlimited-color index, traditional with two-color index, and checkerboard (Azari et al. 2012). The traditional contouring uses a smoothing algorithm to ensure that the displayed contour lines change gradually and incrementally from a minimum value to a maximum value. When the unlimited-color index approach is selected, a large number of shades of primary colors are used in the smoothing algorithm. The two-color index contours contain only two colors delineated by a threshold value. However, a smoothing algorithm is still used to depict the results. The checkerboard algorithm plots a rectangular array of cells. The value for each cell is determined by smoothing the results using the values of that cell and the four adjacent cells to define a surface rectangle. Recent studies have shown that representing the data in a checkerboard format enhances the evaluative power of the results (Azari et al. 2012).

Interpreting the results requires defining the modulus and frequency threshold to delineate between the intact and delaminated areas. In the USW results, the target modulus was set at 0.86 to ensure that the delaminated areas were selected with a confidence level of about 95% (Nazarian et al. 2006). The test points with a modulus less than 0.86 appear in red, indicating that they are defective. The threshold in IE contour maps was based on the thickness of the slab and the depth and extent of delamination. The test points with dominant frequency less than thickness frequency are marked as red (defective).

References

- Azari, H., D. Yuan, S. Nazarian, and N. Gucunski. 2012. Sonic Methods to Detect Delamination in Concrete Bridge Decks: Impact of Testing Configuration and Data Analysis Approach. In *Transportation Research Record: Journal of the Transportation Research Board*, No. 2292, TRB, National Research Council, Washington, D.C., pp. 113–124.
- Nazarian, S., D. Yuan, K. Smith, F. Ansari, and C. Gonzalez. 2006. *Acceptance Criteria of Airfield Concrete Pavement Using Seismic and Maturity Concepts*. Report IPRF-01-G-002-02-2. Skokie, Ill: Innovative Pavement Research Foundation, Airport Concrete Pavement Technology Program.

APPENDIX G

Field Testing with Acoustic Sounding

Introduction

This appendix describes the progress of a particular non-destructive testing (NDT) technique known as acoustic sounding and outlines how this system will work within the framework of the SHRP 2 Renewal Project R06G.

This system is in its final stages of development, and research thus far has shown it to be a promising technique capable of quickly determining the stage of tile debonding in tunnel linings. Because the system remains under development, this appendix discusses how the system will be used in inspection procedures and provides an idea of what the end product will be. An evaluation of public tunnels and a series of test specimens will be conducted for this research and will be discussed in the final report.

Acoustic Sounding Technique

When debonding occurs on tiled surfaces, hammer sounding by ear or by microphone can readily differentiate bonded from debonded tile. Debonded areas have a characteristic lower-frequency pinging relative to fully bonded tiles. The goal here is to devise a less subjective method for inspectors to quickly and efficiently characterize the condition of tile bonding.

Technical Needs

In general, tile debonding can occur for two reasons: improper installation or external influences. Improper installation commonly includes the following:

- Improper use of bonding agent (e.g., mixing ratios or the wrong type of agent);
- Improper tile spacing;
- Excessive open time; and
- A low standard of workmanship (e.g., not “back buttering” the tile).

External influences can include environmental conditions (e.g., thermal expansion) and/or excessive tunnel lining forces (e.g., damage from voids, cracks, delamination, or debonding).

In either case, debonding of the tile does occur and can pose a danger to the public. This SHRP 2 project uses many NDT techniques to identify the onset of damage behind the tiled wall lining before debonding occurs and to quickly and efficiently identify regions that need immediate attention after debonding occurs.

Research Approach

The system under development is used with a laptop computer capable of recording audio signals and installed with a version of MATLAB (developed by MathWorks, <http://www.mathworks.com/products/matlab/>), along with an impact source (preferably a ball-peen hammer). As the operator lightly taps the center of each tile with the hammer, the laptop’s internal microphone records the audio signal. MATLAB software performs a fast Fourier transform on the data set and uses pattern recognition techniques to monitor the fundamental frequencies of flexural vibration for each individual tile. The modes of vibration frequencies in a voided tile can be predicted using acoustic theory for a rectangular plate with simply supported edges (Rossing and Fletcher 2003):

$$f_{mn} = 0.453c_L h \left[\left(\frac{m+1}{L_x} \right)^2 + \left(\frac{n+1}{L_y} \right)^2 \right]$$

where

c_L = longitudinal wave speed,

h = thickness of the tile,

m and n = integers describing the current mode of excitation ($m = n = 0$ for the fundamental frequency of flexural vibration), and

L_x and L_y = respective side lengths of the tile.

The vibration frequencies increase as the voided sections of tile decrease (Liu et al. 2011). Therefore, it is theoretically possible to relate the fundamental frequency to the approximate area of debonding.

This technique can be incorporated into a program that assigns a color scale to the frequency spectrum of a tile wall under inspection. The research team envisions that the final program will be able to operate in two modes. The first is for near-real-time inspection. In this mode of operation, a threshold frequency from an expected frequency band representing sound concrete is established and used to make a pass-fail decision, telling the operator whether a tile is most likely bonded or debonded. The second mode is intended for mapping a large region of tile, and the final result is a map of the tiles showing the degree of expected bond. As in the first mode, the operator selects a section of tile representing a fully bonded state for the program to determine the fundamental frequencies associated with bonded sections. The user then taps each tile in a predetermined order. For instance, the section might consist of an area 13 tiles high by 40 tiles wide. The program prompts the operator to select the layout desired, and after the operator taps each tile in the given order, the program displays a plot showing the frequency spectrum.

Field Application in the Washburn Tunnel

A rudimentary version of this technique was used for a proof-of-concept test in the Washburn Tunnel in Houston, Texas. The Washburn Tunnel is the only underwater vehicle tunnel in operation in Texas and was completed in 1950. It carries a federal road beneath the Houston Ship Channel, joining two Houston suburbs.

The tunnel was constructed using the immersed tube method, with sections joined together in a prepared trench, 26 m (85 ft) below the water line. The entire inner wall is tiled with 110-mm by 110-mm (4.3-in. by 4.3-in.) ceramic tiles. Like many underwater tunnels with tiled walls, this one is experiencing debonding in various areas. Three sections of tile that contained debonded regions (as determined by an inspector performing hammer sounding by ear) were chosen. The regions, shown on the left side of Figure G.1, display the area under consideration outlined with blue painter's tape. The debonded section (determined by human ear) is indicated with a blue painter's tape "x" on the debonded section. On the right side of Figure G.1, scans made via ultrasonic tomography (UST) are shown for each of the three regions. The depths of the C-scans (plan views) in Figure G.1 range from 16 mm to 103 mm (0.63 in. to 4.1 in.). One of the areas investigated (Figure G.1, middle) was evaluated by using a rudimentary version of the acoustic sounding technique and is shown in Figure G.2. This example shows a strong correlation between hammer sounding by ear and the automated acoustic sounding technique.

In Figure G.2, the bottom left plot depicts the tiles color coded in grayscale, with the higher frequencies (predicting a fully bonded state) as white and the lower frequencies (predicting a debonded state) as black. As previously discussed, the lower frequencies should theoretically correspond to larger voided areas behind the tile. The bottom right plot in Figure G.2 shows the output with a pass-fail algorithm denoting tiles that fall below the expected fully bonded state (red is the expected debonded state, and green is the expected fully bonded state).

Testing Criteria

For the automated acoustic sounding device discussed here, no system is commercially available. The following testing criteria are given to estimate the usefulness in designing and implementing this technique.

Precision, Accuracy, and Repeatability

Precision and accuracy criteria will need to be determined on the basis of ground truth data (which were not available for the tunnel lining under inspection) on actual debonded tiles. Technological difficulties prevented the research team from completing a system for validation on test specimens within the time constraints of this project. The system previously described in Field Application in the Washburn Tunnel is only compared with hammer sounding (by ear) and UST, which should not be used in place of ground truth data.

Because the detection of debonded tiles depends on the frequency band chosen to represent bonded tile, the threshold value for a pass-fail decision will vary. The researchers recommend rating the failures (debonded tiles) by color-coded signals based on the proximity of the fundamental frequency response to the chosen threshold. After this is experimentally tried, the precision and accuracy of the technique can be estimated.

Repeatability will depend on the precise location of impact. A great deal of variance is possible depending on how far the point of impact is from the center of the tile.

Calibration Procedures

Calibration will have to be made on a section of tile evaluated by other NDT devices or otherwise assured to be sound. The researchers recommend determining a band from several sample locations of bonded tiles. After this frequency band is determined, it can be used as a threshold value for determining debonded tiles.

Testing Procedures

The research team envisions that a fully developed automated sounding method will be able to operate in two modes. The

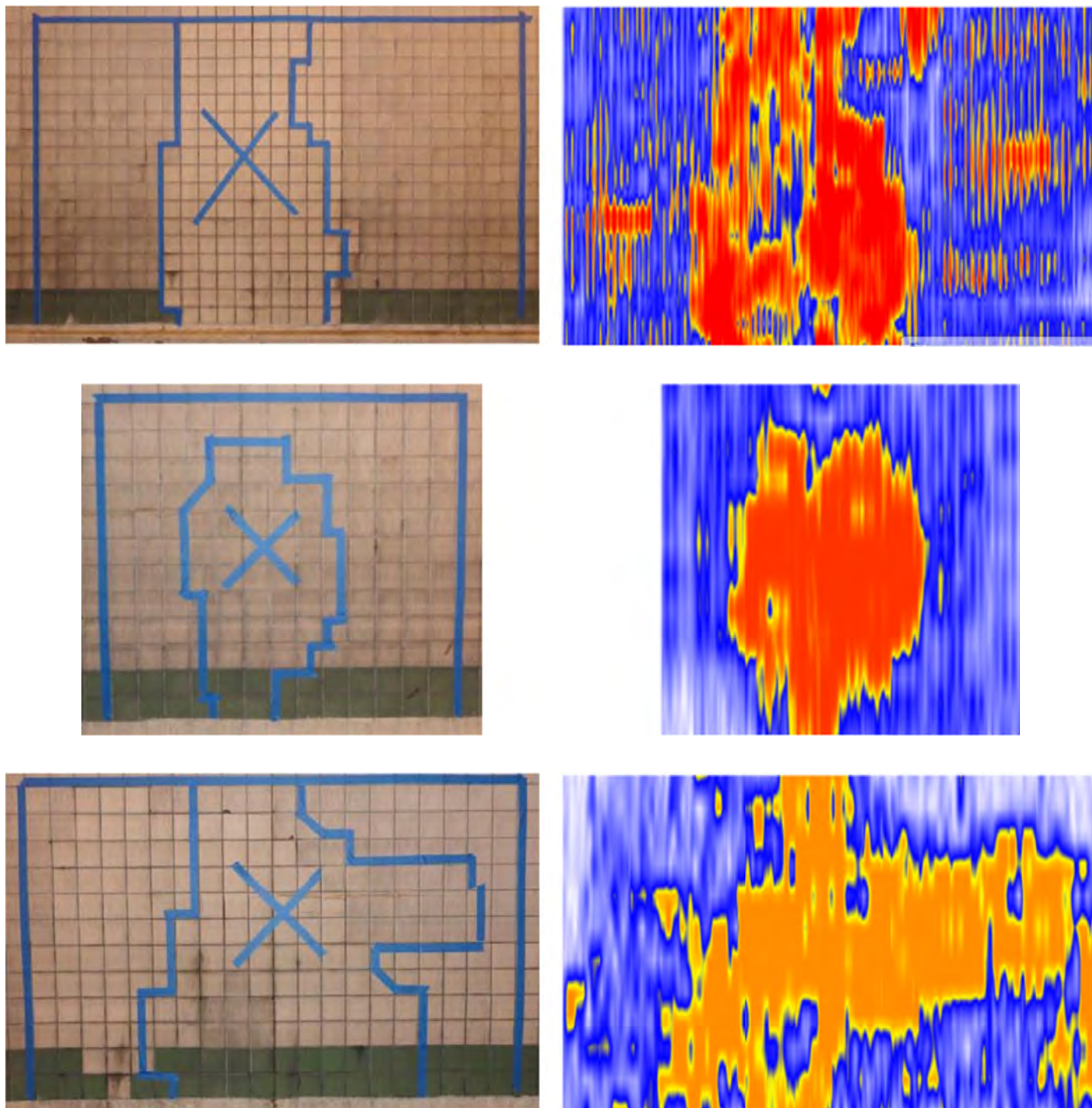


Figure G.1. Debonded regions of tile (left) paired with the associated UST C-scans (right).

first is for near-real-time inspection. In this mode of operation, the threshold frequency from an expected frequency band representing bonded tile; is established and used to make a pass-fail decision, telling the operator whether the tile is most likely bonded or debonded. The second mode is intended for mapping a large region of tile, and the final result is a map of the tiles showing the degree of expected

bond. This pass-fail decision will be based on how close the fundamental frequency of the tile is to the threshold value. As in the first mode of operation, the operator will select a section of tile representing a fully bonded state for the program to determine the fundamental frequencies associated with bonded sections. The user will then tap each tile in a predetermined order.

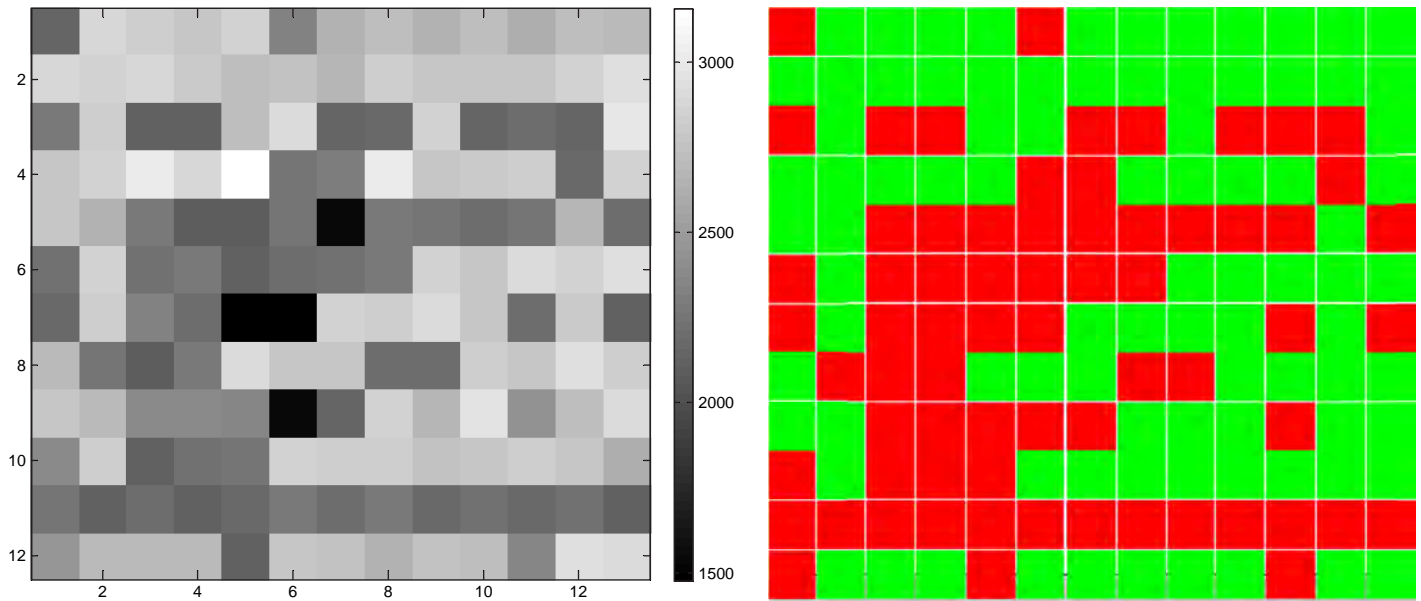
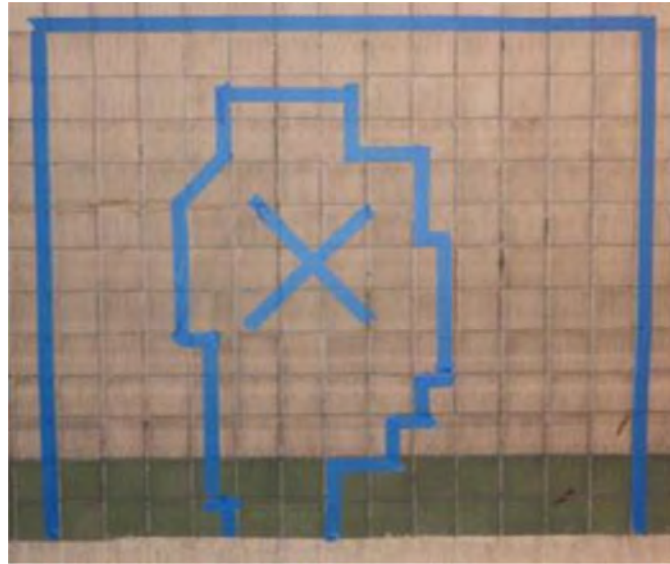


Figure G.2. Debonded regions of tile (top) paired with the acoustic sounding results (bottom).

The research team also recommends developing an application for a smart phone that would signal whether a tile is likely debonded or bonded. A threshold value could be chosen to represent bonded tile, and significant deviations from that threshold would result in a pass (green) or fail (red) screen.

Cost

The research team attempted to construct a viable prototype, but it is in progress and not yet ready for field application. A final and proven technique is expected to be inexpensive.

Limitations

The limitations of this device are as follows:

- *Battery power.* Any remote device will rely on battery-powered operation for long periods of analysis.
- *Consistent impact location.* Repeatability of impact plays a huge role in precision and accuracy. The operator's point of impact should not deviate significantly from the center of the tile.
- *Microphone quality.* The research team is not certain at this time whether the microphone quality from a typical smart phone or laptop computer is sensitive enough to

distinguish fundamental frequencies from the ambient noises present in a tunnel. The proof-of-concept method presented above used recordings from a smart phone video recorder and then processed the data with MATLAB code. When used in the field, the laptop computer had trouble recording usable data.

Data Analysis and Interpretation

The purpose of the automated acoustic sounding technique is to remove the subjective component of the process by allowing the software to make a pass-fail decision. Further analysis and decision making would involve other NDT techniques.

Equipment and Systems Integration Requirements

The research team recommends that devices use MATLAB software on any platform compatible with the version purchased.

Conclusion

This automated sounding technique is still under development. Many factors influence the peak frequencies observed in the frequency spectrum from a single tile tap, including the size of the void, whether or not the hammer tap was directly in the center of the tile, and multiple-mode interference. Preliminary results indicate that this technique, although basic in its approach, will offer the tunnel inspector a quick, efficient, inexpensive, and objective technique that provides sufficient information for repair procedures or further investigation.

References

- Liu, S., F. Tong, B. Luk, and K. Liu. 2011. Fuzzy Pattern Recognition of Impact Acoustic Signals for Nondestructive Evaluation. *Sensors and Actuators A: Physical*, Vol. 167, No. 2, pp. 588–593.
- Rossing, T., and N. Fletcher. 2003. *Principles of Vibration and Sound*, 2nd ed. Springer, New York.

APPENDIX H

Vehicle-Mounted Thermal Camera Testing Criteria

Accuracy

The vehicle-mounted thermal camera system used in this study is described in Appendix J, which discusses the testing done in Finland. A commercially available FLIR A325 camera was used. According to FLIR, the accuracy of the temperature readings is $\pm 3.6^{\circ}\text{F}$ ($\pm 2^{\circ}\text{C}$) or $\pm 2\%$ of the reading.

Images from this system do not indicate depths of defects. However, the images can indicate possible tile debonding, delaminations up to 1 in. deep with a minimum surface area of 1 sq ft, and voids up to 3 in. deep with a minimum surface area of 1 sq ft, based on specimen testing. The system can locate defects within 1 ft of their actual location.

Precision

According to FLIR, the precision of the system is less than 0.09°F (0.05°C). The areas of possible defects can be located within 1 foot of the actual defects with any system as long as the thermal contrast of the area of interest has not changed and the systems are properly calibrated.

Calibration Procedures

Each thermal camera manufacturer has published its own calibration procedures (if needed). With the FLIR cameras used in the Finnish tests, the manufacturer recommends the equipment be calibrated every year. The user cannot make this calibration; the camera has to be sent to the manufacturer or authorized reseller.

Calibration is also needed for the distance measurement indicator (DMI). This usually involves driving the vehicle over a known distance (usually 1,000 ft) and checking the DMI reading against that known distance.

Testing Procedures

The operator needs to ensure that the camera is properly focused before beginning data collection. No other special testing procedures are needed.

Cost

The thermal camera itself—including a 90° wide-angle lens—costs approximately \$15,000. The price for a complete package with racks, software, and positioning system is approximately \$30,000.

Limitations

According to the FLIR A325 camera default calibration, the equipment is not accurate at temperatures below -4°F (-20°C) or above 248°F (120°C). The normal operating temperatures are between 5°F (-15°C) and 122°F (50°C).

Data Management

Data management consists of thermal camera data and positioning data collection and storage. The research team used the Road Doctor CamLink software with the Road Doctor TD Module for data management.

Data Analysis and Interpretation

Data analysis requires specialized software that allows the viewing of thermal camera image data as a video image. The software also needs to be able to create a thermal color map from the tunnel wall or roof that can be used for monitoring real changes in temperature and detecting anomalies. In addition, the software should be able to filter unwanted external noise from the thermal data.

APPENDIX I

Survey of the Chesapeake Bay Bridge-Tunnel

Introduction

Since 1982, SPACETEC has offered a scanner system to monitor disruptions and conditions of tunnel linings (Figure I.1). With this tool, it is possible to validate the effects of degradation—such as crack developments, cavities beneath the surface, changes in material composition, and water intrusions—over time.

The SPACETEC TS3 scanner is able to record high-precision surface, thermographic, and three-dimensional (3-D) images simultaneously with a resolution of 10,000 pixels and a recording angle of 360° (Figure I.2). The scanner is capable of identifying cracks as small as 0.3 mm in width. The rotating mirror speed of up to 300 Hz is one of the crucial features affecting the measuring speed. It can obtain a fast and nondestructive measurement with only a short period of traffic disruption. The scanner is compact and can be installed in almost every road vehicle that offers enough space for the scanner head and the operator console, such as a minivan.

The data are visualized with an easy-to-use, powerful software package displaying all three channels (visual, thermal, and 3-D) simultaneously. In this way, the operator can inspect the tunnel on the screen, with a pixel-by-pixel synchronism of the recordings. This technique helps the operator analyze and identify suspicious anomalies and compare them on all three channels.

Image manipulation is also possible (e.g., adjusting the contrast and brightness of the display, creating 3-D presentations, and performing a 3-D zoom of image details). In many cases, long-term monitoring supports the observation of the tunnel degradation over time with multiple measurements and a recording interval of at least 1 year.

A survey of the Chesapeake Tunnel—a part of the Chesapeake Bay Bridge-Tunnel system in Virginia—was performed in April 2011. The survey was conducted according to the subcontract agreement with the Federal Institute for Materials Research and Testing (BAM) in Germany.

The Chesapeake Bay Bridge-Tunnel is a 37-km-long link crossing the mouth of the Chesapeake Bay and connecting the Delmarva Peninsula's Eastern Shore of Virginia with Virginia Beach and the metropolitan area of Hampton Roads. The bridge-tunnel system combines bridges—connecting four artificial islands—with the Timble Shoal Tunnel (the western side of the bay) and the Chesapeake Tunnel. The Chesapeake Tunnel is one of two immersed, sunken-tube tunnels constructed under the ship channels of Chesapeake Bay in an approximately east–west direction and was opened in 1964. Since it opened, the tunnel has been exposed to extreme environmental conditions. Water intrusion and corrosion have been reported during visual inspections.

The portal-to-portal length of the tunnel is 1,661 m, with a roadway (two-lane) width of 7.3 m plus a sidewalk on one side. The tunnel interior is faced with ceramic tiles, which is uncommon for non-U.S. tunnels. Therefore, the surface of the concrete lining underneath is inaccessible.

This appendix describes the methods and results of the survey and is divided into the following parts:

- Available data channels;
- The recording process, including scanner measurements and scanning parameters;
- A description of results, including a brief introduction to data processing and a detailed description of the data; and
- Working with the data.

The corresponding data sets, including the analysis software package, were shipped with an external hard drive to BAM on January 6, 2011.

Available Data Channels

Visual Images

Visual images (Figure I.3) are most frequently used for general documentation and maintenance purposes. They show the condition of the lining as far as visible phenomena are



Figure I.1. SPACETEC TS3 scanner.

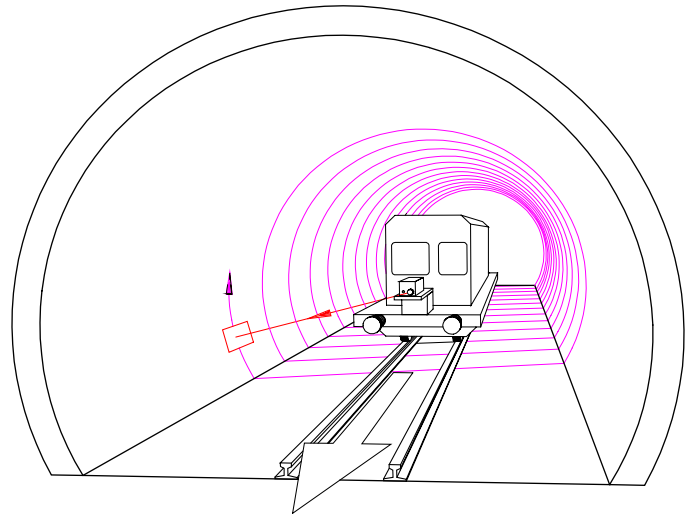


Figure I.2. Scanning principle.



Figure I.3. Visual image of conditions of a shotcrete lining in a motorway tunnel.

concerned. At any time, later data can be consulted to look for changes in those conditions.

Profile Data

Profile data (Figures I.4 and I.5) show the dimensions of the tubes and are used to consider and solve clearance problems. In the small range, the presence of distance measurements at high density allows the inspector to find and identify surface defects (e.g., a chip-off or spalling) in the lining.

Thermal imaging (Figure I.6) measures the surface temperature in the tunnel interior.

Temperature differences determine information about the state of the lining. The differences can result from various interacting processes between the surface of the lining and the air in the tunnel, such as the following:

- Cooling as a result of water evaporating from the surface;
- The reaction of the lining material during cooling or heating;

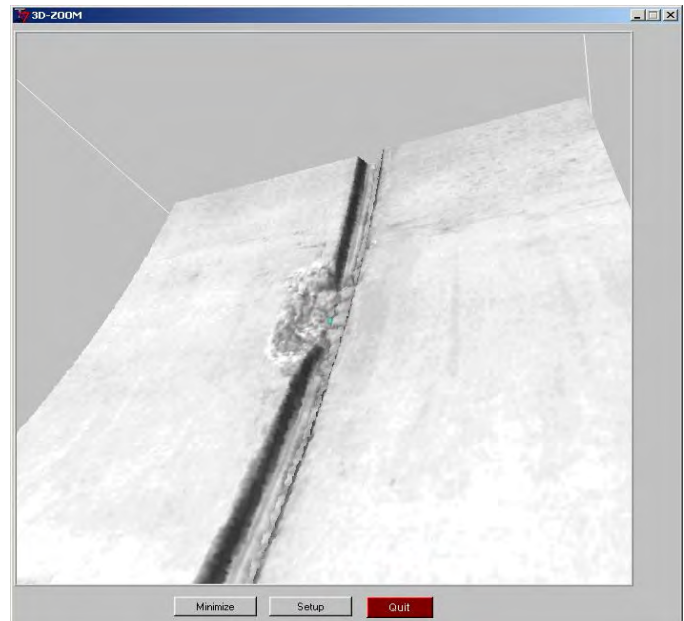


Figure I.5. 3-D view of concrete surface in tunnel with damage (chip-off) near the joint of two sections.



Figure I.4. Structural gauge investigation in motorway tunnel. Red spots indicate obstructions to given clearance profile. Users can determine cut volume and affected area on screen.

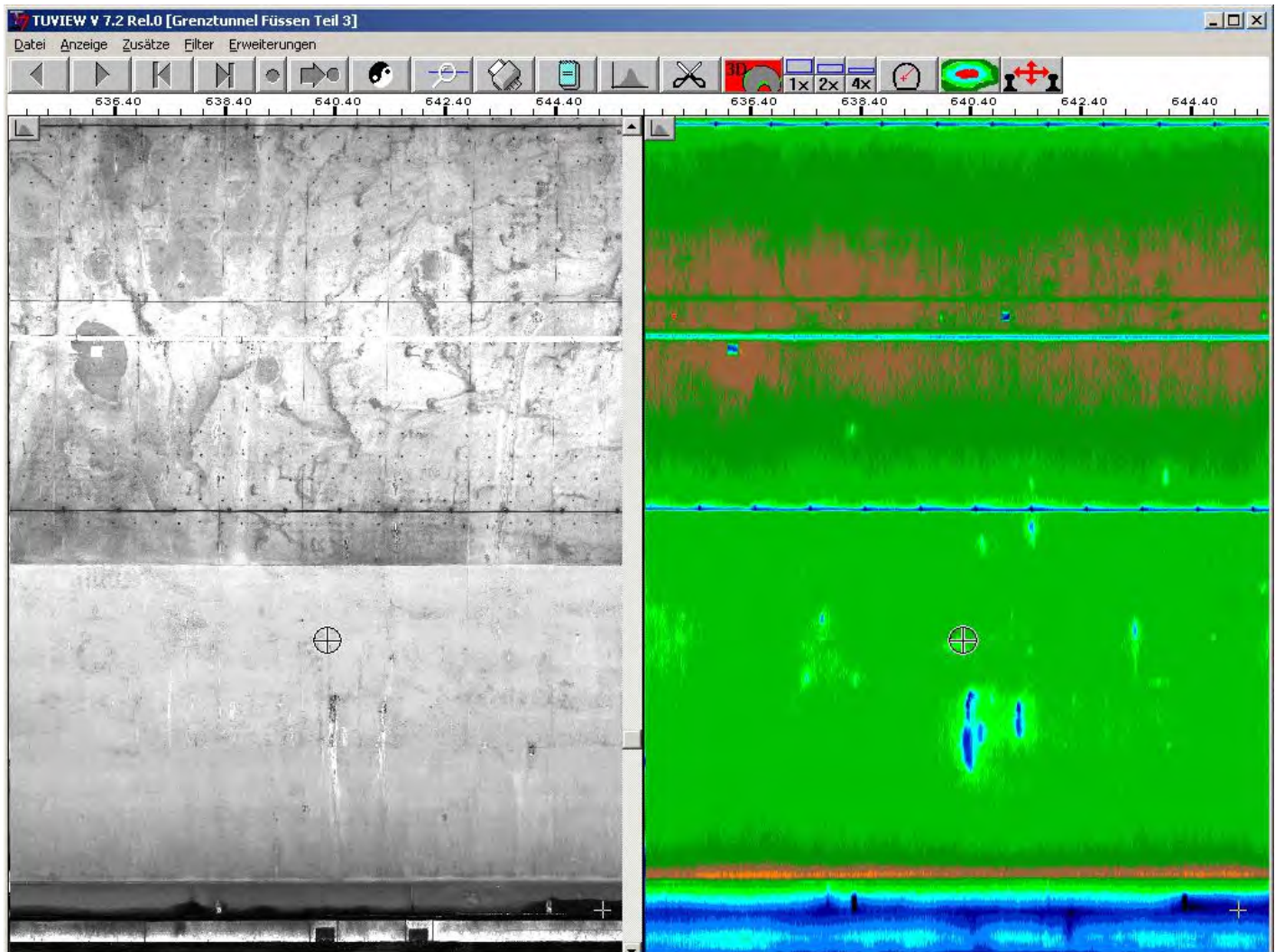


Figure I.6. Example of thermal image showing water infiltration. Water evaporation on the surface yields a clear cold signal. This method marks even smaller water spots clearly.

- The influence of cold and warm temperatures, respectively, at the surface;
- Surface roughness;
- Cavities (gravel nests below the surface, bad contact of the lining to the rock, and gravel rock material); and
- Nonhomogeneous material composition.

Using detailed, known measuring conditions as a comparison, the user can exclude certain thermal interactions and ensure a correct interpretation of the thermal imaging. A quasi-stationary heat flow between the air in the tunnel and the rock behind the lining creates suitable measuring conditions. If the heat-flow conditions are unknown, certain features cannot be clearly identified. Still, the thermographic image displays signals that offer supplemental information to the visual image (see Figure I.6). This information can be used to highlight some effects, like water evaporation.

The premeasurement program used in this project was part of the thermographic survey and evinced proper conditions for the recording. The temperature survey had to be done in a short period because of the constantly changing temperatures in the tunnel. The SPACETEC TS3 scanner system was able to perform such a fast and reliable measurement.

Recording Process

Table I.1 summarizes the data summary from the Chesapeake Tunnel. With the inspection vehicle used for this survey (Figure I.7), the intended driving speed of 1.5 km/h could not always be kept constant (the speed went as high as 3.5 km/h). Therefore, some pixels are stretched in the driving direction. Driving too fast may cause gaps in the laser scan lines at the tunnel wall, which can influence the visibility of cracks. To

Table I.1. Data Summary of the Chesapeake Tunnel

Time of measurement	April 11–12, 2011
Scanning length	1,680 m
Vehicle speed	Approximately 1.5 km/h
Recording channel	Infrared (8–12 μm) 10,000 px/scan Visual 10,000 px/scan Profile 10,000 px/scan
Mirror speed	160 Hz
Temperature resolution	Approximately 0.1°C
Spatial resolution	3 mm by 3 mm at the surface

avoid such problems, a nearly constant speed should be maintained during the survey.

The survey was performed during the night spanning April 11 and 12, 2011. During the survey, a sufficient temperature difference for a quasistationary heat flow was obtained. The TS3 scanner was installed on the roof at the rear of the inspection vehicle (Figure I.7). That placement provided an undisturbed 360° measurement. The highest resolution of 10,000 pixels was used to obtain an appropriate imaging of fine-scale features.

A complete traffic closure was not possible. Thus, the recording was performed twice: once in the north–south direction of the lane to Virginia Beach and once in the opposite lane (south–north) toward the eastern shore of Virginia. Traffic could pass the inspection vehicle, as is visible in the recordings.

Description of Results

Data Processing

The recorded data were corrected for geometry, and the 360° display of the tunnel was projected with a defined scale onto a plane surface (Figure I.8) for a synchronous display of all three channels: visual, thermal, and 3-D.



Figure I.7. Inspection vehicle in Chesapeake Tunnel.

One lane was recorded in the north–south driving direction, and the second lane was recorded in the opposite (south–north) direction. Figure I.8 is labeled with the corresponding driving direction (south or north) and with an absolute true-scale location in meters. Common artificial installations like hand rails, air ports, and electrical and maintenance installations are highlighted. They are clearly visible in both data channels. The cement conduits behind the ceramic tiles are only visible in the thermal image and correlate with information from the construction plans of the tunnel.

A full data set comprised visual, thermal, and 3-D channels and was formatted and edited to evince a true-to-scale display, labeled with a meter range (a change in feet was also possible, if needed). The thermal data were corrected by the commonly existing air temperature drift along the tunnel axis. After leveling, thermal data were displayed with a constant air temperature. Therefore, the same phenomena were displayed with the same colors. The data interpretation was based on local temperature differences (anomalies); thus, an absolute temperature was not needed.

Every thermographic surface point corresponded to a color-coded temperature interval with a temperature resolution of 0.1°C (Figure I.9) and 16 colors ranging from black through blue, green, red, and yellow to white. This color palette gave an intuitive physiological impression of cold (dark to blue) and warm (red to white) temperatures.

Figure I.8 highlights the most common installations in the dataset, which could mainly be ascribed to artificial origins, such as the following:

- Fresh and exhaust air ports and corresponding swirled air;
- Hand railings, niches, and supply boxes installed in the lining wall;
- Traffic lightings and signs; and
- Tubes behind the lining, visible in the thermal image.

Visual Results and Distance Measurements

Since opening in 1964, the Chesapeake Tunnel has been exposed to strong environmental effects such as exhaust gases from traffic, corrosion, and water intrusion. In general, the visual damages are easy to identify and are self-explanatory. Figure I.10 displays split and dirty ceramic tiles, which are the main concern.

Not only are profiles important for clearance considerations in the railway sector, the distance measurements can also be used to characterize damage. The dimensions of the damaged areas can be easily worked out.

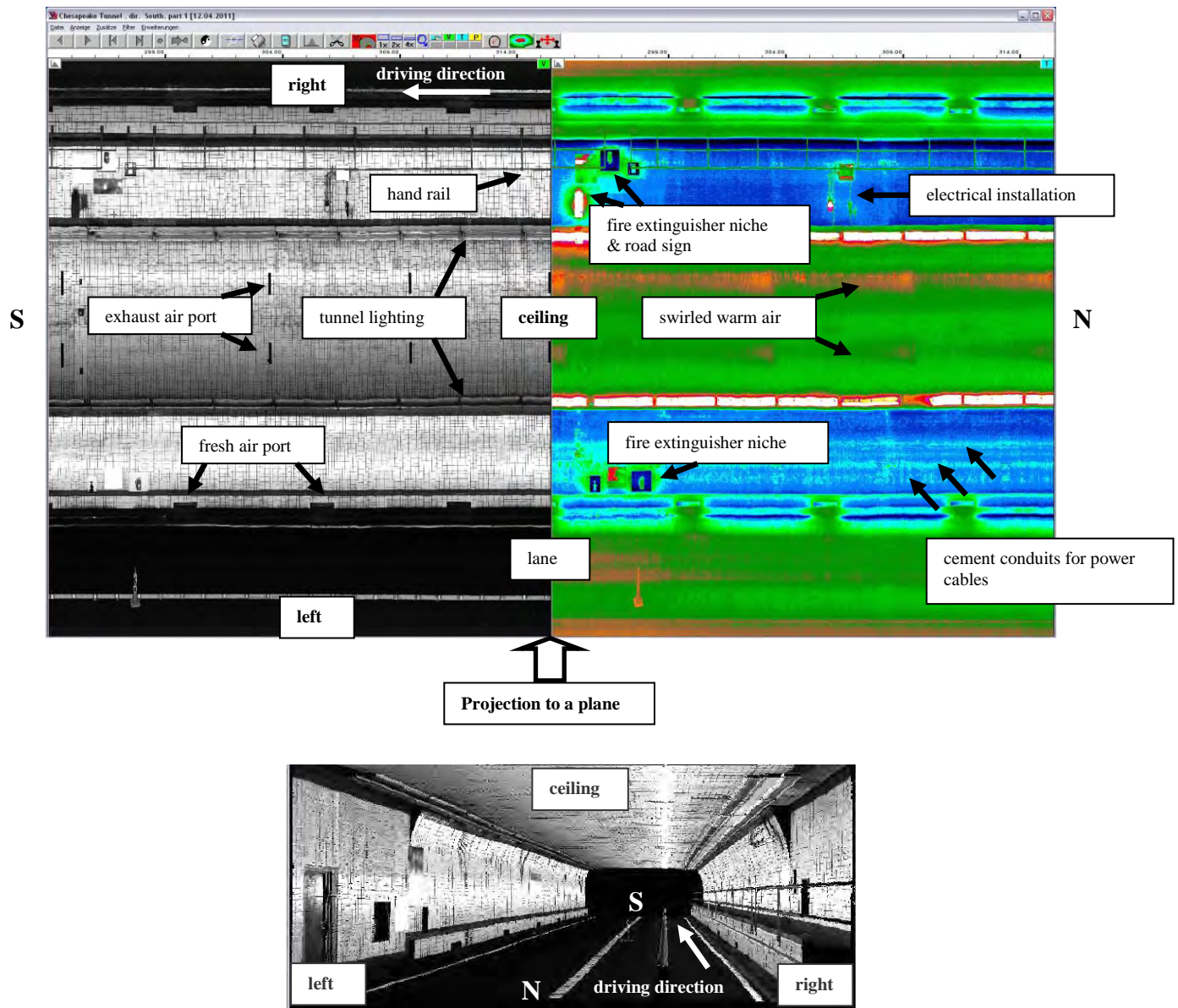


Figure I.8. Perspective view (bottom) demonstrates projection of cylindrical-shaped tunnel onto a plane (top). Top panel displays true-scale projected tunnel with a visual (left) and thermal (right) channel from an interior view. Both synchronized channels show same location and same content with different data sets.



Figure I.9. Color scale for thermographic images.

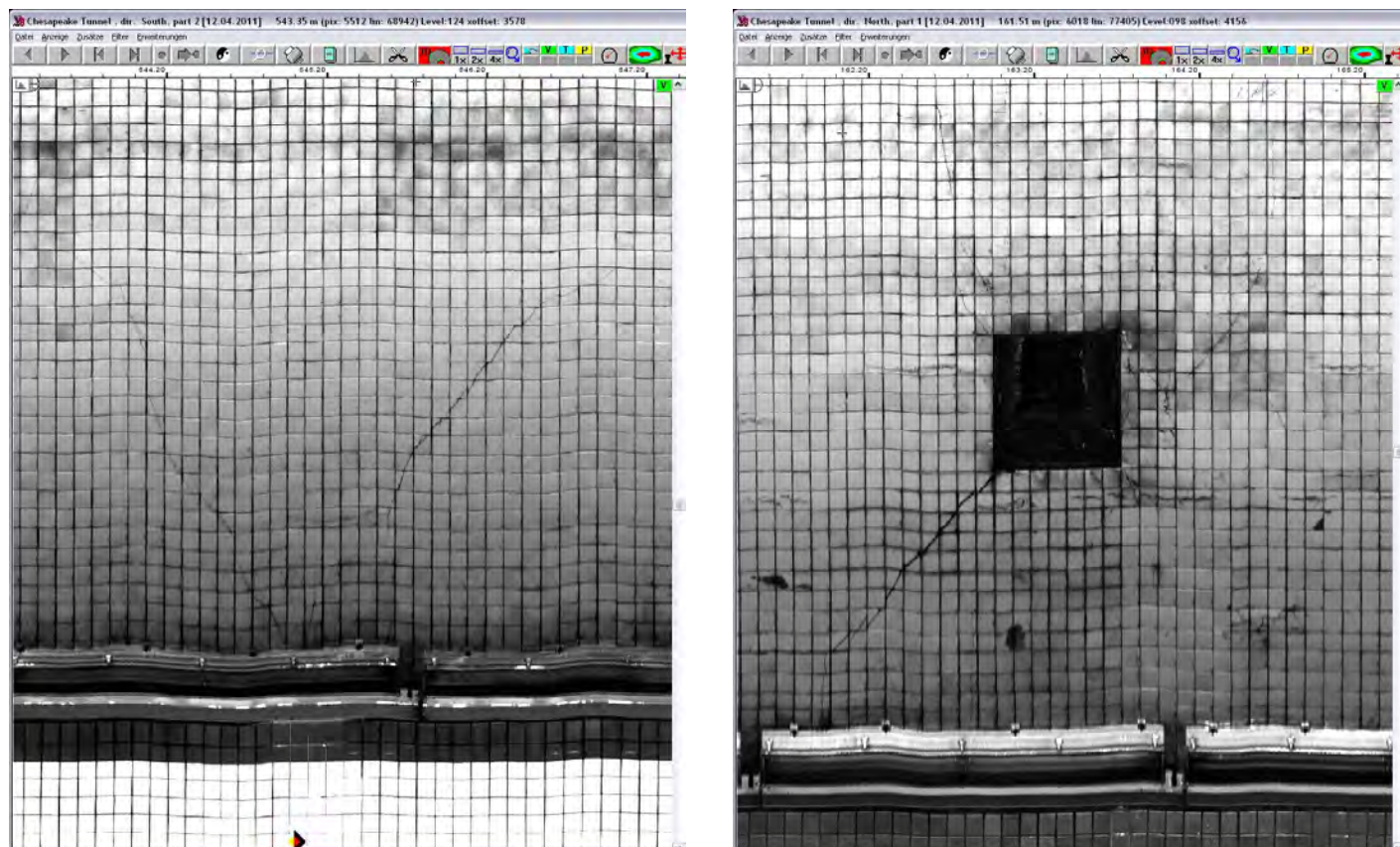


Figure I.10. Development of split ceramic tiles: south, 544 m (left); north, 163 m (right).

Figure I.11 shows one common type of damage—broken or missing tiles—which is clearly evident in the visual channel (upper left). A perspective view of the area (A, lower left) displays more details and is useful for damage assessment. A distance profile (B, lower right) helps estimate the dimensions of the disruptions or highlight artificial installations like emergency lighting. Thermal images usually show a clear cut in the outer rim of disruptions. In this case (upper right), the right side is positioned in the wind shadow and is cooler (darker blue), and the left side is exposed to the warm, lighter air flow coming from the right side of the image. In the area directly ahead and 90° to the side of the detector, the sensor is overmodulated, and the intensities of the reflected signal are high, which is highlighted by an intense horizontal stripe in both channels.

The loose and broken tiles are mainly located on the ceiling of the tunnel (Figures I.10 and I.11).

Classification of Thermal Anomalies

Thermal images consist of a thermal conduction from the tunnel interior into the rock. This determines the qualitative correspondence to the nature of the heat source, as shown in Table I.2.

Some local temperature anomalies can be explained by construction factors, for example, air swirls resulting from obstacles (road signs and traffic lights), niches (which can be recognized in visual images), and tubes behind the linings.

Detailed analysis and interpretation of the data were applied interactively on the screen. Visual and thermal images were analyzed simultaneously to figure out some correspondences between temperature-related patterns and visible construction. The color-coded temperatures and the color resolution were adjusted to the specific temperature anomaly to improve the visibility of the objects.

The Premeasurement Program

A pretesting unit was installed in a fire extinguisher niche 250 m from the western portal (Virginia Beach). The unit could not be installed at the place with the worst-case conditions for thermal measurements in the middle of the tunnel because the distance for data transfer through a cable to the next telephone plug would have been too long.

The premeasurement program was used before and during the recording of the thermal image. It allowed for advanced determination of the time and weather conditions that would be favorable for the purpose of the survey. It documented the

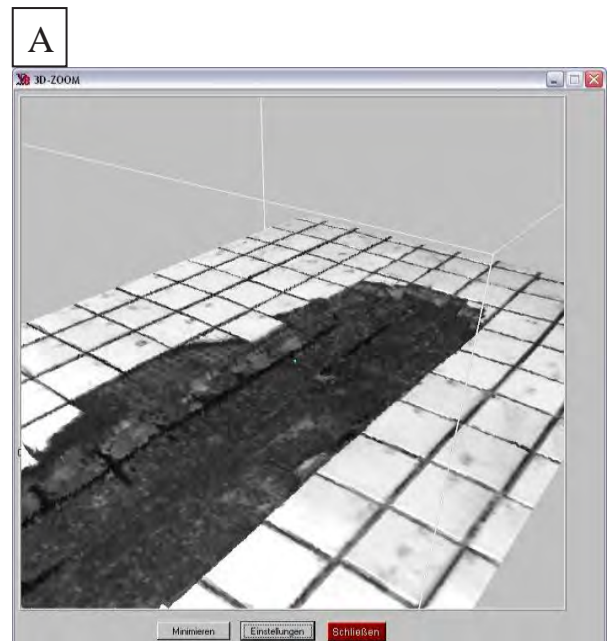
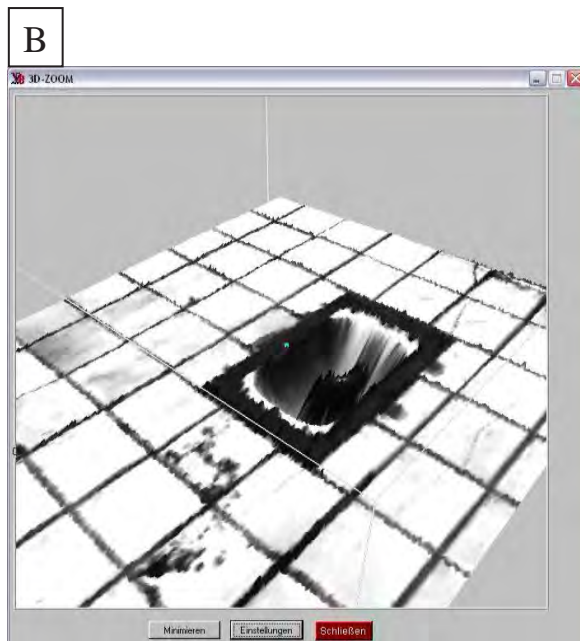
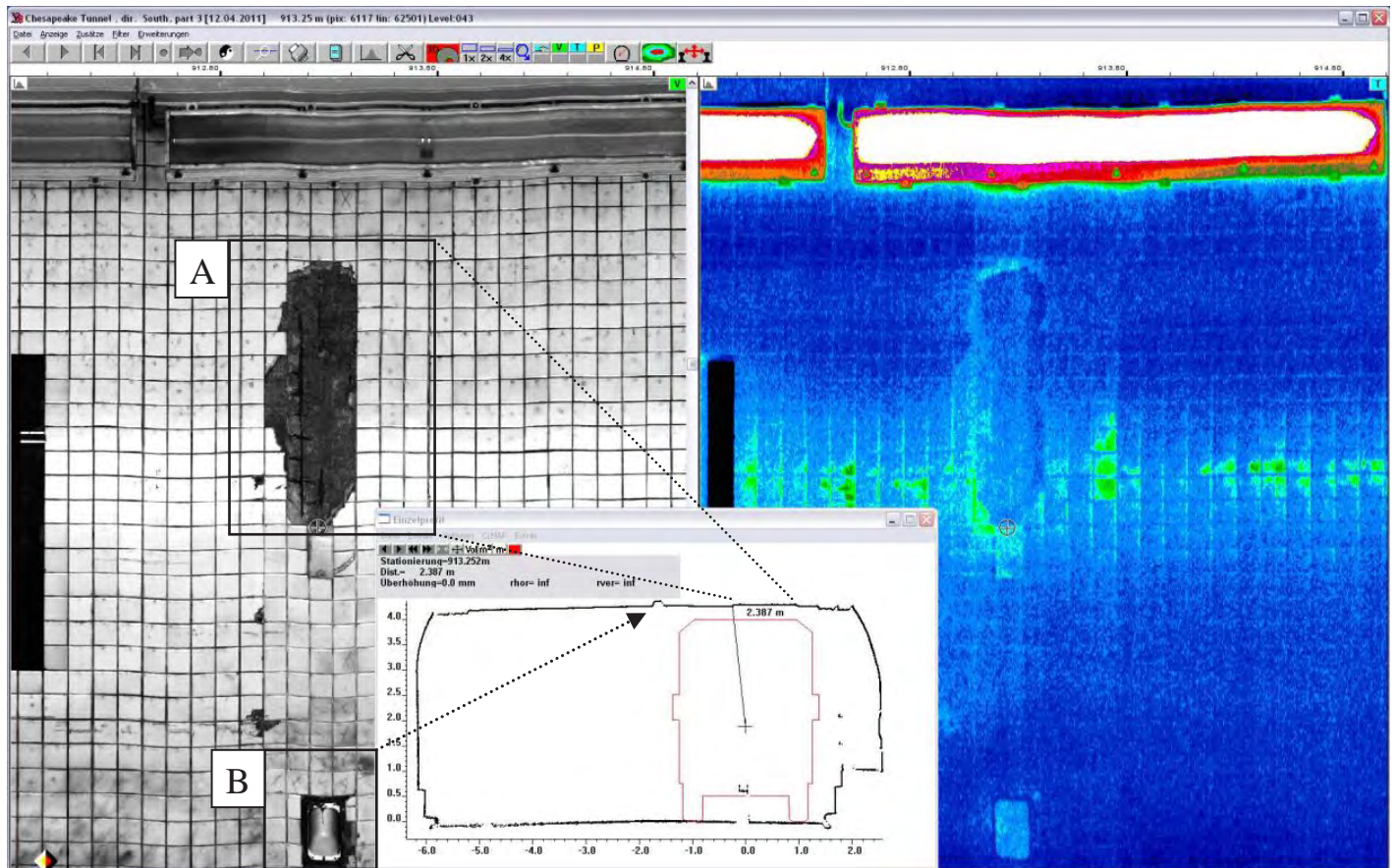


Figure I.11. Views of broken or missing tiles.

Table I.2. Dependency Between Temperature Anomaly and Heat Conduction

Anomaly	Thermal Conduction	Possible Reasons
Cold	Better	Good thermal contact between rock and lining: <ul style="list-style-type: none"> • Water in lining • Higher density of the material
Warm	Worse	Bad thermal contact between rock and lining: <ul style="list-style-type: none"> • Loose, less lithified rock • Lower density of the material • Higher porosity, hollow spaces

required heat flow conditions during the thermal measurement between the lining and the rock to resolve and interpret patterns of heat anomalies.

Temperature sensors were placed in the target structure. One sensor measured the air temperature, the second sensor measured the material temperature near the surface at a depth of 0.075 m, and the third sensor measured deeper depths of 0.3 m. The data logger (master) read and permanently stored the temperature recordings (usually one record per hour) from the sensors (Table I.3). The data could be accessed via telephone line and displayed on the screen (Figure I.12).

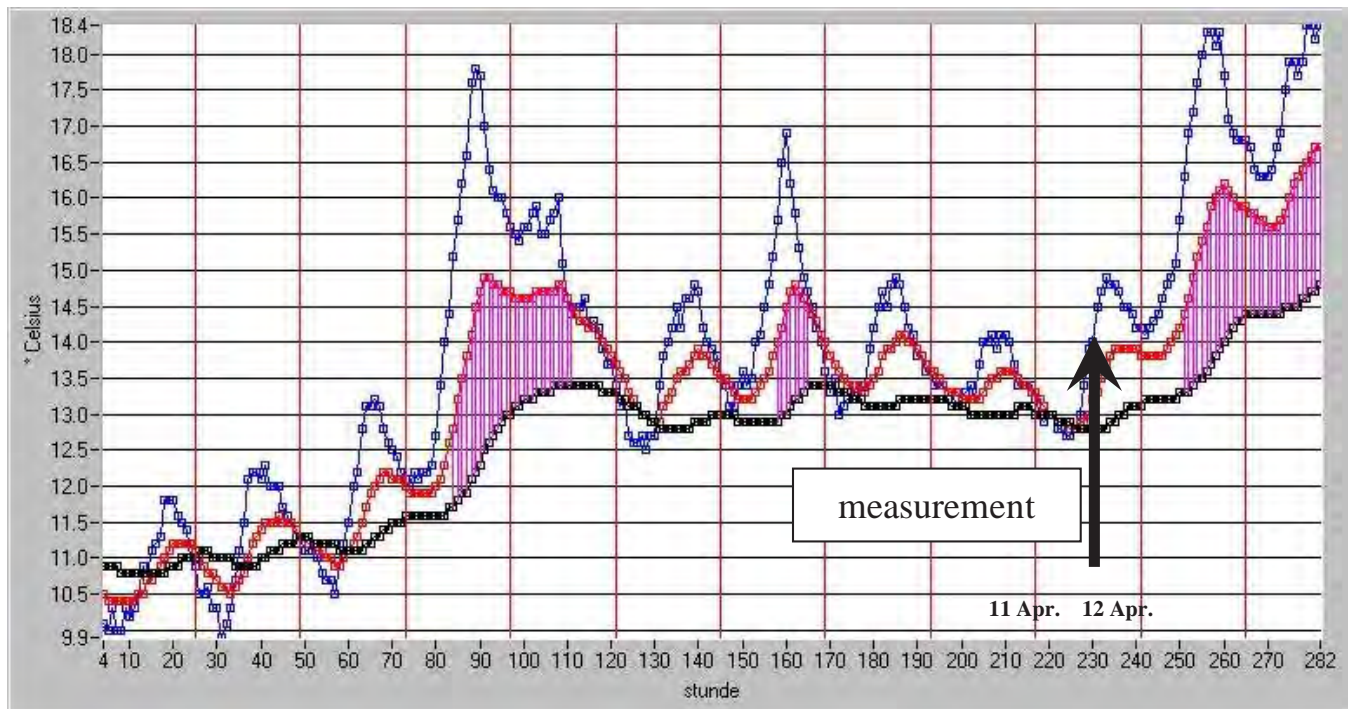
Table I.3. Premeasurement Program in the Chesapeake Tunnel

Location in the Tunnel	Sensor Depth	Remarks
250 m east of the Virginia Beach portal	In front of the lining	Air temperature
	0.075 m into the lining	Temperature difference
	0.3 m into the lining	Temperature difference

Thermal Results

The temperature at the tunnel surface reflected the heat conduction of the lining below the surface. Figure I.13 displays an example of a heat flow under different material conditions with a cavity or wet spots (which are not visible at the surface). The displayed situation is typical for warmer seasons: the air temperature in the tunnel is higher than the rock temperature. The stationary heat flow between the air temperature and the rock resulted in a surface temperature that depended on the heat conductivity of the lining. A cavity reduced the heat conductivity and resulted in a higher surface temperature. Therefore, the tunnel thermography revealed damages in the lining when those damages influenced conductivity.

The quasistationary measuring conditions were adjusted naturally with the corresponding weather conditions and air

**Figure I.12. Temperature alignment before thermographic survey. (Note: stunde = hour.)**

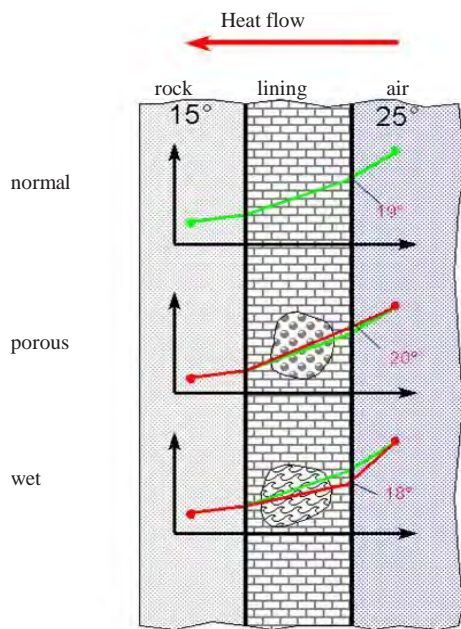


Figure I.13. Dependency of surface temperature on heat conduction of lining material.

temperature when the tunnel had proper air convection—resulting from a chimney effect, caused by different air pressures between the tunnel portals, or from steady traffic. Long-term surveys of other tunnels revealed a number of good measuring conditions during a period of several months.

Figure I.14 displays the effect of the thermal reflections of the installed constructions on the bended corners of the tube. The ceramic tiles seemed to have a higher reflectivity in the infrared spectrum. This is uncommon for concrete or brickwork tunnel linings. Figure I.15 shows the direction of flow of warmer air from the port in the tunnel ceiling.

Figure I.16 reveals some linear structures behind the lining of a side wall, which is referred to as drainage channels with lower heat conductivity and higher temperatures. This indicates that the building documentation needs to be reviewed before further investigations.

In the overall length of the tunnel, several temperature-related anomalies were detected (Figure I.17). Some of the larger temperature anomalies could not be ascribed to artificial sources. The thermography displayed a center with lower temperatures (higher heat conductivity) surrounded by a rim of higher temperatures (lower heat conductivity). The origin of these anomalies was unknown. Figure I.18 displays a common feature that was visible in both the visual and the thermal

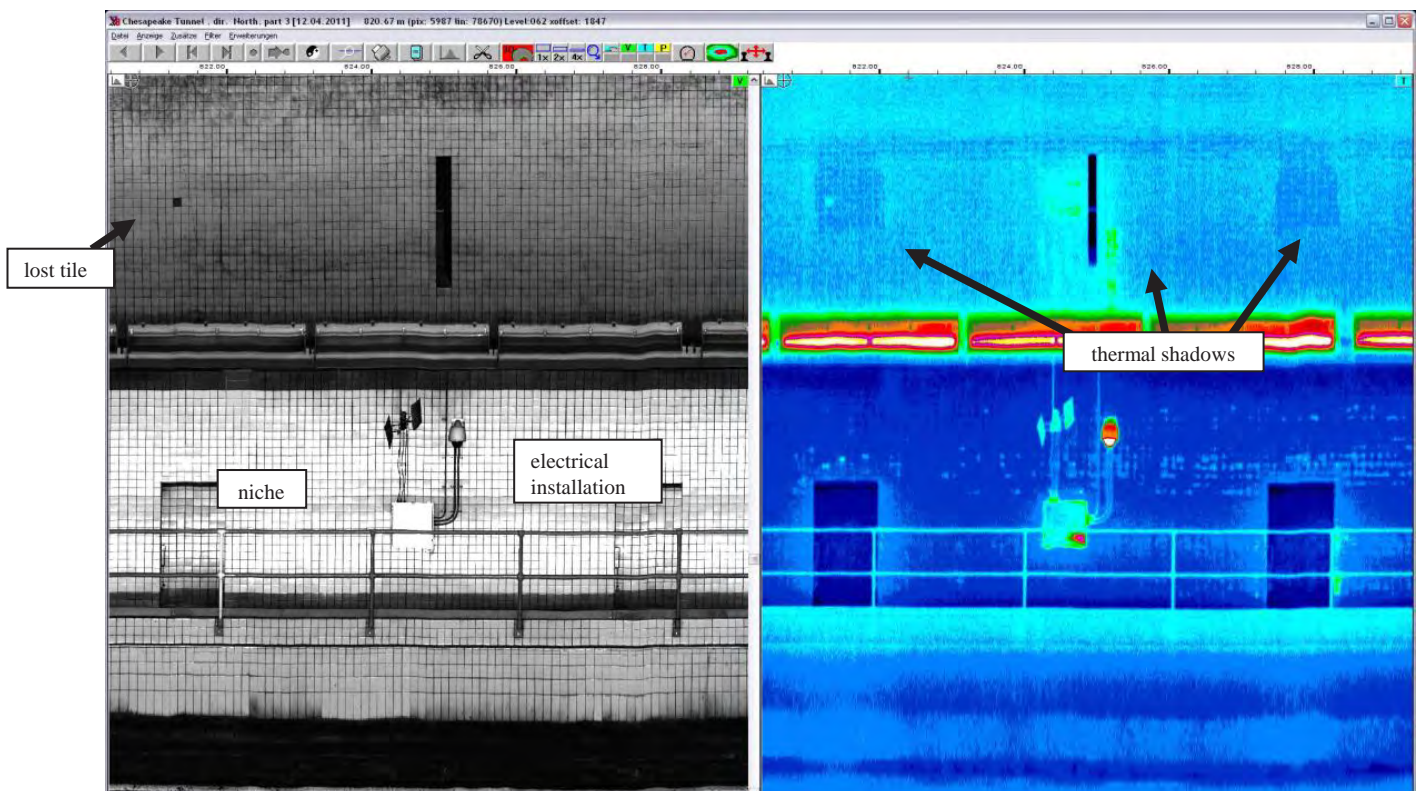


Figure I.14. Thermal shadows of installation. Ceramic tiles have higher reflectivity in infrared spectrum (north, around 825 m).

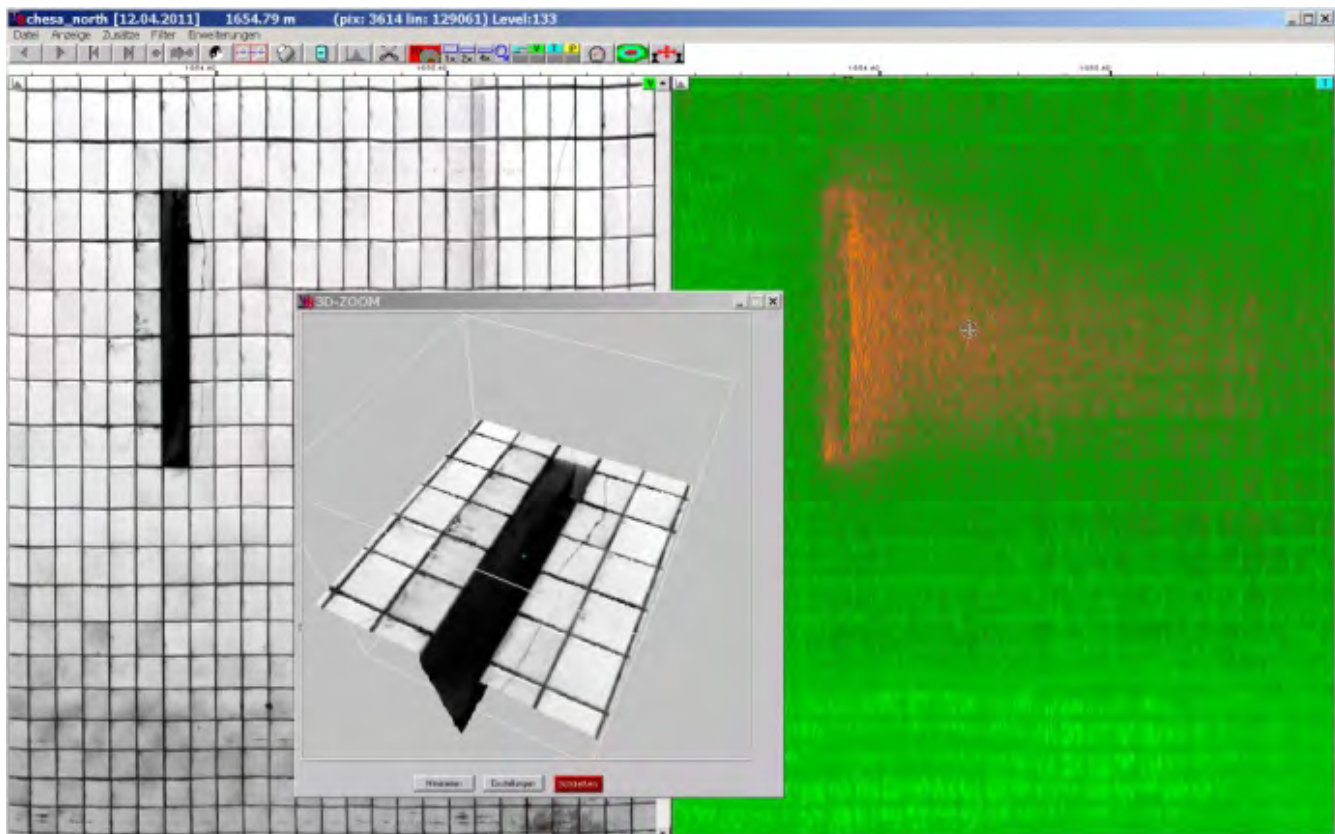


Figure I.15. Air flow from port in tunnel ceiling. Warmer air flows in right-side direction, clearly visible in thermal image (north, 1,654 m).

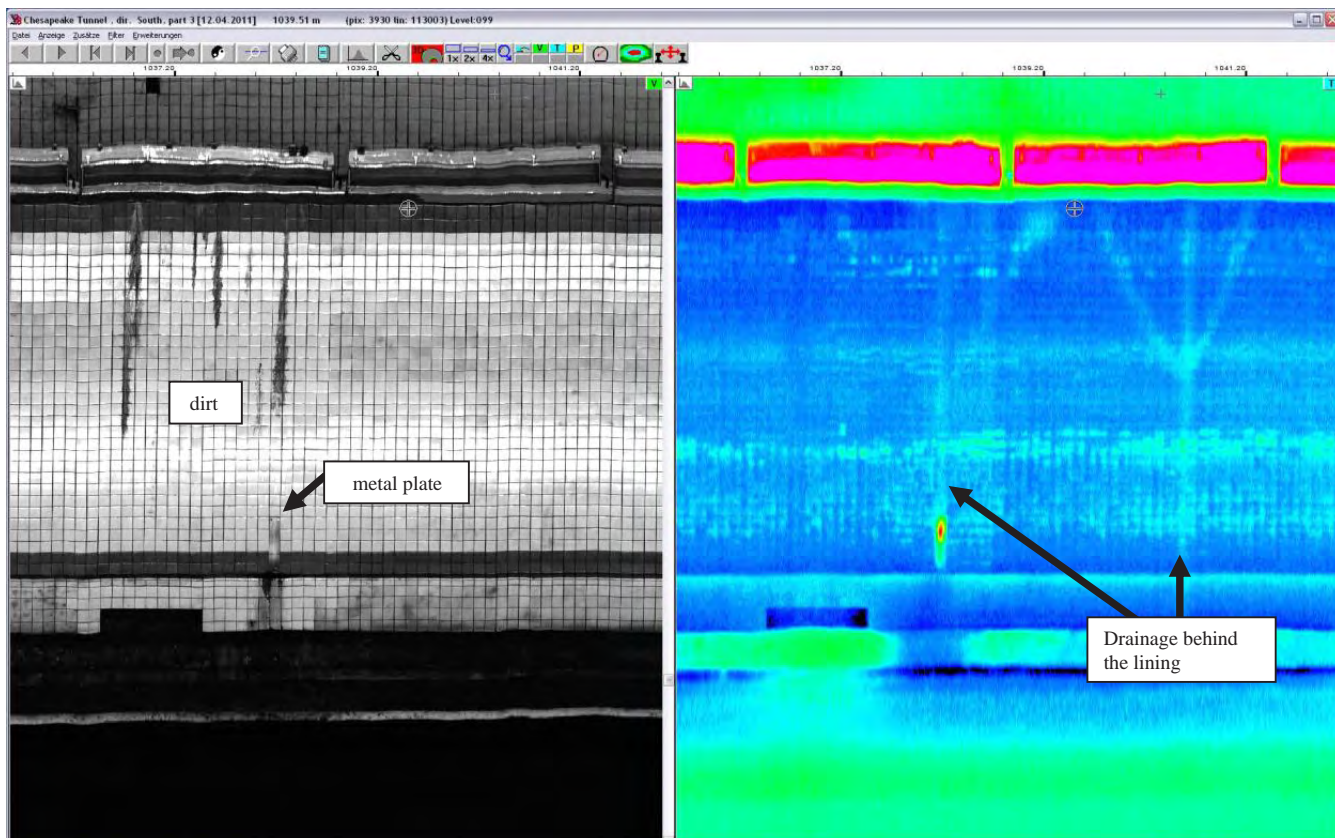


Figure I.16. Visible structures at the surface and drainage behind lining surface (south, 1,038 m).

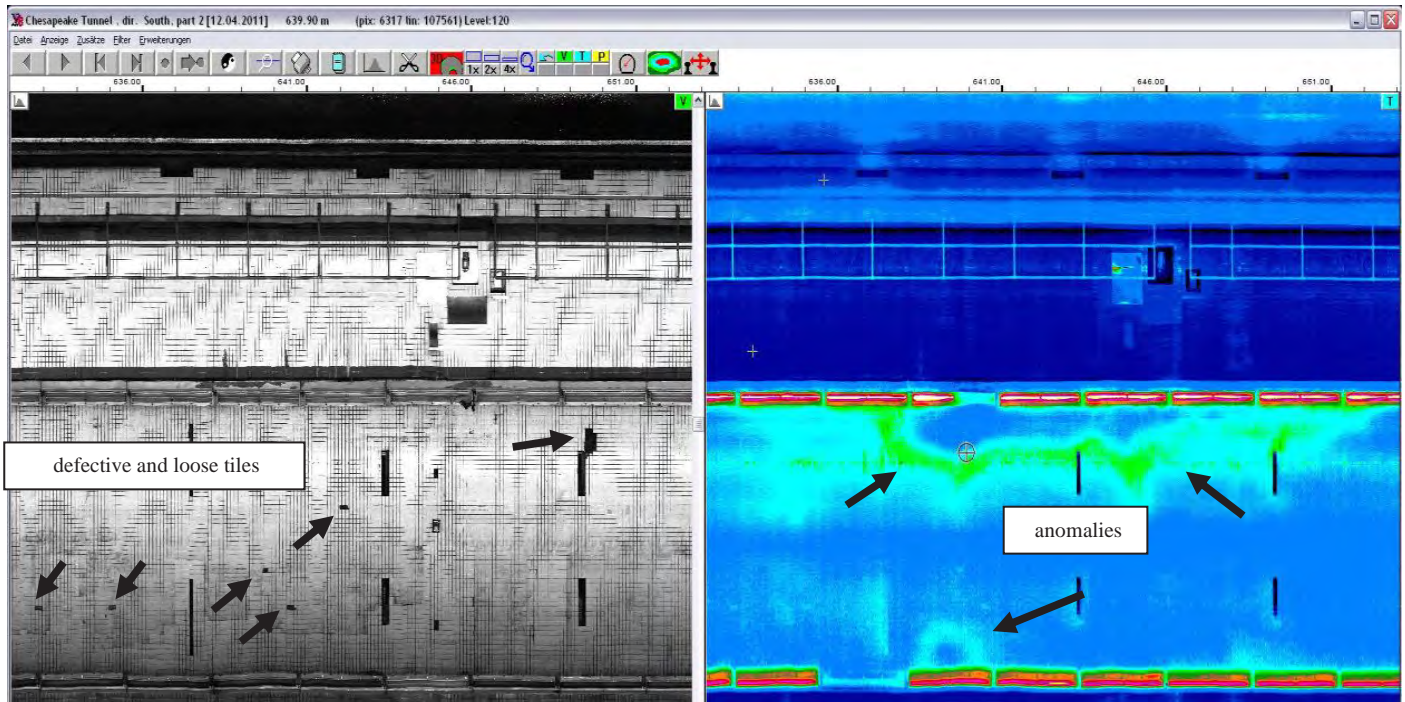


Figure I.17. Loose tiles (left) and warmer temperature anomalies (right) in ceiling area (south, 636–652 m).

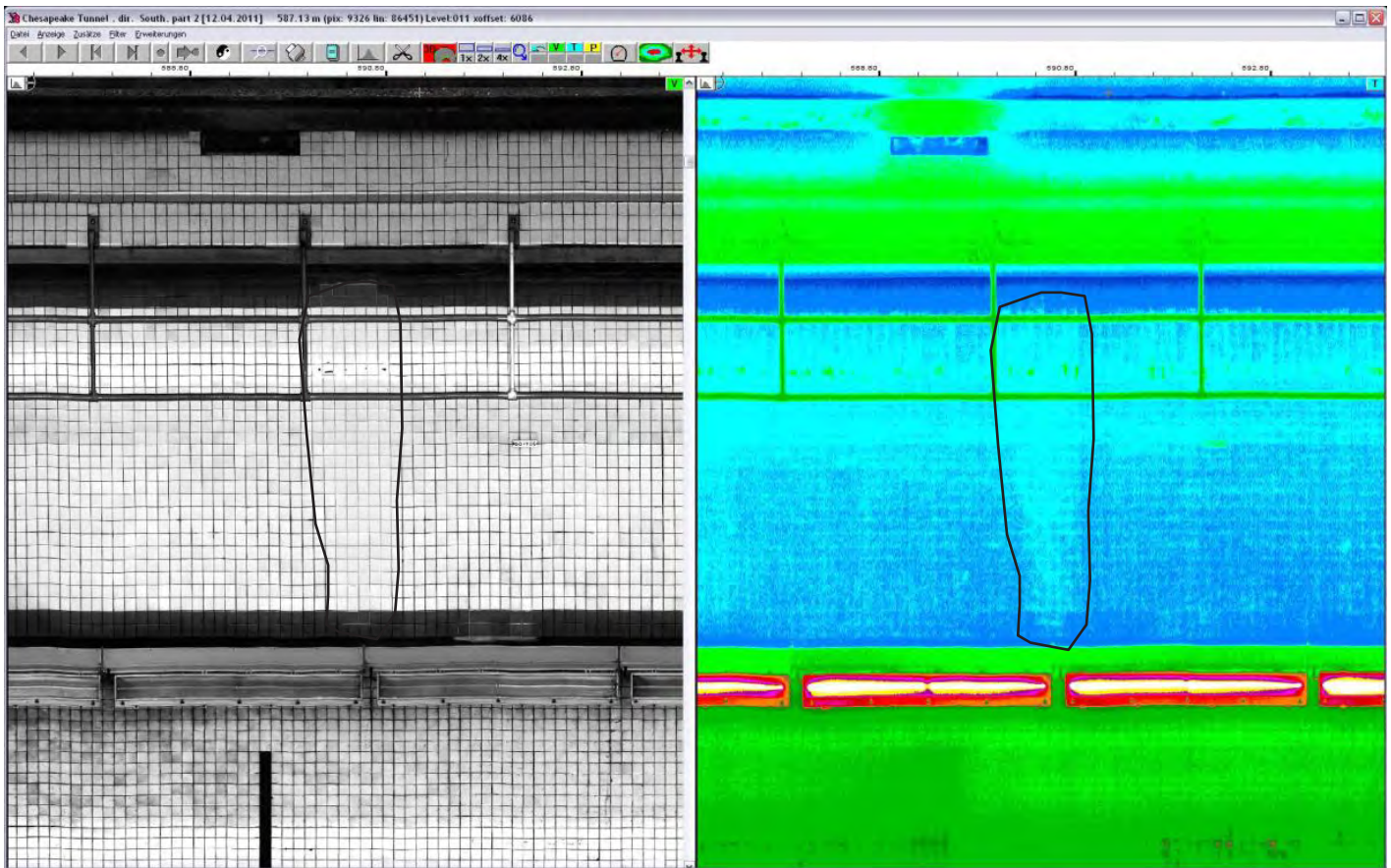


Figure I.18. Renewed tiles with different, compacted material (south, around 675 m).

datasets: joints between the tiles showed a different reflectivity, which seemed to indicate renewed ceramic tiles.

The main findings in the thermographic data set were these:

- Cable channels and drainage tubes behind the linings with lower heat conduction;
- Areas with lighter tile joints, maybe renewed or repaired tiles, with different materials and lower heat flow at the side walls; and
- Areas with larger anomalies behind the ceiling walls.

The thermographic images did not always make clear exactly what was behind a surface. Therefore, further investigation was necessary to determine the reasons for the weak points in the lining.

Working with the Data

The software package TuView was the tool used to analyze and display the data sets of the corresponding three channels. Data access was provided by information files containing the specifications for the image files as well as the true-scale information.

TuView offered the ability to highlight zones of interest with different color codes. The information was saved in notebook files, which were delivered with the report. The notebook files were separated into the following categories: blue, indicating artificial installations like road signs or traffic lights; red, indicating damaged areas (loose and broken tiles); and green, indicating anomalies of unknown origin.

APPENDIX J

Tunnel Tests in Finland 2010–2011

Introduction

A significant component of SHRP 2 is research and development of innovative, high-speed, nondestructive testing and evaluation technologies that promise to accelerate design evaluations and construction inspection for highway renewal projects. One of these research and development projects has focused on nondestructive testing (NDT) of highway tunnels (SHRP 2 Renewal Project R06G).

Tests in Finland have concentrated on the technical feasibility of ground-penetrating radar (GPR) air-coupled antenna (horn antenna) systems, thermal cameras, and laser scanners, as well as their integrated analysis, for tunnel lining condition monitoring. The idea is to test whether these systems can provide reliable and repeatable data and to collect information on the potential sources of error in these techniques. Another goal for these tests is to provide basic information on the potential defects, such as moisture problems close to the surface of tunnel linings. Because all the basic test instruments (GPR, thermal cameras, laser scanners) and survey vans that can be used for the tests are located in Finland, these tests were carried out in two tunnels in the Helsinki area in Finland. The tests were done for the SHRP 2 R06G project by Roadscanners Oy, in cooperation with the Finnish Transport Agency.

Tested Techniques

Ground-Penetrating Radar Technology

The GPR method is based on the use of radio frequency electromagnetic waves with a frequency range from 100 MHz to 5,000 MHz. Physical parameters of the medium affecting the GPR waves are conductivity, dielectricity, and magnetic susceptibility.

Impulse radar is the most popular GPR type. Its working principles are as follows. A short electromagnetic pulse, generated in a transmitter antenna, is sent into the medium. The length of the pulse ranges from less than a nanosecond to tens

of nanoseconds, depending on the frequency. Part of the pulse energy is then reflected from different structural surfaces with different electrical properties, and part of the energy is propagated through the interface and reflected from interfaces beneath. The signal attenuation depends on the geometric attenuation, signal scattering, reflections, and thermal losses. The two-way travel time and reflection amplitudes are recorded with a receiver antenna. Measurements made rapidly over sequential survey points can be viewed as a GPR profile.

The depth penetration of ground-penetrating radar depends on the antenna frequency, that is, the signal wavelength. With higher frequencies, the signal attenuation is greater and the signal depth penetration is smaller. However, the resolution improves.

GPR antennae can be divided roughly into two categories: air-coupled antennae (see data example, Figure J.1) and ground-coupled antennae. These in turn can be either monostatic, in which the same antenna acts as a transmitter and a receiver, or bistatic, in which transmitter and receiver units are different antennae. Most pulse radar antennae are bistatic, but the antenna elements are contained in a single box. The frequency of the ground-coupled antennae ranges from 80 MHz to 2,500 MHz. Their advantage compared with air-coupled antennae is better depth penetration. Ground-coupled antennae have better resolution of individual objects; but with ground-coupled antennae, surveys are done considerably slower.

The point of the tests in Finnish road tunnels was to determine whether air-coupled GPR can be used for different types of tunnel lining measurements. Two tunnels were selected to represent different road tunnel types. The first was a concrete tunnel; in the second tunnel the lining was made of shotcrete. The air-coupled GPR system used in these tests was an SIR-20 mainframe with an air-coupled 1-GHz horn antenna, Model 4108, manufactured in the United States by Geophysical Survey Systems Inc. (GSSI) (Figure J.2).

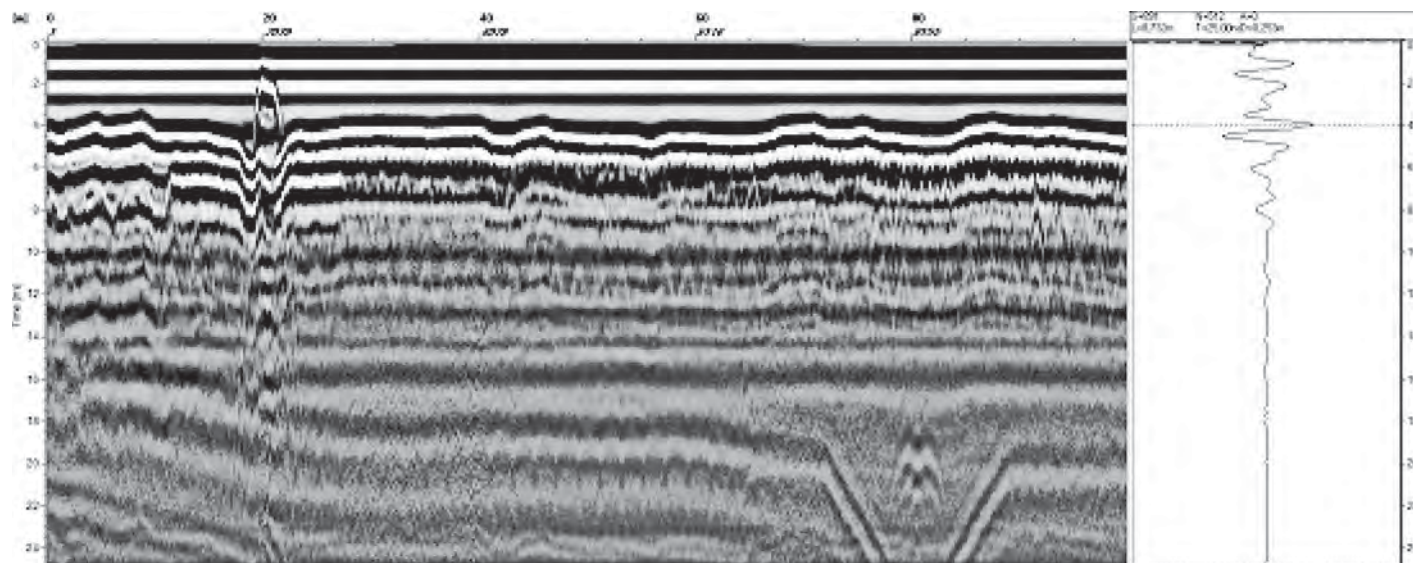


Figure J.1. Example of unprocessed GPR data profile from concrete tunnel wall presented with single scan alongside. Data collected with a 1.0-GHz GSSI air-coupled antenna.

Air-coupled GPR data collection settings were the same as used normally in pavement thickness and quality control surveys. Collected data consisted of 100 scans per meter, 16 bits, and 512 samples per scan. A time window of 30 ns was slightly longer than normally used in pavement surveys. All GPR data processing and analysis were done using Road Doctor Pro software by Roadscanners Oy. The collected data preprocessing was done using standard methods, including automatic air-coupled elevation and amplitude correction, background removal, and vertical time domain filtering. The standard GPR data analysis consisted of reflection amplitude and dielectric value calculations and their analysis.

Thermal Camera Technology

The thermal camera method is based on the use of electromagnetic infrared waves, which means the thermal camera wavelength is located between GPR waves and visual light. Thermal cameras are built to receive and record infrared waves reflected and emitted by objects, thus thermal camera surveys are classified as a nondestructive survey method. Thermal cameras have been used in traffic infrastructure surveys for several decades, but the quality of digital thermal cameras has increased so much that interest in this technology has started to grow. New high-precision thermal cameras

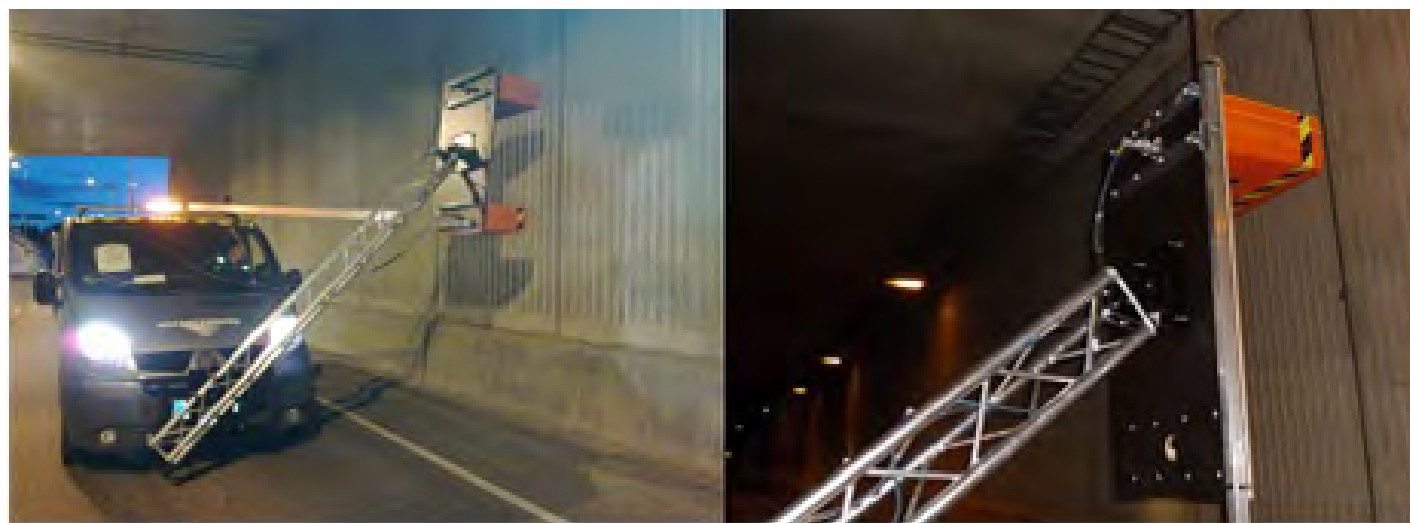


Figure J.2. Survey van equipped with a 1.0-GHz GSSI horn antenna.

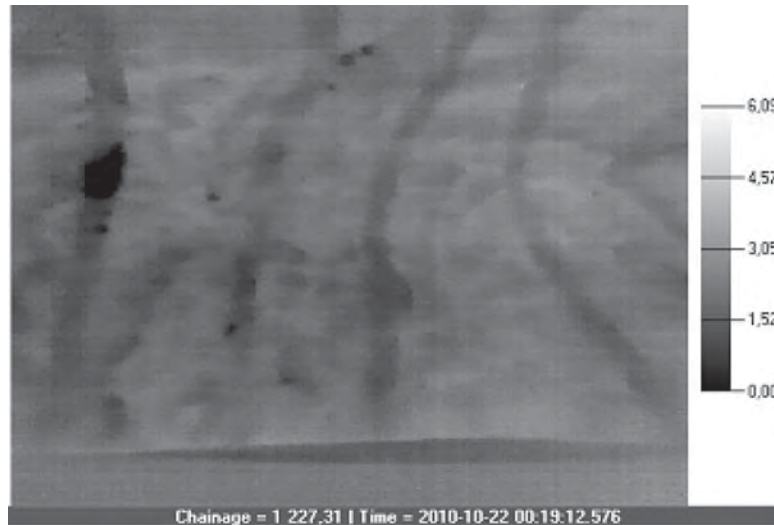


Figure J.3. Thermal video screenshot from Vuosaari Tunnel roof with thermal scale. Darker lines indicate location of drainage pipes beneath shotcrete; black spots are locations of excess moisture.

can measure small changes in surface temperatures, even at the range of 0.05°C . The camera measures infrared radiation with a wavelength of $8\ \mu\text{m}$ to $12\ \mu\text{m}$.

In the SHRP 2 tunnel project, one goal was to test whether and how well digital thermal cameras can detect thermal anomalies in tunnel linings, pointing out areas with moisture, voids, or cracks. A second goal was to test different kinds of data collection and analysis techniques to find an optimal survey method. Tests were done in both a concrete tunnel and a shotcrete tunnel. In this project, the data were collected using a FLIR A325 digital thermal camera made in the United States by FLIR Systems Inc. All thermal data processing and analysis were done using Road Doctor Pro software with the Road

Doctor thermal diagnostics (RD TD) module. Figure J.3 presents a screenshot from the Vuosaari Tunnel roof raw (unprocessed) thermal video data. The screenshot is taken from the RD TD video viewing tool.

The thermal videos were collected using Road Doctor CamLink video equipment made by Roadscanners Oy. In addition to the digital thermal videos, normal digital videos were also recorded. All the collected data were linked to the distance information using CamLink's software synchronization file. In the collected thermal video, the resolution was 320 by 240, and thermal videos were collected using a 60-Hz image frame rate. The device manufacturer declares a $\pm 2^{\circ}\text{C}$ or $\pm 2\%$ accuracy for the thermal camera. Figures J.4 and J.5



Figure J.4. Thermal camera installed on van roof in first measurement.



Figure J.5. Thermal camera installed on end of beam behind van.

present examples of FLIR thermal camera mounting systems used on the survey van. The mounting system presented in Figure J.5 was judged to be better because an analysis of the data indicated that it reduced the thermal reflection of the van, which was causing noise in the data.

Laser Scanner Technology

As with GPR and thermal camera techniques, laser scanner techniques also apply electromagnetic waves. With laser scanning, the distance measurement is based on the laser beam travel time from the scanner to the target and back. In recent years, the greatest advancements in all NDT techniques used in infrastructure surveys have been made in the field of laser scanner techniques. These systems will inevitably become the standard tools for a variety of tasks in traffic infrastructure condition management systems.

A laser scanner has three parts: a laser canon, a scanner, and a detector. The laser canon produces a laser beam, the scanner circulates the laser beam, and the detector measures the reflected signal and defines the distance to the target. The distance measurement is based on the travel time of light or phase shift or a combination of both. The quality and price of mobile laser scanner survey systems vary, but they can be roughly classified into two categories: effective high-accuracy systems (Category A), and cheaper systems with reduced distance measurement capability and accuracy (Category B).

The goal in the laser scanner tunnel tests was to test whether the method could provide valuable information concerning the tunnel lining condition and shape. The Category A laser scanner data were collected by GEOVAP Ltd., from the Czech Republic, using the company's quantum three-dimensional (3-D) technique based on Lynx laser scanner hardware. The GEOVAP survey vehicle and equipment are shown in Figure J.6. Data analysis and all presentations done by GEOVAP used the



Figure J.6. Category A laser scanner survey system used in this research.

company's own software. The Category B laser scanner data were collected by Roadscanners Oy using a model SICK LMS151 laser scanner. The survey van equipment is presented in Figure J.7. The data analysis was done with a new Road Doctor laser scanner module, which is an additional module for the Road Doctor Pro software. The module facilitates integrated analysis of the laser scanner data and other survey data in Road Doctor Pro software.

When the laser beam angle is known, as in the setups described above, and beams are sent in different directions from a moving vehicle with a known position, it is possible to make a 3-D surface image—a point cloud—of the road and its surroundings. A point cloud can have billions of points with accurate x, y, z coordinates and reflection or remission characteristics. Since all points have coordinates, it is possible to measure distances between points and changes between those distances. This gives extra value to tunnel management tasks, for instance,



Figure J.7. Category B laser scanner mounting systems used in this research.

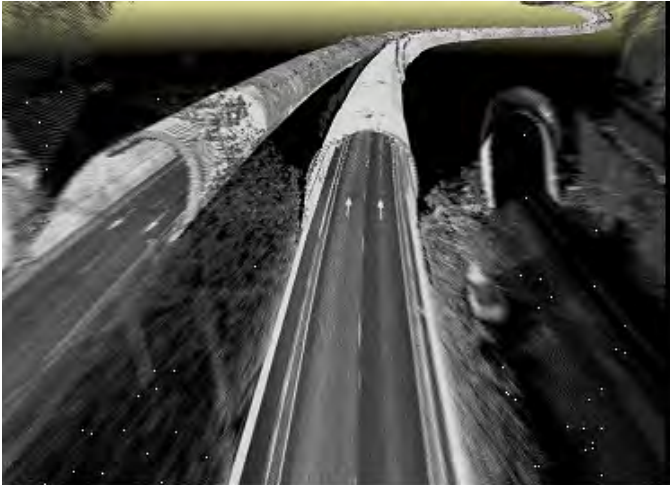


Figure J.8. Three-dimensional surface image of road tunnel produced from Category A laser scanner data (Vuosaari Tunnel mainland opening).

changes in the position of a tunnel lining after an earthquake. For these high-accuracy x , y , z tasks, Category A laser scanner systems are needed. An example of a point cloud view of the Vuosaari Tunnel mouth area is shown in Figure J.8. The accuracy of the laser scanner survey can be reduced by different factors that affect visibility, such as dust, rain, fog, or snow.

SICK laser scanners measure the distance to a reflective objective, as well as the amplitude of reflection, that is, remission. The reflection varies for different materials, textures, and colors; for instance, changes in moisture content in a shotcrete tunnel wall can be detected using the laser scanner remission analysis method. Information from the Category B laser scanner data collected in this study was analyzed in this way. Figure J.9 presents a reflectivity image produced from the Vuosaari Tunnel roof.

Finnish Test Tunnels

Two test tunnels were chosen for this research project in cooperation with Roadscanners and the Finnish Transport Agency. The selected tunnels represent common types of

tunnels in Finland, which are also common in the United States. Both tunnels are located in the Helsinki area of southern Finland. The first test tunnel, called Hakamäentie Tunnel, is a concrete tunnel; the second test tunnel, the Vuosaari Tunnel, is built in igneous bedrock under a sea bay and has a shotcrete surface structure. The tunnels are part of the Finnish public road network and are owned and maintained by the Finnish Transport Agency.

Hakamäentie Tunnel

The Hakamäentie Tunnel, which opened in 2009, is located in the Helsinki City area of Kivihaka. The 320-m long tunnel was built to alleviate traffic jams on the Hakamäki road and consists of two tubes, each with two lanes of traffic flowing in opposite directions (Figure J.10). Most of the traffic consists of private cars and inner-city heavy traffic. The tunnel walls and ceiling consist of cast concrete block elements (Figure J.11). The tunnel is in good condition, and moisture-related problems have not been detected.

All the data collection was done in the southbound tunnel, mostly along the right-side wall. Because of the traffic volumes through the tunnel, all the measurements were done in a closed lane during the night.

Vuosaari Tunnel

The 1,520-m long Vuosaari undersea tunnel, which opened in 2007, is located in the eastern Helsinki area leading from the mainland to the new Vuosaari port. The tunnel consists of three tunnels—one railway tunnel and two road tunnels, both with two lanes (Figure J.12). The tunnel was excavated through bedrock, and the rock surface was covered using 80 mm of shotcrete with steel fibers. Drainage pipes were installed behind the shotcrete. Between the shotcrete and bedrock are two layers of frost insulation, each 50 mm thick (Figure J.13). Heavy trucks heading to and from the Vuosaari port make up the largest part of the tunnel traffic. The tunnel is mainly in good condition, but some water leakage has been detected recently, especially in the roof.

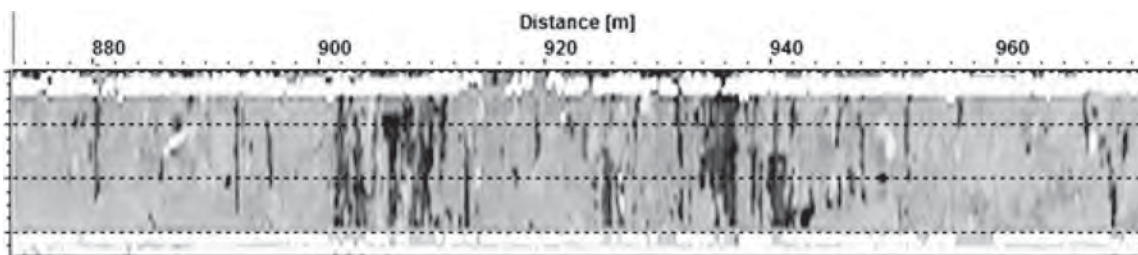


Figure J.9. Remission (reflectivity) surface image from Vuosaari Tunnel roof produced from Category B laser scanner data. Black areas represent areas with higher moisture content in shotcrete surface.



Figure J.10. Hakamäentie Tunnel opening (left) and GPR measurement van in the tunnel (right).

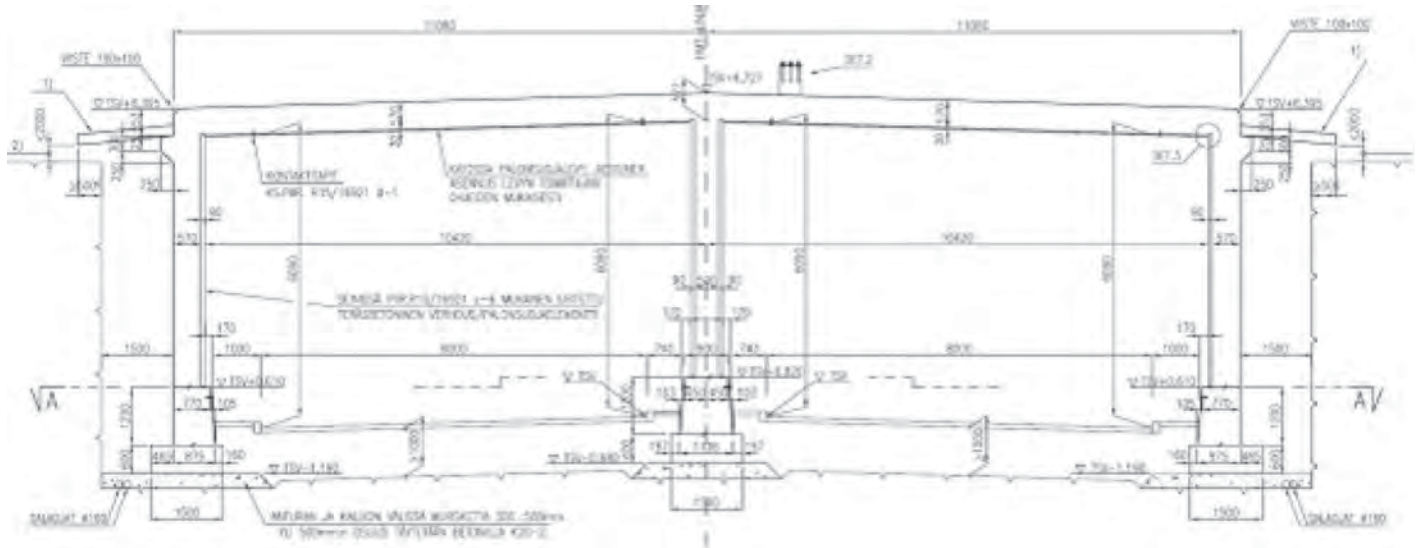


Figure J.11. Hakamäentie Tunnel structure.



Figure J.12. Exterior and interior views of Vuosaari test tunnel. The A-tunnel opening is on the mainland, the railway tunnel is to its right, and the B-tunnel is on the left.

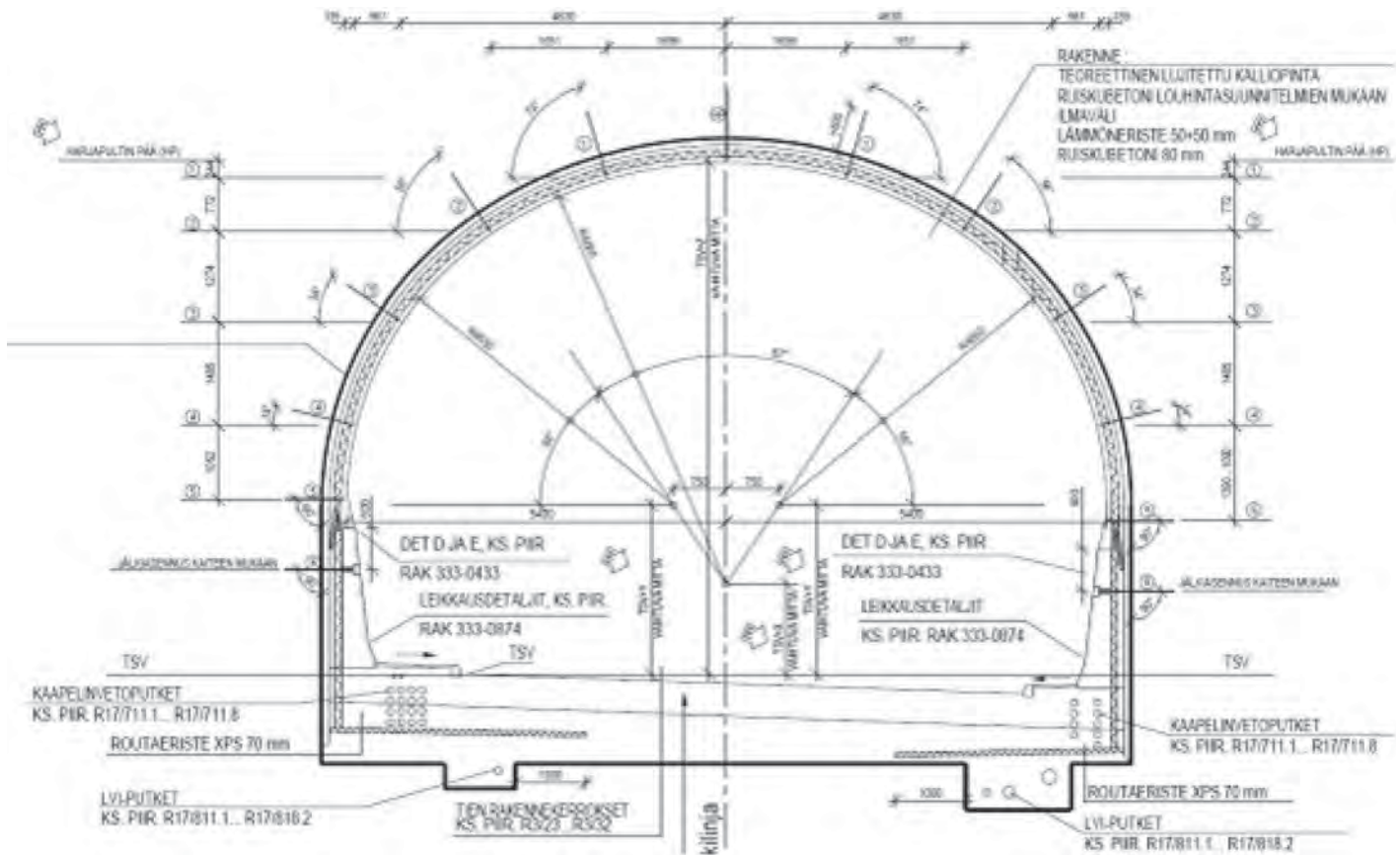


Figure J.13. Vuosaari Tunnel structure.

All the data collection was done in tube A along the right-side wall leading south. Because of traffic in the tunnel, all measurements were done in a closed lane using an automatic lane control system.

Conduct of the Surveys

The survey program consisted of four test trials. The first trial was done to test the data collection technique and procedure in both tunnels, and actual data collection was done in the other three trials. The data collection practice was further developed for each trial on the basis of the experience in the previous trials. Measurements performed and developments in the data collection practice are described below.

Technical Tests, June 2010

Technical tests took place in the Hakamäentie southbound road tunnel in June 2010. The primary goal was to develop GPR measurement techniques and rack systems for air-coupled GPR tunnel measurements (see Figure J.10). The GPR measurements—using two GSSI air-coupled, 1-GHz horn antennae—were performed on the Hakamäentie concrete tunnel walls and roof. Altogether seven survey lines

were measured. GPR tests with GSSI 2.2-GHz antennae were also done, but the results were quite poor because of significant noise in the survey data close to the tunnel mouths caused by a television station nearby. In addition to the GPR tests, short and simple thermal imaging system and laser scanner tests were also performed. The test results provided important knowledge of measurements, and both data collection hardware and software were improved on the basis of the experience.

Fall Tests, October 2010

The second round of tunnel tests with GPR was performed in both the Hakamäentie Tunnel and the Vuosaari Tunnel. Trials took place in October (Week 42) 2010. These dates were chosen for data collection because air temperature and tunnel wall temperature are most likely at the same level in the fall. The right-side wall in both tunnels was selected for further measurements and analysis.

On the technical side of the data collection, the crew tested the new GPR rack system. The system was modified based on the experiences from the first technical tests in June. The new system solved problems with antenna height adjustments. To make the GPR rack system lighter, the second horn antenna

was removed. A rolling beam supported by the pavement surface was added. The new system was more rigid but a bit more difficult to use. With the new rack system antenna, a constant distance between the wall and the antenna was easier to maintain. The GPR measurements in the Hakamäentie Tunnel were made along seven parallel lines on the right-side wall in the southbound tunnel. Data were collected using a single 1.0-GHz horn antenna. Measurements were started at a height of 1.4 m, and each line above that was offset by 0.3 m. The GPR survey in the Vuosaari Tunnel consisted of six parallel lines on the right-side wall in the southbound tunnel. The 1.0-GHz horn antenna was also used. The respective heights of the survey lines were 1.0 m, 1.5 m, 2.0 m, 2.5 m, 3.0 m, and 4.0 m.

Thermal camera measurements were also conducted in both test tunnels. Data were collected at nighttime to minimize the warming effect of the sun at the tunnel ends. Digital thermal videos were recorded in the Hakamäentie Tunnel on the right-side wall of the southbound tunnel. In the Vuosaari Tunnel, thermal data were recorded from the right-side wall and roof in the southbound tunnel. Different data collection speeds were also tested with a thermal camera.

Laser scanner measurements were conducted in both tunnels as well. The laser scanner was positioned as low as possible to obtain coverage as wide as possible. One laser scanner data collection run covered both tunnel walls and the roof. Different data collection speeds were also tested with the laser scanner.

Winter Tests, February 2011

The third round of tunnel measurements was done in the beginning of February (Week 5) 2011. Both the Hakamäentie and Vuosaari tunnels were tested. Surveys consisted of GPR, thermal camera, and laser scanner measurements. Data collection was done using the same technique and procedure as in the previous trial of fall 2010 but, in addition, some new ideas concerning measurement practice were also tested. Some improvements were made to the antenna rack supporting beams and to thermal camera and laser scanner positioning. The main goal of the measurements was to collect data in the winter with air temperatures below 0°C and compare the results to the previously collected fall data.

The GPR measurements in the Vuosaari Tunnel consisted of seven parallel lines on the right-side wall in the southbound tunnel. The first measurement line was at a height of 1.6 m. The second line was at a height of 1.8 m, and the next lines were spaced 0.30 m apart up to 3.3 m. Because of snow and ice at the tunnel mouth, the first section of the tunnel was excluded from the data collection. The GPR measurements in the Hakamäentie Tunnel consisted of four parallel lines on the right-side wall in the southbound tunnel. Measured heights were 1.5 m, 2.0 m, 2.5 m, and 3.0 m. Snow and ice, packed against tunnel wall and road edges, also caused problems for

data collection, so some survey lines measured in the fall tests could not be repeated.

Thermal camera measurements were repeated in the two tunnels. Thermal videos were recorded on the right-side wall in the southbound tunnels. Some problems were encountered with the distance measuring indicator (DMI) due to really slow van speed. This problem was solved before the fourth measurement session. In the early phase of the thermal data analysis, the research team discovered that the thermal emission image of the van reflected from the tunnel wall to the video. To avoid this effect, the thermal camera was mounted on the end of the beam behind the van in the Vuosaari Tunnel.

Laser scanner tests were also improved. Earlier laser scanner measurements provided good results from the tunnel ceiling, but information from the walls' reflection features was limited. To get a better image of the tunnel wall reflectivity, the laser scanner was oriented toward the Vuosaari Tunnel southbound right-side wall. Basic laser scanner measurements were also repeated in both tunnels. Repeated measurements covered the tunnel walls and ceiling with a single measurement.

Summer Tests, June 2011

The fourth and final road tunnel trials were done in mid-June (Week 24) 2011. These surveys consisted of GPR and thermal camera measurements. Measurements were carried out using the same techniques and data collection procedures as in previous measurements. The goal of the measurements was to collect data during the summer when air temperature is high and compare the results to the previously collected fall and winter data. In this survey, tests were also conducted on the effect of data collection speed on the GPR and thermal data quality. An additional goal in the summer tests was to collect GPR horn antenna data at different distances from the tunnel wall to determine possible effects on the data.

The GPR measurements in the Vuosaari Tunnel consisted of four parallel lines on the right-side wall in the southbound tunnel. Measurement lines were at heights of 1.6 m, 2.1 m, 2.4 m, and 3.1 m. The GPR measurements in the Hakamäentie Tunnel consisted of basic measurement lines at heights of 1.5 m, 2.0 m, 2.5 m, and 3.0 m. Additionally, GPR measurement repeatability, measurement speed, and GPR antenna distance from the wall were tested on the tunnel wall at a height of 2 m. Data collection speed tests were conducted using the following speeds: 6 km/h, 20 km/h, and 30 km/h. Antenna distance to the tunnel wall in the speed tests was approximately 80 cm. The effect of GPR antenna distance to the tunnel wall was tested at distances around 0.5 m, 1.0 m, and 1.5 m.

Thermal camera surveys were repeated in the Vuosaari and Hakamäentie tunnels in the summer tests. Thermal videos were recorded in both tunnels on the right-side wall of the southbound tunnels. Additionally, the effect of using different



Figure J.14. GPR antenna mounted on a crane. This system, developed and used by Texas A&M Transportation Institute, was used in SHRP 2 U.S. tunnel tests.

measurement speeds was tested in the Vuosaari Tunnel. Thermal videos were made at van speeds of 20 km/h, 40 km/h, and 60 km/h.

Later in the summer, data were collected from the Vuosaari Tunnel using a quantum 3-D laser scanner technique developed by GEOVAP from the Czech Republic.

Data Collection Practice, Lessons Learned

These data collection tests showed that the GPR antenna rack system used in the Finnish tests was difficult to use. The rack system (Figure J.10) was cheap to build, but the measurement practice was slow and laborious. The height of the antenna using this rack system is adjustable, but the system cannot reach higher than 4 m without special modification. The problem was that the rack became unstable at heights above 3 m. The beam support wheels rolling on the pavement also caused some problems; all objects on the pavement needed to be

cleared before measurement. Manholes and curb stones also caused problems. Compared with the Finnish system, the Texas A&M Transportation Institute (TTI) GPR mounting system used in the U.S. tests was a better solution. The TTI system uses a special truck with an electric crane, allowing adjustment of antenna height, angle, and distance to wall (Figure J.14).

According to the thermal video data analysis, thermal camera position and angle clearly have a great effect on video quality. Thermal noise produced by the vehicle is lower when the camera is placed farther away from the survey van. The thermal camera needs to be installed either in front of or behind the vehicle. The camera also needs to be aimed in such a way that only the area of interest is visible; that way, the most accurate and informative thermal data can be collected. For thermal video logging in the United States, the thermal camera was installed on the end of the beam of the crane. That allowed the research team to get the thermal camera to the correct position, especially in high and wide tunnels (Figure J.15).

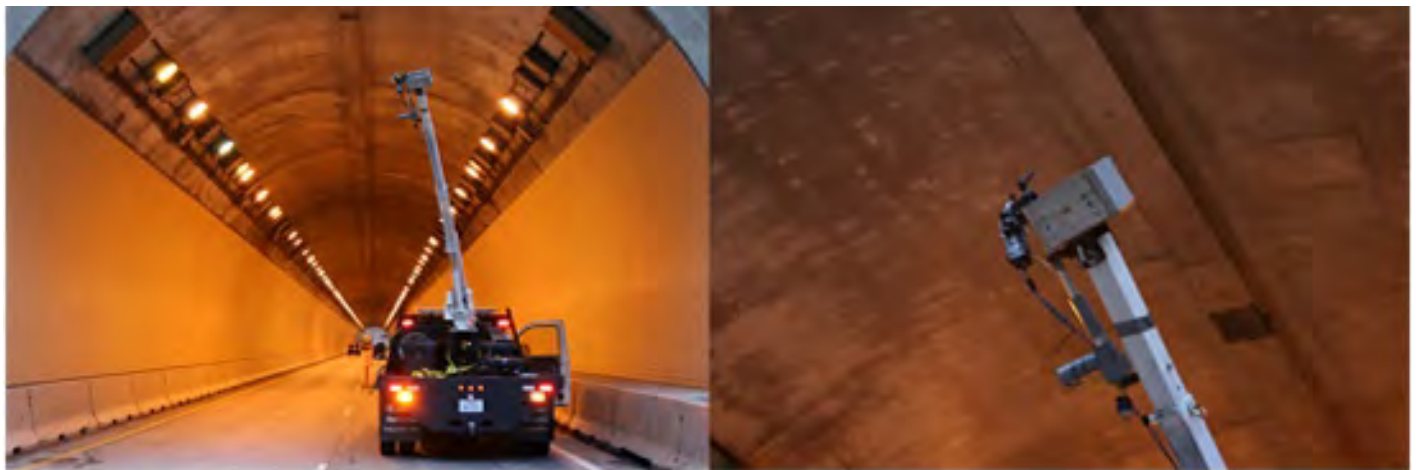


Figure J.15. Thermal video camera mounting used in U.S. tunnel surveys.



Figure J.16. Thermal video collection carts used in tunnel air duct measurements in the United States.

Thermal video collection can also be done without a vehicle; all the required devices can be installed on a cart. Part of the thermal video collection in the United States was done in tunnel air ducts, which were not accessible by vehicle. A thermal video-logging cart consisted of a thermal video camera, normal video camera, DMI kit, control laptop, and battery. This system can also be used when measuring road tunnels and difficult-to-reach locations. Two different carts used in air duct measurements are shown in Figure J.16.

For future surveys, Roadscanners Oy is developing a new rack system for thermal cameras and laser scanners. The new rack system is mounted on a van roof. The rotating rack system can be slid back and forth on the roof. Device angles can be modified to be optimal for different tasks. These rack features make measurement practice easier and thus improve data quality. The rack system is presented in Figure J.17.

Processing and Interpretation of Data Sets

GPR Data Processing, Interpretation, and Outputs

All GPR data preprocessing, processing, and interpretations were done using Road Doctor Pro analysis software and a Road Doctor 3-D module. Preprocessing involves operations that do not change the signal content of the original data. Such operations used in this project were GPR data channel splitting, GPR data scaling, GPR data reversing, and zero-level correction. The GPR data processing operations consist mainly of different filtering operations and amplitude and dielectric value calculations. These operations are fully reversible and changeable. The main target of processing is to make the GPR data more informative so that it will be easy



Figure J.17. New Roadscanners van roof-mounted rack system for laser scanner and thermal camera data collection.

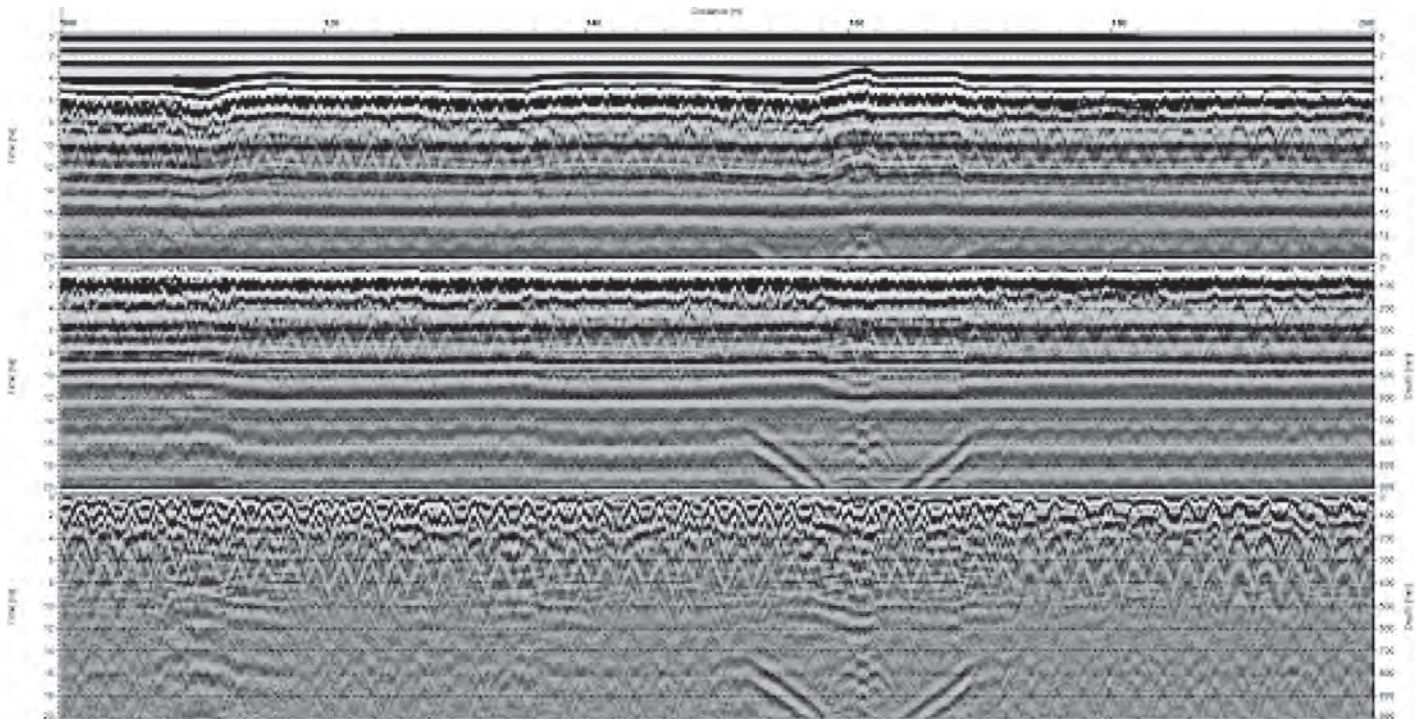


Figure J.18. Raw (top), preprocessed (middle), and processed (bottom) GPR data from Hakamäentie Tunnel right-side wall.

to interpret. Figure J.18 presents examples of how different processing operations affected the GPR data collected from the Hakamäentie Tunnel.

The GPR data interpretations were done using the Road Doctor data interpretation mode. Figure J.19 presents a Road Doctor view of processed data with two-layer interpretation, calculated layer depths, and reflection amplitude of surface, as well as first interpreted layer (concrete surface) and second interpreted layer (reinforcement level).

Thermal Data Processing and Outputs

Thermal videos were collected using the Road Doctor CamLink video-logging package with the RDTD additional module. The following data were collected in each survey run: thermal video (*.SEQ), digital video (*.AVI), and synchronization file (*.SYNC) including distance information. In addition, audio comments were made using Road Doctor CamLink software.

Thermal data processing starts with converting the thermal video data to a Road Doctor-compatible format. This operation is executed with RDTD converter software, which converts the collected *.SEQ raw thermal file to a *.RDTD Road Doctor-compatible thermal file. This operation also links thermal video frames to *.SYNC file distance and coordinate information. The final operation is to link the thermal video to the Road Doctor project. Figure J.20 presents an

example of RDTD converter and *.RDTD file creation. The RDTD converter software and the same initial measurement files can then be used to create thermal color-scale maps. Figure J.21 presents an example of a thermal color-scale map made using RDTD converter software.

The RDTD module allows analysis of the thermal data directly from the thermal video. For that, the supported data type is converted into *.RDTD format. Compared with thermal maps, thermal video analysis is recommended because thermal video analysis gives more detailed information concerning thermal anomalies (Figures J.21 and J.22). A maximum of four thermal videos can be analyzed in the same view at once.

Laser Scanner Data Processing and Outputs

Category B laser scanner data were collected using the Road Doctor CamLink data collection package. Data were collected along with digital video and distance information, and collected data were saved in a Road Doctor-compatible format (*.RDLS). This text file was then opened with Road Doctor using the Road Doctor laser scanner (RDLS) module. Note that in this phase, the operator needs to decide whether distance (shape) or remission information will be written to the new file. The final data file also includes distance information for each laser scan point.

Laser scanner surface shape information can be displayed in Road Doctor in two ways. Data can be viewed as a cross

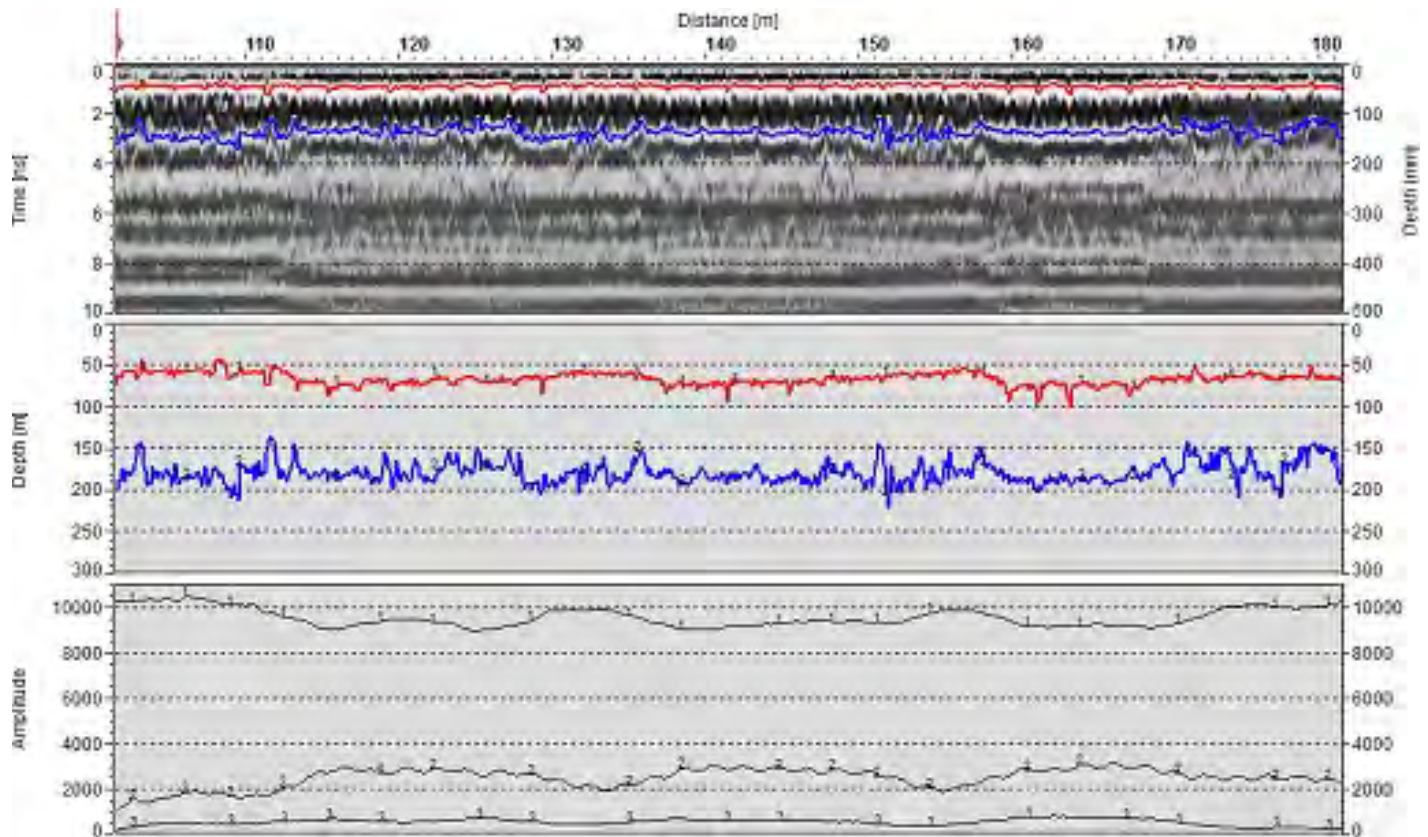


Figure J.19. Processed air-coupled GPR data with two-layer interpretation (top) and calculated layer depths (middle); bottom field presents reflection amplitudes of tunnel wall surface (1, top line), first interpreted layer (2), and second interpreted layer (3).

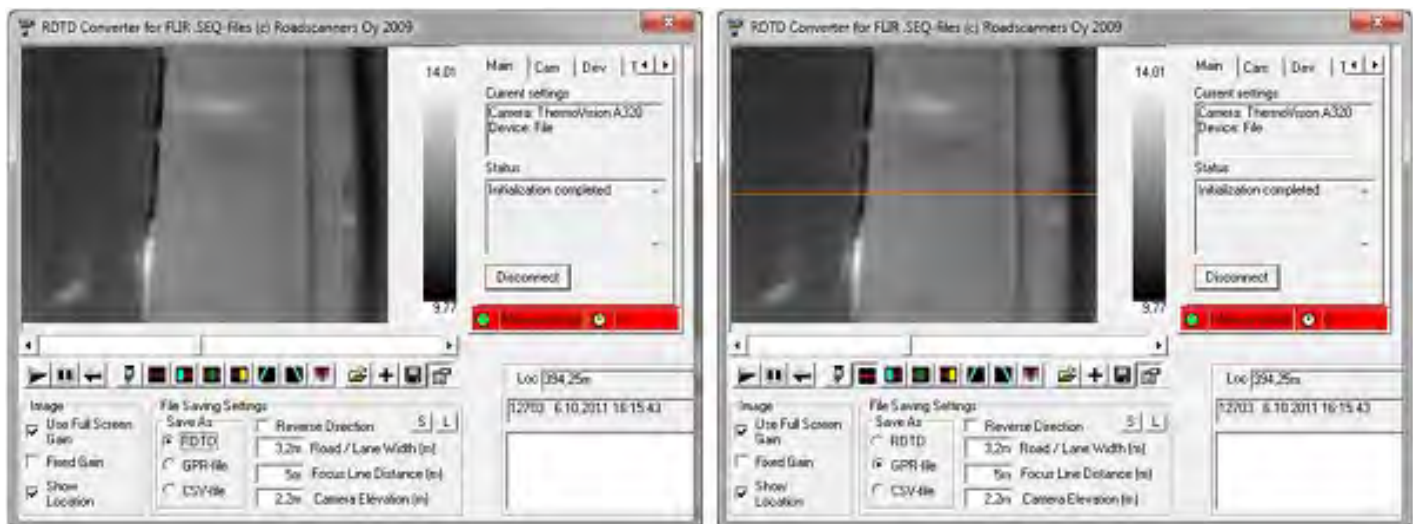


Figure J.20. Road Doctor digital thermal video file creation (left) and thermal color-scale map creation (right). Orange line is position where map database is calculated.

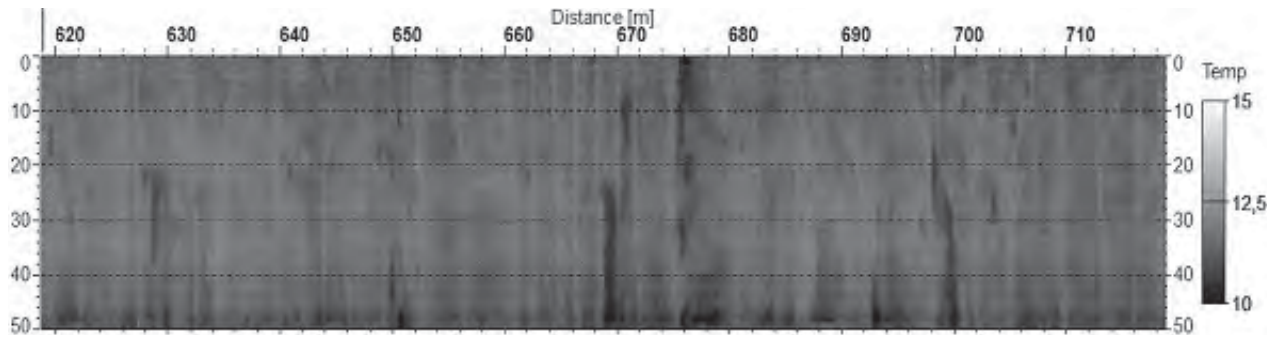


Figure J.21. Thermal color-scale map (temperature scale in degrees Celsius).



Figure J.22. Thermal video view in Road Doctor software display using example from Vuosaari Tunnel roof.

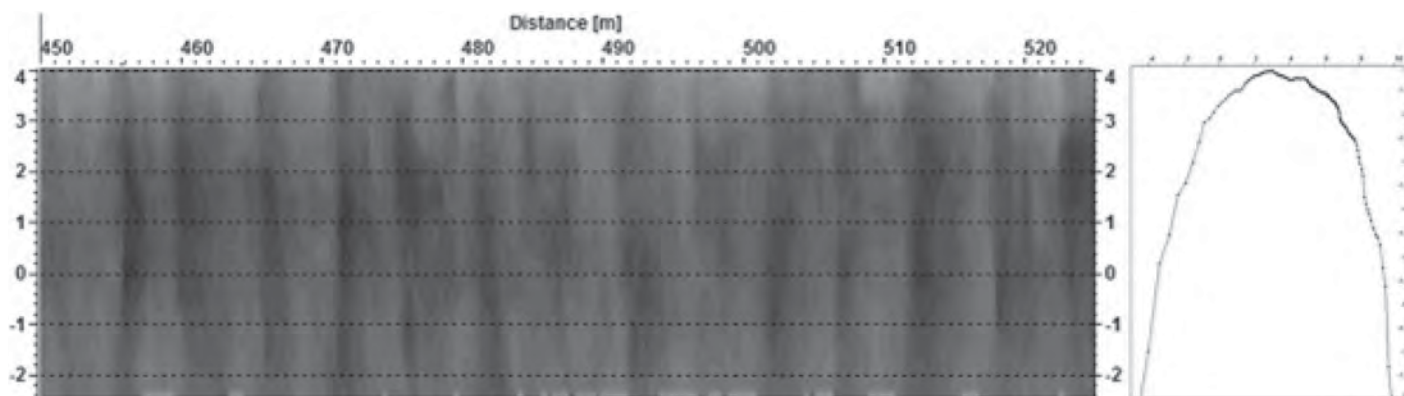


Figure J.23. Cross-section presentation of tunnel shape (right) and contour map of Vuosaari Tunnel right-side wall shape change information (darker colors = longer distance).

section, which gives information on the shape and dimensions of the tunnel (Figure J.23). Surface shape data can also be displayed as a contour map (Figure J.24). Contour maps give more definite information from the chosen tunnel plane. The relationship between the tunnel wall shape with detected water leakages can be analyzed from laser scanner information. Bedrock fracture zones in particular can be identified from this view.

In this project, laser scanner remission information was also analyzed using Road Doctor software. Data were viewed as a color-scale map based on the amplitude of the reflected laser signal. Amplitude depends on the optical reflectivity of the laser beam from the tunnel wall and roof surface and can be used to locate and analyze surface anomalies. In the Vuosaari Tunnel, moist areas can be seen as darker spots; however, detailed reference surveys cannot be done. Digital videos provide valuable supporting information. An example of a Vuosaari Tunnel roof grayscale emission map is presented in Figure J.24.

Category A laser scanner data were collected and processed by GEOVAP using the company's quantum 3-D system. After data preprocessing, the laser scanner data (lidar) were analyzed further using Terrasolid and Point Tools software packages. In this research, only videos produced from point clouds were analyzed. Two grayscale remission videos were created from the Vuosaari Tunnel: a whole-view video and a video toward the right-side wall (Figure J.25). Videos were linked to Road Doctor projects for comparison with other collected data types. The data were measured in a single run through the tunnel. The data collection procedure was fast, and the speed of the survey truck went as high as 50 km/h. However, to get accurate coordinates from the tunnel, measured reference points were needed from certain intervals.

Later, in winter 2011, a new analysis was made with Category A laser scanner point cloud data to try to find more detailed information from the Vuosaari Tunnel roof, where it was difficult to collect data. At that time, the selected view type,

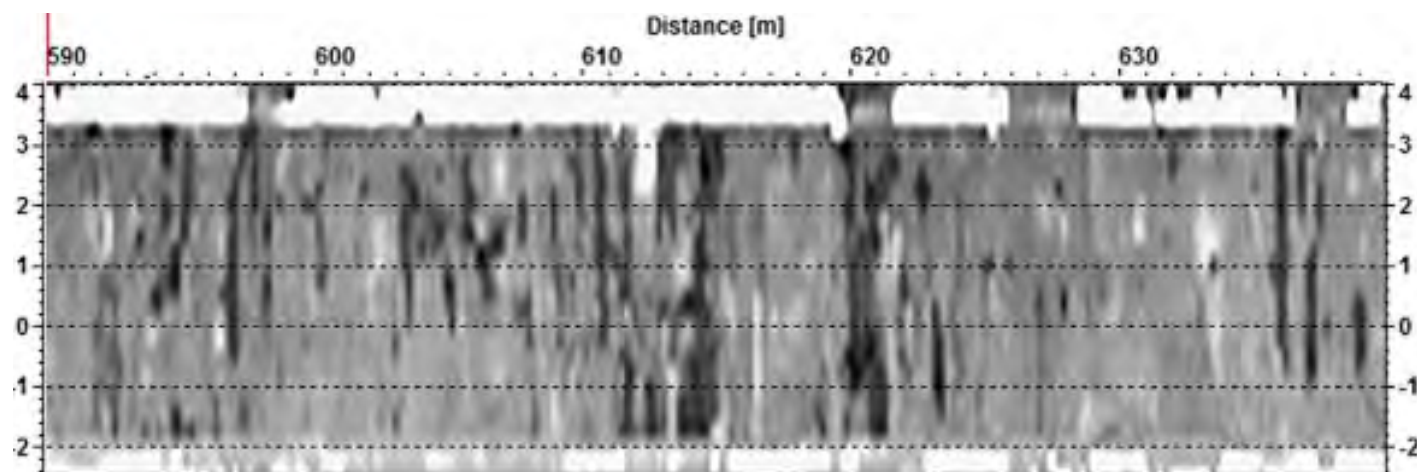


Figure J.24. Road Doctor grayscale emission map of Vuosaari Tunnel roof. Darker areas represent potentially moist areas.

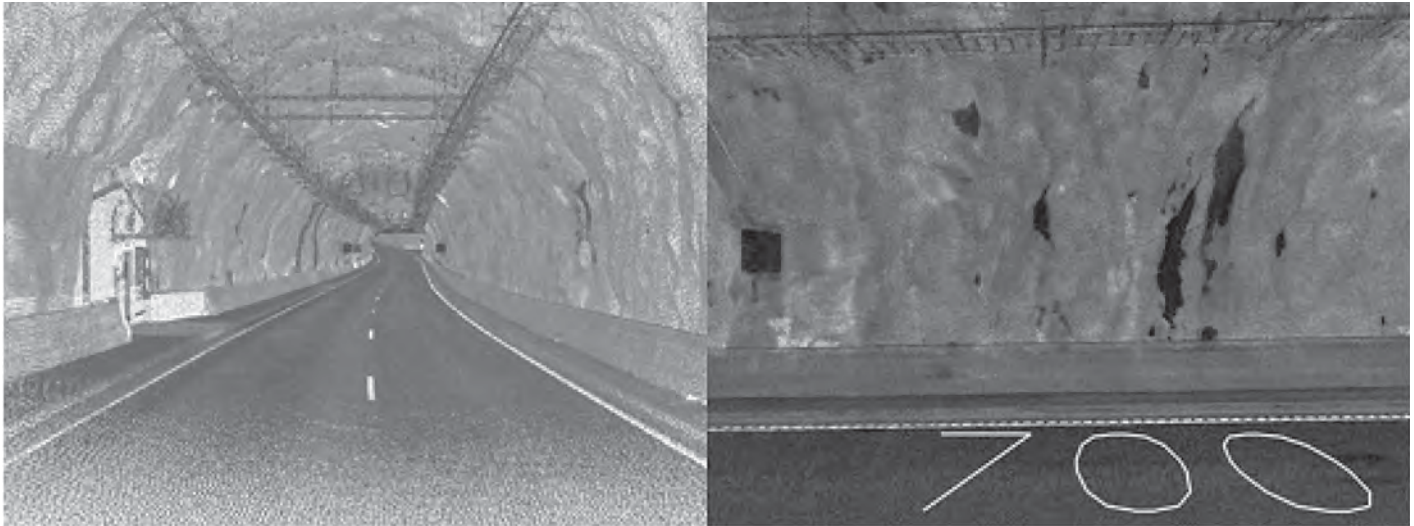


Figure J.25. Screenshots from Vuosaari Tunnel point cloud videos: overall view (left) and targeted view toward right-side wall (right).

from the top down toward the tunnel roof, proved successful, and those data provided valuable information about cracks and water leakage in the tunnel roof (Figure J.26).

Results

General Results

The Vuosaari and Hakamäentie tunnel structures are quite different, so results are presented here separately. The quality and information value of the tested NDT methods also varied in the two test tunnels. The GPR method did not give satisfactory results in the Vuosaari Tunnel because of the steel fibers in shotcrete; however, the thermal camera data provided very good information on the drainage pipes and their condition behind the shotcrete as well as areas of higher moisture

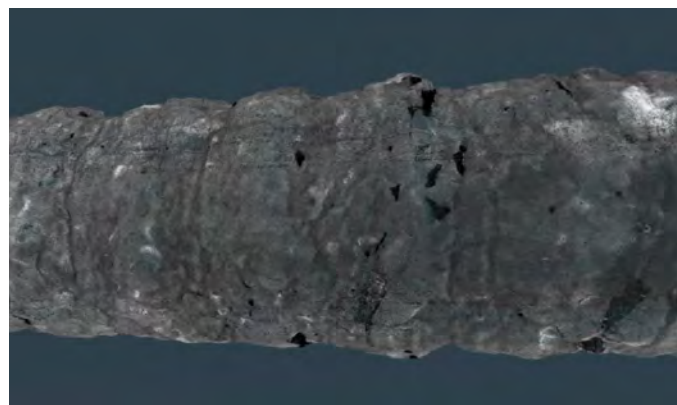


Figure J.26. Point cloud video view from top down in Vuosaari Tunnel roof. Black areas indicate problems with water leakage.

content. In contrast, in the Hakamäentie Tunnel, the GPR method gave very good results, but the thermal camera survey data was inadequate. The Category A laser scanner was tested only in the Vuosaari Tunnel, and the results were very promising. Data can be used in multiple ways, but in this study, only remission and tunnel shape information was used in the analysis. Category B laser scanner data were also good, and the collected data provided information on the tunnel surfaces similar to the Category A laser scanner data. However, data accuracy was not as high.

GPR Test Results

The overall goal of the GPR tests was to determine the suitability of GPR air-coupled antennae for routine tunnel surveys. In addition to structural evaluation, tests were conducted to survey data collection repeatability, antenna-to-wall distance, and speed effect, as well as the effects of seasonal changes on the survey results. The results of these tests are presented in the following sections.

Vuosaari Tunnel

Vuosaari Tunnel air-coupled GPR data processing proved to be much more difficult than expected, and results were not satisfactory, mainly for two reasons. First, the amplitude analysis proved to be sensitive to major antenna-to-wall distance changes. Because it is a shotcrete structure, the Vuosaari Tunnel wall and roof surface is uneven, and antenna-to-wall distance varied along the measurement line. Moderate antenna distance changes can be taken into account, but the correction methods used are not reliable when larger distance changes

are encountered. The Road Doctor software's automatic surface level detection cannot handle such large changes, which were as much as 1.5 m. Second, the Vuosaari Tunnel is surfaced with shotcrete (sprayed concrete), and to improve its technical properties, steel fibers were added. This steel-fiber-strengthened shotcrete reflected the GPR signal so effectively that the detected amplitude values were too high to be used in dielectric analysis. The detected amplitude values also changed along the measurement line, depending on the density and position of iron fibers in the shotcrete. As a result, the GPR reflection amplitude did not provide reliable information concerning moisture conditions. Figure J.27 presents an example of the shotcrete surface amplitude value along a 50-m-long section. The amplitude data show major variation; this result is partly a function of antenna distance to the wall, but the bigger changes were caused by steel fibers.

Hakamäentie Tunnel

Hakamäentie Tunnel air-coupled GPR results were better than the Vuosaari data. Because the surface of the concrete tunnel

walls is relatively even, it was possible to conduct the amplitude and dielectric analyses. Even though the GPR data were sensitive to major antenna-to-wall distance changes, it was not a major problem in the Hakamäentie Tunnel, and Road Doctor software was able to analyze the collected GPR data without problems. Because the Hakamäentie Tunnel is new, only a few weak anomalies were detected. The concrete wall elements were in good condition, and visible damages were rare. Dielectric values higher than 10, indicating major water leakage, were not encountered, but small anomalies were found. Wavy concrete block surface texture had an effect on the measured surface dielectric value, which was lower than predicted. Normally, concrete dielectric values vary between 8 and 12. In this study, the average dielectric value was around 5.

To collect information concerning the effect of seasonal changes on the GPR data results, GPR data were collected in summer, winter, and autumn. Then the surface dielectric values were compared with one another. The comparison data are presented in Figure J.28. The dielectric maps were similar in each season, but the most detailed information was collected in early summer.

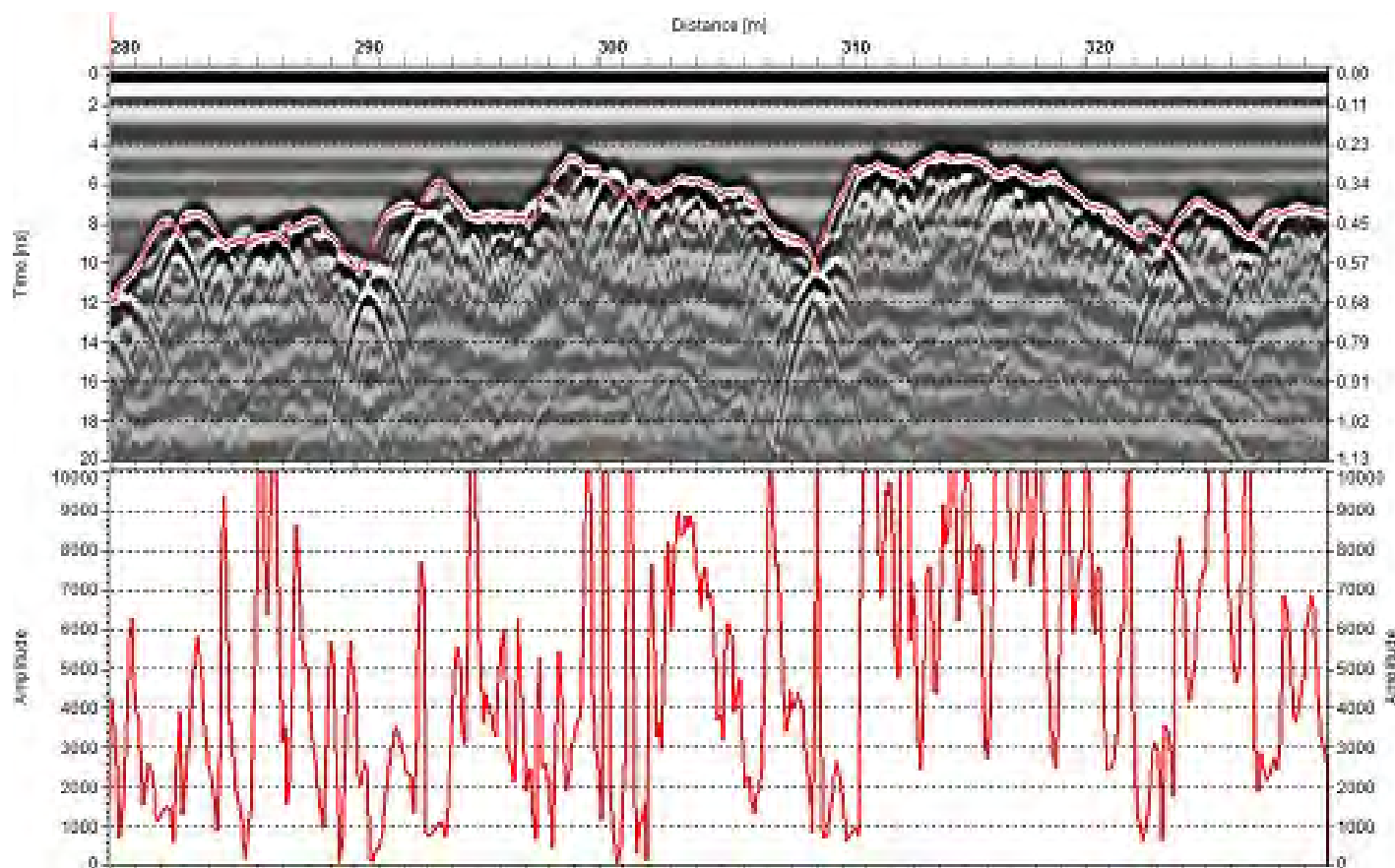


Figure J.27. Interpreted surface reflection of air-coupled 1-GHz horn data (top) and amplitude of interpreted surface reflection (bottom) in Vuosaari Tunnel. Y-axis in GPR data (right) represents distance to wall (calculated with Er:1).

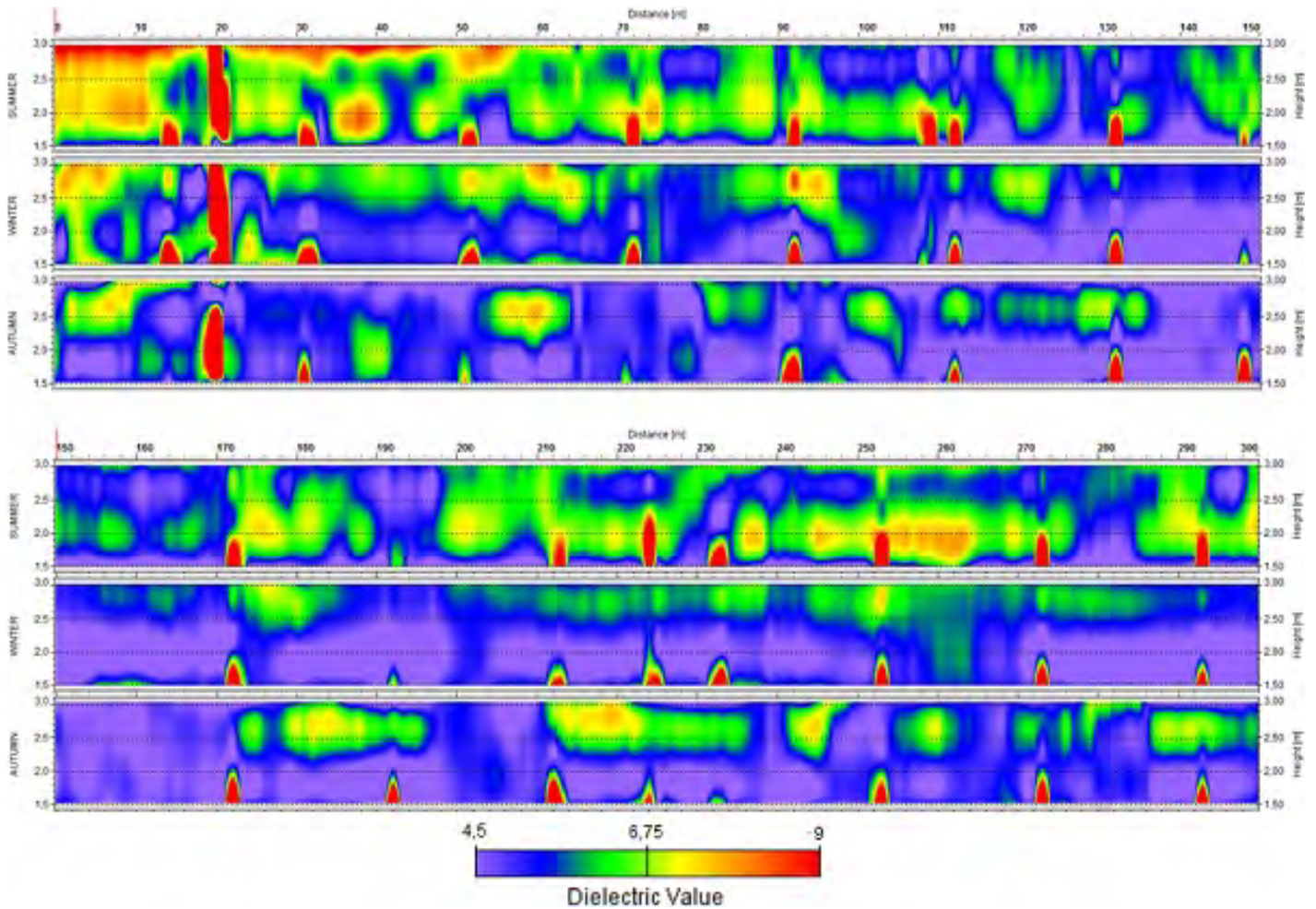


Figure J.28. Dielectric surface maps of Hakamäentie Tunnel right-side wall in summer, winter, and autumn shown at 0–150 m (top) and 150–300 m (bottom).

Repeatability, Antenna-to-Wall Distance Effect, and Data Collection Speed Tests

To test for repeatability, two measurements were taken along the same line, using the same antenna-to-wall distance. The results are shown in Figure J.29. In this figure, the measured dielectric (ϵ_r) is displayed in the top graph, and the corresponding antenna-to-wall distance is in the bottom graph. The graphs show that results were quite repeatable and areas of higher moisture content could be detected even though the value was not exactly the same.

According to the repeatability test results, antenna-to-wall distance seems to have an effect on the measured dielectric value; and increased antenna-to-wall distance seems to have an increasing effect on dielectric value even though the antenna-to-wall distance variation between the two test measurements was quite small (see Figure J.29). When the distance difference is low—2 cm to 3 cm—dielectric results correlate. This means that the elevation correction algorithm used in the analysis was not working as expected (Figure J.30). However, when

antenna-to-wall distance changes are better taken into account, GPR measurements are repeatable.

The antenna-to-wall distance effect was analyzed from data sets measured from three different distances: 0.5 m, 1.0 m, and 1.5 m (Figure J.31). Dielectric values were calculated using metal reflection measured on 0.5-m antenna–plate distance. Performed antenna-to-wall distance tests gave complex results: the results showed that measured surface dielectric value was not acting linearly when antenna-to-wall distance changes were large. This effect can be explained by geometrical signal attenuation when an antenna is moved farther from the wall. Current amplitude correction algorithms are not able to handle these critical distance changes. Figure J.31 also shows that taking measurements farther from the wall (1.0 m and 1.5 m) reduced the general level of the dielectric value compared with the 0.5-m survey distance. Thus, the wall shape starts to have an effect at longer distances. Nonetheless, results from 1.0 m and 1.5 m show similar trends and anomalies.

In further tests, metal plate reflections were also measured using two test distances, but the size of the metal plate—1 m

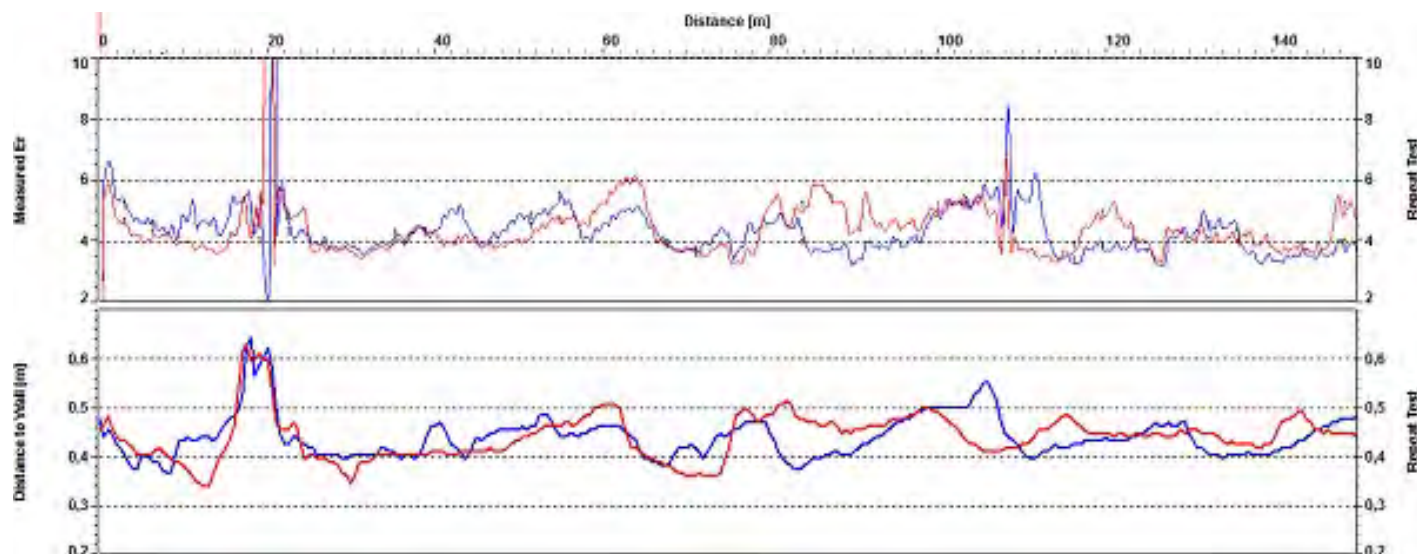


Figure J.29. Results of surface dielectric values repeatability tests (top) and antenna-to-wall distance (bottom). Red, run 1; blue, run 2.

by 1 m—was found to be too small at distances of 1.0 m and 1.5 m (Figure J.32). The GPR signal did not reflect from the metal as expected, and signal loss was too high. From a distance of 1.0 m, the signal was 20% weaker, and from a distance of 1.5 m, it was 50% weaker compared with the signal received from the 0.5-m distance.

In addition, GPR tests were conducted at different speeds to collect information on the effect of the survey van speed on the GPR data. These measurements were performed at three different speeds: 6 km/h, 20 km/h, and 30 km/h. Speeds higher than 30 km/h were not possible because of problems with the antenna support system. The GPR itself has no limits with higher data collections speed; for instance, the maximum speed using a

SIR-20 GPR unit and one air-coupled horn antenna would be around 70 km/h to 80 km/h. The most critical factor affecting speed was the antenna-to-wall distance, which had to stay roughly the same between measurements; when the van speed increased, observing and adjusting the antenna-to-wall distance was more difficult. Test results are presented in Figure J.33, which shows that above 20 km/h, the distance to the wall changed more and affected the measured dielectric value.

All the test results presented above show that horn antennae should be kept relatively close to the wall if the current algorithms will be used. Surveys with longer antenna-to-wall distances and higher speeds have given interesting and promising results, but if such will be used, new calibration methods will be needed for accurate dielectric value calculations. Also, at longer distances, the footprint area from the reflection will be much larger, which means that the GPR survey results will be less detailed.

Finally, when the GPR tests were performed with two antennae side by side (see Figure J.2, left photograph), the performance of the two antennae was not similar.

Other Observations with the GPR Tests—Positioning

The positioning of the GPR data and other data collection is more complex in underground tunnel surveys which cannot use Global Positioning System (GPS) techniques. In detailed tunnel surveys, expensive robot tachymeters can be used, but their use is expensive and time consuming. That is why this study used a survey wheel for positioning. All the data points were stored as a function of a distance from the starting point of the measurement line. A survey wheel is a simple tool for positioning the data, but accuracy is limited.

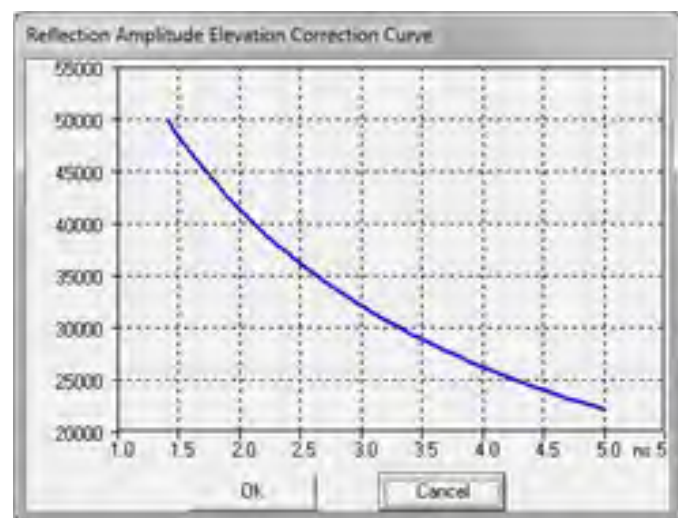


Figure J.30. Reflection amplitude elevation correction curve used in Road Doctor.

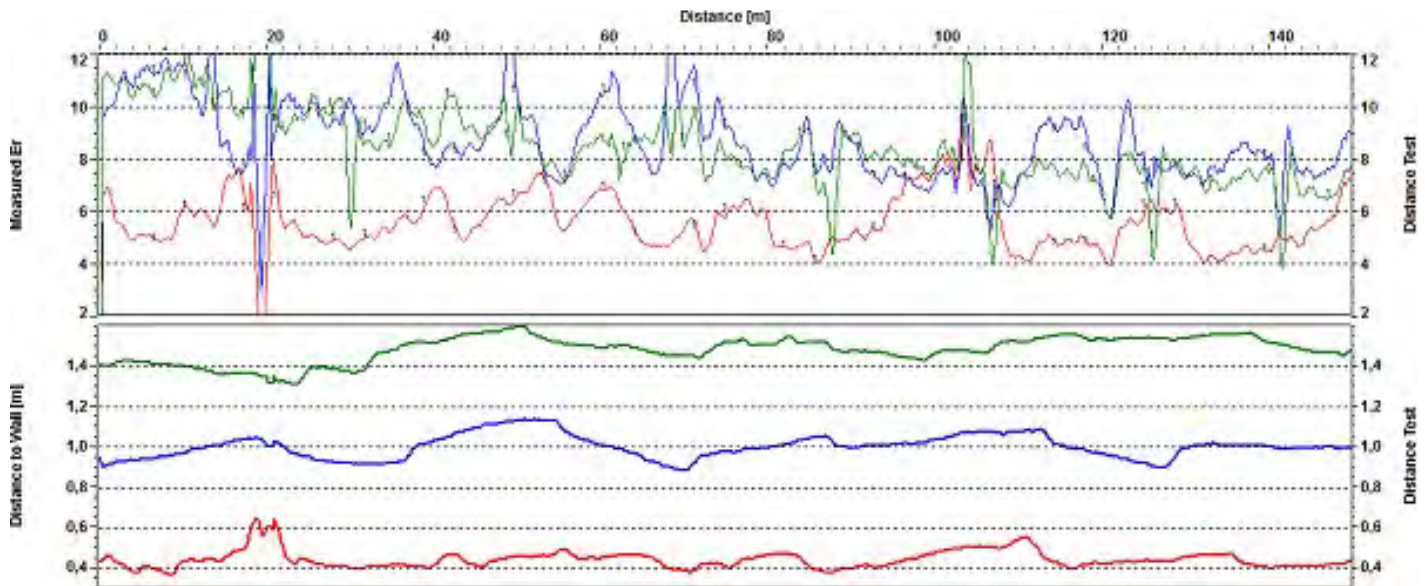


Figure J.31. Surface dielectric values in antenna-to-wall distance tests (top) and antenna-to-wall distance (bottom). Red, 0.5 m; blue, 1.0 m; and green, 1.5 m.

Thermal Camera Test Results

Thermal camera tests gave promising results, especially from the Vuosaari shotcrete tunnel. Some anomalies could be detected in the Hakamäentie Tunnel. The main findings of the thermal camera test are given in the following sections.

Vuosaari Tunnel

The Vuosaari Tunnel proved to be ideal for thermal analysis. Water seeping from the bedrock and infiltrating through the shotcrete was causing strong thermal anomalies, which the thermal camera detected. Leaking and blocked water seem to cause cold thermal anomalies in all outside air temperature



Figure J.32. GPR metal reflection data collection during winter tests in 2011.

conditions. Other visible thermal differences are caused by water drains. These thermal anomalies can be cold or warm, depending on the outside air temperature. In warm conditions, drains can be seen as warm anomalies due to warm air inside the drains. The Vuosaari Tunnel was opened for use in 2007 and is in good condition. Similar studies of older tunnels would reveal more anomalies.

Figure J.34 presents thermal data sets from the Vuosaari Tunnel collected in different seasons. The figure shows that the best and most detailed data was collected in the summer: moisture anomalies (black areas), in particular, are very visible and show where drain pipes are not collecting all the water. In the fall, many of the summer anomalies can also be seen; but in the winter, when the wall was frozen (at the time of the data collection, air temperature ranged from -4°C to 2°C), only small indications of the problem sections can be seen, and the data are more blurry.

Thermal data collected in summer 2011 from the Vuosaari roof also had good quality (Figure J.35). Because the Vuosaari Tunnel is an undersea tunnel, water mostly tries to leak through the roof, which is why the roof data had more thermal anomalies than the wall data. Temperature differences between anomalous and other areas, however, were low, as can be seen in Figure J.35 in which the relative temperature difference is 2°C .

Hakamäentie Tunnel

In the Hakamäentie Tunnel, southbound tunnel right wall thermal camera data collection was done in summer, autumn, and winter. Wall temperatures were constant in every survey season, and thermal anomalies were rare. All spotted anomalies were caused by tunnel technology, water spatters on the wall, and

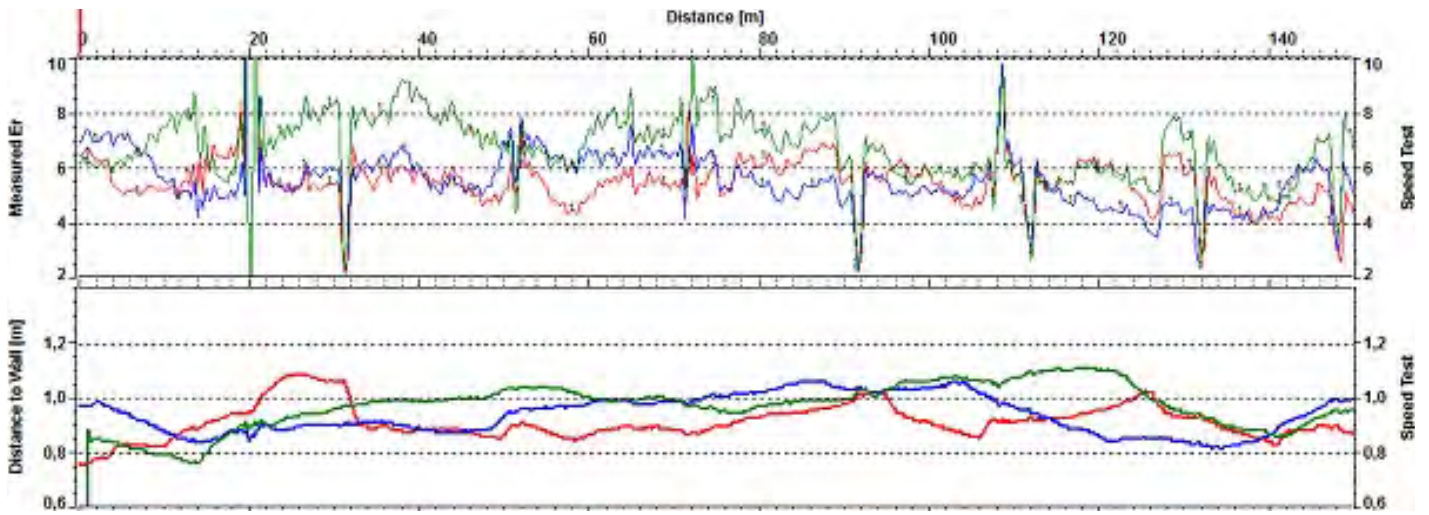


Figure J.33. Surface dielectric values in speed tests (top) and antenna-to-wall distance (bottom). Red, 6 km/h; blue, 20 km/h; and green, 30 km/h.

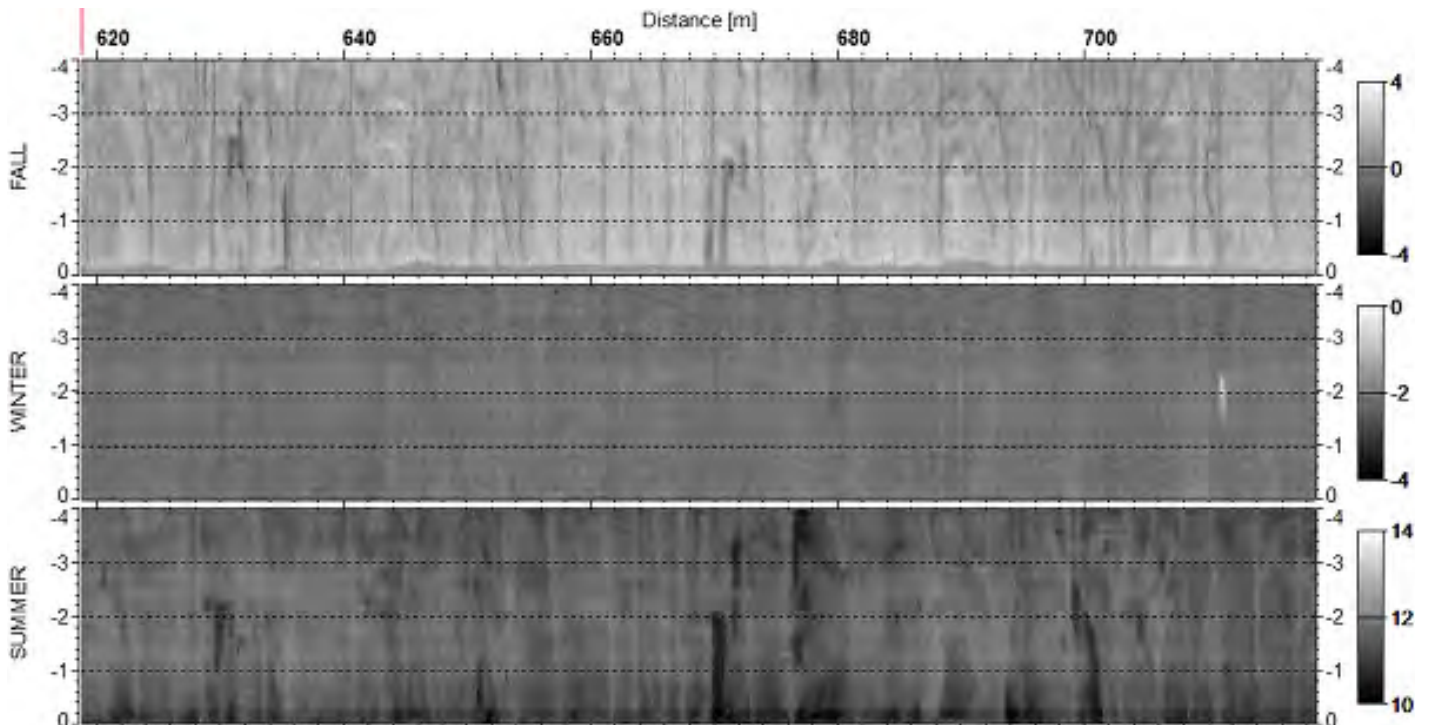


Figure J.34. Comparison of thermal data collected at different times of year (fall, winter, and summer; temperature scale in degrees Celsius).

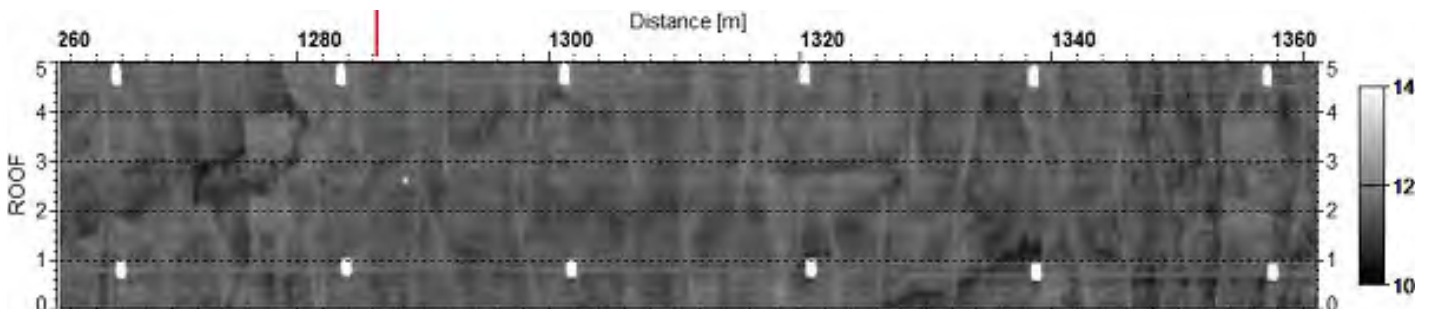


Figure J.35. Thermal color-scale map of Vuosaari Tunnel roof (temperature scale in degrees Celsius). White spots are lamps.

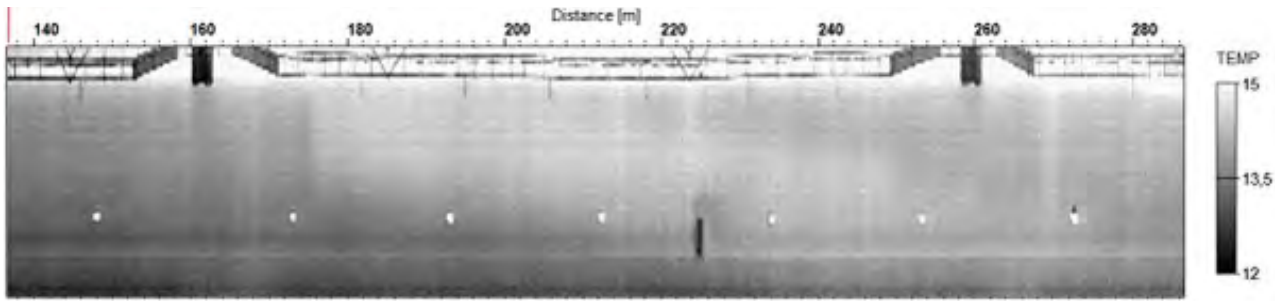


Figure J.36. Thermal color-scale map of Hakamäentie Tunnel southbound right-side wall (summer; temperature scale in degrees Celsius).

snow. Wall temperature variation, regardless the time of the year, was less than 1°C. Compared with the Vuosaari Tunnel, thermal variation was extremely low. Figure J.36 presents the thermal color-scale map from the right-side wall summer data.

Data Collection Speed Tests

Thermal camera data collection speed tests consisted of three measurements on the Vuosaari Tunnel right-side wall with the same camera-to-wall distance. Measurements were performed using van speeds of 20 km/h, 45 km/h, and 60 km/h. Figure J.37 shows an example of test results, which prove that measurements are repeatable at all three tested data collection speeds. The same features can be spotted in all the data sets. Differences in the data sets were caused mainly by the speed of the van. When the camera moved by the objects faster, the anomalies started to fade and blur. Still, up to a speed of 60 km/h, anomalies do not disappear: greater water leak areas can be still detected.

Laser Scanner Test Results

In the Vuosaari Tunnel, laser scanning was performed using two different laser scanner types: effective high-accuracy systems (Category A) and cheaper lower-accuracy systems (Category B). The Hakamäentie Tunnel was measured using only the Category B laser scanner. The key findings are presented in the following sections.

Vuosaari Tunnel

Tests results from both laser scanner systems used in the Vuosaari Tunnel gave promising results. Both systems provided information about the tunnel wall surface shape, and remission data provided information about water leakage areas. Figure J.38 presents an example of the Category B laser scanner shape data, where a tunnel cross section can be seen on the right. Figure J.39 presents an example of the detailed information provided by the Category A laser scanner, which

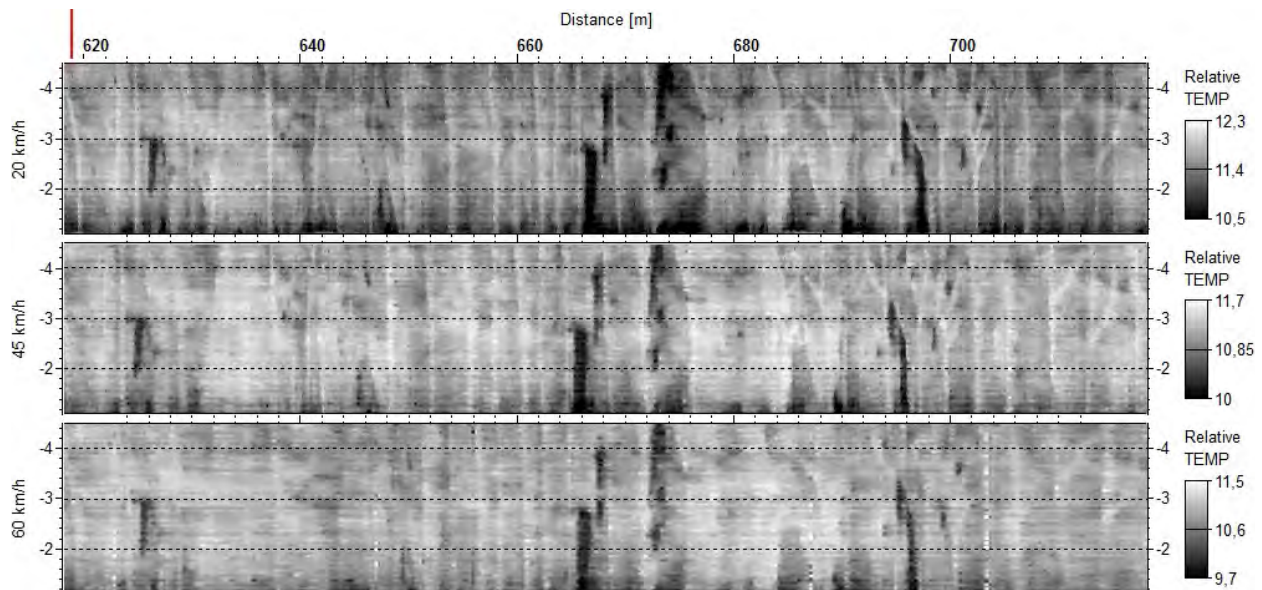


Figure J.37. Repeatability speed test result, example from Vuosaari Tunnel (summer; temperature scale in degrees Celsius).

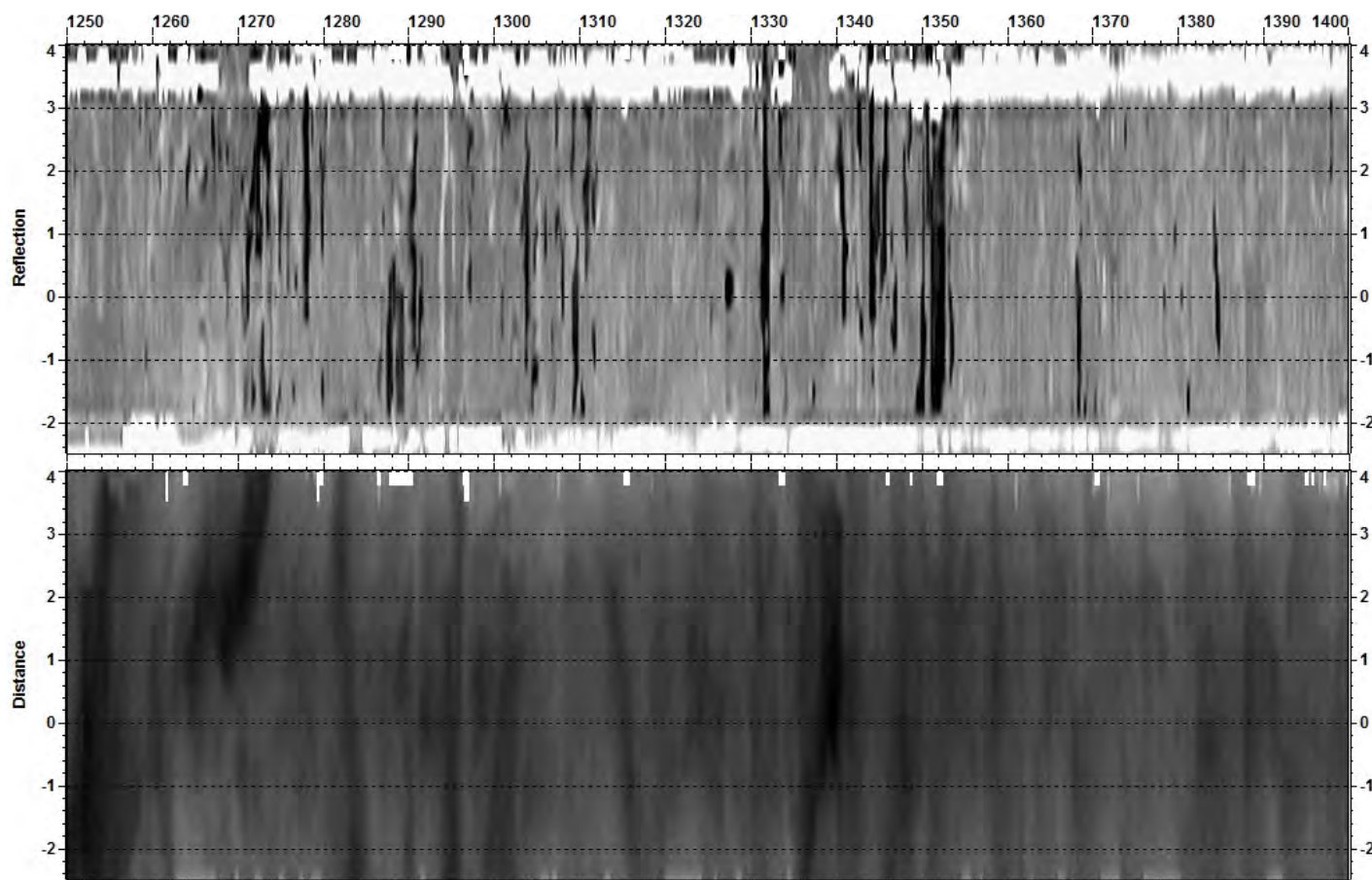


Figure J.38. Category B laser scanner data from Vuosaari Tunnel (right-side wall at 1250–1300 m). In remission data (top data field), darker areas represent potential moisture anomalies; in wall shape information (bottom data field), darker areas are farther from road.

shows points/areas where salty water was leaching through the shotcrete. Figure J.40 presents a comparison of Category A and Category B laser scanner data in the Vuosaari Tunnel roof surveys. It shows that the cheaper Category B laser scanner does detect anomalous areas. The detailed analysis of the high-precision Category A laser scanner data even revealed cracking in the tunnel roof, as Figure J.41 shows.

Laser scanner data are very repeatable, and data collection can be carried out in tunnels with speeds of 30 km/h to 40 km/h. Higher speeds can be used, but problems with accurate positioning can occur when doing so. To get reliable x , y , z position data reference points that can be detected from laser scanner data, collection should be done at 200-m intervals.

Hakamäentie Tunnel

The results of the laser scanner tests in the Hakamäentie Tunnel did not reveal any major problem areas. Figure J.42 presents an example of Category B laser scanning data from the Hakamäentie Tunnel roof. Results showed small anomalies

in concrete block joints and at the joints where the roof meets the wall. Thermal camera data did not show any major thermal anomalies on these locations.

Integrated Analysis of Different Methods

In this study, a comparison of the different data types could be made only with the thermal camera and laser scanner data; GPR data were not usable for data analysis because of the presence of steel fibers. Figure J.43 presents a comparison of the thermal data (in the center) with the point cloud videos (in the corners) in the Vuosaari Tunnel. The connection between the anomalies detected is clear. Where water entered the shotcrete-surfaced tunnel, surface leakages can be seen as darker areas in the laser scanner remission data. In the thermal data, areas with higher water content can be seen as colder anomalies and, with proper color scale, as dark spots. In both data sets, the darkest areas indicate the existence of water in the tunnel structure. Analysis of multiple points showed a high correlation between these points.

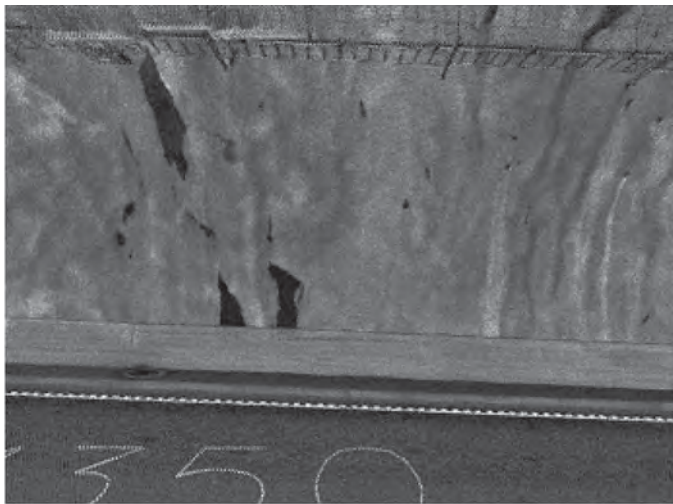


Figure J.39. Category A laser scanner detailed view from Vuosaari Tunnel (right-side wall at 1350 m; see also Figure J.38). Small wet spots are visible on the right; white areas beneath indicate salt.

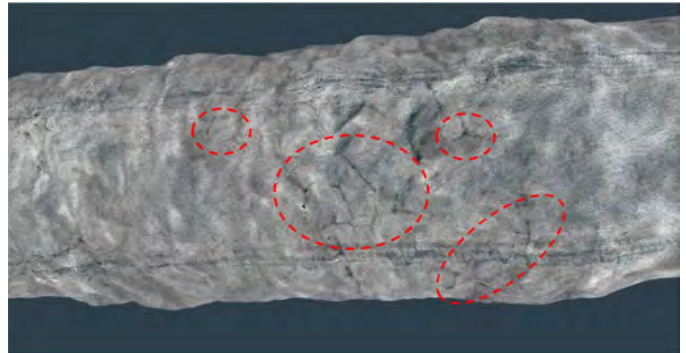


Figure J.41. Example of Category A laser scanner data from Vuosaari Tunnel roof. Areas with cracks in shotcrete are shown with red circles.

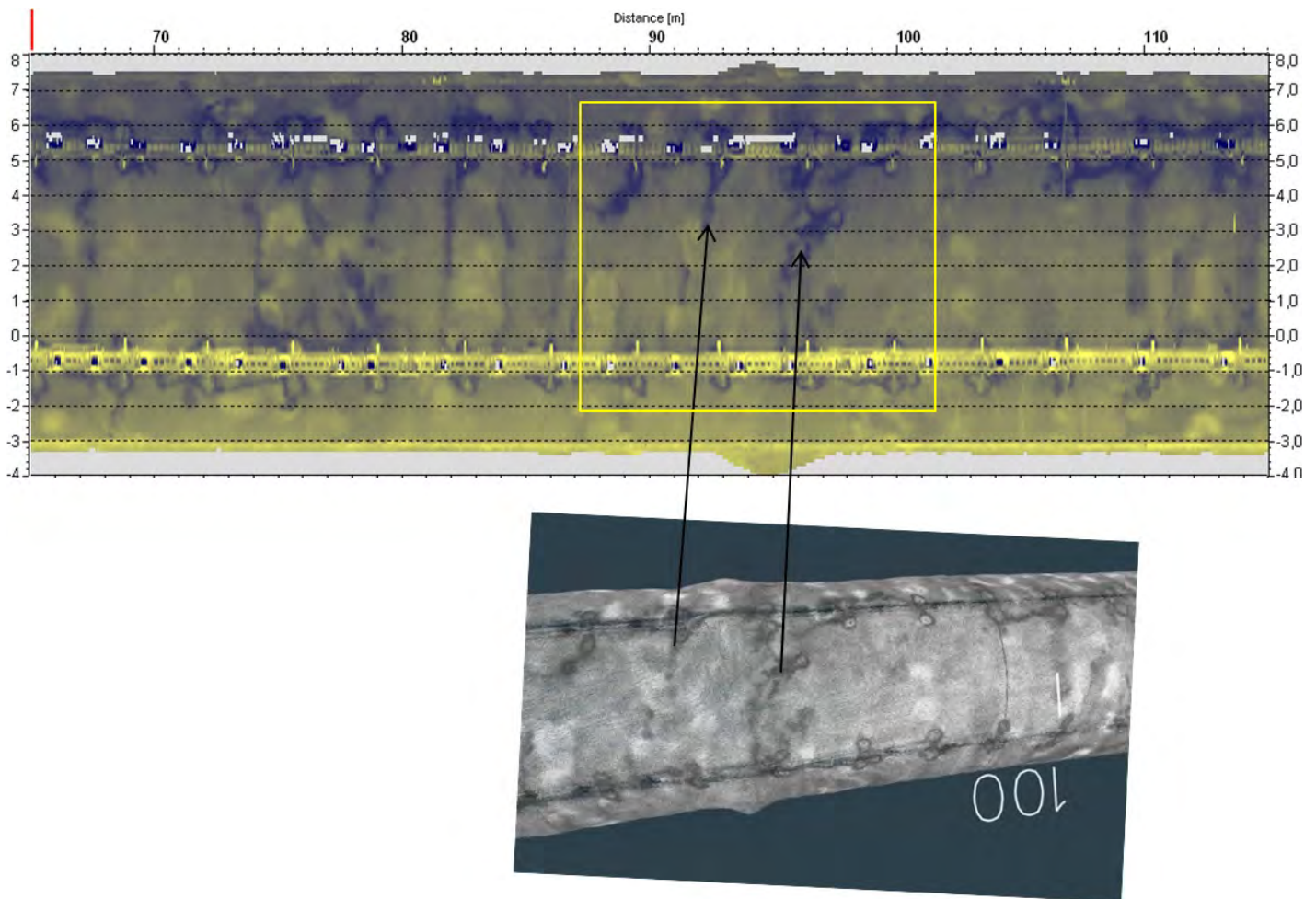


Figure J.40. Comparison of Category B (top) and Category A (bottom) laser scanner data from Vuosaari Tunnel roof (around 100 m at the tunnel roof). The same anomalies can be seen in both data sets.

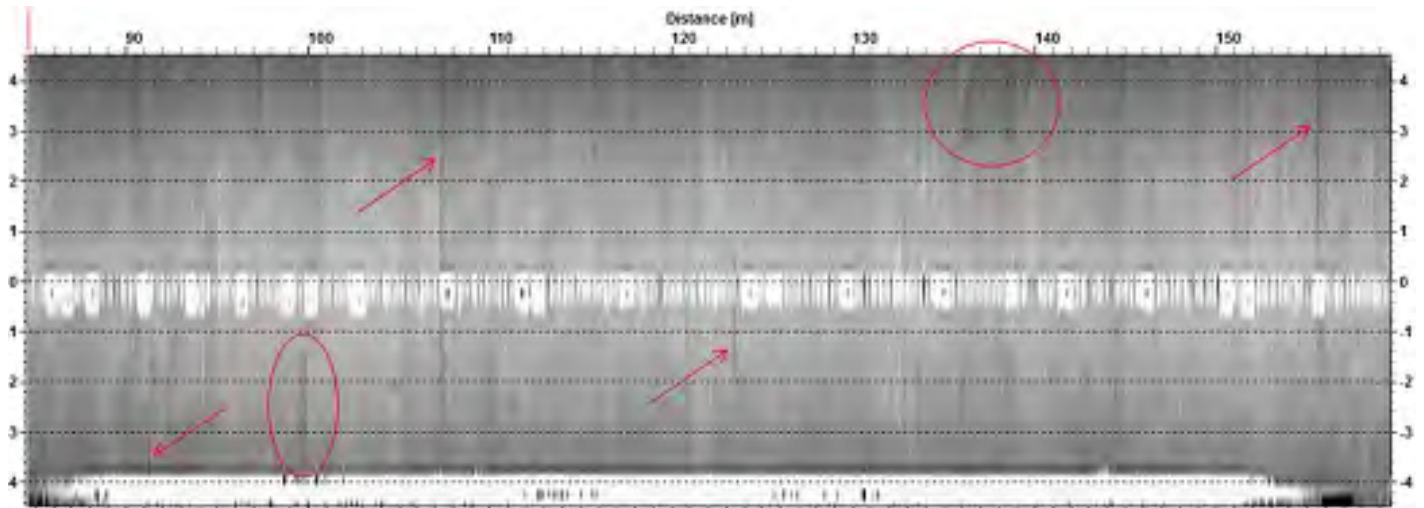


Figure J.42. Category B laser scanner reflection amplitude data from the Hakamäentie Tunnel roof. Red markings point out detected anomalies.

Conclusion

The results of the tunnel tests showed that all three systems are potential tools to be used in surveys of tunnel lining conditions. However, each system has some shortcomings depending on the type of tunnel structure, and these need to be identified before selecting the survey method for each tunnel. The key conclusions for each tested tunnel survey method are presented in the following sections.

GPR Analysis

The key conclusions for the ground-penetrating radar analysis survey method are as follows:

1. GPR horn antenna data provided good quality structural information from the concrete tunnel but could not be used in the shotcrete tunnel because steel fibers were used in the shotcrete. The GPR data provided useful information on structures behind the tunnel linings.

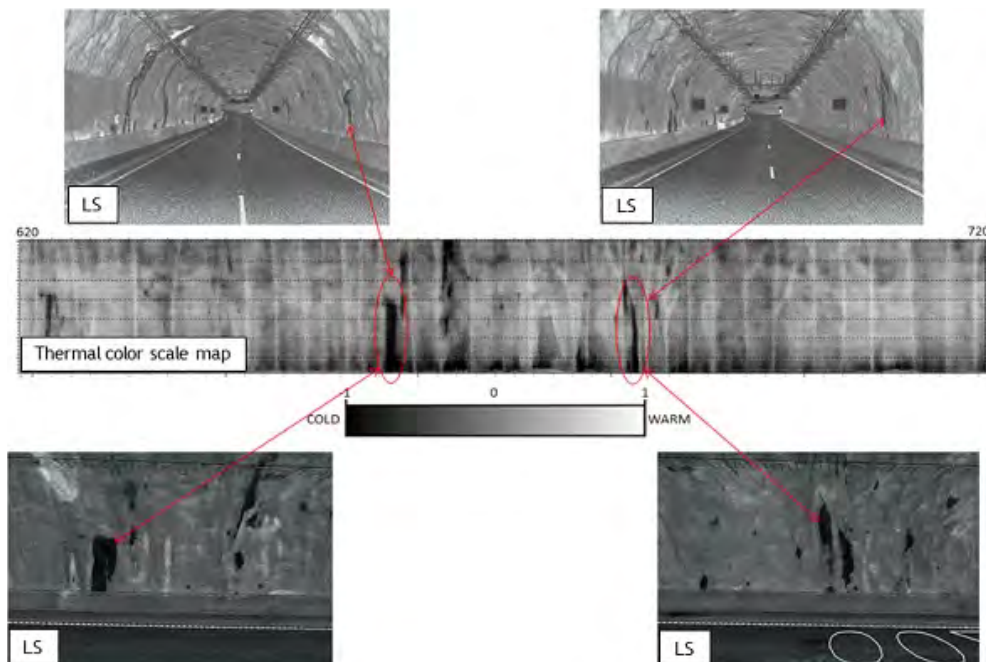


Figure J.43. Thermal color-scale map anomalies' connection to the Category A laser scanning video results, Vuosaari Tunnel right-side wall. LS = laser scan.

2. More research is needed before surface dielectric information can be reliably used to find moisture anomalies in the lining structure. The distance from the antenna to the wall should be kept constant, and better calibration files are needed. The optimal distance is 0.5 m, which allows for safe measurement and is close enough for reliable dielectric value calculation. However, this distance might exclude the horn antenna technique in surveys of tunnel roofs. Also, the surface texture of the wall can affect results; if the surface is smooth, data collection can be done and results will be reliable.
3. Better mounting systems for horn antennae—to protect the antennae in case they hit obstacles—make higher data collection speeds possible.
4. Different GPR horn antennae gave slightly different results, and at this time, only one antenna is recommended for use in one survey.
5. The GPR system is relatively expensive. The price estimate for a complete horn antenna tunnel survey system is \$150,000 to \$200,000.
6. GPR horn antenna data collection and data analysis require well-trained and experienced personnel.

Thermal Camera Surveys

The key conclusions for the thermal camera survey method are as follows:

1. Thermal cameras gave excellent results on the shotcrete tunnel, but in the new Hakamäentie concrete tunnel, hardly any anomalies could be detected with the system. One reason may be a lack of problems close to the surface.
2. The thermal camera is a fast method for tunnel surveys, and first results can be seen *during* data collection. At higher speeds, data are slightly blurred, but bigger anomalies can be reliably detected.
3. Results are repeatable, but changes in tunnel wall surface temperature during the day must be taken into account.
4. Anomalies can be seen in different ways when the surveys are conducted in summer, fall, and winter. The best time for surveys is early summer. However, results surprisingly showed that moisture anomalies were always seen as colder areas.
5. The thermal camera is sensitive to the survey direction toward the tunnel wall and roof, and focusing the camera on white tiles can be difficult. Also, the survey van can cause unwanted infrared reflections.
6. Survey equipment is relatively cheap. The price estimate for the complete hardware package to conduct a thermal camera survey in a tunnel can range from \$40,000 to \$60,000 (excluding the survey van).

7. Thermal cameras are easy to use, and data collection and analysis can be started after 1 to 2 days of training.

Laser Scanning Analysis

The key conclusions for the laser scanning analysis survey method are as follows:

1. Laser scanning systems provided very useful data of the shape and condition of the tunnel linings. The results were excellent, especially in the shotcrete Vuosaari Tunnel, but interesting and valuable information was also detected in the concrete Hakamäentie Tunnel.
2. The Category A laser scanner (lidar) provides very accurate information on the tunnel shape and changes in the shape, especially if good x , y , z reference points are available. The accuracy of the Category B laser scanner is only good enough for rough surface shape analysis.
3. Both systems provided enough detailed remission results to detect moisture anomalies in the tunnel linings. Software plays an important role in presenting the results in the optimal way.
4. The Category A laser scanner (lidar) showed cracking in shotcrete concrete.
5. Laser scanning is repeatable, and surveys can be performed at relatively high speeds.
6. The price of the system varies. A good Category A laser scanning system can cost up to \$1 million, while the price estimate for a complete Category B laser scanner hardware system ranges from \$50,000 to \$70,000.
7. Category A laser scanning system data collection and analysis require experienced personnel with a background in geodesy; training for Category B laser scanning system data collection and analysis takes only 1 to 2 weeks.

Other Instruments Used in the Survey

In addition to the performance of the tested equipment, the tunnel tests in Finland provided useful information on other instruments used in the surveys:

1. The quality of digital videos used in the surveys was not good. For future surveys, video cameras with good luminous power are recommended.
2. Because GPS does not work in tunnels, the quality requirements for encoders are high—with no shift allowable even at very low speeds.
3. Because survey vehicles cannot always drive at exactly the same survey line, the survey tunnels should have referencing systems at about 200-m intervals that can be detected in all survey data (for instance, metallic tapes) and that can be used to scale the data.

APPENDIX K

Air-Coupled Ground-Penetrating Radar Field Tests

Air-Coupled GPR Operating Principles

The Texas A&M Transportation Institute (TTI) air-coupled ground-penetrating radar (GPR) antenna transmits pulses of radar energy with a central frequency of 1 GHz into a tunnel lining. These waves are reflected at significant layer interfaces in the lining. The reflected waves are captured by the system and displayed as a plot of reflection amplitude (voltage) versus arrival time. As shown in Figure K.1, the largest peak is the reflection from the surface. The amplitudes before the surface reflection are internally generated noise and, if significant, should be removed from the trace before signal processing. The reflections that can also be of significance to tunnel personnel are those that occur after the surface echo. These represent significant interfaces within the lining, and the measured travel time is related to the depth to another layer or to a defect. For example, in Figure K.1 the time between the surface echo A1 and A2 is related to the depth to another layer or to a defect.

The software developed at TTI automatically measures the amplitudes of reflection and time delays between peaks. Using these measurements, the operator can calculate layer dielectrics and depths to another layer or defect. The equations used are summarized in Equations K.1 through K.3:

$$\epsilon_a = \left[\frac{1 + \left(\frac{A_1}{A_m} \right)^2}{1 - \left(\frac{A_1}{A_m} \right)^2} \right]^2 \quad (\text{K.1})$$

where

ϵ_a = dielectric of lining surface,

A_1 = amplitude of reflection from the surface in volts (peak A1 in Figure K.1), and

A_m = amplitude of reflection from a large metal plate in volts (this represents the 100% reflection case).

$$h1 = \frac{(c \cdot \Delta t1)}{\sqrt{\epsilon_a}} \quad (\text{K.2})$$

where

$h1$ = depth to another interface (such as to another layer, void, or other defect),

c = constant (speed of the radar wave in air as measured by the system), and

$\Delta t1$ = time delay between peaks A1 and A2 in Figure K.1.

$$\sqrt{\epsilon_b} = \sqrt{\epsilon_a} \left[\frac{\left(1 - \left\{ \frac{A_1}{A_m} \right\}^2 + \left\{ \frac{A_2}{A_m} \right\} \right)}{\left(1 - \left\{ \frac{A_1}{A_m} \right\}^2 - \left\{ \frac{A_2}{A_m} \right\} \right)} \right] \quad (\text{K.3})$$

where

ϵ_b = dielectric of the lower layer, void, or other defect, and

A_2 = amplitude of reflection from the top of the lower layer or defect in volts (peak A2 in Figure K.1).

Dielectric values and depths can be readily determined from two software packages developed by TTI: COLORMAP and Pavecheck. Both software packages are relatively easy to use for production-level purposes.

Air-Coupled GPR Results for the TTI Test Specimens

TTI personnel collected air-coupled GPR data on concrete and shotcrete specimens that contained delaminations or voids. The TTI team determined that the equipment could detect only three simulated voids, all located in the shotcrete sections:

- Specimen D, an air-filled void placed 7.625 in. from the surface;
- Specimen F, an air-filled void placed 3 in. from the surface; and
- Specimen G, a water-filled void placed 3 in. from the surface.

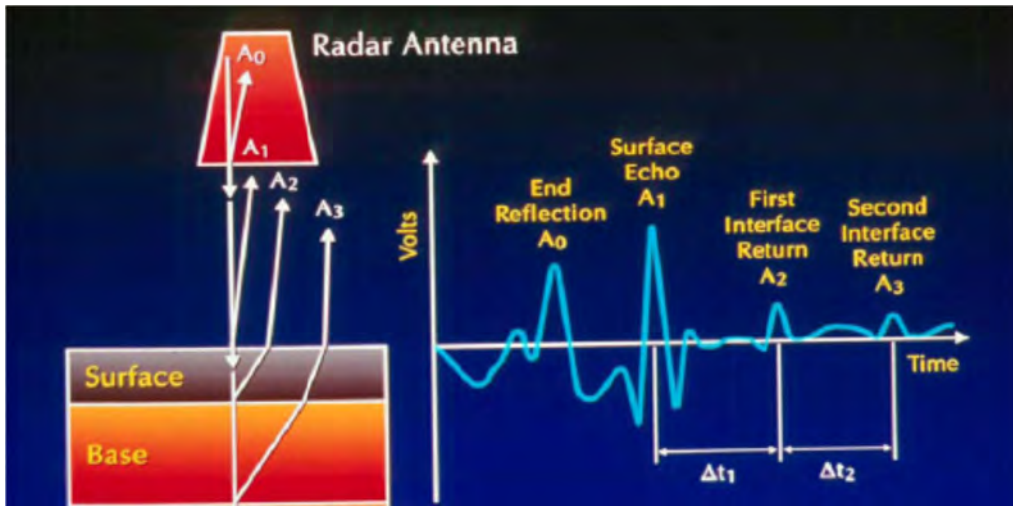


Figure K.1. Air-coupled GPR operation.

The equipment could not detect delaminations or voids in the other sections.

Figure K.2 shows the analysis of the GPR data on Specimen D using the COLORMAP program. The program indicated that the depth to the defect was 7.7 in. The program calculated a surface dielectric of 8.2 and a void dielectric of 6.6. If an air-filled void exists, the calculated dielectric of the void is less than the surface dielectric.

Figure K.3 shows the analysis of the GPR data on Specimen F using the COLORMAP program. The program indicated that the depth to the defect was 2.6 in. The program calculated a surface dielectric of 9.1 and a void dielectric of 7.3. If an air-filled void exists, the calculated dielectric of the void is less than the surface dielectric.

Figure K.4 shows the analysis of the GPR data on Specimen G using the COLORMAP program. The program indicated that

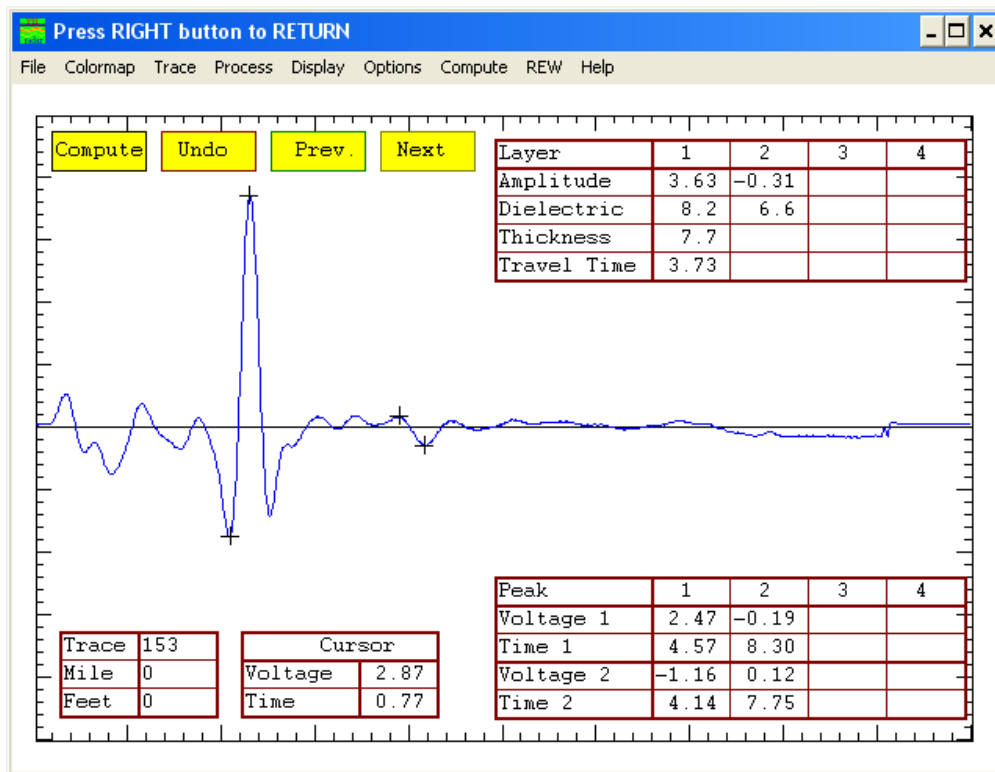


Figure K.2. Analysis of air-coupled GPR data on Specimen D.

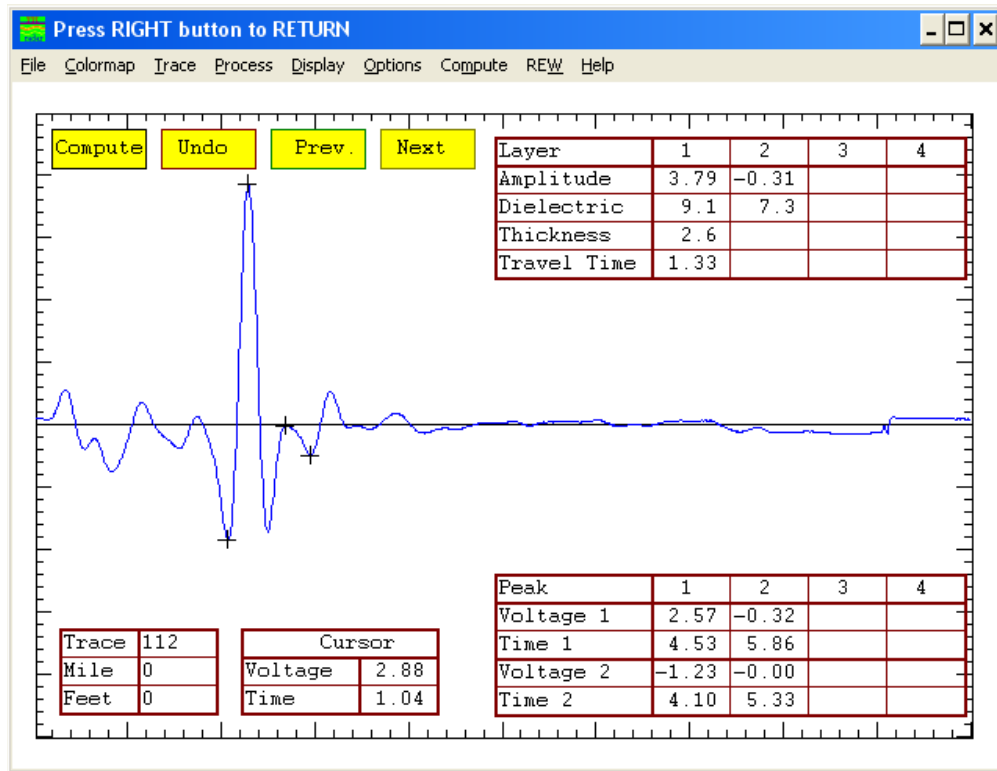


Figure K.3. Analysis of air-coupled GPR data on Specimen F.

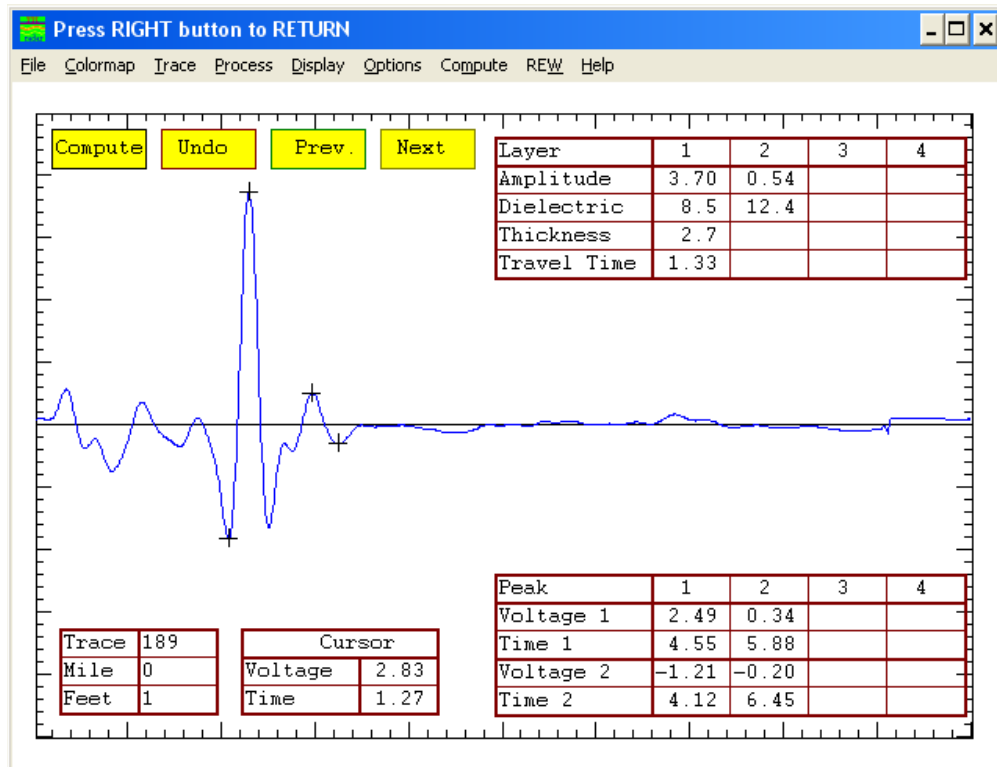


Figure K.4. Analysis of air-coupled GPR data on Specimen G.

the depth to the defect was 2.7 in. The program calculated a surface dielectric of 8.5 and a void dielectric of 12.4. If a water-filled void exists, the calculated dielectric of the void is greater than the surface dielectric.

Air-Coupled GPR Results from Tunnel Testing

Washburn Tunnel

In the Washburn Tunnel, which is completely lined with tiles, the air-coupled GPR data were collected every foot and indicated changes in the surface dielectric along the length of the tunnel. An example of air-coupled GPR data collected in the Washburn Tunnel is shown in Figure K.5. This figure was generated by the Pavecheck program developed by TTI to analyze air-coupled GPR data. The dielectric values shown in Figure K.5 have not been corrected for changes in the distance between the antenna and the tunnel lining. As can be inferred in Figure K.5, the distance between the antenna and the tunnel surface did vary because of the difficulty of keeping the vehicle moving in a straight line. However, the TTI team believes the data are useful in their current form. The

unusually large peak on the left side of the figure is associated with a steel plate installed in the tunnel lining.

Chesapeake Channel Tunnel

At the top of the Chesapeake Channel Tunnel lining, the team used air-coupled GPR data to locate one area with no surface distress for in-depth testing. The data were collected every foot with the antenna aimed directly at the top of the tunnel lining. Data could not be collected from the top sides of the tunnel because of the cables and utilities installed there. The area chosen for testing had a surface dielectric value of 18.7, which is unusually high for concrete, at Station 486+67. Figure K.6 shows the air-coupled GPR data for this area. As can be inferred from Figure K.6, the distance between the antenna and the tunnel lining surface was kept relatively constant (the antenna was mounted on a pushcart and pointed directly at the top of the tunnel lining). The results of the in-depth testing in this area showed that a shallow delamination existed at that location. The team tested other locations at the top of the tunnel and on the tiled tunnel wall.

The team used infrared data from the SPACETEC equipment to determine testing locations on the tiled tunnel wall

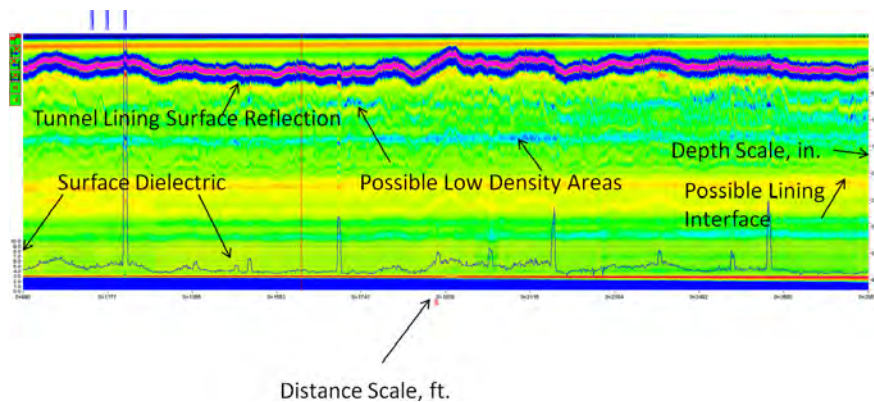


Figure K.5. Air-coupled GPR data collected for the Washburn Tunnel.

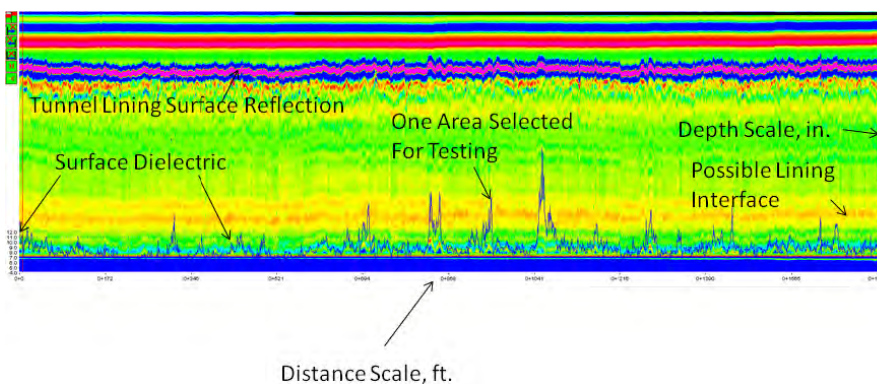


Figure K.6. Air-coupled GPR data collected for the Chesapeake Channel Tunnel roof.

at the Chesapeake Bay. The team could not collect air-coupled GPR data at that location because construction equipment blocked access to the wall at the time of the air-coupled GPR data collection. The in-depth evaluation devices were able to detect defects in the areas tested.

The TTI team also collected handheld infrared camera images in the Chesapeake Channel Tunnel roof and roadway; selected images are shown in Appendix L. The team found few changes in temperature in the tunnel roof. The team found that collecting images on tiled tunnel linings with this equipment was problematic because the tile reflected heat from any heat-generating source, including construction equipment, lights, and people. In addition, the team was not able to effectively compare the SPACETEC results along the area tested by the team because that would have required a lane closure on the other side to effectively obtain images with the handheld device.

The vehicle-mounted thermal camera scans were also affected by construction equipment operations during the scans, so the team could not generate comparisons between the SPACETEC results and that device.

Figure K.7 shows an example of the air-coupled GPR data taken along the tiled tunnel wall. The dielectric values

shown in Figure K.7 have not been corrected for changes in the distance between the antenna and the tunnel lining (a version of this software will be developed soon with this capability). However, the TTI team believes the data are useful in their current form. The unusually large peaks are associated with steel plates or fixtures installed on the tunnel surface.

Eisenhower Memorial Tunnel

In the Eisenhower Memorial Tunnel, the in-depth evaluation devices were able to detect defects in the areas tested. The locations were selected for testing with the in-depth devices based on observed surface distress and feedback from the tunnel operator.

The team encountered problems with collecting air-coupled GPR in the top portion of the Eisenhower Memorial Tunnel with an exposed concrete surface, mainly because cables and other obstructions were in the way. In addition, the team could not collect data at the top of the tunnel because of the distance between the ceiling and the roof. Figure K.8 shows an example of the data collected (the antenna was mounted on a pushcart).

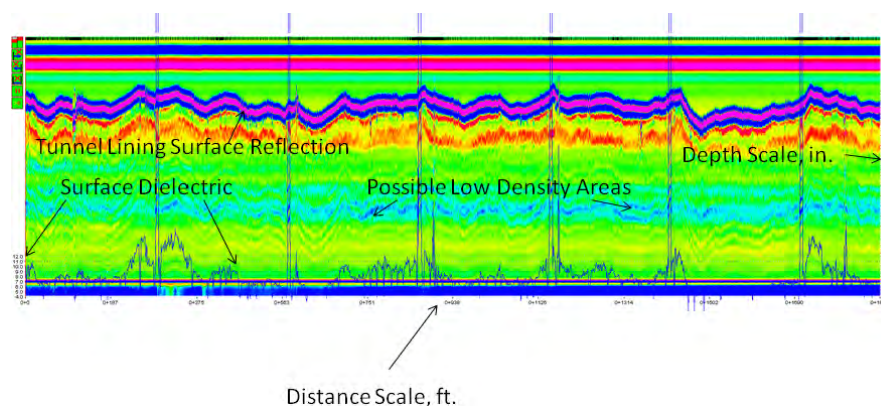


Figure K.7. Air-coupled GPR data collected for the Chesapeake Channel Tunnel tiled wall.

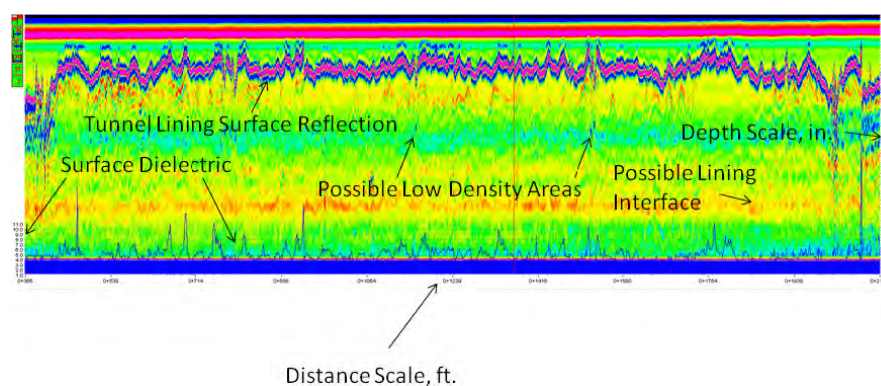


Figure K.8. Air-coupled GPR data collected for the Eisenhower Memorial Tunnel, top portion.

The antenna was pointed at the side of the tunnel; the team had difficulty keeping the pushcart moving in a straight line, so the distance between the antenna and the lining surface varied.

Although GPR data were collected on the tiled roadway section, the data proved not to be usable because the tiles were mounted on steel panels, and the panels were apparently not attached directly to the concrete.

The TTI team also collected handheld infrared camera images in the top section of the Eisenhower Memorial Tunnel and found significant temperature changes. Appendix L contains selected images from the handheld device and the thermal scan.

Hanging Lake Tunnel

In the Hanging Lake Tunnel, the in-depth evaluation devices were able to detect defects in the areas tested on the tunnel

roof. The locations selected for testing with the in-depth devices were requested by the tunnel operator.

Figure K.9 shows an example of the air-coupled data taken on the Hanging Lake Tunnel roof (the antenna was mounted on a pushcart and pointed directly at the top of the lining). As can be inferred from Figure K.9, the distance between the antenna and the tunnel lining surface was kept relatively constant. Also, Figure K.9 shows two distinct interfaces.

Figure K.10 shows an example of the air-coupled GPR data taken on the Hanging Lake Tunnel tiled wall. The dielectric values shown in Figure K.10 have not been corrected for changes in the distance between the antenna and the tunnel lining. However, the TTI team believes the data are useful in their current form. The unusually large peaks are associated with steel plates or fixtures installed on the tunnel surface.

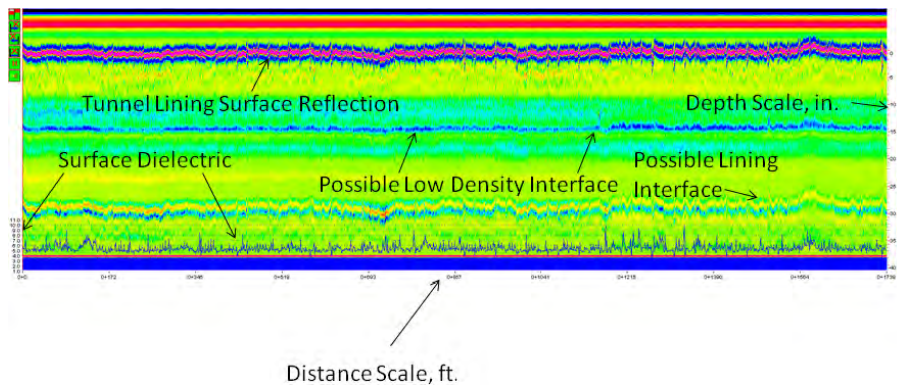


Figure K.9. Air-coupled GPR data collected for the Hanging Lake Tunnel roof.

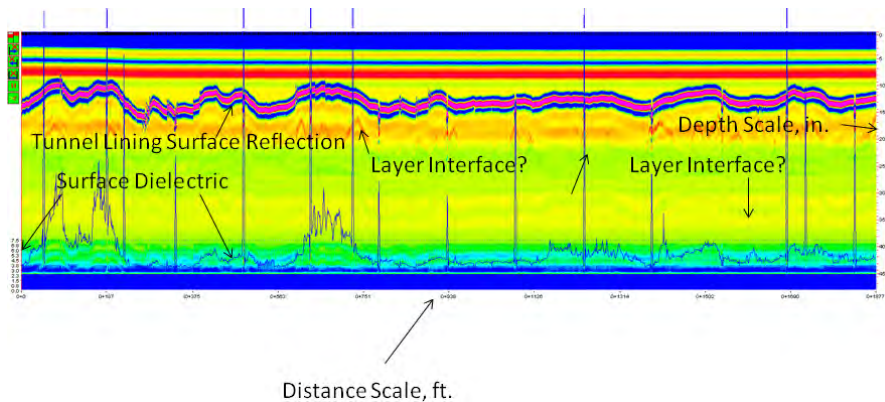


Figure K.10. Air-coupled GPR data collected for the Hanging Lake Tunnel tiled wall.

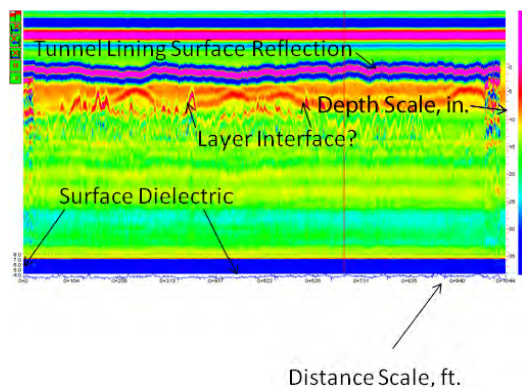


Figure K.11. Air-coupled GPR data collected for the No Name Tunnel.

No Name Tunnel

In the No Name Tunnel, the team collected only air-coupled GPR data. Figure K.11 shows an example of the air-coupled GPR data taken in that tunnel. As can be seen in Figure K.11, the dielectric values are unusually low. The team did not encounter this issue in the other tunnels tested. One explanation is that the antenna was inadvertently set to a lower power output mode, which resulted in lower reflection amplitudes from the tunnel lining. In any case, the air-coupled GPR data indicated possible layer interfaces in this tunnel.

APPENDIX L

Evaluation of Texas A&M Transportation Institute Test Specimens with the Handheld Infrared Camera

Handheld Infrared Camera

The Texas A&M Transportation Institute (TTI) purchased a FLIR T300 handheld infrared camera for this Renewal project. The cost of the camera was approximately \$9,000. Figure L.1 is a photograph of this camera.

Infrared Camera Images for the TTI Test Specimens

TTI personnel collected infrared camera images of ground-penetrating radar (GPR) data on concrete and shotcrete specimens that contained simulated delaminations and voids. As described in Chapter 3 of the main report, the TTI team determined that the infrared camera could detect only three simulated voids, all of which were located in shotcrete sections. Those specimens were

- Specimen F, an air-filled void placed 3 in. from the surface;
- Specimen G, a water-filled void placed 3 in. from the surface; and
- Specimen L, a delamination placed 1 in. from the surface.

Specimen F had the most distinct thermal image.

The following images were taken at night. Figure L.2 shows the infrared image of Specimen F. The blue grid lines are chalk marks placed on the specimen. The spacing between the chalk marks is 50 mm (approximately 2 in.).

Figure L.3 shows the infrared image of specimen G. As shown in Figure L.3, the thermal image is less distinct. The

blue grid lines are chalk marks placed on the specimen. The spacing between the chalk marks is 50 mm.

Figure L.4 shows the infrared image of Specimen L. As shown in Figure L.4, the thermal image is less distinct than the image in Figure L.2. The blue grid lines are chalk marks placed on the specimen. The spacing between the chalk marks is 50 mm.

Selected Infrared Images

Introduction

This section contains selected infrared images from the FLIR T300 handheld infrared camera and the FLIR A325 vehicle-mounted infrared camera. TTI personnel obtained the FLIR T300 images. Roadscanners Oy personnel obtained and analyzed the images from the FLIR A325.

Chesapeake Channel Tunnel Images

Figures L.5 through L.14 show the images obtained in the Chesapeake Channel Tunnel.

Eisenhower Memorial Tunnel Images

Figures L.15 through L.23 show the images obtained from the Eisenhower Memorial Tunnel.

Hanging Lake Tunnel Images

Figure L.24 through Figure L.35 show the images taken in the Hanging Lake Tunnel.



Figure L.1. FLIR T300 infrared camera.

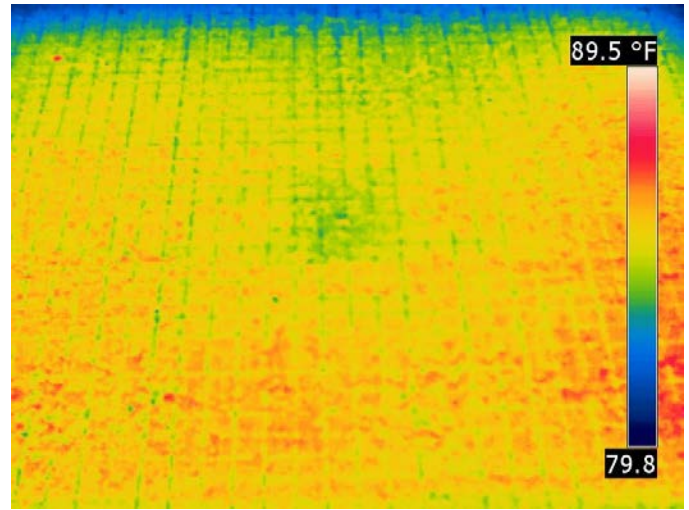


Figure L.4. Infrared camera image of Specimen L.

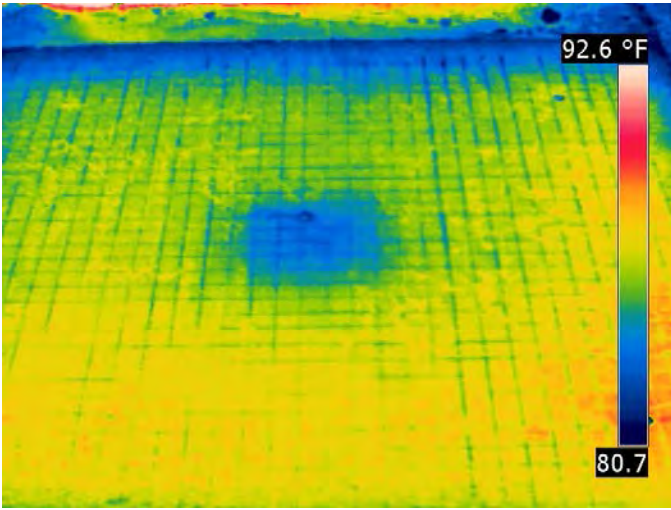


Figure L.2. Infrared camera image of Specimen F.

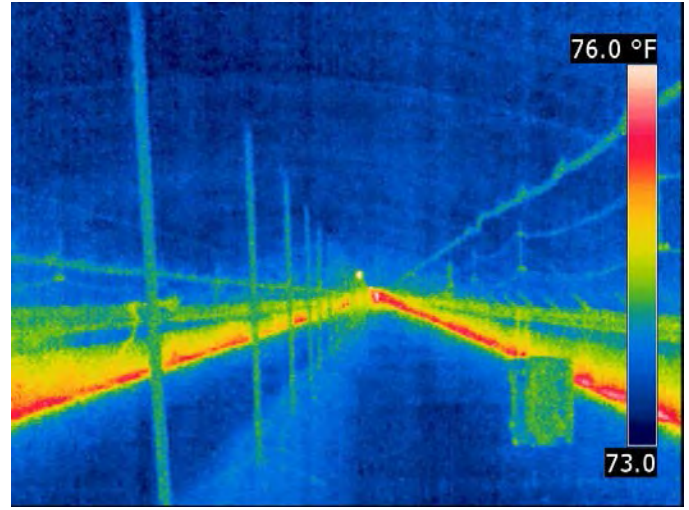


Figure L.5. FLIR T300 infrared image of the top of the Chesapeake Channel Tunnel. Areas in red are air vents.

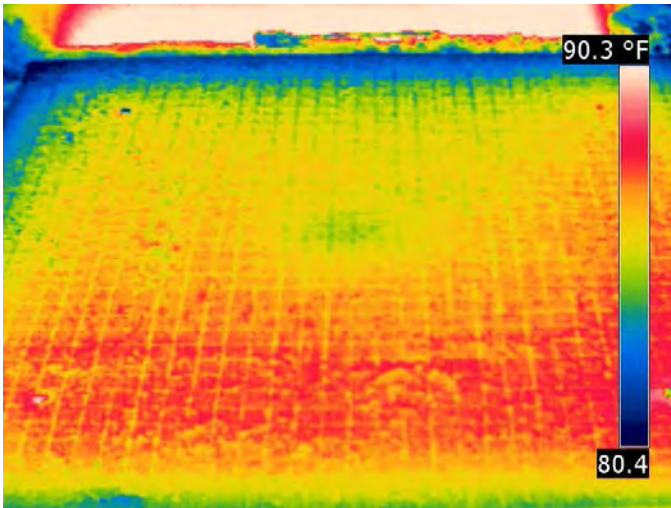


Figure L.3. Infrared camera image of Specimen G.



Figure L.6. Visual image of the top of the Chesapeake Channel Tunnel.

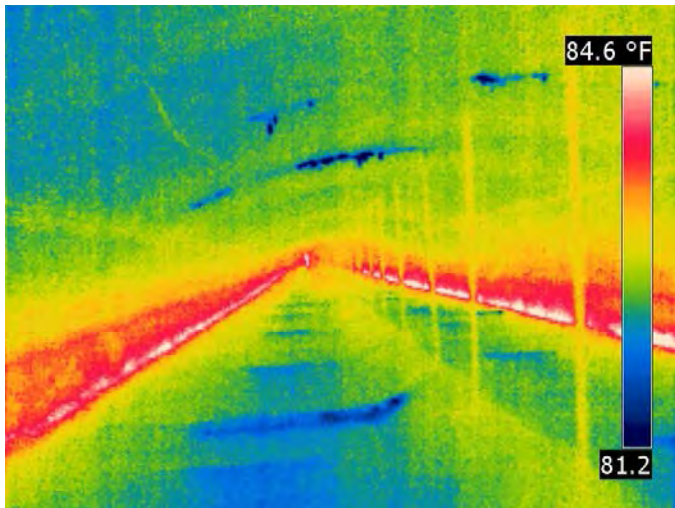


Figure L.7. FLIR T300 infrared image of the top of the Chesapeake Channel Tunnel. Areas in blue at the top of the tunnel are cracks with moisture.



Figure L.9. FLIR T300 visual image of Figure L.8.

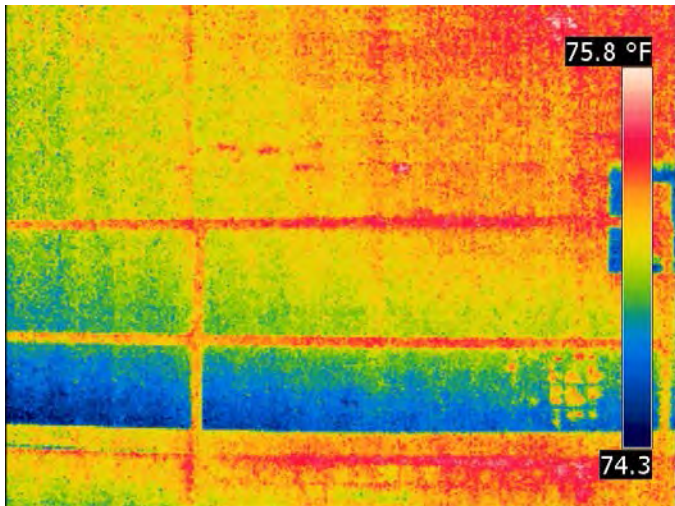


Figure L.8. FLIR T300 infrared image of the tiled lining in the Chesapeake Channel Tunnel.

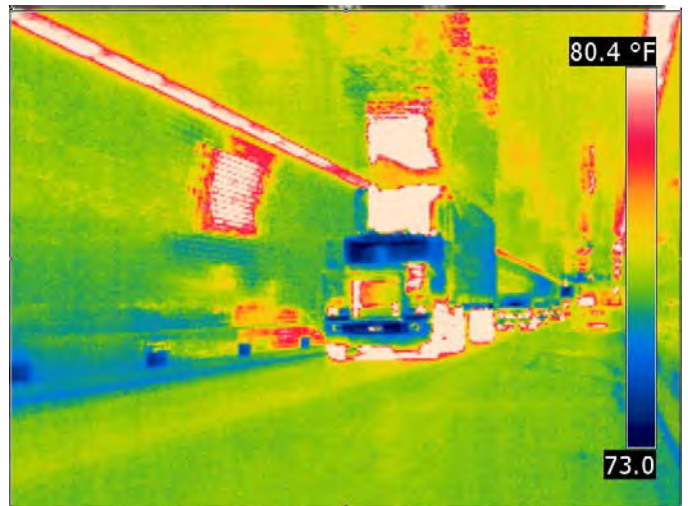


Figure L.10. FLIR T300 infrared image of the tiled lining in the Chesapeake Channel Tunnel. Note the thermal reflection of the vehicles.



Figure L.11. FLIR T300 visual image of Figure L.10.

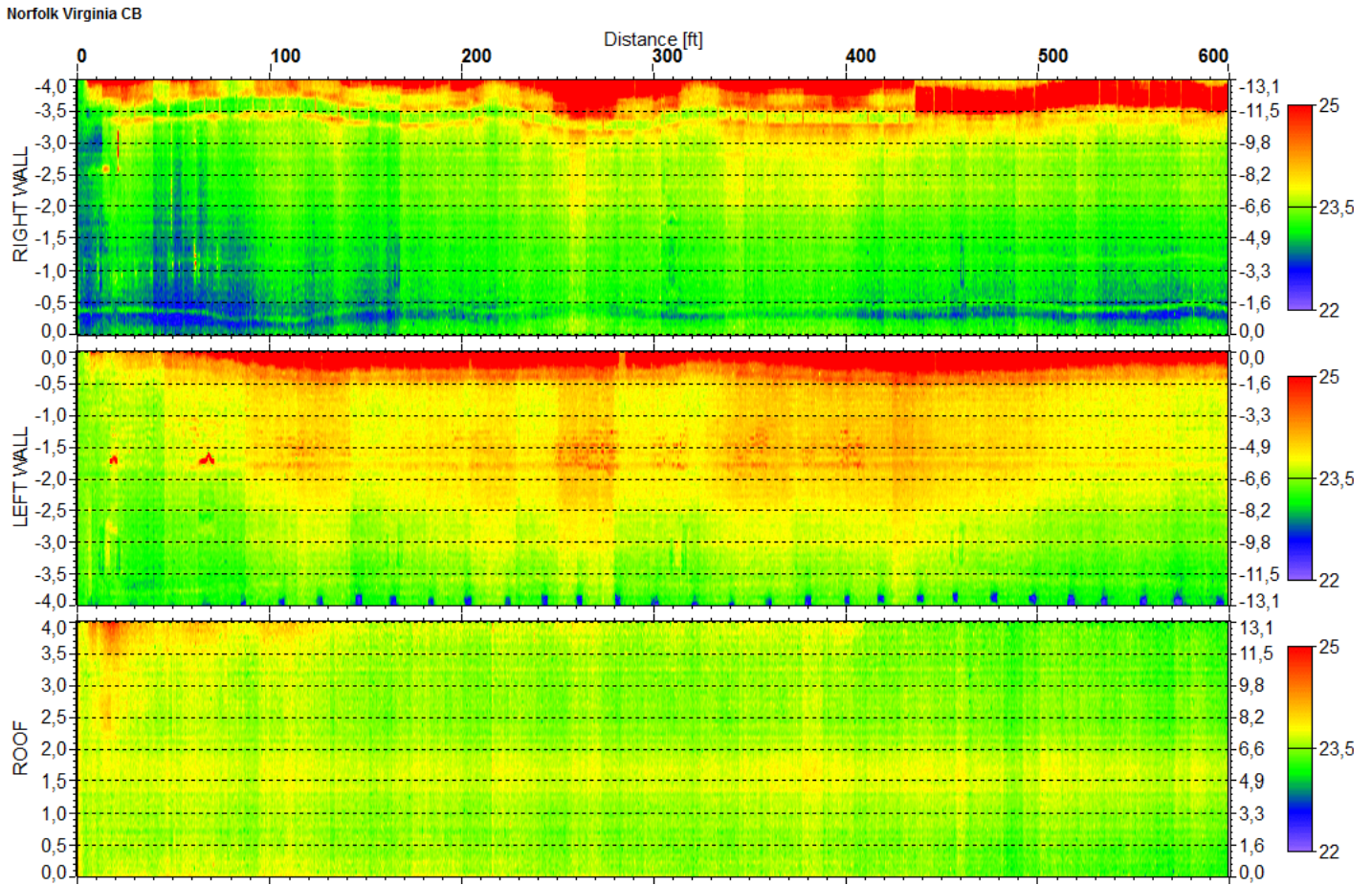


Figure L.12. FLIR A325 scan of the tiled roadway section in the Chesapeake Channel Tunnel. The temperature range is in centigrade (0–600 ft).

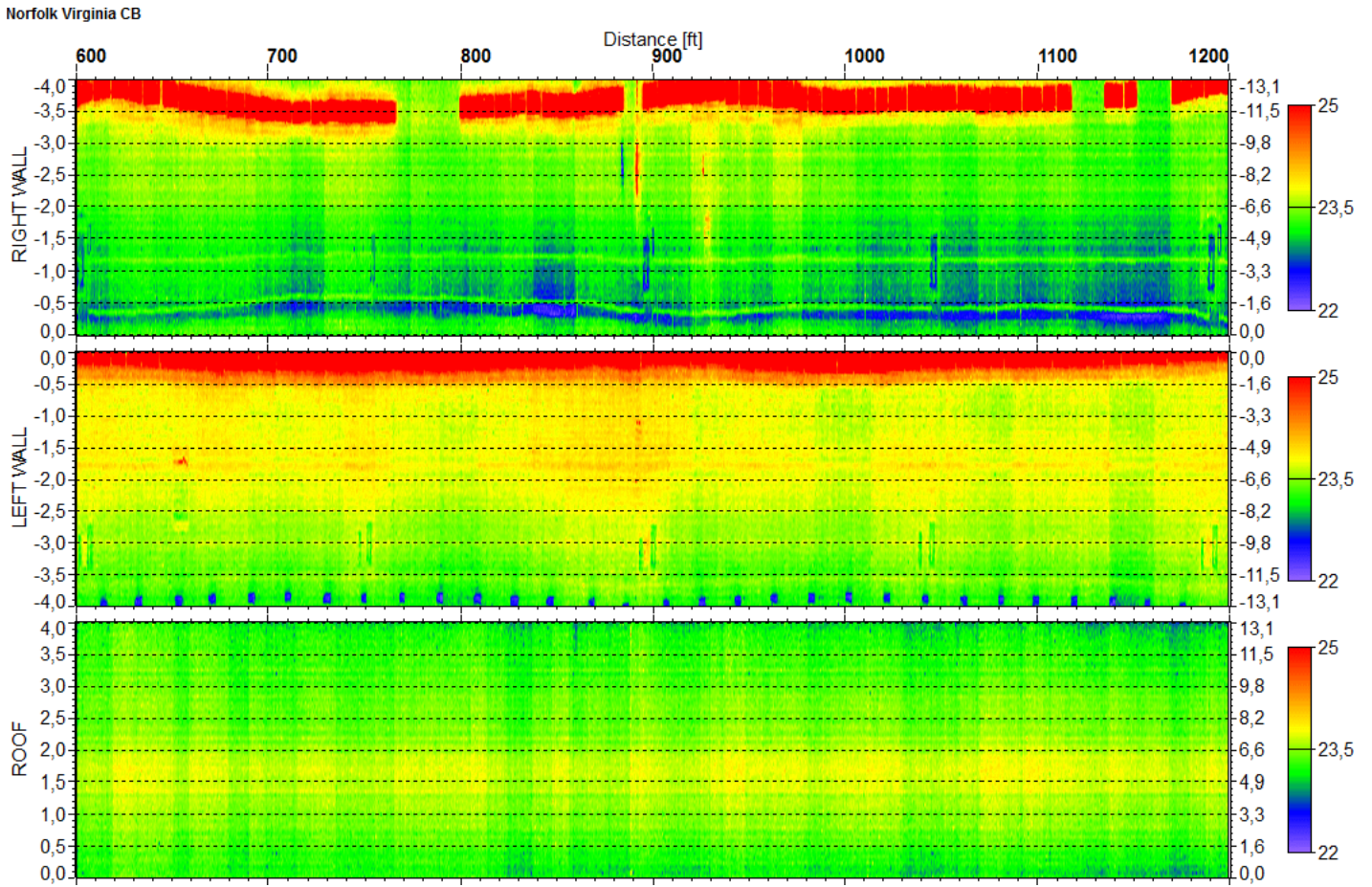


Figure L.13. FLIR A325 scan of the tiled roadway section in the Chesapeake Channel Tunnel. The temperature range is in centigrade (600–1,200 ft).

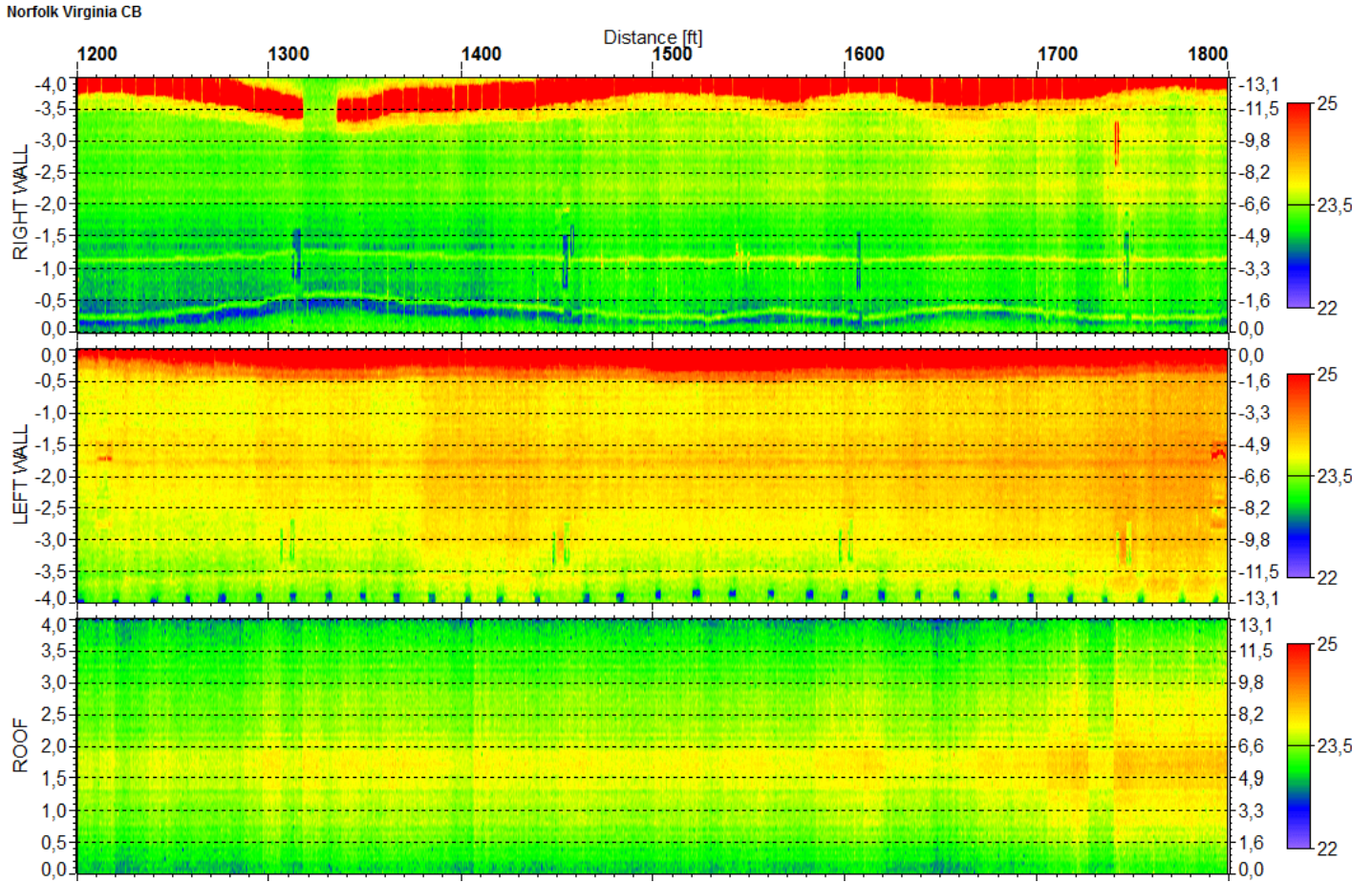


Figure L.14. FLIR A325 scan of the tiled roadway section in the Chesapeake Channel Tunnel. The temperature range is in centigrade (1,200–1,800 ft).

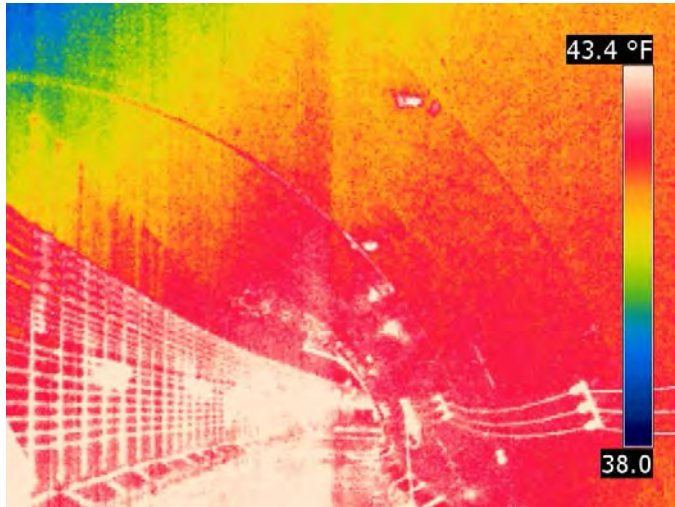


Figure L.15. FLIR T300 infrared image of the top of the Eisenhower Memorial Tunnel. Areas in white are cables.

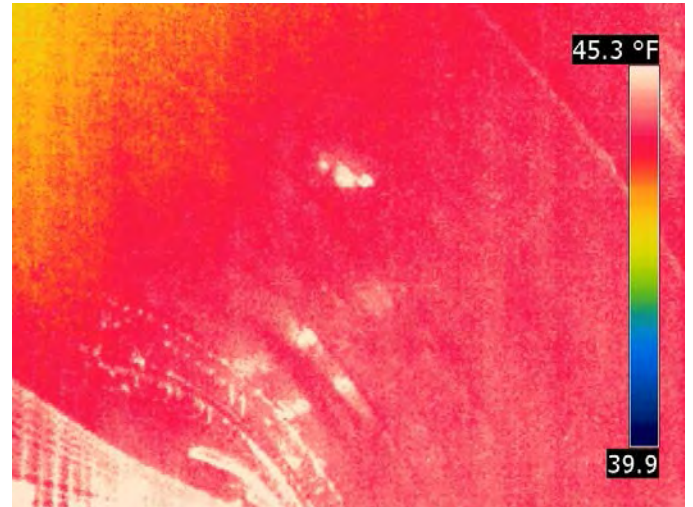


Figure L.16. FLIR T300 infrared image of the top of the Eisenhower Memorial Tunnel.



Figure L.17. Visual image of the top of the Eisenhower Memorial Tunnel.

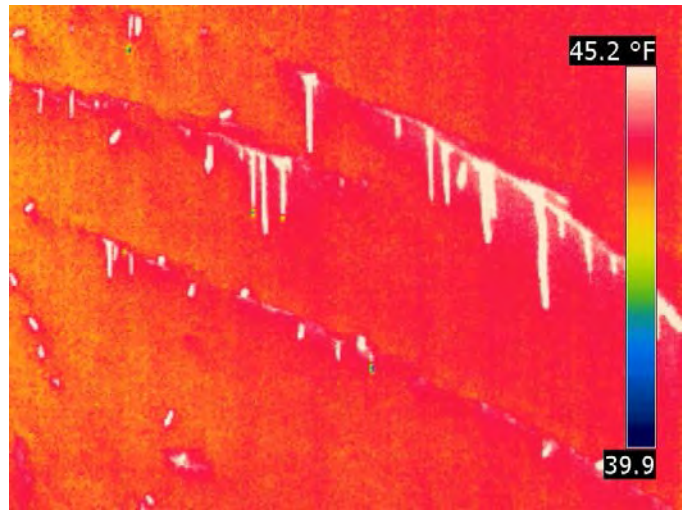


Figure L.18. FLIR T300 infrared image of the top of the Eisenhower Memorial Tunnel showing stalagmites (white).

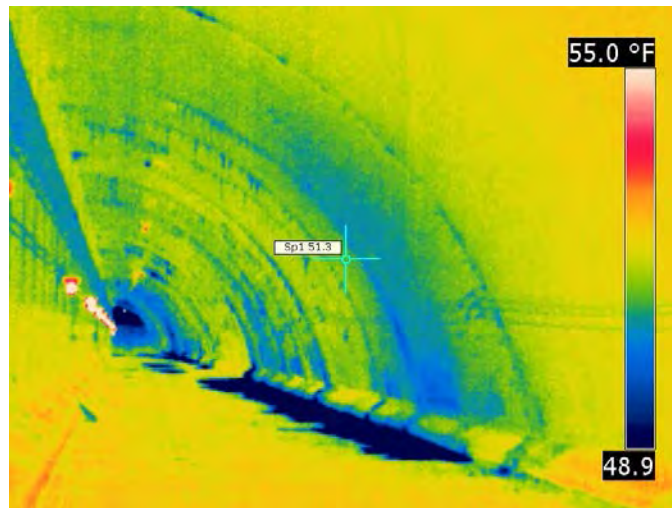


Figure L.19. FLIR T300 infrared image of the top of the Eisenhower Memorial Tunnel.

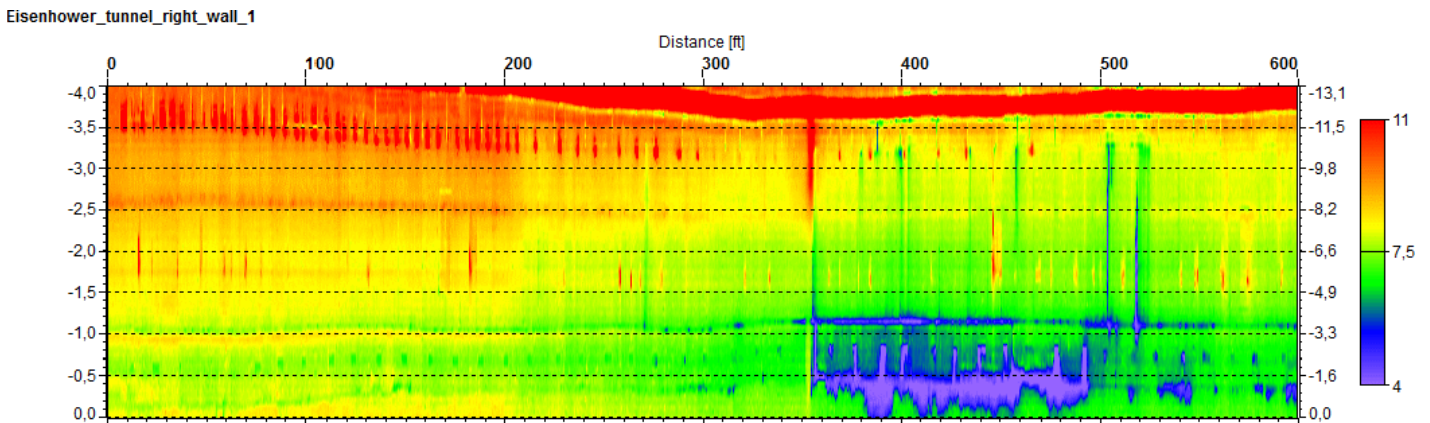


Figure L.20. FLIR A325 scan of the tiled roadway section in the Eisenhower Memorial Tunnel. The temperature range is in centigrade (0–600 ft).

Eisenhower_tunnel_right_wall_1

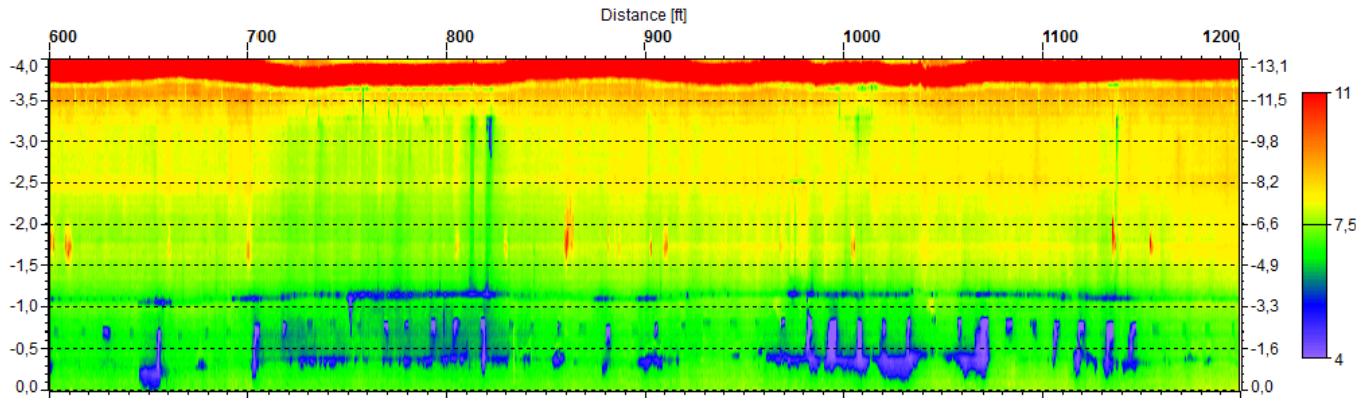


Figure L.21. FLIR A325 scan of the tiled roadway section in the Eisenhower Memorial Tunnel. The temperature range is in centigrade (600–1,200 ft).

Eisenhower_tunnel_right_wall_1

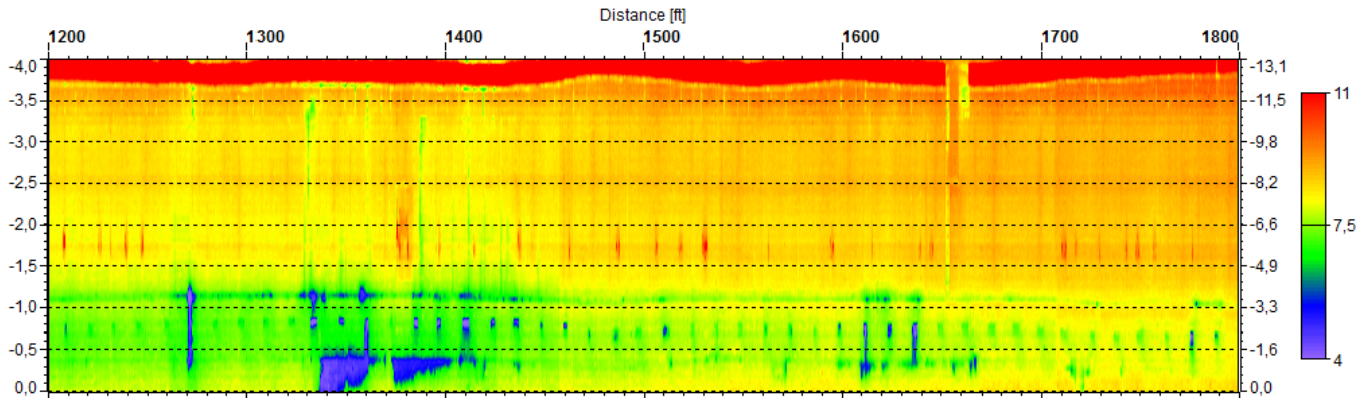


Figure L.22. FLIR A325 scan of the tiled roadway section in the Eisenhower Memorial Tunnel. The temperature range is in centigrade (1,200–1,800 ft).

Eisenhower_tunnel_right_wall_1

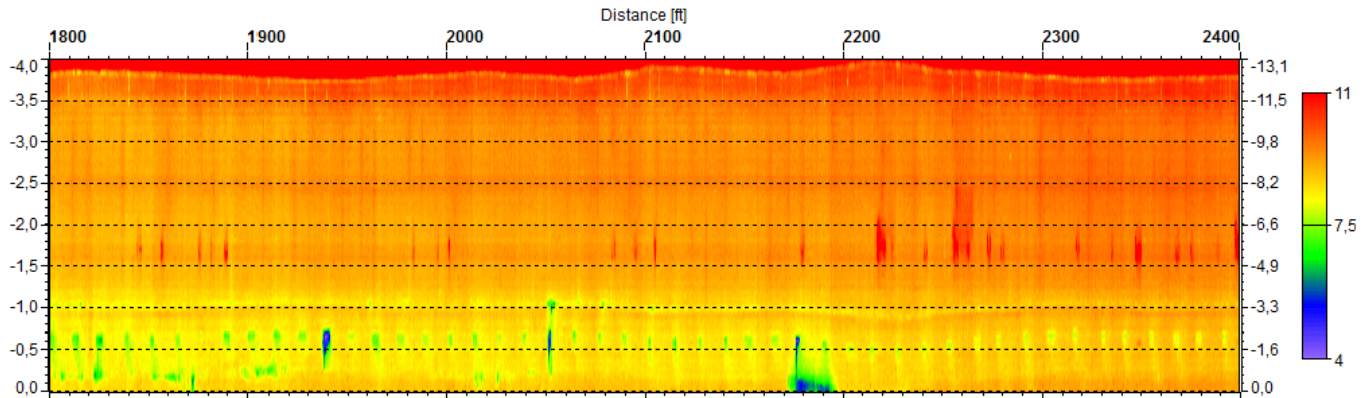


Figure L.23. FLIR A325 scan of the tiled roadway section in the Eisenhower Memorial Tunnel. The temperature range is in centigrade (1,800–2,400 ft).

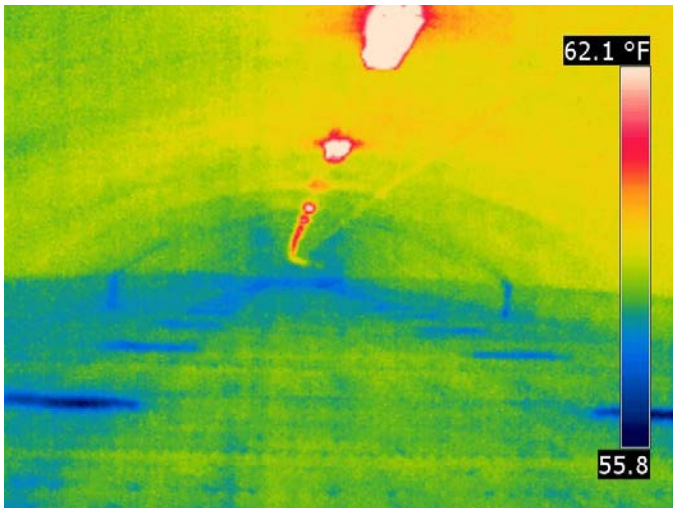


Figure L.24. FLIR T300 infrared image of the top of the Hanging Lake Tunnel.



Figure L.25. Visual image of the top of the Hanging Lake Tunnel. Note staining around cracks.

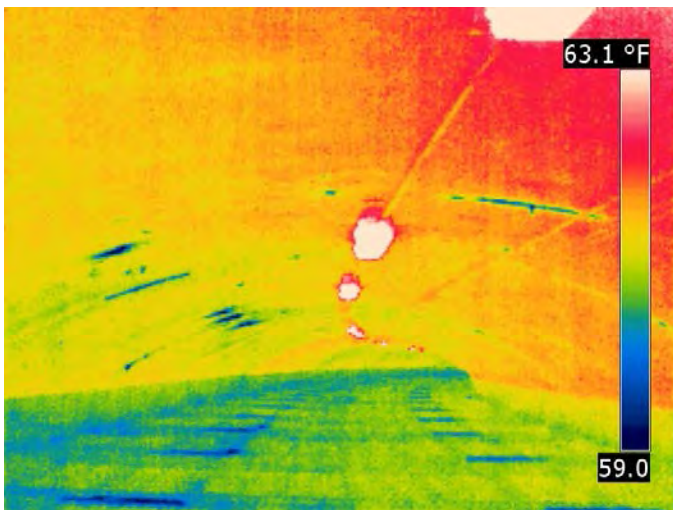


Figure L.26. FLIR T300 infrared image of the top of the Hanging Lake Tunnel. According to visual observations, areas in blue along the tunnel ceiling are cracks with moisture; areas in blue at the bottom are air vents.

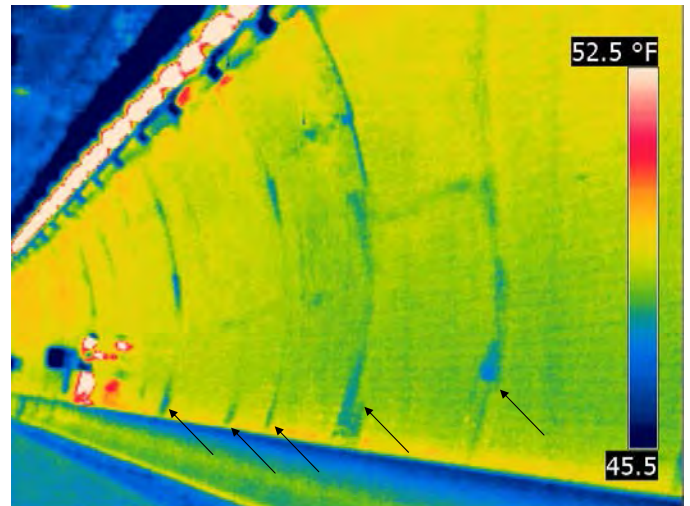


Figure L.27. FLIR T300 infrared image of the tiled tunnel wall in the roadway section (eastbound). According to limited sounding tests, areas in blue appear to be areas of debonded tiles.



Figure L.28. FLIR T300 visual image of Figure L.27.

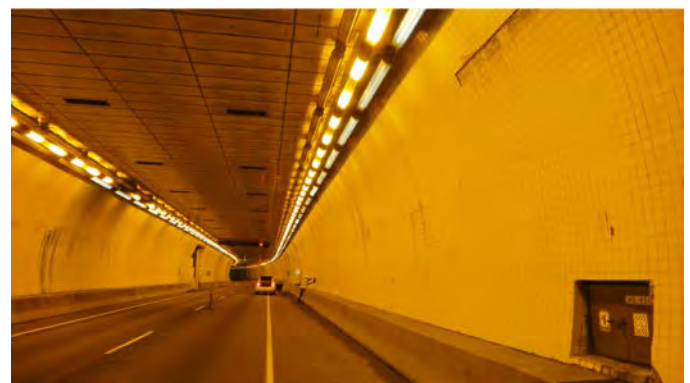


Figure L.29. Visual image of the Hanging Lake Tunnel roadway section.

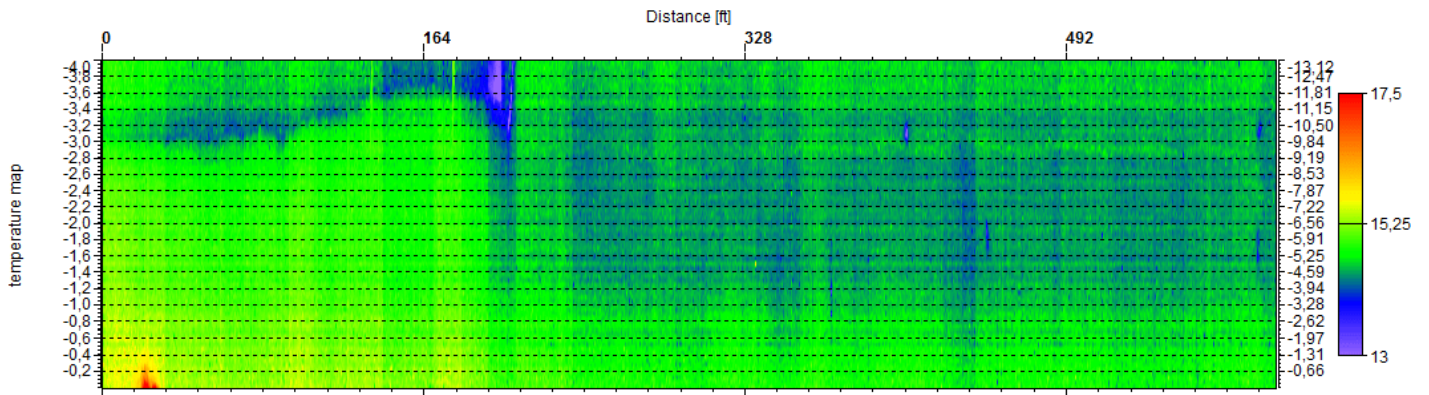


Figure L.30. FLIR A325 scan of the top of the Hanging Lake Tunnel. The temperature range is in centigrade (0–600 ft).

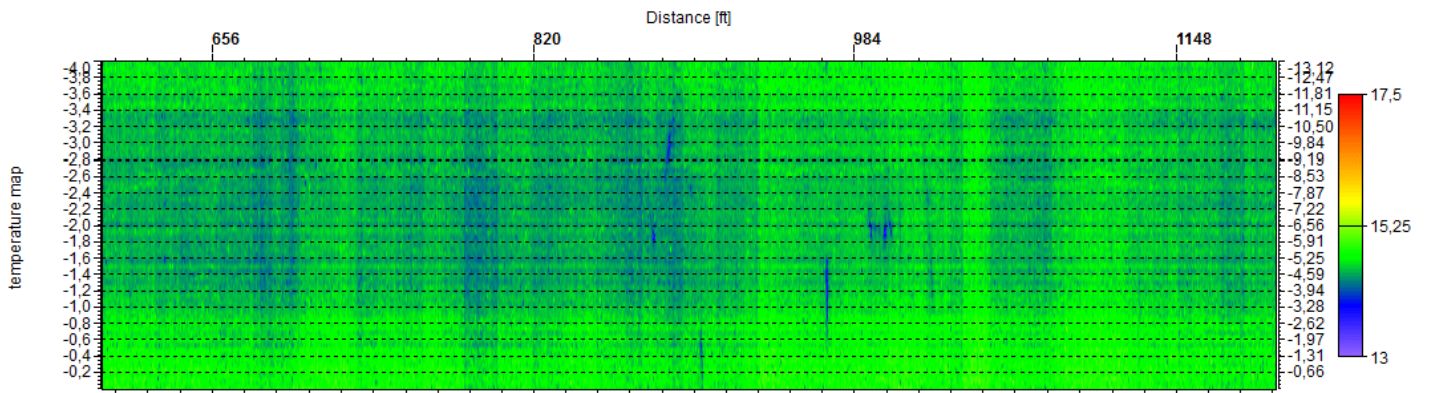


Figure L.31. FLIR A325 scan of the top of the Hanging Lake Tunnel. The temperature range is in centigrade (600–1,200 ft).

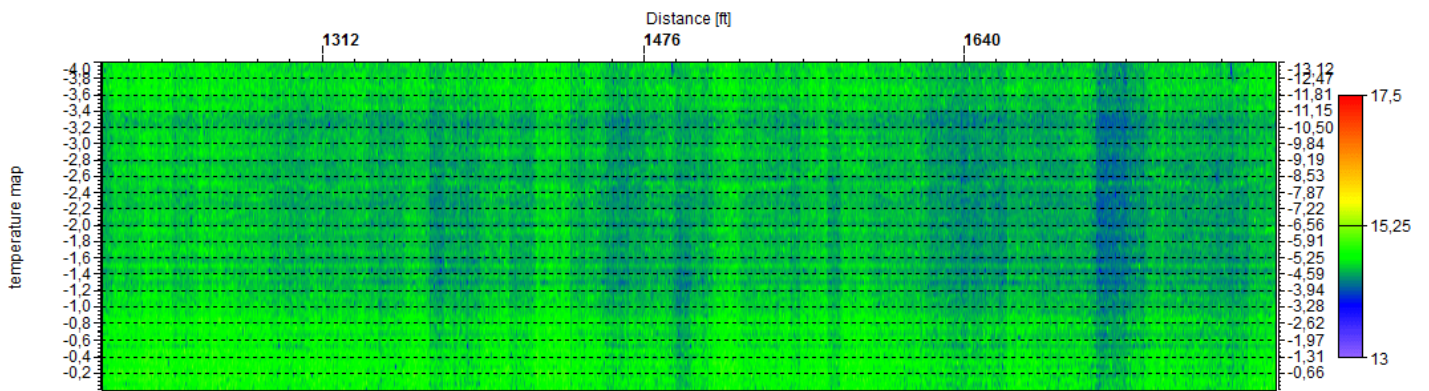


Figure L.32. FLIR A325 scan of the top of the Hanging Lake Tunnel. The temperature range is in centigrade (1,200–1,800 ft).

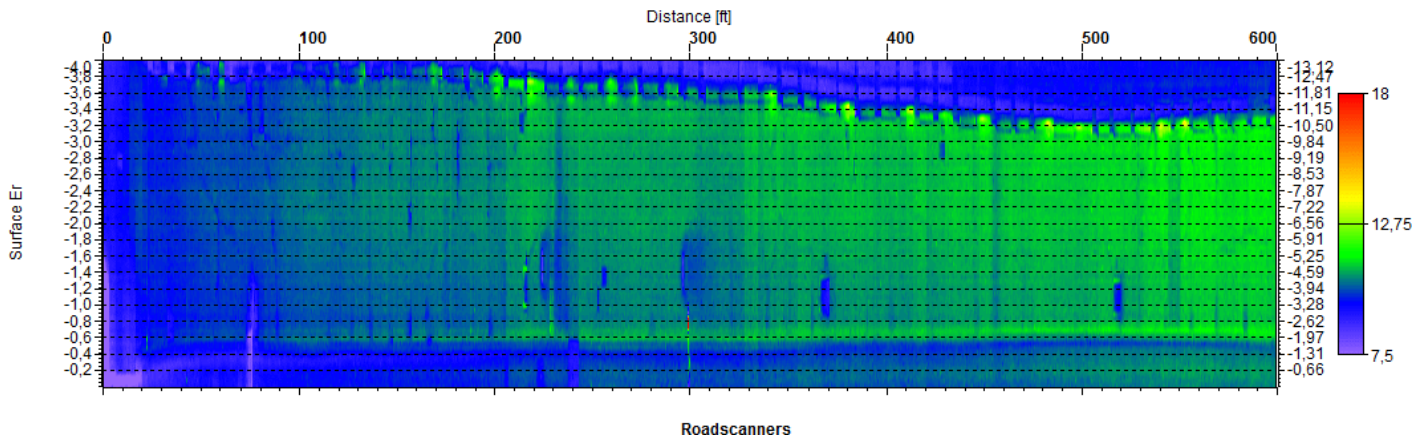


Figure L.33. FLIR A325 scan of the tiled roadway section in the Hanging Lake Tunnel. The temperature range is in centigrade (0–600 ft).

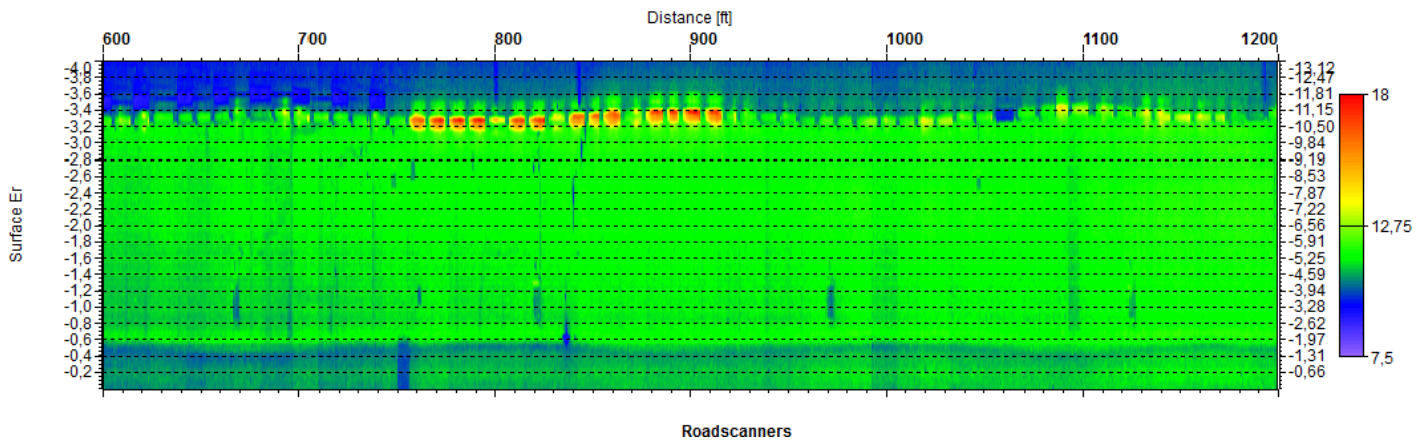


Figure L.34. FLIR A325 scan of the tiled roadway section in the Hanging Lake Tunnel. The temperature range is in centigrade (600–1,200 ft).

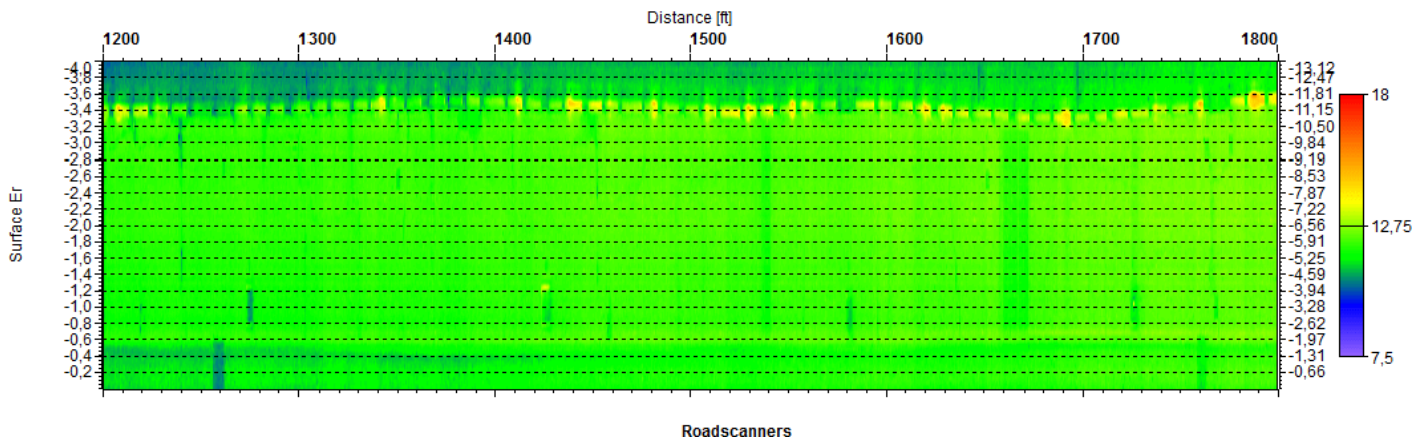


Figure L.35. FLIR A325 scan of the tiled roadway section in the Hanging Lake Tunnel. The temperature range is in centigrade (1,200–1,800 ft).

APPENDIX M

Ultrasonic Tomography Field Tests in the United States

Introduction

Field evaluations of four public tunnels and a series of test specimens were conducted for this research. Because the ultrasonic tomography (UST) technique does not have a testing methodology that is field ready, the system was first evaluated by testing its ability to detect simulated defects in laboratory specimens with simulated defects as well as other available sites (pavements, airport runways, bridge decks) for which ground truth validation was available. After that testing, the system was taken to the field to evaluate natural structural defects within actual tunnel linings. The tunnels tested were the Eisenhower Memorial Tunnel near Dillon, Colorado; Hanging Lake Tunnel near Glenwood Springs, Colorado; Chesapeake Channel Tunnel near Norfolk, Virginia; and Washburn Tunnel in Houston, Texas. Types of concrete defects the system used to detect and localize include air- and water-filled voids, vertical cracks, horizontal delaminations, tile debonding, and abnormalities such as clay lumps. The device is also used to determine reinforcement depth and spacing as well as concrete thickness measurements.

The testing concluded that the UST system is effective in locating horizontal delaminations ranging in thickness from 0.05 mm to 2.0 mm (0.002 in. to 0.079 in.) and is able to differentiate between fully debonded and partially bonded areas. Vertical cracks were only clearly characterized when the polarization of the shear waves was not parallel with the direction of the crack; however, the presence of cracks often resulted in the omission of surface detail in the scanned images because shear waves cannot be supported by air. Backwall surfaces up to a depth of 965 mm (38 in.) were successfully and accurately determined. Air- and water-filled voids ranging from 76 mm to 203 mm (3 in. to 8 in.) in depth, as well as reinforcement details such as layout and depth, were also successfully determined and located. With the exception of some medium-size clay lumps (with a diameter of approximately 102 mm, or 4 in.) surrounding reinforcement, all clay lumps tested were successfully located.

A summary of the ultrasonic tomography technique and field testing results in the United States are provided in this appendix.

Ultrasonic Tomography Technique

The ultrasonic tomography system in this study is a device that uses an array of ultrasonic transducers to transmit and receive acoustic stress waves for the inspection of concrete structures. The system used here, the A1040 MIRA, is produced by Acoustic Control Systems.

The tomograph, shown in Figure M.1 (left), uses a 4-by-12 grid of mechanically isolated and dampened transducers that can fit the profile of a rough concrete testing surface with a variance of approximately 10 mm (0.4 in.). Each row of four transducers transmits stress waves sequentially while the remaining rows act as receivers. In this manner, the tomograph has a wide coverage of shear wave pulses that reflect at internal interfaces where the material impedance changes (Figure M.1, right). With the help of a digitally focused algorithm—an alteration of the synthetic aperture focusing technique (SAFT)—a three-dimensional (3-D) volume is presented with each point of possible reflection in half-space represented by a color scheme, scaled according to reflecting power (Schickert 1995; Schickert et al. 2003). This 3-D image can also be dissected into each of the three planes representing its volume: the B-scan, C-scan, and D-scan (Figure M.2). The B-scan is an image slice showing the depth of the specimen on the vertical (or z) axis versus the width of the scan on the horizontal (or x) axis. This slice is a plane perpendicular to the scanning surface and parallel to the length of the device. The C-scan is an image slice showing the plan view of the tested area, with the y axis of the scan depicting width parallel to the scanning direction and the horizontal (or x) axis of the scan representing the length perpendicular to the scanning direction. The scanning direction is always defined as the y -axis, as seen in Figure M.2.

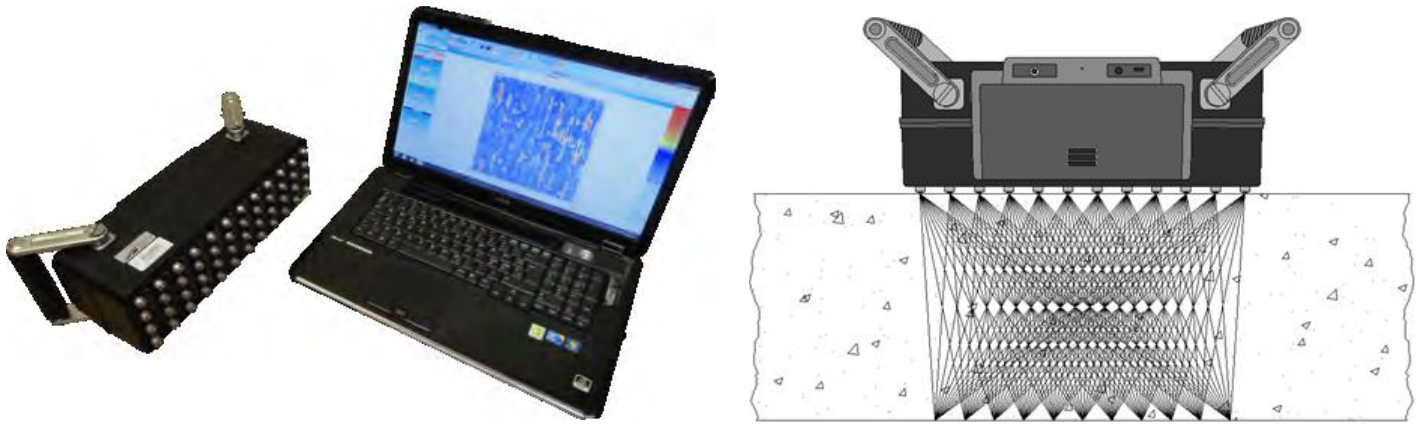


Figure M.1. The A1040 MIRA system (left), and the transmission/reception of acoustic waves (right).

The D-scan is like the B-scan in that it images a plane perpendicular to the testing surface, but it is oriented parallel to the scanning direction. On each of the scans, the various intensities reported by the returned waves are color coded, from light blue to deep red, representing low reflectivity (typically sound concrete) and high reflectivity (any type of impedance), respectively. With this intensity scaling, discontinuities with distinctly different wave speeds—such as voids, delaminations, cracks, and other abnormalities—are easy to discern.

This UST system has had limited exposure to industrial applications but is quickly becoming recognized as a powerful non-destructive testing (NDT) method. The ultrasonic technique in general has been used in concrete structures to identify concrete thickness and elastic modulus, as well as to detect grouting conditions of internal ducts in prestressed structures (Im et al. 2010; De La Haza et al. 2011). Previous uses of the ultrasonic tomograph technique have largely been conducted by the Federal Institute for Materials Research and Testing (BAM) in Germany. BAM collaborated with Acoustic Control Systems in the development of the MIRA system and has successfully detected delaminations at 203 mm (8 in.) below the surface (Shokouhi et al. 2011). The Shokouhi study was conducted on a demolished bridge deck and was limited to delaminations ranging from 76 mm to 203 mm (3 in. to 8 in.) in depth. That study also used a previous version of the UST device (with a 4-by-10

transducer array). Another study conducted by BAM indicated the UST technique could detect grouting conditions in post-tensioned concrete elements (Krause et al. 2009). Overall, the studies conducted by BAM have raised awareness of the abilities of the UST device and encourage more research to evaluate its capabilities and limitations.

Preliminary Evaluation of the UST System

Because the A1040 MIRA device has had limited exposure to industrial applications, the system was first used on a variety of test specimens. The test specimens included mock-up slabs built specifically to mimic defects common in tunnel linings, as well as certain structural applications exhibiting the types of defects of interest. Other sites (highways, bridge decks, airport runways) were made available to the research team and were capable of providing ground truth validation.

The process used for the evaluations was experimentally determined. Experiments with scanning increments, grid locations, device orientations, and other types of configurations were needed to help develop a reliable methodology. The evaluation procedure discussed later in this appendix reflects the insights gained from scanning the following simulated specimens.

Fabrication, Testing, and Validation of Concrete and Shotcrete Specimens with Simulated Delaminations and Voids

Eleven normal-weight concrete slabs and 13 shotcrete slabs were constructed to simulate various defects. The concrete slabs were used to mimic typical concrete tunnel linings with and without reinforcing steel. The shotcrete slabs were constructed to mimic applications in which shotcrete is sprayed on as a finishing layer, as typically found in tunnel linings. A specially designed lattice girder, also typical in tunnel wall construction, was used as reinforcement in the shotcrete slabs (Figure M.3, bottom right).

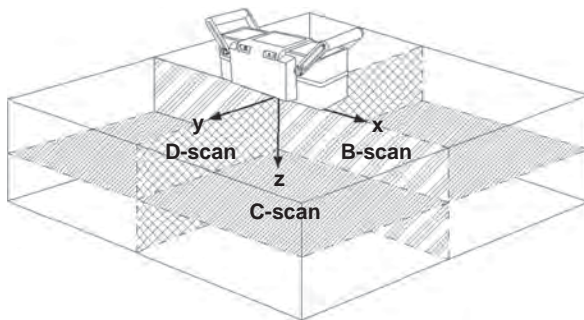


Figure M.2. B-, C-, and D-scans relative to tomograph.



Figure M.3. Construction of slabs with simulated defects.

The simulated delaminations in these slabs were constructed from three types of material. Delaminations were imitated by using 0.05-mm (0.002-in.) plastic square sheets and 0.25-mm (0.01-in.) cloth squares (Figure M.3, top right). Air-filled voids (Figure M.3, top left) were constructed by inserting foam squares 13 mm (0.5 in.) thick in vacuum-sealed plastic bags. Water-filled voids (Figure M.3, bottom left) were constructed in a similar manner by placing water-filled Ziploc bags within vacuum-sealed plastic bags and carefully padding the defect with concrete or shotcrete during construction so as not to puncture the plastic.

The simulated specimens were tested by first placing a 50 mm by 150 mm (2 in. by 6 in.) in a y -increment by x -increment grid on the surface. This grid increment was determined experimentally and is shown to provide optimal resolution for the types of defects under inspection in these slabs. After the grid was constructed, the UST device was manually placed along each marked increment, taking 3 s to 5 s per increment to automatically scan and store the gathered data. At the 50-mm by 150-mm (2-in. by 6-in.) spacing, this process takes approximately 13.5 min/sq m (1.25 min/sq ft).

Some specimens were fully measured twice in opposing directions. This was done for two reasons. First, the reproducibility of the ultrasonic tomography technique when scanned in different directions has to be shown. Second, because the device is polarized—that is, the shear waves are transmitted and received in one direction only (the x -axis)—scanning in

two orthogonal directions allows objects to be measured more accurately.

After the data were gathered, the images produced by the A1040 MIRA proprietary software were analyzed for regions of high reflectivity, which are denoted by red regions in UST images. Because the software output is a color scheme that depicts intensity of reflectivity (low reflectivity or impedance is coded as light blue, high reflectivity or impedance is coded as red, as shown in Figure M.4), great care has to be taken when determining the type of discontinuity under inspection. The software used in this research does not display a waveform in the time domain; therefore, phase changes, which relate directly to the density of the discontinuity, cannot be determined without additional features or post-processing. Also, because the grid increment in the direction normal to the B-scans was 50 mm (2 in.) for these specimens, the B-scans in the inspection software are in 50-mm (2-in.) increments.

With the firmware used for this research, 50 mm (2 in.) is the minimum scanning increment available. Toward the end of the project, a firmware update (3.0-9.1.22) was available for the A1040 MIRA system, which added the ability to scan as closely as 10 mm (0.4 in.). In contrast, C- and D-scans can be viewed in very small increments (1 mm to 2 mm, or 0.04 in. to 0.08 in.) that are associated with the geometry of the transducer spacing and depth of scan; these values are preset by the device manufacturer.

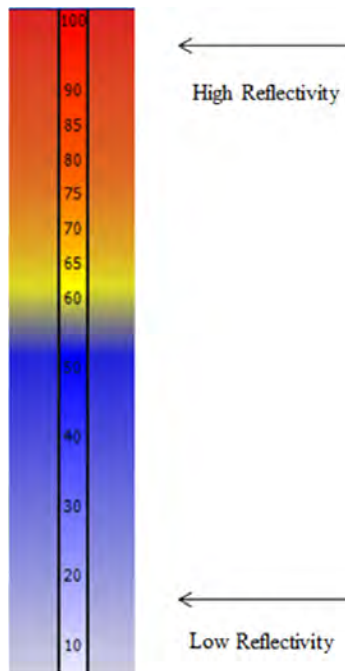


Figure M.4. Scale of reflectivity (or acoustic impedance).

For most concrete structures, a backwall reflection is the first discontinuity that is expected to be readily visible because back-wall surfaces are usually exposed to air, causing almost complete reflection of the sound waves. This is not the case when a layer is fully bonded to a sublayer. When a visible backwall reflection readily correlates with the expected concrete depth, inspection of the area between the testing surface and backwall reflection can take place. As each B-, C-, and D-scan is fully investigated, regions of high reflectivity that appear to indicate damage are catalogued according to the judgment of the operator. If details such as concrete cover and reinforcement direction and spacing are desired, these can be catalogued as well.

C-scans, which offer the most comprehensive visual dimensioning of the simulated delaminations, are shown in Figures M.5 and M.6. The images in these figures are representative of defect visualization for the simulated concrete and shotcrete slabs. Figures M.5 and M.6 depict typical C-scans showing a simulated delamination (top left), an air-filled void (top right), a water-filled void (bottom left), and a slab with only reinforcement (bottom right). A summary of all simulated defects and specimen characteristics for the concrete and shotcrete slabs (as well as the simulated concrete specimens with clay lumps discussed in the next section) is provided in Table M.1. These images demonstrate that the discontinuities in normal-strength concrete are more clearly detectable than in the shotcrete specimens. One explanation is that the shotcrete application, perhaps when misapplied,

can be more porous than typical concrete; within the shotcrete are numerous micro voids that more quickly attenuate the acoustic waves. Even so, delaminations can still be detected. When the system is applied in the field, the images of shotcrete applications are not significantly different from those of typical cast concrete.

Fabrication, Testing, and Validation of Specimens with Simulated Clay Lumps

In addition to the concrete and shotcrete slabs, six concrete slabs were tested that were constructed in the 1990s by the Texas A&M Transportation Institute as part of a previous research project. The slabs contain manufactured clay lumps of different diameters. The clay lumps are a high plasticity clay, classified as Burleson clay CH (AASHTO A-7-6) with a plasticity index range of 35 to 45. The slabs and lumps are shown in Figure M.7 and are summarized in Table M.1 (Specimens A2 through F2). The six specimens consist of two sets of three slabs: one set with steel reinforcement and one set without. In each set, one slab was designated as the control with no clay lump contaminations. The remaining two had various levels of lumps of documented sizes corresponding to three regions of interest: (1) lumps below the reinforcement that represent typical lumps dense enough not to be quickly displaced toward the surface by vibration, (2) those that are caught in the reinforcing steel layer on their path toward the surface, and (3) those that are dispersed between the reinforcement and the top surface. The depth of the slabs is nominally 305 mm (12 in.), but all measurements are approximate because neither ground truth data were retrieved nor any accurate pictures taken to confidently support documented placement.

Similar to the concrete and shotcrete slab specimens discussed previously, the simulated specimens with clay lumps were tested using a 50-mm by 150-mm (2-in. by 6-in.) scanning grid. Because the type of discontinuity under inspection was known beforehand, scanning only took place in one direction, although all the specimens were fully scanned twice to judge repeatability. Scans were needed in only one direction because the objects under inspection had a cross-sectional surface area (parallel to the scanning surface) greater than 50 mm (2 in.) in the y -scanning direction (more on the topic of device polarity and increment sizes can be found in the Conclusions section). A second scan of each specimen was necessary to confirm the detection of each lump. In both sets of measurements taken for repeatability, the clay lumps found in all slabs were in precisely the same location, indicating remarkable repeatability.

Note that the depths of the clay lumps were easily determined from either a single scanned image on the device screen or a more detailed analysis on the computer model. This indicates that the general condition of the structure can be assessed both in the field and in the laboratory. Measurements to the

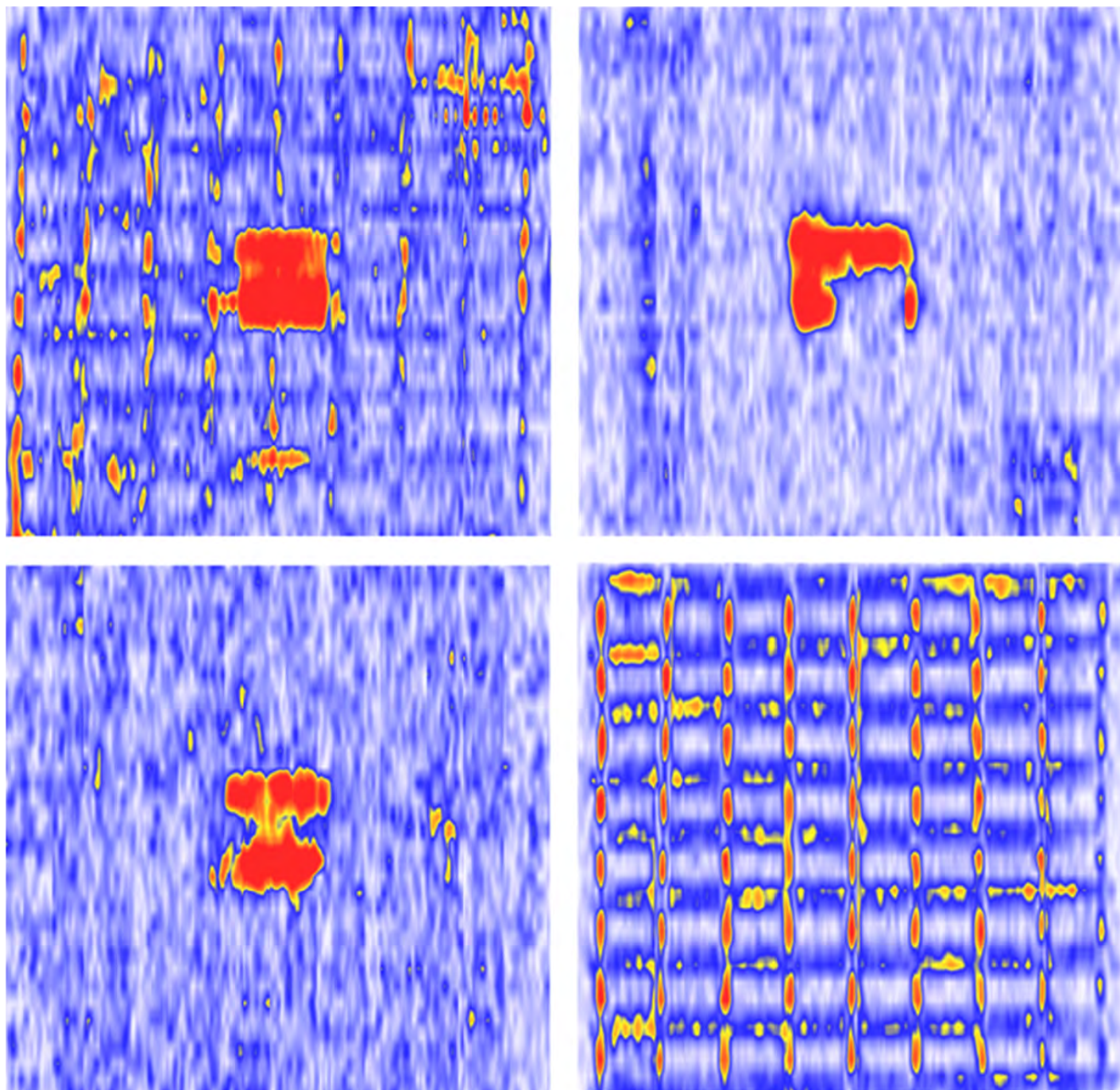


Figure M.5. Typical C-scans of simulated defects in concrete slabs: Specimens Theta (top left), Lambda (top right), Kappa (bottom left), and Gamma (bottom right).

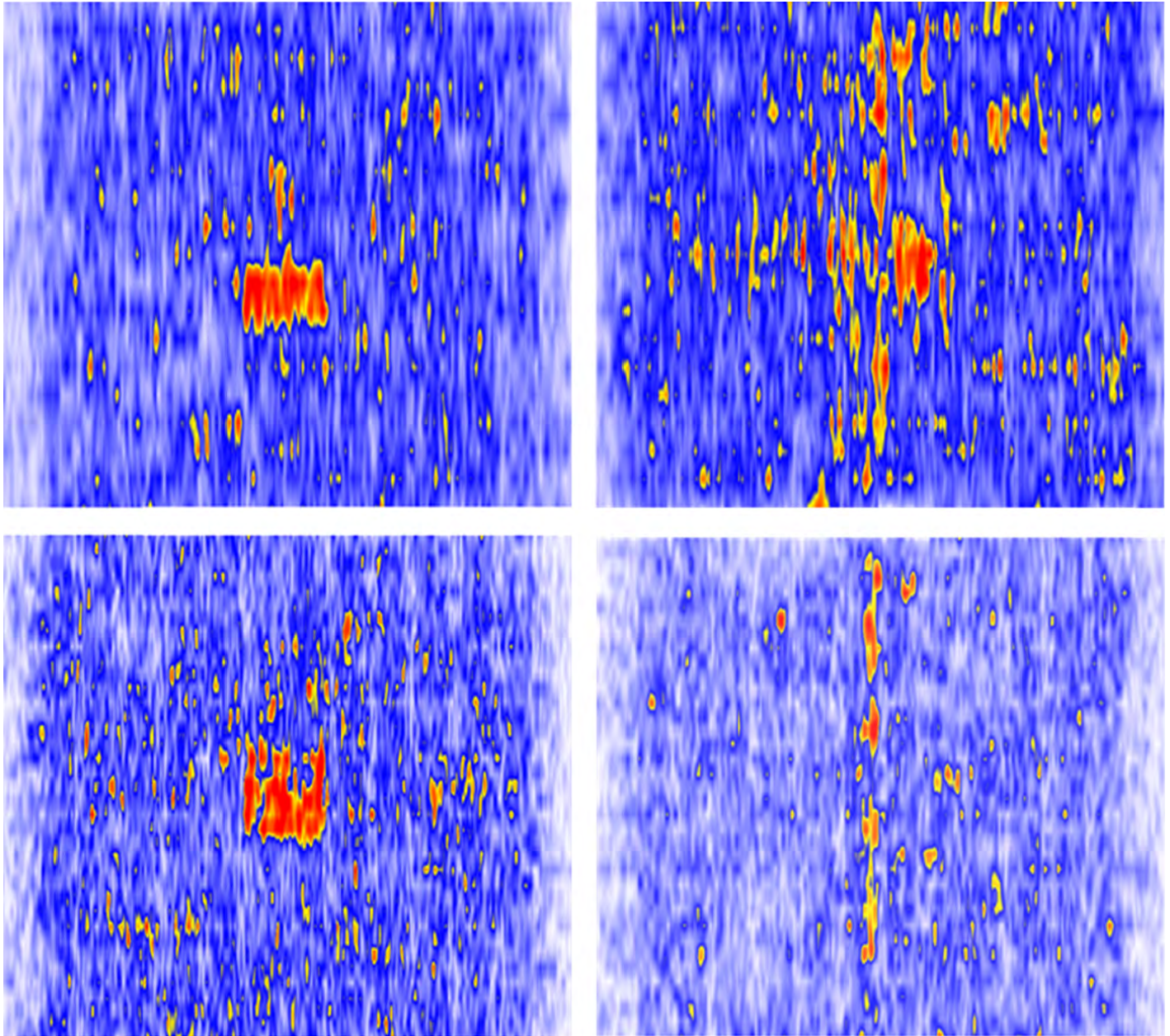


Figure M.6. Typical C-scans for simulated defects in shotcrete slabs: Specimens D (top left), E (top right), I (bottom left), and M (bottom right).

Table M.1. Summary of Concrete and Shotcrete Slab Specimens with Simulated Defects

Specimen Name	Specimen Depth (mm)	Material	Reinforced Detail	Defect	True Depth of Defect (mm)	UST Depth of Defect (mm)
Alpha	305	Concrete	None	None	NA	NA
Beta	457	Concrete	$d = 127 \text{ mm}^a$	Natural crack	NA	NA
Gamma	305	Concrete	$d = 127 \text{ mm}^a$	None	NA	NA
Delta	610	Concrete	None	None	NA	NA
Epsilon	610	Concrete	$d = 127 \text{ mm}^a$	None	NA	NA
Zeta	381	Concrete	$d = 127 \text{ mm}^a$	None	NA	NA
Eta	381	Concrete	$d = 127 \text{ mm}^a$	0.05-mm thin plastic	51 from top	58 from top
Theta	381	Concrete	$d = 127 \text{ mm}^a$	0.05-mm thin plastic	76 from top	89 from top
Iota	381	Concrete	$d = 127 \text{ mm}^a$	0.05-mm thin plastic	25 from top	43 from top
Kappa	381	Concrete	$d = 127 \text{ mm}^a$	Air-filled void (13-mm Styrofoam)	203 from top	203 from top
Lambda	381	Concrete	$d = 127 \text{ mm}^a$	Water-filled void (Ziploc bag)	203 from top	196 from top
A	102	Shotcrete	None	None	NA	NA
B	152	Shotcrete	None	None	NA	NA
C	203	Shotcrete	None	None	NA	NA
D	305	Shotcrete	One lattice girder in center of slab, sitting on bottom form	Air-filled void (13-mm Styrofoam)	193 from top	193 from top
E	305	Shotcrete	One lattice girder in center of slab, sitting on bottom form	Water-filled void (Ziploc bag)	191 from top	193 from top
F	305	Shotcrete	One lattice girder in center of slab, sitting on bottom form	Air-filled void (13-mm Styrofoam)	76 from top	89 from top
G	305	Shotcrete	One lattice girder in center of slab, sitting on bottom form	Water-filled void (Ziploc bag)	76 from top	107 from top
H	305	Shotcrete	One lattice girder in center of slab, sitting on bottom form	0.25-mm thin cloth	203 from top	183 from top
I	305	Shotcrete	One lattice girder in center of slab, sitting on bottom form	0.25-mm thin cloth	102 from top	99 from top
J	305	Shotcrete	One lattice girder in center of slab, sitting on bottom form	0.25-mm thin cloth	76 from top	74 from top
K	305	Shotcrete	One lattice girder in center of slab, sitting on bottom form	0.25-mm thin cloth	51 from top	79 from top
L	305	Shotcrete	One lattice girder in center of slab, sitting on bottom form	0.25-mm thin cloth	25 from top	Only shadow
M	305	Shotcrete	One lattice girder in center of slab, sitting on bottom form	None	NA	NA
A2	305	Concrete	$d = 152 \text{ mm}^a$	None	NA	NA
B2	305	Concrete	$d = 152 \text{ mm}^a$	Large (152 mm \varnothing) clay lumps	152 from top	160 from top
C2	305	Concrete	$d = 152 \text{ mm}^a$	Medium (102 mm \varnothing) clay lumps	76, 152, 229 from top	69, 137, 216 from top
D2	305	Concrete	$d = 152 \text{ mm}^a$	None	NA	NA
E2	305	Concrete	$d = 152 \text{ mm}^a$	Large (152 mm \varnothing) clay lumps	152 from top	107 from top
F2	305	Concrete	$d = 152 \text{ mm}^a$	Medium (102 mm \varnothing) clay lumps	76, 152, 229 from top	61, 137, 198 from top

Note: All slab specimens are nominally 1.83 m by 1.83 m.

^a Two mats of No. 5 rebar, at depth d from top and bottom, 203 mm on center.



Figure M.7. Clay lump slab construction.

centroid of high reflectivity regions, which denote any sort of discontinuity, represent the depth of these anomalies. Keys are provided alongside each ultrasonic image, as in Figures M.8 and M.9, detailing the intended location of the lumps. Note that during concrete pouring and vibrating, the lumps will inevitably be displaced from side to side (e.g., the inward movement of the two center lumps in Figure M.9, left) and upward (e.g., the upward displacement of the lump in Figure M.8, right). The C- and B-scans from Figures M.8 and M.9 show both the large and medium lumps were highly detectable, in slabs both with and without reinforcement. However, if lumps are exactly at the layer of reinforcement (see Figure M.8, right, and the middle set of lumps in Figure M.9, right), it is clear that lumps surrounding reinforcement are highly improbable of detection. It would be difficult or highly improbable to know these areas had clay lumps if the system were to be applied in a field application with lumps caught in the reinforcement.

At these levels within a specimen, it may be inferred that a lump is present, but the clarity is not as persuasive as in the detection of lumps located farther from the reinforcement.

Fabrication, Testing, and Validation of Concrete Bridge Deck with Simulated Defects

In addition to the slabs described above, a bridge deck constructed by the University of Texas at El Paso was available for blind testing. The bridge deck was constructed with known artificial delaminations, cracks, and corroded reinforcement. Several parameters were considered in the construction of the artificial delaminations, including stacked delaminations; delaminations of various thicknesses, ranging from 0.3-mm (0.01-in.) to 2.0-mm (0.08-in.) thickness; sizes ranging from 305 mm by 305 mm to 610 mm by 1,220 mm (12 in. by 12 in. to 24 in. by 48 in.); and depths above reinforcing steel at 64 mm

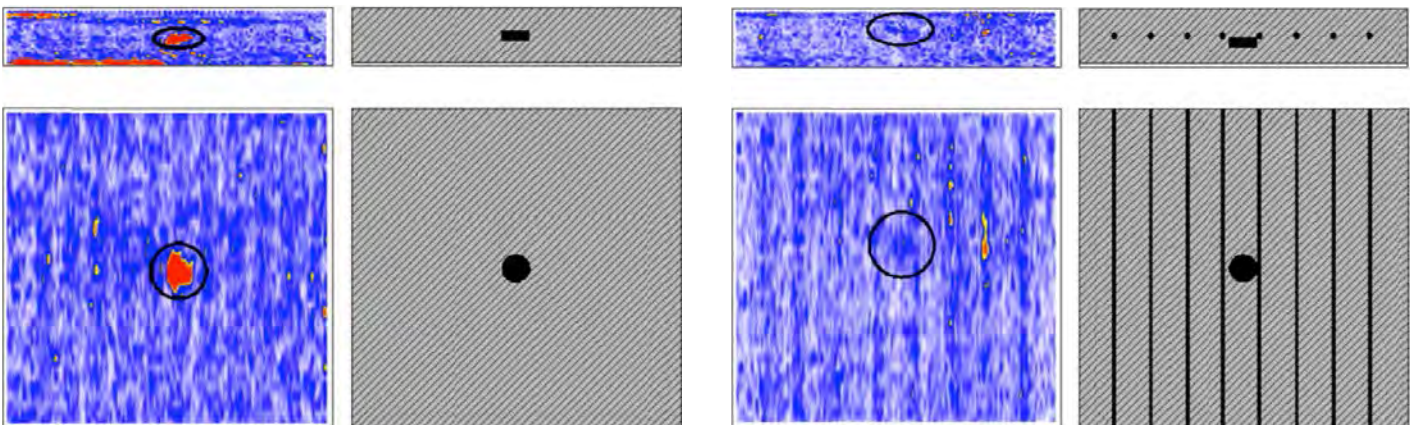


Figure M.8. Large clay lump slabs without reinforcement (left) and with reinforcement (right).

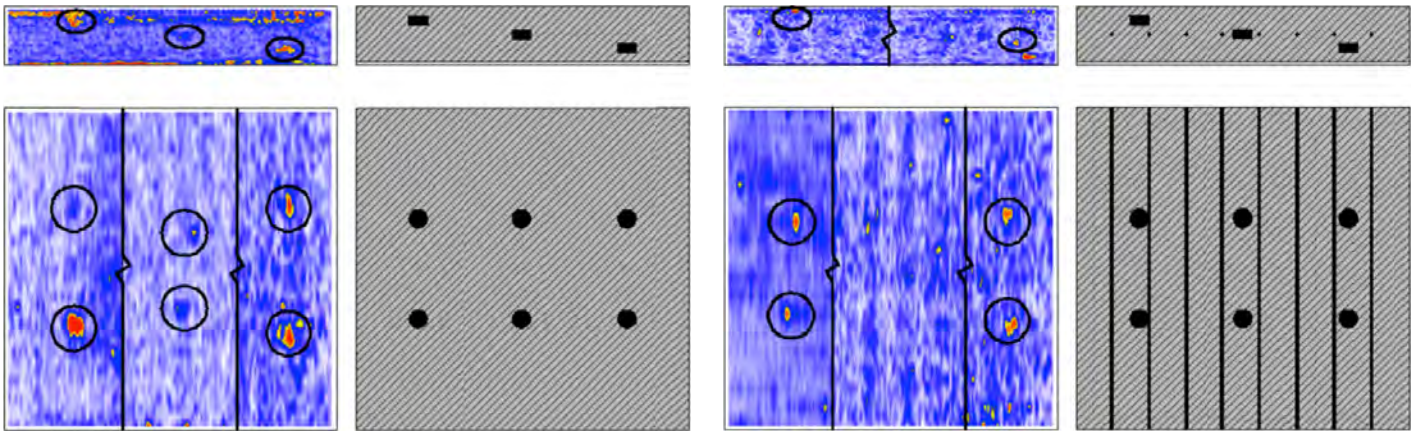


Figure M.9. Medium clay lump slabs without reinforcement (left) and with reinforcement (right).

(2.5 in.) below the surface, and below two layers of reinforcing steel at 152 mm (6 in.), with some located above prestressed girders supporting the slab. The deck, pictured in Figures M.10 and M.11, measures 2.4 m by 6.1 m by 0.2 m (8 ft by 20 ft by 8¾ in.) and rests on three prestressed concrete girders. Simulated defects constructed in the deck consist of nine artificial delaminations, five cracks, and two corroded reinforcement mats, all of which are summarized in Table M.2.

In constructing the deck, 27.6 MPa (4,000 psi) concrete was used, and two layers of No. 5 longitudinal and transverse steel were placed at 254 mm and 203 mm (10 in. and 8 in.) on center, respectively, at centroid depths of 83 mm and 184 mm (3.25 in. and 7.25 in.) from the surface. The 28-day strength and modulus exceeded 34.5 MPa (5,000 psi) and 27.6 MPa (4,000 psi),



Figure M.10. Simulated bridge deck at University of Texas at El Paso.

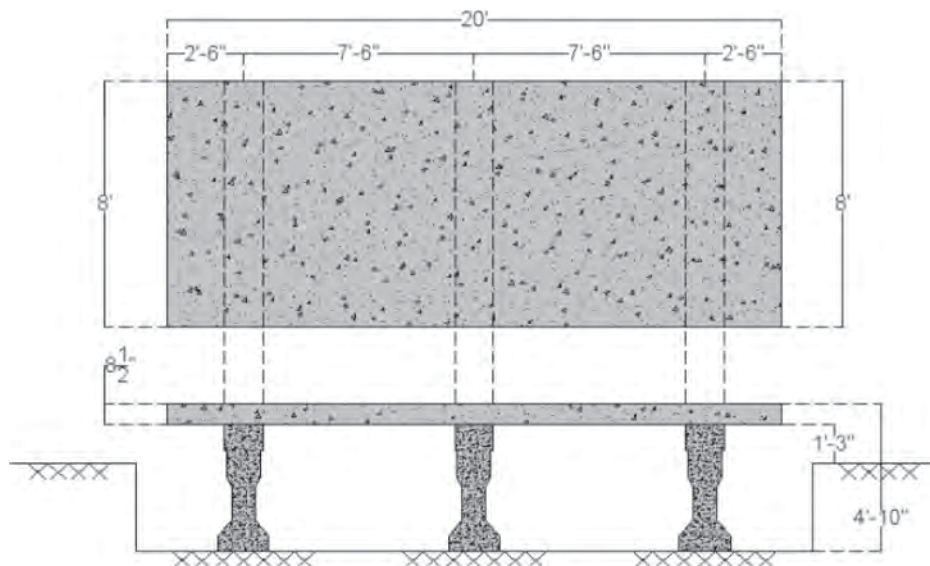




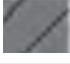













Figure M.11. Layout of constructed bridge deck.

Table M.2. Summary of Simulated Defects in Concrete Bridge Deck

Simulated Defect	Defect Material	Key Legend	Actual Dimension (mm)	Actual Depth (mm)	UST Measured Dimension (mm)	UST Measured Depth (mm)
Delamination (DL1)	Soft, high-strength 1-mm foam		305 by 305	64	301 by 341	65
Delamination (DL2)	Soft, high-strength 1-mm foam		610 by 610	64	578 by 642	71
Delamination (DL3)	Soft, high-strength 1-mm foam		610 by 610	64	603 by 651	81
Delamination (DL4)	Soft, high-strength 2-mm foam		305 by 305	64	333 by 390	69
Delamination (DL5)	Soft, high-strength 2-mm foam		610 by 610	64	587 by 650	81
Delamination (DL6)	Soft, high-strength 2-mm foam		610 by 610	64	587 by 650	54–116
Delamination (DL7)	Soft, high-strength 1-mm foam		610 by 610	152	562 by 667	136
Delamination (DL8)	Soft, high-strength 1-mm foam		610 by 1,219	152	667 by 1,197	150–177
Delamination (DL9)	Soft, 0.25-mm polyester fabric		305 by 610	64	NA ^a	NA ^a
Vertical crack (CK1)	Soft, thin cardboard		305 long	64	NA ^b	NA ^b
Vertical crack (CK2)	Soft, thin cardboard		305 long	64	NA ^b	NA ^b
Vertical crack (CK3)	Soft, thick cardboard		305 long	76	NA ^b	NA ^b
Vertical crack (CK4)	Soft, thick cardboard		305 long	152	NA ^b	NA ^b
Vertical crack (CK5)	Natural crack (observed after construction)		330 long	64	NA ^b	NA ^b
Corroded reinforcement (CR1)	1-mm to 2-mm deep corrosion, No. 5 rebars		762 by 762	76	Identified ^c	Identified ^c
Corroded reinforcement (CR2)	1-mm to 2-mm deep corrosion, No. 5 rebars		762 by 762	165	Identified ^c	Identified ^c

^a NA = not available. Indiscernible because of surface noise and upper transverse reinforcement.

^b NA = not available. Unable to analyze crack details.

^c The corroded steel mats were identified, but the map taken did not completely cover the end of the slab, so dimensions could not be verified.

respectively. A 0.25-mm (0.01-in.) polyester fabric was used to mock an ultrathin horizontal delamination. Vertical cracks were constructed from both thick and thin cardboard sheets. The No. 5 corroded steel mats were electrically merged and attached to the normal reinforcement. The corrosion depth was measured to be 1 mm to 2 mm (0.04 in. to 0.08 in.) before the concrete was poured.

For the UST analysis, the grid increment used on the bridge deck (100 mm by 100 mm, or 4 in. by 4 in.) was greater in the y -scanning direction than the previously evaluated specimens because this deck was actually the first specimen to be tested and an optimal increment was not yet established. In retrospect, this factor contributed to the defects in this specimen being less defined than in the other cases. Figure M.12 shows the defects present at 64 mm (2.5 in.) deep, and Figure M.13 shows the defects present at 152 mm (6 in.) deep. As can be seen from the UST results, six of the seven defects were detected. The one defect undetected was the 0.25-mm (0.01-in.) thin polyester fabric at 64 mm (2.5 in.) below the surface (DL9), as well as details of the various cracks. This scan was not particularly useful for examining cracks, as the data set for the entire scan was too massive for careful evaluations via D-scans,

and the B-scans were spaced too far apart for careful analysis. Nevertheless, a sample crack (CK1) is shown in Figure M.14. The remaining B-scans with their associated end-view keys are shown in Figures M.15 through M.20.

Continuously Reinforced Concrete Pavement on I-20 in Fort Worth, Texas

In the past few decades, I-20 (Figure M.21) has had numerous repairs and overlays, including a section of continuously reinforced concrete pavement (CRCP) in Fort Worth, Texas, west of RM 2871 (~MP 426+0.5). A nominal 254-mm (10-in.) thick CRCP was constructed over a two-lift pavement, which consisted of a top layer of a 51-mm (2-in.) asphalt base. Over time, significant signs of distress began to appear. Ultrasonic tomography was used to evaluate transverse surface cracks on the CRCP and determine the existence of any delamination within the overlay. The four areas tested are shown in Figure M.22. Each area was tested using a 50-mm by 150-mm (2-in. by 6-in.) grid. After scanning the section, cores were taken to verify the predicted overlay depth, reinforcement cover, and delamination depth.

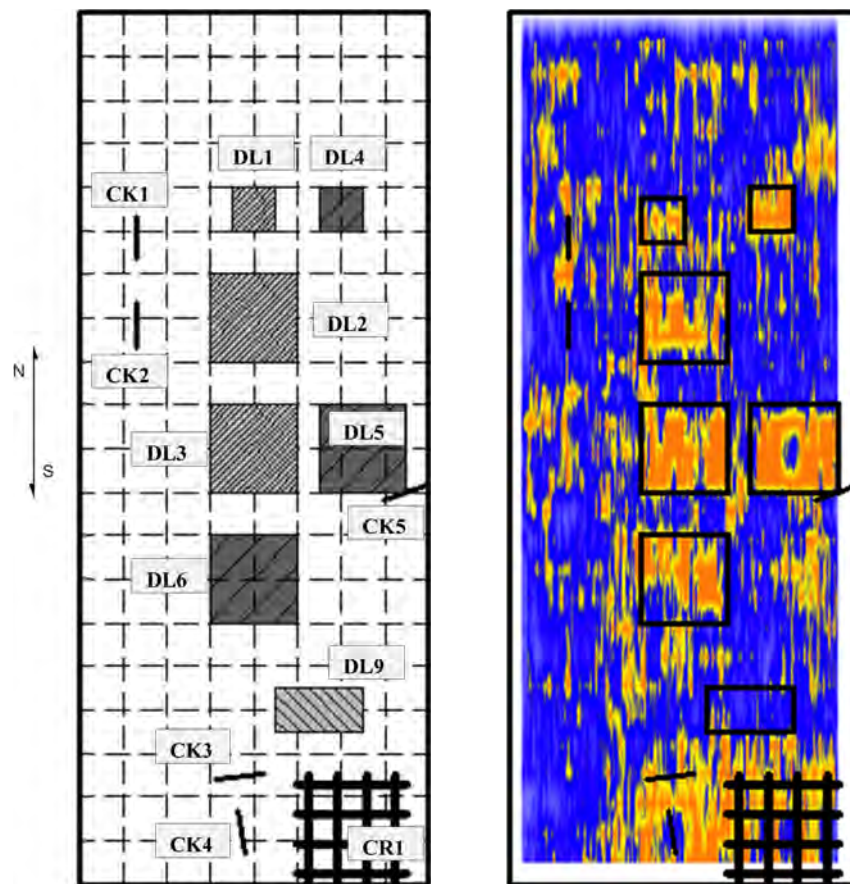


Figure M.12. C-scan at 2.5-in. depth: construction key (left) and UST results (right).

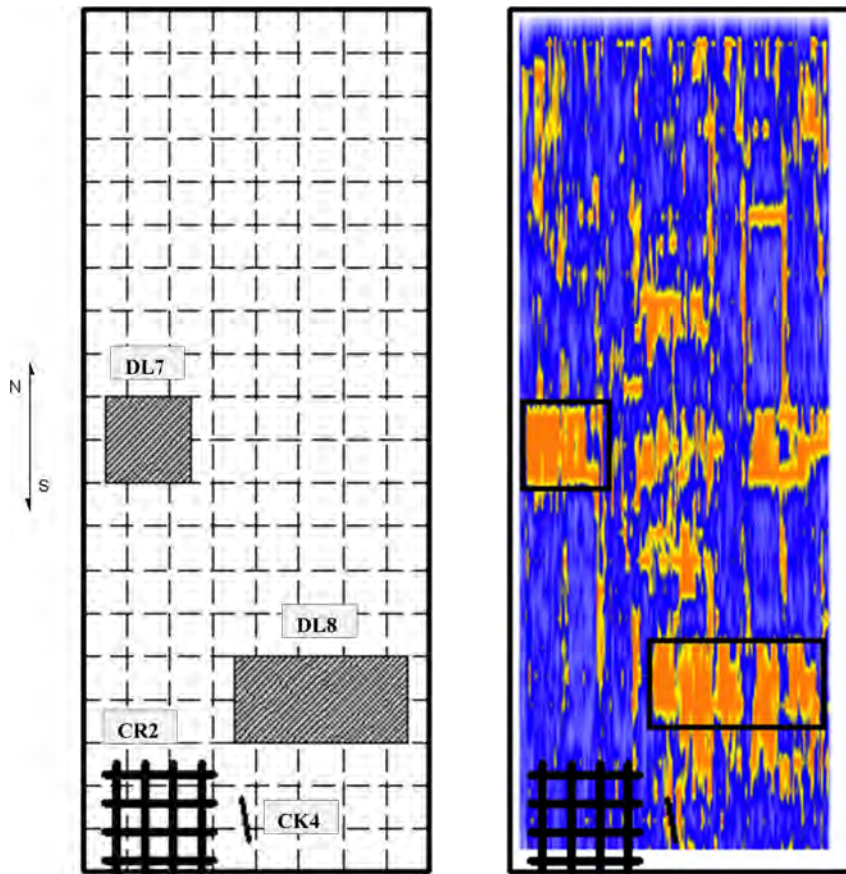


Figure M.13. C-scan at 6-in. depth: construction key (left) and UST results (right).

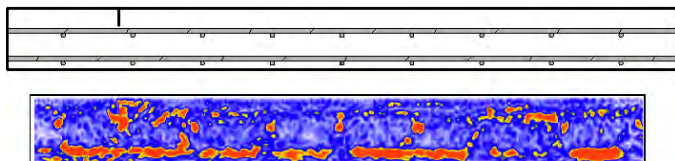


Figure M.14. B-scan showing CK1: construction key (top) and UST results (bottom).

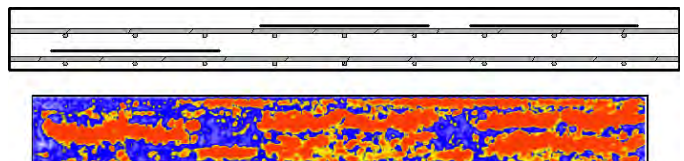


Figure M.17. B-scan showing DL7, DL3, and DL5 (left to right): construction key (top) and UST results (bottom).

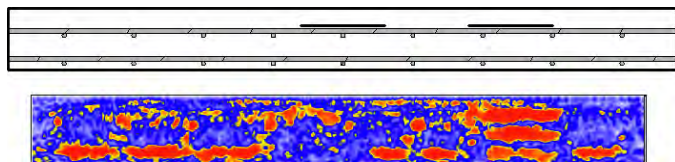


Figure M.15. B-scan showing DL1 and DL4 (left to right): construction key (top) and UST results (bottom).

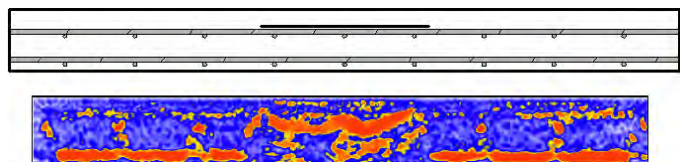


Figure M.18. B-scan showing DL6: construction key (top) and UST results (bottom).

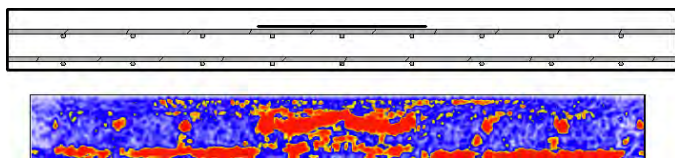


Figure M.16. B-scan showing DL2: construction key (top) and UST results (bottom).

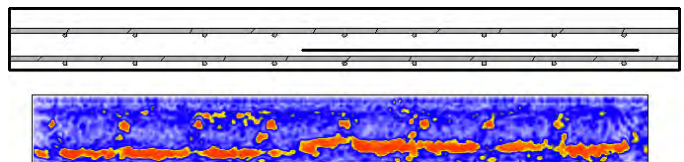


Figure M.19. B-scan showing DL8: construction key (top) and UST results (bottom).

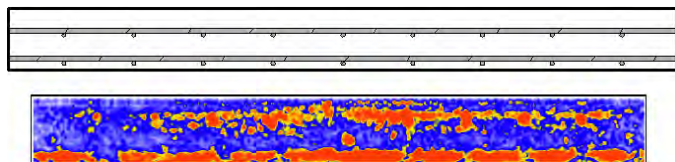


Figure M.20. B-scan showing CR1: construction key (top) and UST results (bottom).

The UST results of the first area tested (Figure M.22, top left) are shown in Figure M.23. These are typical B-, C-, and volume-scans that are seen in the other scanned areas. The two B-scans in Figure M.23 (left) show an area with delamination at the level of longitudinal reinforcement (top B-scan) and an area with no delamination, but a backwall reflection at the top layer interface (bottom B-scan). The C-scan (Figure M.23, center) shows the width of the delamination at the level of reinforcement. Figure M.24 shows all four areas scanned with their appropriate C-scans overlaid on the image. All delaminations in these figures are at the level of reinforcement (see Tables M.3 through M.6 for details).



Figure M.21. I-20 in Fort Worth, Texas.



Figure M.22. Four areas tested on I-20 in Fort Worth, Texas.

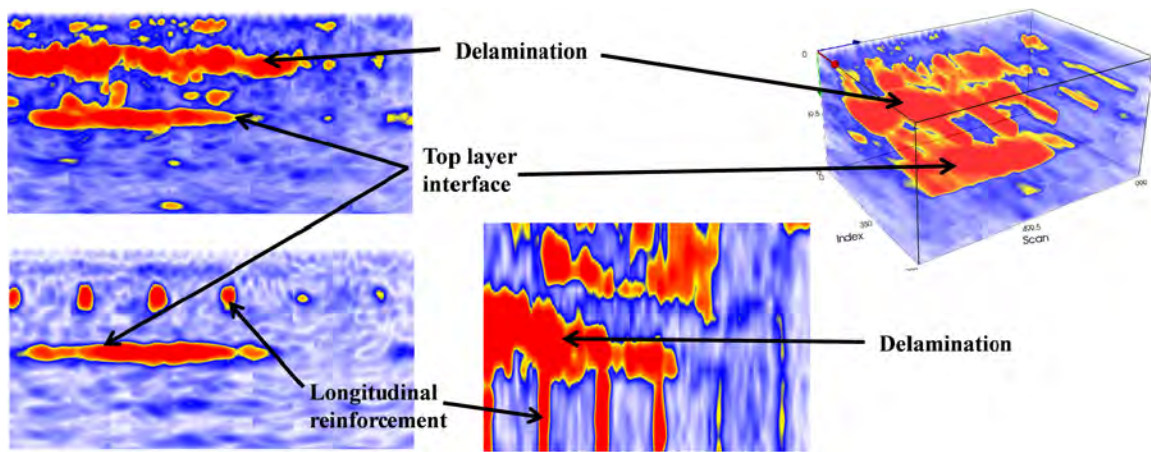


Figure M.23. Typical UST results for I-20 scanning.

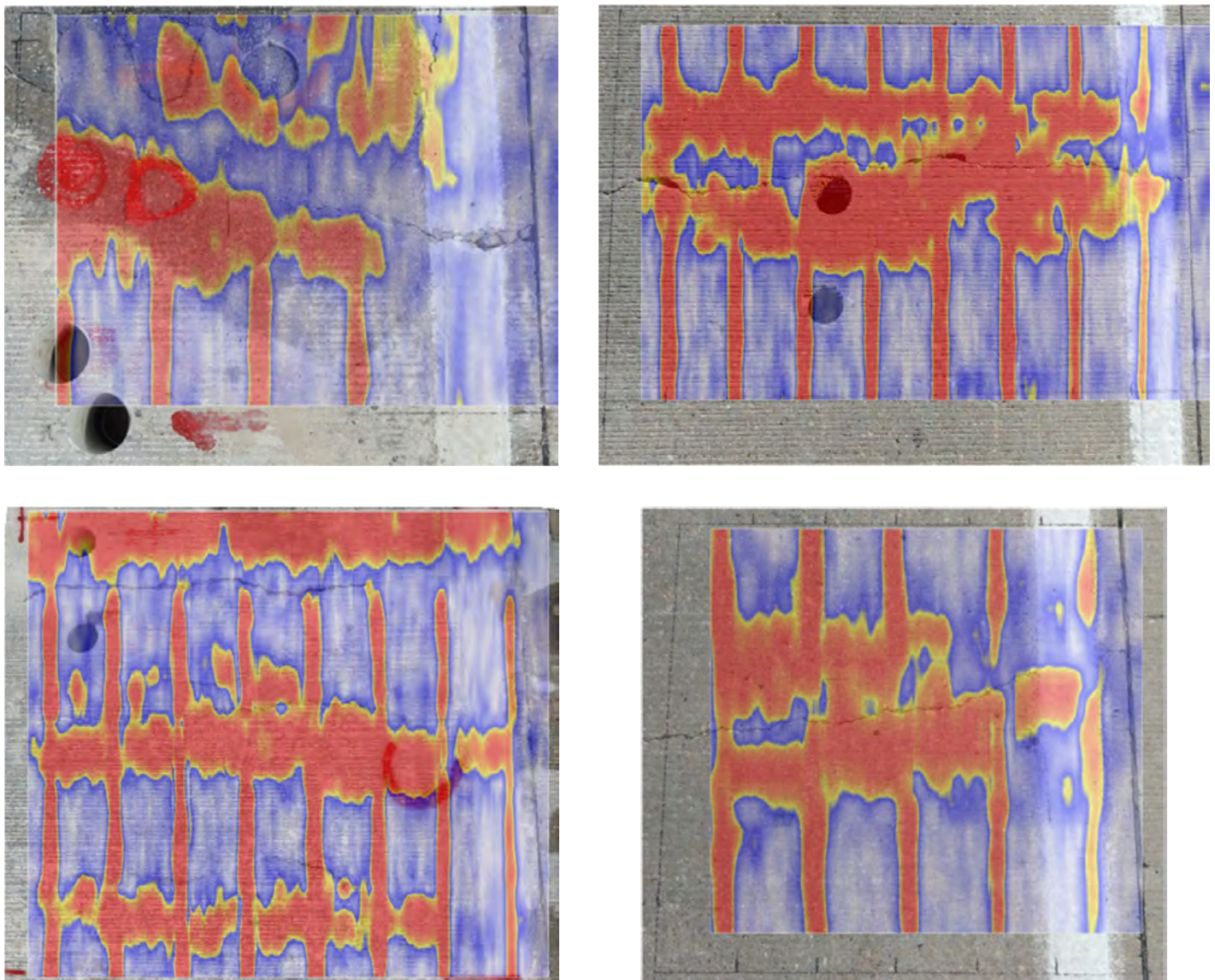


Figure M.24. UST C-scans overlaid on I-20 images: Section A (top left), Section B (top right), Section C (bottom left), and Section D (bottom right).

Table M.3. Section A, I-20 Evaluations

Overlay		
	Tomograph	
Depth to delamination	Varies: 107–127 mm	
Depth to reinforcement	Varies: 117–127 mm	
Core 1		
	Tomograph	Core Results
Depth to asphalt sub-layer	264 mm	259 mm
Depth to delamination	None	None
Depth to reinforcement	127 mm	127 mm
Core 2		
	Tomograph	Core Results
Depth to asphalt sub-layer	254 mm	259 mm
Depth to delamination	None	None
Depth to reinforcement	None	None

Table M.4. Section B, I-20 Evaluations

Overlay		
	Tomograph	
Depth to delamination	Varies: 114–135 mm	
Depth to reinforcement	Varies: 114–132 mm	
Core 3		
	Tomograph	Core Results
Depth to asphalt sub-layer	257 mm	264 mm
Depth to delamination	None	None
Depth to reinforcement	None	None
Core 4		
	Tomograph	Core Results
Depth to asphalt sub-layer	NA	239 mm
Depth to delamination	117 mm	119 mm
Depth to reinforcement	None	None

Note: NA = not available.

George Bush Intercontinental Airport, Houston, Texas

A recent construction project at the George Bush Intercontinental Airport (IAH) in Houston, Texas, entailed overlaying existing runways with a nominal 203-mm (8-in.) jointed plain concrete pavement (Figure M.25). The existing runways were 762-mm (30-in.) sections of concrete pavement: a 457-mm (18-in.) portland cement concrete (PCC) layer over a 305-mm (12-in.) PCC layer. Within 3 months, significant surface cracks on the bonded concrete overlay (BCO) instigated an evaluation

Table M.5. Section C, I-20 Evaluations

Overlay		
	Tomograph	
Depth to delamination	Varies: 117–130 mm	
Depth to reinforcement	Varies: 122–127 mm	
Core 5		
	Tomograph	Core Results
Depth to asphalt sub-layer	257 mm	259 mm
Depth to delamination	None	None
Depth to reinforcement	None	None
Core 6		
	Tomograph	Core Results
Depth to asphalt sub-layer	259 mm	259 mm
Depth to delamination	104–135 mm	137 mm
Depth to reinforcement	None	None

Table M.6. Section D, I-20 Evaluations

Overlay	
	Tomograph
Depth to delamination	Varies: 119–140 mm
Depth to reinforcement	Varies: 122–130 mm

on the source of the cracks. Using a grid spacing of 100 mm by 200 mm (4.0 in. by 7.9 in.), UST was used to completely scan two entire sections of the runway (two 7.6-m by 7.6-m, or 25-ft by 25-ft slabs) to evaluate the extent of the damage. The UST results are shown in Figures M.26 and M.27. The first runway tested showed more than 70% of the area delaminated at the

**Figure M.25. Airport runway at IAH.**

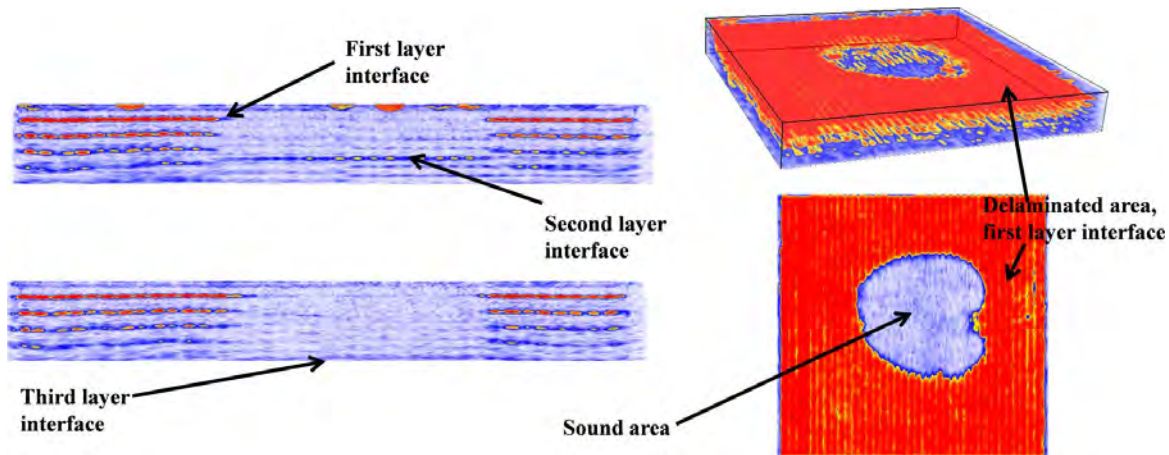


Figure M.26. First segment tested at IAH: B-scans (left), volume-scan (top right), and C-scan (bottom right).

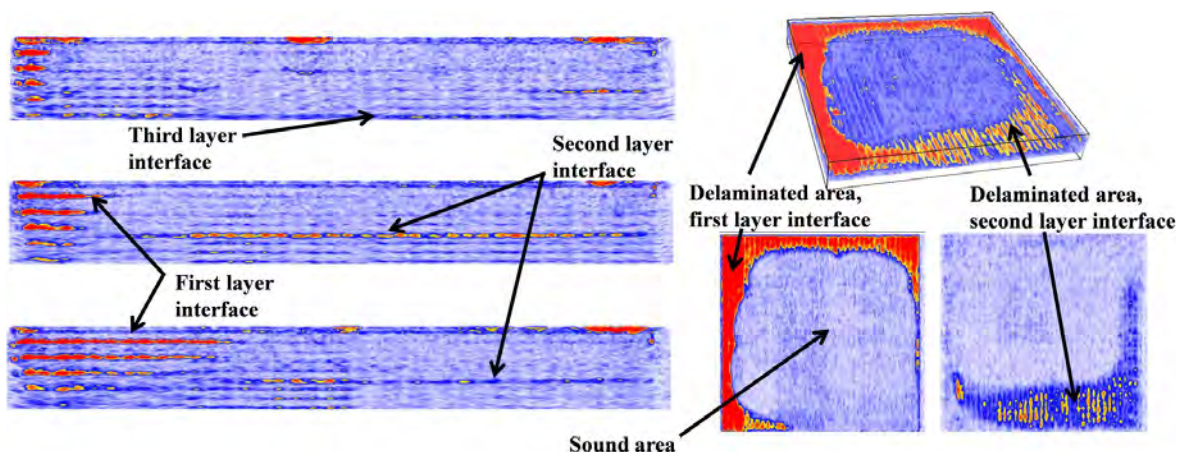


Figure M.27. Second segment tested at IAH: B-scans (left), volume-scan (top right), and C-scans (bottom right).

first layer interface (Figure M.26, C-scan at bottom right, volume-scan at top right). The B-scans on the left of the figure show the first layer interface is 193 mm to 206 mm (7.6 in. to 8.1 in.) deep, the second layer interface is 683 mm (26.9 in.) deep, and the third layer interface is 958 mm (37.7 in.) deep. The second area tested showed approximately 15% of the total area debonded at the first layer interface (Figure M.27, C-scans at bottom right, volume-scan at top right). The partially bonded region at the second layer interface was easily seen.

Cores were taken in both runway sections to verify the degree of bonding based on three locations: where the UST results indicated (1) full bonding, (2) full debonding, and (3) an area in between. Three core strength testing points within location 1 (predicted full bond) indicated tensile strengths ranging from 1,230 Pa to 1,500 Pa (178 psi to 219 psi). A core in Location 2 (predicted partial bond) indicated a tensile strength of 131 Pa (19 psi). Finally, a few cores in Location 3 (predicted full debond) confirmed delamination at the first layer interface.

Assessment for Preliminary Defect Evaluation Using UST

A summary of all simulated defects and specimen characteristics for all specimens tested can be found in Tables M.1 and M.2, above. After scanning each of the concrete and shotcrete slabs, the measurements indicated by UST inspection versus the actual measurement from ground truth data were plotted. A linear regression model was fitted to the data (Figure M.28). The types of discontinuities plotted in this manner were the following:

- Defect depth;
- Defect length (parallel to B-scans, or the x -scanning direction);
- Defect width (parallel to D-scans, or the y -scanning direction);
- Shotcrete specimen thickness;
- Concrete specimen thickness; and
- Reinforcement cover.

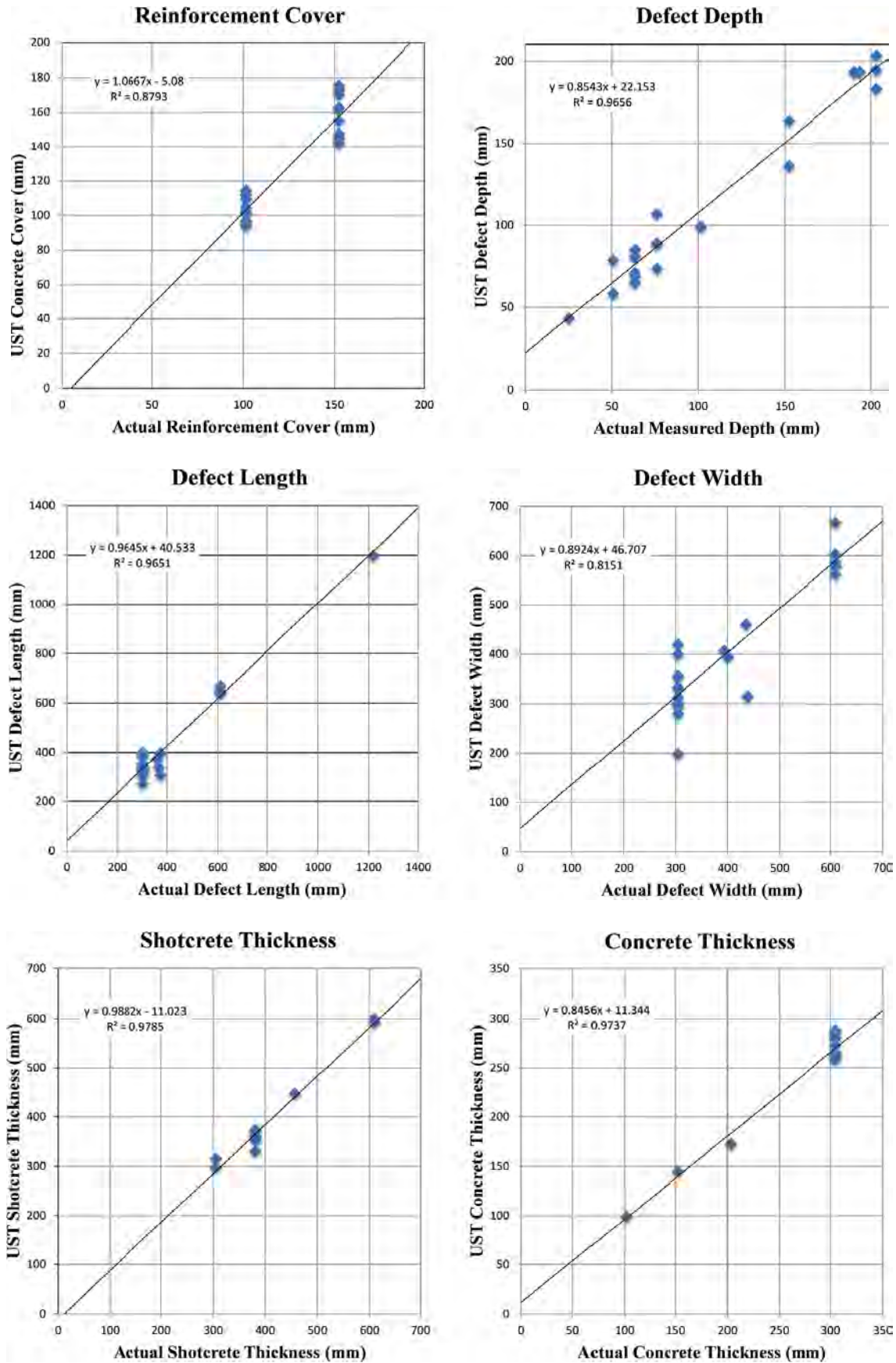


Figure M.28. R^2 for various defect detection parameters in concrete and shotcrete slabs.

The coefficient of determination shows strong agreement between actual discontinuity measurements and measurements taken by ultrasonic tomography. Defect width and length are characteristics that should be determined after scanning the region in more than one scanning direction because the phased-array tomograph is polarized; shear waves are emitted and received in one direction, the x -scanning direction, or direction normal to the D-scans. Objects (such as reinforcement) can therefore appear wider (measured in the y -scanning direction) than they are in reality because the B-scan is an average over a row of four transducers.

The defect location and dimensions, as well as other useful parameters, were plotted against the UST measurements. Linear regression analysis indicated that the coefficient of determination (R^2) varied between 0.82 and 0.98, indicating that 82% to 98% of the variability in defect dimensions (depth from surface, length, and width) or specimen characteristics (thickness, reinforcement cover, and spacing) measured by the UST device was directly related to the variability in the actual defect dimensions or specimen characteristics.

These evaluations on simulated specimens were invaluable for two reasons. Primarily, they instilled confidence that the data collection method would be reliable for inspection of existing structures; this was particularly important because coring or any type of physical validation might not be allowed. The high R^2 values translate into a reliability threshold of the system with which we can confidently map real-life structures. Still, further testing needs to be completed to have a statistical analysis that predicts confidence levels and meaningful probability of detection curves. A limitation of the research performed here is the lack of numerous constructed specimens with similar or repeated defect evaluations.

Many variables can be adjusted when calibrating the tomograph to improve the accuracy of the device, including period of impulse, time-corrected gain, firing impulse pause, and wave velocity. Wave velocity can be accurately estimated by averaging 8 to 10 random readings at different positions on the concrete surface. If physical validation is possible, the wave speed and other variables can be adjusted so that the tomograph is calibrated by a known measurement, such as reinforcement depth or backwall reflection. Because these measurements are rarely known in existing structures to a high level of precision without destructive validation, the device's accuracy can be difficult to fine-tune before testing. For this reason, most of the simulated specimens were tested blindly by an operator who was not familiar with the location or type of defects to accurately mimic field-testing conditions. For all simulated specimens, wave velocity was calculated by averaging 8 to 10 evaluations; no other parameters (period of impulse, time-corrected gain, firing impulse pause) were changed from default settings. In this manner, the accuracy of the device could be predicted in preparation for testing existing structures.

These evaluations were also invaluable because they provided the opportunity to test many variations of grid size, location, and creation for future use on existing structures. Learning how to relate a defect found in the 3-D image reconstruction with the actual grid established on the specimen was critical.

Field Evaluation of the UST System

For the following six test sites, limited ground truth data were available for confirmation of UST defect locations. The descriptions of the test sites, including interpretation of UST evaluations, were made using engineering judgment.

Eisenhower Memorial Tunnel, Colorado

The Eisenhower Memorial Tunnel, located approximately 97 km (60 mi) west of Denver, Colorado, is one of a 2.7-km (1.7-mi) dual bore project started in 1968. Shown in Figure M.29, Eisenhower Memorial Tunnel, which carries I-70 West, is paired with the Edwin C. Johnson Memorial Tunnel, which carries eastbound I-70. Although the eastbound bore was not completed until almost 1980, construction on the Eisenhower bore was completed by 1973. Built using drill and blast methods through a mountain with a maximum overburden of 448 m (1,470 ft), the average tunnel dimensions are 14.6 m in height (48 ft) and 12.2 m (40 ft) in width. In 2011, the average daily traffic was 28,155 vehicles.

All areas of interest in the tunnel were tested from inside the plenum (above the traffic), and evaluations were conducted on the precast concrete divider wall separating the intake and exhaust portions of the plenum and on the lining itself (Figure M.30). Areas tested on the lining included representative locations of relatively sound (uncracked) concrete (Figure M.31a), areas with particularly extensive surface cracks



Figure M.29. Eisenhower Memorial Tunnel, Colorado.

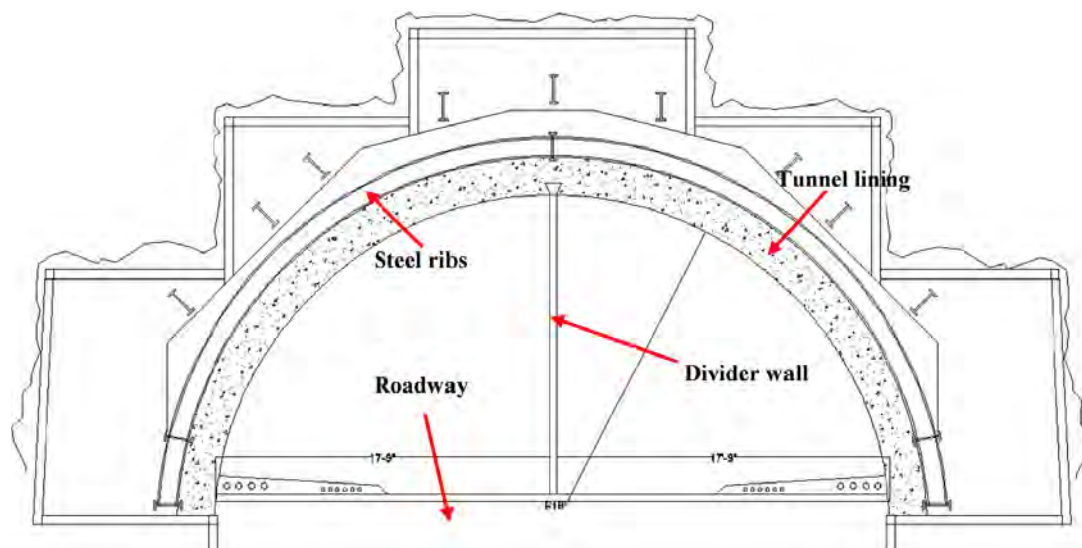


Figure M.30. Eisenhower Memorial Tunnel plenum view indicating interior precast divider wall, structural steel ribs, roadway, and concrete tunnel lining.

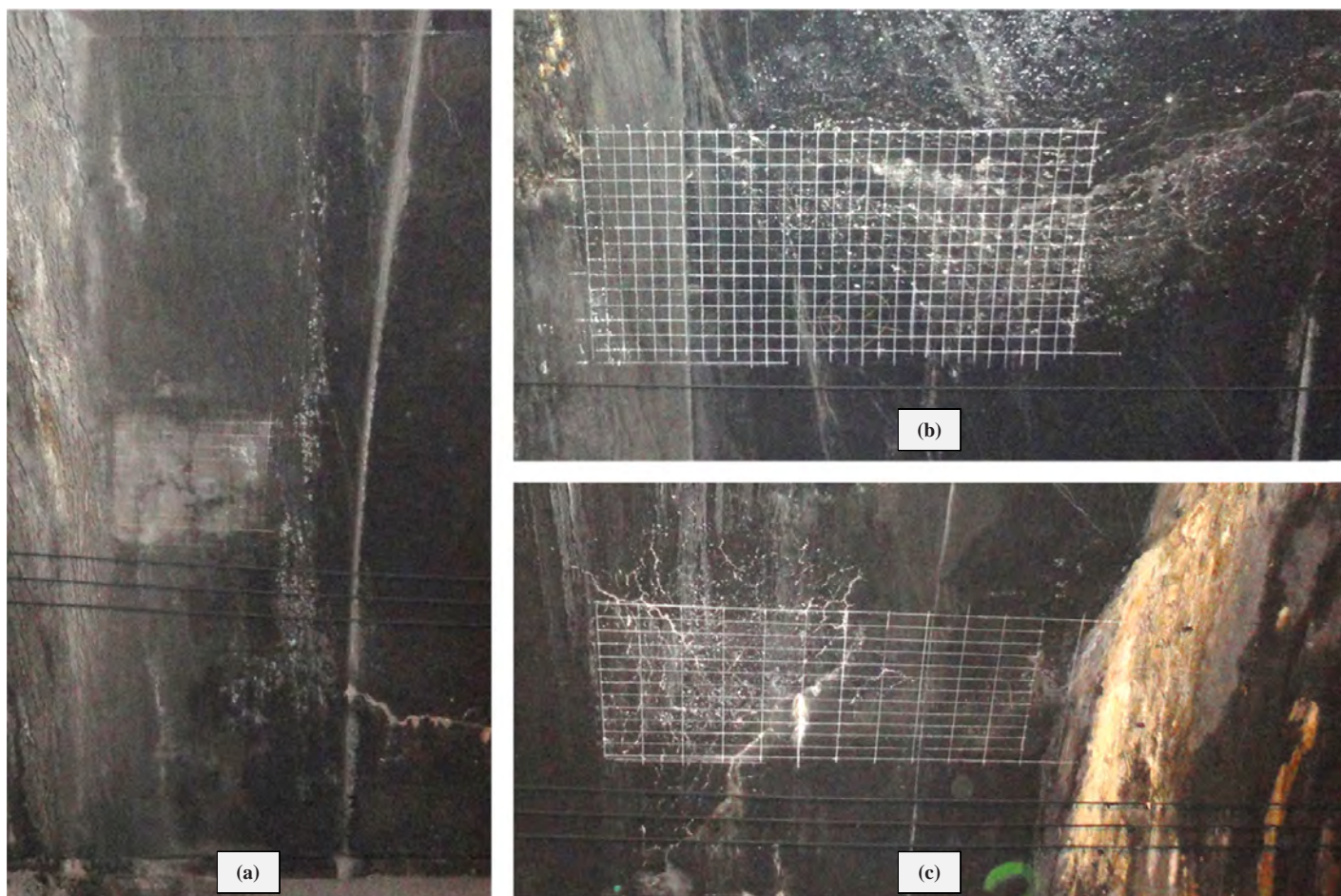


Figure M.31. Scanned areas within Eisenhower Memorial Tunnel: (a) sound concrete, (b) surface cracking and crazing near joint, and (c) surface cracking and crazing near joint and crack with stalactite formation.

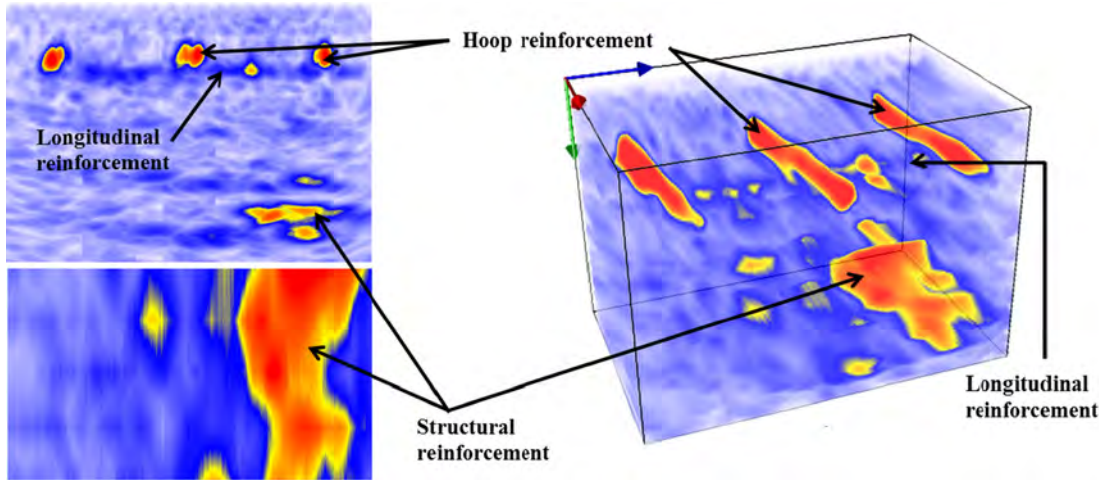


Figure M.32. UST images of sound area: B-scan (top left), C-scan (bottom left), and volume-scan (right).

and crazing near a joint in the tunnel lining (Figure M.31b), and areas near severe vertical cracks with stalactite formations (Figure M.31c).

As expected, the sound concrete area showed no signs of significant delamination, but a clear interface was observed approximately 411 mm (16.2 in.) below the surface (~239 mm, or 9.4 in., wide). (See Appendix N, Ultrasonic Tomography Test Summaries, Figures N.1 and N.2, for images of test site ET 10.4-1, 2.)

This interface was consistently observed at every testing location between Segments 8 and 10 within the Eisenhower Memorial Tunnel lining and is surmised to be part of the structural reinforcement that was in place before the tunnel lining was installed. Detailed tunnel blueprints for verification at this location were not available for confirmation. The scans in Figure M.32 correspond to typical B-, C-, and volume-scans

at this location. In the B-scan, the hoop (or circumferential) reinforcement is clearly observable at approximately 107 mm (4.2 in.) in depth and at 251 mm (9.9 in.) on center. A single rebar as part of the longitudinal reinforcement is seen in the B-scan and volume-scan as well.

As noted earlier, one of the two areas tested displayed significant surface cracking and crazing occurred near a joint. (See Appendix N, Figures N.5 and N.6, for images of test site ET 10.4-4, 5.) At this location, the structural reinforcement is again located approximately 409 mm (16.1 in.) below the surface (~343 mm, or 13.5 in., wide). B-, C-, and volume-scans are shown in Figure M.33. In the B-scan, the longitudinal reinforcement is seen directly under the hoop reinforcement with multiple echoes observed in increments approximately the same as the depth of the longitudinal and hoop reinforcement. These echoes are suspected to be the effect of debonding of

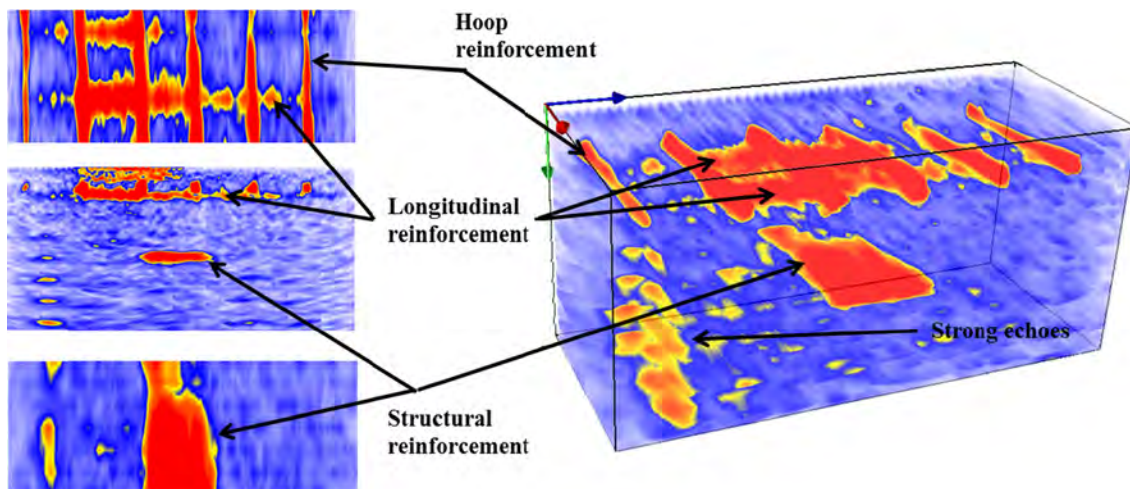


Figure M.33. UST images of surface cracking and crazing area: B-scan (center left), C-scans (top and bottom left), and volume-scan (right).

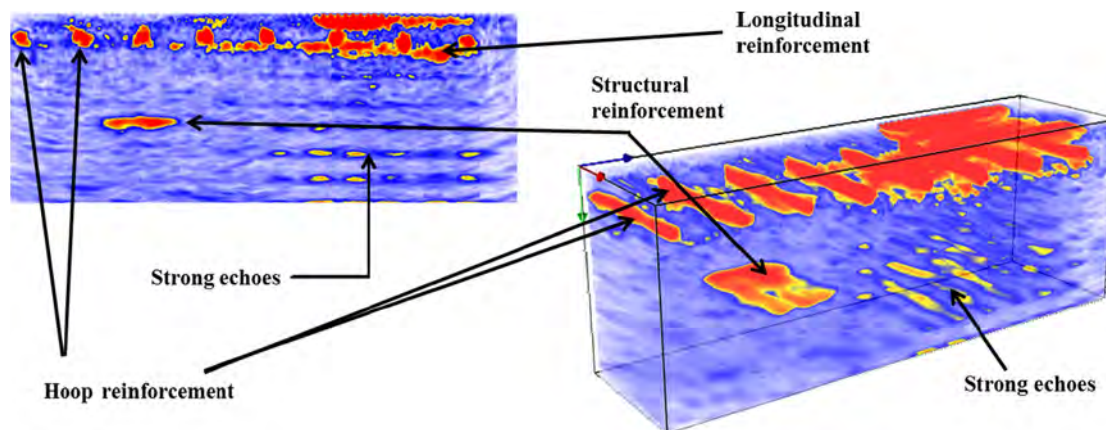


Figure M.34. UST images of surface cracking and crazing area near stalactite formation: B-scan (left) and volume-scan (right).

the longitudinal and hoop reinforcement. Interestingly, this supposed debonding also occurs directly below the lining joint. This may indicate that moisture intrusion has corroded the reinforcement, causing debonding. However, no ground truth data have confirmed this observation.

In the second area that displayed significant surface cracking and crazing near a joint, a severe crack running vertically down the tunnel lining is present. (See Appendix N, Figures N.3 and N.4, for images of test site ET 10.4-3.) The map was built to the side of this crack (Figure M.31c) but because of the stalactite formation and grout fittings, it could not extend over the crack. The same structural reinforcement—approximately 437 mm (17.2 in.) deep and 310 mm (12.2 in.) wide—is present in both the B- and volume-scans (Figure M.34). Also at this location, strong echoes under the region nearest the stalactite formation and crack indicate possible debonding of the hoop and longitudinal reinforcement.

The last areas tested at the Eisenhower Memorial Tunnel were on the interior precast divider wall (particularly surrounding joints) even though significant distress was not visible. Figure M.35 shows the typical B-scan, with the region surrounding the crack completely lacking any reflection. Large cracks (here filled with a caulking sealant) typically completely attenuate all the sound waves emitted, making it difficult to assess the presence of nearby distress. This phenomenon surrounding cracks leads to an important clue in analyzing concrete ultrasound images; the lack of reflection around an area may indicate an unusual amount of air, preventing the shear wave from being transmitted across the boundary since gases and fluids do not support shear wave propagation.

Overall testing at the Eisenhower Memorial Tunnel concluded that the UST system could consistently detect some type of structural reinforcement (other than steel rebars), although the type of reinforcement was not determined. The UST evaluation also revealed possible areas of debonding

near severe cracks and joints. The reinforcement cover and spacing were also detectable.

Hanging Lake Tunnel, Colorado

Completed in 1992 with a maximum length of 1,219 m (4,000 ft) through the southern wall of Glenwood Canyon, Hanging Lake Tunnel (Figure M.36) was the last link in the Interstate highway system. Both bores of the tunnel were built using multiple-face drill and blast methods. Between the westbound and eastbound bores, a four-story control center monitors traffic along I-70, fully equipped with emergency response vehicles and trained staff.

Areas of interest within the tunnel include a number of significant surface cracks (Figure M.37, as well as Figure M.38, a and b), some of which had been partially patched with a skim coat of some type of grout. Other areas include a standard sound concrete region (Figure M.38c), regions surrounding joints (Figure M.38d), and a region of tiled lining in the eastbound lane (Figure M.39).

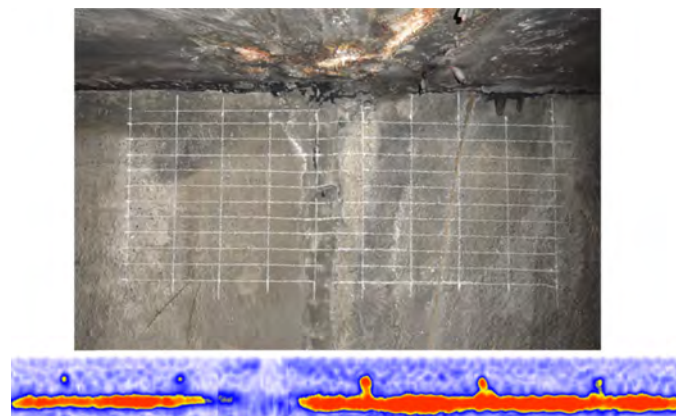


Figure M.35. B-scan of precast divider panel showing backwall reflection and reinforcement.



Figure M.36. Hanging Lake Tunnel: exterior view (left) and interior plenum view (right).

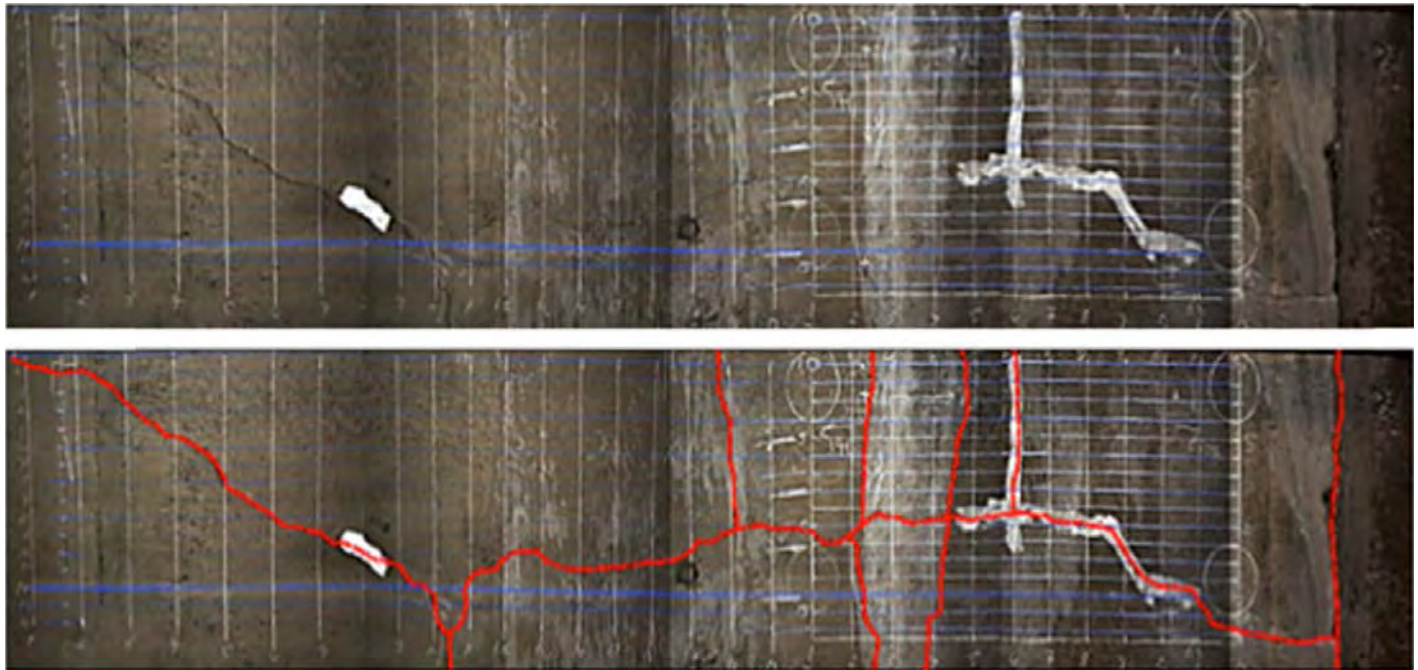


Figure M.37. Image collage of extensive map with cracks (shown in red).

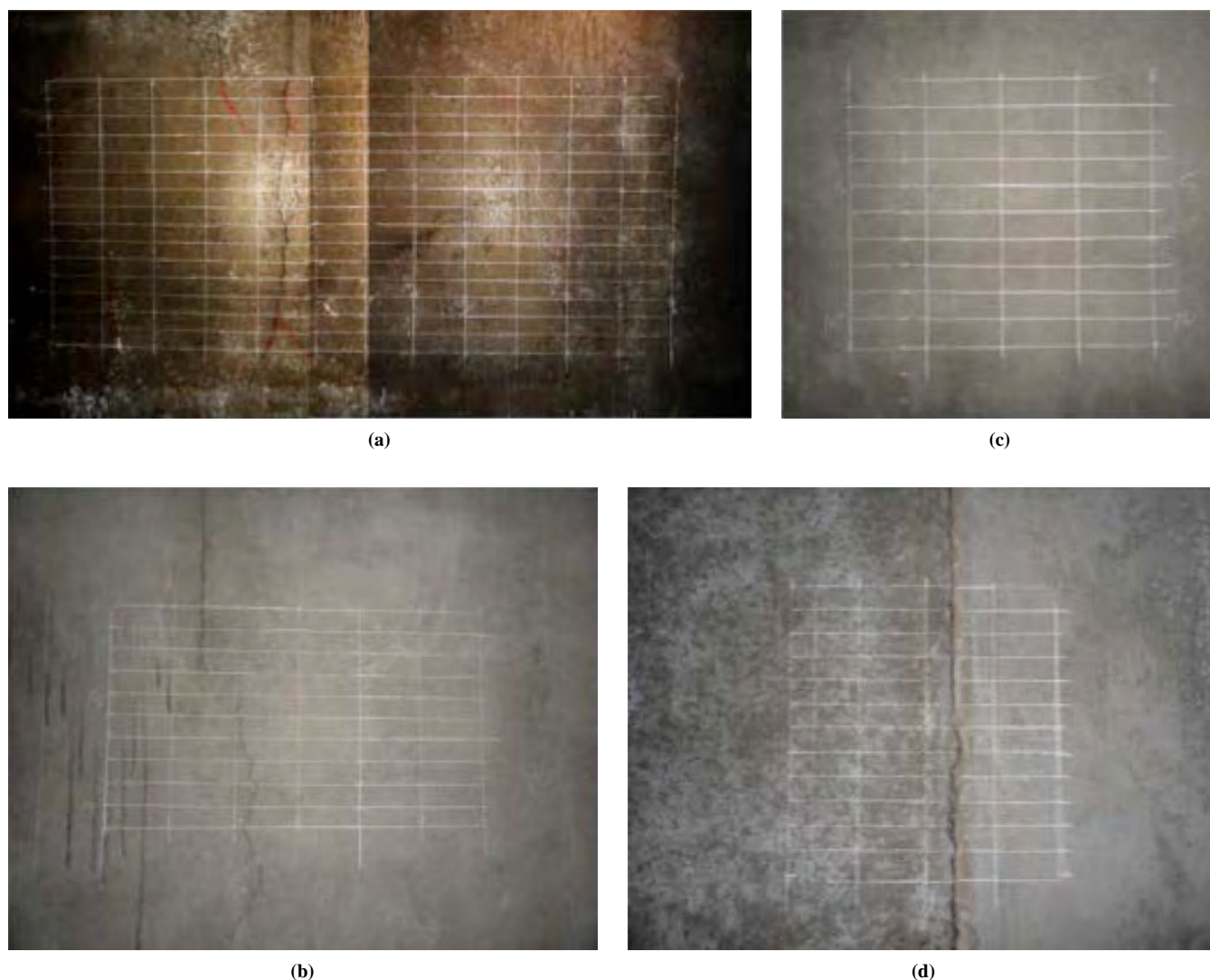


Figure M.38. Images of areas tested at Hanging Lake Tunnel: (a, b) severe vertical cracks, (c) sound concrete, and (d) lining joint.

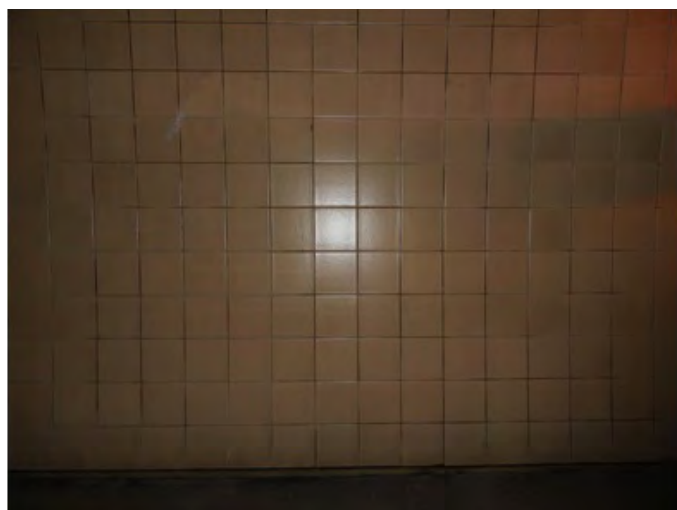


Figure M.39. Image of tile surface evaluated at Hanging Lake Tunnel.

The sound concrete region (Figure M.38c, as well as Figures N.11 and N.12 of test site HLT 10.5-5, 6, 7 in Appendix N) shows that the backwall reflection varies from 752 mm to 823 mm (29.6 in. to 32.4 in.) in depth, with the hoop reinforcement at 109 mm to 130 mm (4.3 in. to 5.1 in.) in depth and a longitudinal rebar on top of the hoop reinforcement.

One area with significant surface cracks revealed shallow delaminations emanating from the surface cracks (see Appendix N, Figures N.7 and N.8, for images of test site HLT 10.5-1, 2, 3). These cracks (Figure M.40, top and bottom left) show what looks to be the beginning stages of spalling, with the curved cracks penetrating approximately 312 mm (12.3 in.) in depth and closing toward each other. This map also revealed a backwall surface at 701 mm (27.6 in.). The hoop and longitudinal reinforcement can be seen in all scans.

Another area with significant cracking (see Appendix N, Figures N.13 and N.14, for images of test site HLT 10.5-8, 9)

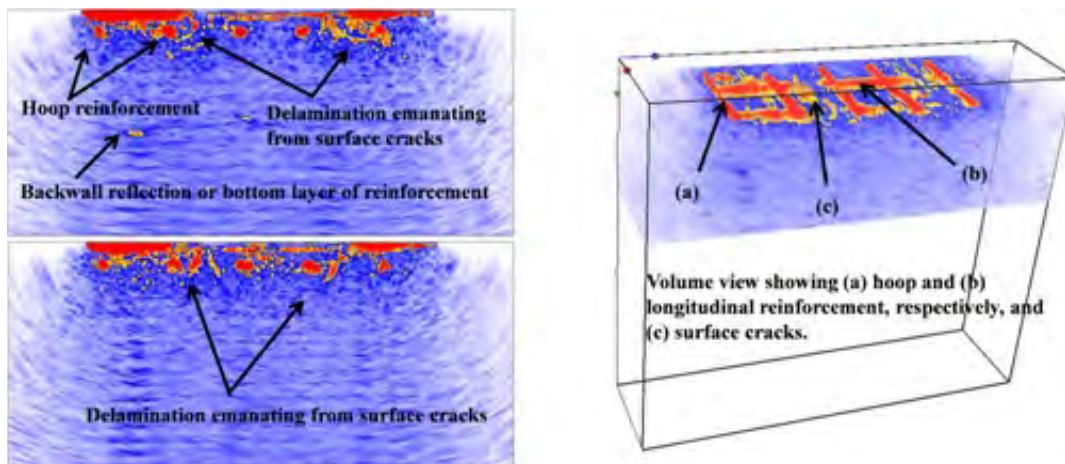


Figure M.40. UST images showing surface cracks and delamination: B-scans (left) and volume-scan (right).

did not show any sign of delamination; the surface crack appeared only to follow a single hoop reinforcing rebar. The backwall, however, was clearly distinguished at approximately 752 mm (29.6 in.) in depth (Figure M.41). Above this backwall reflection is an area of high reflectivity that either corresponds to shallow (51-mm to 76-mm, or 2-in. to 3-in.) backwall delamination or the lower layer of reinforcing steel.

Another area showing significant cracking was originally mapped to cover a small area (~1.2 m, or 4 ft, wide). After the data was collected, however, a delamination appeared around the boundary of the grid. The grid was extended to cover as much of the delamination as possible, eventually reaching over 4.9 m (16 ft). This map (see Appendix N, Figures N.15 and N.16, for images of test site HLT 10.5-10, 11, 12) is shown as a collage of photographs in Figure M.37. The B-scan shown in Figure M.42 (top) reveals an extensive delamination ranging

from 203 mm to 508 mm (8 in. to 20 in.) below the surface and stretching over 3.4 m (11 ft). The C-scans in Figure M.42 (bottom right) show the hoop and longitudinal reinforcement, as well as a plan view of the curved delamination's planar spread. Because of the significant reflection from the delamination's boundaries, the backwall reflection is not detectable.

The map tested over a joint (see Figure M.38d, as well as Figures N.9 and N.10 of test site HLT 10.5-4 in Appendix N) showed possible signs of debonding or the presence of voids and/or shallow delaminations at a maximum depth of 229 mm, or 9 in. (Figure M.43). Also, similar to the suspected debonding at the Eisenhower Memorial Tunnel locations in Figures M.33 and M.34, multiple reflections are seen at increments corresponding to the reinforcing steel depth. As noted before, these characteristic echoes are suspected to be present when debonding of the reinforcement occurs as a result of corrosion.

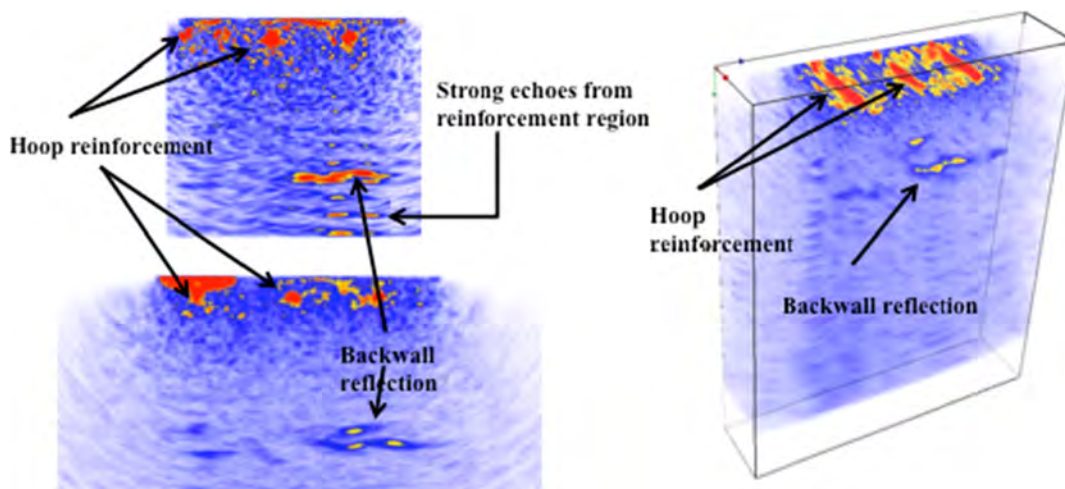


Figure M.41. UST images showing possible deep delamination: B-scans (left) and volume-scan (right).

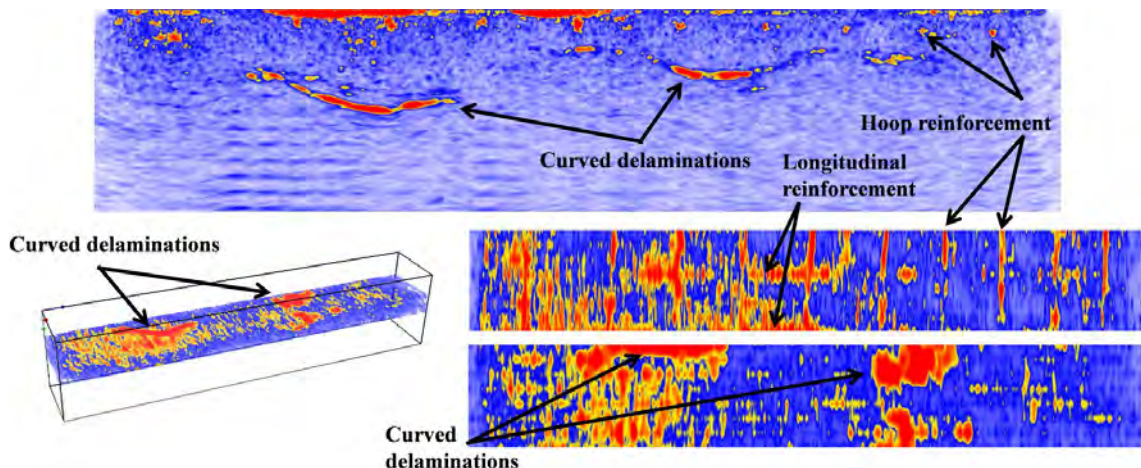


Figure M.42. UST images showing significant deep delamination: volume-scan (bottom left), B-scan (top), and C-scans (bottom right).

The last area tested at the Hanging Lake Tunnel was a section of tile inside the eastbound bore along the outer wall (see Figure M.39, as well as Figures N.17 and N.18 of test site HLT 10.5-13 in Appendix N). Although no backwall surface was detectable, all reinforcement could be clearly seen.

Overall, testing at this tunnel indicated shallow delaminations emanating from surface cracks (approximately 312 mm [12.3 in.] in depth), as well as severe delaminations at an approximate depth of 508 mm (20 in.). The UST evaluation also revealed possible areas of debonding near severe cracks and joints. The reinforcement cover and spacing were also detectable. Unfortunately, validation of delamination and crack depth was not available at this tunnel.

Chesapeake Channel Tunnel, Virginia

The Chesapeake Channel Tunnel (Figure M.44) is one of two tunnels that make up the Chesapeake Bay Bridge-Tunnel

system, joining southeastern Virginia to the Delmarva Peninsula. Hailed worldwide as a modern engineering wonder, the 37-km-long (23-mi-long) system includes 3.2 km (2 mi) of causeway, four manmade islands, 8.9 km (5.5 mi) of approach roads, 19.3 km (12 mi) of low-level trestle, two 1.6-km (1-mi) steel tunnels, and two bridges. The Chesapeake Channel Tunnel (during construction and briefly afterward called the Baltimore Channel Tunnel) was constructed using a cut-and-cover method. Precast steel tubes, fabricated and assembled in Orange, Texas, were floated to a shipyard in Norfolk, Virginia, where the reinforced concrete linings and roadway were constructed. The sections were floated to the site and then sunk into a trench. Each steel tube, 90 m (300 ft) in length and 11 m (37 ft) in diameter, was joined to the other one, sealed, and connected to its adjoining section. As each steel section was welded together, patches between the 90-m (300-ft) sections had to be formed with concrete to make an overlapping seal.

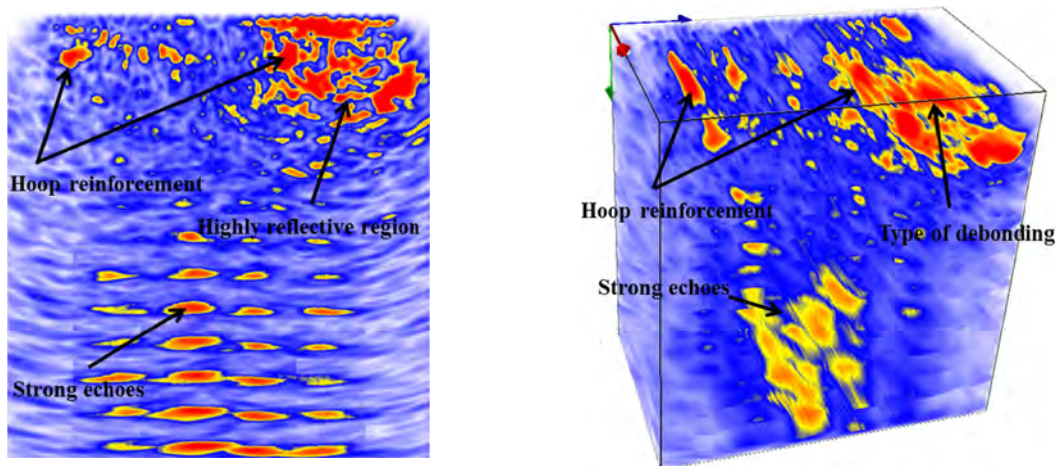


Figure M.43. UST images over lining joint: B-scan (left) and volume-scan (right).

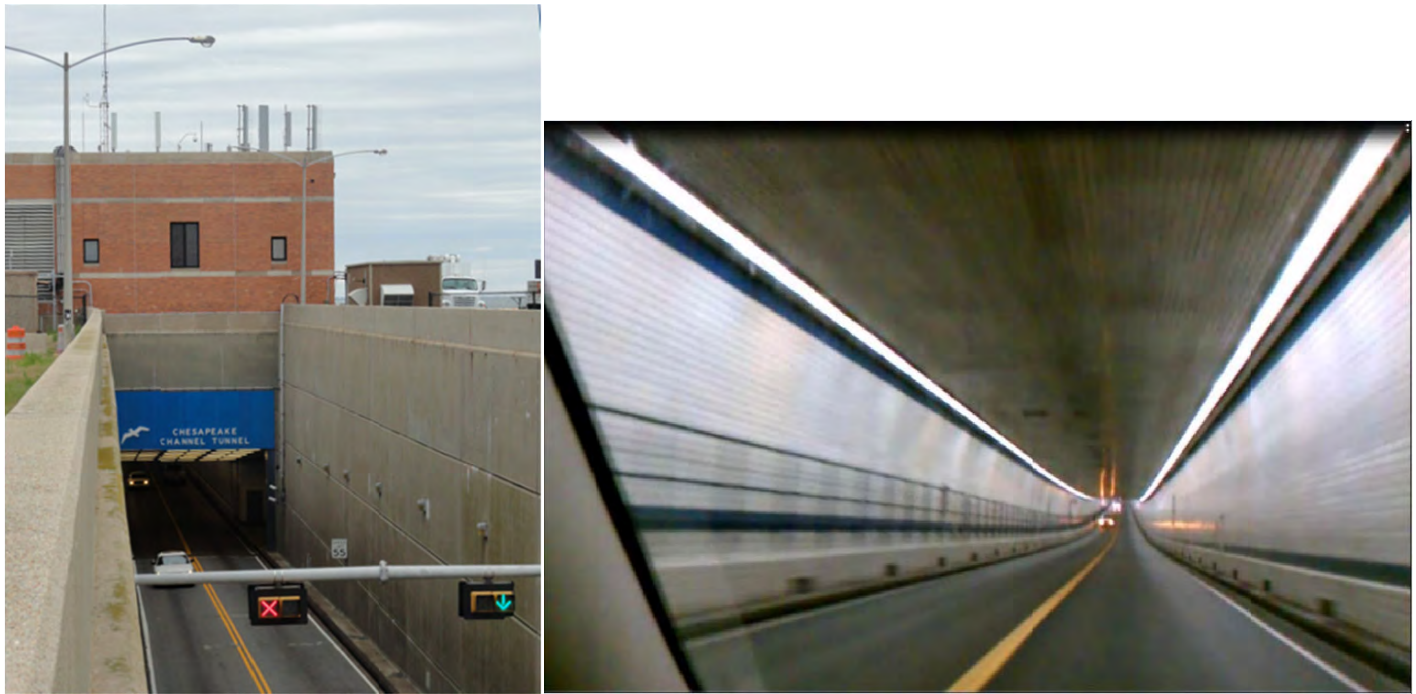


Figure M.44. Chesapeake Channel Tunnel: entrance (left) and interior view (right).

As testing for this SHRP 2 Renewal project began, a cart with an attached ground-penetrating radar (GPR) antenna was wheeled throughout the entire length of the 1.6-km (1-mi) tunnel in various configurations. The data from the GPR evaluations revealed two significant features. The first was a change in steel layout. In two segments at the entrance to the tunnel, the layer of reinforcement in the GPR scan showed a change, although specifics of the change were indiscernible. Two maps were built on what appeared to be a representation of sound concrete: one before the change shown in the GPR and one after the change (see Appendix N, Figures N.19 through N.22, for images of test sites CBBT 10.11-1 through 10.11-4). The first area, shown in Figure M.45a, revealed that the hoop reinforcement was approximately 61 mm (2.4 in.) in depth and 112 mm (4.4 in.) on center with the longitudinal reinforcement located directly beneath it. The backwall at this location was determined to be 627 mm (24.7 in.) from the surface. The second area, shown in Figure M.45b, revealed the hoop reinforcement to be 58 mm (2.3 in.) in depth and 300 mm (11.8 in.) on center, with the longitudinal reinforcement located directly beneath it. The backwall at this location was 620 mm (24.4 in.) from the surface. Blueprints for the two areas verified that the first bridge section on both ends was constructed with the hoop reinforcement at 114 mm (4.5 in.) on center, and the rest of the sections were constructed at 305 mm (12 in.) on center. The plans also indicate that all wall thicknesses are a nominal 610 mm (24 in.) in depth. A comparison of the B-scans of the two areas, showing the difference in hoop rebar layout, is shown in Figure M.46.

The second significant feature of the GPR data was the frequent spike in dielectric. Almost every observed spike in dielectric corresponded to a lining seam or crack and was marked for ultrasonic inspection.

Spalling and corrosion are the two predominant damages this tunnel is facing (see Figure M.47 for typical spalling and corrosion damage); therefore, the areas of greatest interest were identified to be cracks through which water seeps (live cracks). The primary objective was to cover a variety of cracking conditions and as many of the cracks located by the GPR dielectric as possible. The most significant live cracks, shown in Figure M.45 (c and d), were evaluated by building a map that spanned the crack in such a way as to capture the origin of the crack. This method would theoretically cover the entire surface area of the visible crack for detailed analysis. Because of time constraints, this was not possible at every location. These maps, though large, required only 30 min to 1.5 h for data collection.

Figure M.48 displays the scanning results of a live crack at Station 474+27 ft (see Figure M.45c, as well as Figures N.23 and N.24 of test site CBBT 10.11-5 in Appendix N). The backwall surface, clearly located at 612 mm (24.1 in.) below the surface, is consistent with tunnel blueprints that show the lining is approximately 610 mm (24 in.) in depth. Also in line with the tunnel blueprints for this section of tunnel is the reinforcement spacing. The tomograms indicate the hoop reinforcement is located at approximately 305 mm (12.0 in.) on center, at a depth of 51 mm to 66 mm (2.0 in. to 2.6 in.), along with longitudinal reinforcement located directly beneath. The blueprints for this section indicate the hoop

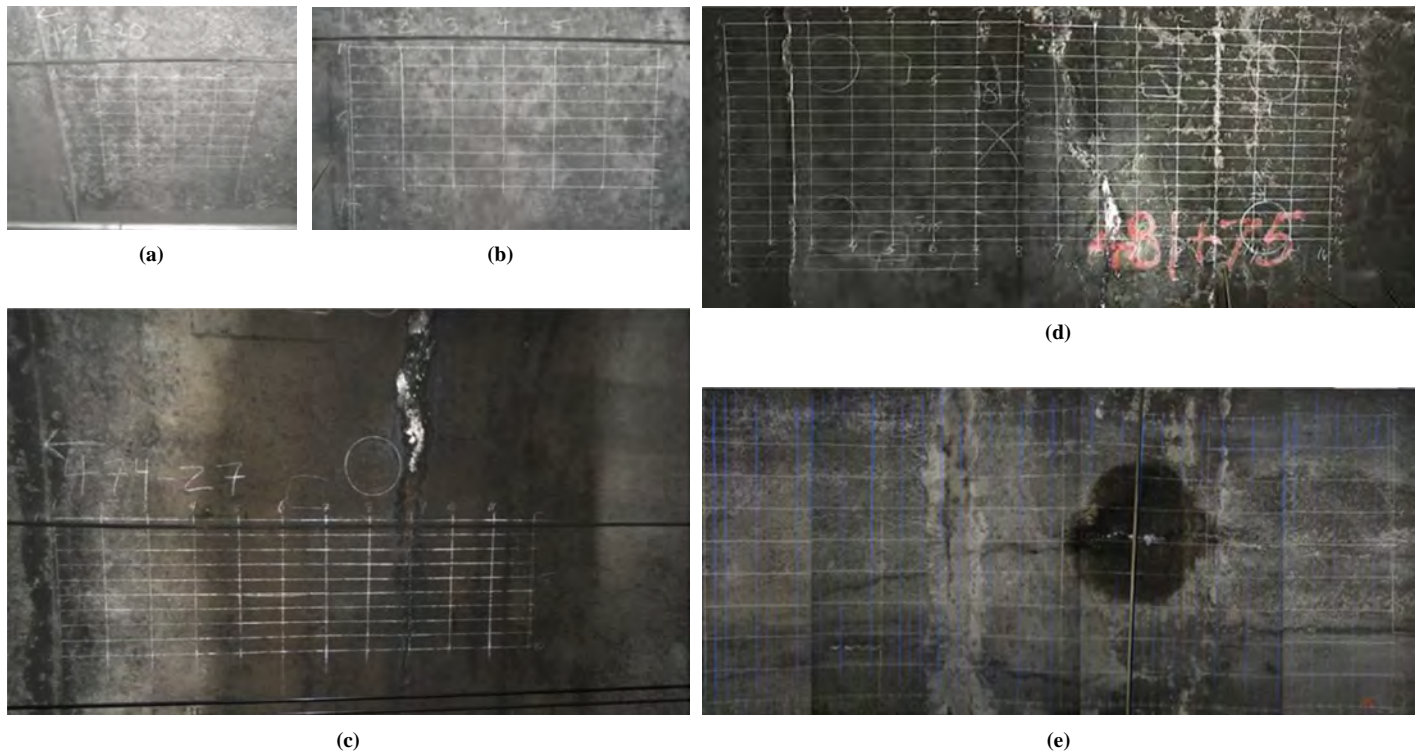


Figure M.45. Areas tested at Chesapeake Channel Tunnel.

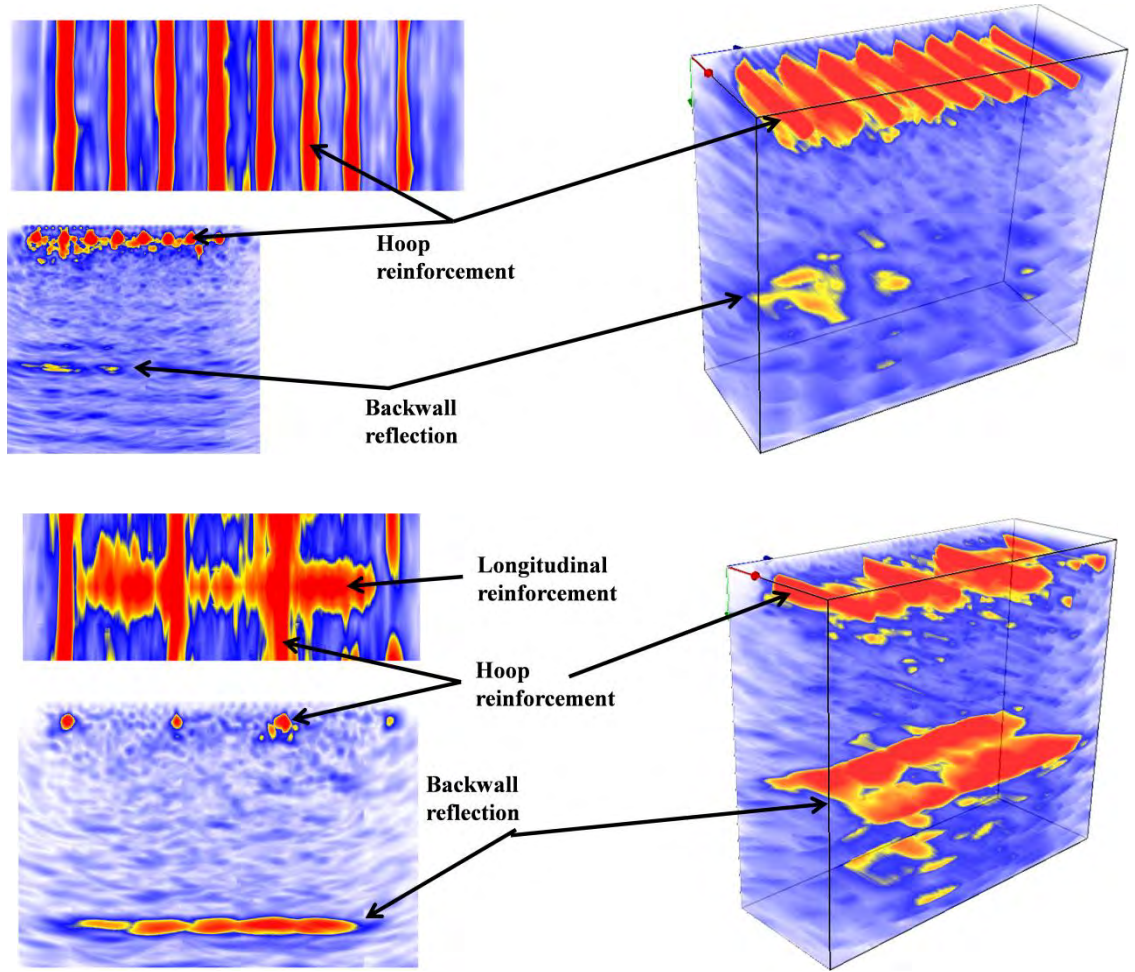


Figure M.46. Comparison of steel layout differences.



Figure M.47. Typical spalling and corrosion.

reinforcement is 305 mm (12 in.) on center, with the longitudinal reinforcement directly underneath.

Surrounding the surface cracks, the tomograms also indicate severe shallow defects, including cracks as deep as 229 mm (9 in.) and possibly shallow delaminations approximately 51 mm (2 in.) below the surface. The heavy ringing

surrounding the cracked region (see Figure M.48, top left and both bottom images) indicates suspected discontinuities surrounding the reinforcement. The discontinuities are presumed to have resulted from corrosion of the top layer of reinforcement.

Another map covering a severe crack, located at Station 481+76 ft (see Appendix N, Figures N.35 and N.36, for images of test site CBBT 10.11-13), was built to completely capture the width of a delamination less than 102 mm (4 in.) below the bottom surface (from the steel plate). Shown in Figure M.49, this delamination may originate from the layer of hoop reinforcement nearest the steel skin. The backwall surface, a little more than the typical 610 mm (24 in.) in depth, varied between 676 mm and 721 mm (26.6 in. and 28.4 in.). The delamination was approximately 513 mm (20.2 in.) below the surface and approximately 696 mm (27.4 in.) in width. The hoop reinforcement is located approximately 307 mm (12.1 in.) on center, at a depth of 51 mm to 91 mm (2.0 in. to 3.6 in.), along with longitudinal reinforcement located directly beneath. The blueprints for this section indicate the hoop reinforcement is 305 mm (12 in.) on center with the longitudinal reinforcement directly underneath.

Another area of interest involved a circumferential crack that had only just begun to indicate signs of moisture intrusion

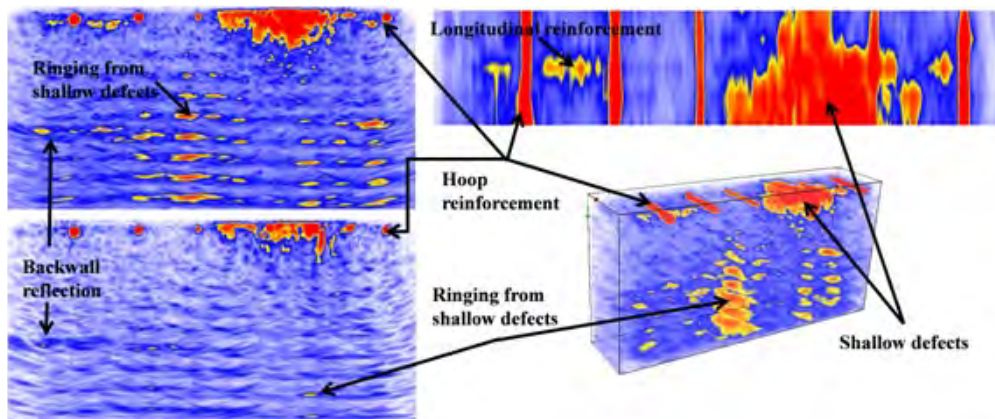


Figure M.48. Area surrounding live crack.

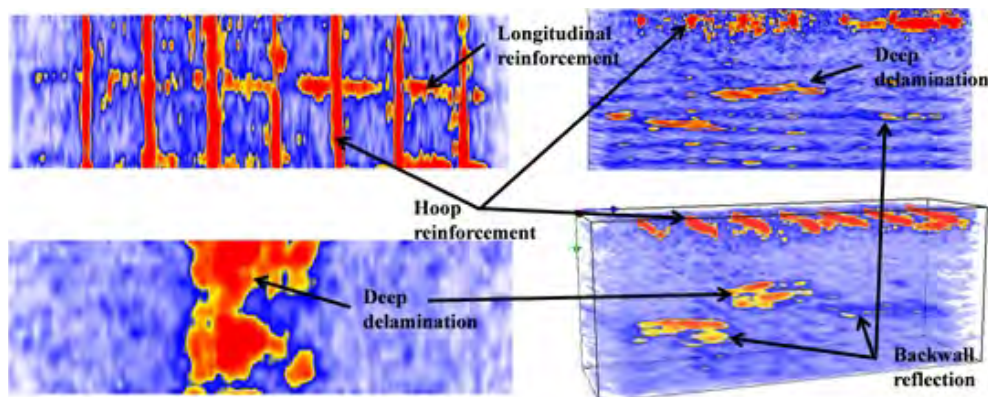


Figure M.49. UST images at Station 481+76 ft showing deep delamination.

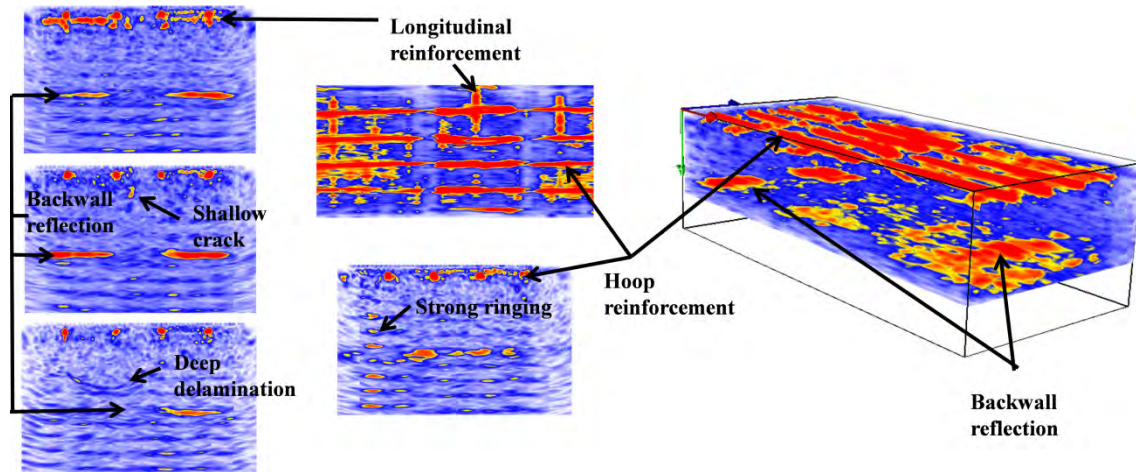


Figure M.50. UST images surrounding circumferential crack.

(see Figure M.45e, as well as Figures N.29 and N.30 of test site CBBT 10.11-10 in Appendix N). A map was built around this crack, attempting to cover as much of the length of the crack as possible from inside the plenum. Another feature that made this crack interesting was the presence of a longitudinal crack between the stainless steel ceiling hangers (visible in Figure M.45e approximately one-third of the distance from the left side of the image). The backwall surface was clearly distinguishable and ranged from 577 mm to 658 mm (22.7 in. to 25.9 in.) below the surface (Figure M.50). The hoop reinforcement measured 69 mm to 81 mm (2.7 in. to 3.2 in.) in depth and 307 mm (12.1 in.) on center, and the longitudinal reinforcement measured 434 mm (17.1 in.) on center. This matches with the blueprint's details of 305 mm (12.0 in.) on center for the hoop reinforcement, but the plans do not indicate spacing for the longitudinal reinforcement. As seen in Figure M.50 (top left B-scan), two layers of hoop reinforcement appear to be present; but as that is not indicated in the blueprints, this could be an area of a splice. Light reflections, or echoes, are seen throughout the entire region of the crack, specifically surrounding the reinforcement nearest the moisture. Debonding of the reinforcement here is probably due to corrosion.

The gap in the backwall reflection (Figure M.50, B-scans on left) and the omission of some of the hoop reinforcement (Figure M.50, volume-scan on right and C-scan at top center) indicate the presence of a crack. When cracks are present, the ultrasonic waves are strongly attenuated, causing the reception of the signals to be scarce if not completely absent. The other noticeable feature in this map is the possibility of a curved delamination approximately 450 mm (17.7 in.) in depth and up to 483 mm (19 in.) wide (Figure M.50, bottom left). Figure M.50 (center left B-scan) also makes apparent that surface cracks appear to extend a maximum of 249 mm (9.8 in.) in depth.

The last section tested within the plenum was a location detected by a high spike in GPR dielectric. Upon investigation,

no live crack was found, but rather a dry seam. Although no visible signs of distress were apparent, hammer tapping revealed an extremely shallow delamination that appeared close to separating and falling. A grid was applied to the region surrounding the seam and shallow delamination, and the area was broken up into two sections: Region I (see Figures N.27 and N.28 for images of test site CBBT 10.11-9 in Appendix N) and Region II (see Figures N.25 and N.26 for images of test site CBBT 10.11-7, 8 in Appendix N), as shown in Figure M.51. Both regions showed strong ringing emanating from the layer of reinforcement, indicating potential reinforcement debonding.

Region I UST evaluations revealed significant cracks and/or voids as deep as 218 mm, or 8.6 in. (Figure M.52, bottom left). The hoop reinforcement was shown to vary between 51 and 76 mm (2.0 and 3.0 in.) in depth at approximately 310 mm (12.2 in.) on center, with the longitudinal reinforcement located directly beneath at 503 mm (19.8 in.) on center. The backwall in this section varied from 617 to 660 mm (24.3 to 26.0 in.).

Region II UST evaluations, depicted in Figure M.53, showed the delaminated region (marked as "shallow delamination") and also showed the presence of cupped delaminations as deep as 488 mm (19.2 in.) below the surface, or approximately the same depth as the lower reinforcement closest to the tube skin. The backwall in this area ranged from 612 mm to 660 mm (24.1 in. to 26.0 in.). The hoop reinforcement at 56 mm (2.2 in.) deep was found to be 307 mm (12.1 in.) on center, with the longitudinal rebars underneath at 411 mm (16.2 in.) on center.

The last two areas tested within the Chesapeake Channel Tunnel were both located in the driving lane, along the tiled wall lining. One of the areas with potential deterioration was discovered in the data from SPACETEC, a German company that uses a contact-free scanning system that provides detailed images, profiles, and thermal data for tunnel linings (<http://www.spacetec.de>). SPACETEC's analysis of the Chesapeake

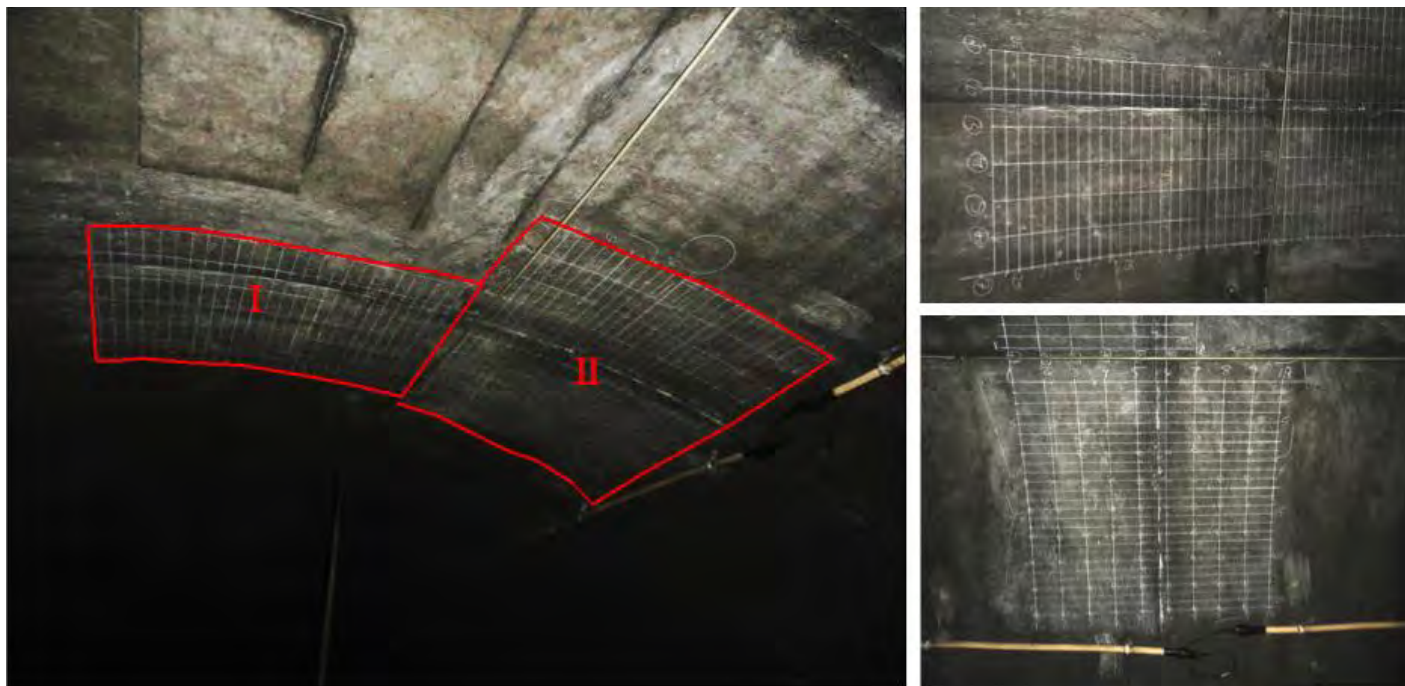


Figure M.51. Images depicting Region I (top right) and Region II (bottom right).

Channel Tunnel revealed an area detected by the infrared scan, indicating possible debonding. When debonding occurs beneath tile, hammer sounding by ear or by microphone can readily differentiate bonded from debonded tile. Debonded tile can occur for two reasons: (1) improper installation (wrong type of thin set; disproportionate water ratios; improper mixing; and/or low standard of workmanship, that is, not back-buttering the tile); or (2) presence of degrading agent (typically water) behind the tile lining. If the debonding occurs for the first reason, reapplication of the tile lining can solve the problem. However, when debonding occurs because of cracks that facilitate the degradation of the thin set by moisture entrainment, NDT techniques may help determine the source of the

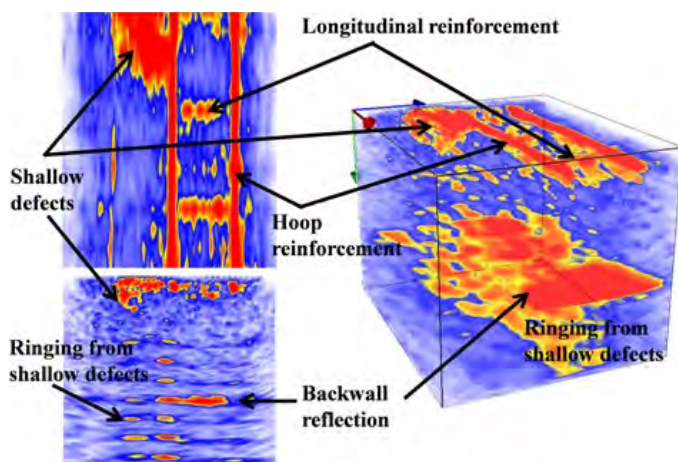


Figure M.52. Region I UST images.

moisture. Therefore, one goal was to search for a damaged area that was not verifiable by sounding techniques or, in other words, to determine the beginning stages of tile debonding before debonding actually occurred to a noticeable extent. SPACETEC's data served this purpose well by identifying an area (Figure M.54, left) that showed signs of possible delamination but the delamination was not detectable by hammer sounding. Figure M.54, right, shows a damaged area that includes debonded tile detectable by hammer sounding. The UST results from scanning the area identified by SPACETEC's data are shown in Figure M.55. The three B-scans (Figure M.55, left images) indicate the backwall reflection varies between 714 mm and 787 mm (28.1 in. and 31.0 in.). This variance can be seen in the D-scan in Figure M.55 (far right image, the dark blue curved strip on the right of the figure), which shows the curvature of the tube's skin. Also in the same figure is a C-scan image of the area tested at a depth of 102 mm (4 in.) directly beneath the reinforcement. When compared to SPACETEC's infrared analysis, this outline correlates strongly with the infrared image. A significant delamination appears to be present at the level of reinforcement and above, but it has yet to cause significant debonding of the tile. The top left image in Figure M.55 shows much of the shallow surface cracks and possible shallow delaminations above the reinforcement, and the center left image depicts a deep crack (directly left of the last hoop rebar on the right). Notice the hoop and longitudinal reinforcement are both detectable at 122 mm to 239 mm (4.8 in. to 9.4 in.) below the surface at 297 mm (11.7 in.) on center (again, refer to the D-scan in Figure M.55 and the hoop reinforcement profile).

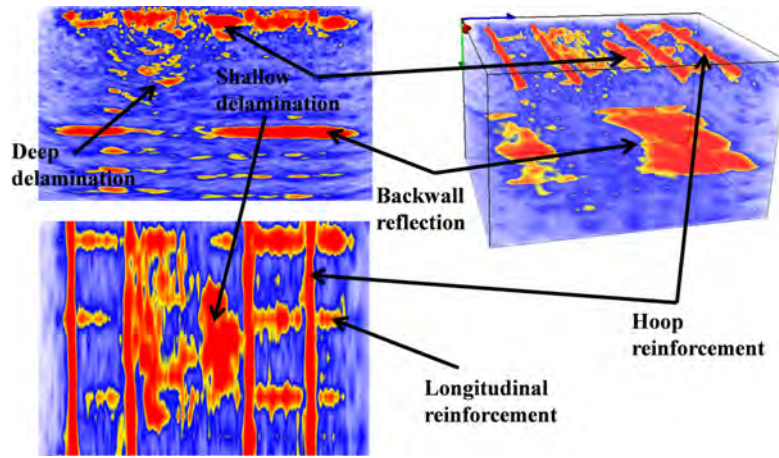


Figure M.53. Region II UST images.

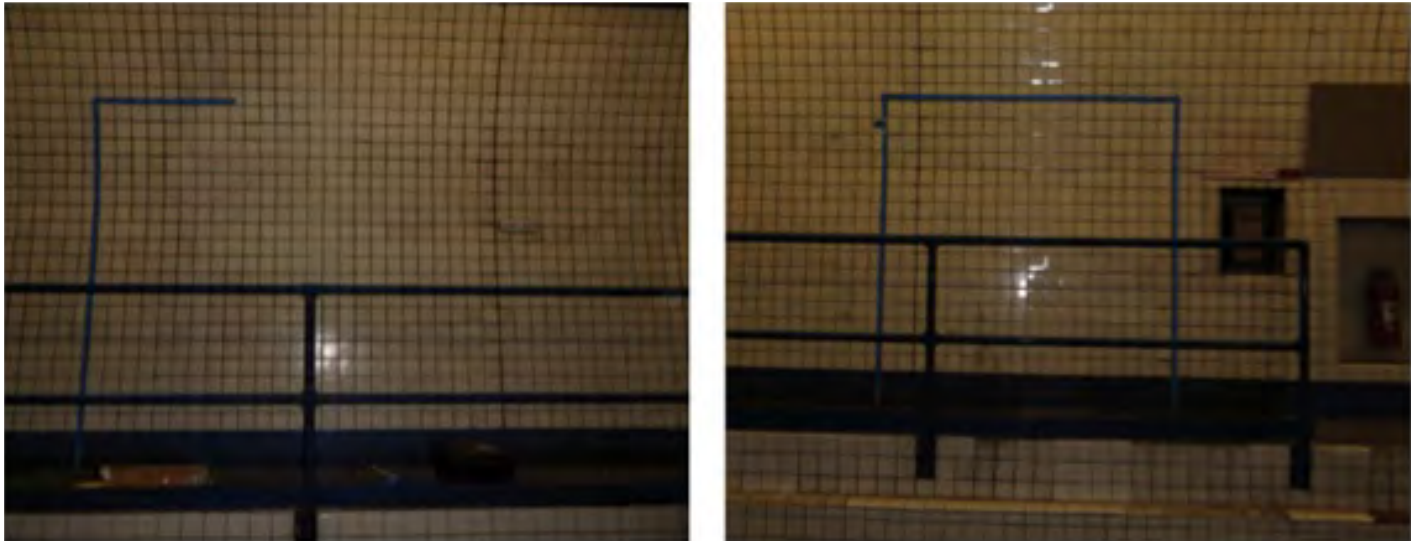


Figure M.54. Tile lining sections in Chesapeake Channel Tunnel.

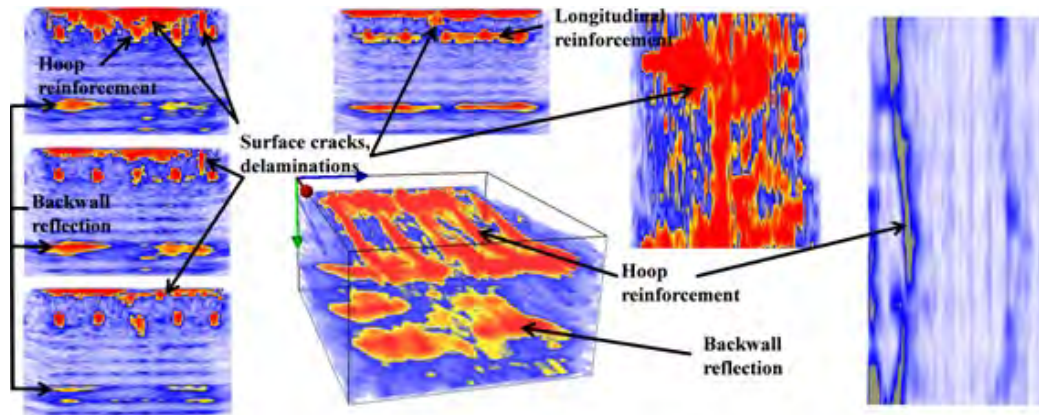


Figure M.55. First tile lining area tested, discovered by SPACETEC scanning.

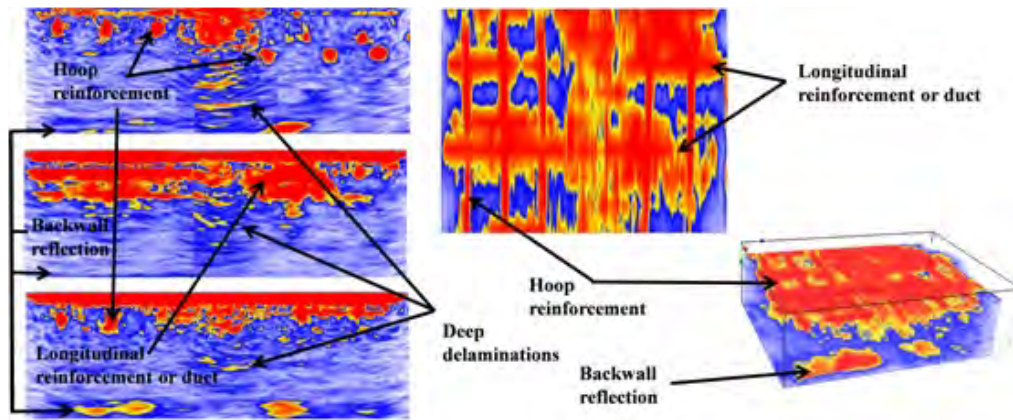


Figure M.56. Second tile lining area tested.

The longitudinal reinforcement is seen, but differentiating between the actual longitudinal rebars and the 51-mm (2-in.) diameter electrical ducts that are present can be difficult. If the scanning direction were oriented perpendicular to the rebar/ducts, this distinction could be made.

The UST results from the second area tested (Figure M.54, right) are shown in Figure M.56. The region of debonded tile correlated greatly with a joint in the tube lining as supported by the extensive delamination noted mid-image in the B-scans (Figure M.56, left images). The backwall in this region varied from 635 mm to 762 mm (25 in. to 30 in.), for the same reasons of tube curvature discussed in the previous map. The hoop reinforcement was 109 mm to 196 mm (4.3 in. to 7.7 in.) in depth and approximately 307 mm (12.1 in.) on center. As in the previous map, the longitudinal reinforcement is hard to distinguish from the 51-mm (2-in.) diameter electrical ducts present. The top left image is likely evidence of a lap splice (notice two distinct layers of steel rebar to the right of the joint, where different tube sections could have different splice

locations). During assembly of the tubes underwater, as noted earlier, steel skins were connected by bolting and welding overlapped hoods. After this mechanical lock connection was complete, concrete was poured around the joint location to make the interior steel-reinforced concrete continuous and waterproof. Although no detailed plans show the width of this scratch joint, the question remains as to whether the deep delaminations seen in the B-scans could be a result of degrading concrete joints.

Washburn Tunnel, Texas

The Washburn Tunnel (Figure M.57), the only underwater vehicle tunnel in operation in Texas, was completed in 1950 and carries a federal road beneath the Houston Ship Channel, joining two Houston suburbs. The tunnel was constructed using the immersed tube method, with sections joined together in a prepared trench, 26 m (85 ft) below water.

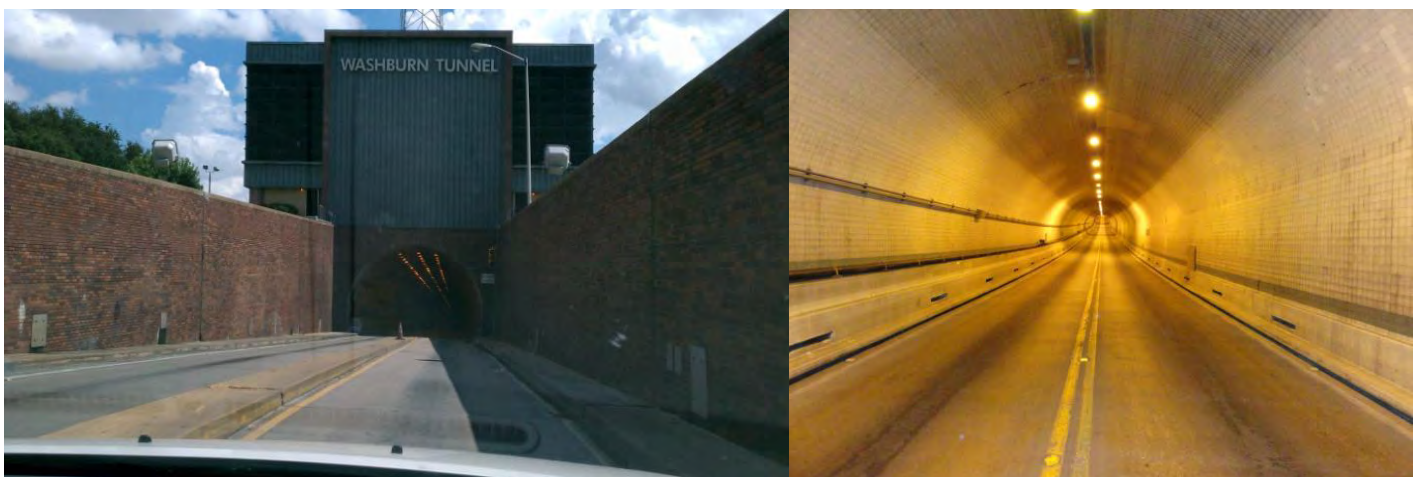


Figure M.57. Washburn Tunnel: entrance (left) and interior view (right).

A specific area of interest in this tunnel was tile debonding. As noted earlier, in tile-lined tunnels such as these, acoustic sounding with hammer tapping can quickly reveal debonded tiles. When an object such as a hammer is lightly tapped (or even dragged) along the surface, the lower frequencies perceived by the ear as pinging typically indicates debonding. Most debonding of tiles happens as water infiltrates the lining, deteriorating the mortar that holds the tile. However, trouble arises when trying to locate the source of the water infiltration; while hammer sounding is effective in locating debonded tiles, it does not necessarily locate the source of the water. In this tunnel, four areas that indicated debonding through hammer sounding were evaluated. Blue painter's tape was used to outline both the grid and the outside perimeter of the area that the human ear perceived as a debonded section.

The first three sections are shown in Figure M.58. The images have blue painter's tape outlining debonded areas (detected by hammer sounding) and are paired with the associated C-scans that show shallow delaminations ranging from 16 mm to 103 mm (0.63 in. to 4.1 in.) deep. The area marked off by hammer sounding closely matches the region of shallow debonding.

Representations of typical B-, C-, and volume-scans for the three regions in Figure M.58 are shown below in Figure M.59. Again, large areas depicting shallow debonding are visible, as well as regions of delamination surrounding the reinforcement. The B-scans clearly show that significant damage penetrates as deep as 457 mm (18 in.). These B- and C-scans are representative of the other areas tested in the Washburn Tunnel.

The last section tested, depicted in Figure M.60, reveals shallow debonding (note the C-scan image of the debonded area 16 mm, or 0.63 in., below the surface in Figure M.60, bottom center). The B-scan (Figure M.60, bottom left) shows areas suspected of having deep delamination. This delamination is also seen in the volume-scan on the right.

Overall, testing at the Washburn Tunnel showed significant damage behind debonded tile, leading to the conclusion that the debonding resulted from lining stresses (i.e., not from tile workmanship).

Conclusions

The UST system was used to perform evaluations on more than 30 concrete and shotcrete specimens containing simulated defects, numerous concrete pavements, airport runways, and bridge decks. These defects included air-filled and water-filled voids, vertical cracks, horizontal delaminations, and abnormalities such as clay lumps. The device was also used to determine specimen characteristics such as reinforcement depth and spacing, as well as concrete thickness

measurements. After evaluating the system's capabilities and establishing confidence in the methodology, the system was used on four existing tunnels. When possible, ground truth data were further used to determine the precision and accuracy of the system with various types of defects. Table M.7 shows the maximum and minimum features detected by this research. Note that these values do not necessarily express the limits of the device but the limits of the performed research. Further research should expand the variety of structural defects (both size and location) to determine maximum and minimum detectable features along with confidence levels for each type of defect.

Limitations of the UST System

The limitations of the device are as follows:

- *Speed of data acquisition.* If the system is used for detailed mapping in the Map Mode, the user should expect the scanning process to take between 9 min/sq m and 25 min/sq m (0.8 min/sq ft and 2.3 min/sq ft). The Review Mode can be used for single-point evaluations at much faster rates of inspection (3–5 s per scan), but only limited-width B-scans are available for evaluation in this mode.
- *No indication of phase change.* The color palette response represents quantity of reflectivity regions and is a measurement relative to the medium (in which zero reflectivity, the blue spectrum, should ideally exist). The type of defect is largely guesswork on the part of the user, and interpreting these signals requires greater skill and knowledge of ultrasonics.
- *Detection of layered defects.* If defects are stacked, particularly in such a manner that air gaps are located above other types of defects, then the device can rarely determine anything below the initial air-filled gaps. Ultrasonic pulses attenuate at air boundaries. If pulses are able to transmit past air interfaces, then the received signal is extremely weak and should be examined to be certain it is not a multiple or echo of the initial flaw.
- *Shallow defects.* Because of the spacing of the transducer array and the beam spread of the individual transducers, defects that exist approximately 25 mm (1 in.) from the surface cannot be expected to be received by other transducers and carry accurate information regarding the depth and lateral dimensions of the shallow defects. However, near-surface defects can leave a shadow on the data collected below the near-surface defects. Examples of this are the shotcrete Specimen L and concrete Specimen Iota, in which the defects left a shadow beneath their presence. Though the defects are too shallow to reflect the actual boundary, their presence inhibits ultrasonic pulses from being transmitted (or received) beyond them.

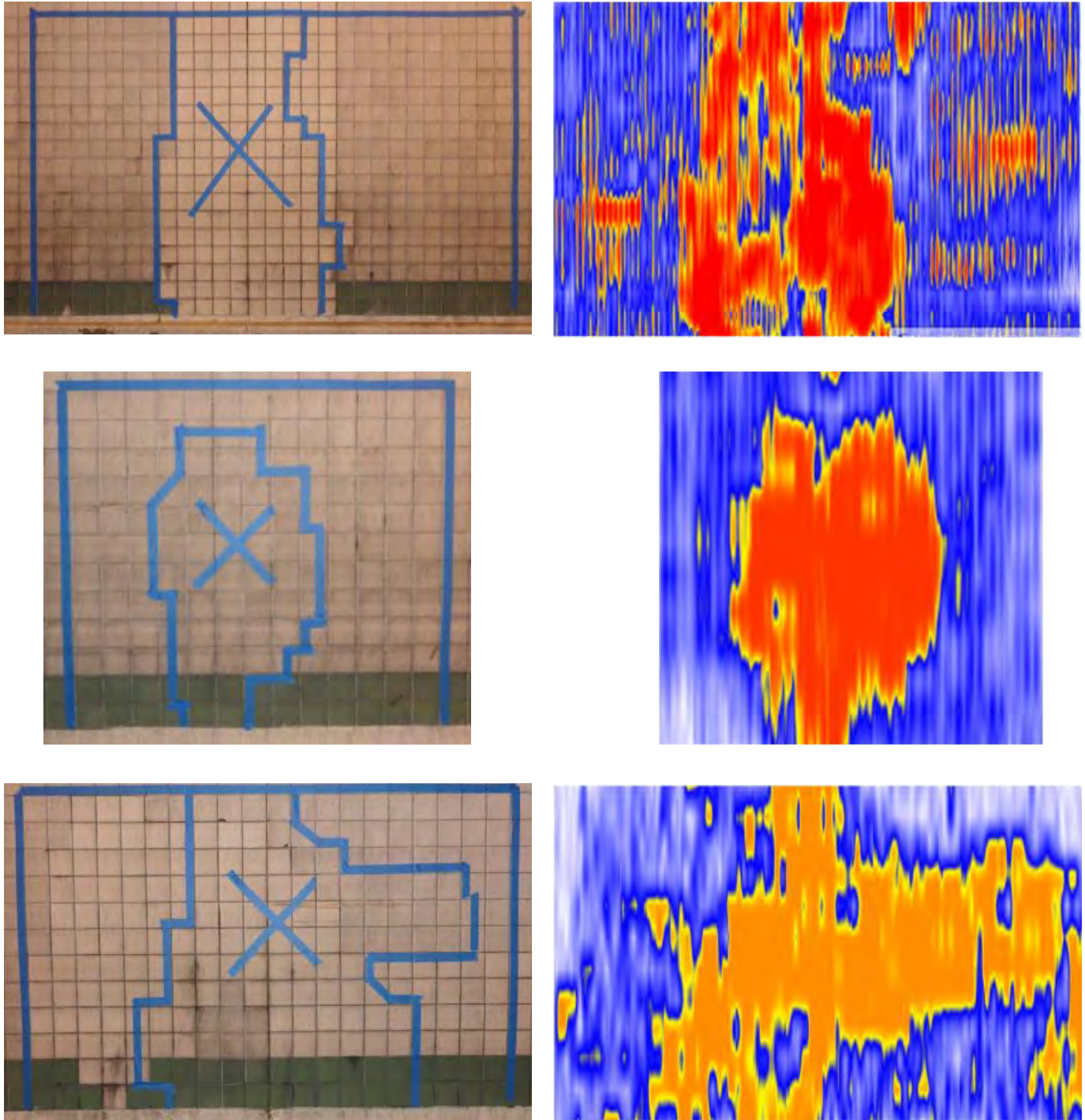


Figure M.58. *Tile linings via UST (left) paired with the associated C-scans (right).*

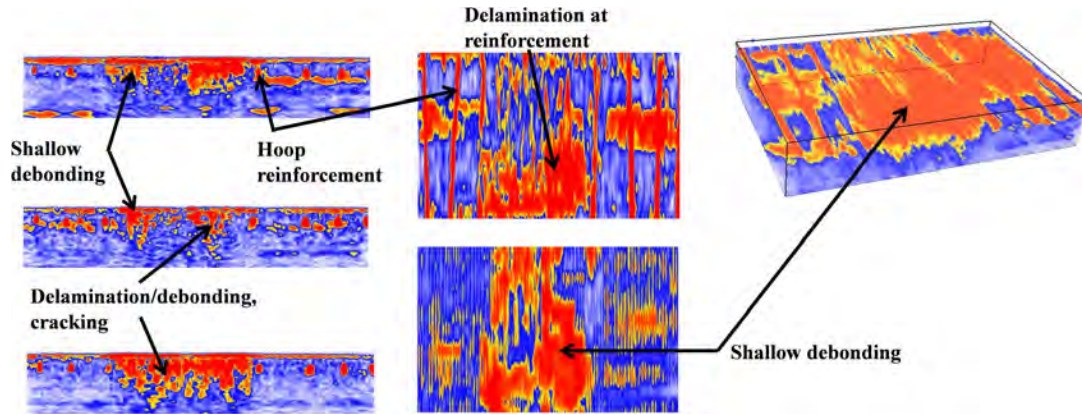


Figure M.59. Areas tested surrounding debonded tiles: B-scans (left), C-scans (center), and volume-scan (right).

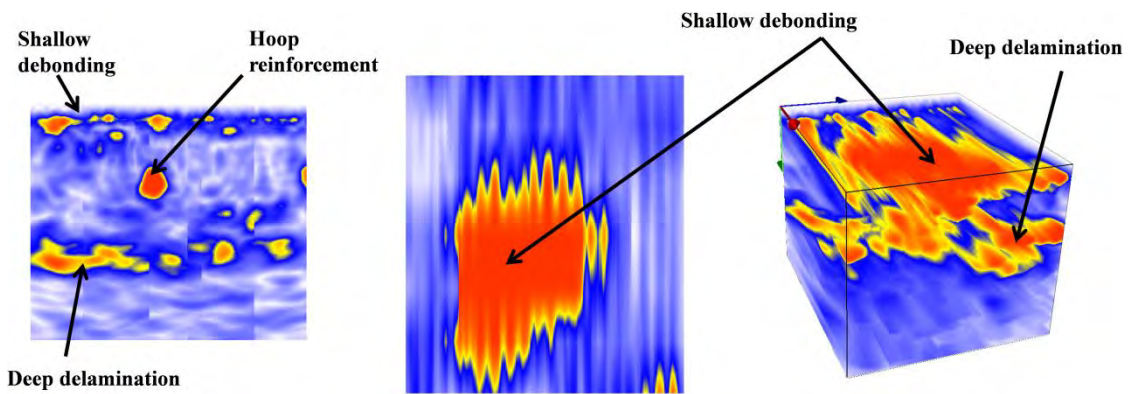


Figure M.60. Tile lining tested at Washburn Tunnel.

Table M.7. Minimum and Maximum Detected Features Tested by the A1040 MIRA System

Component Detected	Component Extremes	Minimum Depth Detected	Maximum Depth Detected
Reinf. diameter ^a	Minimum diameter: No. 5	83 mm (to center)	184 mm (to center)
	Maximum diameter: No. 11	51 mm (to center)	196 mm (to center)
Reinf. cover	NA	No. 11 at 33 mm	No. 9 at 377 mm
Secondary reinf. layer	Minimum diameter: No. 5	184 mm (to center)	184 mm (to center)
	Maximum diameter: No. 9	210 mm (to center)	377 mm (to center)
Delamination thickness ^a	Minimum thickness: 0.05 mm	43 mm (to center)	89 mm (to center)
	Maximum thickness: 2.0 mm	69 mm (to center)	69 mm (to center)
Delamination depth	NA	0.05-mm thickness at 43-mm depth (to center)	0.25-mm thickness at 183-mm depth (to center)
Clay lump diameter (all 51 mm thick)	Minimum diameter: 102 mm	61 mm (to center)	216 mm (to center)
	Maximum diameter: 152 mm	107 mm (to center)	160 mm (to center)
Specimen thickness (structural depth)	NA	102 mm	711 mm
Air-filled voids	Only thickness tested: 13 mm	76 mm (to center)	203 mm (to center)
Water-filled voids	Water-filled Ziploc bag: ~13 mm	76 mm (to center)	203 mm (to center)

^a Size only verified by ground truth data; feature is not able to be detected by the A1040 MIRA system.

Note: All testing performed with 50-kHz scanning frequency; NA = not available.

Conclusions of Tunnel Testing

The conclusions of the tunnel testing are as follows:

- The UST system is exceptional at locating horizontal delaminations ranging in thickness from 0.05 mm to 2.0 mm (0.002 in. to 0.079 in.) and is able to differentiate between fully debonded and partially bonded areas within a single map on the basis of the color distribution. It is not, however, able to directly measure the thickness of delaminations.
- Cracks were only clearly characterized when they formed nonperpendicular to the testing surface; however, the presence of perpendicular cracks could be assumed by the omission of surface detail. Note that no crack depths were confirmed by ground truth validation and this finding should be a focus of further research.
- Backwall surfaces up to a depth of 965 mm (38 in.) were successfully and accurately determined. Assuming the plan details were correct (no ground truth validation was available to verify), the UST system predicted this depth within an accuracy of 5 mm (0.3 in.).
- Both air-filled and water-filled voids ranging from 76 mm to 203 mm (3 in. to 8 in.) in depth could be detected, but differentiation between the two was difficult because shear waves are not supported by air or water, and almost all of the acoustic energy is reflected by these types of voids. Further study could be conducted to analyze the difference between phase changes involving these two types of voids.
- As long as the device is polarized in the correct direction, reinforcement layout and depth were also successfully determined, the only exception being in some shotcrete applications. When potentially porous materials such as the shotcrete specimens were evaluated, the presence of very small air voids made internal inspection very difficult.
- With the exception of some medium-size clay lumps (with a diameter of approximately 102 mm, or 4 in.) surrounding reinforcement, the testing of all clay lumps was also highly successful.
- Two MIRA systems were used to compare the system's abilities to reproduce the same wave speed. For a test involving 16 specimens, a strong positive correlation existed (with a coefficient of determination of 0.952), with a standard error of approximately 33 m/s (108 ft/s).
- Precision in detecting the depth of delaminations using the same device with the same testing procedures and input parameters (e.g., wave speed, frequency, gain selection) was typically on the order of 1 mm to 3 mm (0.04 in. to 0.12 in.) and is more likely to be explained by user error/interpretation than device error. The same is true for water-filled and air-filled voids.
- Reproducibility, using separate devices with the same testing procedures and input parameters (e.g., wave speed, frequency, gain selection), indicated a consistent offset of 9 mm to 13 mm (0.35 in. to 0.51 in.) between the two systems, with a single system always revealing the deeper measurement. The research team is pursuing an explanation for this

offset with the device's manufacturer. Reproducibility using separate devices with the same testing procedures and an individual calculation of wave speed (with all other parameters equal) indicated a strong positive correlation between defect depths (coefficient of determination of 0.9965) with a standard error of 3.85 mm.

- The minimum area able to be tested with the MIRA system is merely tied to the size of the device: 370 mm by 170 mm (14.6 in. by 6.7 in.).

References

- De La Haza, A., C. Peterson, and A. Samokrutov. n.d. *Three Dimensional Imaging of Concrete Structures Using Ultrasonic Shear Waves*. Acoustic Control Systems. http://acsys.ru/eng/article/files/Imaging_of_concrete_structures.pdf.
- Im, S., S. Hurlebaus, and D. Trejo. 2010. Inspection of Voids in External Tendons of Posttensioned Bridges. *Transportation Research Record: Journal of the Transportation Research Board*, Vol. 2172, TRB, National Research Council, Washington, D.C., pp. 115–122.
- Krause, M., B. Gräfe, F. Mielentz, B. Milmann, M. Friese, and H. Wiggenhauser. 2009. Ultrasonic Imaging of Post-Tensioned Concrete Elements: New Techniques for Reliable Localization of Grouting Defects. *Proc., 2nd International Conference on Concrete Repair, Rehabilitation and Retrofitting*, Concrete Repair, Rehabilitation, and Retrofitting II, Cape Town, South Africa, pp. 215–216.
- Schickert, M. 1995. Towards SAFT-Imaging in Ultrasonic Inspection of Concrete. *Proc., International Symposium on Non-Destructive Testing in Civil Engineering*, NDT-CE, Berlin, Germany, Vol. 1, pp. 411–418.
- Schickert, M., M. Krause, and W. Müller. 2003. Ultrasonic Imaging of Concrete Elements Using Reconstruction by Synthetic Aperture Focusing Technique. *Journal of Materials in Civil Engineering*, Vol. 15, No. 3, pp. 235–246.
- Shokouhi, P., J. Wöstmann, G. Schneider, B. Milmann, A. Taffe, and H. Wiggenhauser. 2011. Nondestructive Detection of Delamination in Concrete Slabs. *Transportation Research Record: Journal of the Transportation Research Board*, Vol. 2252, TRB, National Research Council, Washington, D.C., p. 103.

APPENDIX N

Ultrasonic Tomography Test Summaries

Introduction

This appendix summarizes the field evaluations of the non-destructive testing (NDT) technique known as ultrasonic tomography (UST). The tests were performed within the framework of the second Strategic Highway Research Program (SHRP 2) Renewal Project R06G. The objectives of this project have been listed in the Executive Summary of the main report.

Thirty specimens with simulated defects were tested before the UST equipment was used in the field. Table N.1 summarizes those tests.

Following are evaluation summaries of the test sites located at Eisenhower Memorial Tunnel near Dillon, Colorado; Hanging Lake Tunnel near Glenwood Springs, Colorado; Chesapeake Channel Tunnel near Norfolk, Virginia; Washburn Tunnel in Houston, Texas; continuously reinforced concrete pavement on I-20 in Fort Worth, Texas; and bonded concrete overlays at the George Bush International Airport in Houston, Texas (Figures N.1–N.56).

Table N.1. Detailed Defect Dimensions, Depth, and Cover and Spacing (in.)

Specimen Name and Material	Actual Reinforcement Cover and Spacing	Measured Reinforcement Cover and Spacing	Type of Defect	Actual Dimensions of Defect	Actual Depth of Defect	Measured Dimensions of Defect	Measured Depth of Defect	Actual Specimen Depth	Measured Specimen Depth
Alpha, concrete	None	na	None	na	na	na	na	12	12.4
Beta, concrete	^a	4.0 at 8.0 on center	None	na	na	na	na	18	17.6
Gamma, concrete	^a	4.3 at 7.9 on center	None	na	na	na	na	12	11.7
Delta, concrete	None	na	None	na	na	na	na	24	23.6
Epsilon, concrete	^a	4.1 at 8.0 on center	None	na	na	na	na	24	23.3
Zeta, concrete	^a	3.8 at 7.9 on center	None	na	na	na	na	15	14.1
Eta, concrete	^a	4.5 at 7.9 on center	plastic	12 by 12 by 1	2	11.7 by 12.8	2.3	15	14.2
Theta, concrete	^a	4.4 at 8.0 on center	plastic	12 by 12 by 1	3	11.7 by 13.5	3.5	15	13.9
Iota, concrete	^a	4.0 at 8.0 on center	plastic	12 by 12 by 1	1	7.8 by 12.3	1.7	15	13.0
Kappa, concrete	^a	3.8 at 8.0 on center	Styrofoam	12 by 12 by 1	8	15.7 by 15.7	8.0	15	14.7
Lambda, concrete	^a	3.7 at 8.1 on center	Water-filled void	12 by 12	8	16.5 by 15.4	6.5–8.8	15	14.6
A, shotcrete	None	na	None	na	na	na	na	4	3.9
B, shotcrete	None	na	None	na	na	na	na	6	5.7
C, shotcrete	None	na	None	na	na	na	na	8	6.8
D, shotcrete	^b	6.9	Air-filled void	17.25 by 14.75	7 ⁵ / ₈	12.4 by 12.1	7.6	12	11.3
E, shotcrete	^b	6.4	Water-filled void	15.75 by 14.5	7 ¹ / ₂	15.5 by 13.3	7.6	12	11.0
F, shotcrete	^b	6.7	Air-filled void	17.125 by 14.75	3	18.1 by 15.6	3.5	12	11.2
G, shotcrete	^b	6.8	Water-filled void	15.5 by 14.25	3	16.0 by 14.7	4.2	12	10.7

(continued on next page)

Table N.1. Detailed Defect Dimensions, Depth, and Cover and Spacing (in.) (continued)

Specimen Name and Material	Actual Reinforcement Cover and Spacing	Measured Reinforcement Cover and Spacing	Type of Defect	Actual Dimensions of Defect	Actual Depth of Defect	Measured Dimensions of Defect	Measured Depth of Defect	Actual Specimen Depth	Measured Specimen Depth
H, shotcrete	^b	6.4	Thin cloth	12 by 12	8	14.0 by 10.7	7.2	12	10.2
I, shotcrete	^b	5.7	Thin cloth	12 by 12	4	11.0 by 14.0	3.9	12	10.4
J, shotcrete	^b	6.1	Thin cloth	12 by 12	3	13.1 by 12.0	2.9	12	10.4
K, shotcrete	^b	5.6	Thin cloth	12 by 12	2	12.3 by 13.4	3.1	12	10.2
L, shotcrete	^b	5.6	Thin cloth	12 by 12	1	14.0 by 13.3	Very shallow	12	10.3
M, shotcrete	^b	5.8	None	na	na	na	na	12	10.4
A2, concrete	^c	NA	None	na	na	na	na	na	na
B2, concrete	^c	NA	1 clay lump	6-Ø by 2	~6	6.1	6.3	na	na
C2, concrete	^c	NA	6 clay lumps	4-Ø by 2	~3, 6, 9	3.1–4.1	2.7, 5.4, 8.5	na	na
D2, concrete	^c	6.0 at 8.0 on center	None	na	na	na	na	na	na
E2, concrete	^c	6.0 at 8.0 on center	1 clay lump	6-Ø by 2	~6	4.2	4.6	na	na
F2, concrete	^c	6.0 at 8.0 on center	6 clay lumps	4-Ø by 2	~3, 6, 9	2.9–3.9	2.4, 5.4, 7.8	na	na

Note: na = not applicable; NA = not available.

^a Two mats of No. 5 rebar, 4 in. from top and bottom, 8 in. on center.

^b One lattice girder in center of slab, sitting on bottom form, centroid of upper bar 5.25 in. from bottom, or ~6.25 in. from top.

^c One mat of No. 5 rebar, 6 in. from top, 8 in. on center.



Eisenhower Memorial Tunnel, Dillon, CO			
Defects	Notes	Reinf. Detail	
No significant defect noticed, except for strip of area (~9.4" wide, 16.2" deep) consistently found in other maps. Possibly structural steel reinforcement.	Backsurface not discernible. Area tested as representative of sound concrete.	Hoop reinf: ~4.2" deep @ ~9.9" on center. Longitudinal reinf: below hoop reinforcement.	$V_{\text{shear}} = 2751 \text{ m/s}$ X-step: 150 mm Y-step: 50 mm Max Depth: 1000 mm Frequency: 50 kHz Dillon, CO Eisenhower Tunnel ET 10.4-1, 2 Segment 8 TAMU/TII 10/2011



Figure N.1. Images of test site ET 10.4-1, 2.

Eisenhower Memorial Tunnel, Dillon, CO			
Defects	Notes	Reinf. Detail	$V_{\text{shear}} = 2751 \text{ m/s}$ X-step: 150 mm Y-step: 50 mm Max Depth: 1000 mm Frequency: 50 kHz
No significant defect noticed, except for strip of area (~9.4" wide, 16.2" deep) consistently found in other maps. Possibly structural steel reinforcement.	Backsurface not discernible. Area tested as representative of sound concrete.	Hoop reinf: ~4.2" deep @ ~9.9" on center. Longitudinal reinf: below hoop reinforcement.	

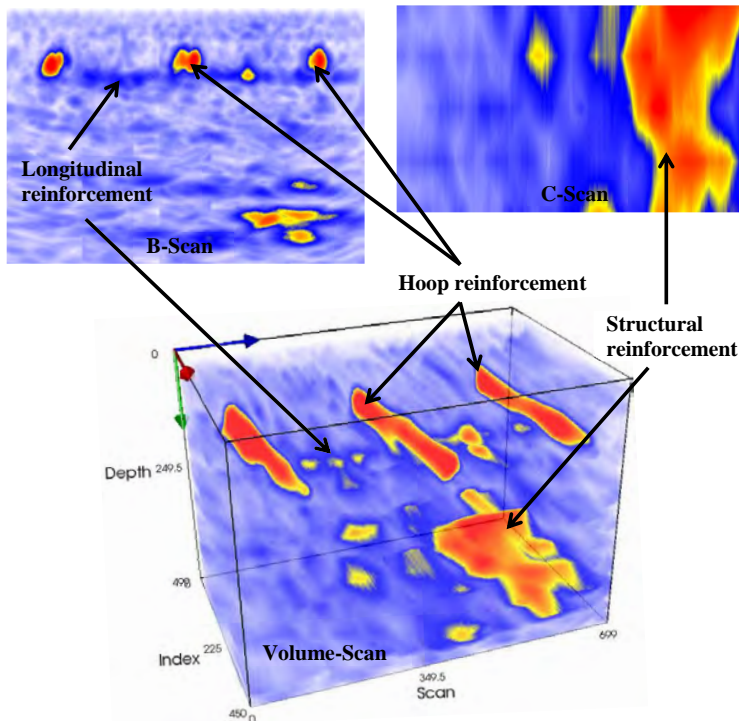


Figure N.2. UST images of test site ET 10.4-1, 2.



Eisenhower Memorial Tunnel, Dillon, CO			
Defects	Notes	Reinf. Detail	
No significant defect noticed, except for strip of area (~12.2" wide, 17.2" deep) consistently found in other maps. Possibly steel structural reinforcement.	Backsurface not discernible. Area tested because of surface cracking and crazing, nearby stalactite formation. Could not test over stalactite crack due to obtrusions.	Hoop reinf: ~3.7"-5.1" deep @ ~10.1" on center. Longitudinal reinf: below hoop reinforcement.	$V_{\text{shear}} = 2751 \text{ m/s}$ X-step: 150 mm Y-step: 50 mm Max Depth: 750 mm Frequency: 50 kHz Dillon, CO Eisenhower Tunnel ET 10.4-3 Segment 8 TAMU/TTI 10/2011



Figure N.3. Image of test site 10.4-3.

Eisenhower Memorial Tunnel, Dillon, CO			
Defects	Notes	Reinf. Detail	
No significant defect noticed, except for strip of area (~12.2" wide, 17.2" deep) consistently found in other maps. Possibly steel structural reinforcement.	Backsurface not discernible. Area tested because of surface cracking and crazing, nearby stalactite formation. Could not test over stalactite crack due to obtrusions.	Hoop reinf: ~3.7"-5.1" deep @ ~10.1" on center. Longitudinal reinf: below hoop reinforcement.	$V_{shear} = 2751$ m/s X-step: 150 mm Y-step: 50 mm Max Depth: 750 mm Frequency: 50 kHz Dillon, CO Eisenhower Tunnel ET 10.4-3 Segment 8 TAMU/TTI 10/2011

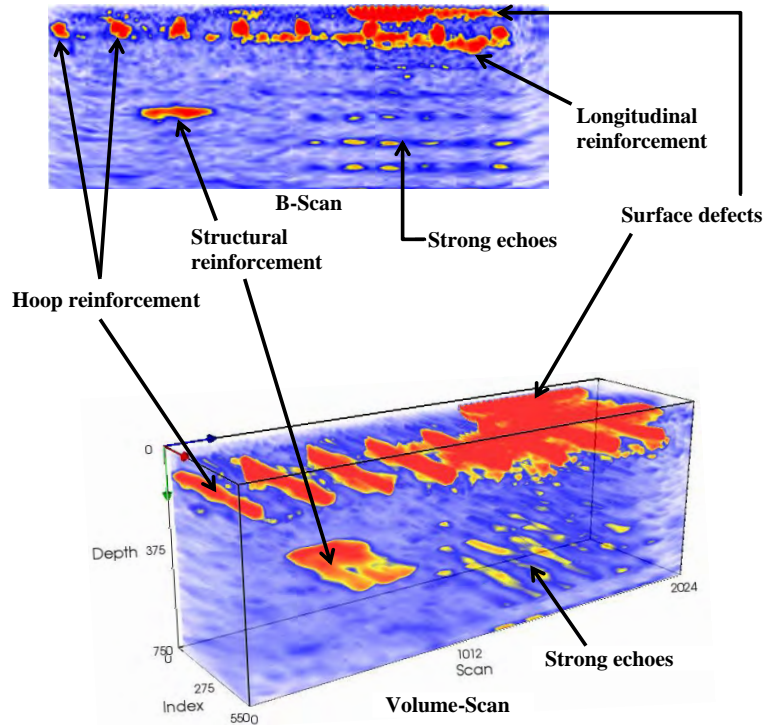



Figure N.4. UST images of test site 10.4-3.

Eisenhower Memorial Tunnel, Dillon, CO			
Defects	Notes	Reinf. Detail	
No significant defect noticed, except for strip of area (~13.5" wide, 16.1" deep) consistently found in other maps. Possibly steel structural reinforcement.	Backsurface not discernible. Area tested because of surface cracking and crazing and nearby joint.	Hoop reinf: ~4.1" deep @ ~10.1" on center. Longitudinal reinf: below hoop reinforcement.	$V_{\text{shear}} = 2751 \text{ m/s}$ X-step: 150 mm Y-step: 50 mm Max Depth: 750 mm Frequency: 50 kHz Dillon, CO Eisenhower Tunnel ET 10.4-4, 5 Segment 10 TAMU/TTI 10/2011

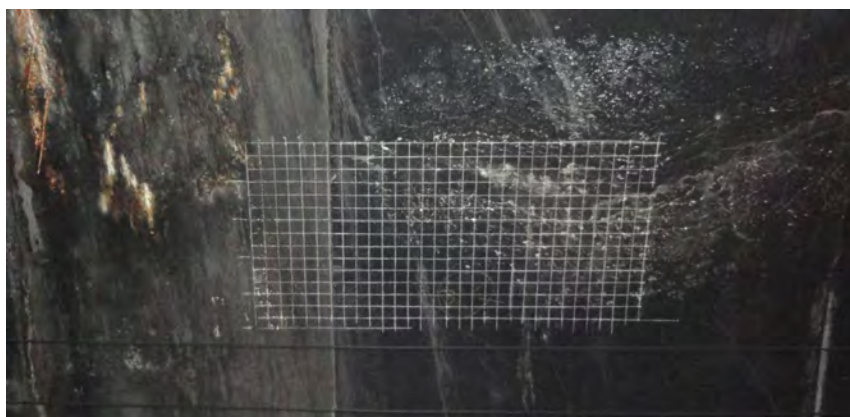



Figure N.5. Image of test site ET 10.4-4, 5.

Eisenhower Memorial Tunnel, Dillon, CO			
Defects	Notes	Reinf. Detail	
No significant defect noticed, except for strip of area (~13.5" wide, 16.1" deep) consistently found in other maps. Possibly steel structural reinforcement.	Backsurface not discernible. Area tested because of surface cracking and crazing and nearby joint.	Hoop reinf: ~4.1" deep @ ~10.1" on center. Longitudinal reinf: below hoop reinforcement.	$V_{shear} = 2751 \text{ m/s}$ X-step: 150 mm Y-step: 50 mm Max Depth: 750 mm Frequency: 50 kHz Dillon, CO Eisenhower Tunnel ET 10.4-4, 5 Segment 10 TAMU/TTI 10/2011

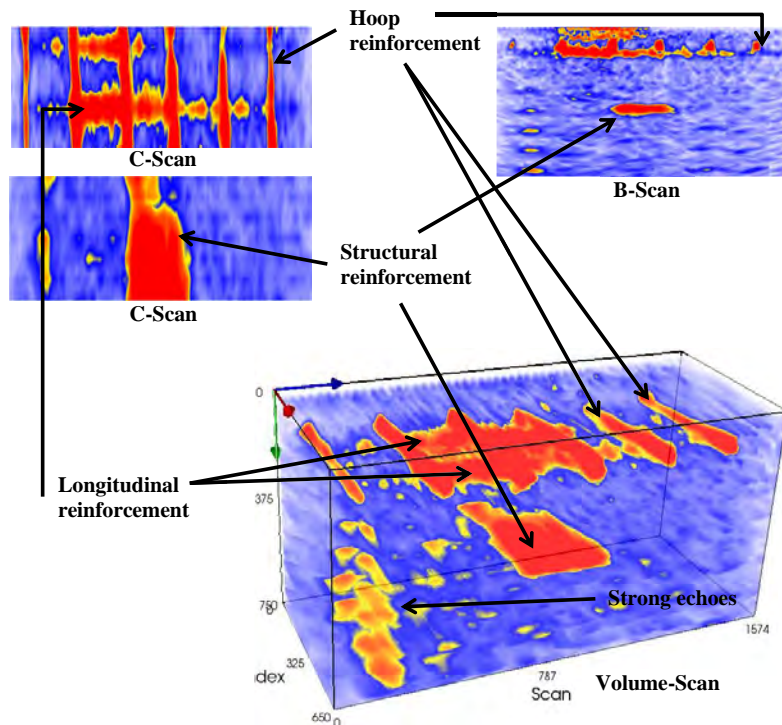


Figure N.6. UST images of test site ET 10.4-4, 5.



Hanging Lake Tunnel, Glenwood Springs, CO			
Defects	Notes	Reinf. Detail	
Apparent delamination extending 12.3" deep, originating from surface crack; possibly connecting to another crack located approximately 35" to the right of surface crack	Backsurface possibly seen at 27.6" in depth. Severe cracking. Area also tested by BAM.	Hoop reinf: 4.6"- 6.2" deep @ 15.7" on center. Longitudinal reinf: above and possibly below hoop reinforcement @ 14.1" on center.	V _{shear} = 2159 m/s X-step: 150 mm Y-step: 50 mm Max Depth: 2500 mm Frequency: 50 kHz Glenwood Springs, CO Hanging Lake Tunnel HLT 10.5-1, 2, 3 Segment 57 + 3.4 TAMU/TTI 10/2011



Figure N.7. Image of test site HLT 10.5-1, 2, 3.

Hanging Lake Tunnel, Glenwood Springs, CO			
Defects	Notes	Reinf. Detail	
Apparent delamination extending 12.3" deep, originating from surface crack; possibly connecting to another crack located approximately 35" to the right of surface crack	Backsurface possibly seen at 27.6" in depth. Severe cracking. Area also tested by BAM.	Hoop reinf: 4.6" - 6.2" deep @ 15.7" on center. Longitudinal reinf: above and possibly below hoop reinforcement @ 14.1" on center.	Vshear = 2159 m/s X-step: 150 mm Y-step: 50 mm Max Depth: 2500 mm Frequency: 50 kHz Glenwood Springs, CO Hanging Lake Tunnel HLT 10.5-1, 2, 3 Segment 57 + 3.4 TAMU/TTI 10/2011

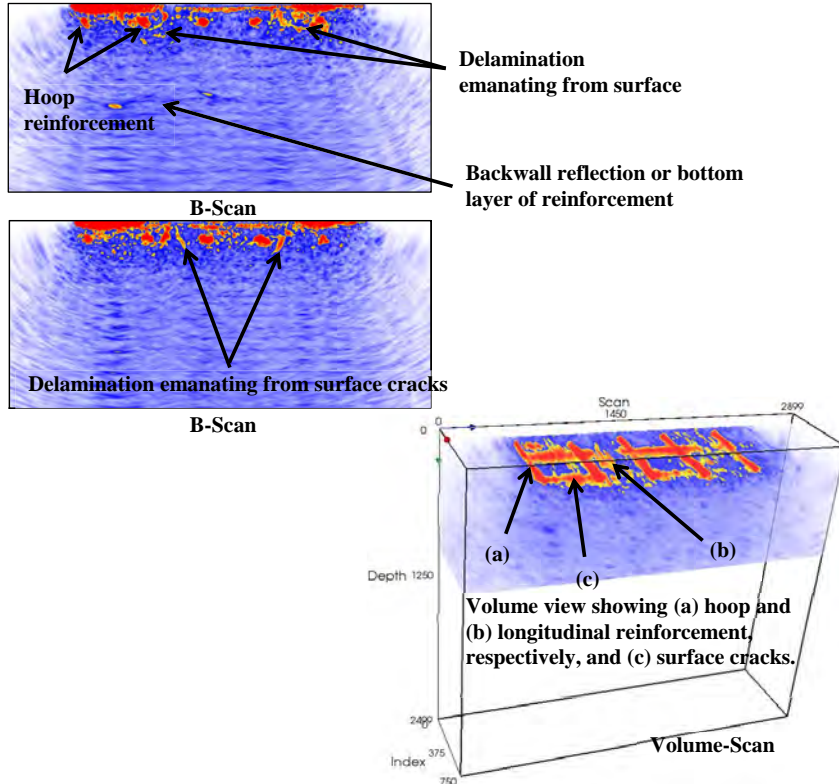


Figure N.8. UST images of test site HLT 10.5-1, 2, 3.



Hanging Lake Tunnel, Glenwood Springs, CO			
Defects	Notes	Reinf. Detail	
Suspected debonding around east (right) side of joint. Surface crack around area might support this. Suspected debonding extends a maximum of 9" deep.	Backsurface not detected. Area tested because of natural joint. This map should be extended east to detail more of possible debonding.	Hoop reinf: ~3.6" deep on center.	V _{shear} = 2159 m/s X-step: 150 mm Y-step: 50 mm Max Depth: 1000 mm Frequency: 50 kHz
			Glenwood Springs, CO Hanging Lake Tunnel HLT 10.5-4 Segments 54/55 Joint TAMU/TTI 10/2011



Figure N.9. Images of test site HLT 10.5-4.

Hanging Lake Tunnel, Glenwood Springs, CO			
Defects	Notes	Reinf. Detail	
Suspected debonding around east (right) side of joint. Surface crack around area might support this. Suspected debonding extends a maximum of 9" deep.	Backsurface not detected. Area tested because of natural joint. This map should be extended east to detail more of possible debonding.	Hoop reinf: ~3.6" deep on center.	Vshear = 2159 m/s X-step: 150 mm Y-step: 50 mm Max Depth: 1000 mm Frequency: 50 kHz <hr/> Glenwood Springs, CO Hanging Lake Tunnel HLT 10.5-4 Segments 54/55 Joint TAMU/TTI 10/2011

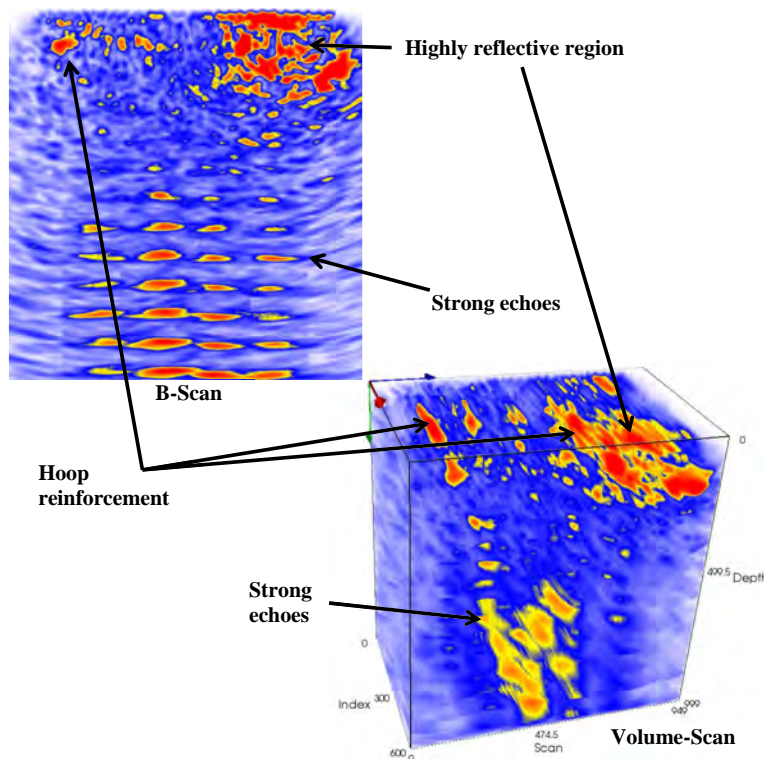



Figure N.10. UST images of test site HLT 10.5-4.

Hanging Lake Tunnel, Glenwood Springs, CO			
Defects	Notes	Reinf. Detail	
No significant defect noticeable. Backwall reflection varies 2-3" in depth. This may be lower reinforcement reflection or backwall delamination (see HLT 10.5-8,9).	Backsurface possibly 29.6" 32.4" deep. Area tested as a representation of sound concrete-no apparent cracks or defects.	Hoop reinf: ~4.3"-5.1" deep @ 16.6" on center. Longitudinal reinf: above hoop reinforcement.	Vshear = 2159 m/s X-step: 150 mm Y-step: 50 mm Max Depth: 2500 mm Frequency: 50 kHz Glenwood Springs, CO Hanging Lake Tunnel HLT 10.5-5, 6, 7 Segments 49 TAMU/TTI 10/2011

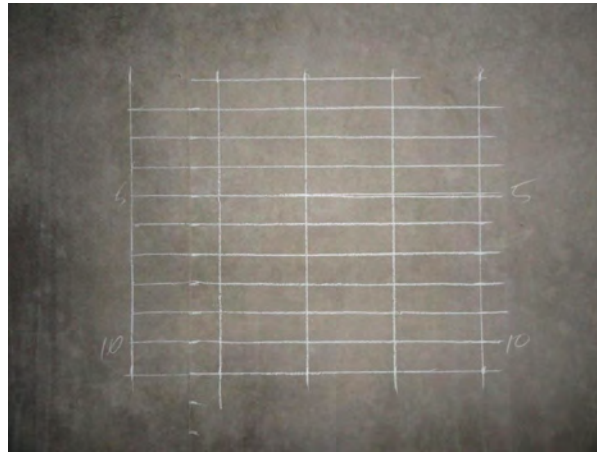



Figure N.11. Image of test site HLT 10.5-5, 6, 7.

Hanging Lake Tunnel, Glenwood Springs, CO			
Defects	Notes	Reinf. Detail	
No significant defect noticeable. Backwall reflection varies 2-3" in depth. This may be lower reinforcement reflection or backwall delamination (see HLT 10.5-8,9).	Backsurface possibly 29.6" 32.4" deep. Area tested as a representation of sound concrete-no apparent cracks or defects.	Hoop reinf: ~4.3"-5.1" deep @ 16.6" on center. Longitudinal reinf: above hoop reinforcement.	Vshear = 2159 m/s X-step: 150 mm Y-step: 50 mm Max Depth: 2500 mm Frequency: 50 kHz Glenwood Springs, CO Hanging Lake Tunnel HLT 10.5-5, 6, 7 Segments 49 TAMU/TTI 10/2011

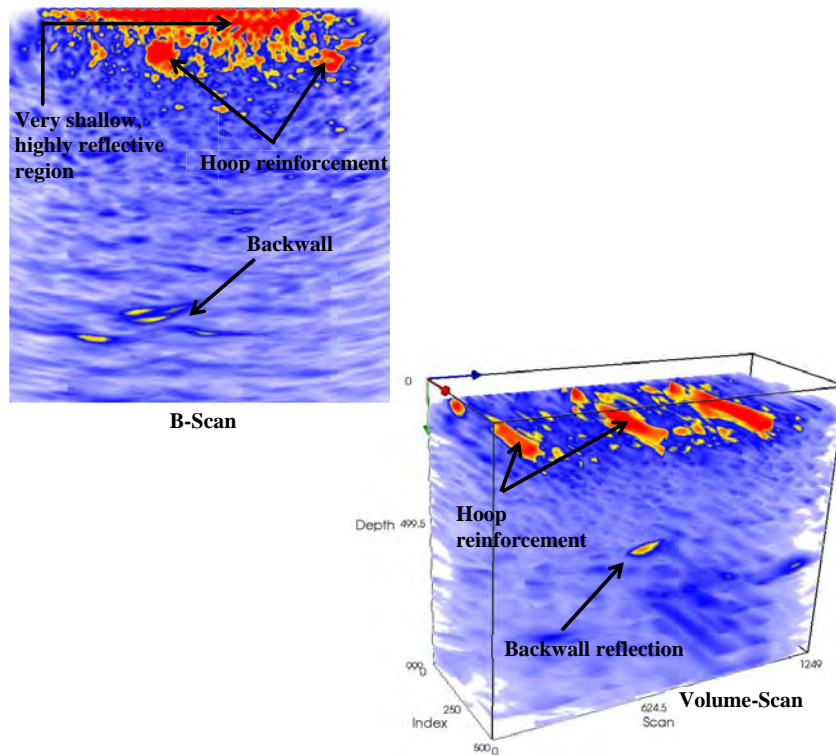


Figure N.12. UST images of test site HLT 10.5-5, 6, 7.



Hanging Lake Tunnel, Glenwood Springs, CO			
Defects	Notes	Reinf. Detail	
No significant defect noticeable. Backwall reflection varies 2-3" in depth. This may be lower reinforcement reflection or backwall delamination (see HLT 10.5-8,9).	Backsurface possibly 24.5" - 29.6" deep. Area tested because of single surface crack. Note strong echoes emanating from region of reinforcement. This is possible sign of debonding.	Hoop reinf: ~3.7" deep @ 15.9" on center. Longitudinal reinf: below hoop reinforcement. .	Vshear = 2159 m/s X-step: 150 mm Y-step: 50 mm Max Depth: 2500 mm Frequency: 50 kHz
			Glenwood Springs, CO Hanging Lake Tunnel HLT 10.5-8, 9 Segments 49 TAMU/TTI 10/2011



Figure N.13. Image of test site HLT 10.5-8, 9.

Hanging Lake Tunnel, Glenwood Springs, CO			
Defects	Notes	Reinf. Detail	
No significant defect noticeable. Backwall reflection varies 2-3" in depth. This may be lower reinforcement reflection or backwall delamination (see HLT 10.5-8,9).	Backsurface possibly 24.5" - 29.6" deep. Area tested because of single surface crack. Note strong echoes emanating from region of reinforcement. This is possible sign of debonding.	Hoop reinf: ~3.7" deep @ 15.9" on center. Longitudinal reinf: below hoop reinforcement. .	Vshear = 2159 m/s X-step: 150 mm Y-step: 50 mm Max Depth: 2500 mm Frequency: 50 kHz Glenwood Springs, CO Hanging Lake Tunnel HLT 10.5-8, 9 Segments 49 TAMU/TTI 10/2011

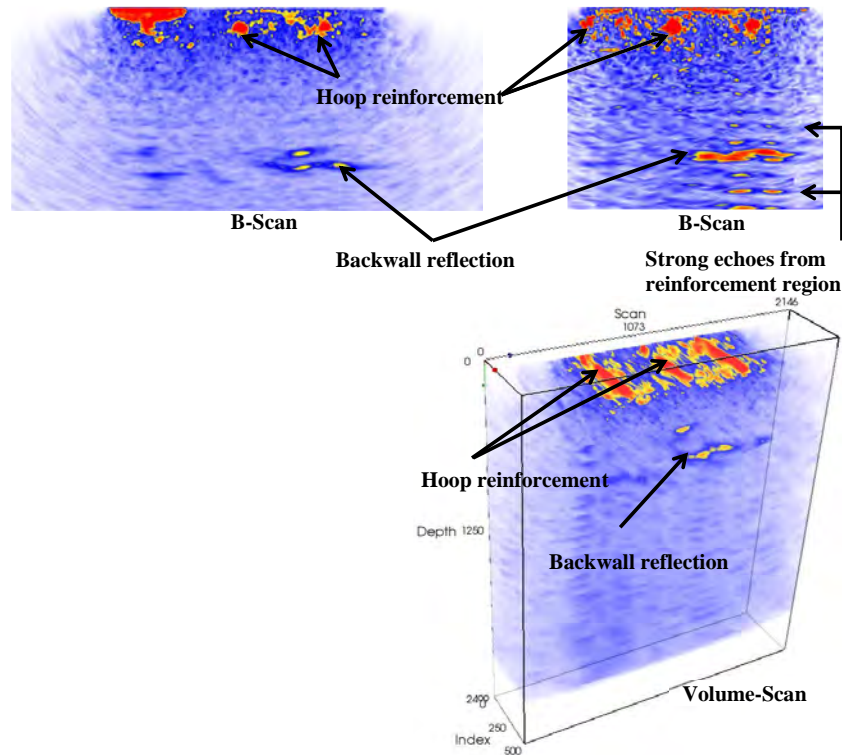


Figure N.14. UST images of test site HLT 10.5-8, 9.



Hanging Lake Tunnel, Glenwood Springs, CO			
Defects	Notes	Reinf. Detail	
Significant delamination/debonding discovered which stretched over 11', ranging from 8"-20" below the surface.	Backsurface not discernible due to high presence of delamination/debonding. Area tested because of severe surface cracking.	Hoop reinf: ~2.9"-5.1" deep @ ~16.4" on center. Longitudinal reinf: above hoop reinforcement.	V _{shear} = 2159 m/s X-step: 150 mm Y-step: 50 mm Max Depth: 1000 mm Frequency: 50 kHz
			Glenwood Springs, CO Hanging Lake Tunnel HLT 10.5-10, 11, 12 Segment 55 TAMU/TTI 10/2011



Figure N.15. Images of test site HLT 10.5-10, 11, 12.

Hanging Lake Tunnel, Glenwood Springs, CO			
Defects	Notes	Reinf. Detail	
Significant delamination/debonding discovered which stretched over 11', ranging from 8"-20" below the surface.	Backsurface not discernible due to high presence of delamination/debonding. The B-scan below shows variance in depth and the C-scans show the horizontal spread of the delamination/debonding.	Hoop reinf: ~2.9"-5.1" deep @ ~16.4" on center. Longitudinal reinf: above hoop reinforcement.	Vshear = 2159 m/s X-step: 150 mm Y-step: 50 mm Max Depth: 1000 mm Frequency: 50 kHz Glenwood Springs, CO Hanging Lake Tunnel HLT 10.5-10, 11, 12 Segment 55 TAMU/TTI 10/2011

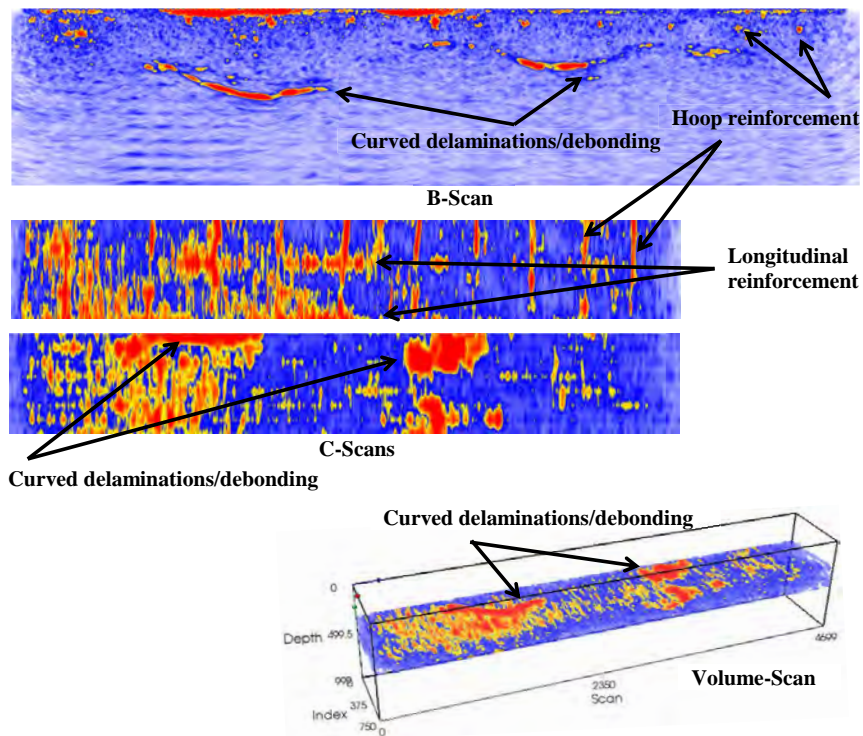


Figure N.16. UST images of test site HLT 10.5-10, 11, 12.



Hanging Lake Tunnel, Glenwood Springs, CO			
Defects	Notes	Reinf. Detail	
No significant defect noticed.	Backsurface not discernible. Area tested on surface of tile. Hair-line crack present.	Hoop reinf: ~5.1" deep @ ~16.3" on center. Longitudinal reinf: below and possible above hoop reinforcement @ ~14.0" on center.	Vshear = 2159 m/s X-step: 150 mm Y-step: 50 mm Max Depth: 1000 mm Frequency: 50 kHz
			Glenwood Springs, CO Hanging Lake Tunnel HLT 10.5-13 Interior Tile Lining TAMU/TII 10/2011



Figure N.17. Image of test site HLT 10.5-13.

Hanging Lake Tunnel, Glenwood Springs, CO			
Defects	Notes	Reinf. Detail	
No significant defect noticed.	Backsurface not discernible. Area tested on surface of tile. Hair-line crack present.	Hoop reinf: ~5.1" deep @ ~16.3" on center. Longitudinal reinf: below and possible above hoop reinforcement @ ~14.0" on center.	Vshear = 2159 m/s X-step: 150 mm Y-step: 50 mm Max Depth: 1000 mm Frequency: 50 kHz Glenwood Springs, CO Hanging Lake Tunnel HLT 10.5-13 Interior Tile Lining TAMU/TTI 10/2011

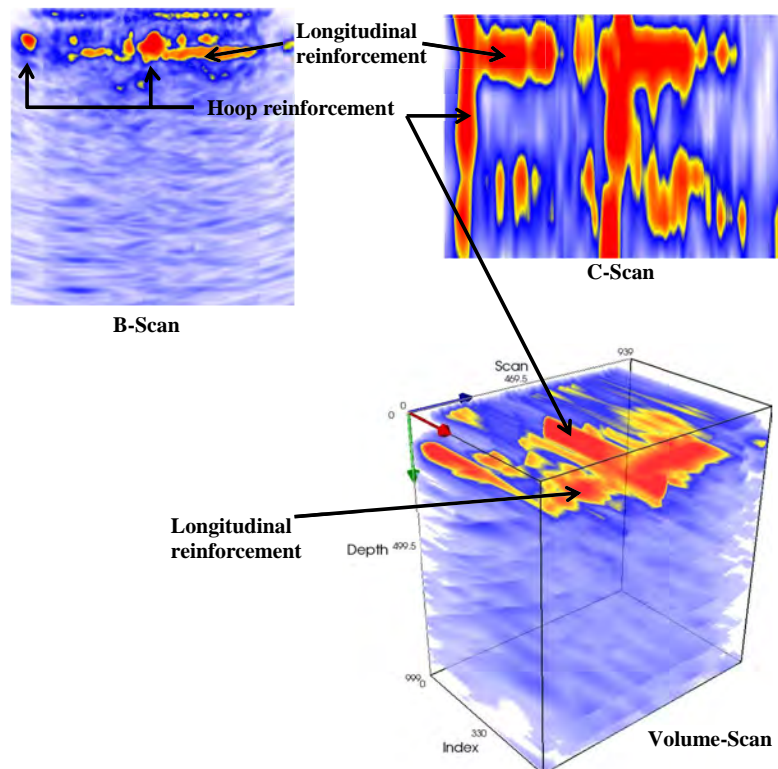



Figure N.18. UST images of test site HLT 10.5-13.

Chesapeake Channel Tunnel, Norfolk, VA			
Defects	Notes	Reinf. Detail	
No significant defect noticed.	Backsurface at ~24.7" deep. Area tested as representative of sound concrete. Also tested because GPR data revealed different steel detail (c.f. with CBBT 10.11-3,4).	Hoop reinf: ~2.4" deep @ ~4.4" on center. Longitudinal reinf: below hoop reinforcement.	Vshear = 2710 m/s X-step: 150 mm Y-step: 50 mm Max Depth: 1000 mm Frequency: 50 kHz <hr/> Norfolk, VA Chesapeake Tunnel CBBT 10.11-1, 2 Sta. 471+80 TAMU/TTI 10/2011

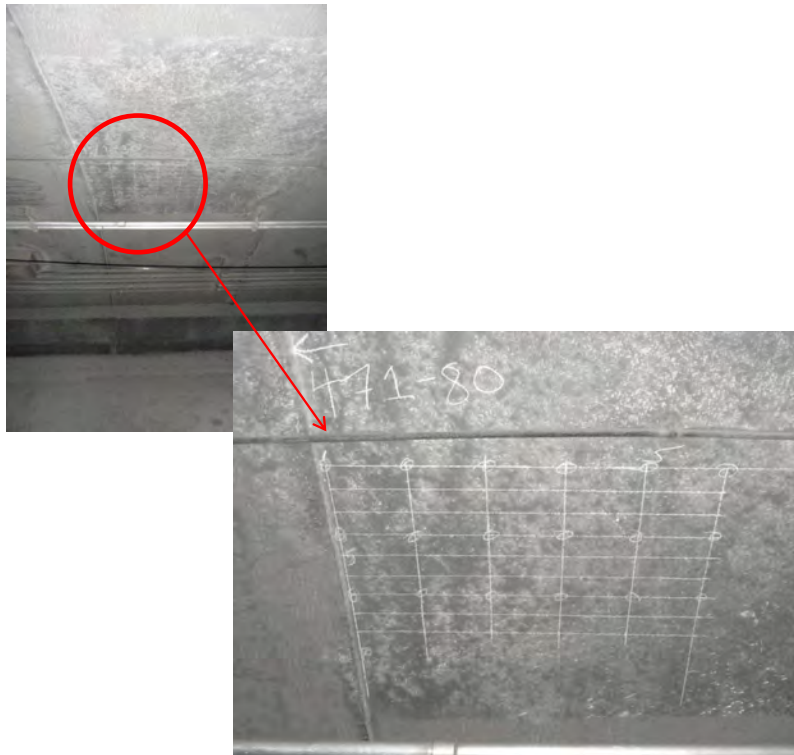



Figure N.19. Images of test site CBBT 10.11-1, 2.

Chesapeake Channel Tunnel, Norfolk, VA			
Defects	Notes	Reinf. Detail	
No significant defect noticed.	Backsurface at ~24.7" deep. Area tested as representative of sound concrete. Also tested because GPR data revealed different steel detail (c.f. with CBBT 10.11-3,4).	Hoop reinf: ~2.4" deep @ ~4.4" on center. Longitudinal reinf: below hoop reinforcement.	Vshear = 2710 m/s X-step: 150 mm Y-step: 50 mm Max Depth: 1000 mm Frequency: 50 kHz Norfolk, VA Chesapeake Tunnel CBBT 10.11-1, 2 Sta. 471+80 TAMU/TTI 10/2011

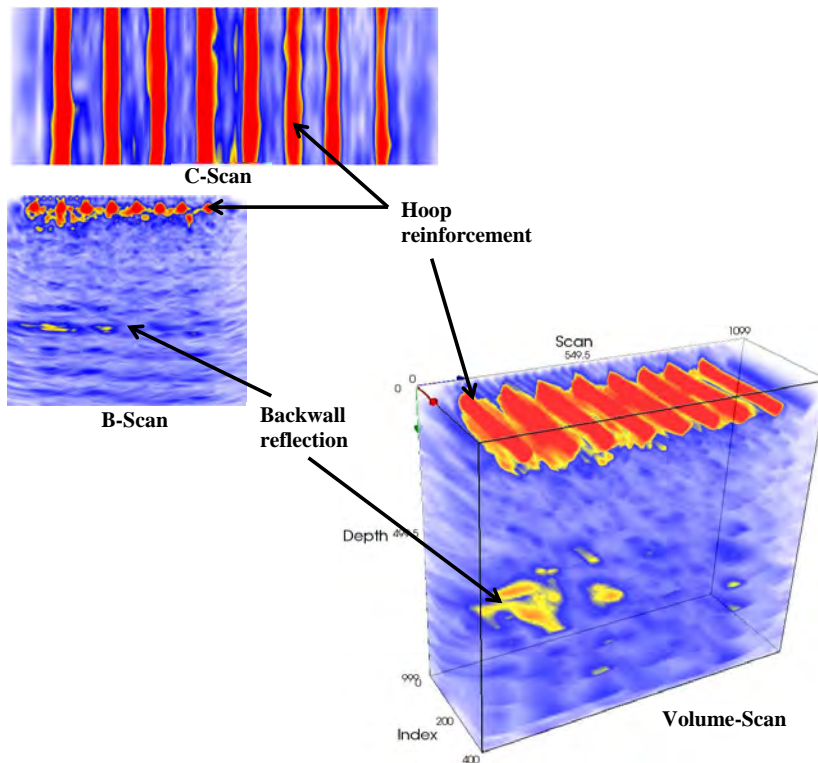



Figure N.20. UST images of test site CBBT 10.11-1, 2.

Chesapeake Channel Tunnel, Norfolk, VA			
Defects	Notes	Reinf. Detail	
No significant defect noticed.	Backsurface at ~24.4" deep. Area tested as representative of sound concrete. Also tested because GPR data revealed different steel detail (c.f. with CBBT 10.11-1,2).	Hoop reinf: ~2.3" deep @ ~11.8" on center. Longitudinal reinf: below hoop reinforcement.	Vshear = 2710 m/s X-step: 150 mm Y-step: 50 mm Max Depth: 1000 mm Frequency: 50 kHz <hr/> Norfolk, VA Chesapeake Tunnel CBBT 10.11-3, 4 Sta. 473+56 TAMU/TTI 10/2011

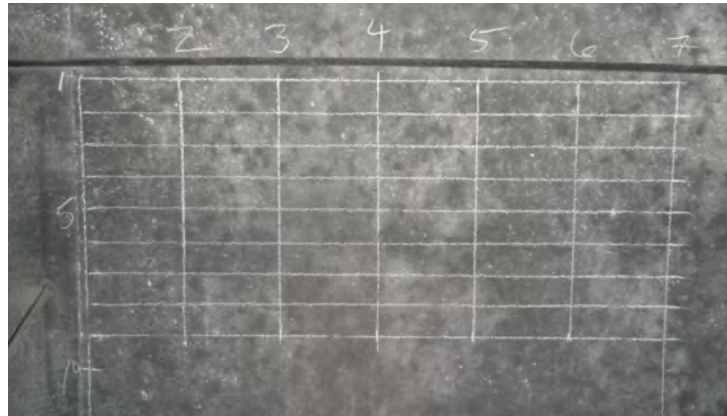



Figure N.21. Image of test site CBBT 10.11-3, 4.

Chesapeake Channel Tunnel, Norfolk, VA			
Defects	Notes	Reinf. Detail	V _{shear} = 2710 m/s X-step: 150 mm Y-step: 50 mm Max Depth: 1000 mm Frequency: 50 kHz
No significant defect noticed.	Backsurface at ~24.4" deep. Area tested as representative of sound concrete. Also tested because GPR data revealed different steel detail (c.f. with CBBT 10.11-1,2).	Hoop reinf: ~2.3" deep @ ~11.8" on center. Longitudinal reinf: below hoop reinforcement.	Norfolk, VA Chesapeake Tunnel CBBT 10.11-3, 4 Sta. 473+56 TAMU/TTI 10/2011

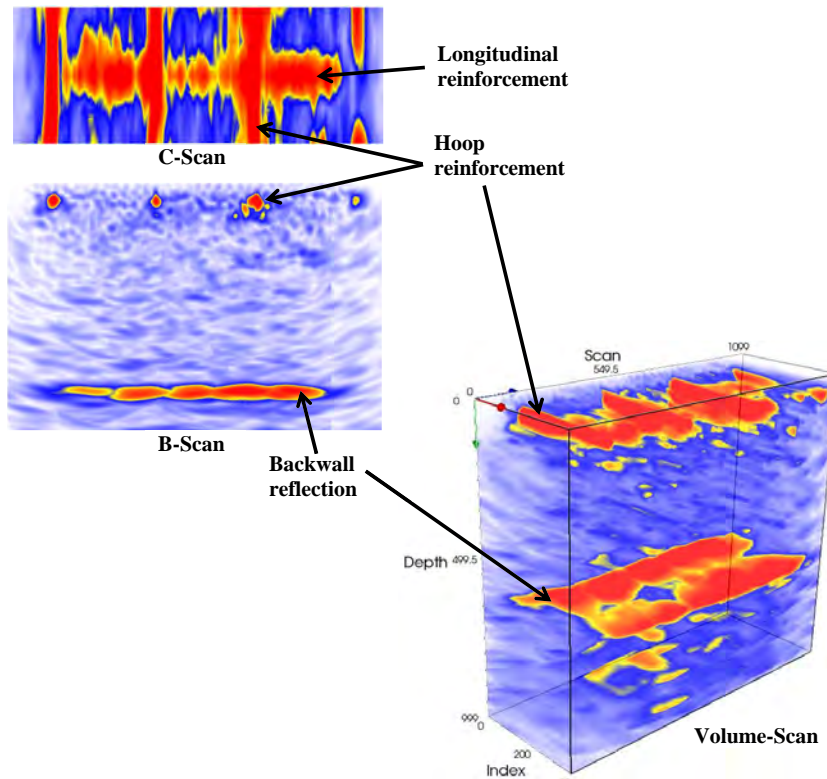



Figure N.22. UST images of test site CBBT 10.11-3, 4.

Chesapeake Channel Tunnel, Norfolk, VA			
Defects	Notes	Reinf. Detail	
Significant shallow defects, such as shallow cracks (~9" deep) and possibly shallow delaminations (~2" deep), which seem to produce the ringing.	Backsurface at ~24.1" deep. Area tested because of live crack. Significant ringing may suggest debonding of longitudinal reinforcement.	Hoop reinf: ~2.0"-2.6" deep @ ~12.0" on center. Longitudinal reinf: below hoop reinforcement.	Vshear = 2710 m/s X-step: 150 mm Y-step: 50 mm Max Depth: 1000 mm Frequency: 50 kHz Norfolk, VA Chesapeake Tunnel CBBT 10.11-5 Sta. 474+27 TAMU/TTI 10/2011

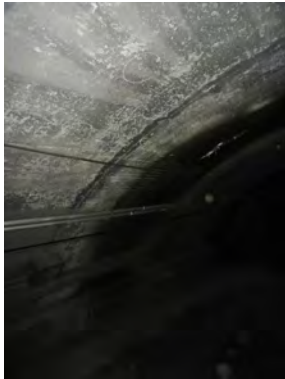



Figure N.23. Images of test site CBBT 10.11-5.

Chesapeake Channel Tunnel, Norfolk, VA			
Defects	Notes	Reinf. Detail	
Significant shallow defects, such as shallow cracks (~9" deep) and possibly shallow delaminations (~2" deep), which seem to produce the ringing.	Backsurface at ~24.1" deep. Area tested because of live crack. Significant ringing may suggest debonding of longitudinal reinforcement.	Hoop reinf: ~2.0"-2.6" deep @ ~12.0" on center. Longitudinal reinf: below hoop reinforcement.	Vshear = 2710 m/s X-step: 150 mm Y-step: 50 mm Max Depth: 1000 mm Frequency: 50 kHz
			Norfolk, VA Chesapeake Tunnel CBBT 10.11-5 Sta. 474+27 TAMU/TTI 10/2011

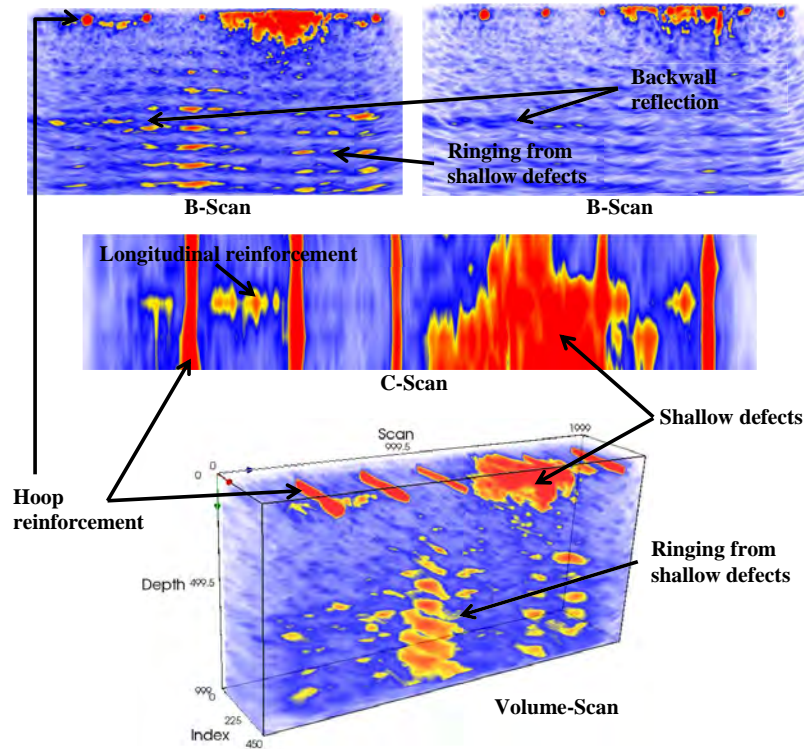



Figure N.24. UST images of test site CBBT 10.11-5.

Chesapeake Channel Tunnel, Norfolk, VA			
Defects	Notes	Reinf. Detail	
Hammer tapping revealed hollow region as shown by shallow reflective region in the C- and B-scans. Significant cupped-shaped delaminations as deep as 19.2"	Backsurface at 24.1"-26.0" deep. Area tested because of high dielectric reading from GPR scan. No significant visual distress noticeable, but hammer sounding revealed shallow delamination in Region II.	Hoop reinf: ~2.2" deep @ ~12.1" on center. Longitudinal reinf: below hoop reinforcement @ 16.2" on center.	V _{shear} = 2710 m/s X-step: 150 mm Y-step: 50 mm Max Depth: 1000 mm Frequency: 50 kHz Norfolk, VA Chesapeake Tunnel CBBT 10.11-7, 8 (Region II) Sta. 486+67 TAMU/TTI 10/2011

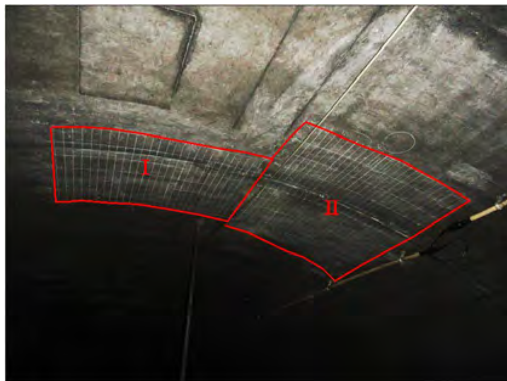



Figure N.25. Images of test site CBBT 10.11-7, 8.

Chesapeake Channel Tunnel, Norfolk, VA			
Defects	Notes	Reinf. Detail	Vshear = 2710 m/s X-step: 150 mm Y-step: 50 mm Max Depth: 1000 mm Frequency: 50 kHz Norfolk, VA Chesapeake Tunnel CBBT 10.11-7, 8 (Region II) Sta. 486+67 TAMU/TTI 10/2011
Hammer tapping revealed hollow region as shown by shallow reflective region in the C- and B-scans. Significant cupped-shaped delaminations as deep as 19.2"	Backsurface at 24.1"-26.0" deep. Area tested because of high dielectric reading from GPR scan. No significant visual distress noticeable, but hammer sounding revealed shallow delamination in Region II.	Hoop reinf: ~2.2" deep @ ~12.1" on center. Longitudinal reinf: below hoop reinforcement @ 16.2" on center.	

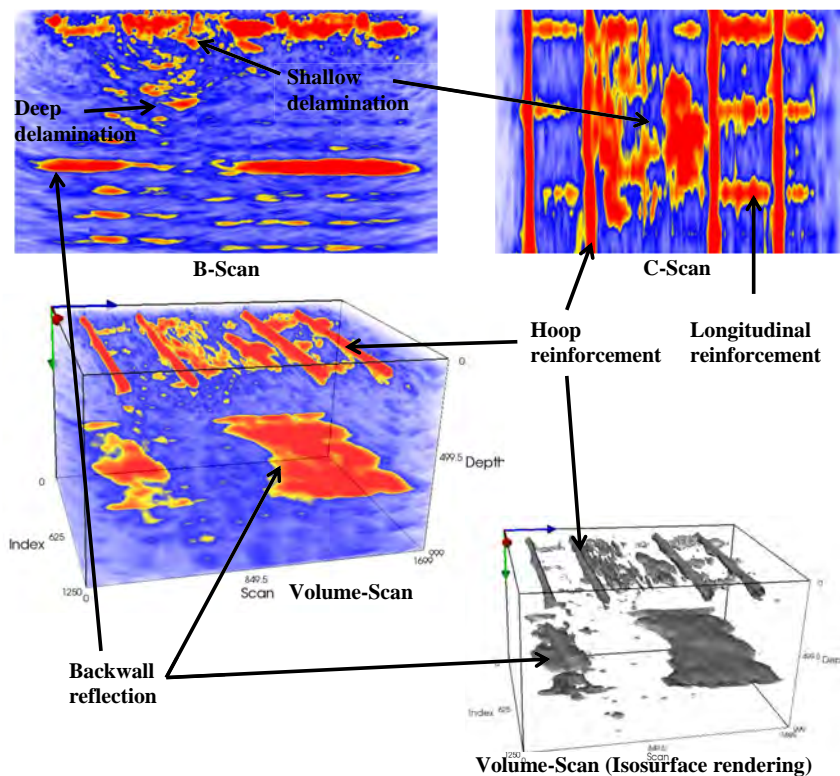



Figure N.26. UST images of test site CBBT 10.11-7, 8.

Chesapeake Channel Tunnel, Norfolk, VA			
Defects	Notes	Reinf. Detail	
Significant cracks up to 8.6" deep.	Backsurface at 24.3"-26.0" deep. Area tested because of high dielectric reading from GPR scan. No significant visual distress noticeable.	Hoop reinf: ~2.0"-3.0" deep @ ~12.2" on center. Longitudinal reinf: below hoop reinforcement @ 19.8" on center.	Vshear = 2710 m/s X-step: 150 mm Y-step: 50 mm Max Depth: 1000 mm Frequency: 50 kHz Norfolk, VA Chesapeake Tunnel CBBT 10.11-9 (Region I) Sta. 486+67 TAMU/TTI 10/2011

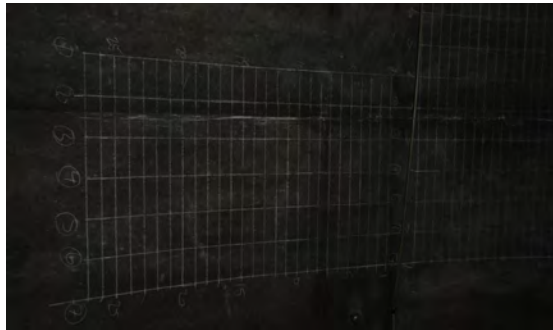
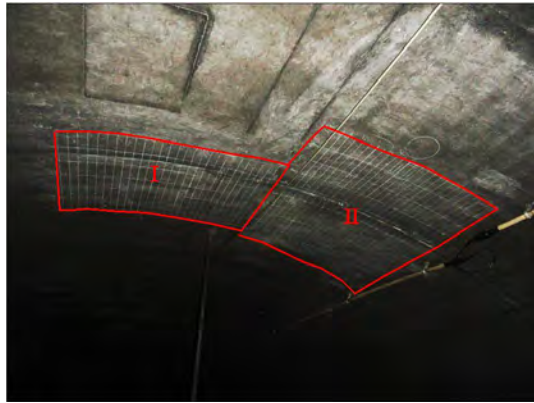



Figure N.27. Images of test site CBBT 10.11-9.

Chesapeake Channel Tunnel, Norfolk, VA			
Defects	Notes	Reinf. Detail	
Significant cracks up to 8.6" deep.	Backsurface at 24.3"-26.0" deep. Area tested because of high dielectric reading from GPR scan. No significant visual distress noticeable.	Hoop reinf: ~2.0"-3.0" deep @ ~12.2" on center. Longitudinal reinf: below hoop reinforcement @ 19.8" on center.	V _{shear} = 2710 m/s X-step: 150 mm Y-step: 50 mm Max Depth: 1000 mm Frequency: 50 kHz Norfolk, VA Chesapeake Tunnel CBBT 10.11-9 (Region I) Sta. 486+67 TAMU/TTI 10/2011

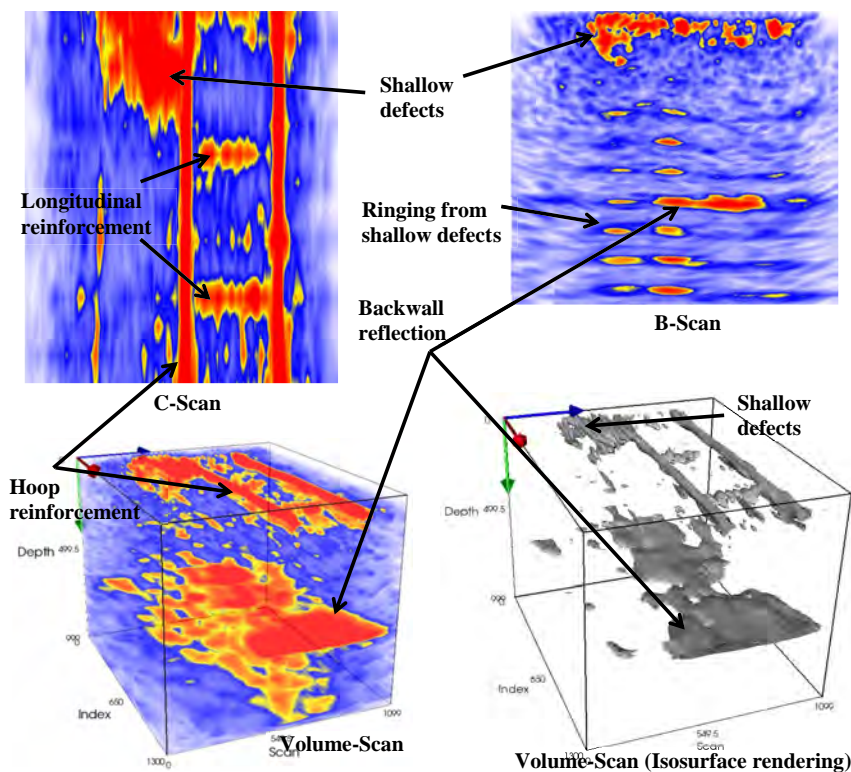


Figure N.28. UST images of test site CBBT 10.11-9.



Chesapeake Channel Tunnel, Norfolk, VA			
Defects	Notes	Reinf. Detail	
Heavy ringing made internal inspection difficult. Possible deep delamination (~17.7" deep and possibly 19" wide) and evidence of surface crack extending ~9.8" deep.	Backsurface at 22.7"-25.9" deep. Area tested because of large surface crack and small area of water intrusion.	Hoop reinf: ~2.7"-3.2" deep @ ~11.7"-12.4" on center. Second layer of hoop reinf. directly beneath top layer. Longitudinal reinf: below first layer of hoop reinforcement @ ~17.1" on center.	Vshear = 2710 m/s X-step: 150 mm Y-step: 50 mm Max Depth: 1000 mm Frequency: 50 kHz
			Norfolk, VA Chesapeake Tunnel CBBT 10.11-10 Sta. 491+25 TAMU/TTI 10/2011



Figure N.29. Images of test site CBBT 10.11-10.

Chesapeake Channel Tunnel, Norfolk, VA			
Defects	Notes	Reinf. Detail	Vshear = 2710 m/s
Heavy ringing made internal inspection difficult. Possible deep delamination (~17.7" deep and possibly 19" wide) and evidence of surface crack extending ~9.8" deep.	Backsurface at 22.7"-25.9" deep. Area tested because of large surface crack and small area of water intrusion.	Hoop reinf: ~2.7"-3.2" deep @ ~11.7"-12.4" on center. Second layer of hoop reinf. directly beneath top layer. Longitudinal reinf: below first layer of hoop reinforcement @ ~17.1" on center.	X-step: 150 mm Y-step: 50 mm Max Depth: 1000 mm Frequency: 50 kHz
			Norfolk, VA Chesapeake Tunnel CBBT 10.11-10 Sta. 491+25 TAMU/TTI 10/2011

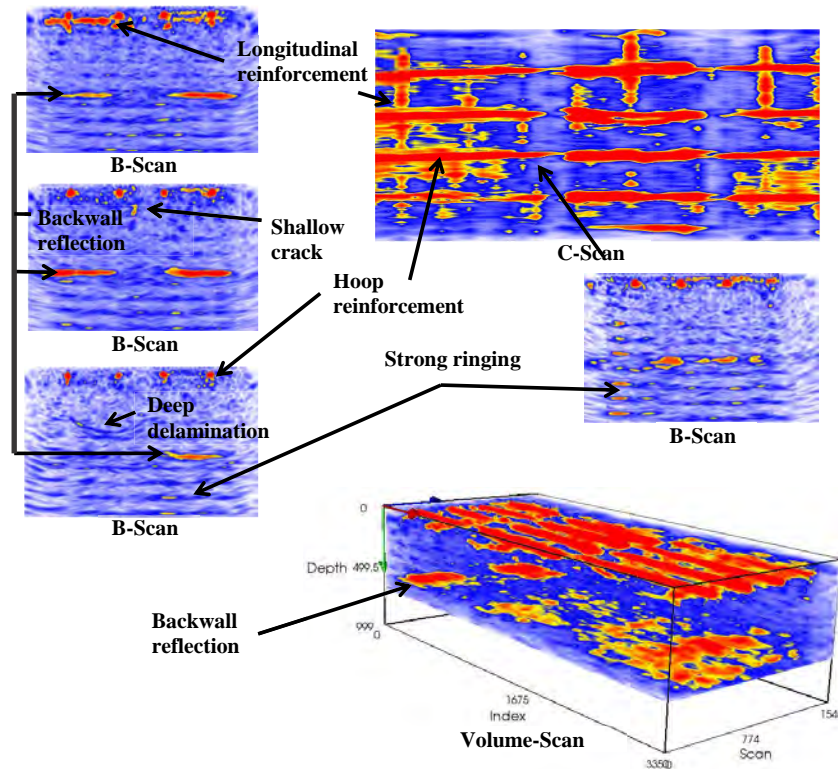


Figure N.30. UST images of test site CBBT 10.11-10.



Chesapeake Channel Tunnel, Norfolk, VA			
Defects	Notes	Reinf. Detail	
Heavy ringing made internal inspection difficult. Possible deep delamination (~15.7" deep and 20.3" wide).	Backsurface at 25.0"-30.0" deep. Area tested was tiled lining over a joint where tile has debonded. Determined area via hammer sounding.	Hoop reinf: ~4.3"-7.7" deep @ ~12.1" on center. Second layer of hoop reinf. seen beneath top layer in one location-possibly splice area. Longitudinal reinf: below hoop reinforcement @ ~13.0" on center.	Vshear = 2710 m/s X-step: 110 mm Y-step: 110 mm Max Depth: 750 mm Frequency: 50 kHz Norfolk, VA Chesapeake Tunnel CBBT TILE 10.11-11 Approx. Sta. 488 TAMU/TTI 10/2011



Figure N.31. Image of test site CBBT TILE 10.11-11.

Chesapeake Channel Tunnel, Norfolk, VA			
Defects	Notes	Reinf. Detail	Vshear = 2710 m/s X-step: 110 mm Y-step: 110 mm Max Depth: 750 mm Frequency: 50 kHz Norfolk, VA Chesapeake Tunnel CBBT TILE 10.11-11 Approx. Sta. 488 TAMU/TTI 10/2011
Heavy ringing made internal inspection difficult. Possible deep delamination (~15.7" deep and 20.3" wide).	Backsurface at 25.0"-30.0" deep. Area tested was tiled lining over a joint where tile has debonded. Determined area via hammer sounding.	Hoop reinf: ~4.3"-7.7" deep @ ~12.1" on center. Second layer of hoop reinf. seen beneath top layer in one location-possibly splice area. Longitudinal reinf. below hoop reinforcement @ ~13.0" on center.	

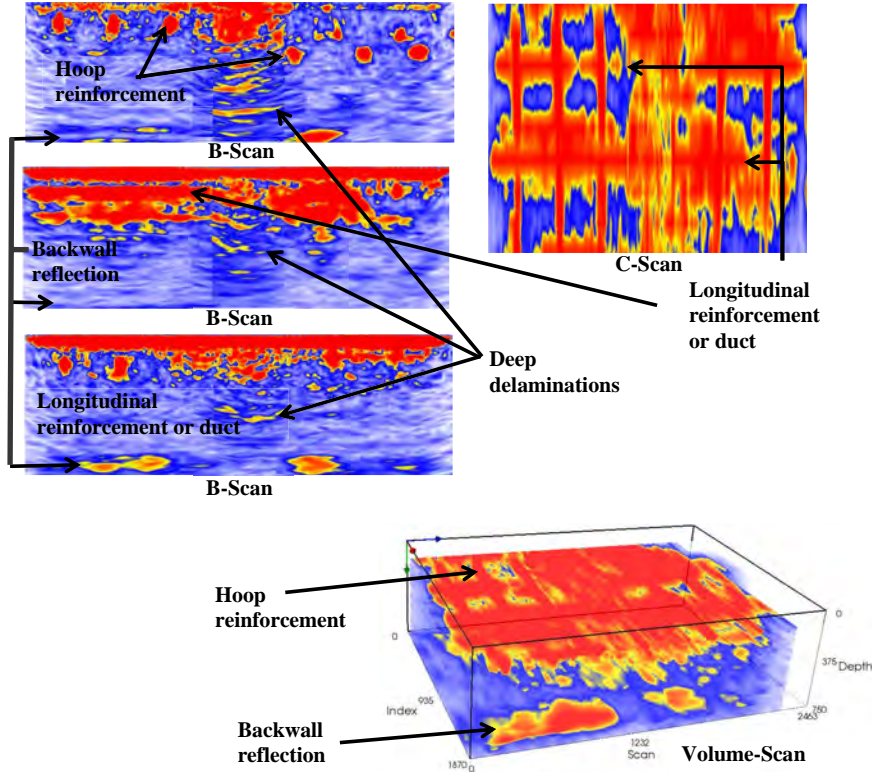


Figure N.32. UST images of test site CBBT TILE 10.11-11.



Chesapeake Channel Tunnel, Norfolk, VA			
Defects	Notes	Reinf. Detail	
Heavy ringing made internal inspection difficult. Possibly multiple cracks as deep as 8.6".	Backsurface at 28.1"-31.0" deep. Area tested was tiled lining. Hammer sounding did not indicate debonding, but SPACETEC infrared scans showed area of question..	Hoop reinf: ~4.8"-9.4" deep @ ~11.7" on center. Longitudinal reinf: below and possibly above hoop reinforcement.	Vshear = 2710 m/s X-step: 110 mm Y-step: 110 mm Max Depth: 1000 mm Frequency: 50 kHz Norfolk, VA Chesapeake Tunnel CBBT TILE 10.11-12 Sta. 486-09 TAMU/TTI 10/2011



Figure N.33. Image of test site CBBT TILE 10.11-12.

Chesapeake Channel Tunnel, Norfolk, VA			
Defects	Notes	Reinf. Detail	
Heavy ringing made internal inspection difficult. Possibly multiple cracks as deep as 8.6".	Backsurface at 28.1"-31.0" deep. Area tested was tiled lining. Hammer sounding did not indicate debonding, but SPACETEC infrared scans showed area of question..	Hoop reinf: ~4.8"-9.4" deep @ ~11.7" on center. Longitudinal reinf: below and possibly above hoop reinforcement.	Vshear = 2710 m/s X-step: 110 mm Y-step: 110 mm Max Depth: 1000 mm Frequency: 50 kHz Norfolk, VA Chesapeake Tunnel CBBT TILE 10.11-12 Sta. 486-09 TAMU/TTI 10/2011

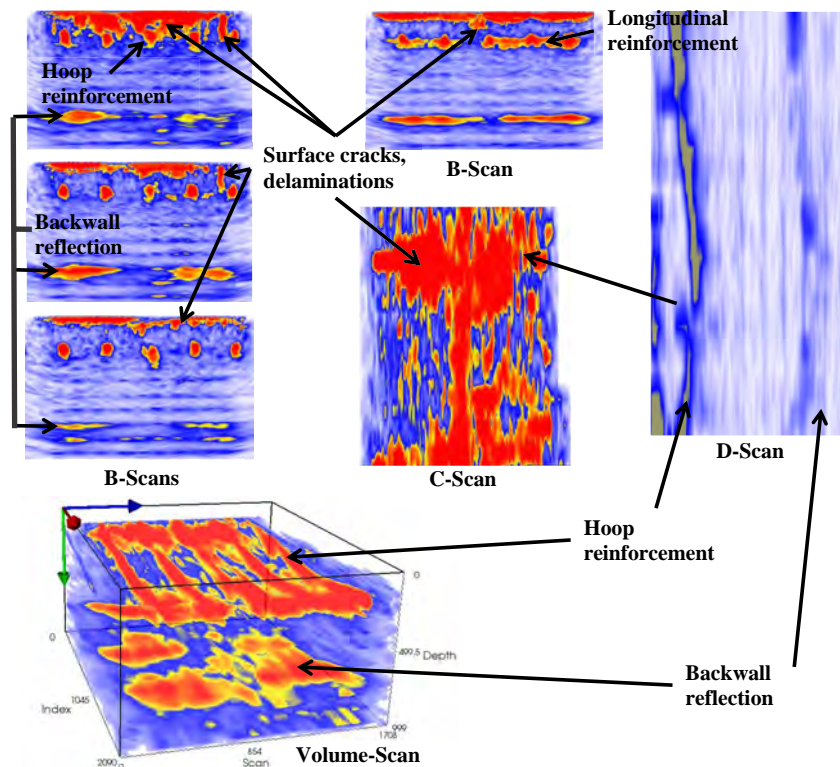



Figure N.34. UST images of test site CBBT TILE 10.11-12.

Chesapeake Channel Tunnel, Norfolk, VA			
Defects	Notes	Reinf. Detail	
Apparent delamination 20.2" deep and 27.4" wide.	Backsurface at 26.6"-28.4" deep. Area tested because of surface crack and varying backwall reflections from single-point evaluations.	Hoop reinf: ~2.0"-3.6" deep @ 12.1" on center. Longitudinal reinf: below hoop reinforcement.	Vshear = 2710 m/s X-step: 150 mm Y-step: 50 mm Max Depth: 1000 mm Frequency: 50 kHz Norfolk, VA Chesapeake Tunnel CBBT 10.13 Sta. 481+76 TAMU/TTI 10/2011

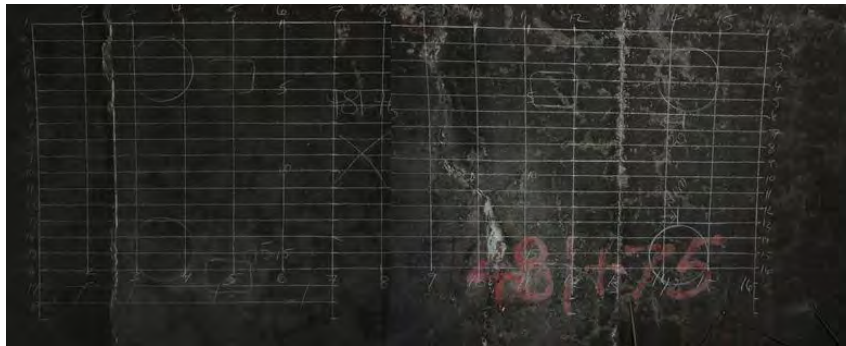



Figure N.35. Image of test site CBBT 10.11-13.

Chesapeake Channel Tunnel, Norfolk, VA			
Defects	Notes	Reinf. Detail	
Apparent delamination 20.2" deep and 27.4" wide.	Backsurface at 26.6"-28.4" deep. Area tested because of surface crack and varying backwall reflections from single-point evaluations.	Hoop reinf: ~2.0"-3.6" deep @ 12.1" on center. Longitudinal reinf: below hoop reinforcement.	Vshear = 2710 m/s X-step: 150 mm Y-step: 50 mm Max Depth: 1000 mm Frequency: 50 kHz Norfolk, VA Chesapeake Tunnel CBBT 10.13 Sta. 481+76 TAMU/TTI 10/2011

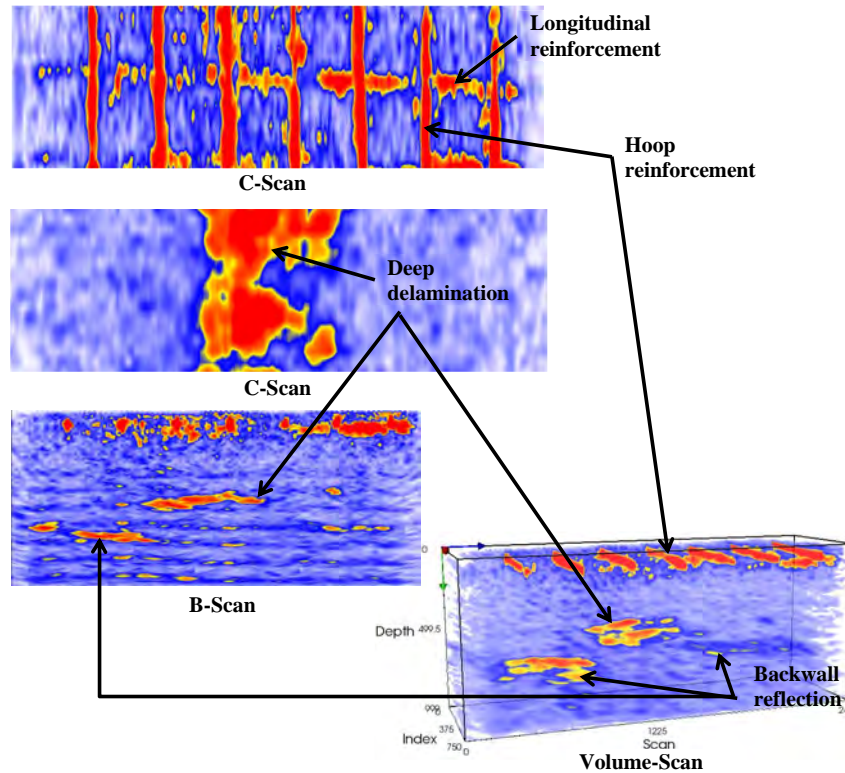



Figure N.36. UST images of test site CBBT 10.11-13.

Washburn Tunnel, Houston, TX			
Defects	Notes	Reinf. Detail	
Significant shallow debonding/delamination. Deep delamination approximately 13" deep (B-scan image).	Backsurface not discernible. Area tested because of debonding located via hammer sounding.	Hoop reinf: ~6.8" deep.	V _{shear} = 2710 m/s X-step: 110 mm Y-step: 110 mm Max Depth: 500 mm Frequency: 50 kHz Houston, TX Washburn Tunnel WT 9.16-1 West Side TAMU/TI 9/2011

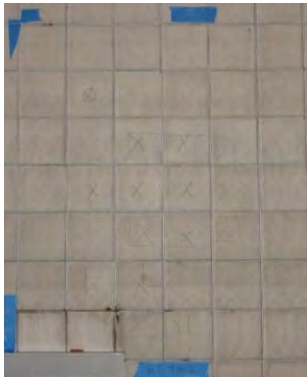



Figure N.37. Images of test site WT 9.16-1.

Washburn Tunnel, Houston, TX			
Defects	Notes	Reinf. Detail	
Significant shallow debonding/delamination. Deep delamination approximately 13" deep (B-scan image).	Backsurface not discernible. Area tested because of debonding located via hammer sounding.	Hoop reinf: ~6.8" deep.	Vshear = 2710 m/s X-step: 110 mm Y-step: 110 mm Max Depth: 500 mm Frequency: 50 kHz
			Houston, TX Washburn Tunnel WT 9.16-1 West Side TAMU/TTI 9/2011

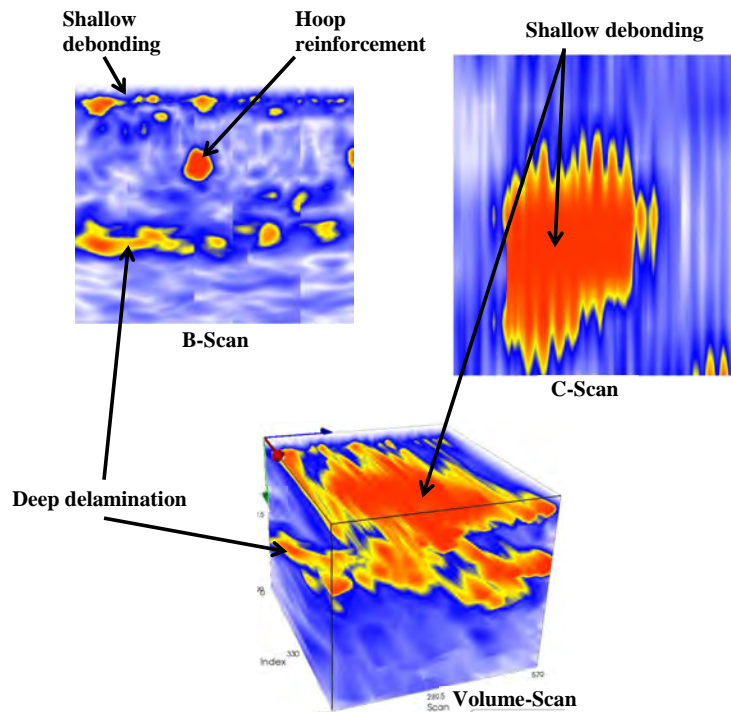


Figure N.38. UST images of test site WT 9.16-1.



Washburn Tunnel, Houston, TX			
Defects	Notes	Reinf. Detail	
Significant shallow and deep debonding/delamination. Delamination as deep as approximately 18" deep (B-scan image).	Backsurface not discernible. Area tested because of debonding located via hammer sounding.	Hoop reinf: ~4.8"-5.2" deep @ 12.2 on center. Longitudinal reinf: below hoop reinforcement.	Vshear = 2710 m/s X-step: 110 mm Y-step: 110 mm Max Depth: 500 mm Frequency: 50 kHz
			Houston, TX Washburn Tunnel WT 9.16-2 West Side TAMU/TTI 9/2011



Figure N.39. Image of test site WT 9.16-2.

Washburn Tunnel, Houston, TX			
Defects	Notes	Reinf. Detail	
Significant shallow and deep debonding/delamination. Delamination as deep as approximately 18" deep (B-scan image).	Backsurface not discernible. Area tested because of debonding located via hammer sounding.	Hoop reinf: ~4.8"-5.2" deep @ 12.2 on center. Longitudinal reinf: below hoop reinforcement.	V _{shear} = 2710 m/s X-step: 110 mm Y-step: 110 mm Max Depth: 500 mm Frequency: 50 kHz
			Houston, TX Washburn Tunnel WT 9.16-2 West Side TAMU/TTI 9/2011

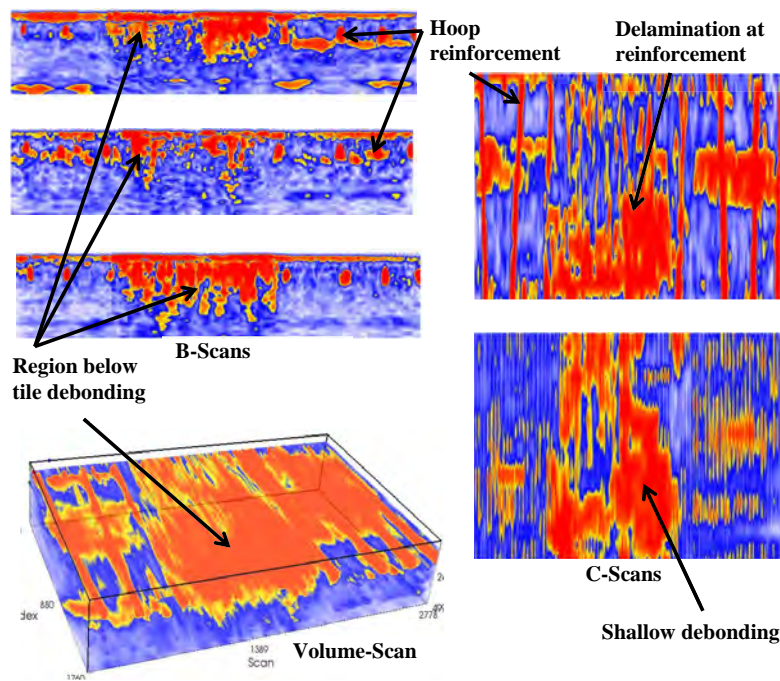


Figure N.40. UST images of test site WT 9.16-2.



Washburn Tunnel, Houston, TX			
Defects	Notes	Reinf. Detail	
Significant delaminations/debonding throughout. Delaminations as deep as 10.7" below surface.	Backsurface not discernible. Area tested because of debonding located via hammer sounding.	Hoop reinf: ~4.9" deep @ 13.4" on center. Longitudinal reinf: below hoop reinforcement.	V _{shear} = 2710 m/s X-step: 110 mm Y-step: 110 mm Max Depth: 500 mm Frequency: 50 kHz
			Houston, TX Washburn Tunnel WT 9.16-3 West Side TAMU/TI 9/2011



Figure N.41. Image of test site WT 9.16-3.

Washburn Tunnel, Houston, TX			
Defects	Notes	Reinf. Detail	
Significant delaminations/debonding throughout. Delaminations as deep as 10.7" below surface.	Backsurface not discernible. Area tested because of debonding located via hammer sounding.	Hoop reinf: ~4.9" deep @ 13.4" on center. Longitudinal reinf: below hoop reinforcement.	Vshear = 2710 m/s X-step: 110 mm Y-step: 110 mm Max Depth: 500 mm Frequency: 50 kHz Houston, TX Washburn Tunnel WT 9.16-3 West Side TAMU/TTI 9/2011

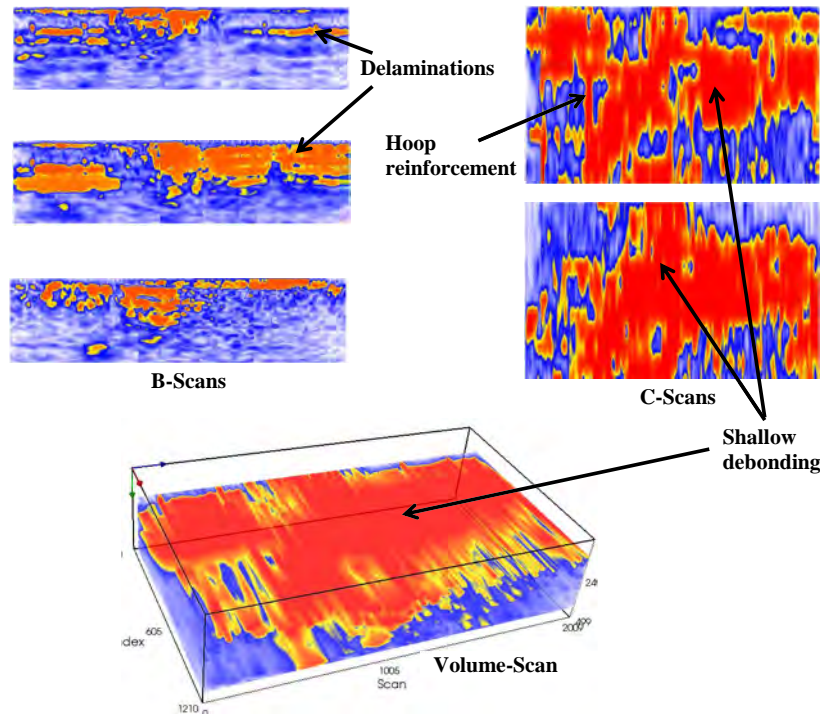


Figure N.42. UST images of test site WT 9.16-3.



Washburn Tunnel, Houston, TX			
Defects	Notes	Reinf. Detail	
Significant delaminations/debonding throughout. Possible delaminations 11.7" deep.	Backsurface not discernible. Area tested because of debonding located via hammer sounding.	Hoop reinf: ~4.7" deep @ 11.7" on center. Longitudinal reinf: below hoop reinforcement.	Vshear = 2710 m/s X-step: 110 mm Y-step: 110 mm Max Depth: 500 mm Frequency: 50 kHz
			Houston, TX Washburn Tunnel WT 9.16-4 West Side TAMU/TTI 9/2011



Figure N.43. Image of test site WT 9.16-4.

Washburn Tunnel, Houston, TX			
Defects	Notes	Reinf. Detail	Vshear = 2710 m/s
Significant delaminations/debonding throughout. Possible delaminations 11.7" deep.	Backsurface not discernible. Area tested because of debonding located via hammer sounding.	Hoop reinf: ~4.7" deep @ 11.7" on center. Longitudinal reinf: below hoop reinforcement.	X-step: 110 mm Y-step: 110 mm Max Depth: 500 mm Frequency: 50 kHz
			Houston, TX Washburn Tunnel WT 9.16-4 West Side TAMU/TTI 9/2011

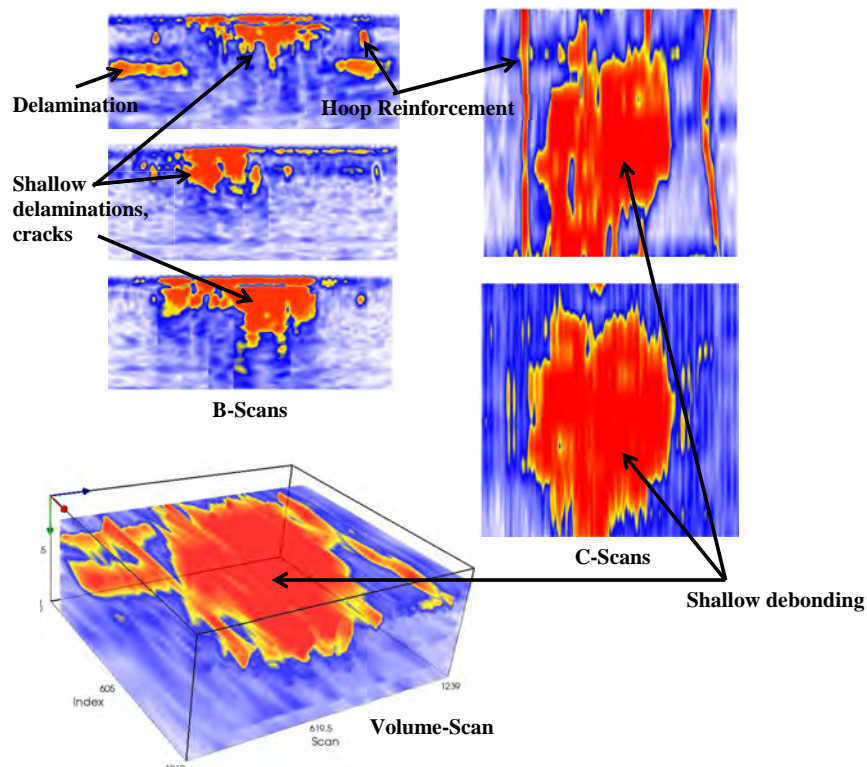


Figure N.44. UST images of test site WT 9.16-4.



Interstate 20, Ft. Worth, TX			
Defects	Notes	Reinf. Detail	
Significant delamination on both sides of surface crack, ranging from 4.2"-5.0" from top surface.	Top layer of pavement 10.2" below surface. Area tested because of transverse surface cracking. Pavement depth confirmed by 2 cores, both indicating 10.2" thickness and one indicating 5.0" reinf.	Longitudinal reinf.: ~4.6"- 5.0" deep @ 5.6" on center. No transverse reinforcement located in this area.	V _{shear} = 2770 m/s X-step: 150 mm Y-step: 50 mm Max Depth: 500 mm Frequency: 50 kHz Ft. Worth, TX I-20 IH20 9.27-1 MP 426 + 0.5, RM 2871 TAMU/TTI 9/2011



Figure N.45. Images of test site WT 9.27-1.

Interstate 20, Ft. Worth, TX			
Defects	Notes	Reinf. Detail	
Significant delamination on both sides of surface crack, ranging from 4.2"-5.0" from top surface.	Top layer of pavement 10.2" below surface. Area tested because of transverse surface cracking. Pavement depth confirmed by 2 cores, both indicating 10.2" thickness and one indicating 5.0" reinf.	Longitudinal reinf.: ~4.6"- 5.0" deep @ 5.6" on center. No transverse reinforcement located in this area.	V _{shear} = 2770 m/s X-step: 150 mm Y-step: 50 mm Max Depth: 500 mm Frequency: 50 kHz Ft. Worth, TX I-20 IH20 9.27-1 MP 426 + 0.5, RM 2871 TAMU/TTI 9/2011

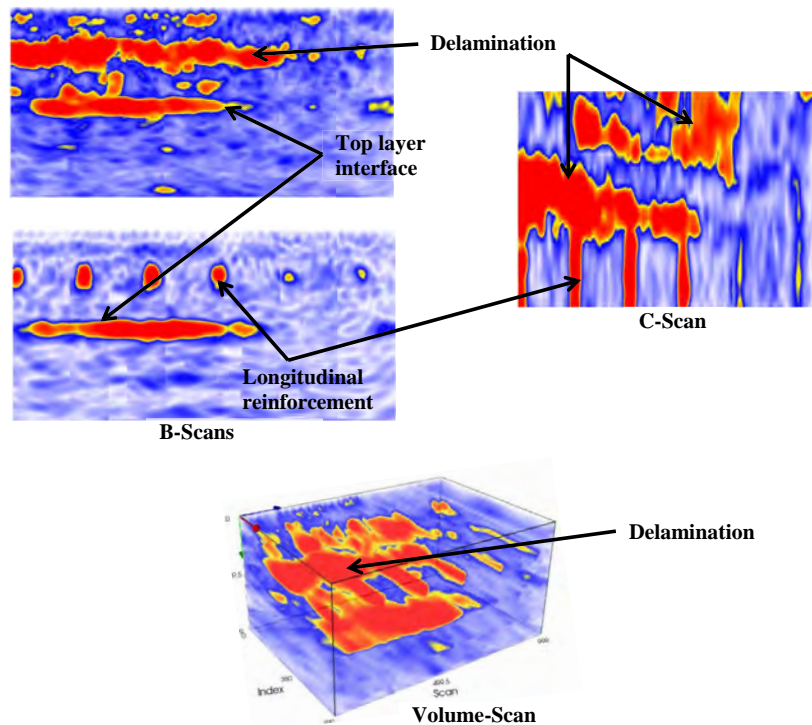


Figure N.46. UST images of test site IH20 9.27-1.



Interstate 20, Ft. Worth, TX			
Defects	Notes	Reinf. Detail	
Significant delamination on both sides of surface crack, ranging from 4.5"-5.3" from top surface.	Top layer of pavement 10.4" below surface. Area tested because of transverse surface cracking. Pavement depth confirmed by 2 cores, indicating 9.4"-10.4" thickness.	Longitudinal reinf.: ~4.5"- 5.2" deep @ 7.1" on center. No transverse reinforcement located in this area.	Vshear = 2770 m/s X-step: 150 mm Y-step: 50 mm Max Depth: 500 mm Frequency: 50 kHz Ft. Worth, TX I-20 IH20 9.27-2 MP 426 + 0.5, RM 2871 TAMU/TTI 9/2011



Figure N.47. Images of test site IH20 9.27-2.

Interstate 20, Ft. Worth, TX			
Defects	Notes	Reinf. Detail	
Significant delamination on both sides of surface crack, ranging from 4.5"-5.3" from top surface.	Top layer of pavement 10.4" below surface. Area tested because of transverse surface cracking. Pavement depth confirmed by 2 cores, indicating 9.4"-10.4" thickness.	Longitudinal reinf.: ~4.5"- 5.2" deep @ 7.1" on center. No transverse reinforcement located in this area.	V _{shear} = 2770 m/s X-step: 150 mm Y-step: 50 mm Max Depth: 500 mm Frequency: 50 kHz Ft. Worth, TX I-20 IH20 9.27-2 MP 426 + 0.5, RM 2871 TAMU/TTI 9/2011

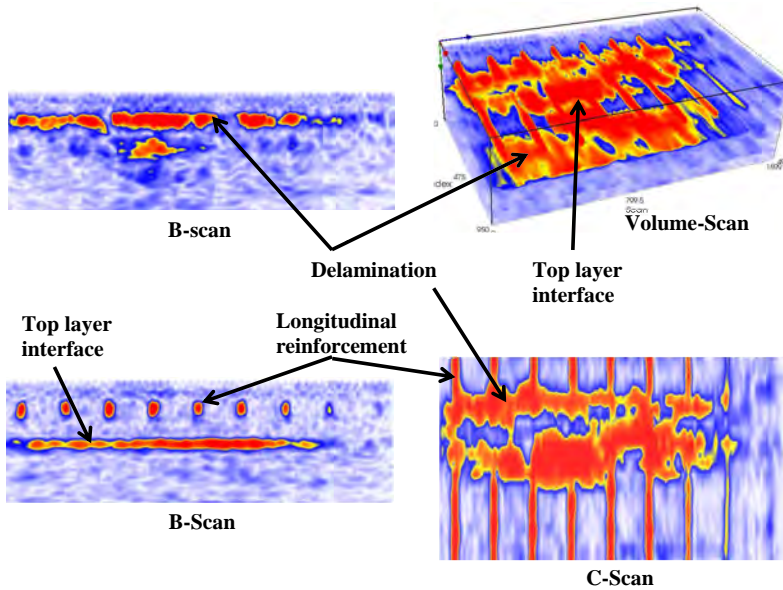



Figure N.48. UST images of test site IH20 9.27-2.

Interstate 20, Ft. Worth, TX			
Defects	Notes	Reinf. Detail	
Significant delamination on both sides of surface crack, ranging from 4.6"-5.1" from top surface.	Top layer of pavement approximately 10.2" below surface. Area tested because of transverse surface cracking. Pavement depth confirmed by 2 cores, indicating 10.2" thickness.	Longitudinal reinf.: ~4.8"- 5.0" deep @ 7.2" on center. No transverse reinforcement located in this area.	V _{shear} = 2770 m/s X-step: 150 mm Y-step: 50 mm Max Depth: 500 mm Frequency: 50 kHz Ft. Worth, TX I-20 IH20 9.27-3 MP 426 + 0.5, RM 2871 TAMU/TTI 9/2011

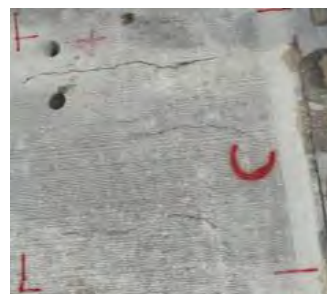
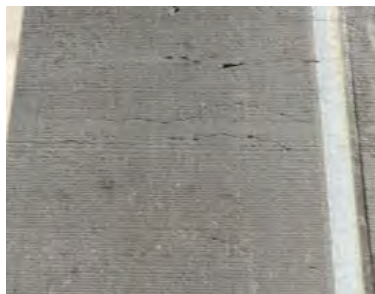



Figure N.49. Images of test site IH20 9.27-3.

Interstate 20, Ft. Worth, TX			
Defects	Notes	Reinf. Detail	
Significant delamination on both sides of surface crack, ranging from 4.6"-5.1" from top surface.	Top layer of pavement approximately 10.2" below surface. Area tested because of transverse surface cracking. Pavement depth confirmed by 2 cores, indicating 10.2" thickness.	Longitudinal reinf.: ~4.8"- 5.0" deep @ 7.2" on center. No transverse reinforcement located in this area.	V _{shear} = 2770 m/s X-step: 150 mm Y-step: 50 mm Max Depth: 500 mm Frequency: 50 kHz Ft. Worth, TX I-20 IH20 9.27-3 MP 426 + 0.5, RM 2871 TAMU/TTI 9/2011

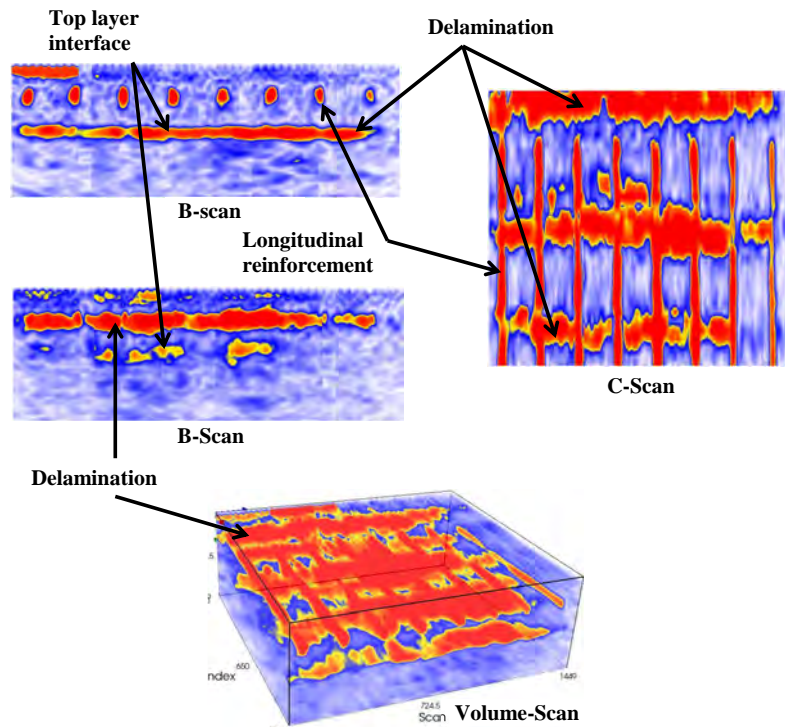


Figure N.50. UST images of test site IH20 9.27-3.



Interstate 20, Ft. Worth, TX			
Defects	Notes	Reinf. Detail	
Significant delamination on both sides of surface crack, approximately 5.0" from top surface.	Top layer of pavement approximately 10.1" below surface. Area tested because of transverse surface cracking. No cores taken in this location.	Longitudinal reinf.: ~4.6"- 5.2" deep @ 7.0" on center. No transverse reinforcement located in this area.	Vshear = 2770 m/s X-step: 150 mm Y-step: 50 mm Max Depth: 500 mm Frequency: 50 kHz Ft. Worth, TX I-20 IH20 9.27-5 MP 426 + 0.5, RM 2871 TAMU/TTI 9/2011



Figure N.51. Image of test site IH20 9.27-5.

Interstate 20, Ft. Worth, TX			
Defects	Notes	Reinf. Detail	V _{shear} = 2770 m/s
Significant delamination on both sides of surface crack, approximately 5.0" from top surface.	Top layer of pavement approximately 10.1" below surface. Area tested because of transverse surface cracking. No cores taken in this location.	Longitudinal reinf.: ~4.6"- 5.2" deep @ 7.0" on center. No transverse reinforcement located in this area.	X-step: 150 mm Y-step: 50 mm Max Depth: 500 mm Frequency: 50 kHz
			Ft. Worth, TX I-20 IH20 9.27-5 MP 426 + 0.5, RM 2871 TAMU/TTI 9/2011

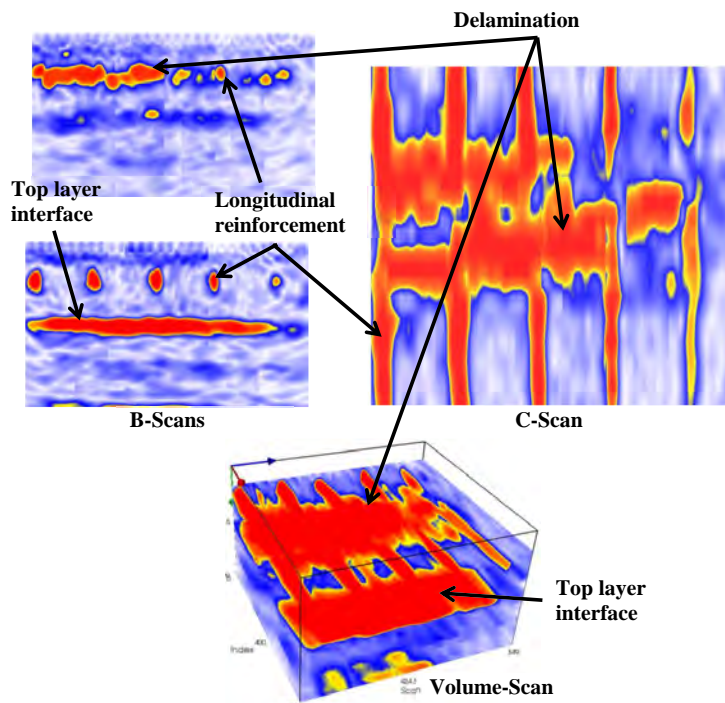


Figure N.52. UST images of test site IH20 9.27-5.



George Bush International Airport, Houston,			
Defects	Notes	Reinf. Detail	
Significant debonding at at runway/subbase (7.6"-8.1" deep) and verified by coring. Possible further debonding in deeper layers (26.9" and 37.7" deep).	Top layer of pavement approximately 7.6"-8.1" below surface; second layer 26.9" below surface; third layer 37.7" below surface. Area tested because of surface cracking and hammer sounding revealing possible debonding. Image is of typical runway segment.	None.	Vshear = 2885 m/s X-step: 200 mm Y-step: 100 mm Max Depth: 1000 mm Frequency: 50 kHz Houston, TX IAH IAH 6.9-1 Sta 83+00 T/W WA E TAMU/TI 6/2011



Figure N.53. Image of test site IAH 6.9-1.

George Bush International Airport, Houston,			
Defects	Notes	Reinf. Detail	
Significant debonding at at runway/subbase (7.6"-8.1" deep) and verified by coring. Possible further debonding in deeper layers (26.9" and 37.7" deep).	Top layer of pavement approximately 7.6"-8.1" below surface; second layer 26.9" below surface; third layer 37.7" below surface. Area tested because of surface cracking and hammer sounding revealing possible debonding. Image is of typical runway segment.	None.	Vshear = 2885 m/s X-step: 200 mm Y-step: 100 mm Max Depth: 1000 mm Frequency: 50 kHz
			Houston, TX IAH IAH 6.9-1 Sta 83+00 T/W WA E TAMU/TTI 6/2011

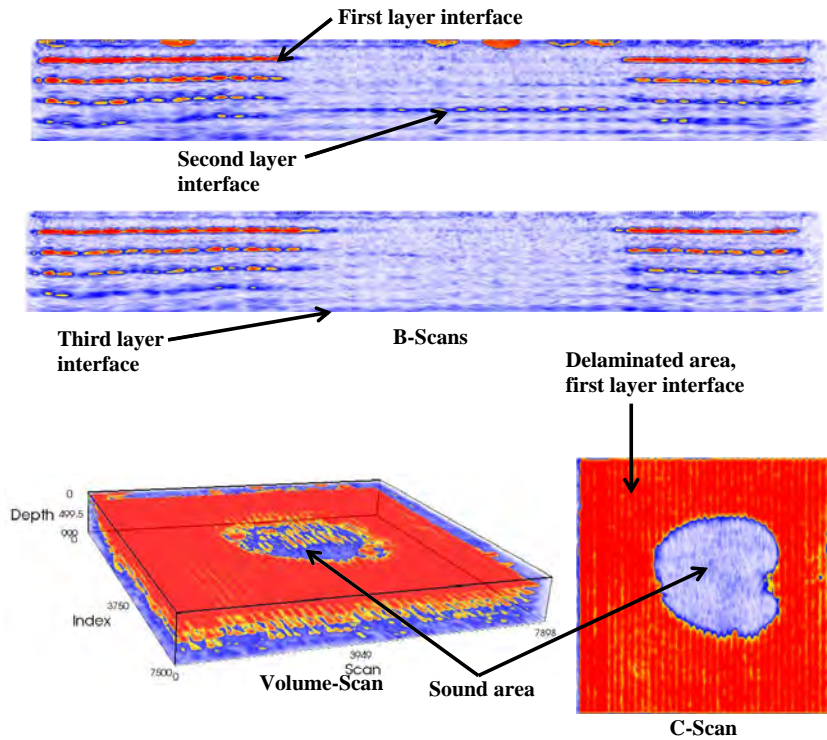


Figure N.54. UST images of test site IAH 6.9-1.



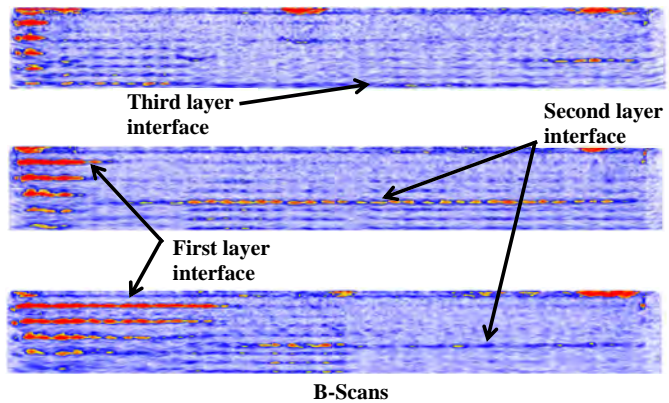
George Bush International Airport, Houston,			
Defects	Notes	Reinf. Detail	
Significant debonding at at runway/subbase (7.1" deep) and verified by coring. Possible further debonding in deeper layers (25.6" and 37.5" deep).	Top layer of pavement approximately 7.1" below surface; second layer 25.6" below surface; third layer 37.5" below surface. Area tested because of surface cracking and hammer sounding revealing possible delaminations. Image is of typical runway segment.	None.	Vshear = 2885 m/s X-step: 200 mm Y-step: 100 mm Max Depth: 1000 mm Frequency: 50 kHz Houston, TX IAH IAH 6.9-2 Sta 82+75 T/W WA E TAMU/TTI 6/2011

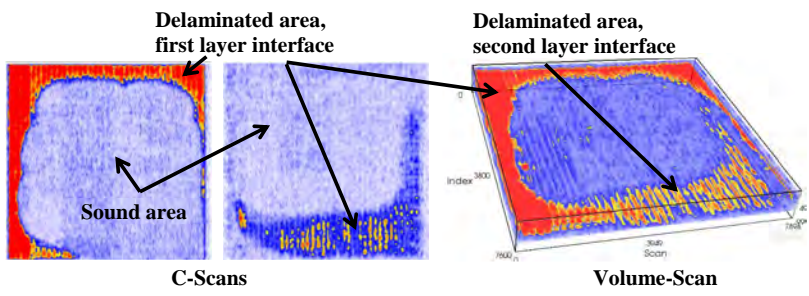


Figure N.55. Image of test site IAH 6.9-2.

George Bush International Airport, Houston,			
Defects	Notes	Reinf. Detail	Vshear = 2885 m/s
Significant debonding at at runway/subbase (7.1" deep) and verified by coring. Possible further debonding in deeper layers (25.6" and 37.5" deep).	Top layer of pavement approximately 7.1" below surface; second layer 25.6" below surface; third layer 37.5" below surface. Area tested because of surface cracking and hammer sounding revealing possible delaminations. Image is of typical runway segment.	None.	X-step: 200 mm Y-step: 100 mm Max Depth: 1000 mm Frequency: 50 kHz
			Houston, TX IAH IAH 6.9-2 Sta 82+75 T/W WA E TAMU/TTI 6/2011



B-Scans



C-Scans

Volume-Scan

Figure N.56. UST images of test site IAH 6.9-2.

APPENDIX O

Evaluation of Tiled Tunnel Linings by Using Acoustic Sounding

Introduction

This appendix describes the progress of a particular non-destructive testing (NDT) technique known as acoustic sounding and outlines how this system will work within the framework of the second Strategic Highway Research Program (SHRP 2) Renewal Project R06G.

This system requires further development to be efficiently implemented for tile debonding in tunnel linings. But research thus far has shown it to be a promising technique capable of quickly determining the stage of tile debonding in tunnel linings. This appendix discusses how the system will be used in inspection procedures and provides an idea of what the end product will be. Evaluations of public tunnels and test specimens have been conducted and the preliminary results are given.

Acoustic Sounding Technique

When debonding occurs on tiled surfaces, hammer sounding by ear or by microphone can readily differentiate bonded from debonded tile. Debonded areas have a characteristic lower-frequency pinging relative to fully bonded tiles. The goal here is to devise a less subjective method for inspectors to quickly and efficiently characterize the condition of tile bonding.

Technical Needs

In general, tile debonding can occur for two reasons: improper installation or external influences. Improper installation commonly includes the following:

- Improper use of bonding agent (e.g., the wrong mixing ratios or the wrong type of agent);
- Improper tile spacing;
- Excessive open time; and

- A low standard of workmanship (e.g., not “back buttering” the tile).

External influences can include environmental conditions (e.g., thermal expansion) and/or excessive tunnel lining forces (e.g., damage from voids, cracks, delamination, or debonding).

In either case, debonding of the tile does occur and can pose a danger to the public. This SHRP 2 project uses many NDT techniques to identify the onset of damage behind the tiled wall lining before debonding occurs and to quickly and efficiently identify regions that need immediate attention after debonding occurs.

Research Approach

The system under development is used with a laptop computer capable of recording audio signals and installed with a version of MATLAB (developed by MathWorks, <http://www.mathworks.com/products/matlab/>), along with an impact source (preferably a ball-peen hammer). As the operator lightly taps the center of each tile with the hammer, the laptop’s internal microphone records the audio signal. MATLAB software performs a fast Fourier transform (FFT) to the data set and uses pattern recognition techniques to monitor the fundamental frequencies of flexural vibration for each individual tile. The modes of vibration frequencies in a voided tile can be predicted with acoustic theory for a rectangular plate with simply supported edges (Rossing and Fletcher 2003):

$$f_{mn} = 0.453c_L h \left[\left(\frac{m+1}{L_x} \right)^2 + \left(\frac{n+1}{L_y} \right)^2 \right]$$

where c_L is the longitudinal wave speed, h is the thickness of the tile, m and n are the integers describing the current mode of excitation ($m = n = 0$ for the fundamental frequency of

flexural vibration), and L_x and L_y are the respective side lengths of the tile. The vibration frequencies increase as the voided section of tile decreases (Liu et al. 2011). Therefore, it is theoretically possible to relate the fundamental frequency to the approximate area of debonding.

This technique can be incorporated into a program that assigns a color scale to the frequency spectrum of a tile wall under inspection. The research team envisions that the final program will be able to operate in two modes. The first is for near-real-time inspection. In this mode, a threshold frequency from an expected frequency band representing sound concrete is established and used to make a pass-fail decision, telling the user whether a tile is most likely bonded or debonded. The second mode is intended for mapping a large region of tile, and the final result is a map of the tiles showing the levels of expected bond. As in the first mode, the user selects a section of tile representing a fully bonded state for the program to determine the fundamental frequencies associated with bonded sections. The user then taps each tile in a predetermined order. For instance, the section might consist of an area 13 tiles high by 40 tiles wide. The program prompts the user to select the layout desired, and after the user taps each tile in the given order, the program will output a plot showing the frequency spectrum.

Field Application in the Washburn Tunnel

A rudimentary version of this technique was used for a proof-of-concept test in the Washburn Tunnel in Houston, Texas. The Washburn Tunnel (Figure O.1) is the only underwater vehicle tunnel in operation in Texas and was completed in 1950. It carries a federal road beneath the Houston Ship Channel, joining two Houston suburbs.

The tunnel was constructed via the immersed tube method, with sections joined together in a prepared trench, 26 m (85 ft) below the water line. The entire inner wall is tiled with 110-mm by 110-mm (4.3-in. by 4.3-in.) ceramic tiles. Like many underwater tunnels with tiled walls, this one is experiencing debonding of tile in various areas. Three sections of tile that contained debonded regions (as determined by an inspector performing hammer sounding by ear) were chosen. The regions, shown on the left side of Figure O.2, show the area under consideration outlined with blue painter's tape. The debonded section (determined by human ear) is indicated with a blue painter's tape "x" on the debonded section. On the right side of Figure O.2, scans made via ultrasonic tomography (UST) are shown for each of the three regions. (The ultrasonic tomography technique and its specific application to the Washburn Tunnel can be read in Appendix M) The depths of the C-scans (plan views) in Figure O.2 range from 16 mm to 103 mm (0.63 in. to 4.1 in.). One of the areas investigated (Figure O.2, top) was evaluated using a rudimentary version of the acoustic sounding technique and is shown in Figure O.3. This example demonstrates a strong correlation between hammer sounding by ear and the automated acoustic sounding technique.

In Figure O.3, the bottom left plot depicts the tiles color coded in grayscale, with the higher frequencies (predicting a fully bonded state) as white and the lower frequencies (predicting a debonded state) as black. As previously discussed, the lower frequencies observed should theoretically correspond to larger voided areas behind the tile. The bottom right plot in Figure O.3 shows the output with a pass-fail algorithm denoting tiles that fall below the expected fully bonded state (red is the expected debonded state, green is the expected fully bonded state).

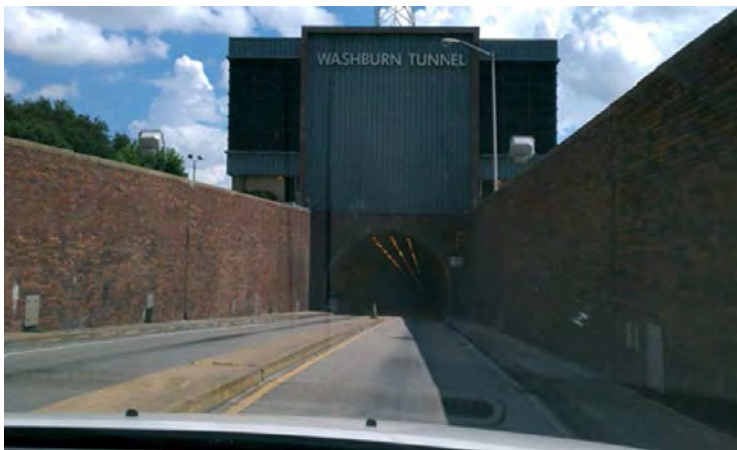


Figure O.1. Washburn Tunnel: exterior view (left) and interior view (right).

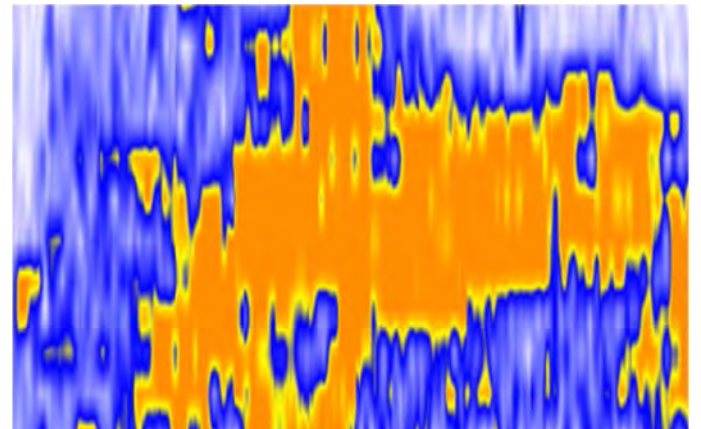
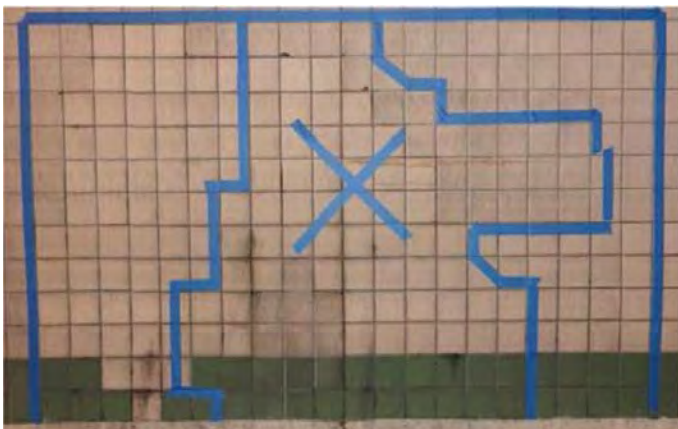
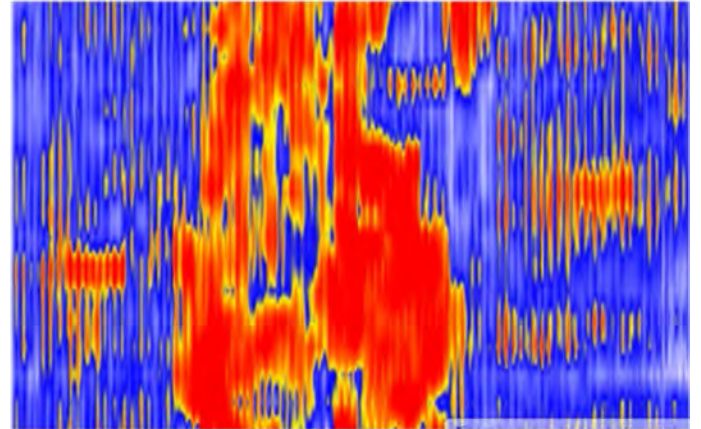
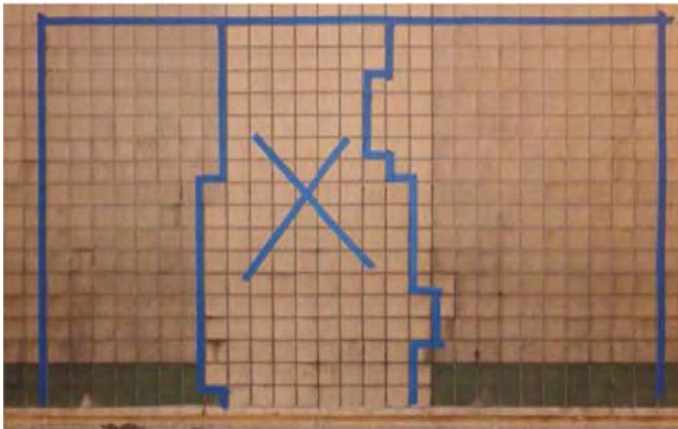
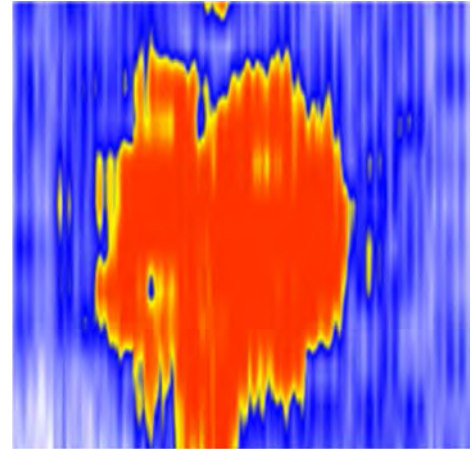
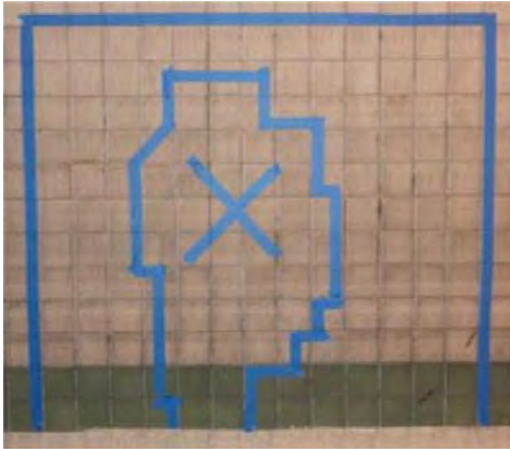


Figure O.2. Debonded regions of tile (left) paired with the associated UST C-scans (right).

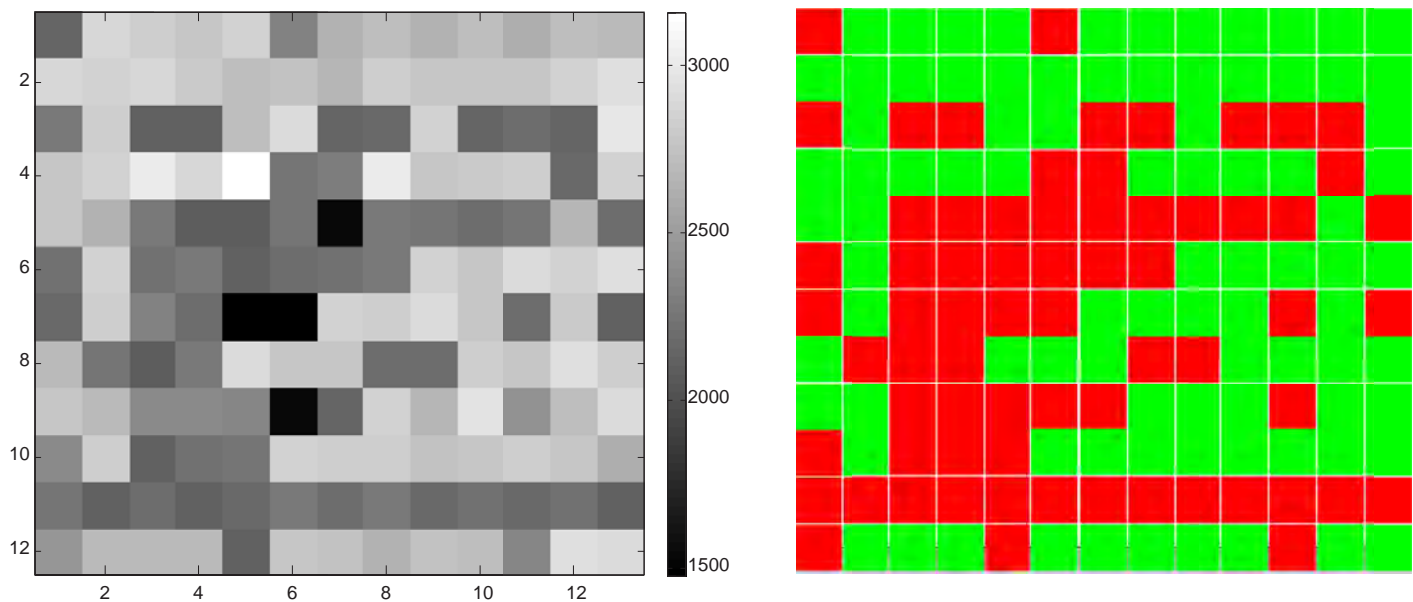
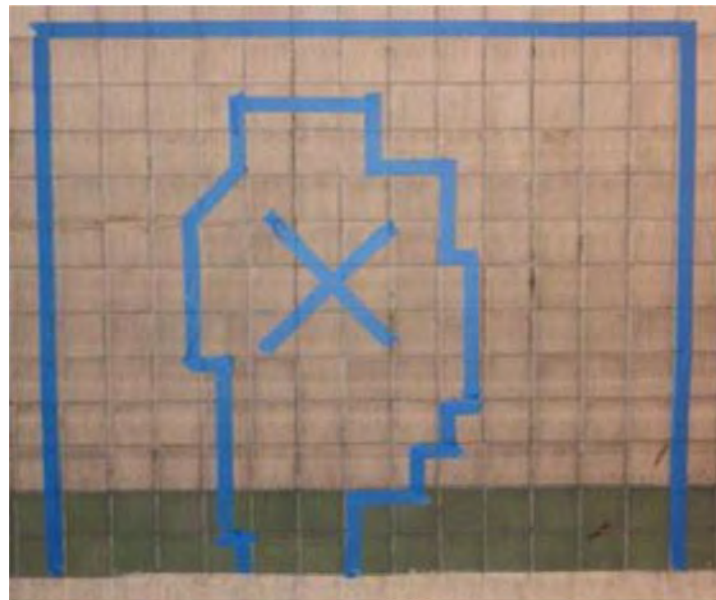


Figure O.3. Debonded regions of tile (top) paired with the acoustic sounding results (bottom).

Conclusion

This automated sounding technique is still under development. Many factors influence the peak frequencies observed in the frequency spectrum from a single tile tap, including the size of the void, whether or not the hammer tap is directly in the center of the tile, and multiple mode interference. Preliminary results indicate that this technique, although basic in its approach, will offer the tunnel inspector a quick, efficient, inexpensive, and

objective technique that provides sufficient information for repair procedures or further investigation.

References

- Liu, S., F. Tong, B. Luk, and K. Liu. 2011. Fuzzy Pattern Recognition of Impact Acoustic Signals for Nondestructive Evaluation. *Sensors and Actuators: A. Physical*, Vol. 167, No. 2, pp. 588–593.
- Rossing, T., and N. Fletcher. 2003. *Principles of Vibration and Sound*, 2nd ed. Springer, New York.

APPENDIX P

Portable Seismic Property Analyzer Field Tests in the United States

Introduction

A survey of several tunnels linings was carried out with a portable seismic property analyzer (PSPA) within the framework of the SHRP 2 Renewal Project R06G. The main objectives of the research project are summarized in the Executive Summary of the main report.

Two tunnels in Colorado and one tunnel in Virginia were involved in this study. The Eisenhower Memorial Tunnel in Colorado was investigated on October 3 and 4, 2011, and the Hanging Lake Tunnel in Colorado was assessed on October 5 and 6, 2011. The evaluation of the Chesapeake Channel Tunnel in Virginia was performed October 11 through 12, 2011. The scope of the University of Texas at El Paso study was to evaluate the performance of the PSPA in locating defects behind or within tunnel linings. This appendix describes the tests executed and the results obtained.

Description of PSPA and Testing Methods

PSPA is a portable device that can perform two tests—impact echo (IE) and ultrasonic surface wave (USW)—simultaneously. The PSPA consists of two receivers and a source packaged into a handheld portable device. The near and far receiver spacing from the source are 4 in. and 10 in., respectively. The impact duration (contact time) is about 60 μ s, and the data acquisition system has a sampling frequency of 390 kHz. The advantage of combining these two methods in a single device is that once the test is performed, the variations in the modulus (an indication of the quality of concrete) and return resonance frequency (an indication of the full thickness or depth of delamination) of a slab can be assessed concurrently. The following sections discuss the principles of the two seismic methods, along with interpretation approaches.

Impact Echo Method

The IE method is one of the most commonly used non-destructive testing (NDT) methods for detecting delamination in concrete (Carino et al. 1986). This method works by striking a plate-like object such as a tunnel lining with an impactor that generates stress waves at frequencies up to 20 kHz to 30 kHz and collecting signals with a receiver (Figure P.1a). By using a fast Fourier transform (FFT) algorithm, the recorded time domain signal is converted into a frequency domain function (amplitude spectrum) and the peak frequency is monitored. For an intact point on a slab or an intact portion of a slab, the thickness (h) is then determined from the compression wave velocity (V_p) and the return frequency (f) as shown in Equation P.1:

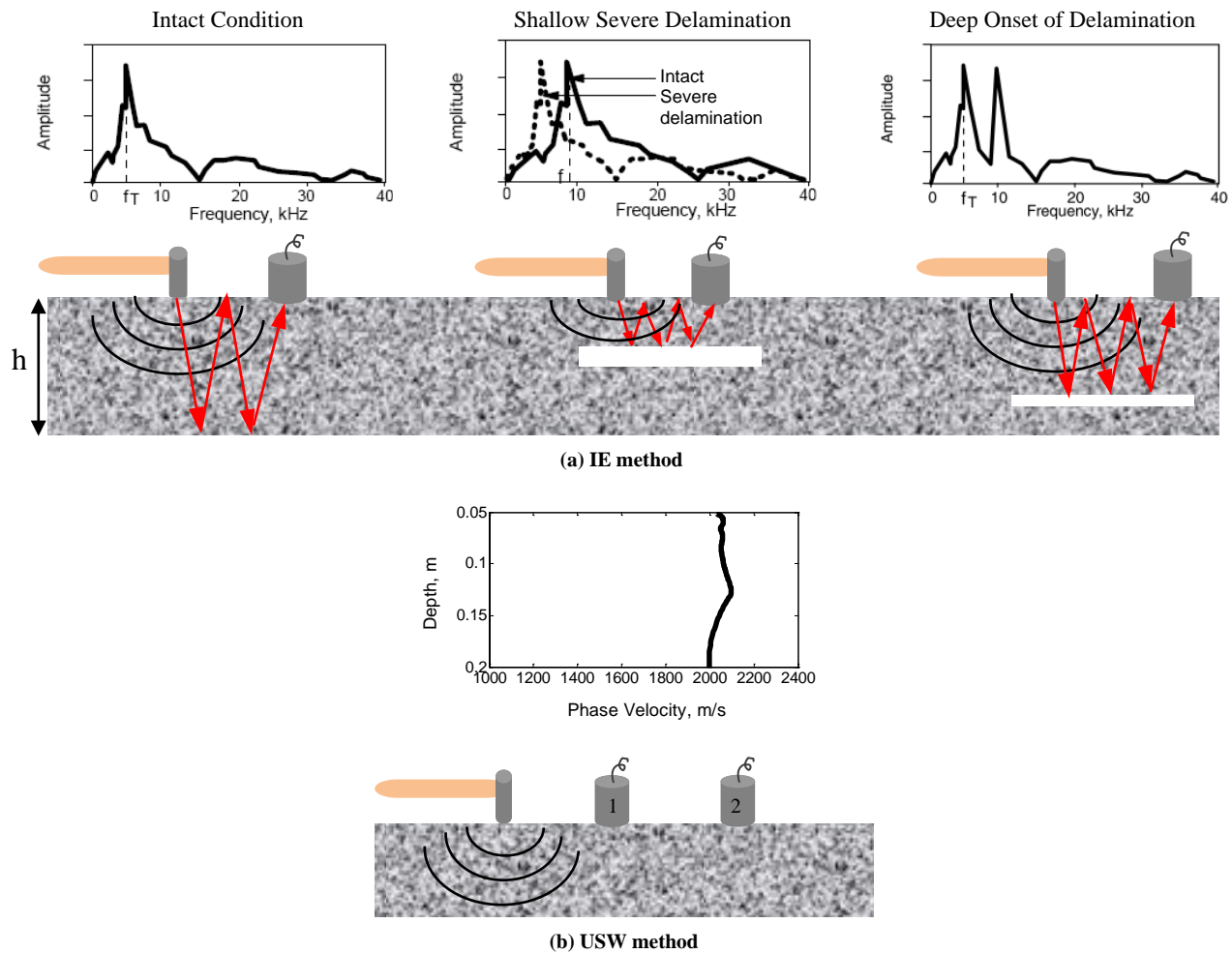
$$h = \alpha \frac{V_p}{2f} \quad (\text{P.1})$$

where α is about 0.96 for concrete slabs.

For a deep and relatively small delaminated location in a concrete slab, the return frequency may shift to a higher frequency corresponding to the depth of the delamination. As shown in Figure P.1b, a shallow or a deep but extensive and severely delaminated area is usually manifested by a low peak frequency, indicating that little or no energy propagates toward the bottom of the deck, and a flexural mode dominates the frequency response. In this case, Equation P.1 is not applicable to measure the depth of delamination since it is influenced by several factors.

Ultrasonic Surface Waves Method

The USW method is used to estimate the average velocity of propagation of surface waves in a medium, based on the time at which different types of energy arrive at each sensor (Figure P.1b). The velocity of propagation, V_R , is typically



Source: Gucunski and Maher 1998.

Figure P.1. Schematic illustration of the test methods.

determined by dividing the distance between two receivers, ΔX , by the difference in the arrival time of a specific wave, Δt . Knowing the wave velocity, E , the modulus can be determined from shear modulus, G , through Poisson's ratio (ν) by using Equation P.2:

$$E = 2(1 + \nu)G \quad (\text{P.2})$$

Shear modulus can be determined from shear wave velocity, V_S , by using Equation P.3:

$$G = \frac{\gamma}{g} V_S^2 \quad (\text{P.3})$$

The modulus from surface wave velocity, V_R , first converted to shear wave velocity, can be determined with Equation P.4:

$$V_S = V_R(1.13 - 0.16\nu) \quad (\text{P.4})$$

In the USW method, the variation in velocity with wavelength is measured to generate a dispersion curve. For a

uniform or intact concrete slab, the dispersion curve shows more or less a constant velocity within the wavelengths no greater than the thickness of the slab. When a delamination or void is present in a concrete slab or the concrete has deteriorated, the average surface wave velocity (or modulus) becomes less than the actual modulus because of interference from the defect. In this case, the velocity or modulus obtained may be called an apparent velocity or modulus.

Description of Sites

The three tunnels visited in this study are described below.

Eisenhower Memorial Tunnel

An outside view of the Eisenhower Memorial Tunnel is shown in Figure P.2. The tunnel was originally designed as a twin bore tunnel—the Eisenhower bore and the Edwin C. Johnson bore. This two-bore tunnel is located approximately 60 mi



Figure P.2. Outside view of Eisenhower Memorial Tunnel.

west of Denver, Colorado, on I-70. The tunnel is about 1.7-mi long, and the plenum is up to 18-ft high, with a nominally 2-ft-thick liner. Some sections of the ventilation plenum were investigated in this study.

Hanging Lake Tunnel

Hanging Lake Tunnel also consists of two bores and is located approximately 10 mi east of Glenwood Springs, Colorado, on I-70. The tunnel is about 0.7-mi long, and the ventilation plenum is 7-ft high, with a nominally 15-in.-thick liner, as shown in Figure P.3. Some sections of the plenum were evaluated.

Chesapeake Channel Tunnel

This one-bore subsea tunnel is part of a 17-mi-long bridge-tunnel connecting southeastern Virginia to the Delmarva



Figure P.3. Outside view of Hanging Lake Tunnel.



Figure P.4. Outside view of Chesapeake Channel Tunnel.

Peninsula on U.S. Hwy 13. The tunnel is about 1-mi long with a nominally 2-ft-thick liner. An outside view of the tunnel is shown in Figure P.4. A section of about 2,600 ft of the ventilation plenum and a section of 200 ft on the wall of the roadway were involved in this study.

Data Collection Process

In the Eisenhower Memorial Tunnel, data were collected point by point, mostly every 5 ft, along a line in each selected section. The selection was based on the detected anomalies with infrared thermography. In the Hanging Lake Tunnel, besides the line testing, data were collected along a test grid. The selection of test sections was based on visual inspection and previous investigation of the tunnel.

In the Chesapeake Channel Tunnel, both the ventilation plenum and roadway wall were evaluated with NDT. All tests, including those with PSPA in this study, were conducted at or within a number of areas. The selection was based on the distribution of major anomalies with a dielectric constant. The testing schedules and locations for the tunnels are presented in Table P.1. Table P.2 lists the selected areas on the plenum ceiling of the Chesapeake Channel Tunnel, which include three spots one an area and 10 selected anomaly areas characterized by a high dielectric constant (greater than 15, compared with 4.5 for typical dry concrete) and, for most of them, by cracking with more or less water dropping.

Eisenhower Memorial Tunnel

In the Eisenhower Memorial Tunnel, each bore was investigated in 1 day. Six 50-ft-long sections (from Section 8 to Section 13) were tested on October 3 in the eastbound bore. About

Table P.1. Testing Schedules and Locations of the Tunnels

Location and Schedule	Eisenhower Memorial Tunnel		Hanging Lake Tunnel		Chesapeake Channel Tunnel	
Location	Dillon, Colorado		Glenwood Springs, Colorado		Cape Charles, Virginia	
Date	October 3	October 4	October 5	October 6	October 11	October 12
Direction	Eastbound	Westbound	Eastbound	Eastbound	Plenum	Plenum and wall
Section tested	8 to 13	148 to 166	57 to 61	57	Not applicable	
Number of blocks (areas) tested	60	190	50	2	7	14
Number of points tested	57	151	42	42	46	52

19 sections (from Section 148 to Section 166) were investigated on October 4 in the westbound bore. The selection of sections was based on visual inspection and a preliminary infrared testing. In both bores, the investigation was mostly performed every 5 ft at the center of each block. Several extra points were tested around the cracked and delaminated areas. It took about 10 min for each 50-ft section to be tested. The rest of the time was allotted to documenting the data collection information and taking some pictures. The main challenge while using the PSPA device was the dirt on the wall that caused an occasional slip of the device during testing. Therefore, some points had to be tested several times to get a clear signal.

Hanging Lake Tunnel

In the Hanging Lake Tunnel, five 50-ft-long sections (from Section 57 to Section 61) were investigated on October 5 in the westbound bore. Similar to the Eisenhower Memorial Tunnel, the selection of sections was based on visual inspection and the severity of visible cracks. The data were collected at the center of each block as well as around the cracks and delaminated areas. In addition to 10 min of testing for each block, extra time was allotted to documenting the data collection information and taking pictures. On October 6, two blocks in Section 57 were tested in more detail with denser measurements. These two blocks were investigated through seven horizontal and six vertical lines (see Figure P.5). It took about 2 h to test the two blocks. The main challenge while using the PSPA was the areas with large curvature, which prevented the device from maintaining full contact with the surface in some places.

Table P.2. Approximate Locations of the Areas Tested with PSPA in the Plenum of the Chesapeake Channel Tunnel

Area	Intact	Defective									
Location	470+50 to 470+75	473+56	474+27	477+60	478+85	481+76	486+67	486+81	491+25	493+15	496+25

Chesapeake Channel Tunnel

Because this tunnel has been previously evaluated by other NDT methods, the focus of this study was on a number of areas or spots on the plenum and the roadway wall where high dielectric constants were measured. Forty-six points within seven areas on the ceiling of the plenum were evaluated on October 11. Thirty-eight points within six areas on the ceiling of the plenum and 14 points at 11 spots on the wall of the roadway were evaluated on October 12. All tests were stopped at midnight that day because the traffic lane had to be reopened due to foggy weather.

Test Results

Because the IE and USW methods used in this study are point inspection methods, the results are best visualized using a contour map rather than evaluating them individually. However, typical IE and USW results for an intact area and defective area are shown for each tunnel.

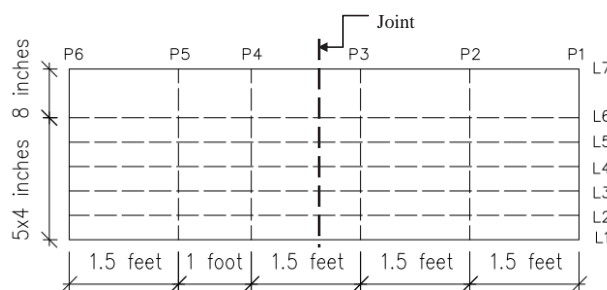
Eisenhower Memorial Tunnel

IE Method

The amplitude spectra for an intact point and two defective points along with the photograph taken through visual inspection are shown in Figure P.6. Compared with the intact point, either lower or higher peak frequencies control the response at defective points, as discussed above. Based on an average compression wave velocity of 13,800 ft/s measured for the concrete and Equation P.1, a nominal



(a) The actual photograph



(b) Plan of the tested blocks

Figure P.5. Tested blocks with denser grid measurement in Hanging Lake Tunnel.

frequency of around 3.5 kHz approximately corresponds to the thickness of the liner (2 ft), whereas the frequency of 6.8 kHz for the shallow delamination approximately corresponds to a thickness of 1 ft. The response from the severely delaminated area corresponds to the flexural mode of vibration.

Figures P.7a and P.7b show the spectral B-scan of the IE results along several blocks in the eastbound and westbound bores, respectively. At some points, a frequency of about 3 kHz to 3.5 kHz governs the response, which indicates the thickness of the liner. On the remaining areas, either a low- or high-frequency amplitude governs the response. The low-frequency flexural mode results from a shallow or a deep but extensive delamination. Therefore, its peak frequency does not correspond to any thickness measurement, and the depth of defect can be estimated from a USW B-scan. However, the high-frequency response could be attributed to the onset of delamination. In that case, the depth of delamination is estimated from Equation P.1 and confirmed with the USW B-scan. In the presence of a crack, data analysis is more complicated. Multiple frequencies are present in the response when a crack is between the source and receiver in an IE

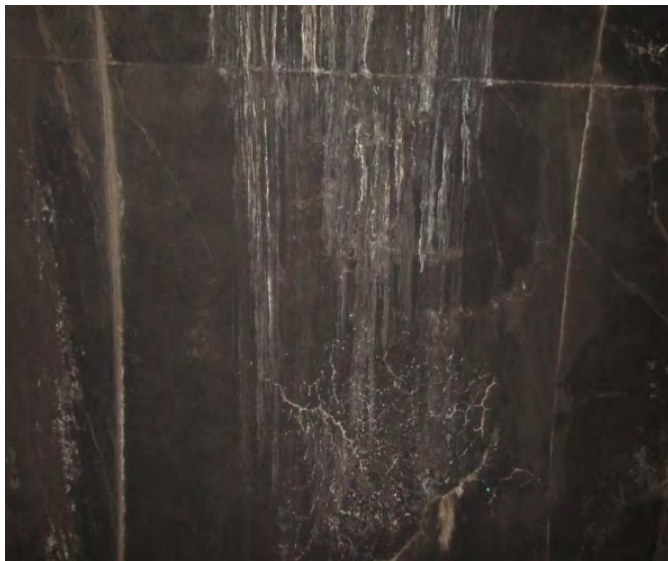
B-scan, and the crack is recognized through high average moduli in the USW B-scan.

USW Method

Figure P.8 shows a typical USW dispersion curve for an intact area and a defective point along with actual photographs. The dispersion curve shifts to lower moduli where severe flaws are present.

The cross sections of variation in modulus with wavelength, which can be viewed qualitatively as a scaled variation in modulus with depth, are shown in Figure P.9 for the eastbound and westbound bores. The problematic areas manifest themselves as areas with lower average moduli.

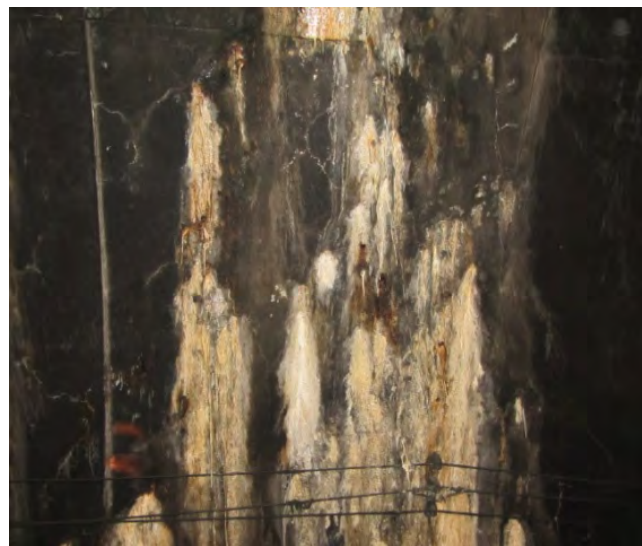
Combining the IE and USW results builds confidence in the interpretation of the location and depth of the problematic areas. In other words, the combined tests allow for a better delineation between shallow/deep and initial/extensive defects. For instance, a low-frequency dominant frequency in the IE results in Figures P.7a and P.7b is an indication of a shallow or a very deep and extensive delamination, and the depth can be estimated from USW B-scans (Figures P.9a and



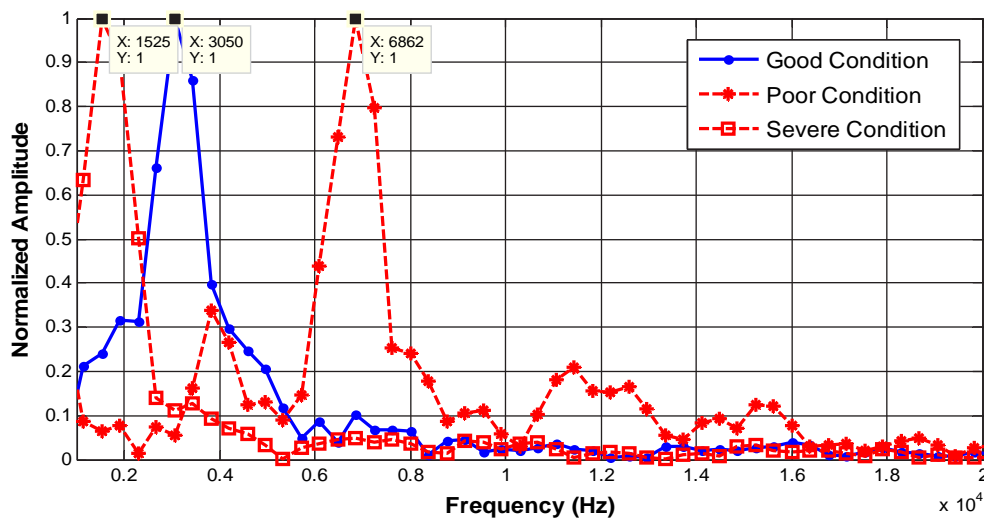
(a) Good condition



(b) Poor condition



(c) Severe condition



(d) Representative amplitude spectrum for intact and defective points

Figure P.6. Amplitude spectra along with actual photographs for intact and defective points in Eisenhower Tunnel showing good, poor, and severe conditions, and representative amplitude spectrum for intact and defective points.

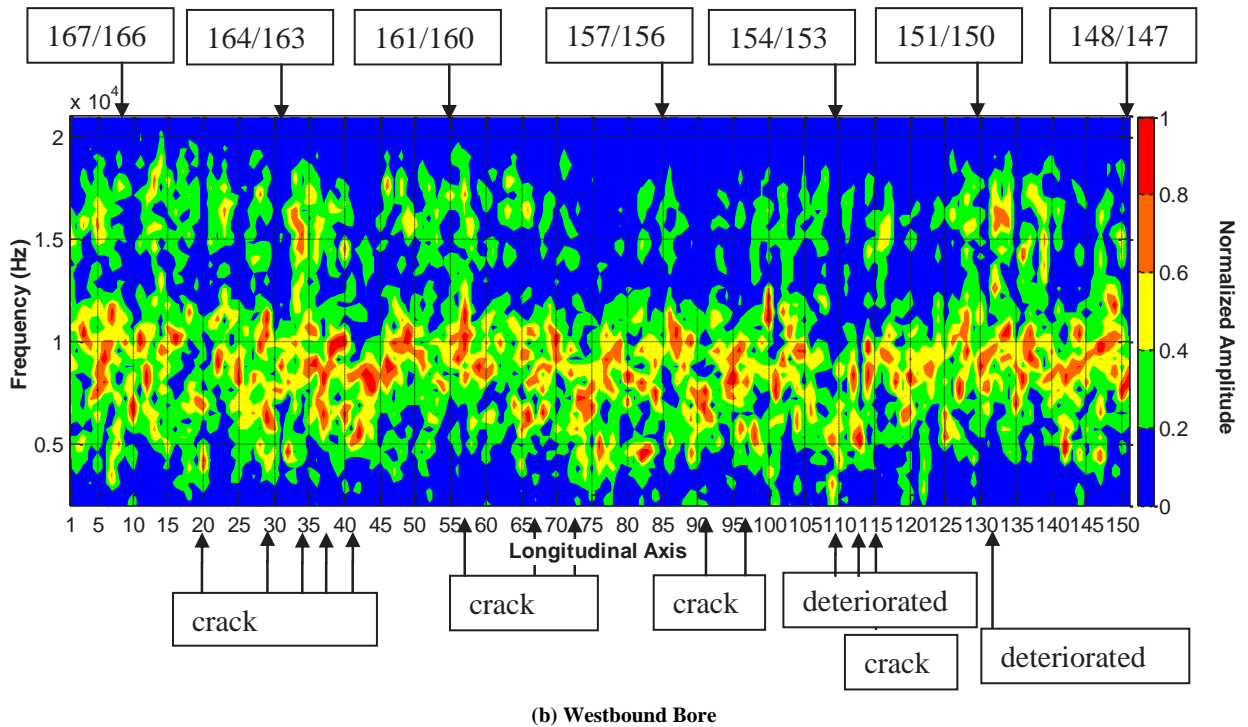
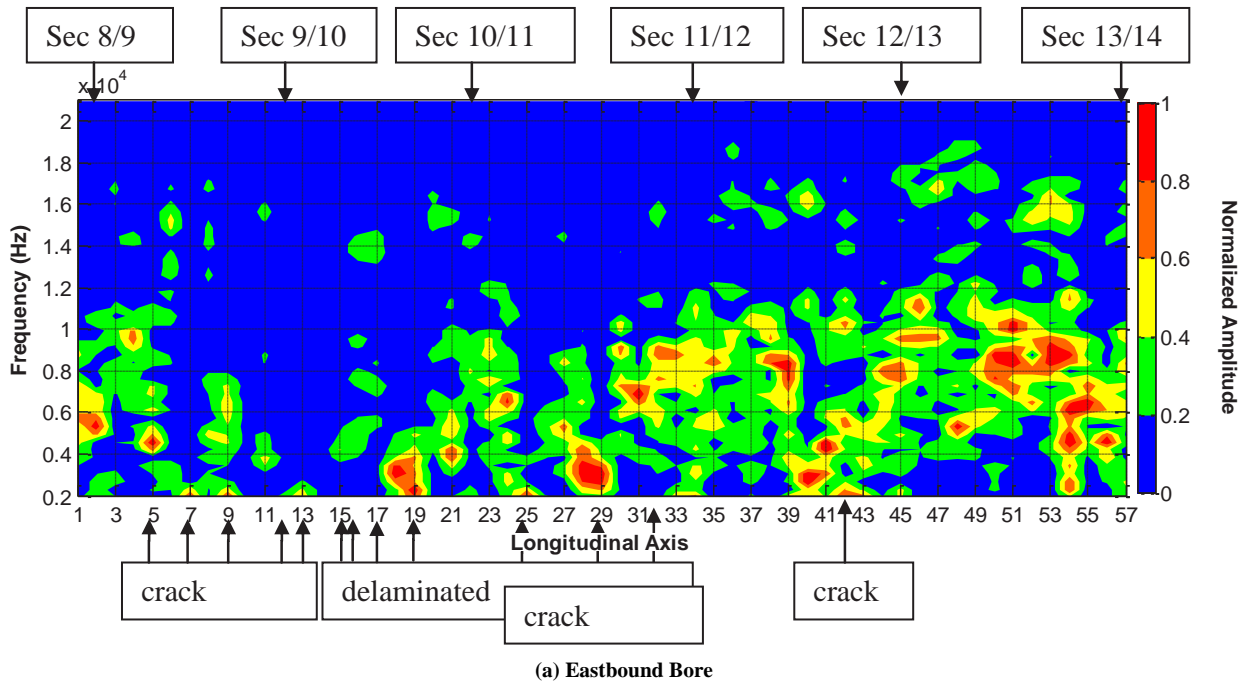


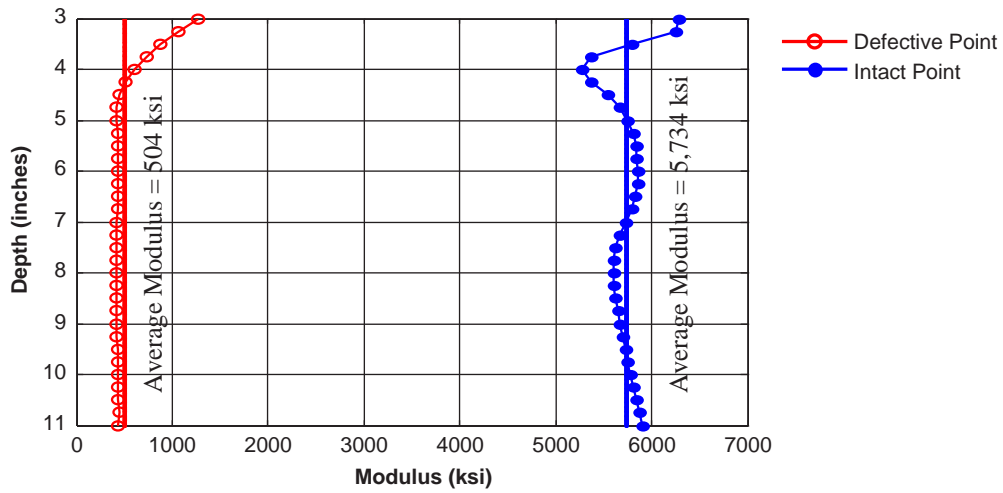
Figure P.7. IE spectral B-scans along Eisenhower Memorial Tunnel.



(a) Intact location



(b) Defective location



(c) Representative dispersion curve for intact and defective points

Figure P.8. Photographs of intact and defective points along with representative dispersion curve for both points, in Eisenhower Memorial Tunnel.

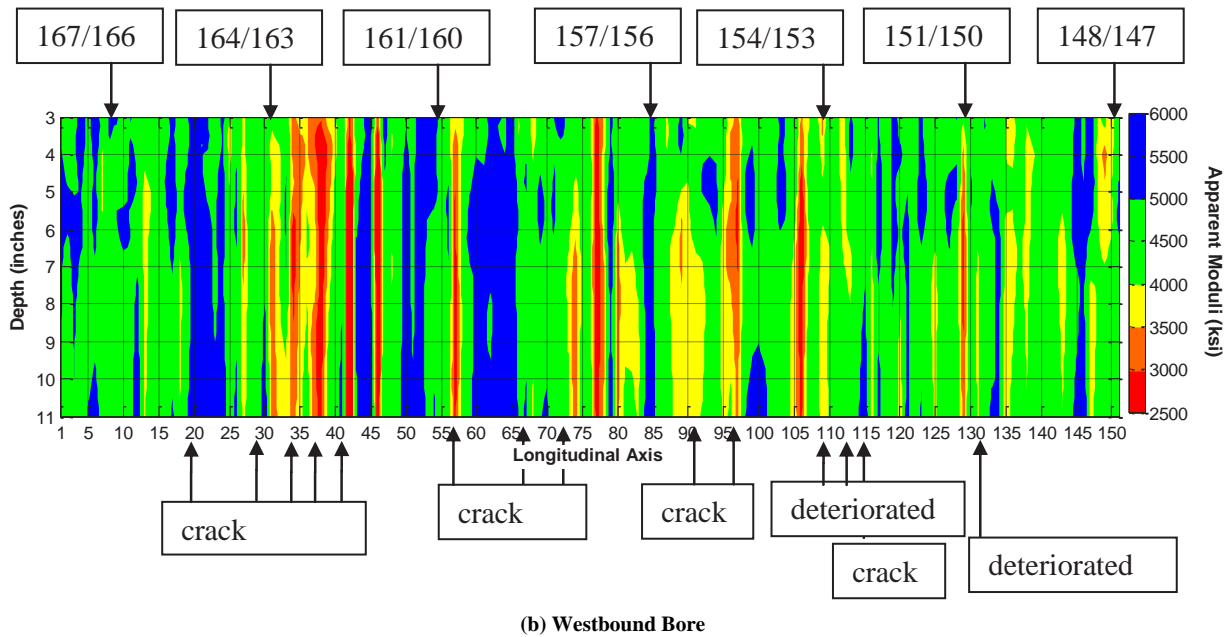
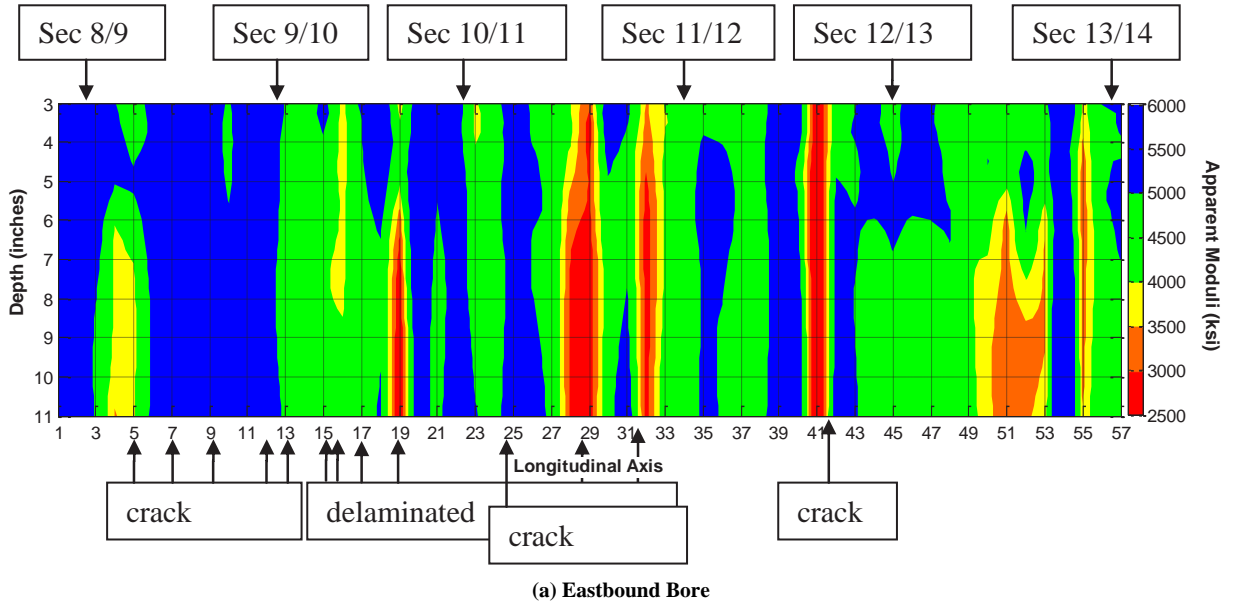


Figure P.9. Variation of modulus with depth, in Eisenhower Memorial Tunnel.

P.9b). The areas with high-frequency dominant amplitudes (around 16 kHz) in Figures P.7a and P.7b are deep delamination, with the depth of the delamination around 5 in. (according to Equation P.1). At several points in Figures P.9a and P.9b, the manifestation of defect starts at 6 in. On the majority of testing areas, multiple frequencies control the response in the IE B-scans indicating the presence of cracks. Comparable results are obtained from the USW B-scans. When the crack is between the source and first receiver, the USW modulus is typically greater than normal because of the travel path of the wave. Similarly, when the crack is between the two sensors, the reported USW modulus is lower than normal. The results for these points agree well with the actual condition that was documented during visual inspection.

Hanging Lake Tunnel

IE Method

The actual condition of liners at the time of testing is shown in Figures P.10a and P.10b. The amplitude spectra for selected intact and defective points are shown in Figure P.10c. Based on an average compression wave velocity of about 14,000 ft/s measured for the concrete, the dominant frequency corresponding to the tunnel thickness (15 in.) is around 5.4 kHz. Compared with the intact point, higher peak frequencies mostly control the response at the defective points.

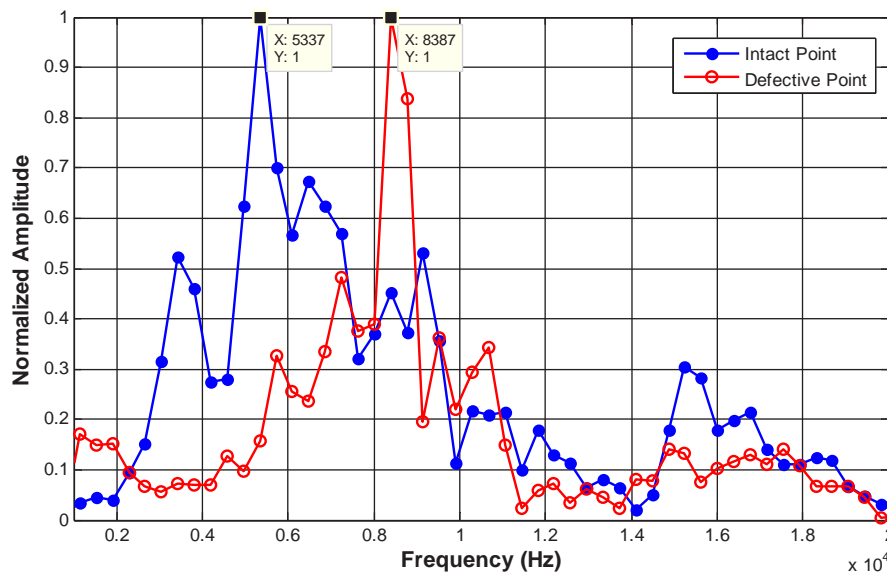
Figure P.11 shows the spectral B-scan of the IE results along several blocks in the westbound bore. At some points, a frequency of 5.4 kHz dominates the response, which



(a) Intact location



(b) Defective location



(c) Representative amplitude spectrum for intact and defective points

Figure P.10. Photographs of intact and defective points, along with representative amplitude spectrum for both points, in Hanging Lake Tunnel.

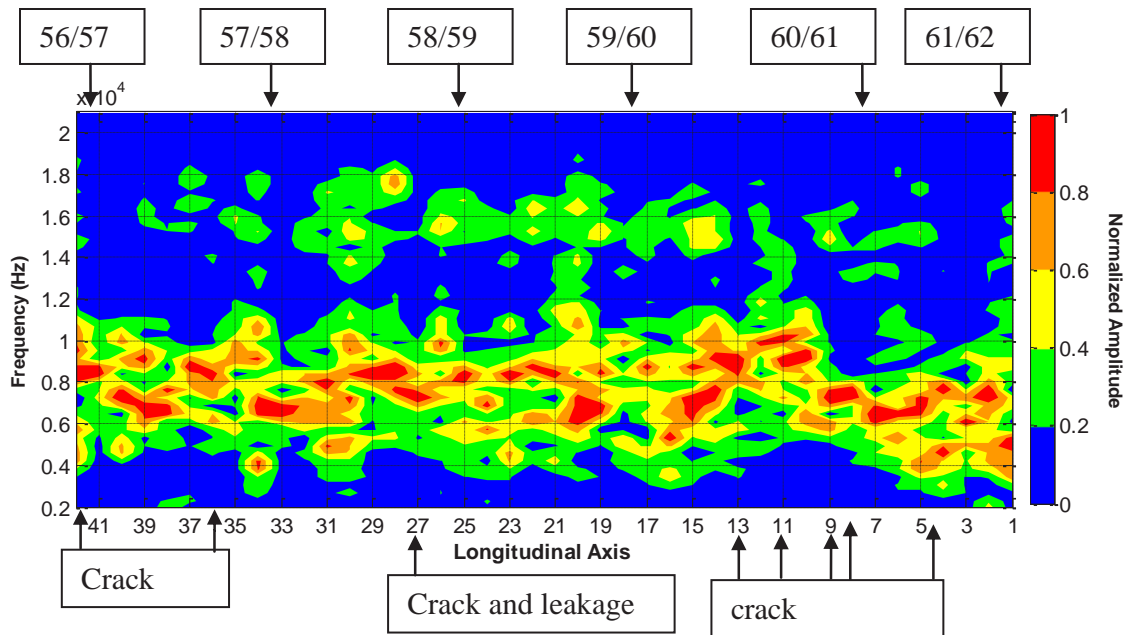


Figure P.11. IE spectral B-scan along Hanging Lake Tunnel.

indicates intact areas. On the remaining areas, mostly high frequency governs the response, which is an indication of a deep (but not extensive) delamination or crack. A better delineation between delamination and crack can be obtained through the USW B-scan.

Figure P.12 presents the contour map of the peak frequency on the defined test grid. As mentioned earlier, the thickness frequency is around 5.4 kHz. The threshold in color index is set according to the dominant frequency on intact areas. Frequencies lower than 4 kHz and higher than 8 kHz are considered as the dominant low and high frequency, respectively. The spectral B-scan of the IE results along Line 2 is shown in Figure P.13. The red stripe around 5.4 kHz corresponds to the tunnel thickness and indicates echo mode. The rest of the

spectral B-scans of IE results are shown in Appendix P1, at the end of this appendix.

USW Method

Figure P.14 compares typical USW dispersion curves from an intact area and a defective area with their actual conditions, as was documented during visual inspection. In defective areas, the dispersion curve shifts to lower moduli.

The variation in modulus with wavelength (or depth) along several blocks of the eastbound bore of the Hanging Lake Tunnel is shown in Figure P.15. The problematic areas are marked with red, which indicates a lower modulus. The IE B-scan (Figure P.11) and the USW B-scan (Figure P.15)

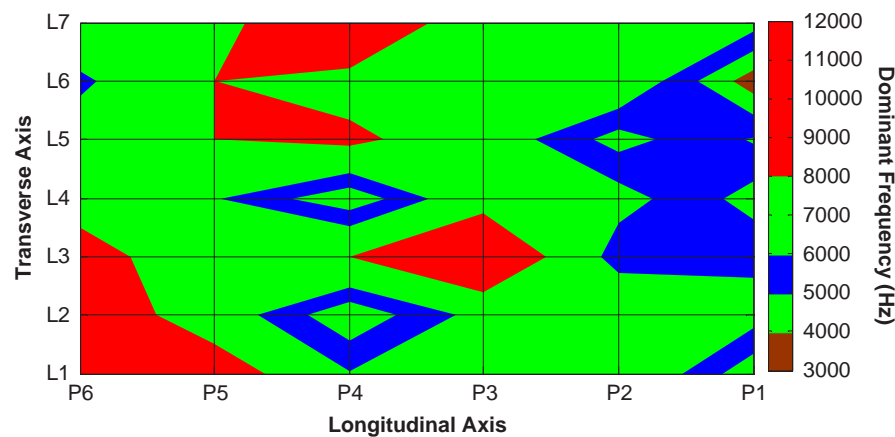


Figure P.12. Planar variation of the dominant frequency on meshed block, in Hanging Lake Tunnel.

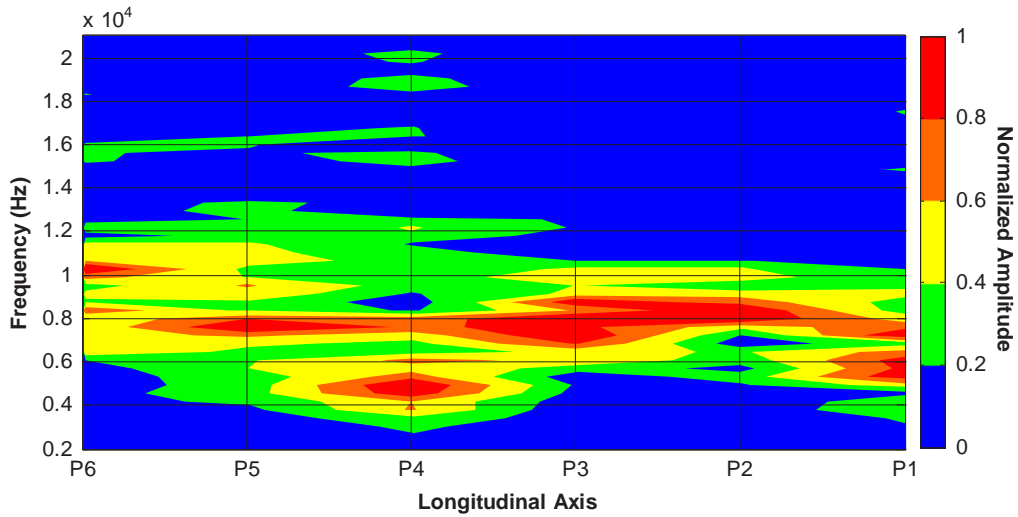


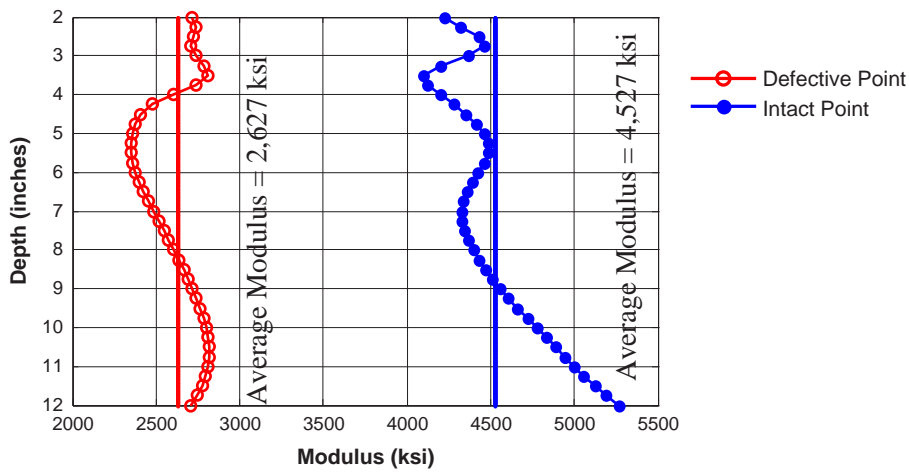
Figure P.13. IE spectral B-scan along L2 on meshed block, in Hanging Lake Tunnel.



(a) Intact location



(b) Defective location



(c) Representative dispersion curve for intact and defective points

Figure P.14. Photographs of intact and defective points, along with representative dispersion curve for both points, in Hanging Lake Tunnel.

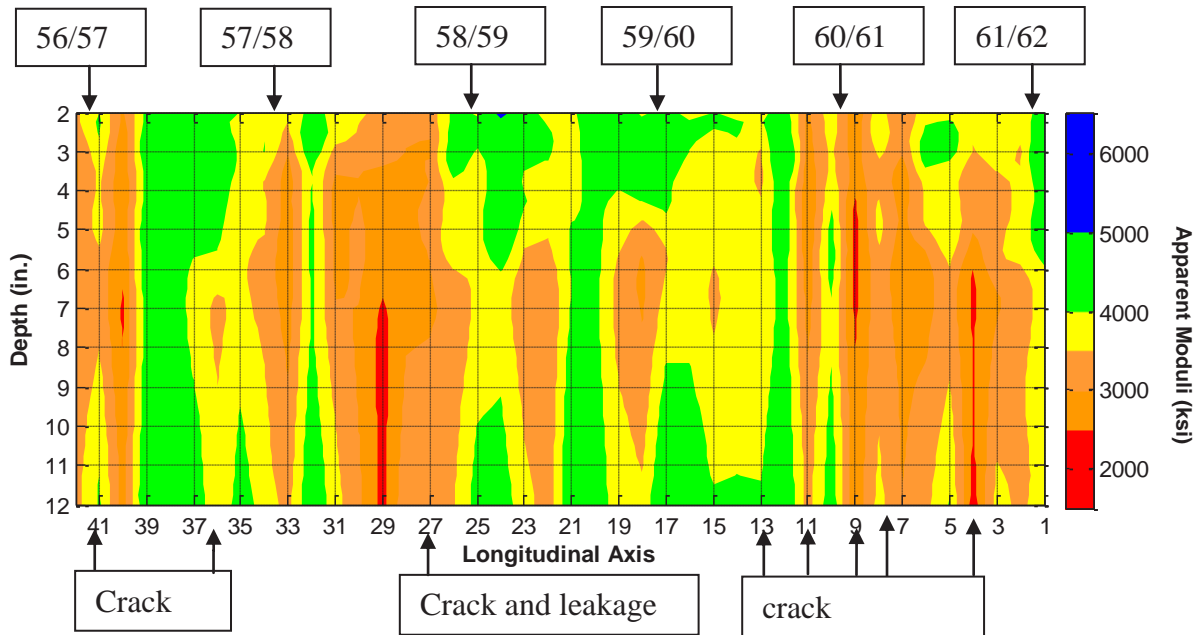


Figure P.15. Variation of apparent modulus with depth along Hanging Lake Tunnel.

result in similar defect maps (both for location and depth). The points with multiple peak frequencies in Figure P.11 are recognizable in Figure P.15 through a low modulus starting at the surface (indication of crack). Other defective points that manifest themselves by high frequency (between 15 kHz and 17 kHz) in the IE B-scan might be delamination at the depth of 5 in. to 5.5 in. (calculated using Equation P.1). Similarly, the indication of lower moduli starts at a depth of around 5 in. in the USW B-scan at those points.

The planar contour map of the variations of the average modulus on the meshed blocks is presented in Figure P.16. The defective areas manifest themselves as the areas with lower moduli and are marked in red.

Another way to represent the USW outcomes is through a line scan, which is shown in Figure P.17 for Line 2. The depths

of suspected delamination areas can be approximated through the B-scan. The line scans from the remaining lines are presented in Appendix P1. As shown in Figure P.17, the defective areas manifest themselves as areas with lower average moduli.

The planar variations in modulus, obtained by the USW method at two different depths, are shown in Figure P.18. All planar variations of modulus are presented in Appendix P1.

Chesapeake Channel Tunnel

Ceiling of Plenum

Figure P.19 shows the results from the IE and USW analyses of the data collected in the intact areas where no cracks or other surface damages were observed and with low dielectric constants (significantly less than 10).

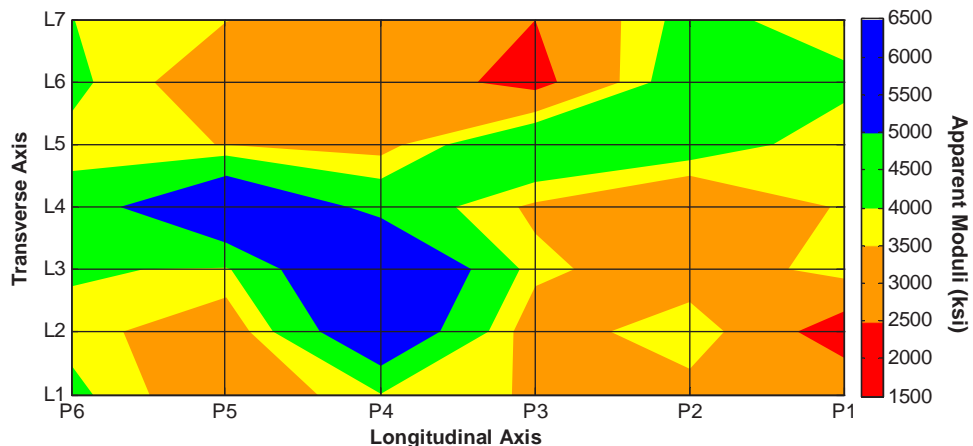


Figure P.16. Planar variation of average apparent modulus on meshed block, in Hanging Lake Tunnel.

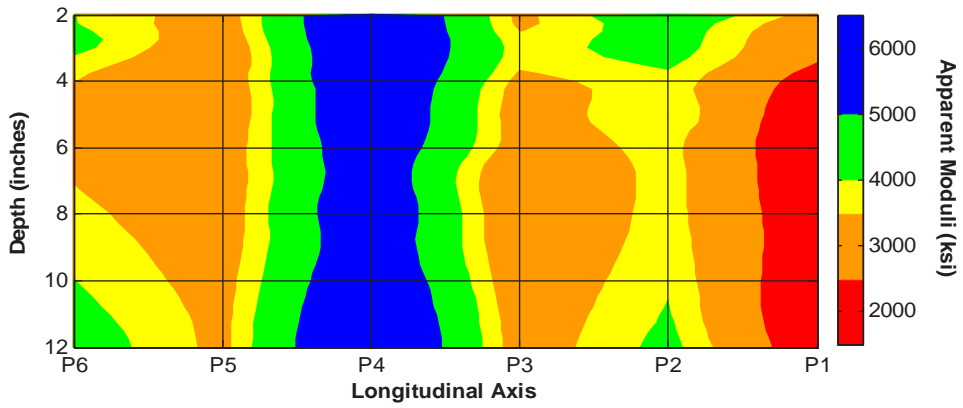


Figure P.17. Variation of apparent modulus with depth along L2 on meshed block, in Hanging Lake Tunnel.

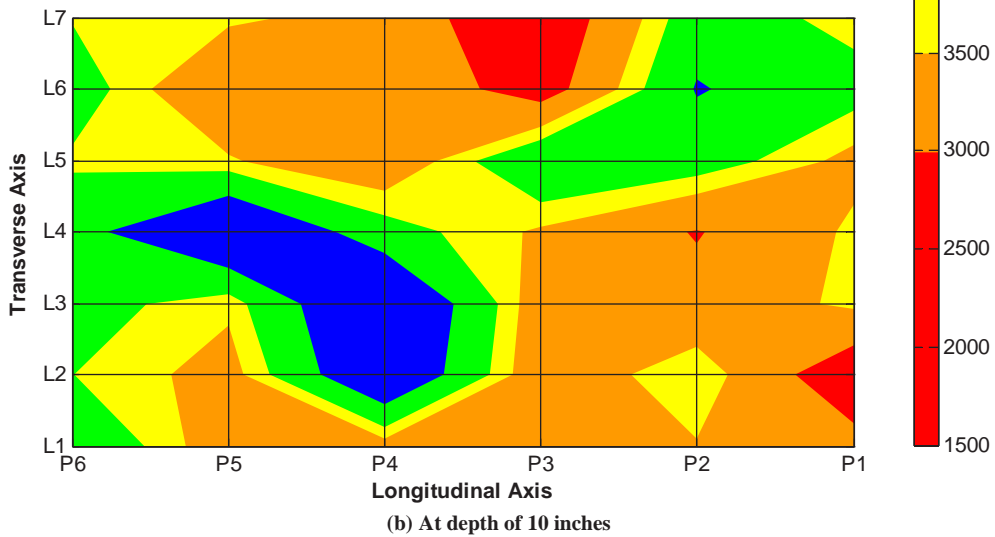
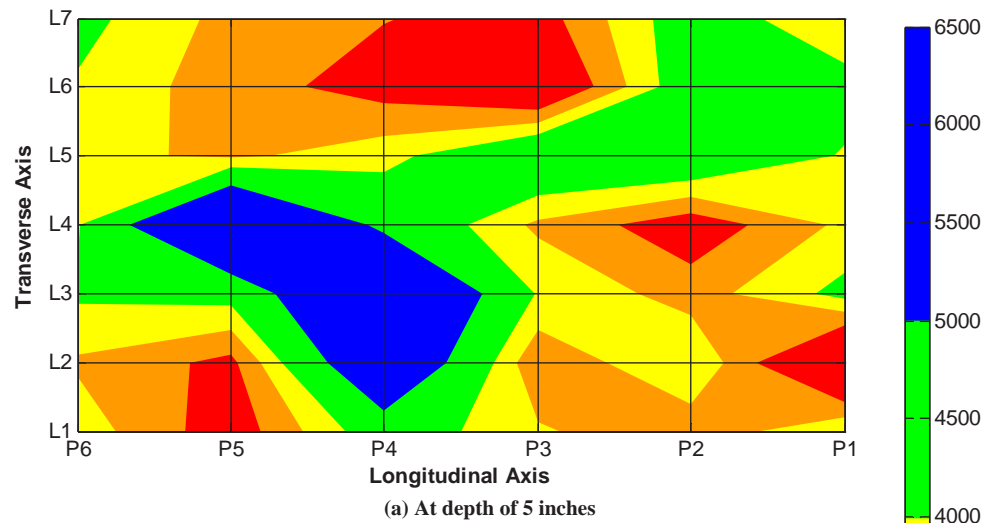


Figure P.18. Planar variation of apparent modulus at depths of 5 in. and 10 in. of meshed block, in Hanging Lake Tunnel.

The data used in Figure P.19 were actually from three separated intact spots within a distance of about 20 ft. Since they have the similar feature, the results are represented together. As shown in Figure P.19a, a clear and almost constant peak frequency of about 3 kHz represents the thickness echo of the concrete liner. This frequency results in a thickness of 2 ft for the concrete liner with an average compressive velocity of 13,800 ft/s per Equation P.1. However, Figure P.19b indicates that the concrete liner at these spots is quite uniform, with an average modulus of more than 4,000 ksi up to 12-in. penetration. The very high modulus values (indicated in blue in Figure P.19b) may reflect the high-velocity surface conditions.

The results from the PSPA tests for the 10 defective areas are shown in Figures P.20 through P.29. In general, the IE method exhibited higher peak frequencies compared with the thickness frequency, and the USW method showed lower moduli compared with the modulus of normal concrete at those defective areas or spots. For instance, in areas 477+60, 481+76, and 486+81, higher peak frequencies dominated the responses at several points in the IE B-scans. The calculated depths of delamination (by Equation P.1) agreed well with the depths of delamination in the USW B-scans. The anomalies or defects mainly distributed along the

transverse cracks on the plenum ceiling. Some exceptions occurred, such as in areas 473+56 and 491+25, where the IE and USW analyses were not consistent. That result can be attributed to the edge effect near the crack and placement of the PSPA sensor unit relative to the crack. When the crack is between the source and first receiver, the USW modulus is typically greater than normal because of the travel path of the wave. However, when the crack is between the two sensors, the reported USW modulus is lower than normal. The interpretation of the existence of the crack agrees well with the actual condition that was documented during visual inspection.

Wall of the Roadway

Tests with the PSPA on the wall of the roadway covered a distance of approximately 150 ft from Station 485+6 to Station 486+54 with uneven intervals, following the blue marks on the wall. Results are shown in Figure P.30. Test points 9 to 12 were actually restricted in a very small area about 2 ft by 2 ft. This area was characterized by an extremely low modulus and higher IE peak frequencies compared with the thickness frequency of the liner, indicating that a severe delamination or void was just behind the tile of the wall.

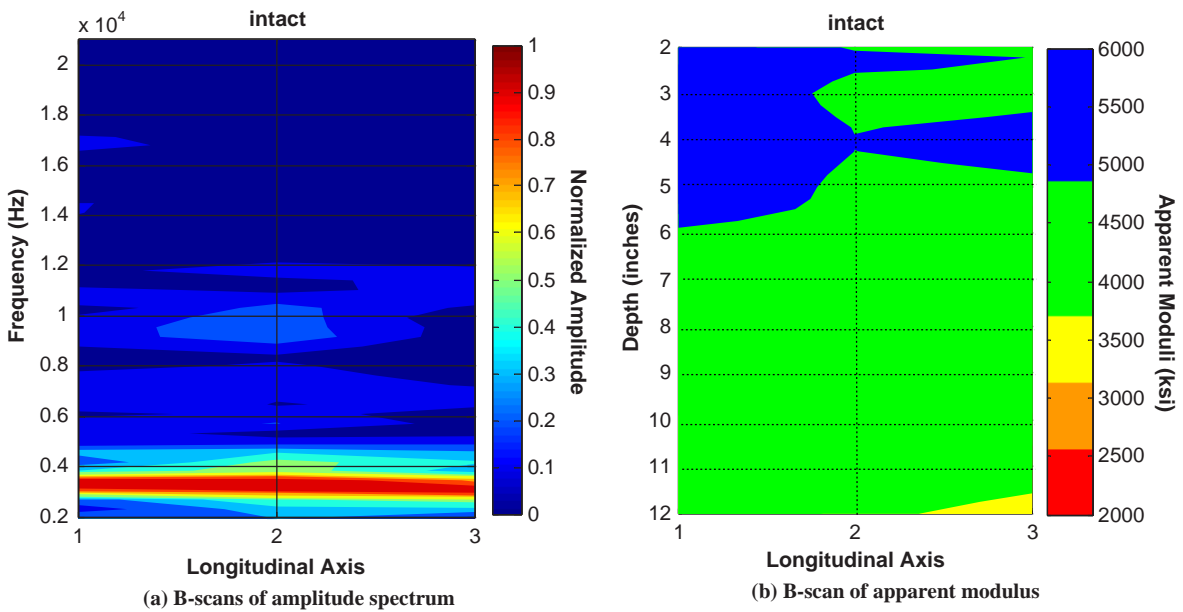


Figure P.19. PSPA results in an intact area on plenum ceiling, in Chesapeake Channel Tunnel.

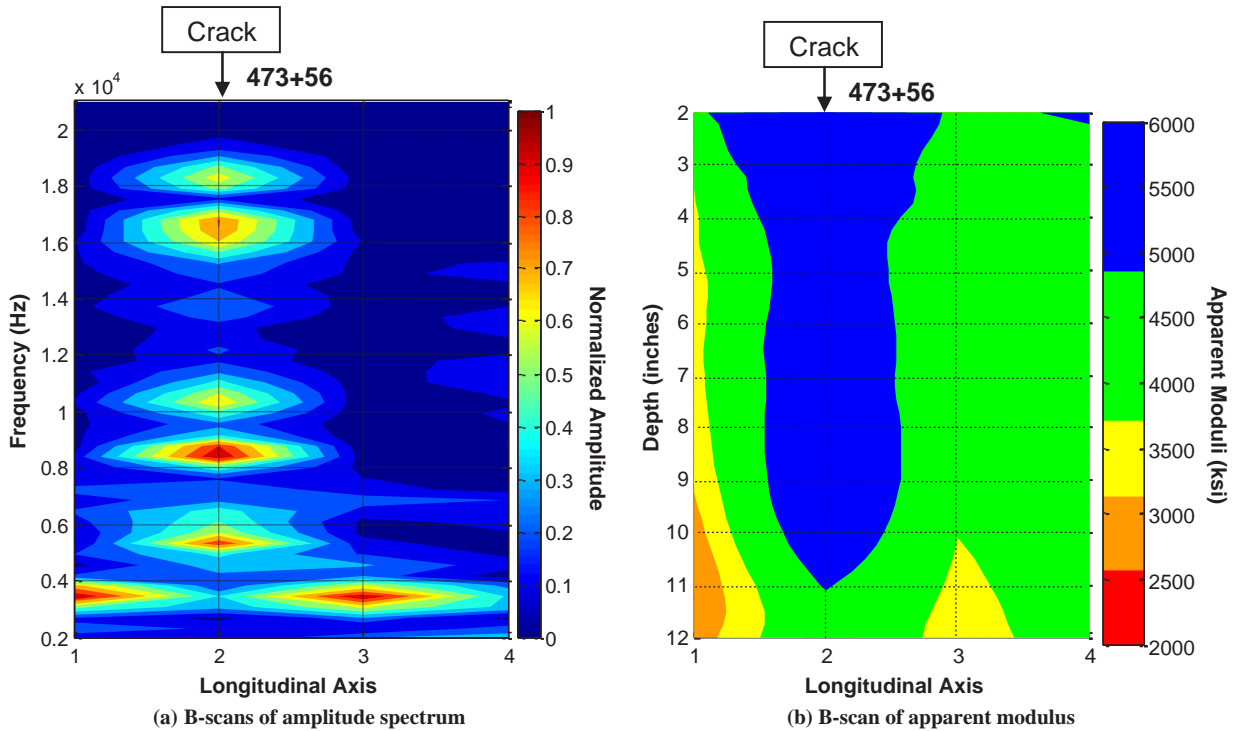
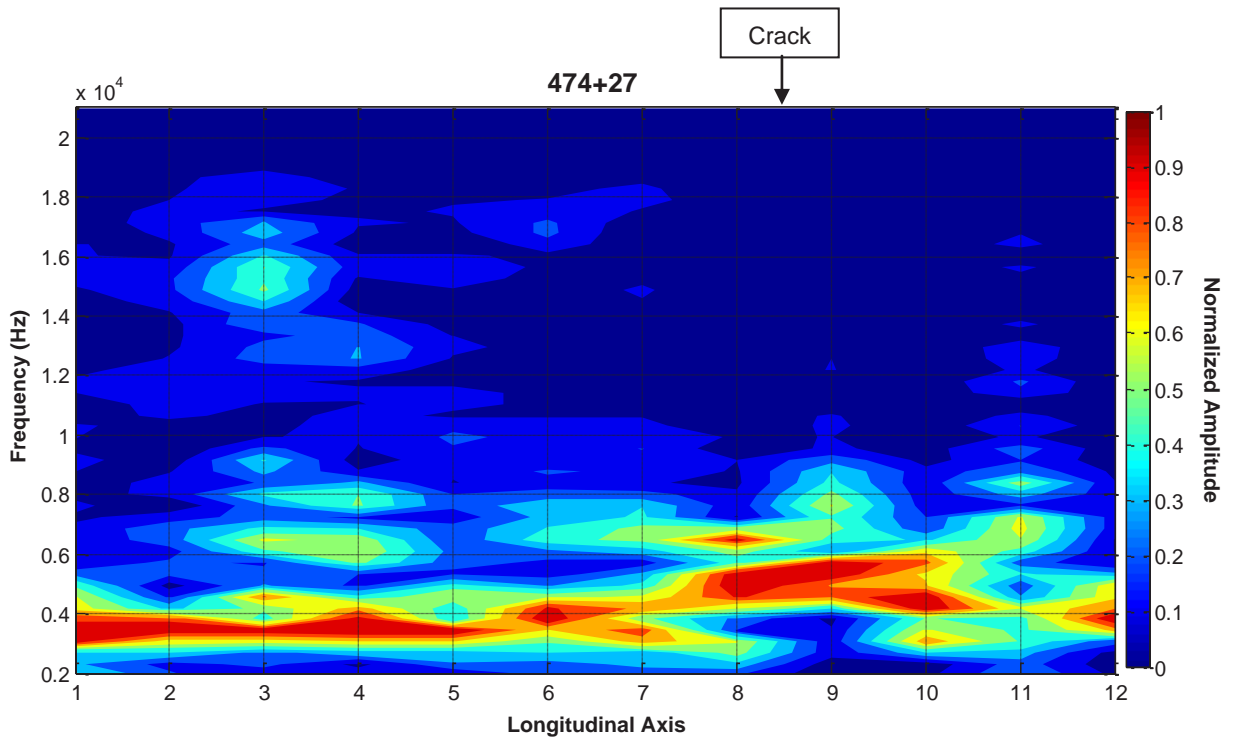
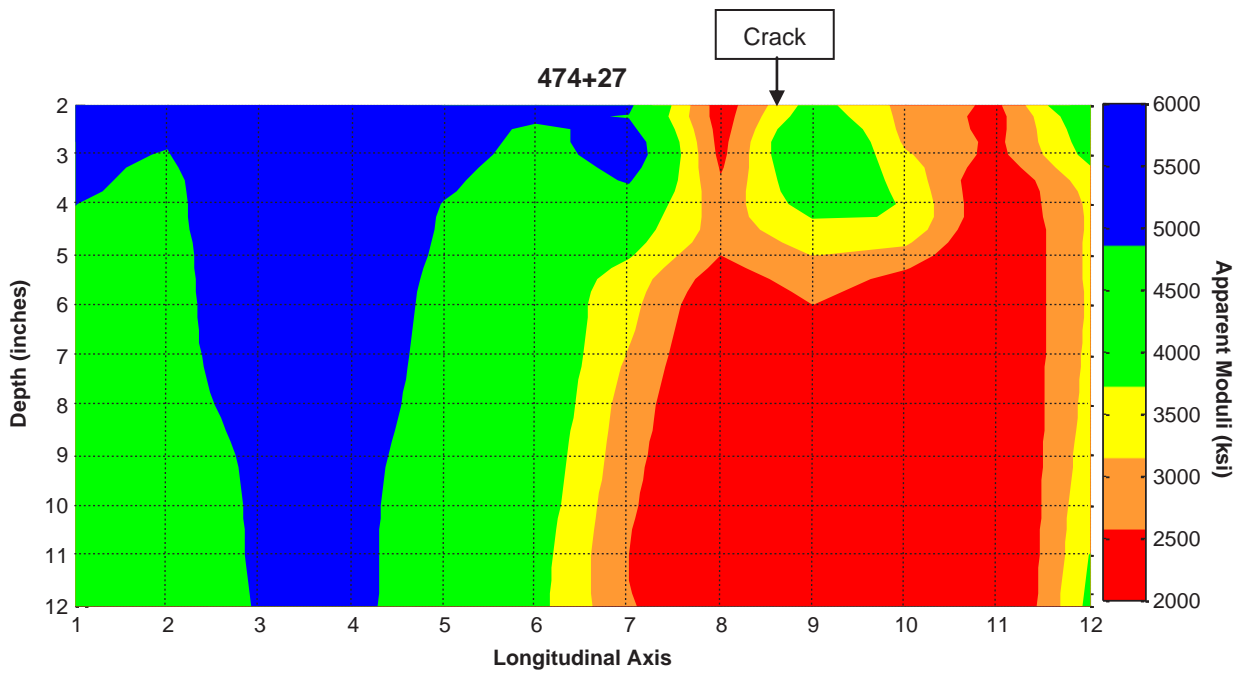


Figure P.20. PSPA results on plenum ceiling in area 473+56, in Chesapeake Channel Tunnel.



(a) B-scans of amplitude spectrum



(b) B-scan of apparent modulus

Figure P.21. PSPA results on plenum ceiling in area 474+27, in Chesapeake Channel Tunnel.

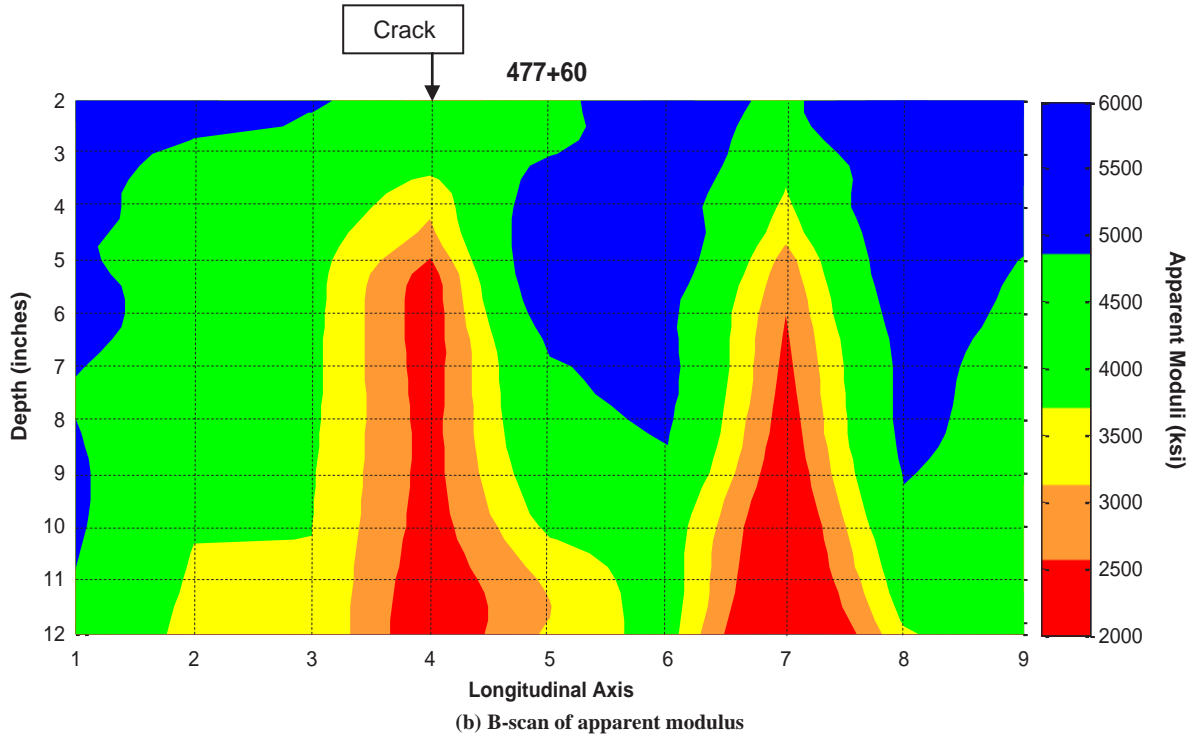
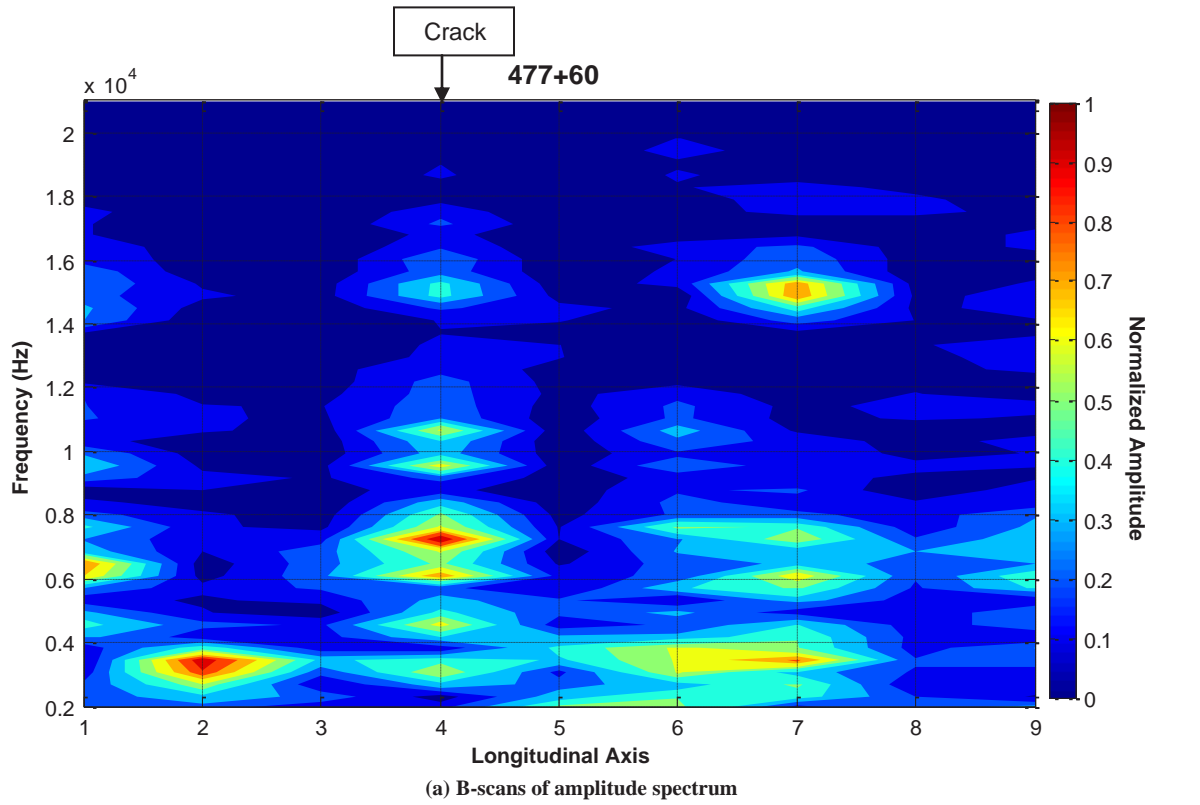


Figure P.22. PSPA results on plenum ceiling in area 477+60, in Chesapeake Channel Tunnel.

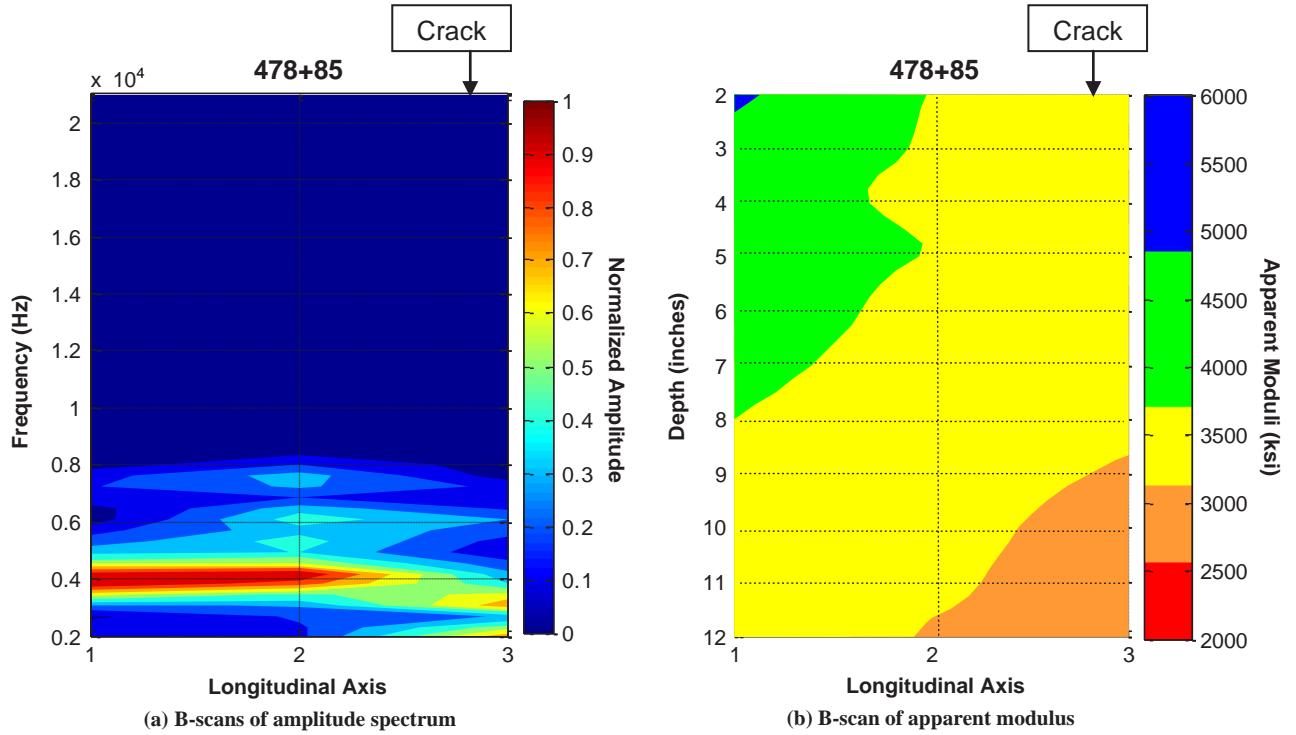


Figure P.23. PSPA results on plenum ceiling in area 478+85, in Chesapeake Channel Tunnel.

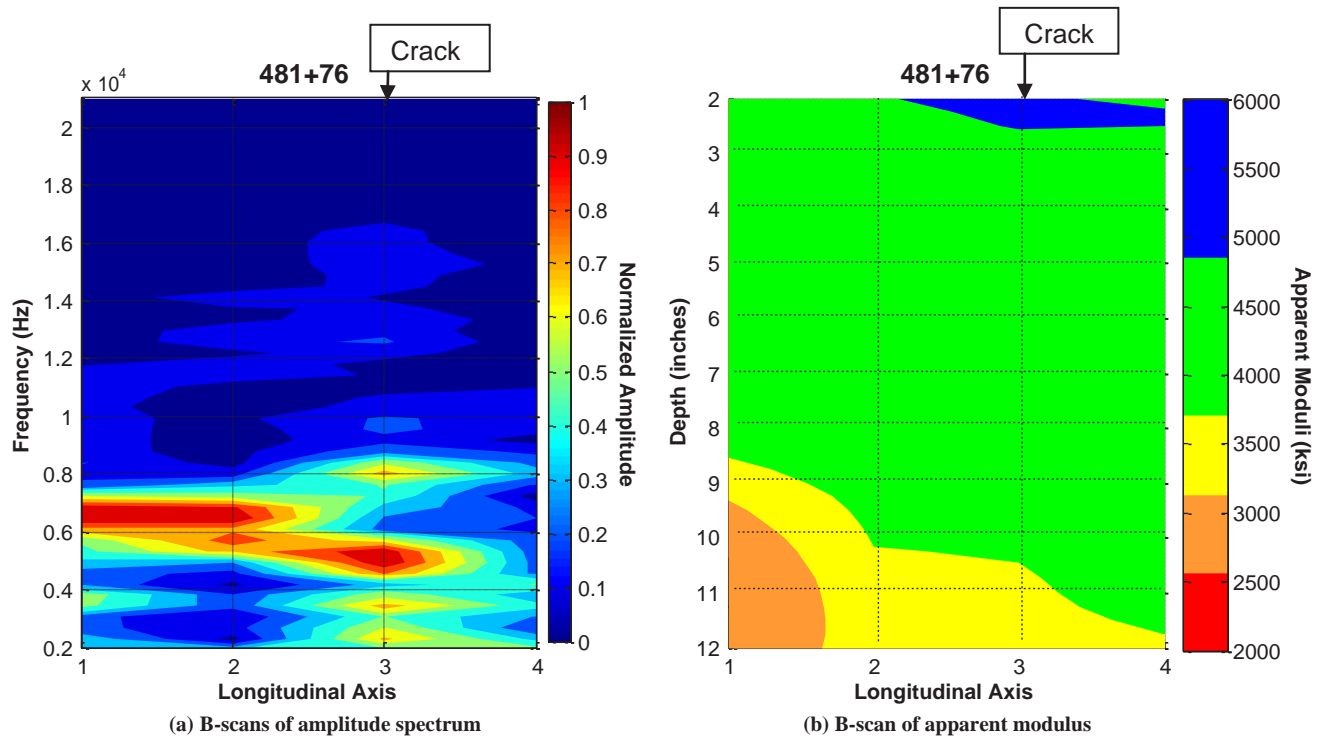


Figure P.24. PSPA results on plenum ceiling in area 481+76, in Chesapeake Channel Tunnel.

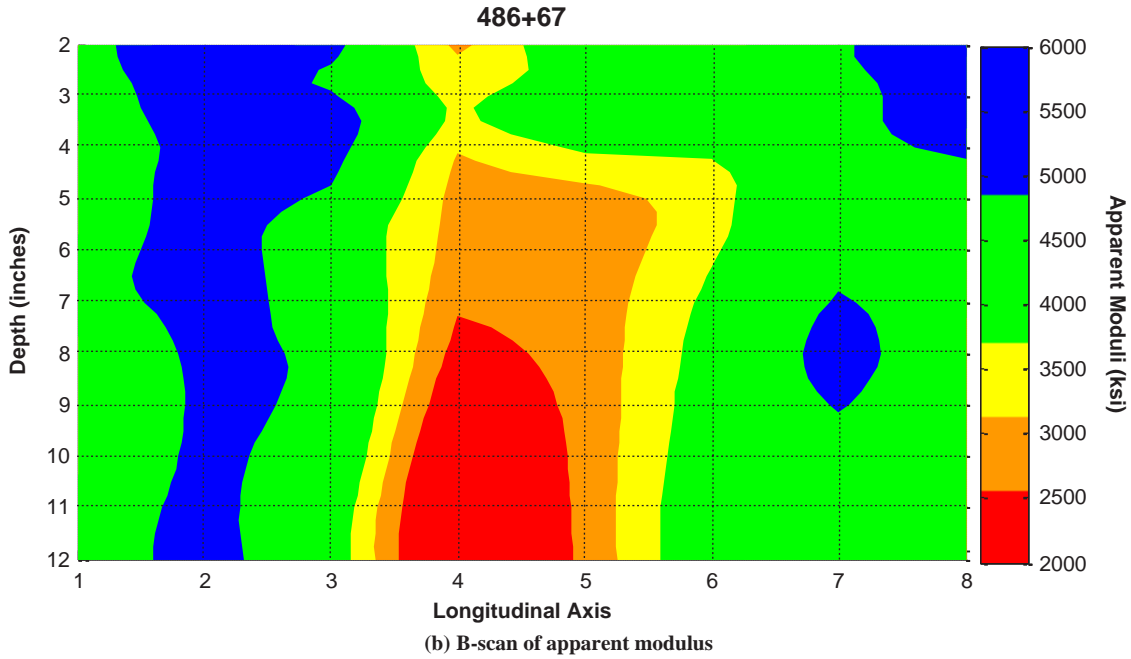
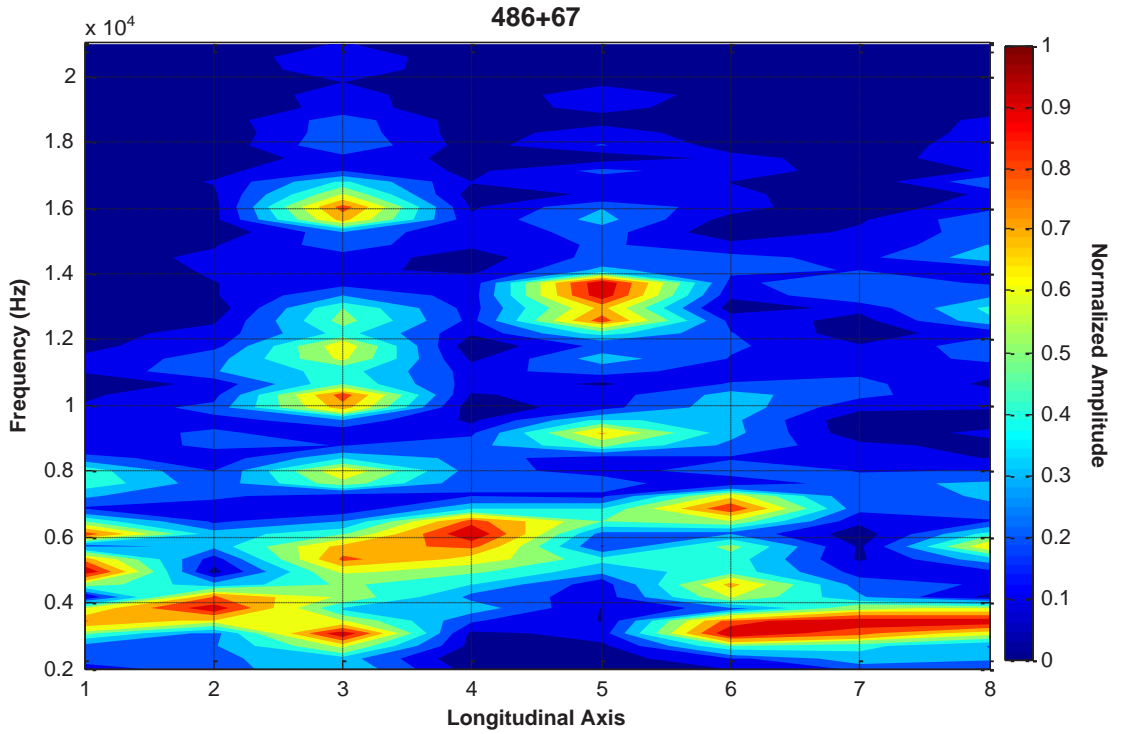


Figure P.25. PSPA results on plenum ceiling in area 486+67, in Chesapeake Channel Tunnel.

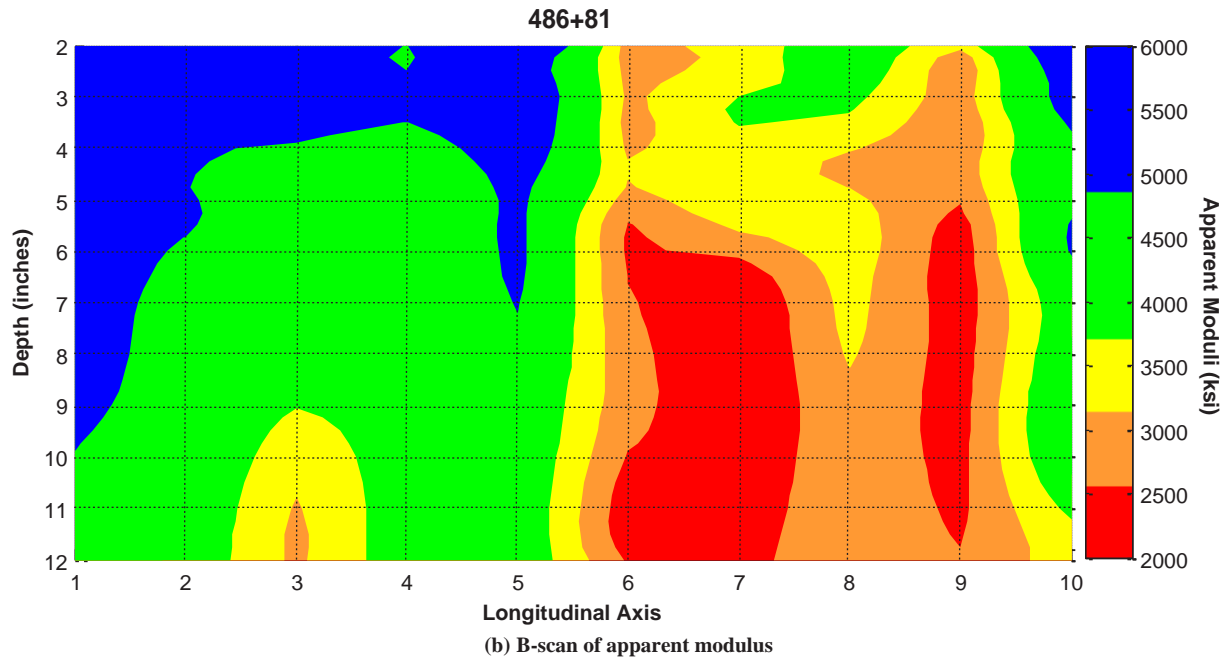
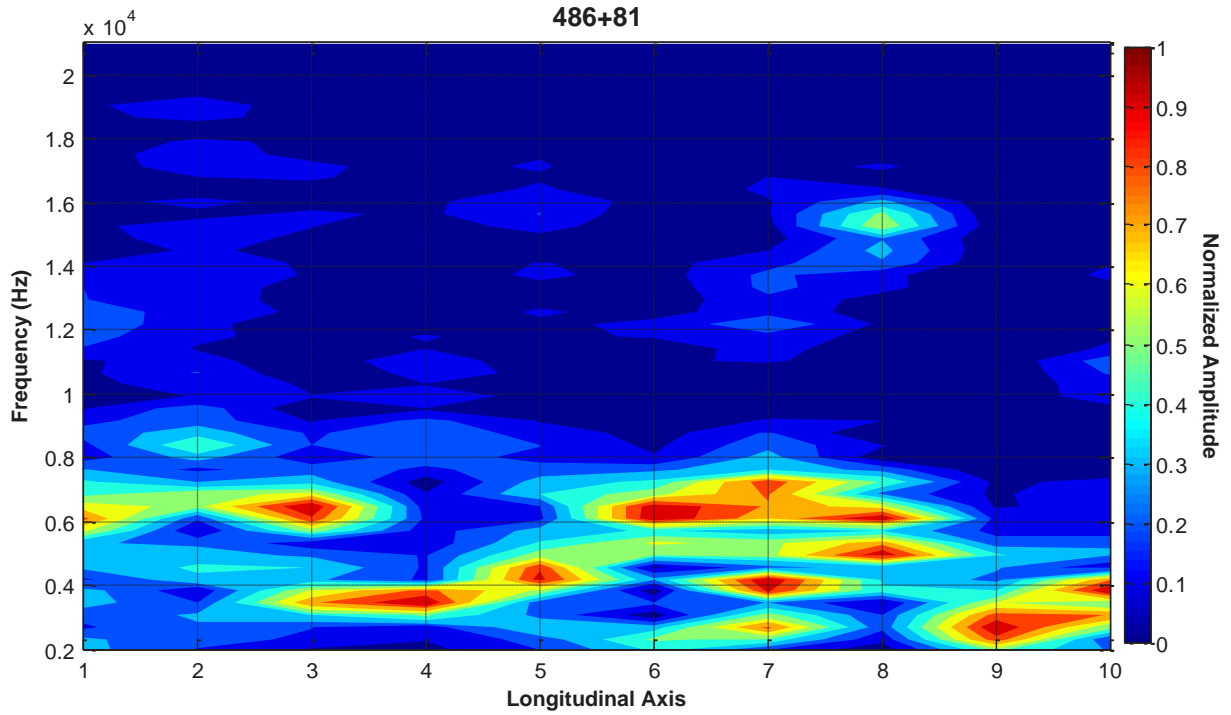


Figure P.26. PSPA results on plenum ceiling in area 486+81, in Chesapeake Channel Tunnel.

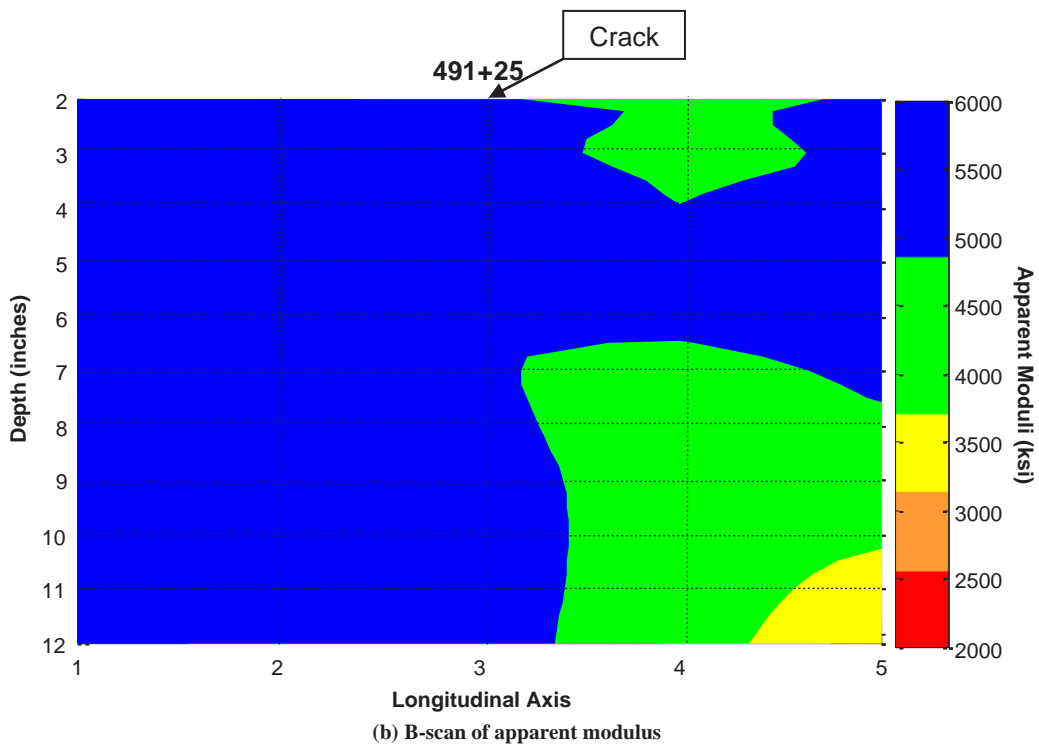
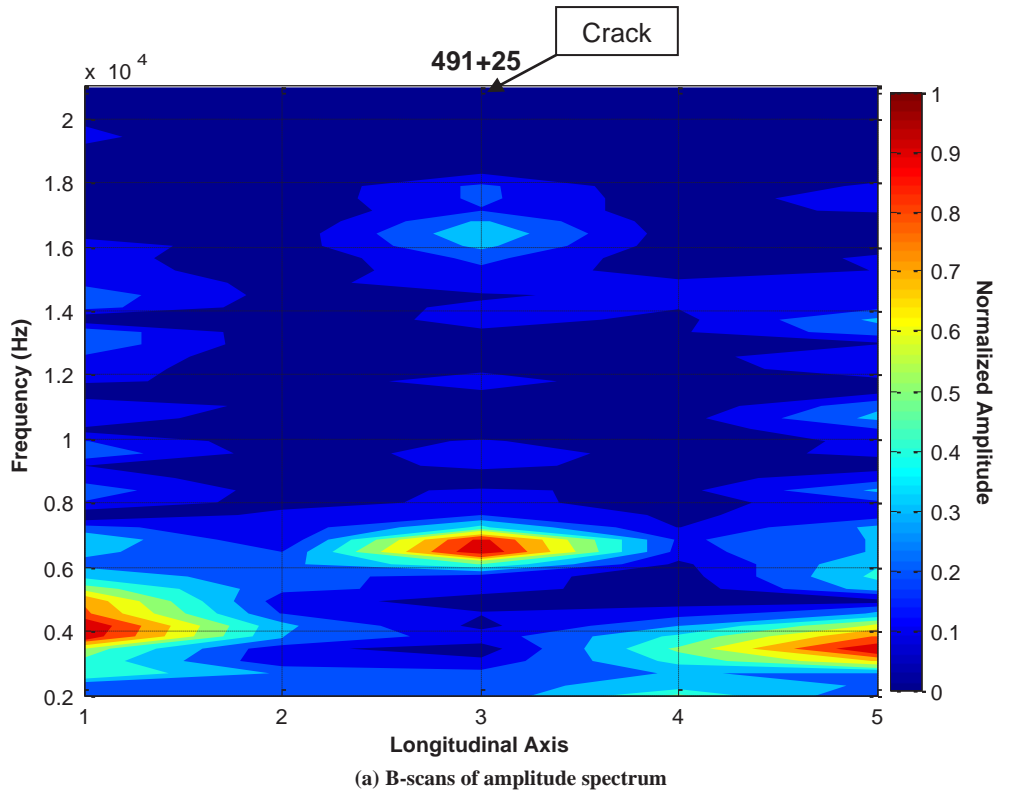


Figure P.27. PSPA results on plenum ceiling in area 491+25, in Chesapeake Channel Tunnel.

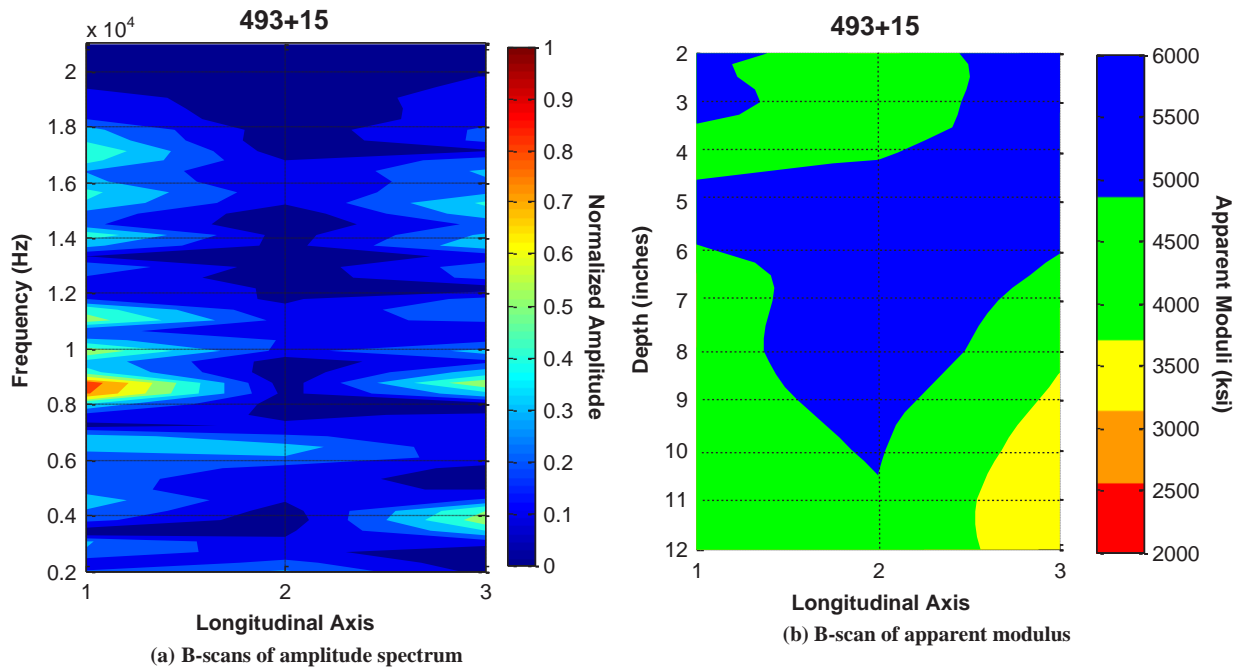


Figure P.28. PSPA results on plenum ceiling in area 493+15, in Chesapeake Channel Tunnel.

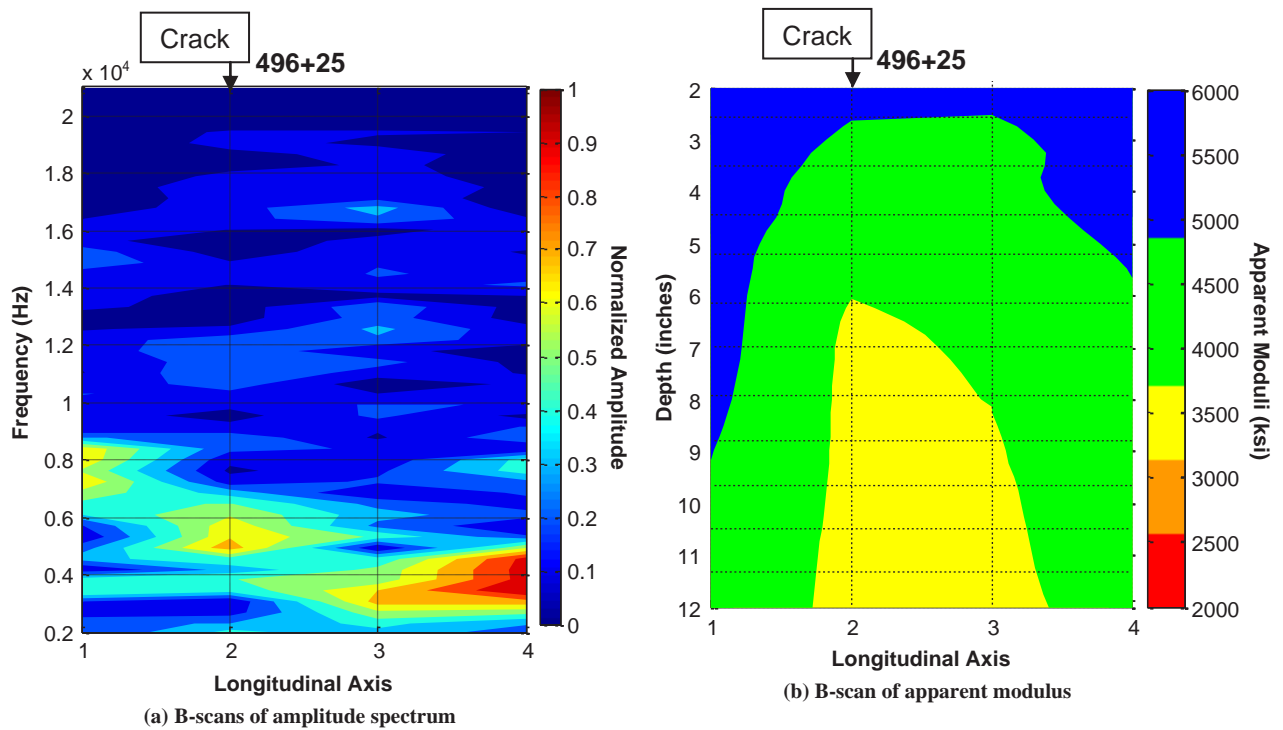
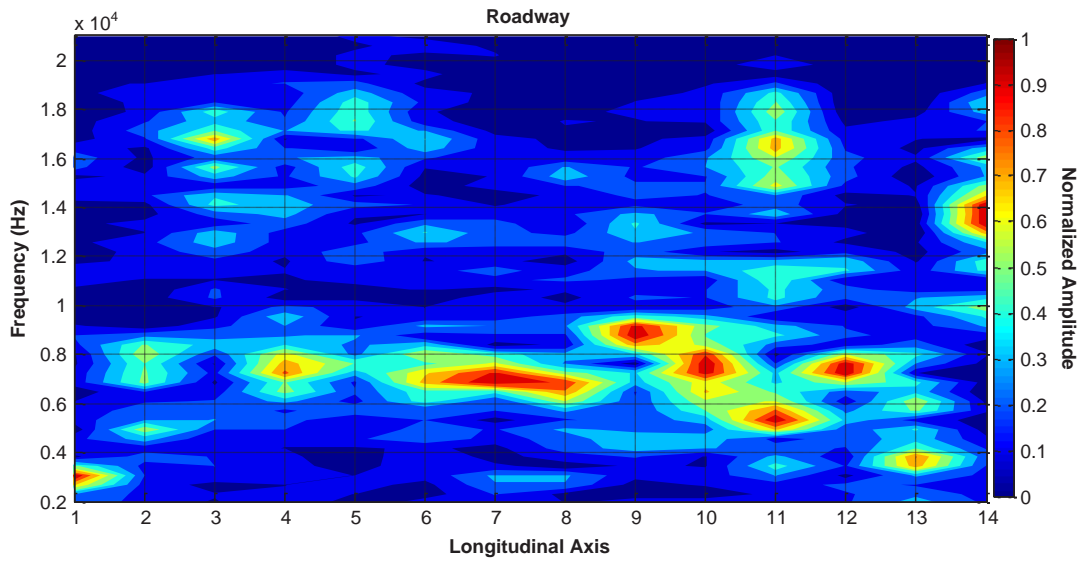
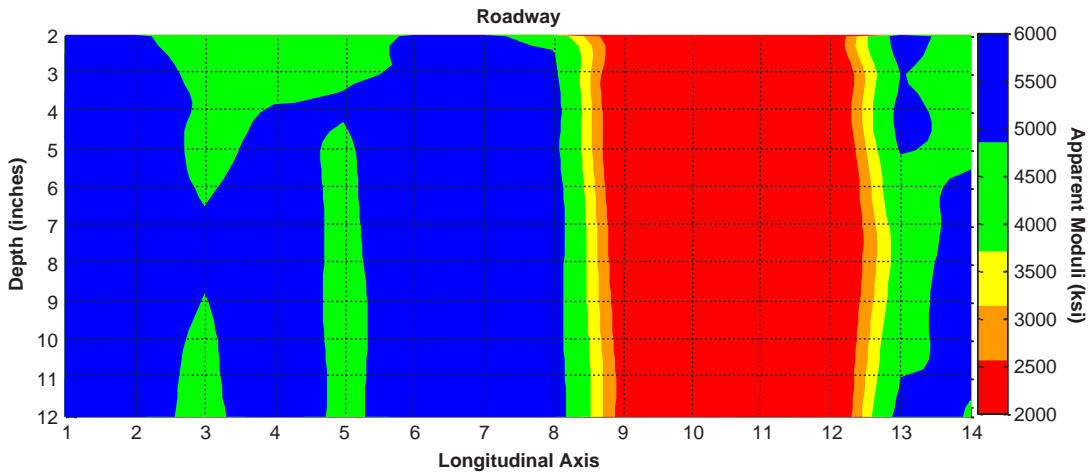


Figure P.29. PSPA results on plenum ceiling in area 496+25, in Chesapeake Channel Tunnel.



(a) B-scans of amplitude spectrum



(b) B-scan of apparent modulus

Figure P.30. PSPA results on wall of roadway, in Chesapeake Channel Tunnel.

Appendix P1

The remaining line scans and planar variations of modulus are presented here.

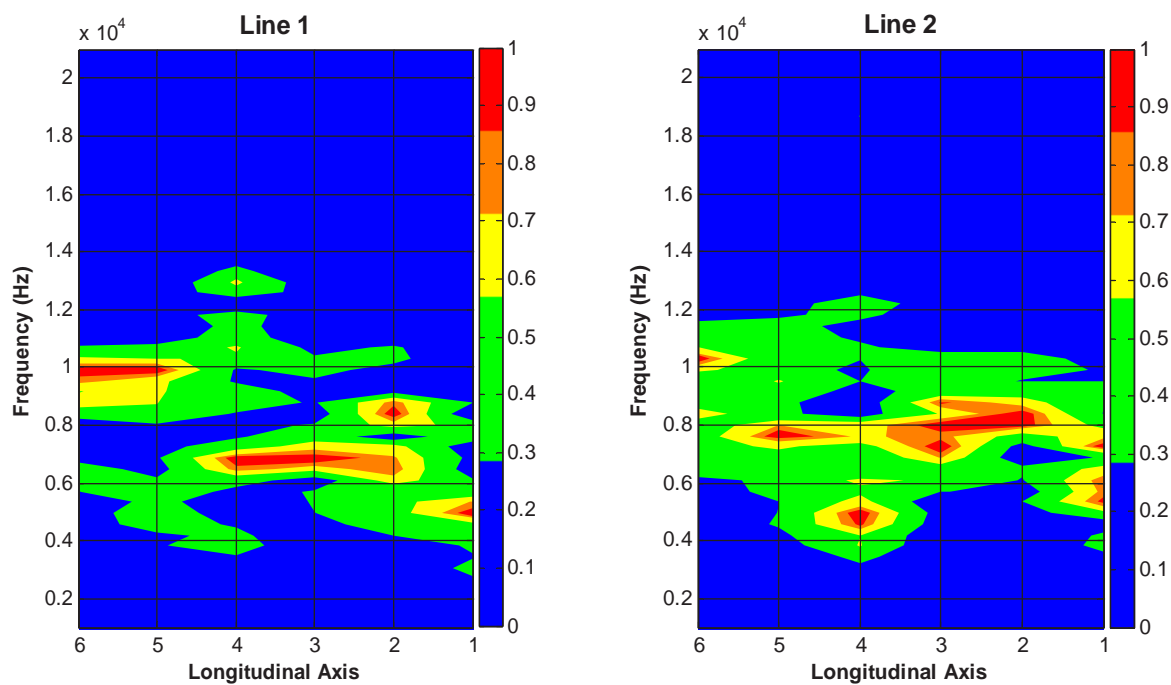


Figure P1.1. IE Spectral B-scans on meshed blocks, in Hanging Lake Tunnel. (Continued on next page.)

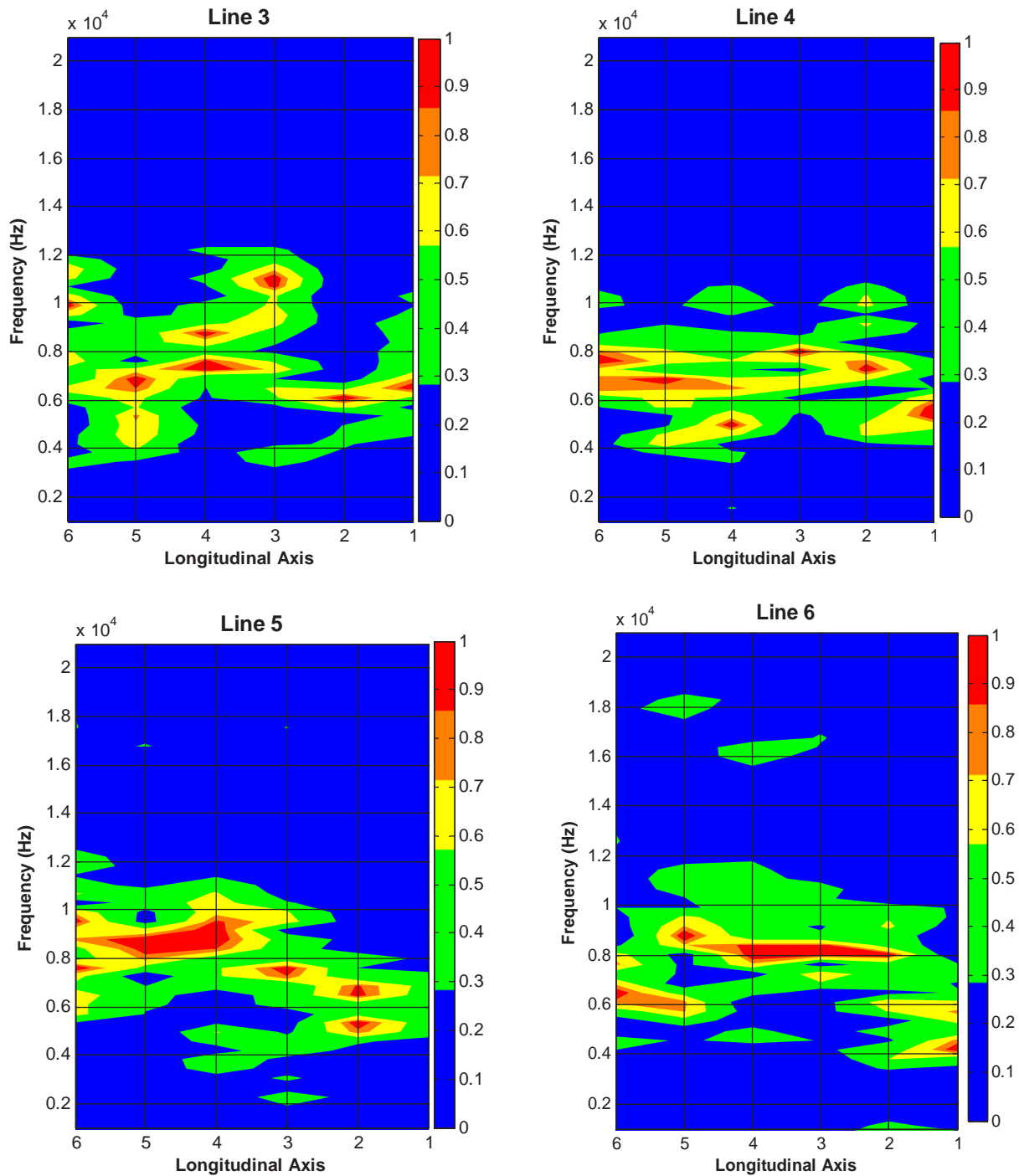


Figure P1.1. (Continued.)

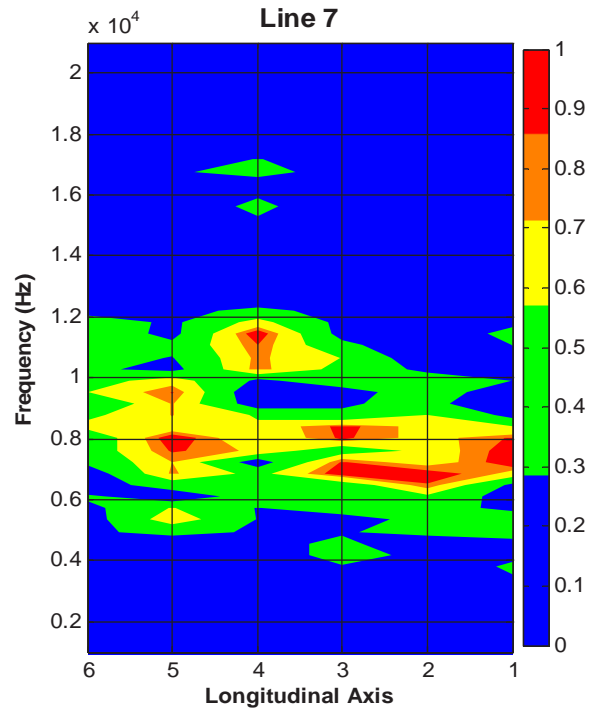


Figure P1.1. (Continued.)

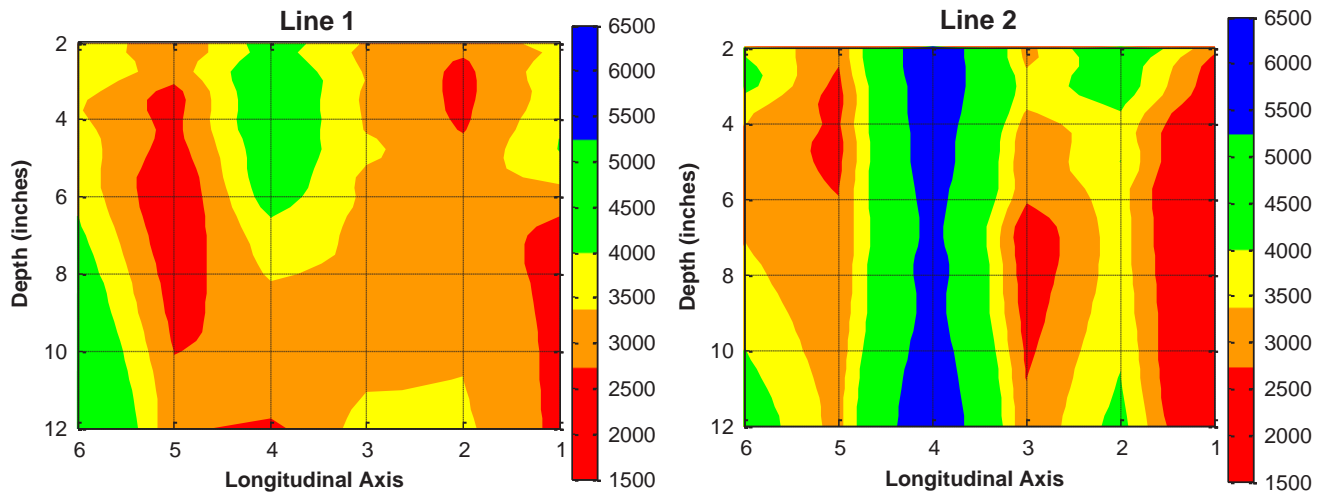


Figure P1.2. Variation of apparent modulus with depth on meshed block, in Hanging Lake Tunnel. (Continued on next page.)

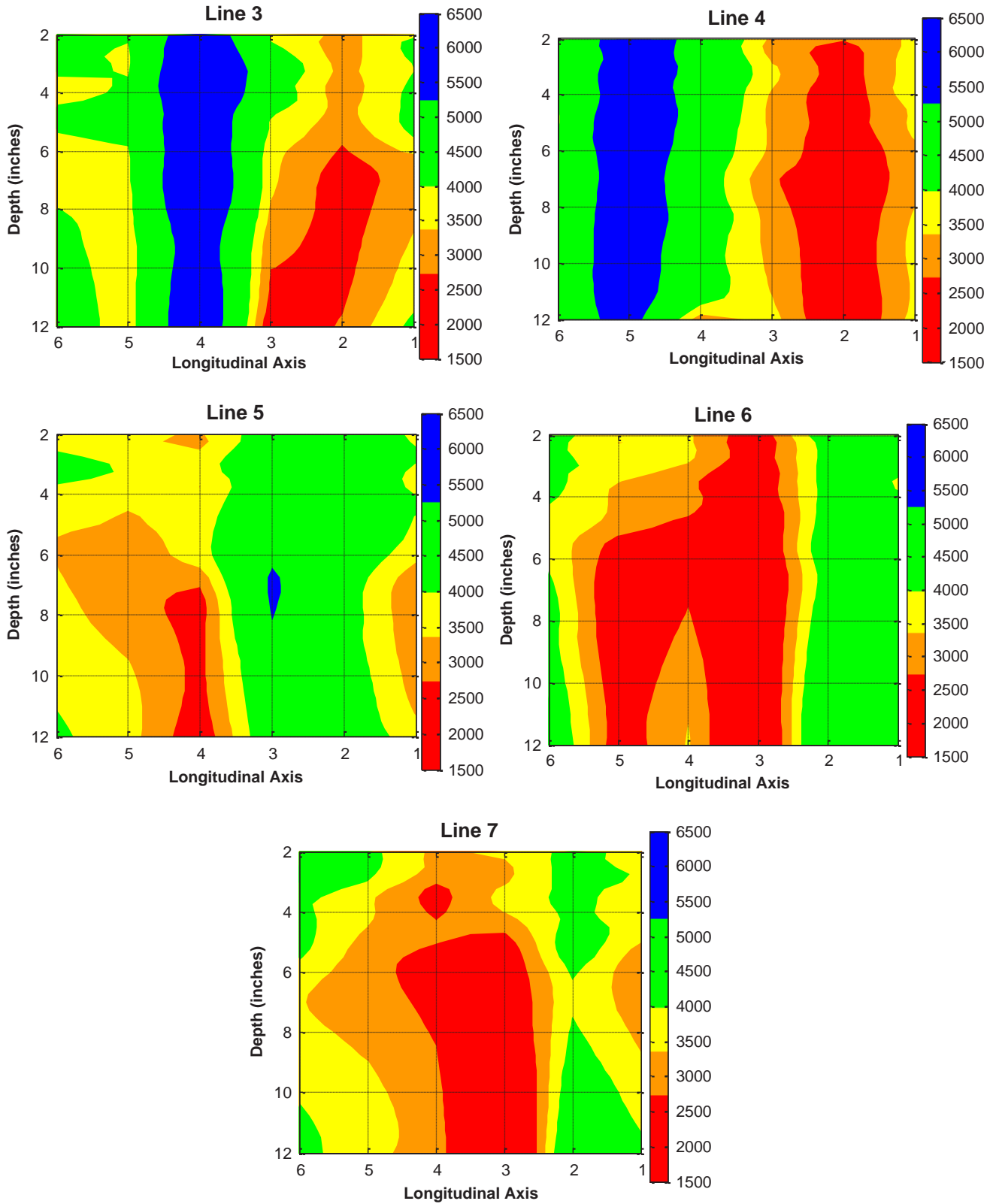


Figure P1.2. (Continued.)

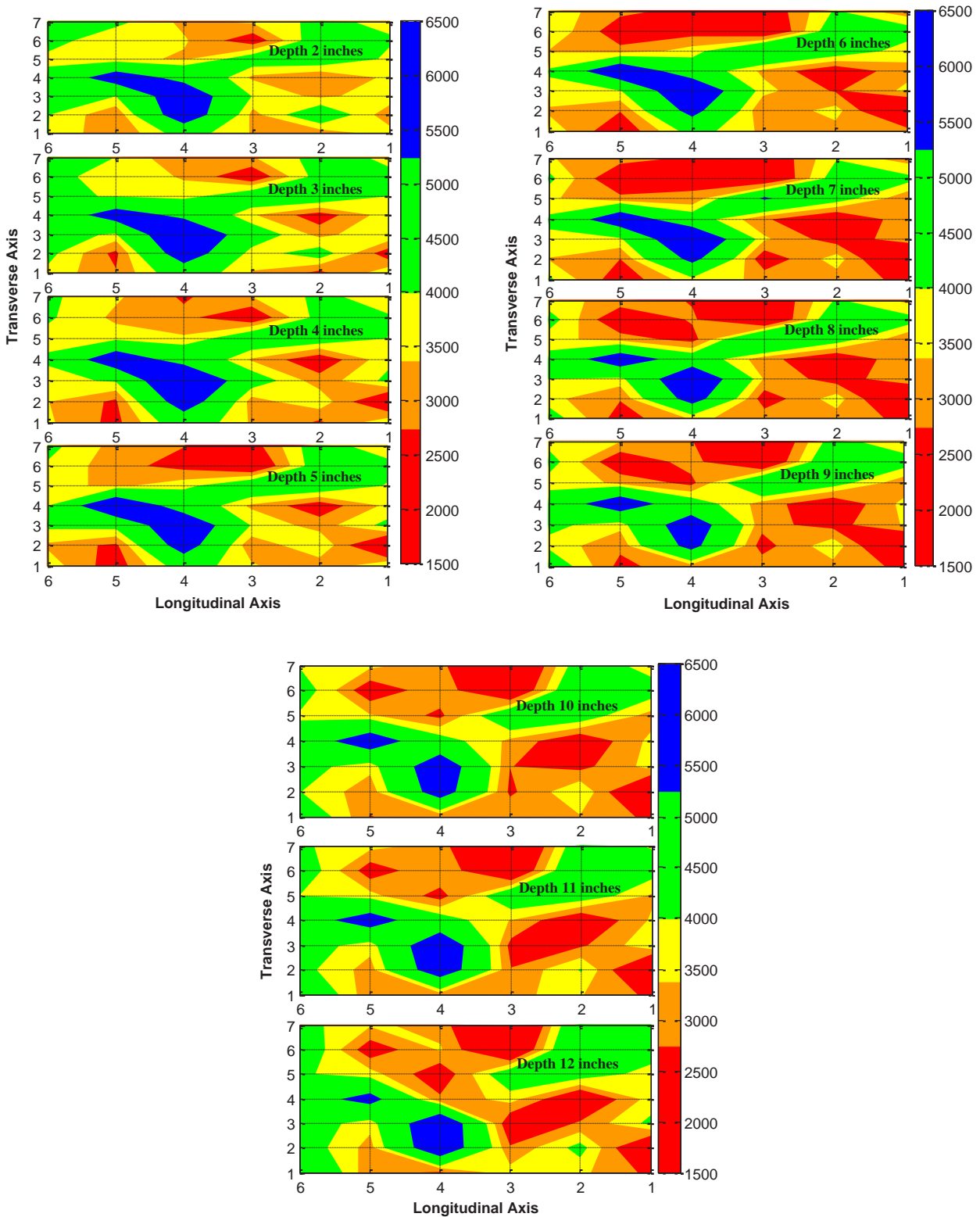


Figure P1.3. Planar variation of apparent modulus at different depths for meshed block, in Hanging Lake Tunnel.

References

Carino, N. J., M. Sansalone, and N. N. Hsu. 1986. A Point Source–Point Receiver, Pulse-Echo Technique for Flaw Detection in Concrete. *ACI Material Journal*, Vol. 83, No. 2, pp. 199–208.

Gucunski, N., and A. Maher. 1998. Bridge Deck Condition Monitoring by Impact Echo Method. *Proc., International Conference MATEST '98—Life Extension*, Brijuni, Croatia, pp. 39–45.

APPENDIX Q

BAM Testing in U.S. Tunnels

Testing Program

The Federal Institute for Materials Research and Testing (BAM) in Germany carried out field testing between October 3 and 12, 2011, in three tunnels in the United States: two in Colorado (Eisenhower Memorial Tunnel and Hanging Lake Tunnel) and one in Virginia (Chesapeake Bay Bridge-Tunnel). In each tunnel, selected areas were tested using three nondestructive testing (NDT) techniques: ground-penetrating radar (GPR), ultrasonic echo (designated as US in test area sketch figures), and impact echo (IE). The allocated testing time in each tunnel was limited. The number and location of the test areas were selected on the basis of either preanalysis (mostly thermography) or the existence of visual distress. The on-site working conditions were also taken into account. Table Q.1 provides the details of the test program, including the number and size of test areas in each tunnel as well as the testing methods.

Tunnel Description

Eisenhower Memorial Tunnel

The Eisenhower Memorial Tunnel is located approximately 60 mi west of Denver, Colorado, on I-70 and is a part of the Colorado Department of Transportation. It is the highest vehicular tunnel in the world, located, on average, at an elevation of 11,112 ft. It is 1.693 mi long and runs through a mountain within the Arapaho National Forest. Figure Q.1 shows a construction information bulletin from the tunnel side. Figure Q.2 shows the entrance to the tunnel as well as one of the supply air ducts where measurements took place. Construction started in March 1968 and was completed in March 1973. The information about this tunnel was obtained from the Colorado Department of Transportation website (Colorado DOT 2011).

Hanging Lake Tunnel

The Hanging Lake Tunnel stretches more than 4,000 ft through a mountain bordering the Glenwood Canyon in Colorado as

part of I-70. The most noteworthy feature of the tunnel is the direct change of I-70 from bridge to tunnel (Figure Q.3). Construction started in 1980 and was completed in 1992. The entrance to the tunnel and the supply air duct are shown in Figure Q.3.

Chesapeake Bay Bridge-Tunnel

The Chesapeake Bay Bridge-Tunnel is part of a bridge-tunnel system connecting Virginia's Eastern Shore with its mainland. The tunnel itself is 1 mi long, going under the Atlantic Ocean. Construction started in November 1960, and the first part was opened in April 1964. Figure Q.4 shows a bulletin board from the side and a view of the supply air duct where most measurements were taken.

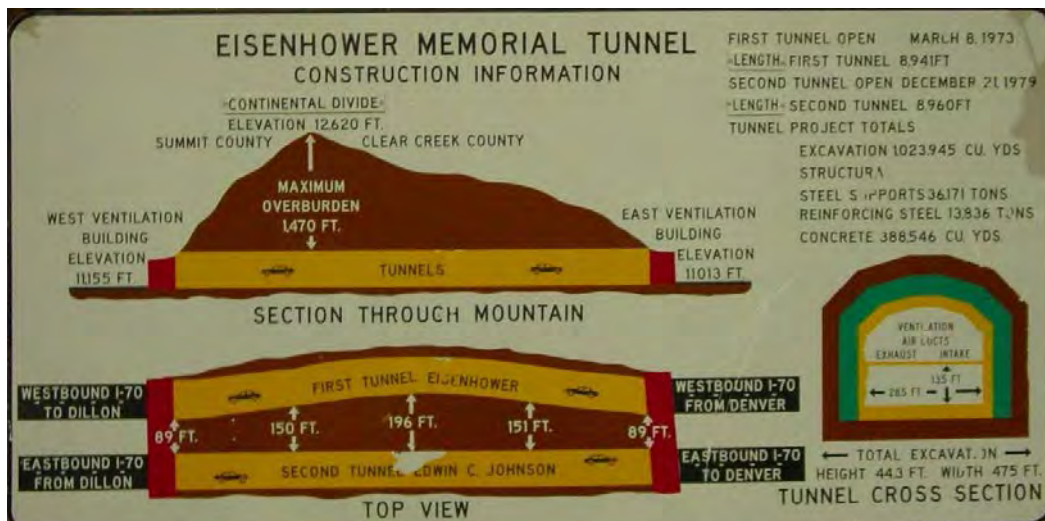
Measurement Techniques

The different measurement equipment BAM used for this project can be mounted on an automated scanning device developed by BAM. The ZFP scanner (Figure Q.5) (Zoega et al. 2012) can be used on horizontal surfaces as well as vertical surfaces, including overhead testing, even in narrow areas. The scanner is fixed to the surface using vacuum “feet” or plates. When running acoustic tests requiring contact, choosing 1-in.-grid spacing allows a speed of operation of 11 sq ft/h (1 sq m/h). With noncontact transducers such as air-coupled radar antenna, testing at a speed of 156 sq ft/h would be possible. The field of measurement can be up to 17.6 sq ft (4.2 ft by 4.2 ft).

The advantage of the ZFP scanner is its easy and fast on-site assembly. It can be carried in a relatively light and small package. Its size allows the scanner to be transported in cars and carried through small openings to reach difficult-to-access areas such as the vents above tunnels. The commonly used equipment for NDT of structures—including GPR, ultrasonic echo, and IE devices—can be easily attached to the scanner for testing and detached after completing the measurements. The scanning and NDT data acquisition are controlled by a single

Table Q.1. Overview of BAM Field-Testing Program, October 2011

Code	Tunnel	Location	Date	Technique	Size (in.)	Spacing (in.)	Notes
EH1	Eisenhower	Seg 3 Block 2-3	10/03/2011	US	40 × 40	1	
				IE	2 × 24	1	
EH2	Eisenhower	Seg 11 Block 1	10/04/2011	US	40 × 24	1	anomaly, reinforcement
				IE	40 × 24	1	
				GPR	40 × 24	2	anomaly, reinforcement
HL1	Hanging Lake	Seg 56/57	10/05/2011	US	48 × 24	1	anomaly
				IE	48 × 24	1	anomaly
				GPR	48 × 24	2	beam, dowels, reinforce
HL2	Hanging Lake	Seg 57	10/05/2011	US	48 × 24	1	crack, reinforcement
				IE	48 × 24	1	backwall?
				GPR	48 × 24	2	crack, reinforcement
HL3	Hanging Lake	Seg 57/58	10/06/2011	US	48 × 24	1	reinforcement
				IE	48 × 24	1	
				GPR	48 × 24	2	joint, dowels
CPB1	Chesapeake Bay Bridge	St.No. 474+27	10/11/2011	US	48 × 24	1	anomaly, backwall, reinforce.
				IE	46 × 24	1	anomaly, backwall
				GPR	48 × 24	2	reinforcement
CPB2	Chesapeake Bay	St.No. 481-76	10/12/2011	US	40 × 24	1	backwall, anomaly, reinforce.
				IE	40 × 24	1	backwall, anomaly
				GPR	40 × 24	2	reinforcement
CPB3	Chesapeake Bay	St.No. 486-67	10/12/2011	US	48 × 24	1	anomaly, backwall, reinforce.
				IE	48 × 24	1	backwall, anomaly
				GPR	48 × 24	2	reinforcement
CPB4	Chesapeake Bay	St.No. 487	10/12/2011	US	48 × 36	1	
				IE	4 × 36	1	condition of tile bonding
				GPR	48 × 36	2	reinforcement



Source: Colorado DOT 2012

Figure Q.1. Construction information, Eisenhower Memorial Tunnel.



(a)



(b)

Figure Q.2. Entrance to the Eisenhower Memorial Tunnel (a) and the interior of the supply air duct where measurements took place (b).

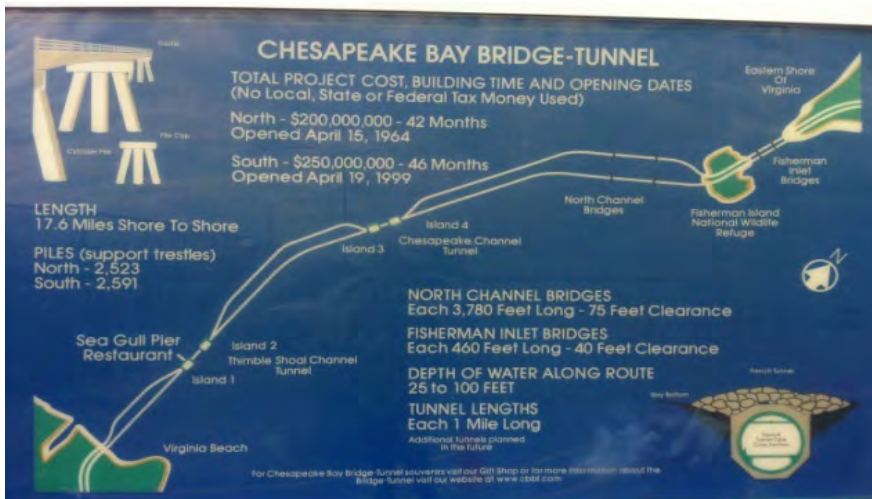


(a)



(b)

Figure Q.3. Hanging Lake Tunnel entrance (a) (Salek 2002) and supply air duct where measurements took place (b).



(a)



(b)

Figure Q.4. Construction information for the Chesapeake Bay Bridge-Tunnel (a) and supply air duct where most measurements took place (b).



(a)



(b)

Figure Q.5. ZFP scanner packed in its custom-made box (a) and on site in Chesapeake Bay Bridge-Tunnel with ultrasonic echo transducer mounted on it (b).

notebook. This simplifies the control and reduces the equipment and weight of the measurement system.

The three NDT techniques and the typical data from each are briefly discussed below.

GPR

Basic Operation Principles

Ground-penetrating radar is a widely used subsurface scanning tool that was employed here to detect subsurface defects in tunnel linings. GPR sends discrete electromagnetic pulses into the structure and then captures the reflections from subsurface layer interfaces. Radar is an electromagnetic wave and therefore obeys the laws governing reflection and transmission of electromagnetic waves in layered media. At each interface within a structure, a part of the incident energy is reflected and a part is transmitted. The ratio of reflected to transmitted energy depends on the electromagnetic contrast of the material on either side of the interface.

Two main types of GPR equipment are typically used for civil structure investigations. High-speed air-coupled GPR systems are capable of testing at speeds up to about 50 mph

and can penetrate up to 24 in. in some materials. They are excellent tools for network-level data collection. High-frequency ground-coupled GPR systems provide better depth penetration and high densities of readings and are excellent for project-level data collection and applications concerned with locating steel and defects such as voids in concrete. Their limitation is that they must stay in close contact with the material being tested, making the speed of data collection relatively slow (1 mph to 5 mph).

GPR antennas can emit electromagnetic pulses of different frequencies. The choice of frequency depends on the required depth of penetration and depth resolution. In general, lower-frequency antennae have a better resolution in deeper depth. Higher-frequency antennae show better details of reflectors close to the surface but do not penetrate the test object as deeply. Determining which antenna to use therefore depends on the task, the experience of the user, and other NDT methods used at the scene.

In this study, BAM used a ground-coupled GPR from Geophysical Survey Systems Inc. (GSSI), with a center frequency of about 1.5 GHz (Figure Q.6).

Typical Results

Ground-coupled GPR has proved very useful in discovering reinforcements, dowels, surface cracks, moisture, and other intrusions. As shown in Figure Q.7, scanner testing on fine grids provides the opportunity to generate B-, C-, and D-scans from the measurements. Reinforcement bars and dowels are best seen in C-scans and recognized by their unusually high reflection amplitudes of positive phase (white strips) and linear geometries. Surface cracks are best seen in B- or D-scans and recognized by near-surface hyperbolas. Any unusual feature detected in the radar scans is hereafter referred to as an *anomaly*. Anomalies are usually reflections of significant amplitude or extent, where reflections from the geometrical boundaries are not expected. For example, in Figure Q.7d the area in the C-scan exhibiting unusually high amplitudes with reverse phase is designated as an anomaly.

Ultrasonic Echo

Basic Principles of Operation

In this test, a single ultrasonic transducer was used to generate and detect ultrasonic waves in the structure. Ultrasonic is based on the measurement of propagation time to localize cracks, voids, and deteriorations, as well as the thickness of a structure. The speed of ultrasonic pulses propagating through the structure is often correlated to material strength and thus a measure of material quality. Ultrasonic echo was employed here to inspect tunnel linings to estimate the thickness of the

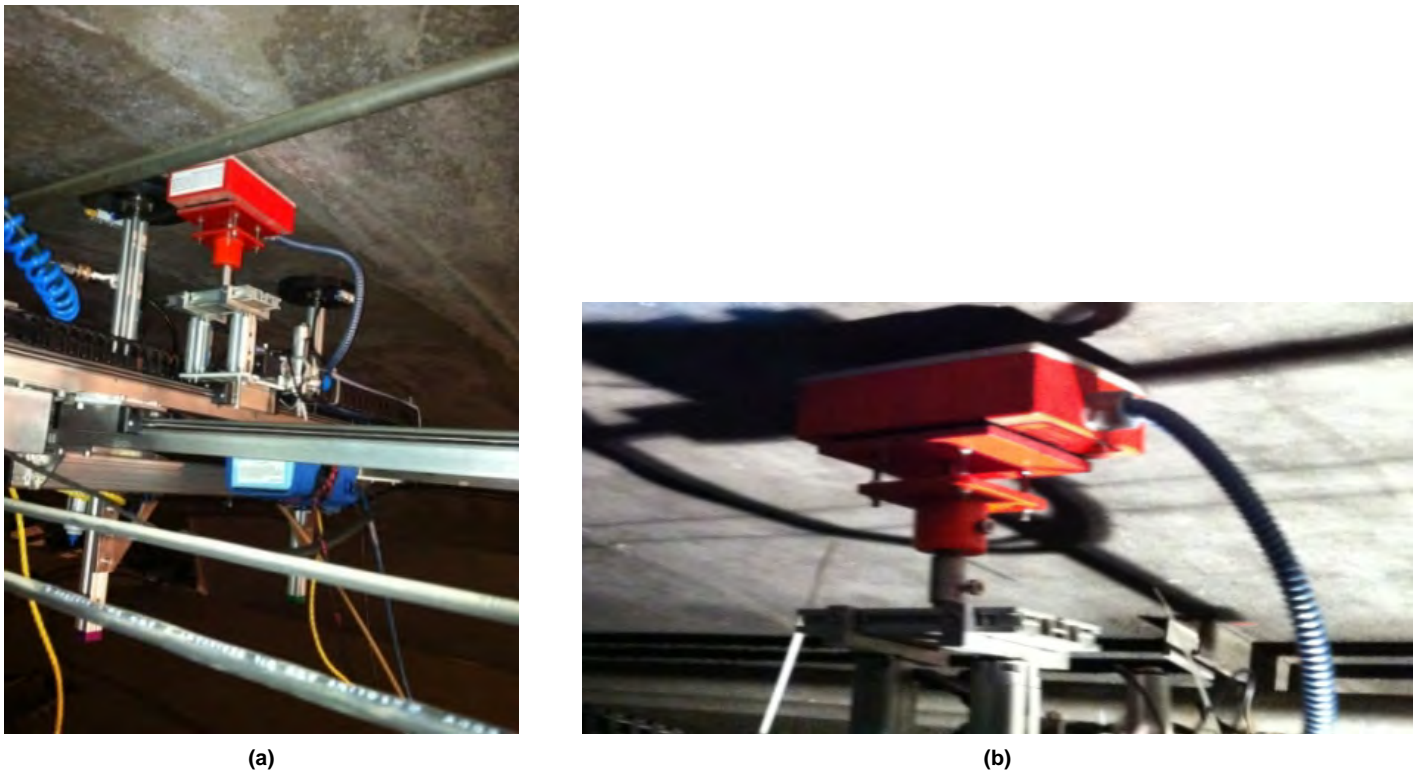


Figure Q.6. 1.5-GHz ground-coupled GPR antenna mounted on the scanning system (a) and close-up view (b).

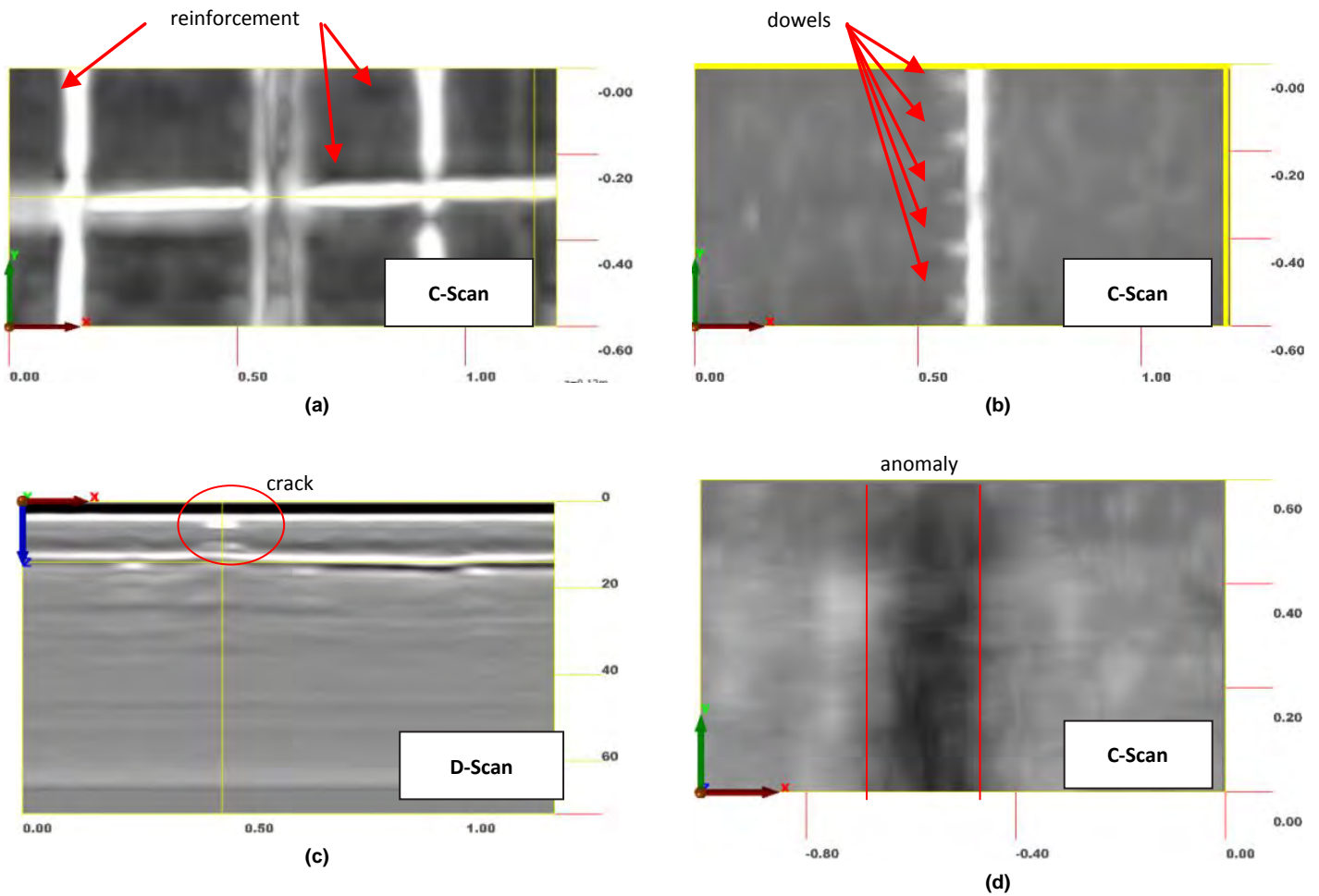


Figure Q.7. Typical radar scans illustrating (a) reinforcement, (b) dowels, (c) surface crack, and (d) anomaly.

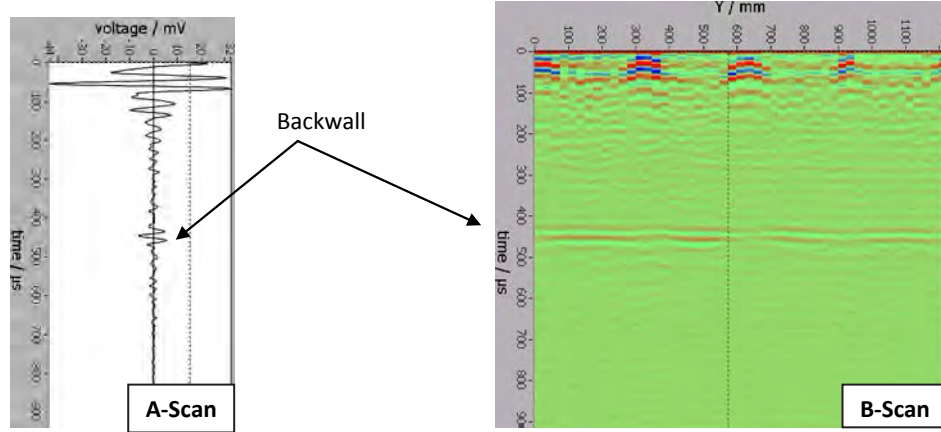


Figure Q.8. Typical A-scan and B-scan along Chesapeake Bay Bridge-Tunnel lining.

lining and detect/locate defects and anomalies within the lining. In the absence of ground truth data, the wave-speed of the lining material was either assumed or estimated from surface measurements. As such, the thickness of the tunnel lining as well as the depth of the reflectors could only be approximated. Ultrasonic data collection was done automatically using the previously described scanning system.

As data collection was conducted point-by-point following a predefined grid, the resulting signals (A-scans) were processed and presented in real time as evolving B-, C-, and D-scans. Figure Q.8 shows typical A- and B-scans obtained in one of the tunnels. The A-scan shows the intensities of the reflections over time for each point of measurement. The evolution of the A-scans along the profile can be seen in the B-scan. Heterogeneities are recognized by their high reflection amplitudes. Knowing the wave propagation speed made it possible to estimate the depth of the reflector, which could

be the tunnel lining backwall or defects. The collected data set could be further processed using the synthetic aperture focusing technique (SAFT) algorithm (Schickert et al. 2003) to give a clearer image (higher signal-to-noise ratio) of the internal structure of the test volume; see Figure Q.9).

The phase diagram shows the change in phase of ultrasonic waves at the detected interfaces within the material. The color-coded local phase diagram helps distinguish between the reflections from steel objects and from air interfaces. Relative to concrete, steel is of higher and air is of lower impedance. Therefore, the phase of the reflected waves at concrete-steel interfaces and concrete-air interfaces are different. This can be seen in Figure Q.9 where a 180° phase shift (red color) is visible at the location of the rebars, while the backwall reflections exhibit negative phase shifts of 0° to -100° .

The advantage of ultrasonic testing is its potential to detect different types of defects such as voids, cracks, honeycombs,

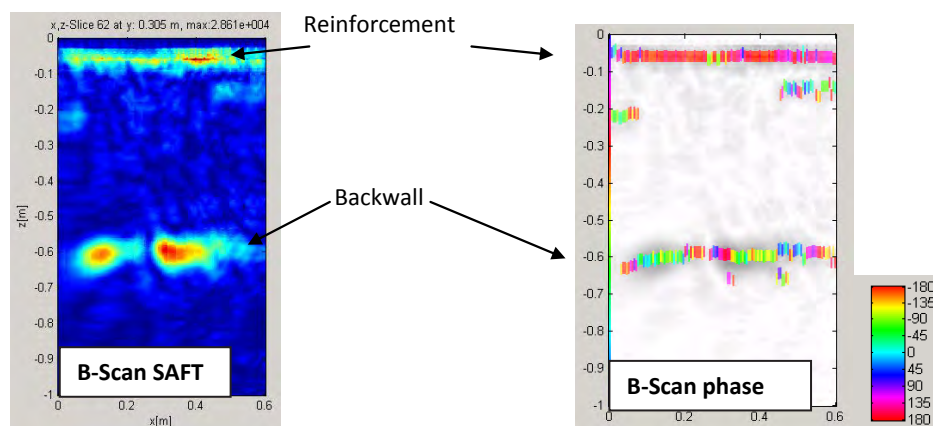


Figure Q.9. Postprocessed ultrasonic data using SAFT, including both amplitude and phase evaluation.

and delaminations directly or indirectly, in real time. Furthermore, it can estimate the strength of the material and estimate the structure thickness. Conventional ultrasonic equipment is available and fairly inexpensive. The main limitation is that the transducers must be in contact with the surface of the structure, which slows down the speed of the automated scanning systems.

The ultrasonic equipment used by BAM was the A1220. It is a low-cost, multisensor, dry-contact, low-frequency, shear wave transducer developed by Acoustic Control Systems, Ltd. in cooperation with BAM. It includes 24 spring-mounted ultrasonic transducers with a nominal frequency of 50 kHz, out of which 12 serve as transducers and the other 12 as receivers. This construction ensures that a higher amount of ultrasonic energy is transmitted and the reflected and recorded signals can be averaged, thereby minimizing the scatter noise. The images in Figure Q.10 depict the A1220 being used as a handheld device and mounted on the ZFP scanner. For postprocessing of the data (i.e., analysis, SAFT, and phase evaluation), two different programs were used: one program was developed at BAM by Rüdiger Feldmann and the other program at the University of Kassel by Dr. Klaus Meyer.

Typical Results

Ultrasonic echo was able to detect the backwall of tunnel linings directly, reinforcement directly, possible delamination directly and indirectly, surface cracks indirectly, and intrusions in an otherwise homogeneous volume directly (see Figure Q.11). The indirect detection of reflectors was possible by the “shadow effect,” that is, by recognizing a missing portion

of an otherwise consistent element of the tunnel lining, such as backwall or reinforcement.

Impact Echo

Basic Principles of Operation

IE involves introducing a stress pulse into concrete, commonly by application of a mechanical impact on the surface of the structure. A broadband transducer located on the surface close to the impact source (usually at a distance of 2 in. to 4 in.) is used to record vertical deformations of the surface caused by the arrival of incident and reflected waves (or echoes). The response of solid or delaminated plates subjected to IE testing is distinctly different: thickness resonance vibrations in case of solid plates, and plate-like flexural vibrations in the presence of shallow, severe delaminations (Shokouhi 2005). Intermediate conditions result in a response superimposing these two.

The time and frequency characteristics of the recorded response can be used to deduce the condition of the structure. Figure Q.12 shows two typical time signals (top) and frequency spectra, one corresponding to a supposedly sound area of a tunnel lining with the backwall as the only reflector with a frequency peak at 3.15 kHz, and the other on a supposedly delaminated area, where the spectrum has multiple peaks. The peak in the frequency spectrum of the supposedly sound area is the resonance frequency of the tunnel lining depth. The dominant response of a severely delaminated deck to an impact is characterized by a low-frequency response because of oscillations of the upper delaminated portions of the deck. This response is almost always in the audible frequency range. Because it is significantly lower

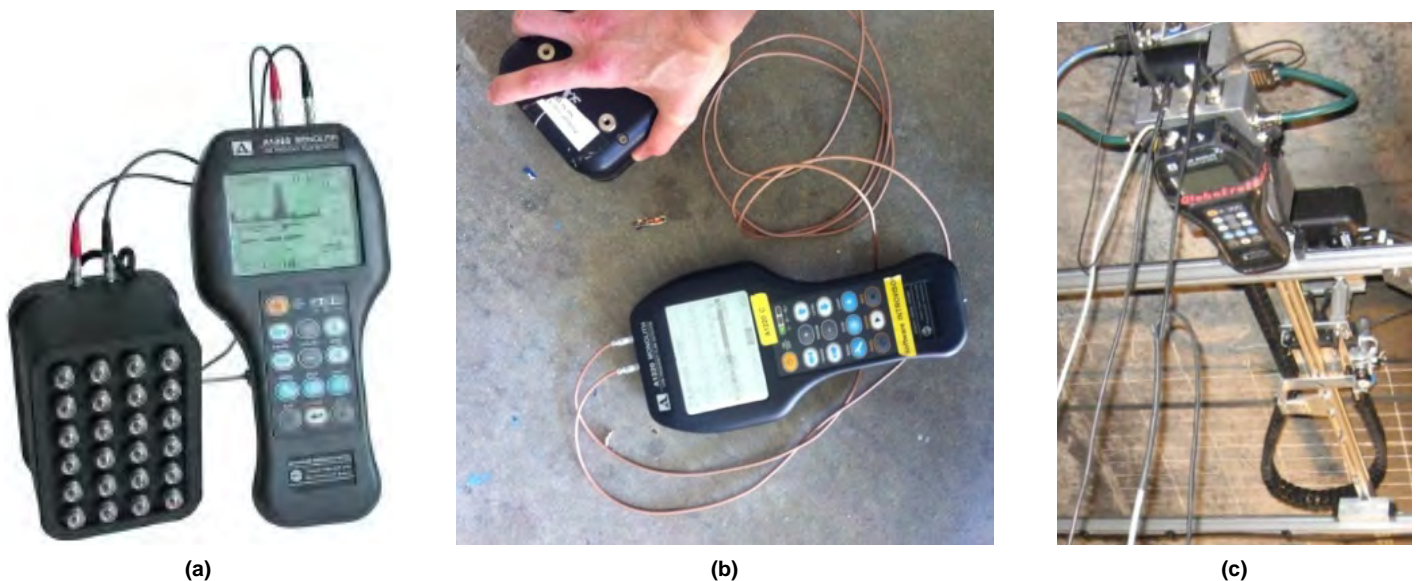


Figure Q.10. Ultrasonic A1220 from Acoustic Control Systems (a) used for point measurements by hand (b) and used for profile measurements by automated scanning device (c).

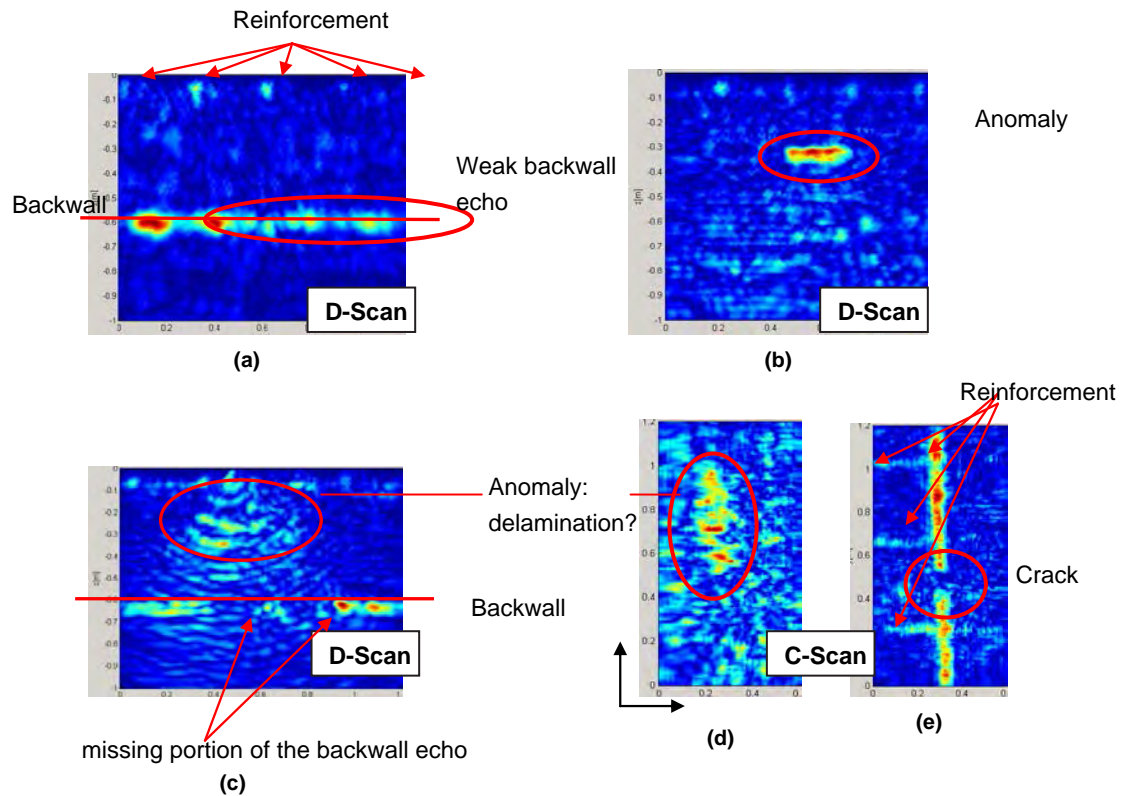


Figure Q.11. Typical ultrasonic echo results: (a) backwall and reinforcement in D-scan, (b) unknown detection of a reflector in a D-scan, (c) direct detection of a delamination-like anomaly in a D-scan, (d) direct detection of delamination-like anomaly in a C-scan, and (e) indirect detection of surface crack considering missing reinforcement in the C-scan.

than the return frequency for the tunnel lining backwall, it produces an apparent reflector depth that is larger than the full thickness (Shokouhi 2005).

When using automated scanning devices, the single point-by-point measurements along a profile add up to B- and C-, and D-scans as time/depth/frequency slices (Figure Q.13).

Typical Results

IE is best known for thickness evaluation and delamination detection in plate-like structures. Depending on the mechanical

source used, shallow or deep structures or defects may be investigated. IE can detect the backwall, even at delaminated areas, provided that the delaminations are not severe. Figure Q.12a shows an example of a sound tunnel lining with the backwall resonant single frequency peak at 3.4 kHz. Considering the P -wave velocity of about v_p in concrete, $\sim 4,000$ m/s, this amounts to a depth of about ~ 2 ft. Frequency domain D-scans along two selected test lines are shown in Figure Q.13. The D-scan in Figure Q.13a was taken over a sound area, and the D-scan in Figure Q.13b was taken across a supposedly delaminated area.

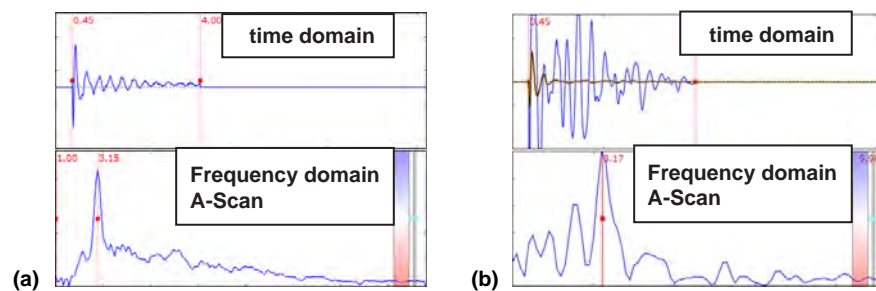


Figure Q.12. Sound area of tunnel lining with single frequency peak at 3.15 kHz (a) and supposedly delaminated area with several low-frequency peaks (b) from Chesapeake Bay Bridge-Tunnel, Area 3.

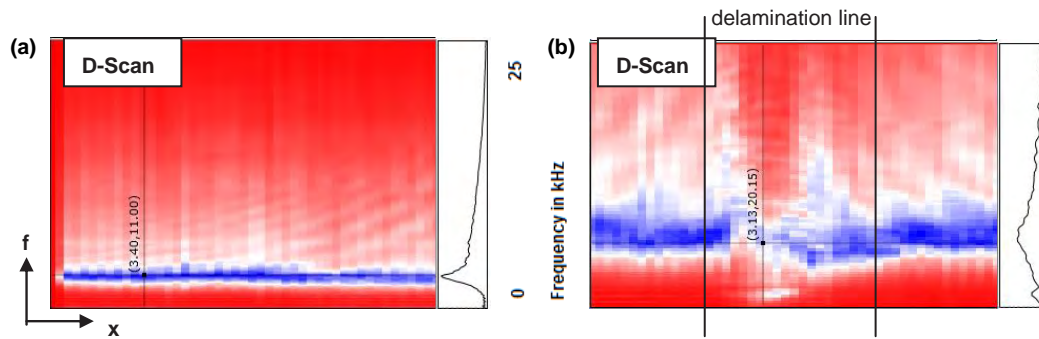


Figure Q.13. Frequency domain D-scans of test line on sound portion of one tunnel lining with backwall at 3.4 kHz (a) and on supposedly delaminated area of another tunnel lining (b).

Measurement Results for Eisenhower Memorial Tunnel

Description of the Test Area

Measurements in the Eisenhower Memorial Tunnel were performed over two days: October 3 and 4, 2011. The unusually high elevation of the tunnel (11,112 ft) created a few challenges. The ZFP scanner is attached to the surface using four vacuum feet. Because of the high tunnel altitude, the compressor could not maintain the pressure necessary to create the vacuum under the feet. Two areas were examined. The first area was regarded as an equipment test. The

second area was properly examined with all three NDT methods.

The second test area was located within Segment 11, Block 1 of the Eisenhower Memorial Tunnel and was tested from east to west, starting in the lower right corner, then moving up and left. This test area is hereafter referred to as EH2. As shown in Figure Q.14, the 40-in. by 24-in. test area was located 26 in. east of a joint between Segments 10 and 11. The starting scanning point was located at the lower right corner of the scanner field. The scanner moved up and then left, in this case from east to west. The feet of the scanner slid down 0.5 in. during the testing (because of the difficulties in

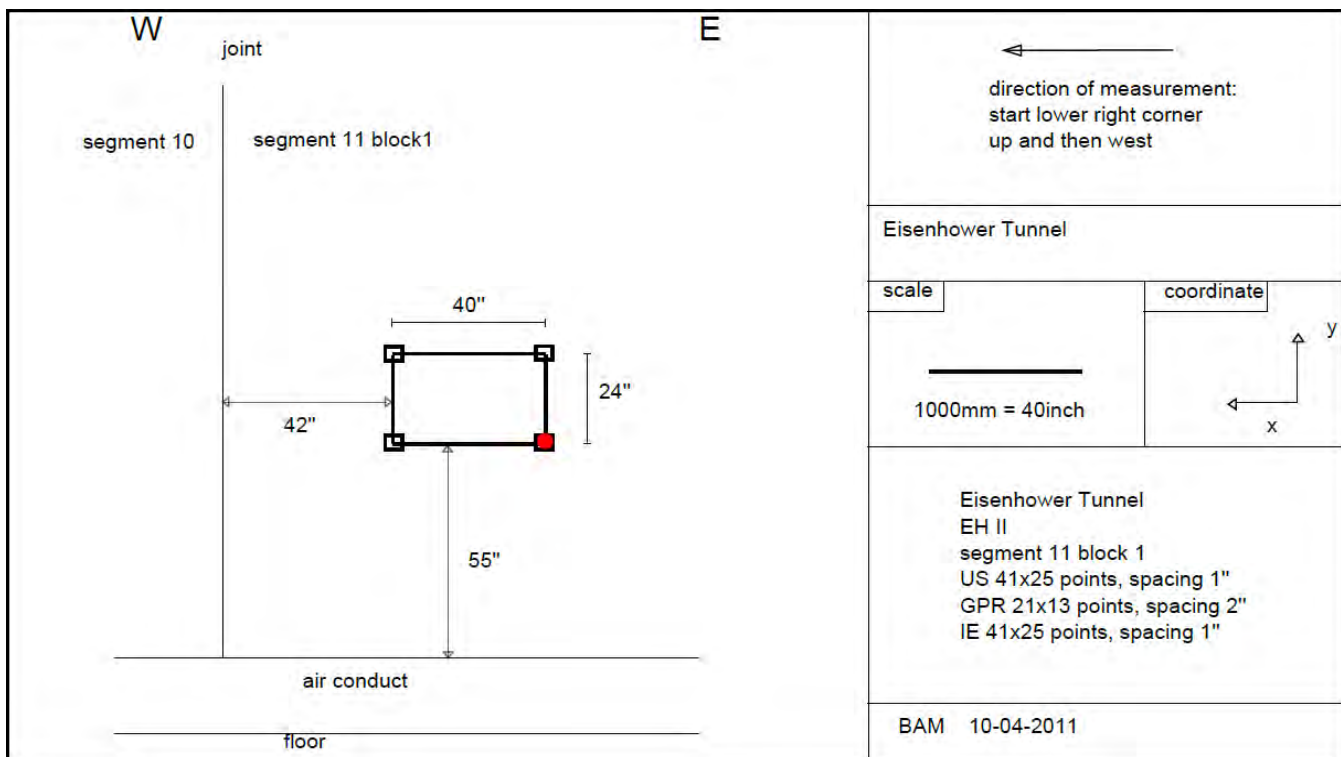
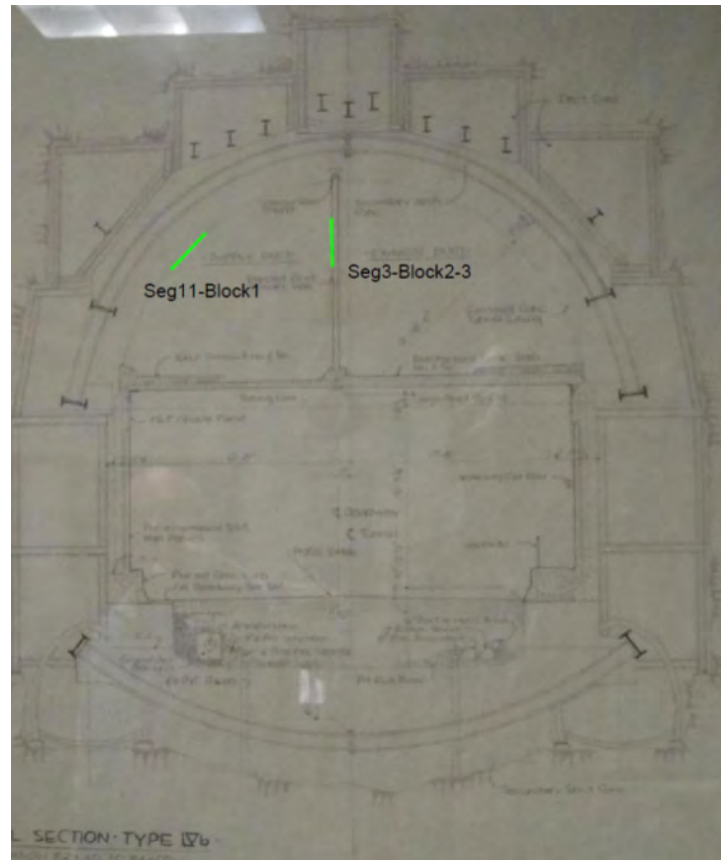


Figure Q.14. Sketch of test area EH2, located within Segment 11, Block 1.



(a)



(b)

Figure Q.15. Test area in Eisenhower Memorial Tunnel: (a) test setup of scanner on EH2 and (b) cross section of tunnel showing locations of the two test areas.

maintaining suction). Figure Q.15a shows the setup on the first area, and Figure Q.15b is a photograph of a page of an information bulletin that shows a cross section of the tunnel with the two fields of testing marked on it. The grid spacing was 1 in. for ultrasonic echo and IE tests and 2 in. for GPR. The position of the test apparatus and the feet of the scanner were marked with chalk. The lengths of the ultrasonic echo, IE, and GPR transducers were parallel to the centerline of the tunnel.

The results obtained from each of the three tests performed are discussed below.

GPR Results

With the GSSI 1.5-GHz GPR antenna, the rebar mesh at a depth between 2 in. and 3 in. was clearly detected. Moreover, an anomaly (reflector of unknown origin) at 16-in. deep was detected. According to the GPR results, the reinforcement bars within the test area along the y -direction were positioned regularly at 10-in. intervals: $x = 8$ in., $x = 18$ in., $x = 28$ in., and $x = 38$ in. The ones along the x -direction had a 10-in.

distancing as well, located at $y = 10$ in. and $y = 20$ in. The detected anomaly had an x -dimension of 10 in. extending from $x = 18$ in. to $x = 28$ in. and ran along the entire y -dimension of the test area. Figure Q.16 is a three-dimensional (3D) image of the volume with the slices (B-, C-, and D-scans) positioned to reveal the anomaly and the reinforcing elements. Figure Q.17 shows a selection of the B-, C-, and D-scans from EH2, including the detected reflectors: (a) is a D-scan of the reinforcement bars in the y - and x -direction as well as the anomaly, (b) and (c) are B-scans, and (d) and (e) are C-scans showing the reinforcement bars and the anomaly at their respective depths.

Ultrasonic Echo Results

Using ultrasonic echo, reinforcements at a depth between $z = 2$ in. and $z = 3$ in. were detected. An anomaly (i.e., a reflector of an unknown origin) was also detected at an approximate depth of 16 in. The reinforcement bars along the y -direction were 10 in. apart, located at $x = 8$ in., $x = 18$ in., $x = 28$ in., and $x = 38$ in. The bars along the x -direction were not very clear

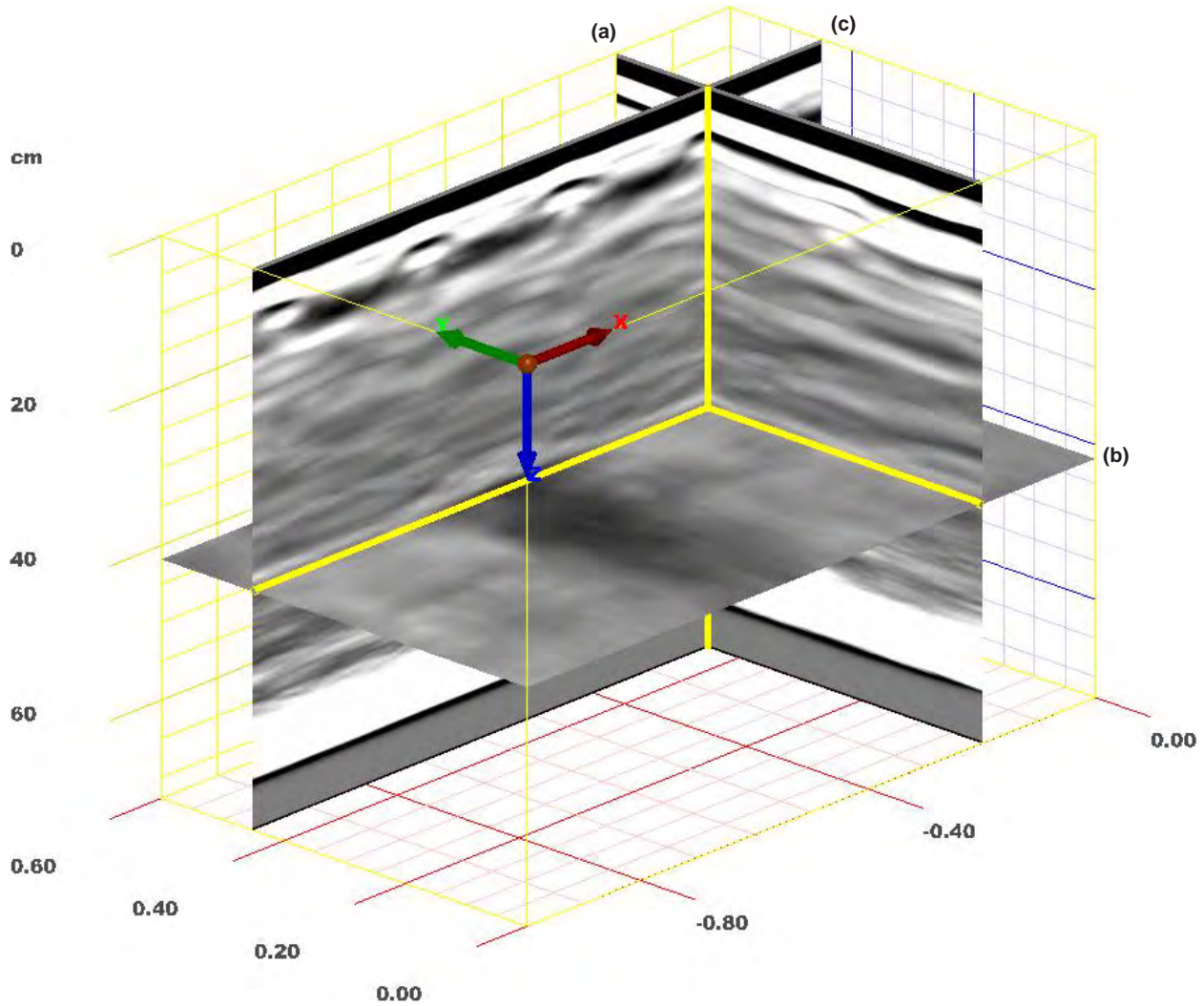


Figure Q.16. EH2, GPR: 3-D image of volume positioned to reveal anomaly, with B-scan (a) positioned at $x = 8$ in., C-scan (b) at $z = 16.8$ in., and D-Scan (c) at $y = 18$ in.

(because of the positioning and polarization of the probe) and thus could only be vaguely traced at $y = 10$ in. (Figure Q.18). Figure Q.19 is a 3-D image of the volume with the slices (B-, C-, and D-scans) positioned to reveal the anomaly. The local phase at rebar reflections was, as expected, between 90° and 180° (red color), indicating an impedance higher than the surrounding concrete. The anomaly was 10 in. in width and lay between $x = 18$ in. and $x = 28$ in. in the direction of x , as seen in Figure Q.20. It ran completely across the y -dimension of the test area. The local phase was negative, between 0° and -110° (green, yellow), indicating an impedance lower than concrete.

Impact Echo Results

IE could not register either reinforcement or the anomaly detected by GPR and ultrasonic echo. The frequency spectra

did not have clear amplitude peaks but was rather a plateau of many overlapping peaks (Figure Q.21). IE could not yield any reliable information about the backwall of the tunnel lining. Assuming a shear wave velocity of 3,400 m/s, the longitudinal wave velocity was approximately 5,889 m/s.

Comparison of Results

As expected, GPR proved to be the best tool in identifying and locating the reinforcement within the EH2 test volume. Ultrasonic echo, however, could locate the anomaly of unknown origin more clearly. The negative local phase of the amplitudes at the mysterious reflector led to the assumption that the anomaly would have a lesser impedance than the surrounding concrete. The fact that GPR registered the anomaly at a depth of 16 in. led to speculations about it having a higher impedance than the surrounding concrete. Wood

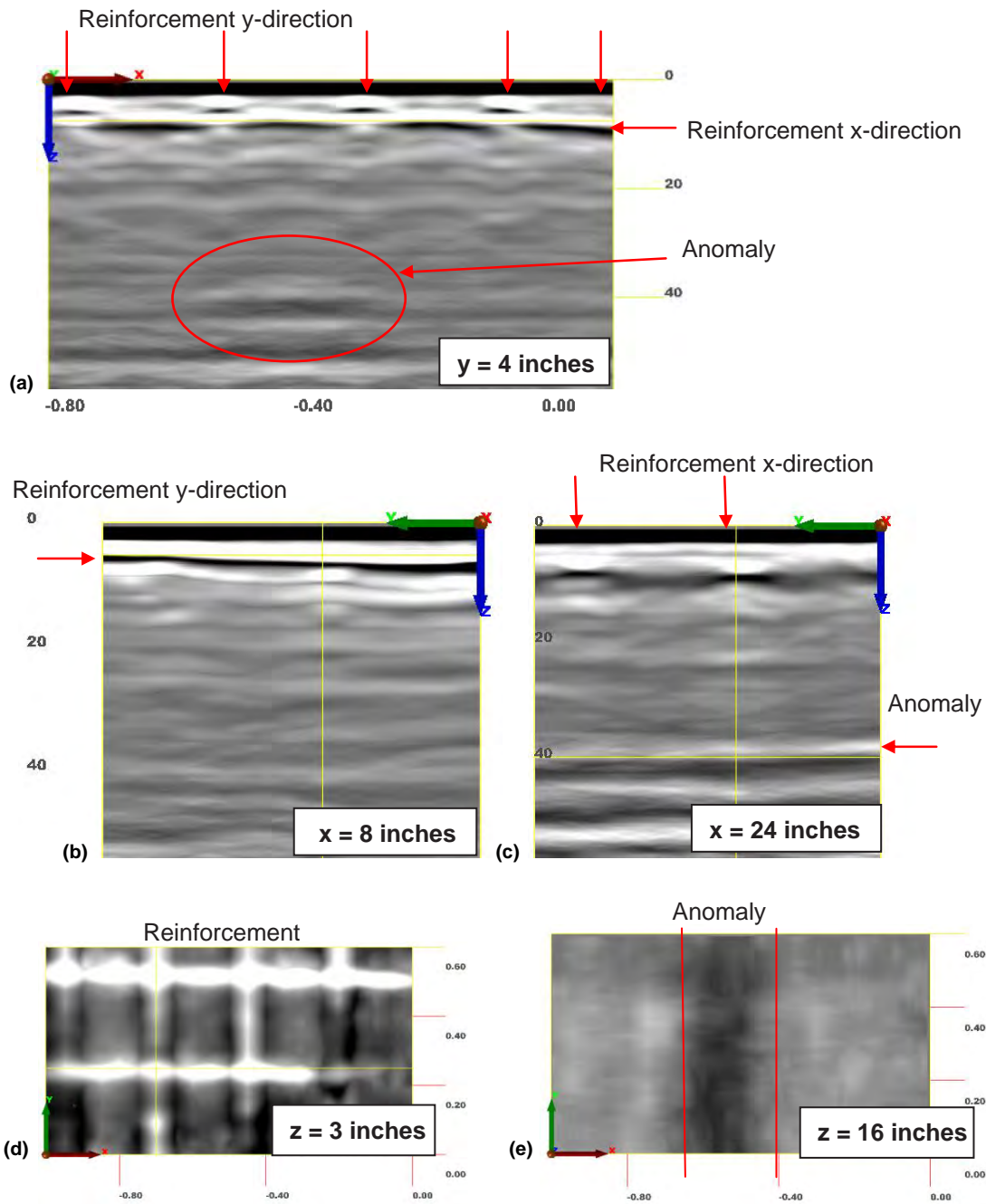


Figure Q.17. EH2, GPR: Collection of B-, C-, and D-scans from test area displaying main GPR results.

and air voids in such a depth could not likely be seen with a 1.5-GHz antenna as clearly as the anomaly seen in the radargrams.

One hypothesis is that the anomaly could be one of the steel beams shown in Figure Q.22. This assumption raises the question of how the local phase normally associated with reflections from wood or air could appear. One theory is that the concrete around the metal beams may not be properly bonded to the steel anymore, leaving a thin layer of air between the two mediums. The local phase reflects

the phase shift at the concrete-air interface rather than the steel underneath.

In general, both the GPR and ultrasonic echo methods were effective in detecting reflectors within the Eisenhower Memorial Tunnel lining. A combination of the two result sets would provide the most detailed and reliable results. Both methods detected the reinforcement and an unknown anomaly. GPR was more effective in detecting the former and ultrasonic echo in detecting the latter. The backwall could not be seen with any of the employed techniques here.

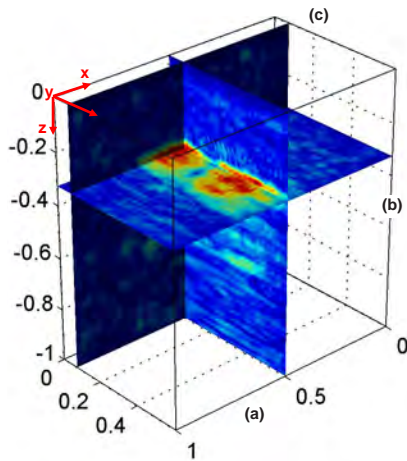


Figure Q.18. EH2, ultrasonic echo: 3-D image of volume positioned to reveal anomaly, with B-scan (a) positioned at $x = 19$ in., 6-in. width; C-scan (b) at $z = 14$ in., 3-in. width; and D-scan (c) at $y = 4$ in., 2-in. width.

Measurement Results for Hanging Lake Tunnel

Testing in the Hanging Lake Tunnel took place on October 5 and 6, 2011. As noted in Figure Q.23, three test areas were measured with GPR, ultrasonic echo, and IE.

Test Area 1

Description of the Test Area

The first test area was situated in Section 56 of the tunnel and is hereafter referred to as HL1. No referencing system for this tunnel was available. The test area was believed to be within Section 56 because 56/57 was marked with spray paint on the floor, looking south on the right side of the test location (see Figure Q.23a). On the left side, E16 was written. A repaired crack ran across the selected test area (see Figure Q.23b). As shown schematically in Figure Q.24, the 48-in. by 24-in. test area was located between two joints at a distance of 27 in. from the north joint and 56 in. from the south joint. The scanning started at the point closest to the centerline. It then moved away from the centerline and farther south, toward the tunnel entrance. The grid spacing was 1 in. for ultrasonic echo and IE testing and 5 in. for GPR testing. The length (larger dimension) of the ultrasonic echo, IE, and GPR transducer was parallel to the centerline of the tunnel.

GPR Results

Using the GSSI 1.5-GHz GPR antenna, the reinforcement mesh and other reinforcing elements (possibly dowels) at depths (z) between 1 in. and 6 in. could be detected, as well as an extended anomaly at $z = 12$ in. Figure Q.25 is a 3-D image of the volume with the slices (B-, C-, and D-scans) positioned to reveal the anomaly and the reinforcing elements. At a

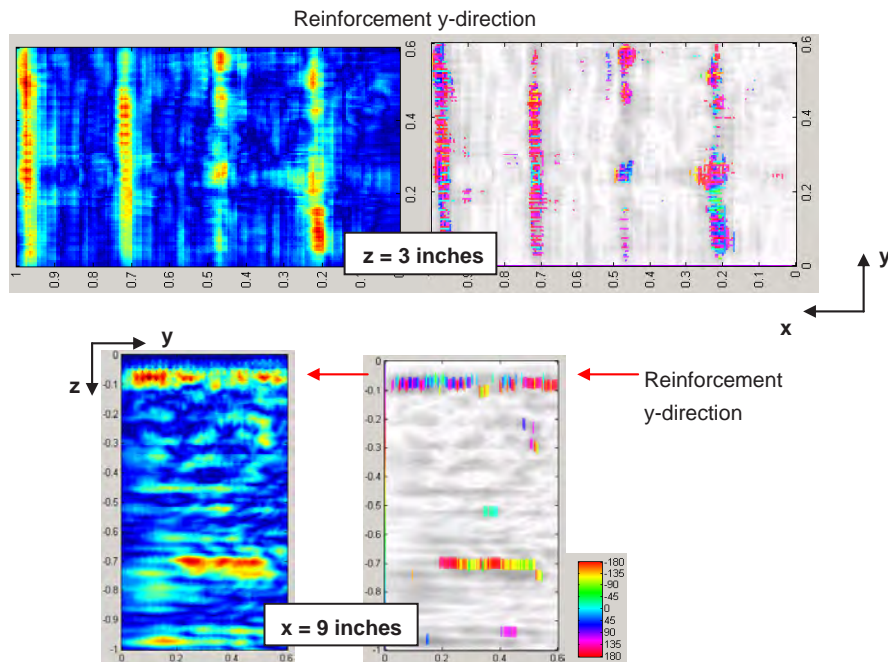


Figure Q.19. EH2, ultrasonic echo: B- and C-scans, displaying reinforcement. Reflector at 0.7 m could not be identified, as it showed up inconsistently.

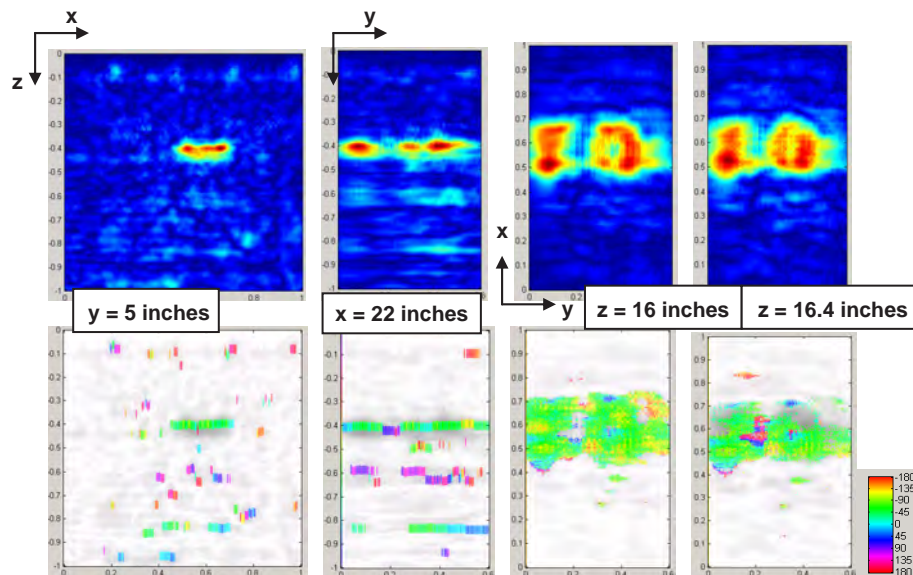


Figure Q.20. EH2, ultrasonic echo: B-, C-, and D-scans and corresponding local phase diagram, displaying a reflector.

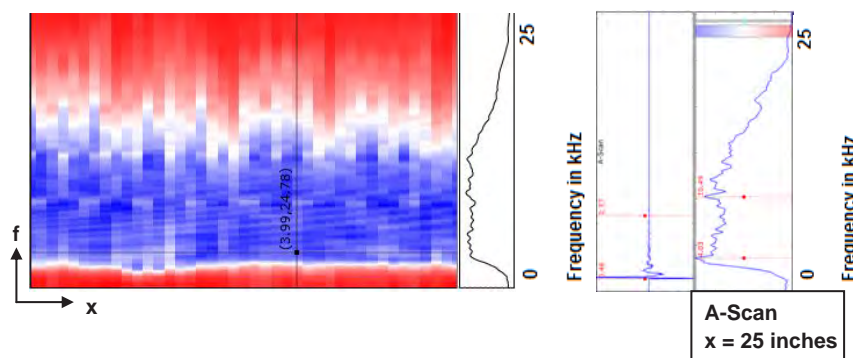


Figure Q.21. EH2, IE: A- and D-scans. No information about possible anomalies, reinforcements, or lining thickness could be drawn.



Figure Q.22. Photograph of construction of Eisenhower Memorial Tunnel sometime between 1968 and 1973 (Colorado DOT 2011). Steel beams could be anomaly seen in GPR and ultrasonic echo data.

depth of 1 in., rebar-like reflections at $x = 24$ in. were detected. At this depth, reflections also appeared from a series of shorter elements (dowels) between the two rebar-like reflections. The shorter elements were regularly spaced and oriented perpendicular to the rebar-like reflections. The C-scan in Figure Q.26c shows the reinforcement mesh in both directions, with the bars along the y -direction at $x = 6$ in. and $x = 38$ in. The D-scans in Figure Q.27 and the B-scan in Figure Q.28 show the third rebar, along the y -direction positioned at $x = 22$ in., whose reflections could not be distinguished in the C-scans because of the overlap with other reinforcing elements present. The depth of the rebars along the y -direction was between $z = 5$ in. and $z = 6$ in.

Besides the reinforcing elements, at a depth of $z = 5.5$ in., an anomaly appeared from $z = 12$ in., down to $z = 16$ in., which

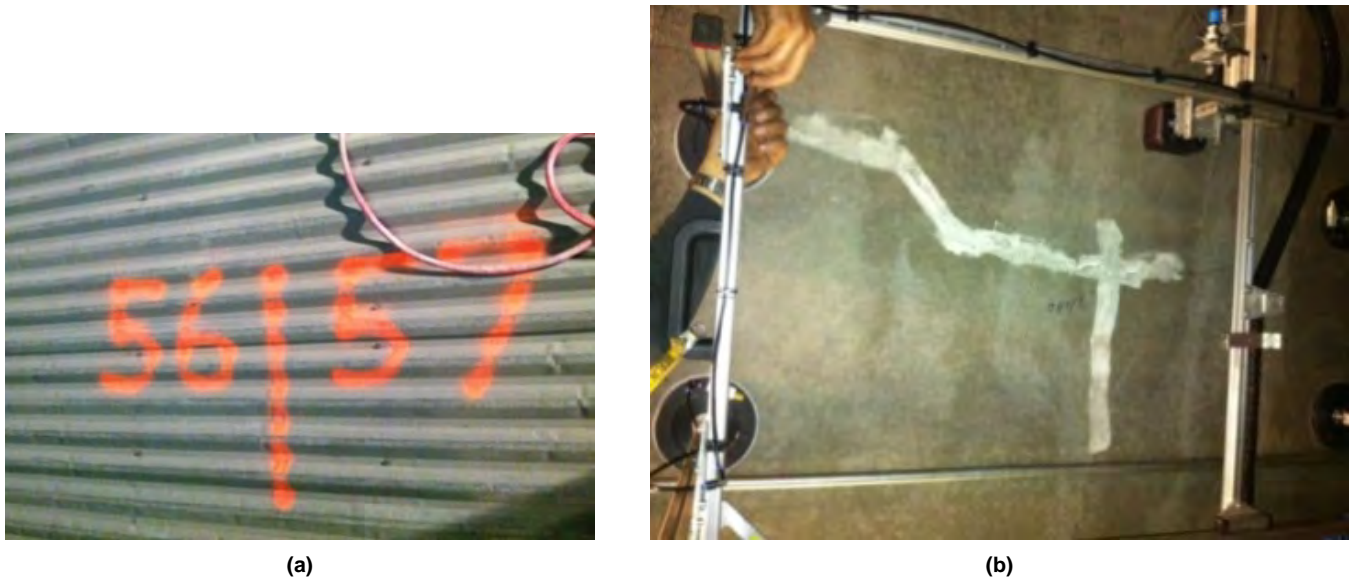


Figure Q.23. Mark on tunnel vent floor of HL1 used as reference to identify sections (a) and location of repaired crack across test field in relation to scanner aperture (b).

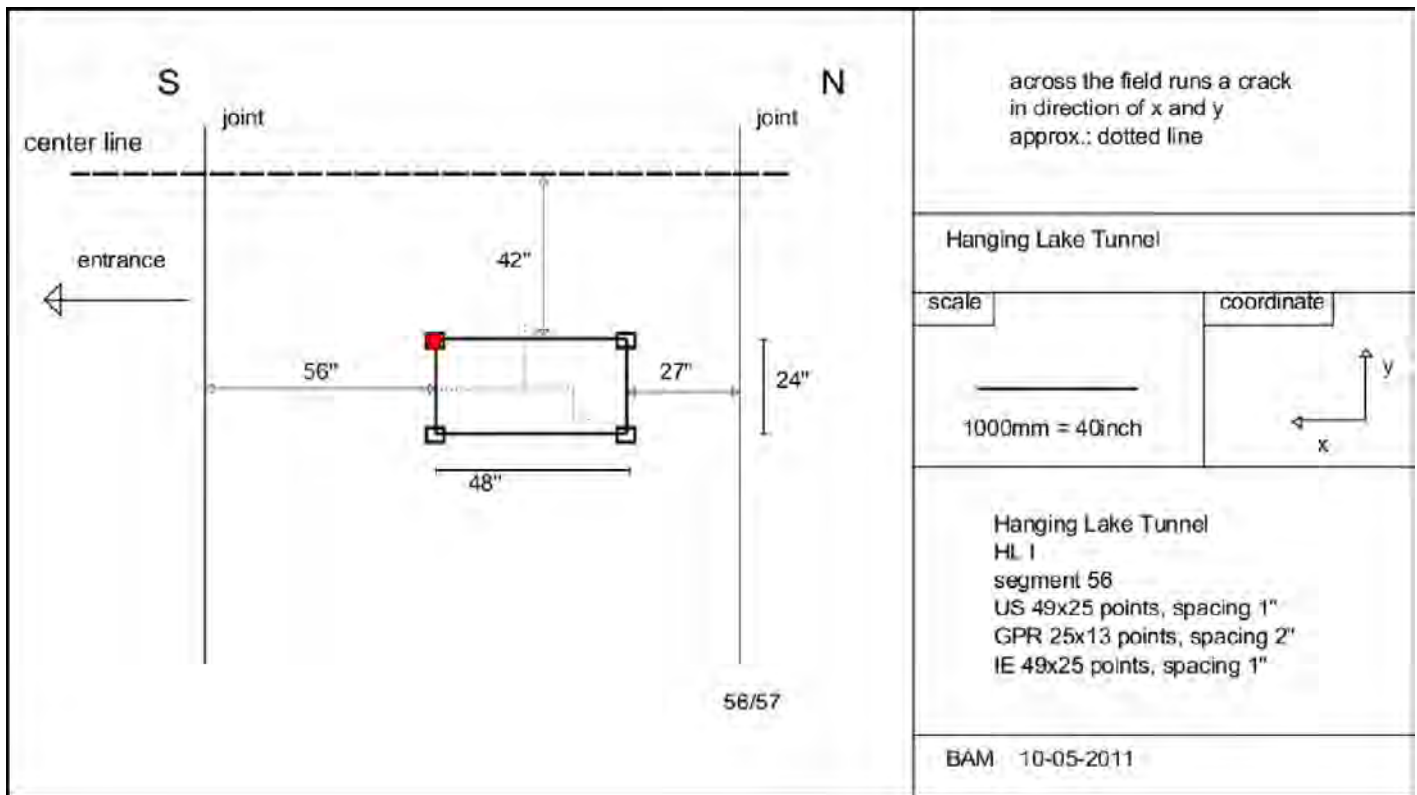


Figure Q.24. Sketch of test area, HL1, Segment 56.

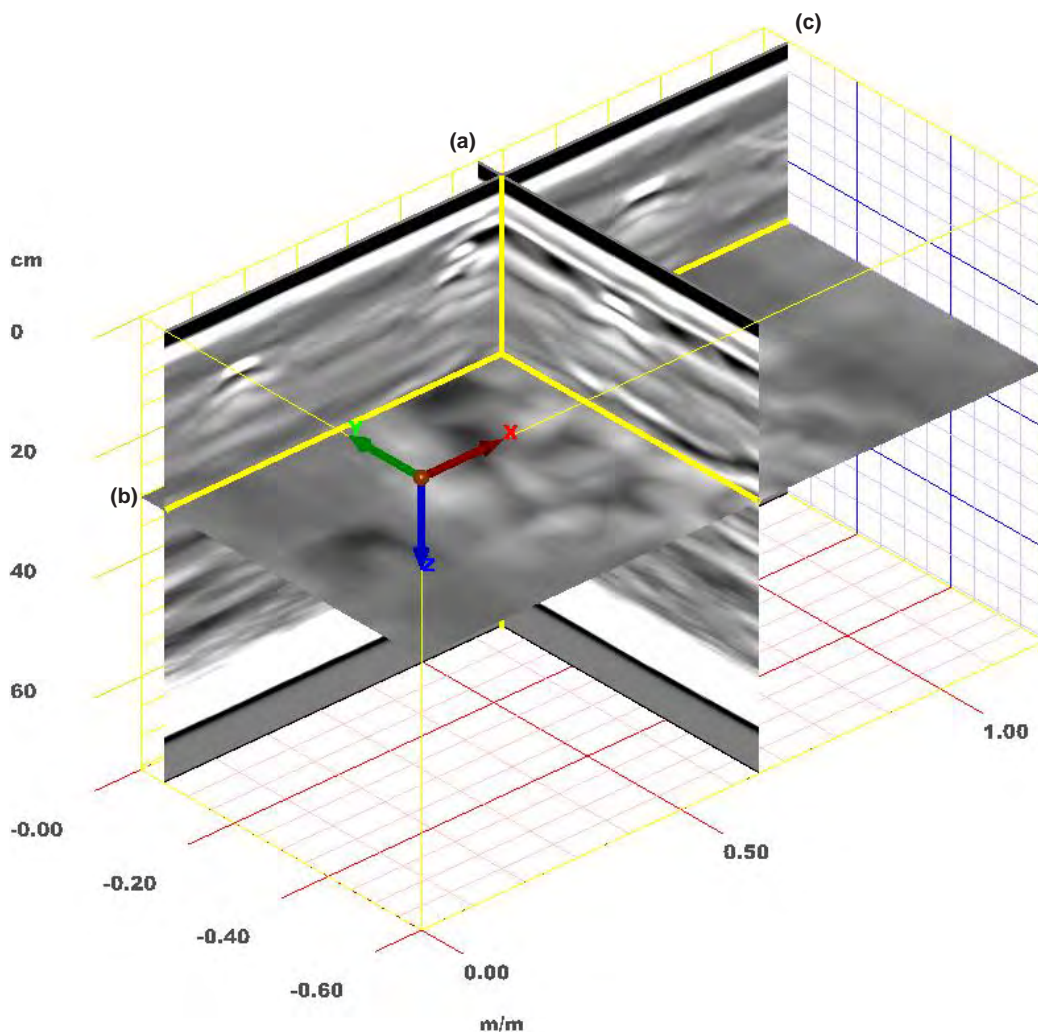


Figure Q.25. HL1, GPR: 3-D image of volume positioned to reveal anomaly and reinforcing elements, with B-scan (a) positioned at $x = 22$ in., C-scan (b) at $z = 12$ in., and D-scan (c) at $y = 1$ in.

led to the rise of amplitudes over an area (Figure Q.26d, Figure Q.27c, Figure Q.28b, and Figure Q.28c).

The backwall could not be seen in the GPR radargrams.

Ultrasonic Echo Results

The reinforcement bars could not clearly be detected in ultrasonic results. No usable C-scan at the depth of the reinforcement. And no horizontal (the same depth) backwall could be identified. However, a deeper reflector plane (relative to the rebar mesh) of variable depth could be detected.

Figure Q.29 shows a D-scan taken at $y = 5$ in. along with the corresponding phase diagram. The reinforcement was seen vaguely at depths between $z = 4$ in. to $z = 6$ in. However, an anomalous reflector of mostly negative phase shift appeared at a depth between $z = 12$ in. and $z = 16$ in.

The B-scans at $x = 6$ in. and $x = 23$ in. are shown in Figure Q.30. Figure Q.31, a 3D image of the volume, gives another view on the anomaly.

Impact Echo Results

The IE spectra contained peaks of frequencies much higher than the expected backwall resonance frequency.

Figure Q.32 is a D-scan cut through the short side of the rectangular test area, therefore along the length. Many frequency peaks occurred within the frequency spectrum. The first peak of the individual spectra appeared at around 3,700 Hz and 3,400 Hz, corresponding to depths of $z = 22$ in. and $z = 24$ in., respectively (assuming a longitudinal wave velocity of 4,000 m/s). A recurring second peak occurred at about 6,700 Hz, corresponding to a shallower reflector, at about

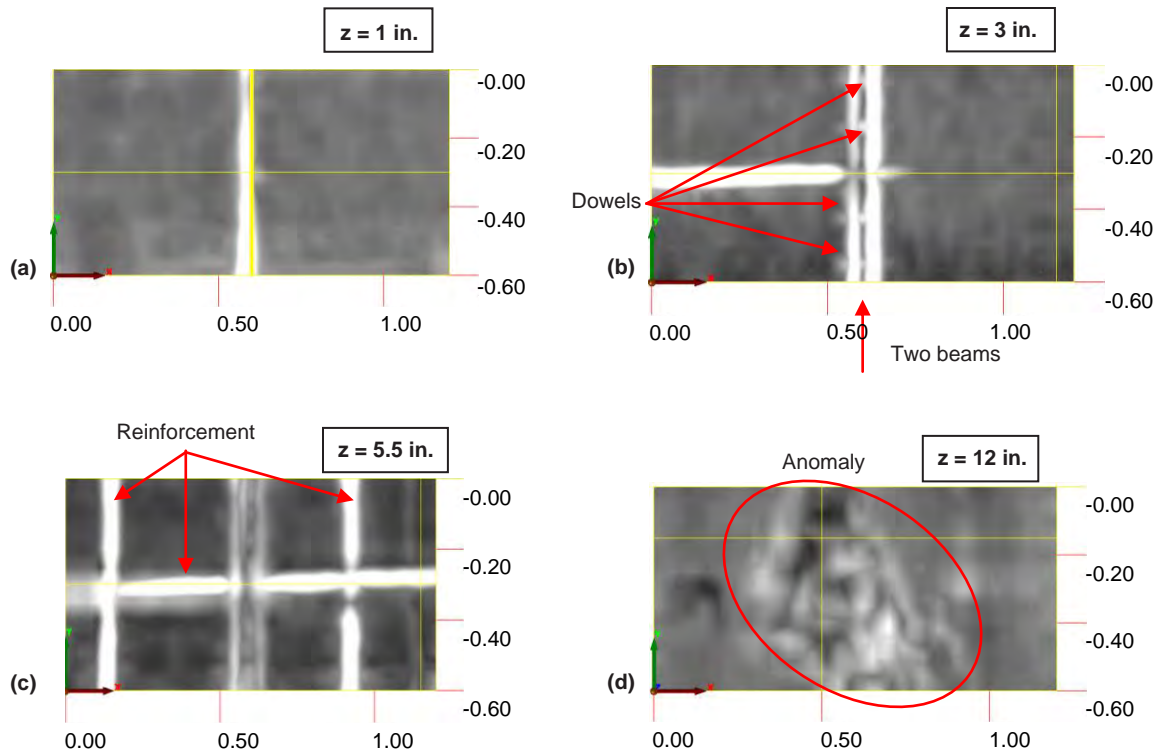


Figure Q.26. HL1, GPR: C-scans with (a) rebar-like reflection, (b) reflections from two rebars appearing close to each other with dowel-like elements in between along with shallower part of reinforcement bar in x -direction seen at $y = 12$ in., (c) reinforcement mesh in both directions, and (d) anomaly.

$z = 12$ in. Because the amplitude spectrum along the profile seemed rather scattered, no reliable conclusions about the nature of the reflector could be drawn.

Comparison of Results

For this test area (HL1), GPR proved to be the only method to identify the reinforcement mesh and the reinforcing elements. The fine measurement grid and 3-D data collection allowed detection of reinforcing elements overlapping each other in some views. The ultrasonic echo technique, however, was able to detect a deeper anomaly and establish that the anomaly under the test area is located at different depths. The phase diagram provided some information about the possible nature of the anomaly, which appears to have a lower impedance relative to its surrounding concrete. IE spectra contained high-frequency energy, but no reliable information could be extracted from either IE time histories or spectra.

Comparing the results reveals the need to employ at least two complementary NDT techniques to locate different reflectors within the tunnel lining. GPR is best for locating the metallic reflectors within the penetration range of the antenna. To locate reflectors of different acoustic impedance

such as voids and delaminations, the acoustic wave methods should be used. A change of structure seems to occur in the middle of the test area; unusual dowel-like reinforcing elements are present around this location and the depth of the detected anomaly changed abruptly in the ultrasonic results.

None of the NDT techniques that were used were able to reliably identify the extent of the tunnel lining. Obviously, the impedance contrast between the tunnel lining and the surrounding rock formations was not detectable. The backwall was located outside the penetration range of GPR and possibly the zone of influence of ultrasonic echo. Moreover, the reflection and scattering effects due to the presence of reinforcement and anomalies weaken the propagating wave and limit its penetration depth.

Test Area 2

Description of the Test Area

The second test area at Hanging Lake Tunnel (HL2) took place in Segment 57 (segment number was assumed based on the marking on the ground as shown in Figure Q.23a). The 48-in. by 24-in. test area was located 52 in. north of the joint

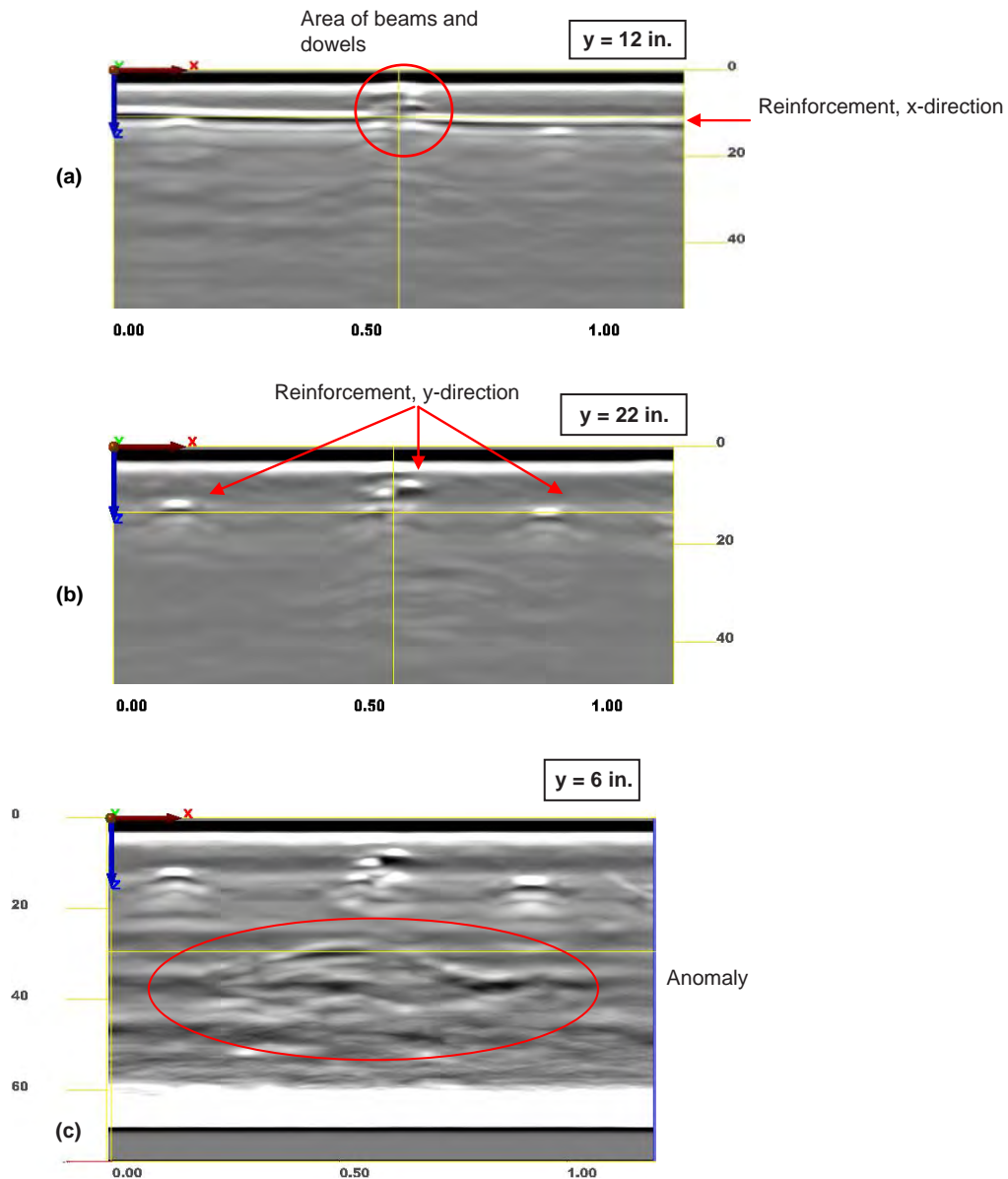


Figure Q.27. HL1, GPR: D-scans. Area of beams and dowels (a) as well as reinforcement in x- and y-direction can be seen as a cut through. Reinforcement in x-direction starts at $z = 3$ in. and leads to $z = 5$ in. Third reinforcement bar along y-direction at $x = 22$ in. is located beneath other reinforcing elements at $x = 24$ in. (b), which makes it difficult to distinguish them in C-scan. Image (c) shows anomaly starting from $z = 12$ in. and going to $z = 16$ in. Image has higher gain than other images to clarify the anomaly.

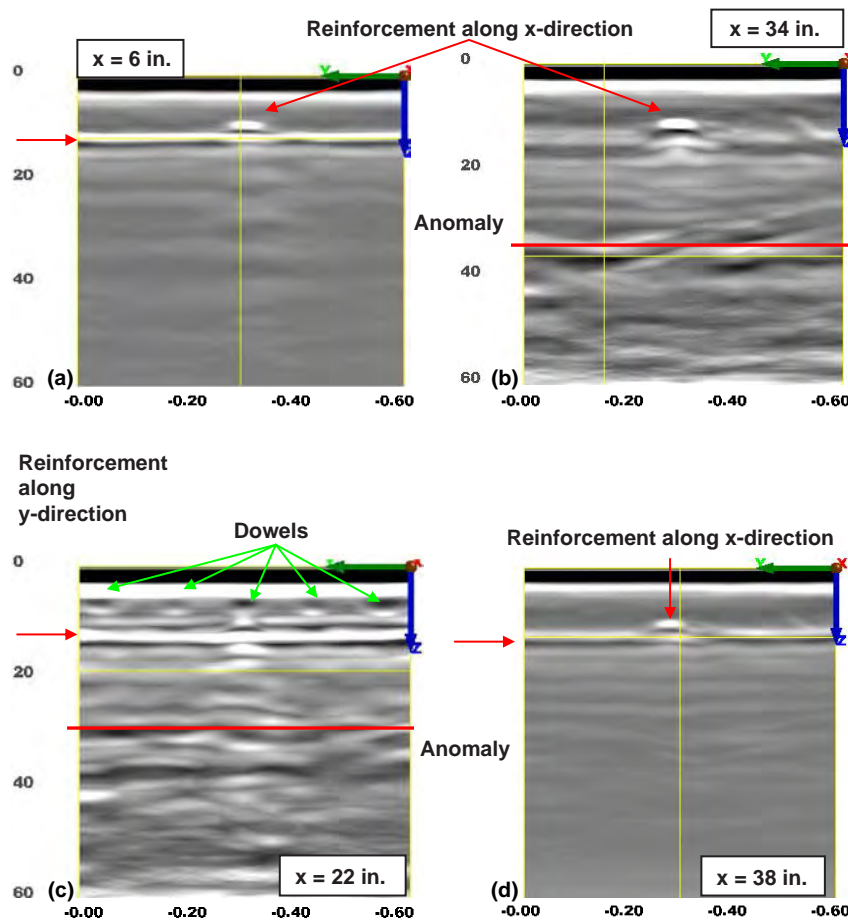


Figure Q.28. HL1, GPR: B-scans. First reinforcement bar along y-direction at $x = 6$ in. (a). At $x = 34$ in., bar along x-direction positioned at $y = 12$ in. (b) as well as anomaly at $z = 16$ in. is seen. Second bar along y-direction at $x = 22$ in. under other reinforcing elements and anomaly at $z = 12$ in. (c), and third bar along y-direction at $x = 38$ in. (d) are also shown.

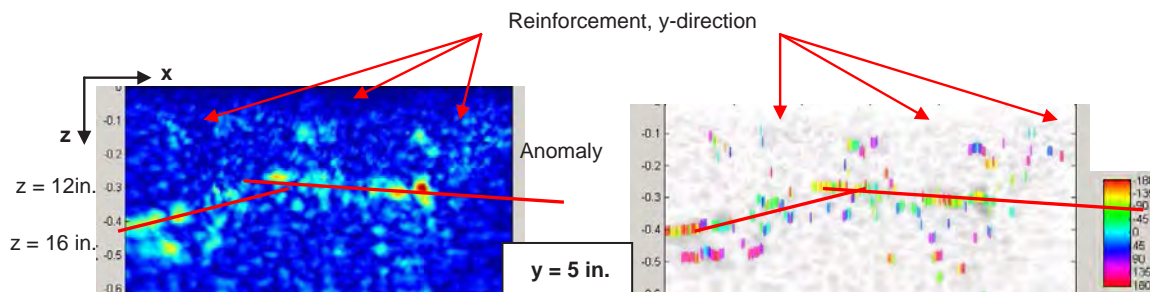


Figure Q.29. HL1, ultrasonic echo: D-scan at $y = 5$ in. Curved anomalous reflector of mostly negative phase detected between $z = 12$ in. and $z = 16$ in.

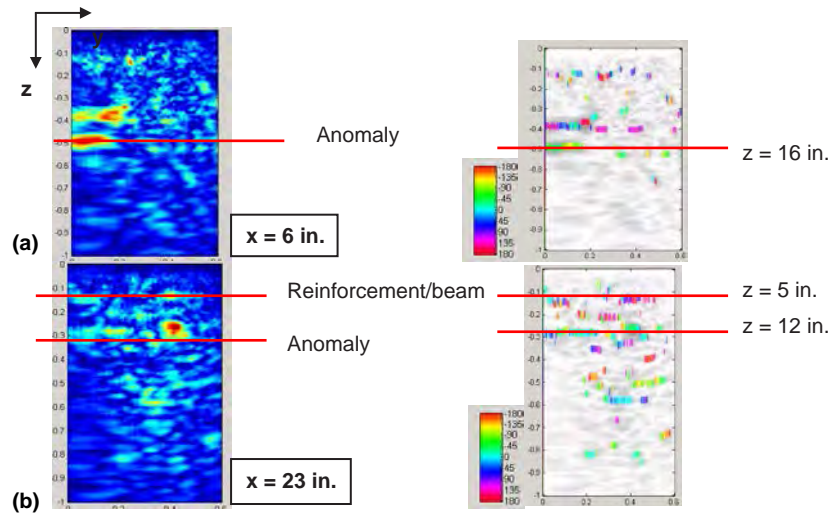


Figure Q.30. HL1, ultrasonic echo: B-scans to evaluate extent of anomaly. B-scan crossing through deeper reflector (a) and B-scan crossing through shallower anomaly (b).

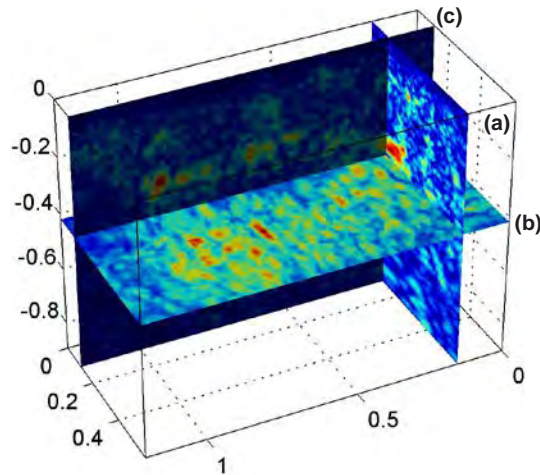


Figure Q.31. HL1, ultrasonic echo: 3-D image of volume positioned to reveal anomaly, with B-scan (a) positioned at $x = 6$ in.; C-scan (b) at $z = 21$ in., 4-in. width; and D-scan (c) at $y = 6$ in.

dividing segments 56 and 57. Its upper edge (toward the tunnel crest) was about 100 in. from the centerline. Figure Q.33 shows a sketch of HL2. An unrepaired crack ran across the test area, as shown in Figure Q.34a. Figures Q.34a and Q.34b, show the ZFP scanner. The scanning started at the point closest to the centerline, first moving down and away from the centerline, then south toward the tunnel entrance. The grid spacing for both the ultrasonic echo and IE tests was 1 in. and for GPR was 2 in. The ultrasonic echo, IE, and GPR transducers were mounted such that their length (large dimension) was parallel to the centerline of the tunnel. One profile line of the GPR data was missing (at $y = 20$ cm, or 8 in.), which caused a discontinuity in the B-scans and C-scans. Consequently, no D-scan was available for $y = 8$ in.

GPR Results

Figure Q.35 is a 3-D image of the volume intended to give an overall view of the reinforcement.

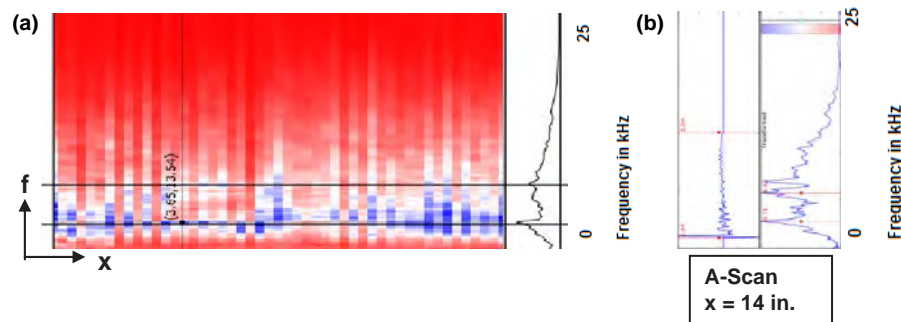


Figure Q.32. HL1, IE: D-scan (a) and A-scan (b).

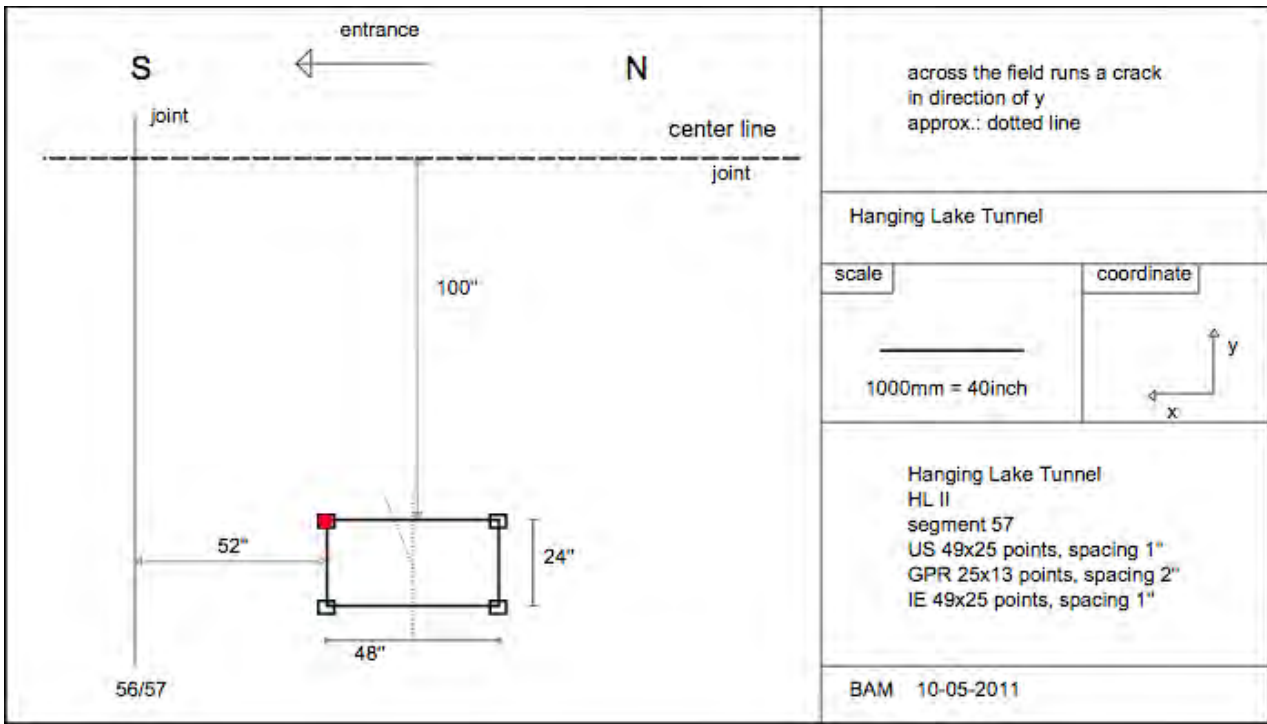
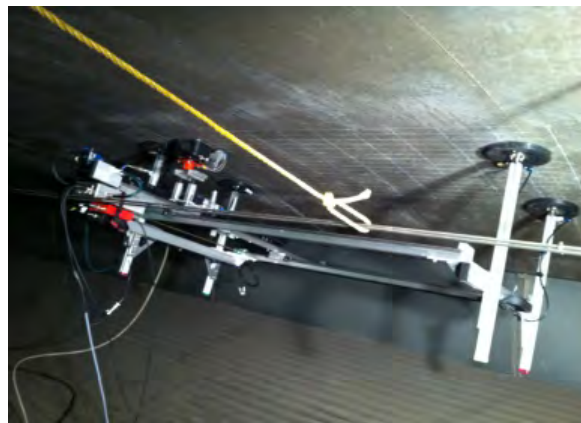


Figure Q.33. Sketch of test area HL2, Segment 57.



(a)



(b)



(c)

Figure Q.34. HL2: (a) crack running across test area, (b) NDT scanner mounted on tunnel ceiling, and (c) scanning of test area.

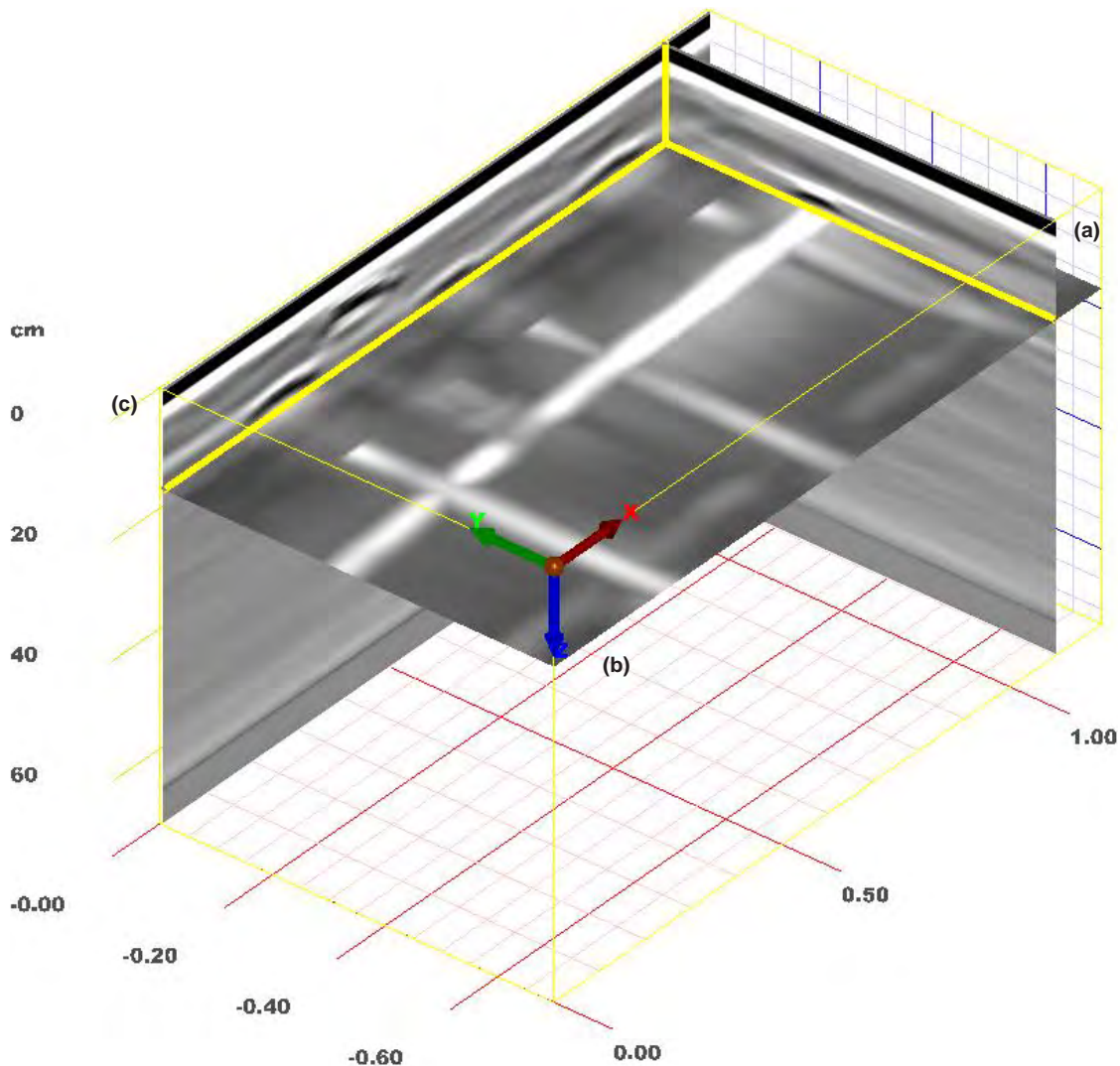


Figure Q.35. HL2, GPR: 3-D image of volume positioned to reveal reinforcing elements, with B-scan (a) positioned at $x = 44$ in.; C-scan (b) at $z = 6.5$ in., 3-in. width; and D-scan (c) at $y = 0$ in.

In the C-scan at a depth of $z = 5$ in., a reinforcement bar in the general x -direction could be seen running across the test area roughly from $y = 16$ in. on the south side of the area to about $y = 12$ in. on the north side (Figure Q.36b). The D-scan in Figure Q.36c shows that this reinforcement bar ran above the bars perpendicular to it. Figure Q.36a is the B-scan at $x = 2$ in., where the bar at $y = 16$ in. was marked.

The C-scan at $z = 8$ in. showed another, albeit weak, reinforcement bar along the x -axis, at about $y = 24$ in. (see Figure Q.37b). A D-scan through the bar at $y = 24$ in. (Figure Q.37c) and a B-scan at $x = 2$ in. (Figure Q.37a), with the weak reflection from the bar marked, are shown as well.

The reinforcement bars in the y -direction at a depth of $z = 6$ in. are shown in Figure Q.38b. Figure Q.38c shows the D-scan at $y = 24$ in. with the reinforcements marked at a depth of 8 in. The B-scan (Figure Q.38a) through the bar at $x = 9$ in. revealed that the bars did not run parallel to the surface

but were bent from $z = 6$ in. down to $z = 8$ in. This explained the weak reflections over half of the C-scans at $z = 6$ in.

Figure Q.39 shows images resulting from the crack on the surface, which manifested itself by a changed impedance because of the intrusion of moisture into the very first layers of the lining. Figure Q.39b is a slice in the depth, this time at $z = 3$ in. The circled area shows the reflection caused by moisture as a result of the crack on the surface. It ran in that depth until $y = 12$ in. ($y = 30$ cm). The upper part until $y = 6$ in. ($y = 15$ cm) does not seem to fit onto the lower part. The reason for this is a missing profile line caused by a failure during the measurements, which cannot be reconstructed properly by the program. Figure Q.39c shows the same reflector at a depth of $z = 3$ in., which does not show up at the other D-scans above, meaning it was local. The B-scan at $x = 19$ in. (Figure Q.39a) shows the extent of the reflector better: it was down to 3.4-in. deep and nearly 16 in. into the field of measurement.

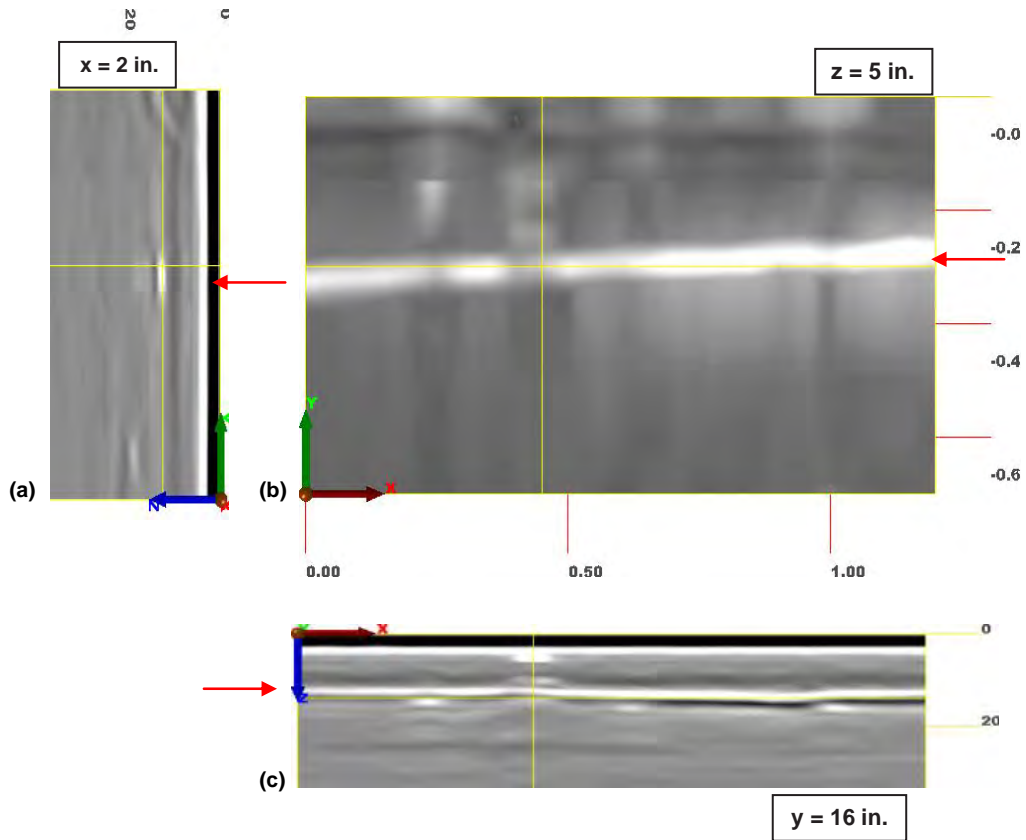


Figure Q.36. HL2, GPR: B-, C-, and D-scans showing first reinforcement bar along x-direction at depth of $z = 5$ in.

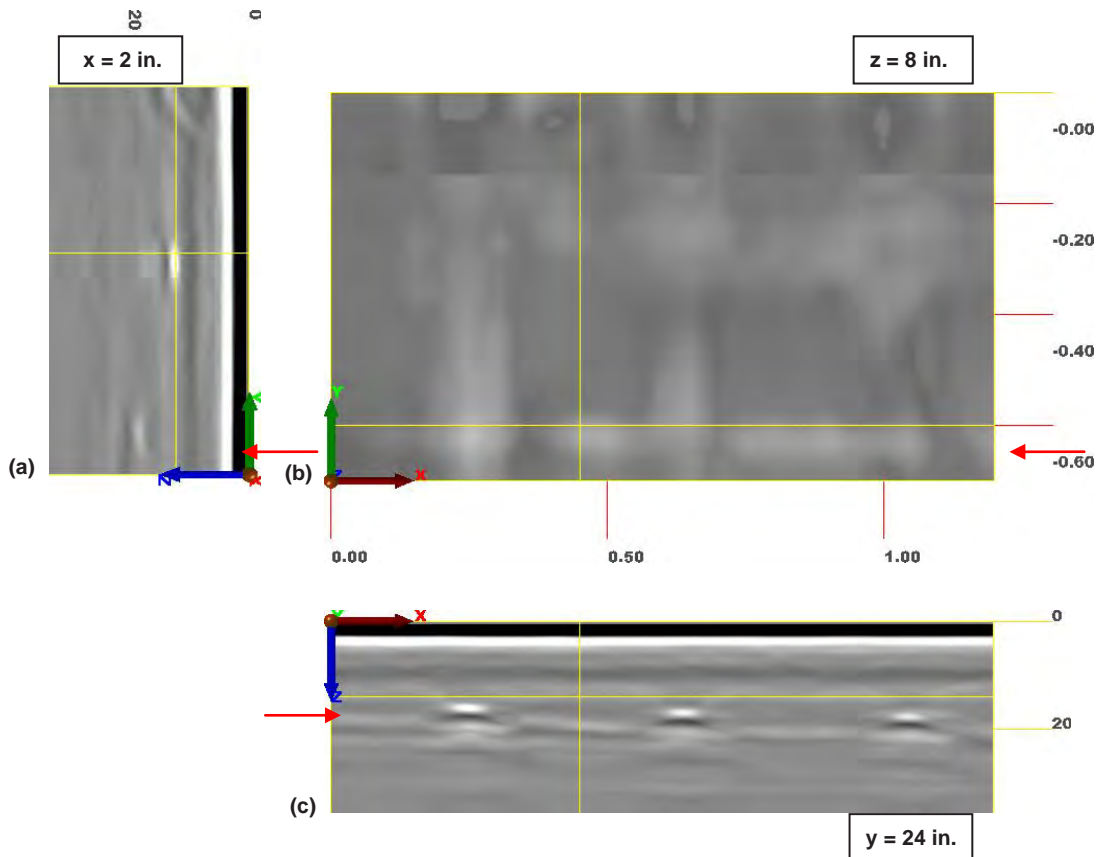


Figure Q.37. HL2, GPR: B-, C-, D-scans showing second reinforcement bar in x-direction at a depth of $z = 8$ in.

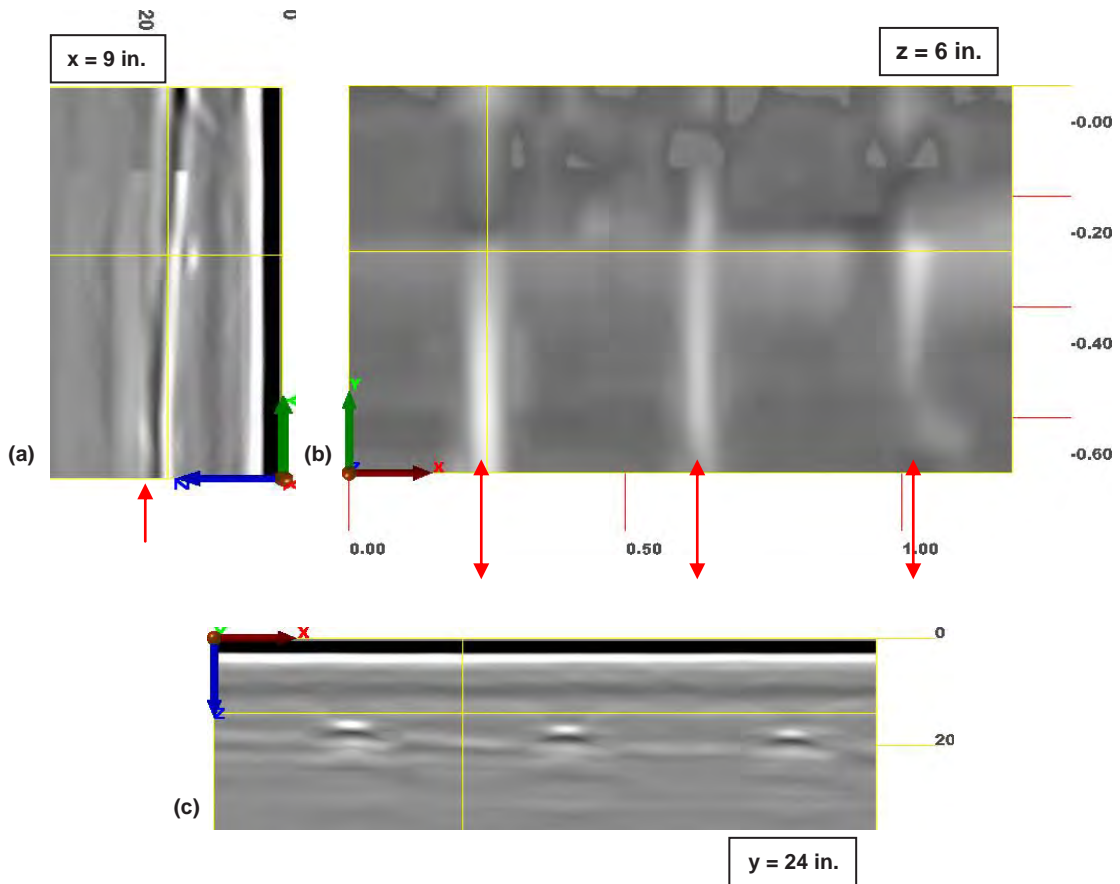


Figure Q.38. HL2, GPR: B-, C-, D-scans showing reinforcement bars in y-direction at depths between 6 in. and 8 in.

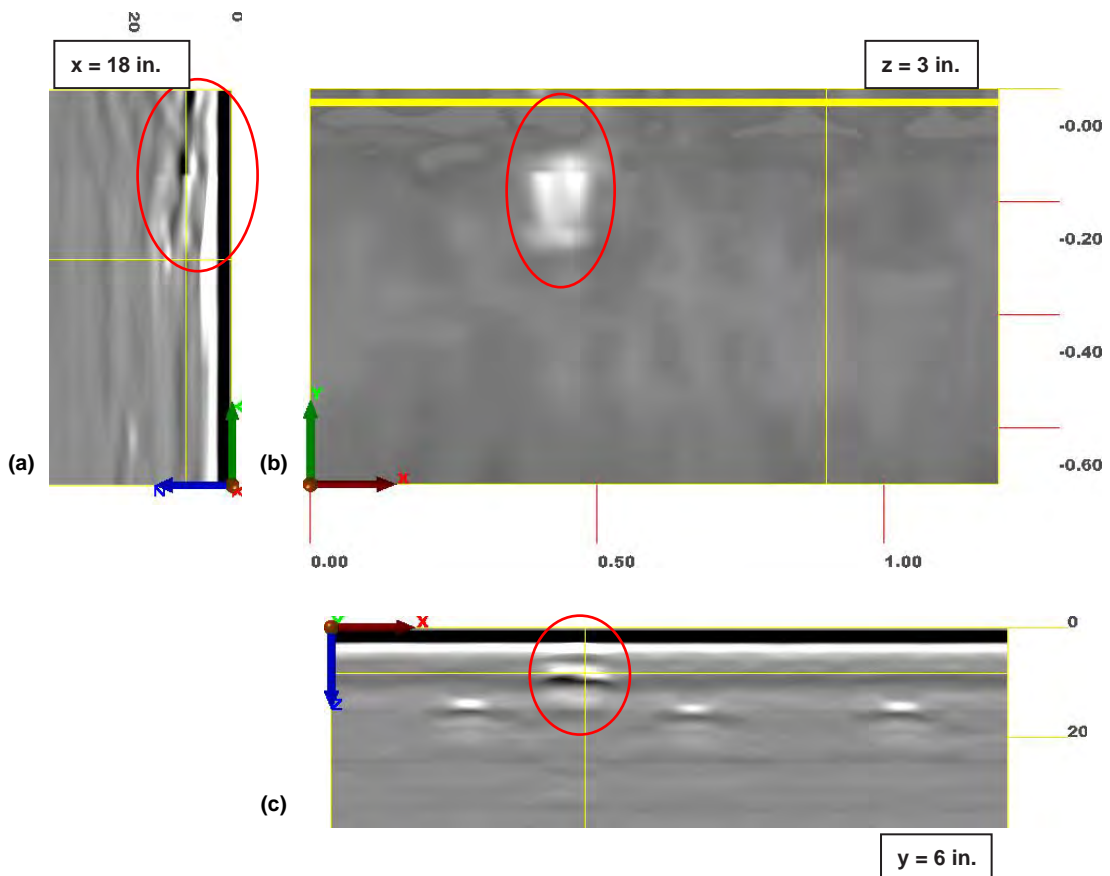


Figure Q.39. HL2, GPR: B-, C-, D-scans showing reflections caused by presence of a surface crack.

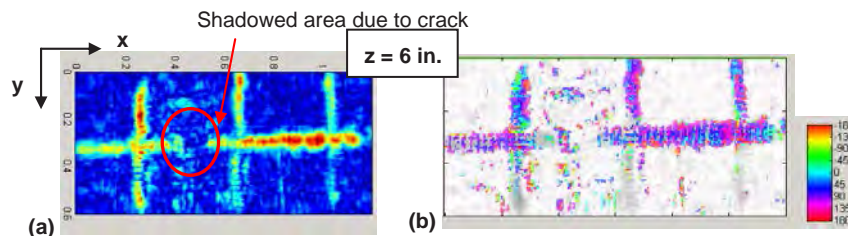


Figure Q.40. HL2, ultrasonic echo: C-scan at $z = 6$ -in. amplitude (a) and corresponding phase diagram (b). Missing part of reinforcement bar is due to surface crack within test area.

Ultrasonic Echo

The reinforcement mesh could be clearly seen in the ultrasonic echo C-scan at a depth of $z = 6$ in. (Figure Q.40). The corresponding phase diagram is also included in Figure Q.40b. As expected, the local phase of the reinforcement bars' reflections appeared mostly positive, which represented impedance higher than the surrounding concrete, that is, steel.

The B-scan (a) and D-scans (b) in Figure Q.41 show the steel bars in both directions. The reinforcement bar along the x -axis at an approximate depth of $z = 8$ in. (Figure Q.41c) would not be identified without previous knowledge of its existence through GPR data. The reinforcement bars in the y -direction were, however, easily detectable. The hole in the reinforcing bar reflections in Figure Q.40 and Figure Q.41b are due to the presence of moisture that intruded through the surface crack. It caused the US signal energy to be absorbed.

Figure Q.42 is a 3-D image of the volume intended to give an overall view of the reinforcement.

Impact Echo

Some of IE spectra showed a dominant frequency peak at about 3,600 Hz, which equals a depth of $z \sim 22$ in. However, in the B- and D-scans, no clear backwall could be seen. Figure Q.43 shows a typical example of the obtained IE D-scan

(Figure Q.43a) and A-scan (Figure Q.43b). The IE data for this test area yielded no reliable information about either the thickness of the lining or the presence of possible anomalies.

Comparison of Results

Reinforcement could be detected using both GPR and ultrasonic echo, although GPR exhibited a clear advantage in detecting deep steel bars, which could not be reliably identified in ultrasonic echo results. The surface crack was seen in the GPR data as a near-surface reflector, maybe because of moisture penetrating the tunnel lining through the crack, resulting in a change of the dielectric constant. The signature of this crack in the ultrasonic echo data was a hole in the reflections from the reinforcement bars. Neither GPR nor ultrasonic echo could give any indication of the thickness of the lining. IE spectra contained a repeated frequency peak at a frequency resonating at a depth of about $z \sim 22$ in., which could possibly have been the backwall.

GPR proved to be the most effective NDT method to detect the reinforcement as well as the effects of a surface crack. Even the extent of the affected area could be detected, as the anomaly was directly influencing the data. The crack could be indirectly detected in the ultrasonic echo results because the reflections from the reinforcements were shadowed by it. It is

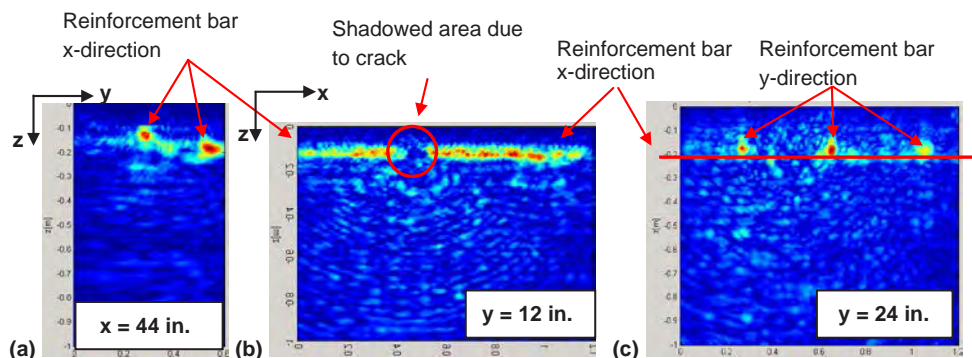


Figure Q.41. HL2, ultrasonic echo: B-scan (a) and D-scans (b) and (c) showing reinforcement in the x -direction (a) and (b) and in the y -direction (c). Reinforcement bar along x -axis at $z = 8$ in. is very weak (c).

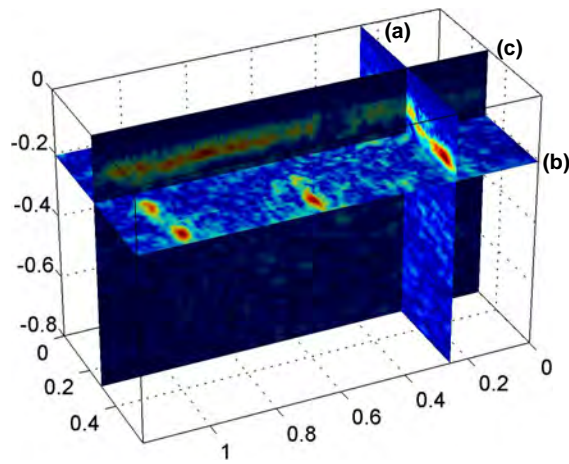


Figure Q.42. HL2, ultrasonic echo: 3-D image of volume positioned to reveal reinforcing elements, with B-scan (a) positioned at $x = 10.5$ in., C-scan (b) at $z = 8$ in., and D-scan (c) at $y = 12$ in. Missing reinforcement due to crack is also seen in D-scan.

a curious finding that the thickness of the lining could not be detected by either method, as the tunnel is relatively recent. IE, however, could provide some hints about the thickness of the tunnel. Ground truth information on the lining thickness would help verify the accuracy of the IE results.

Test Area 3

Description of the Test Area

The third test area at Hanging Lake Tunnel (HL3) was also near Section 57/58 of the tunnel, which was marked as such with spray on the floor (Figure Q.44a). The test area included a small crack (Figure Q.44b). A transverse joint crossed through the test field, and the area was relatively close to the

centerline of the tunnel. The field had an area of 48 in. by 24 in. The distance of the field to permanent features of the tunnel was not measured; therefore, the sketch in Figure Q.45 has no offsets marked. The grid spacing for ultrasonic echo and IE was 1 in., and for GPR was 2 in. Figure Q.44c shows an image of the ZFP scanner on the test area. During the testing, the longer side (length) of the GPR, ultrasonic echo, and IE transducers was set parallel to the centerline of the tunnel.

GPR Results

Figure Q.46 shows the reinforcement in the x -direction in B-, C-, and D-scans. One bar is at the edge of the test area. The steel bars ran from around $y = 8$ in. to $y = 6.5$ in. at a depth of $z = 5$ in., and from around $y = 24$ in. to $y = 22.5$ in. at a depth of $z = 4$ in. The transverse joint running across the test field was encircled on the radarscans. The reinforcement bars in the y -direction were positioned at $x = 10$ in., $x = 24$ in., and $x = 42$ in., at a depth of $z = 6$ in. (Figure Q.47). The scans from the joint crossing the test field at $x = 6$ in. in $z = 2$ in. are shown in Figure Q.48. Dowel-like steel elements traversing the joint at $z = 3$ in. can be seen in the B- and D-scans.

The line scans at $y = 0.45$ cm (18 in.), $y = 0.4$ cm (16 in.), and $y = 0.35$ cm (14 in.) were missing.

Figure Q.49 is a 3-D image of the volume intended to give an overall view of the reinforcing elements.

Ultrasonic Echo Results

The reinforcement running along both x - and y -directions at about $z = 6$ in. could be seen in the ultrasonic echo results, although the rebars along the x -axis at $y = 8$ in. and $y = 24$ in. did not appear as clearly as the ones along the y -axis at $x = 9$ in., $x = 24$ in., and $x = 40$ in. (Figure Q.50). The joint could not be identified in the ultrasonic echo results.

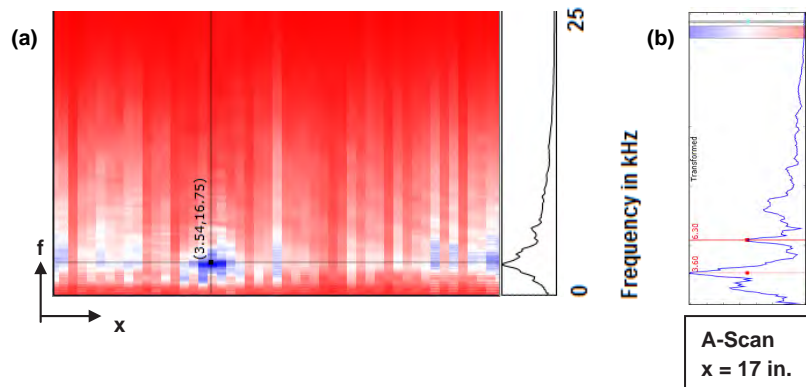


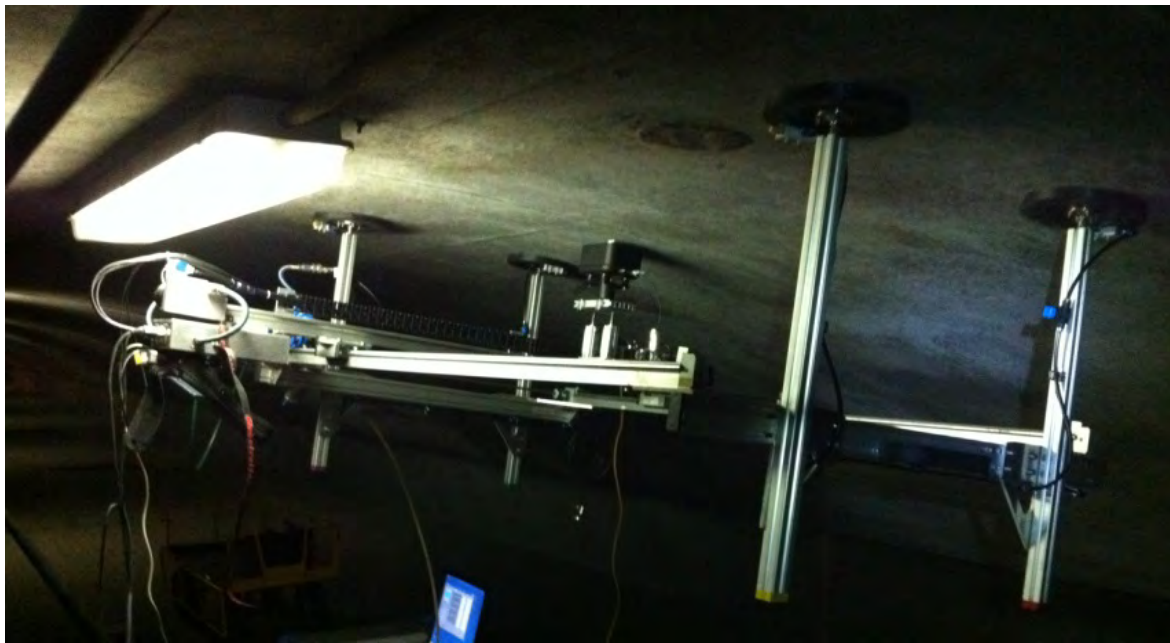
Figure Q.43. HL2, IE: D-scan (a) and A-scan (b). First frequency peak at 3,600 Hz could represent backwall in depth of $z \sim 22$ in.



(a)



(b)



(c)

Figure Q.44. HL3: (a) section marking on the floor, (b) crack across the field, and (c) ZFP scanner.

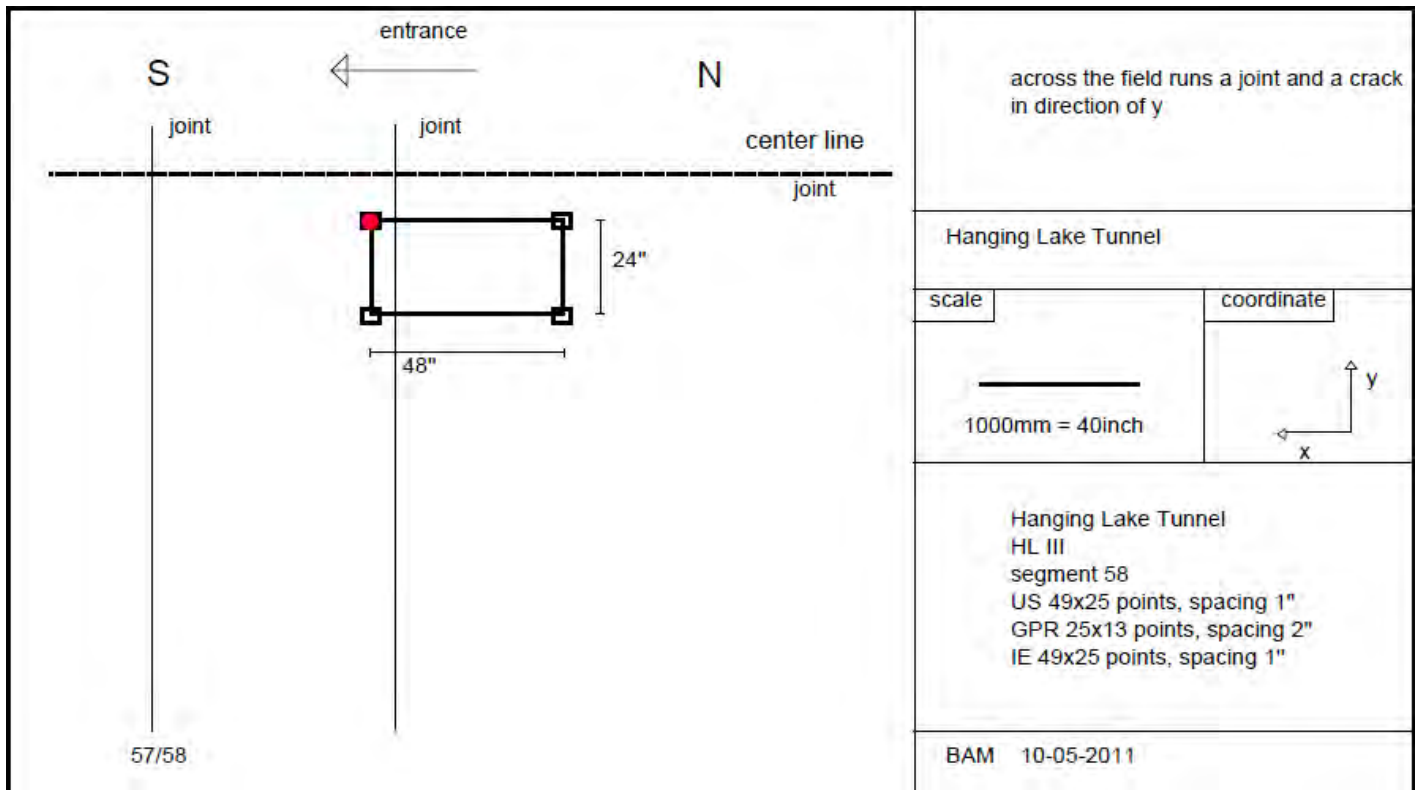


Figure Q.45. Sketch of test area HL3, segment 58, Hanging Lake Tunnel.

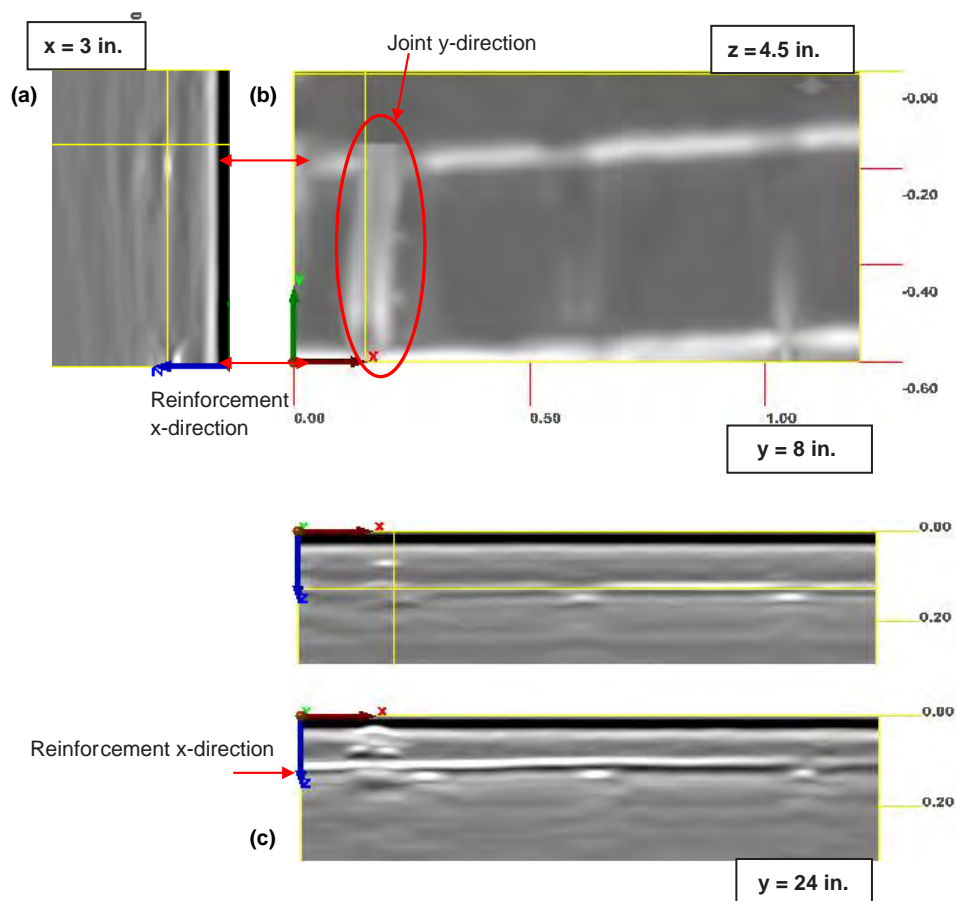


Figure Q.46. HL3, GPR: B-, C-, and D-scans of reinforcement in x-direction running along at a depth of $z = 5$ in. and $z = 4$ in. B-scan taken at $x = 3$ in. (a). C-scan at $z = 4.5$ in. with a width of 1.5 in. (b). D-scans taken from points $y = 8$ in. and $y = 24$ in. (c). Circled reflector is the joint.

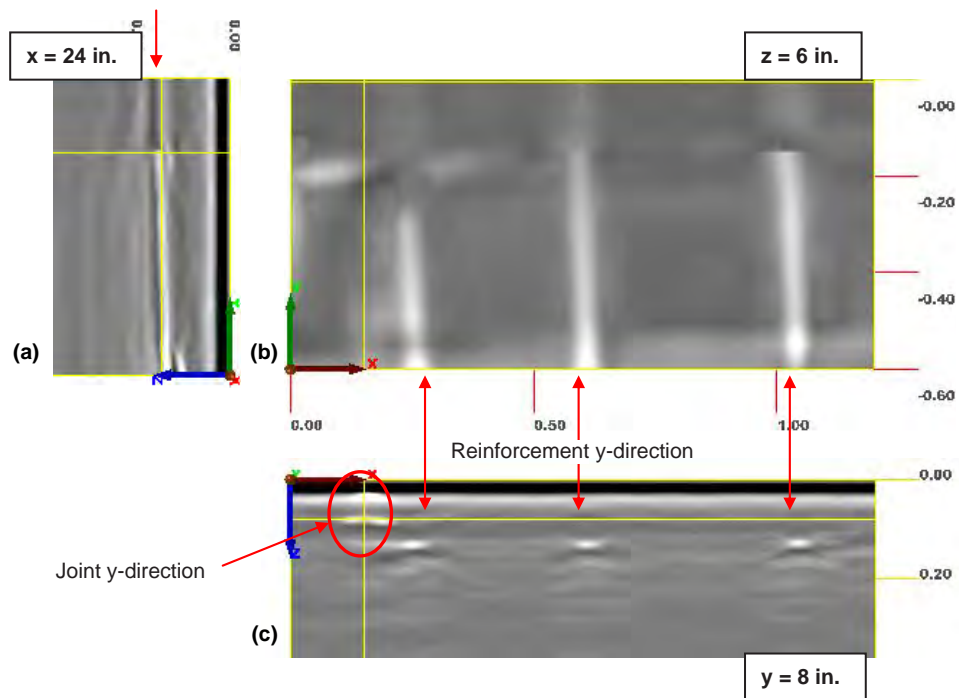


Figure Q.47. HL3, GPR: B-, C-, and D-scans of reinforcement bars running along y-direction at a depth of $z = 6$ in. B-scan taken at $x = 24$ in. (a). C-scan at $z = 6$ in. (b). D-scan at $y = 8$ in. (c). Circled reflector is the joint.

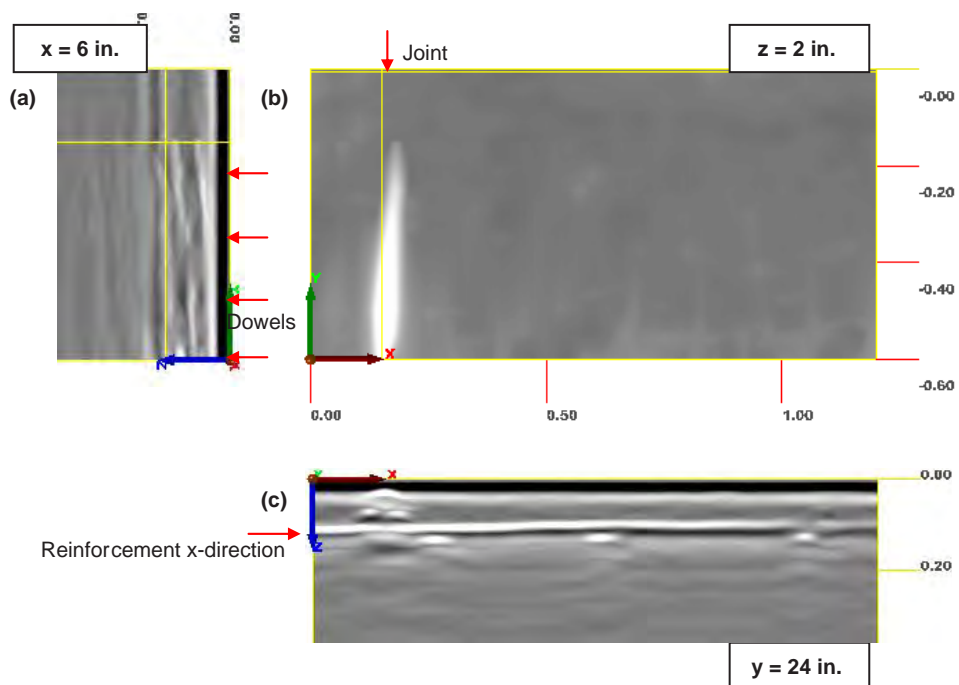


Figure Q.48. HL3, GPR: B-, C-, D-scans corresponding to location of joint at $x = 6$ in.

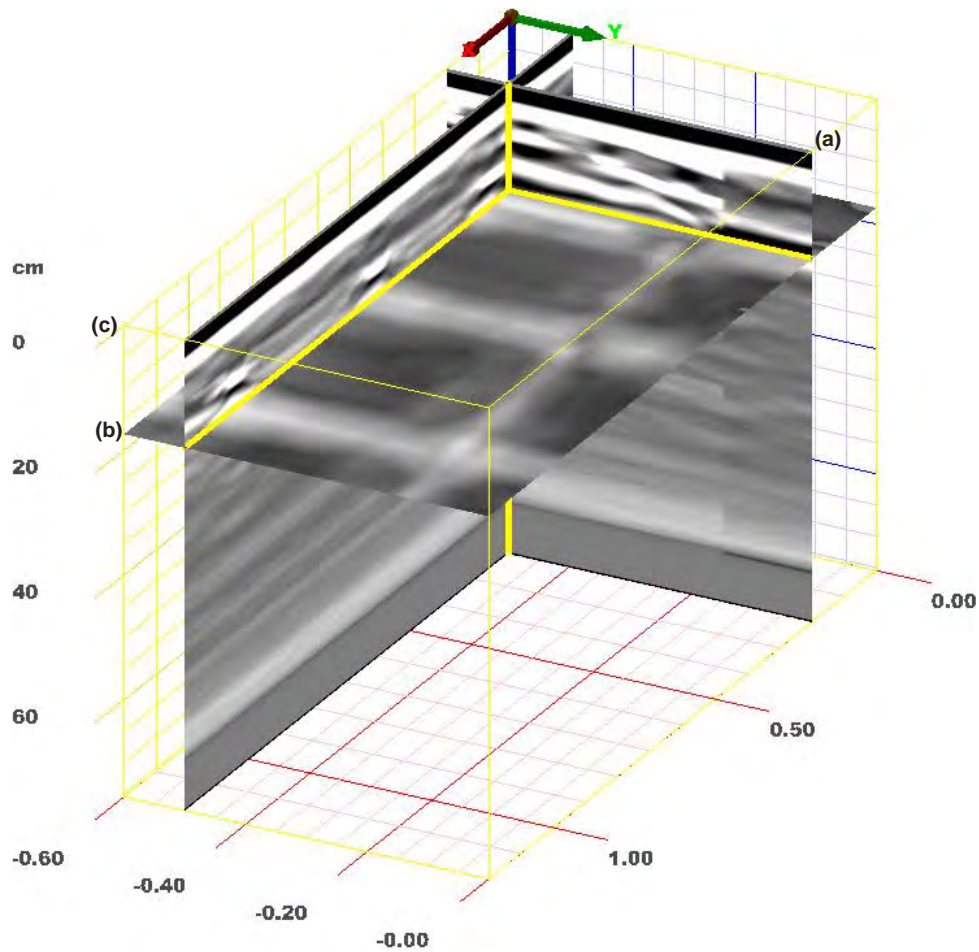


Figure Q.49. HL3, GPR: 3-D image of volume positioned to reveal reinforcing elements, with B-scan (a) positioned at $x = 8$ in.; C-scan (b) at $z = 7$ in., 1 in. wide; and D-scan (c) at $y = 16$ in.

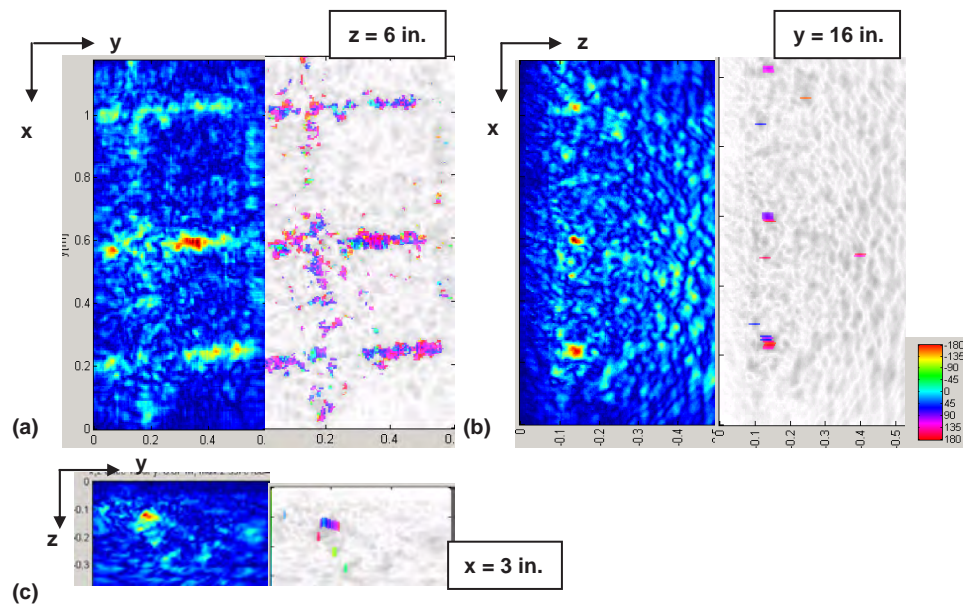


Figure Q.50. HL3, ultrasonic echo: B-, C-, D-scans showing reinforcement bars running along x - and y -direction at depth of $z = 6$ in.

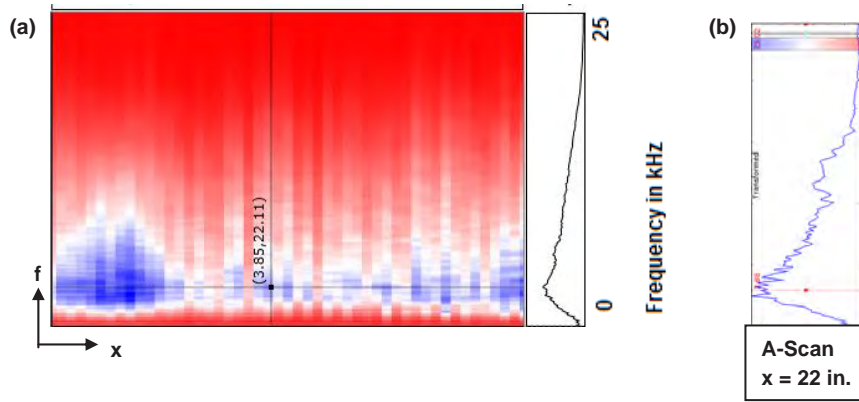


Figure Q.51. HL3, IE: Typical D-scan (a) and A-scan (b). No clear frequency peaks, which could have represented a possible backwall or other reflectors, could be identified.

Impact Echo Results

No features were resolved on the basis of the IE results, as the frequency peaks were generally too broad to point to any particular resonating feature (Figure Q.51).

Comparison of Results

Reinforcement could be detected with both GPR and ultrasonic echo, but they were much clearer with GPR. The joint seen on the surface of the field could only be detected with GPR, as well as two beams. None of the NDT methods resolved the end of the tunnel lining.

Measurement Results for Chesapeake Bay Bridge-Tunnel

Measurements in the Chesapeake Channel Tunnel (a part of the Chesapeake Bay Bridge-Tunnel system) were taken over

two days: October 11 and 12, 2011. Four test fields were tested, three of which were located in the tunnel's exhaust air duct (shown in Figure Q.52). The fourth test area was on the tiles of the tunnel wall itself.

Test Area 1

Description of the Test Area

The first test field (CPB1) was located at Station 474+27. A sketch of the field showing its positioning in the tunnel is shown in Figure Q.53. The 48-in. by 24-in. test area started immediately above the pipe. A joint ran across the field, parallel to its shorter side, at one-fourth its length. The center of the ZFP scanner's feet were at 14 in. to the left of the joint marked Station 474+27, facing the tunnel wall and about 29 in. down from the joint running along the tunnel. When looking north, this joint was about 7 in. to the left of the vertical stands (centerline). The tunnel's entrance is at Station 470 south end. The

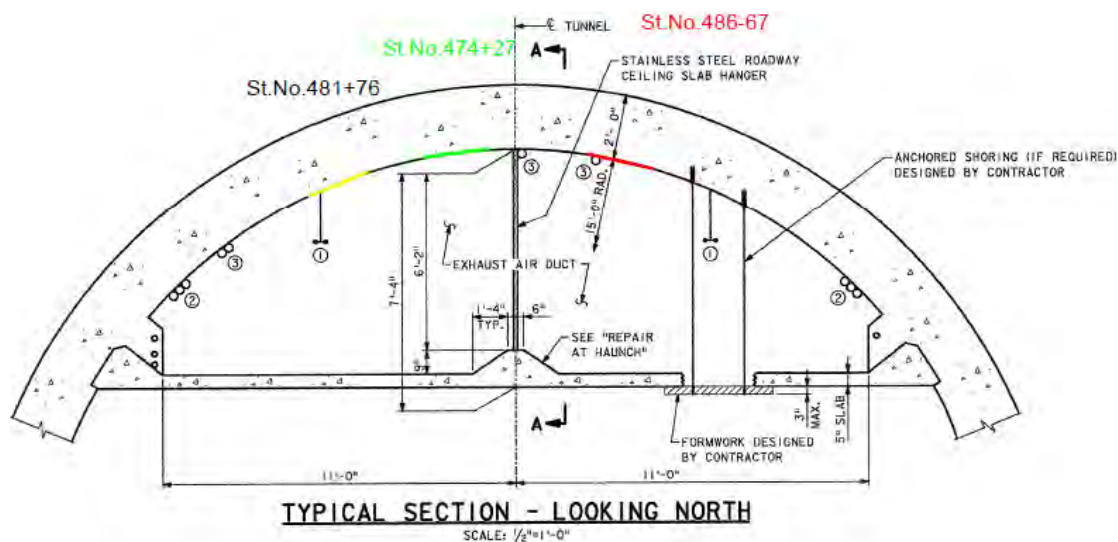


Figure Q.52. Cross section of exhaust air duct of Chesapeake Channel Tunnel.

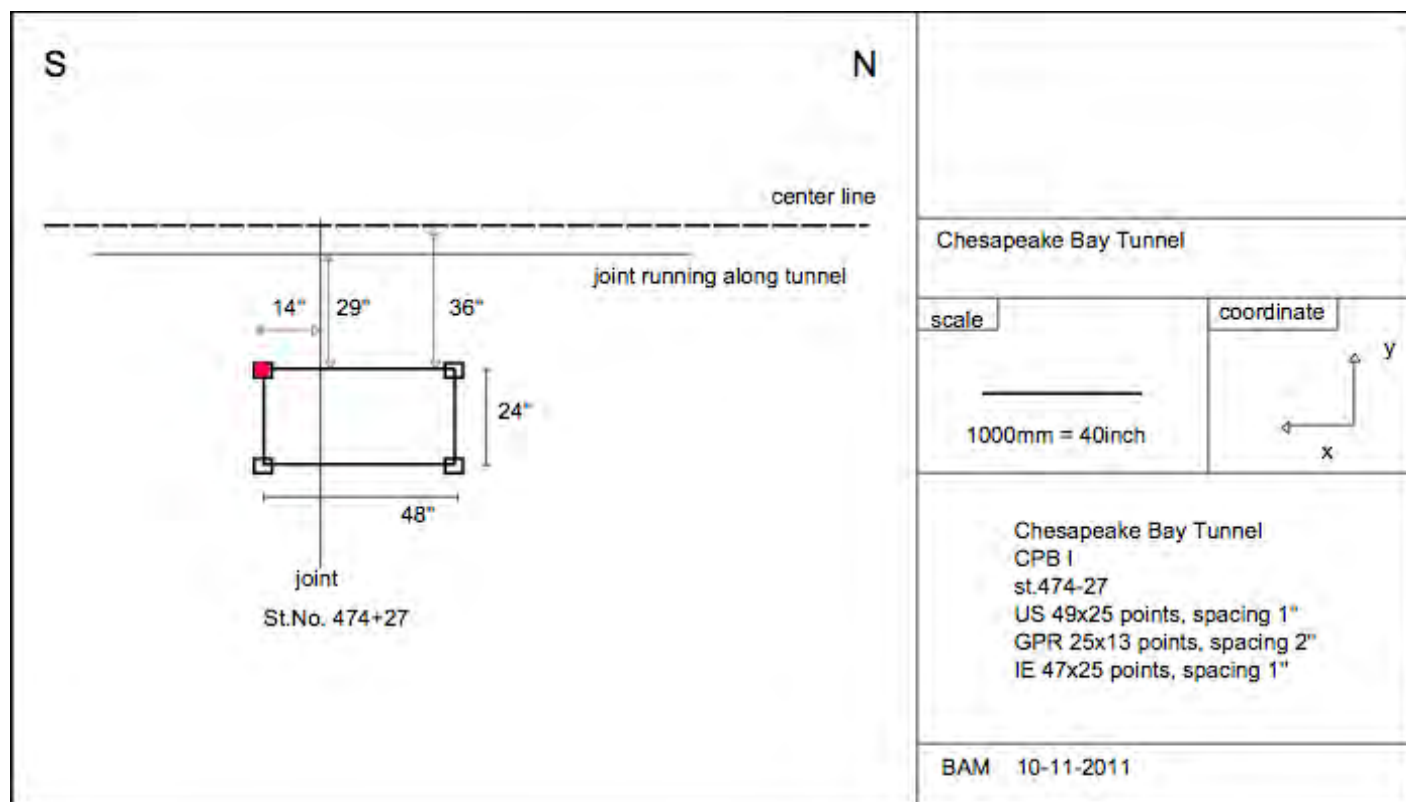


Figure Q.53. Sketch of test area CPB1, Station 474-27, Chesapeake Channel Tunnel.

backwall has a nominal thickness of 24 in., according to the tunnel's blueprints, and has a so-called steel skin.

The grid spacing for ultrasonic echo and IE testing was set to 1 in., and for GPR, 2 in. During the testing, the GPR, ultrasonic echo, and IE transducers were positioned such that their lengths were parallel to the centerline of the tunnel.

GPR Results

Figure Q.54 gives an overview of the reinforcement within the volume.

The reinforcements in the y -direction at a depth of $z = 1.5$ in. and in the x -direction at a depth of $z = 3$ in. are depicted in the C-scans of Figure Q.55. The transverse bars along the y -axis were detected at $x = 0$ in. (i.e., under one of the shorter sides of the test area), $x = 12$ in., $x = 24$ in., and $x = 42$ in. The longitudinal reinforcement was detected at $y = 16$ in.

Figure Q.56 includes two D-scans, one at $y = 22$ in. and another one at $y = 16$ in. that cuts through the longitudinal rebar appearing in Figure Q.55b. A selection of B-scans cutting through the transverse rebars at $x = 24$ in. and $x = 42$ in. is shown in Figure Q.57.

Ultrasonic Echo Results

Transverse steel bars along the y -direction could be clearly detected and identified using the ultrasonic echo technique as

well (see the C-scan of Figure Q.58 taken at $z = 2$ in.). The reflections from the longitudinal bar in the x -direction in the C-scan were vaguely seen, although they could be more clearly seen in the later B-scans. This repeating observation resulted from the orientation of the ultrasonic echo transducer, which made it more sensitive to transverse reinforcement (the polarization effect). When examining the C-scans (Figure Q.59) at different depths, the steel skin of the tunnel at about $z = 24$ in. was detected. The shear wave velocity was adjusted to about 2,710 m/s such that the backwall reflections occurred at the known depth of 24 in. A shallower anomaly was detected at $z = 15$ in., spreading from $x = 20$ in. to $x = 40$ in. and $y = 6$ in. to $y = 14$ in., detected both directly and indirectly through its shadowing of the skin reflections. The corresponding phase diagrams exhibited a positive phase for the reinforcement bars and steel skin and a mixture of positive and negative angles (inconclusive) for the anomaly.

Looking at the D-scan at $y = 12$ in. (Figure Q.60), the rebars and the backwall at $z = 24$ in. are clearly seen. About one-half of the backwall (with $x > 24$ in.) exhibited weakened reflections or even missing reflections. The phase evaluation offered more information about why the backwall reflections appeared weaker: at a depth of around $z = 16$ in. was a confined anomaly that shadowed the backwall reflection between $x = 22$ in. and $x = 30$ in. This anomaly was the same as seen in the C-scan in Figure Q.59.

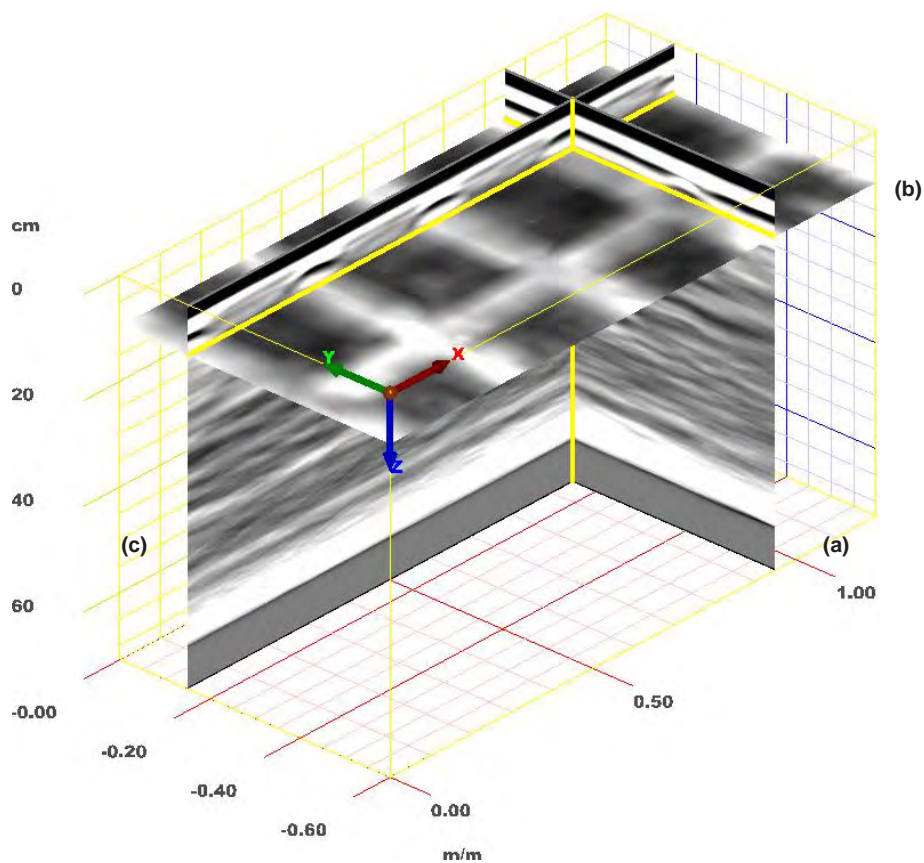


Figure Q.54. CPB1, GPR: 3-D image of volume positioned to reveal reinforcing elements, with B-scan (a) positioned at $x = 38$ in.; C-scan (b) at $z = 4$ in., 1 in. wide; and D-scan (c) at $y = 6$ in.

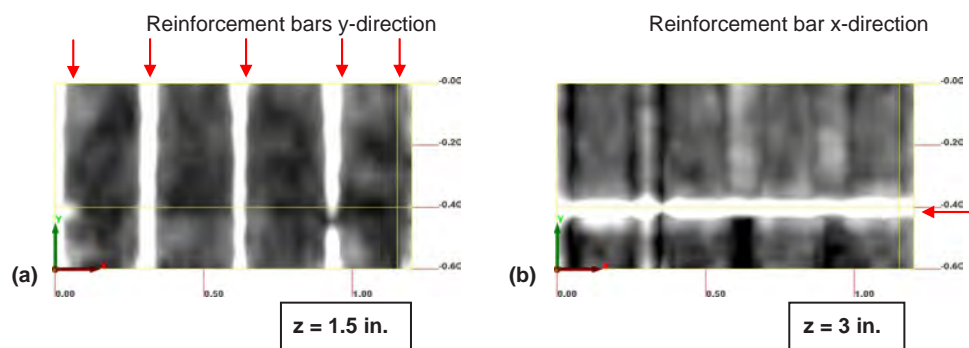


Figure Q.55. CPB1, GPR: C-scans depicting reinforcement bars (a) along y -directions at $z = 1.5$ in. and (b) in the x -direction at a depth of about $z = 3$ in.

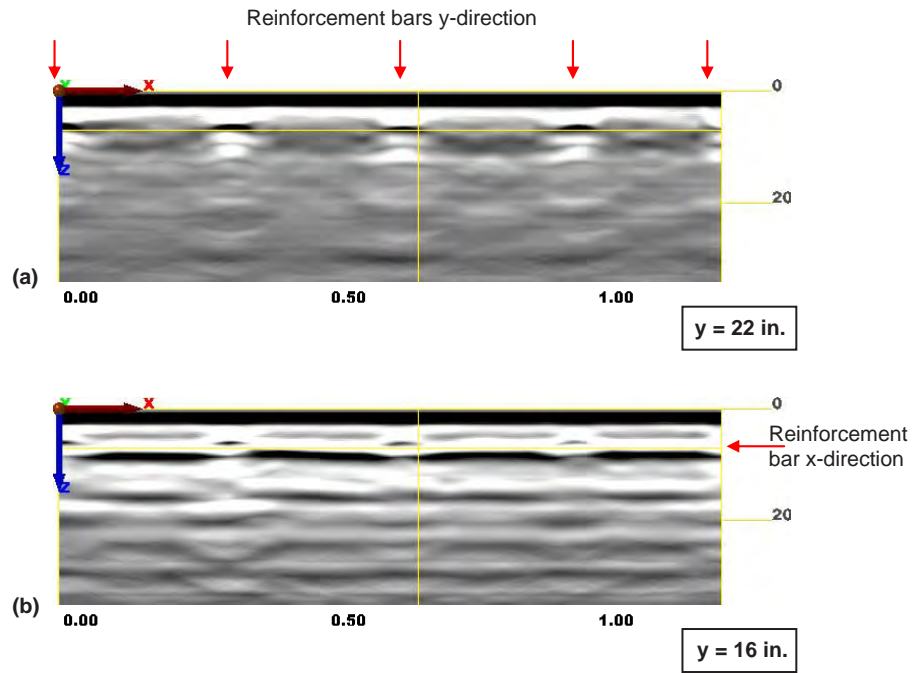


Figure Q.56. CPB1, GPR: D-scans showing reinforcement bars (a) along y-direction at location $y = 22$ in. and (b) x-direction at location $y = 16$ in.

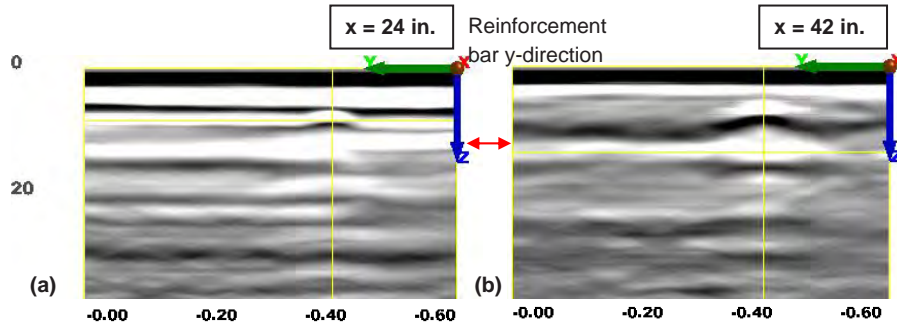


Figure Q.57. CPB1, GPR: B-scans of transverse rebar (along y-direction) taken at (a) $x = 24$ in. and (b) $x = 42$ in.

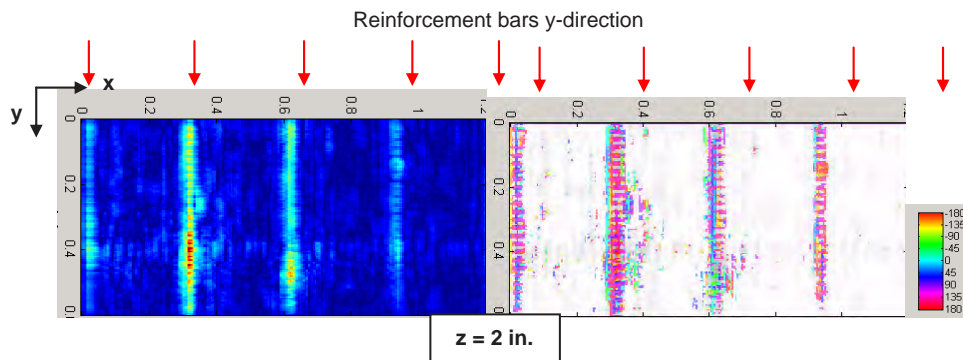


Figure Q.58. CPB1, ultrasonic echo: C-scan showing transverse reinforcement in y-direction at $z = 2$ in.

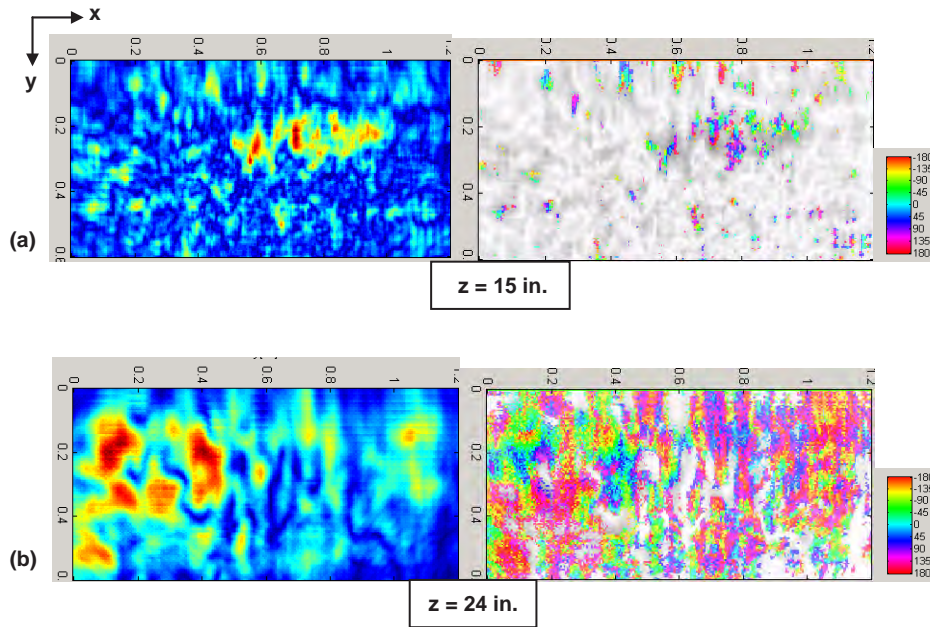


Figure Q.59. CPB1, ultrasonic echo: C-scans showing reflection from anomaly (a) and tunnel skin (b).

The B-scans in Figure Q.61 were chosen to represent areas of the test volume with and without anomaly. The left image in Figure Q.61 is a B-scan at $x = 3$ in., with no anomaly. The backwall and reinforcement bar in x -direction (at $y = 16$ in.) can be clearly seen. The other B-scan was obtained by cutting through the anomaly at $x = 28$ in. The backwall is missing between $y = 8$ in. and $y = 12$ in. and some reflections from about $z = 13$ in. downwards can be seen. The corresponding phase diagrams are not conclusive.

Figure Q.62 is a 3-D image of the volume, showing the backwall and anomaly.

Impact Echo Results

The IE spectra contained a clear thickness resonance frequency peak at a frequency between 3,600 Hz and 3,400 Hz,

representing a thickness of about $z = 22$ in. to $z = 24$ in., assuming a longitudinal wave velocity of 4,000 m/s. Figure Q.63 shows the selected B-scan (Figure Q.63a) and D-scan (Figure Q.63b) of the test volume along with a representative A-scan and frequency spectrum. The amplitudes of the backwall echo in the D-scan between $x = 27$ in. and $x = 46$ in. were weaker than in the area $x < 27$ in., indicating the presence of an inhomogeneity between the sensor and the backwall absorbing the wave energy. The same was true for the B-scan between $y = 0$ in. and $y = 8$ in.

Comparison of Results

While GPR proved to be the most reliable NDT method for detecting and identifying reinforcement bars, it could not detect a 15-in.-deep localized anomaly. The ultrasonic echo

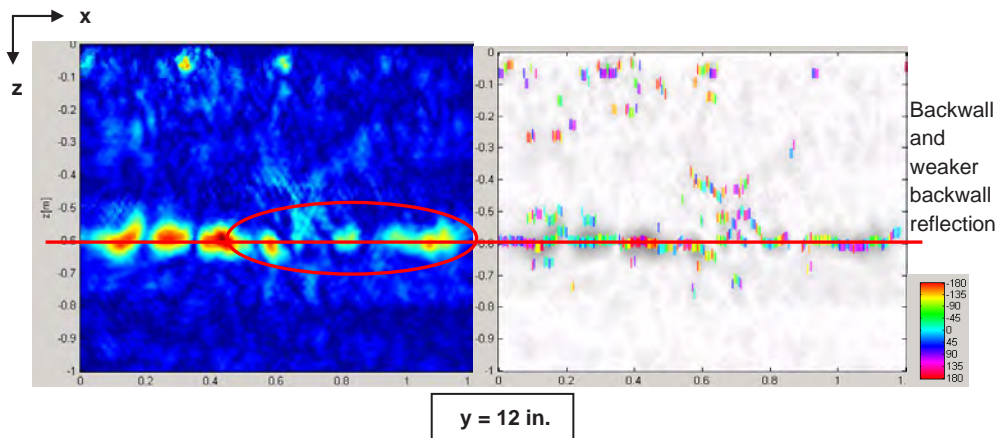


Figure Q.60. CPB1, ultrasonic echo: D-scan showing reinforcement and tunnel skin. Weakened reflection from backwall is marked.

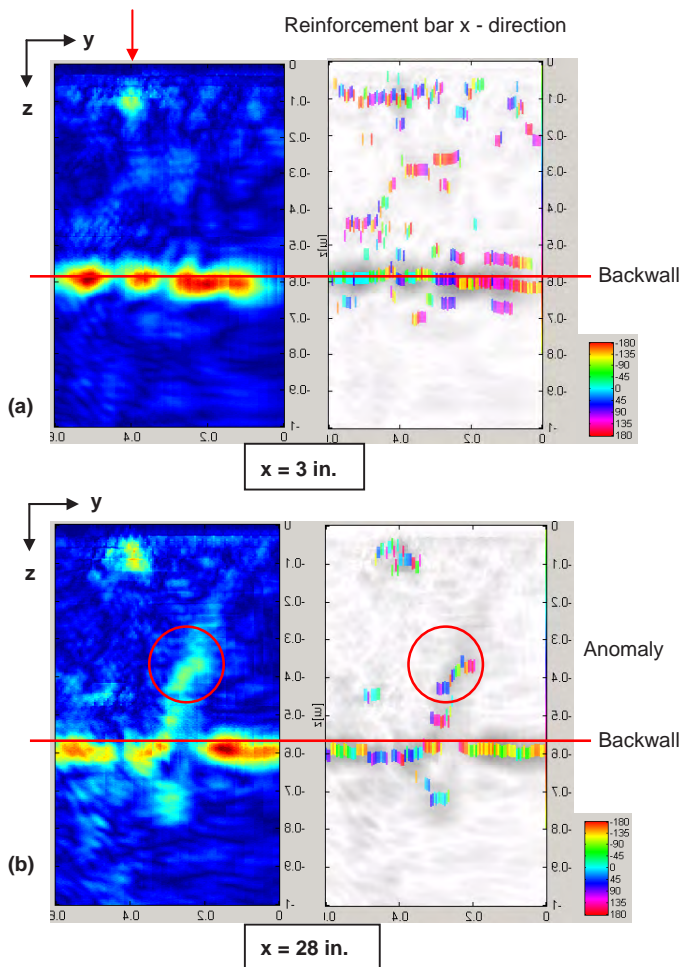


Figure Q.61. CPB1, ultrasonic echo: B-scan showing longitudinal reinforcement bar (along x-direction) and backwall, where no anomaly was detected (a), and where an anomaly was detected (b).

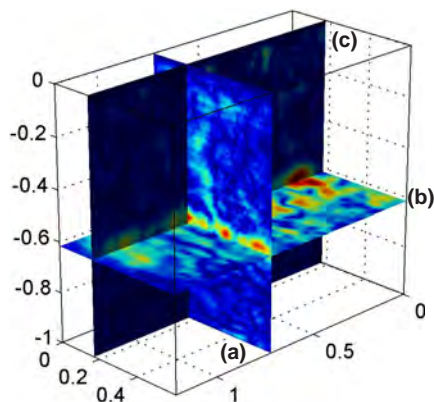


Figure Q.62. CPB1, ultrasonic echo: 3-D image of volume positioned to reveal backwall and anomaly, with B-scan (a) positioned at x = 29 in., C-scan (b) at z = 24 in., and D-scan (c) at y = 7 in.

technique, however, was not as clear in detecting the steel bars (due to the polarization effects) but indicated the presence of an anomaly, directly and indirectly (directly by evaluating the reflections from the anomaly and indirectly based on the weakened and even missing backwall echo).

Both ultrasonic echo and IE could yield the thickness of the tunnel lining. The phase diagrams allowed the ultrasonic echo results to even indicate that the impedance of the tunnel's skin was higher than that of the lining and, therefore, of steel. This could be verified by the tunnel's blueprint indicating the presence of a steel skin.

Considering the obtained data from all three employed NDT methods together, a clearer picture of the geometry and condition of the tunnel emerged.

Test Area 2

Description of the Test Area

The test area CPB2 was located on the west side of the tunnel, facing north. It was located south of the joint marked Station 481+76, and the entire area was on a single block. The 48-in. by 24-in. test area was oriented such that its length was parallel to the centerline of the tunnel. The near and far shorter sides of the scanning aperture were 9 in. and 49 in. south of Station 481+76. The longer side was 47 in. away from the tunnel's centerline, where the vertical stands were. Figure Q.64 provides a rough sketch of the test area and its positioning within the tunnel.

The grid spacing for ultrasonic echo and IE testing was set to 1 in., and for GPR, it was 2 in. The GPR, ultrasonic echo, and IE transducers were oriented such that their lengths were parallel to the centerline of the tunnel. Note that the GPR measurements for this test area were shifted 1.5 in. in the x-direction compared with those from IE and ultrasonic echo.

GPR Results

Figure Q.65 is a 3-D image of the volume with the slices (B-, C-, and D-scans) positioned to reveal the reinforcing elements.

Transverse reinforcement in the y-direction could be detected at a depth of z = 2.5 in. with the bars positioned at x = 0 in., x = 12 in., x = 24 in., and x = 36 in. Two longitudinal steel rebars in the x-direction appeared 4-in. deep at y = 8 in. and y = 24 in. The one at y = 24 in. ran out of the test field and was only partly visible.

Figure Q.66 provides C-scans showing the reinforcement mesh at two different depths. D-scans taken at y = 8 in. and y = 24 in. showed the rebars in the y-direction as well as one of the rebars in the x-direction (see Figure Q.67). One B-scan at x = 12 in. cutting through one of the transverse rebars and a second one at x = 16 in. cutting between the transverse rebars, showing the longitudinal rebars, are shown in Figure Q.68.

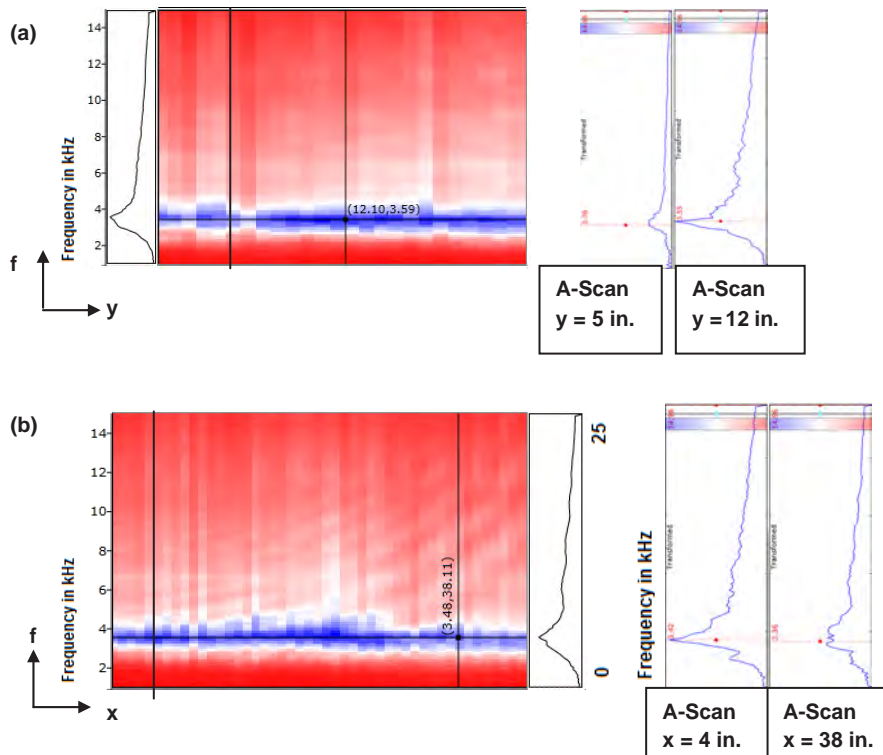


Figure Q.63. CPB1, IE: (a) B-scan and (b) D-scan of profile lines along y- and x-axes of field coordinate system. A-scans (right): Frequency peaks represent tunnel lining thickness. Areas with weaker amplitudes indicate wave energy absorbing inhomogeneity.

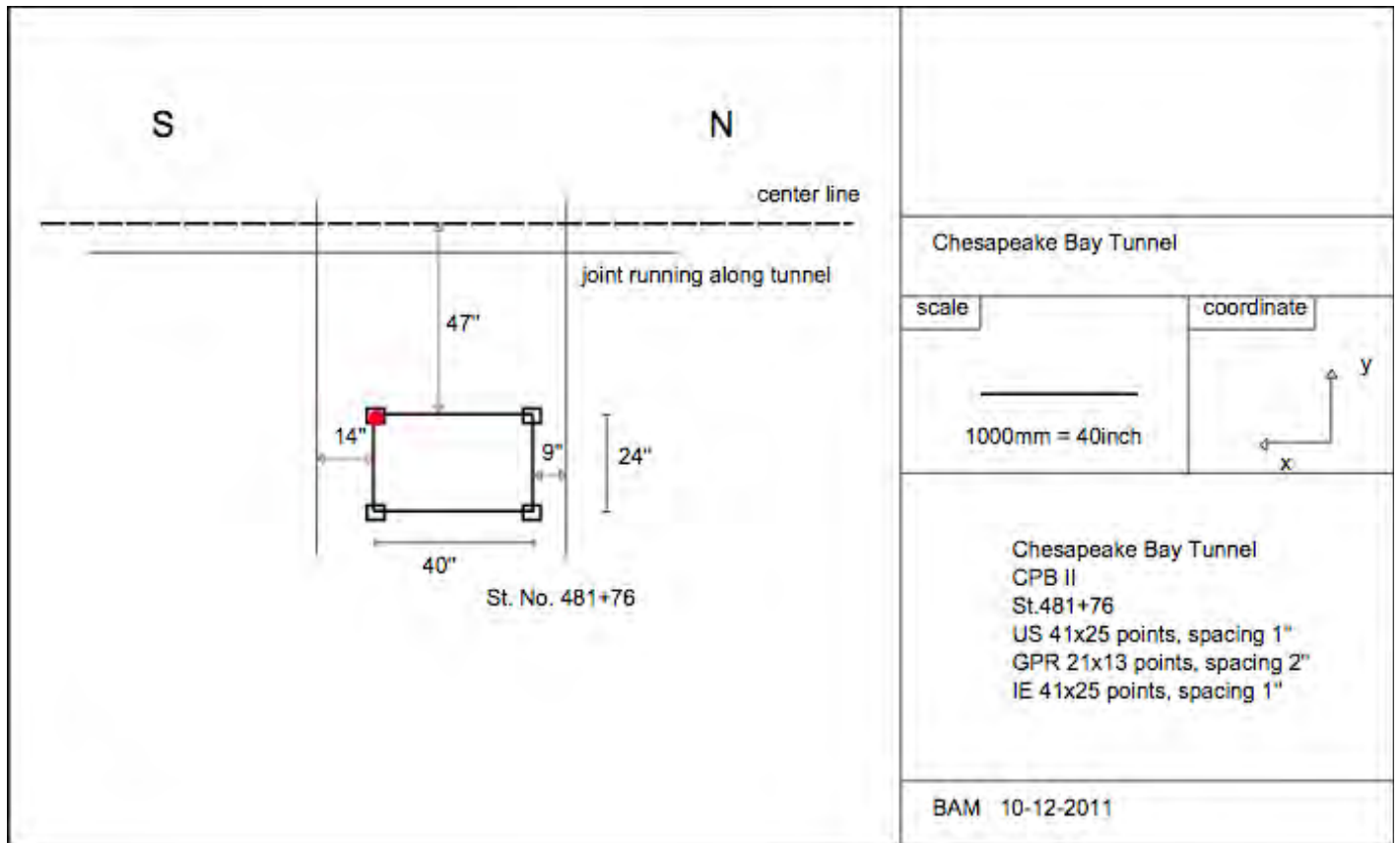


Figure Q.64. Sketch of test area CPB2 south of Station 481+76, Chesapeake Channel Tunnel.

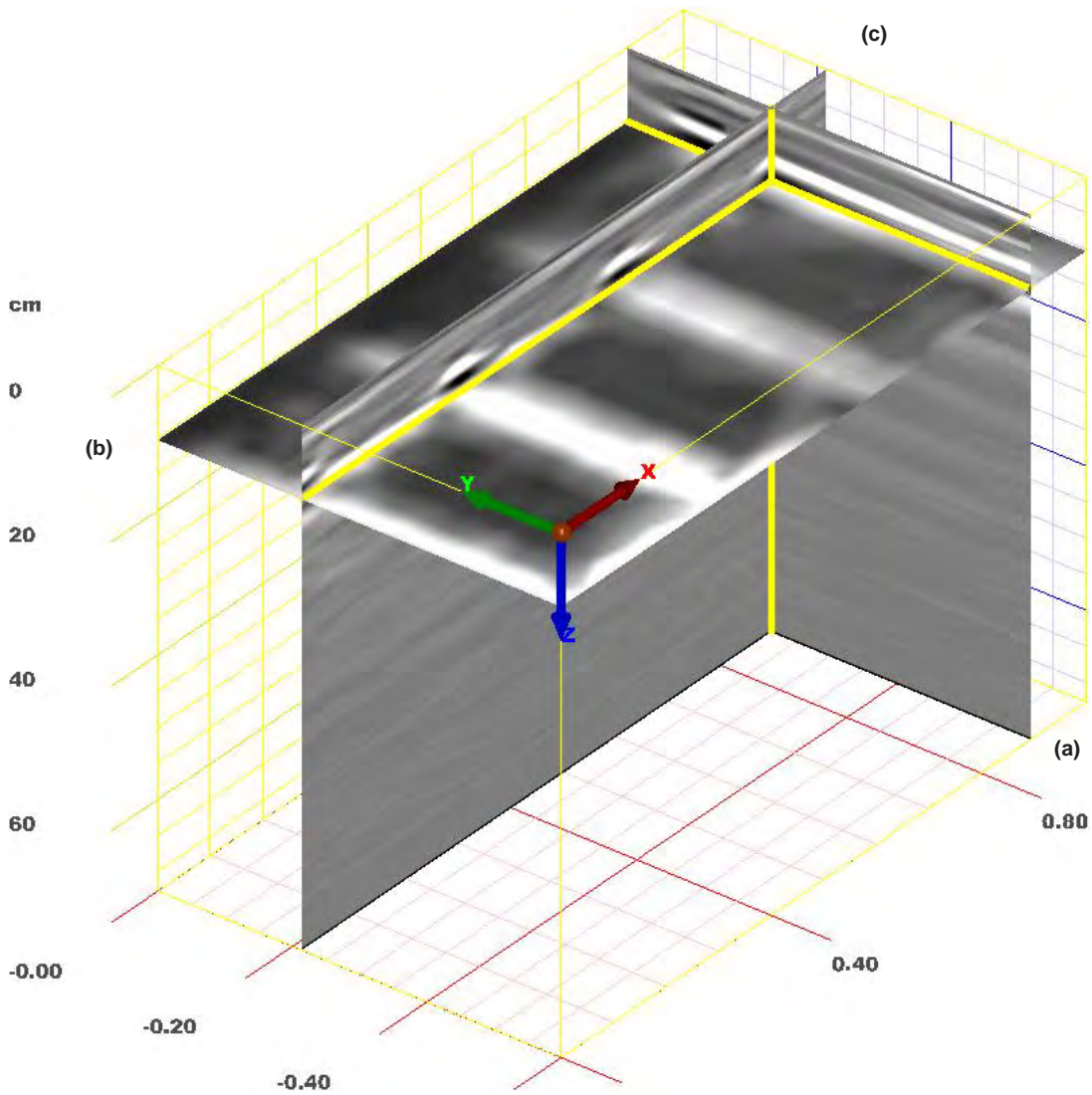


Figure Q.65. CPB2, GPR: 3D image of volume positioned to reveal reinforcing elements, with B-scan (a) positioned at $x = 36$ in.; C-scan (b) at $z = 4$ in., 4 in. wide; and D-scan (c) at $y = 8$ in.

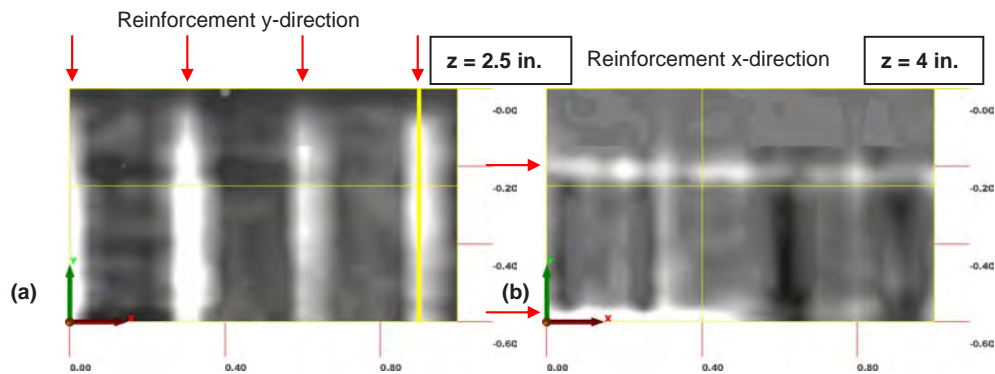


Figure Q.66. CPB2, GPR: C-scans at $z = 2.5$ in. and $z = 4$ in. showing rebars in y -direction (a) and x -direction (b).

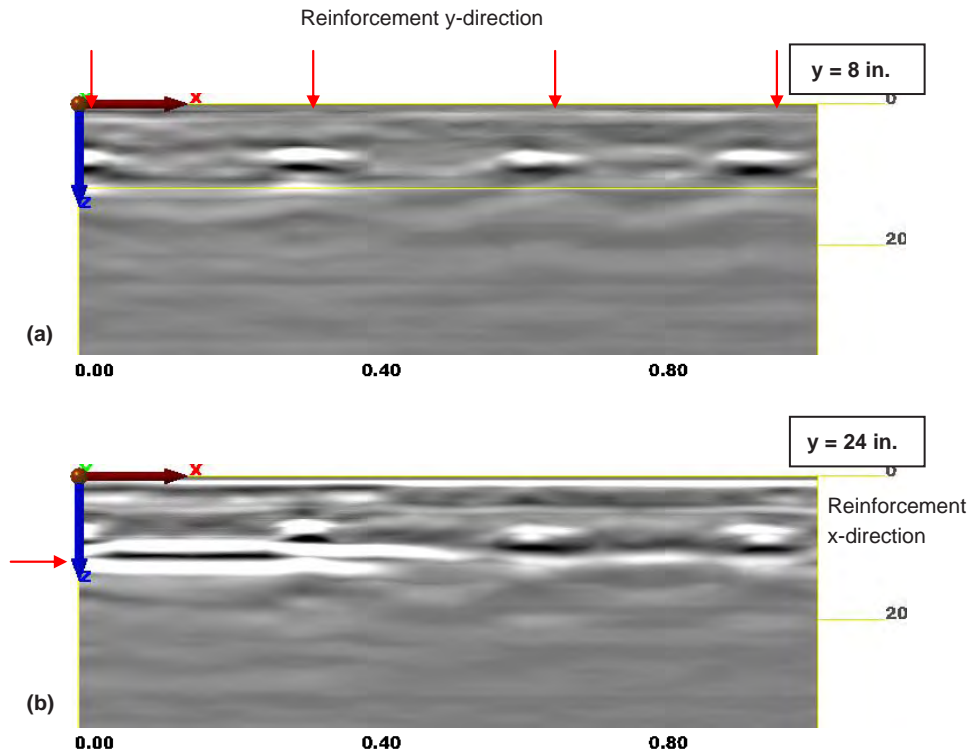


Figure Q.67. CPB2, GPR: D-scans through test volume at positions $y = 8$ in. and $y = 24$ in. showing reinforcement in y -direction (a) and in x -direction (b).

Ultrasonic Echo Results

Figure Q.69 shows a 3-D image of the volume focusing on the backwall and an anomaly shadowing it.

The reinforcement mesh was not clear in the ultrasonic echo C-scans. The transverse bars along the y -axis were most clearly seen in the C-scan at $z = 2$ in. (Figure Q.70a), and those along the x -axis at $z = 4$ in. (Figure Q.70b).

Besides the reinforcements, an anomaly at $z = 20$ in. (Figure Q.71a) and the backwall at $z = 28$ in. (Figure Q.71b) could also be detected in the C-scans. The anomaly had a phase shift between 45° and -45° (of lower acoustic impedance than concrete). The backwall exhibited a phase shift between -90° and -180° (of higher acoustic impedance than concrete).

To analyze the ultrasonic echo data, a transversal wave velocity of 2,710 m/s was assumed (taken from the measurements at CPB1).

By examining D-scans (Figure Q.72) and B-scans (Figure Q.73), the extent of the anomaly could be approximated as running along the entire width of test field CPB2 (i.e., y -direction) but confined between $x = 8$ in. and $x = 28$ in. in the x -direction.

Impact Echo Results

The IE spectra contained two distinct frequency peaks at about 2,900 Hz and 4,100 Hz (see spectral A-scans of

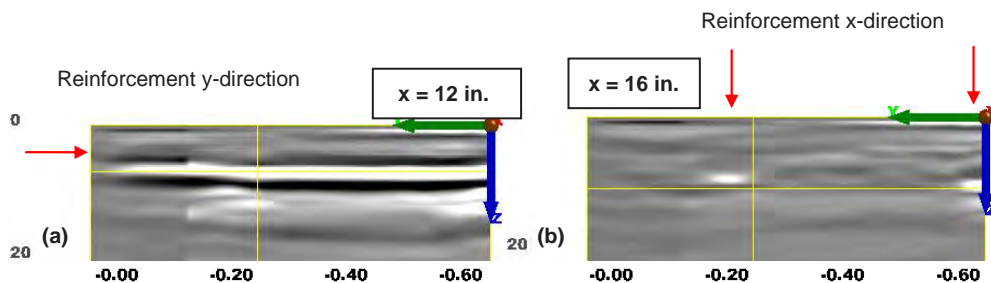


Figure Q.68. CPB2, GPR: B-scans taken at $x = 12$ in. and $x = 16$ in. showing rebars in y -direction (a) and in x -direction (b).

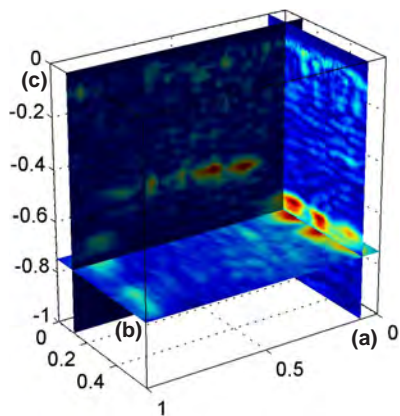


Figure Q.69. CPB2, ultrasonic echo: 3-D image of volume positioned to reveal backwall and anomaly, with B-scan (a) positioned at $x = 3$ in.; C-scan (b) at $z = 25$ in., 5 in. wide; and D-scan (c) at $y = 4$ in.

Figure Q.74) corresponding to the reflector depths of $z = 27$ in. (Figure Q.74a) and $z = 20$ in. (Figure Q.74b), respectively.

The D-scan in Figure Q.75 shows a clear shift in the frequency peak from 3,000 Hz up to 3,700 Hz, corresponding to the approximate depths of $z = 27$ in. (lining thickness) and $z = 21$ in. (anomaly).

Comparison of Results

Steel reinforcement was best located with GPR. Two reflectors at two different depths were detected by both ultrasonic echo and IE. Phase analysis of the ultrasonic echo results showed different phase shifts at the reflectors: the phase shift at the shallower reflector (at 20 in.) indicated an impedance lower than concrete, while the deeper reflector (at 28 in.) had an acoustic impedance higher than concrete. This higher impedance is typical of concrete-metal interfaces and leads to the assumption of it being the echo of the metal skin surrounding the tunnel, although the estimated depth of 28 in. does not match the

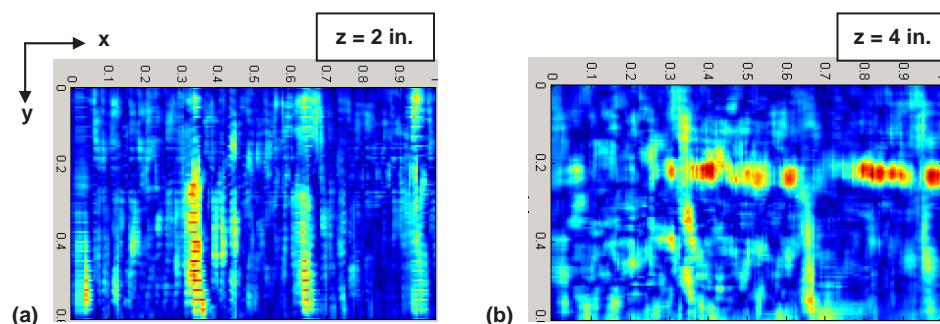


Figure Q.70. CPB2, ultrasonic echo: C-scans at $z = 2$ in. and $z = 4$ in. showing the reinforcement along (a) y - and (b) x -directions.

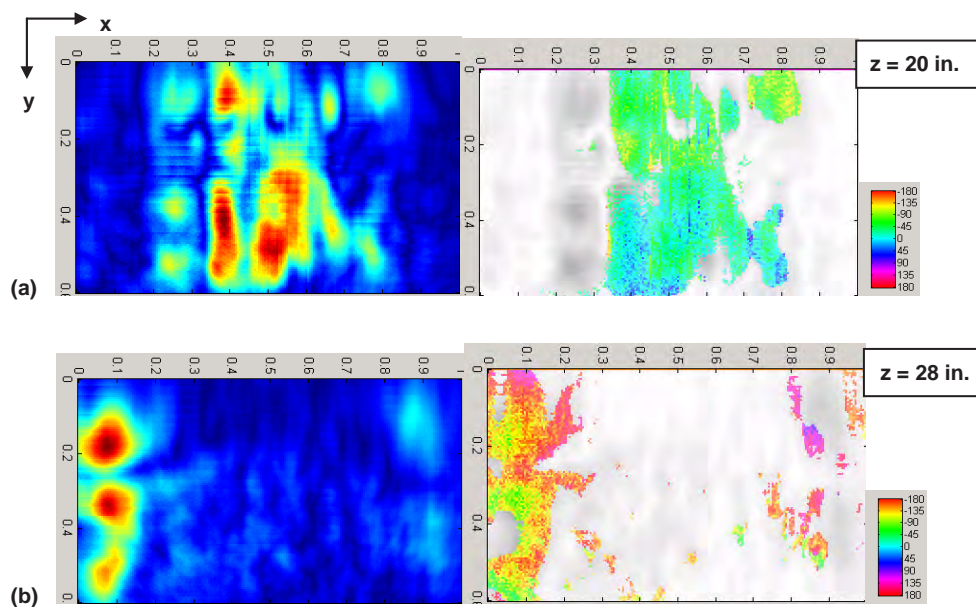


Figure Q.71. CPB2, ultrasonic echo: C-scans at different depths: (a) depth of anomaly at 20 in. and (b) depth of tunnel lining at 28 in.; image of amplitudes (left), image of corresponding phase (right).

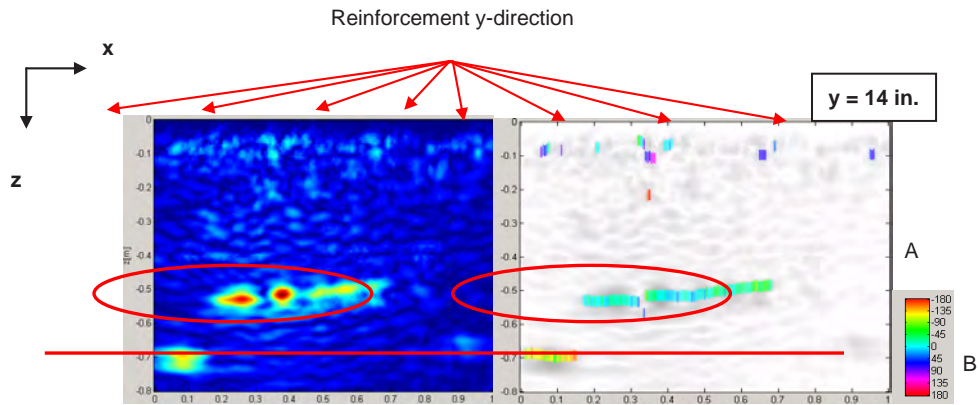


Figure Q.72. CPB2, ultrasonic echo: D-scan at $y = 14$ in. and corresponding phase diagram.

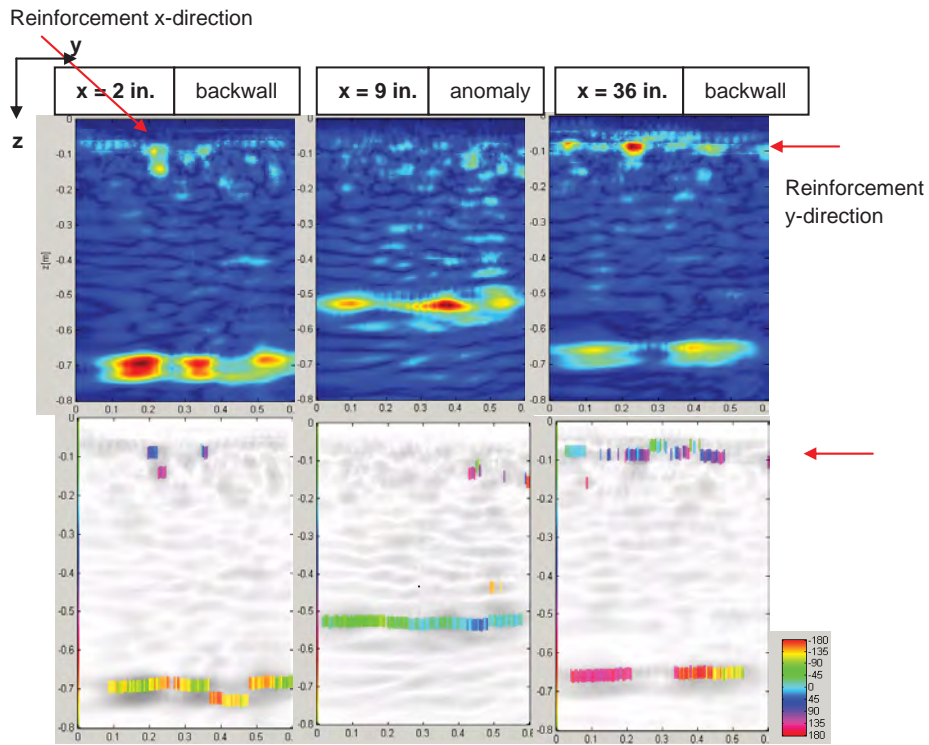


Figure Q.73. CPB2, ultrasonic echo: B-scans through anomaly and backwall taken at $x = 2$ in., $x = 9$ in., and $x = 36$ in.

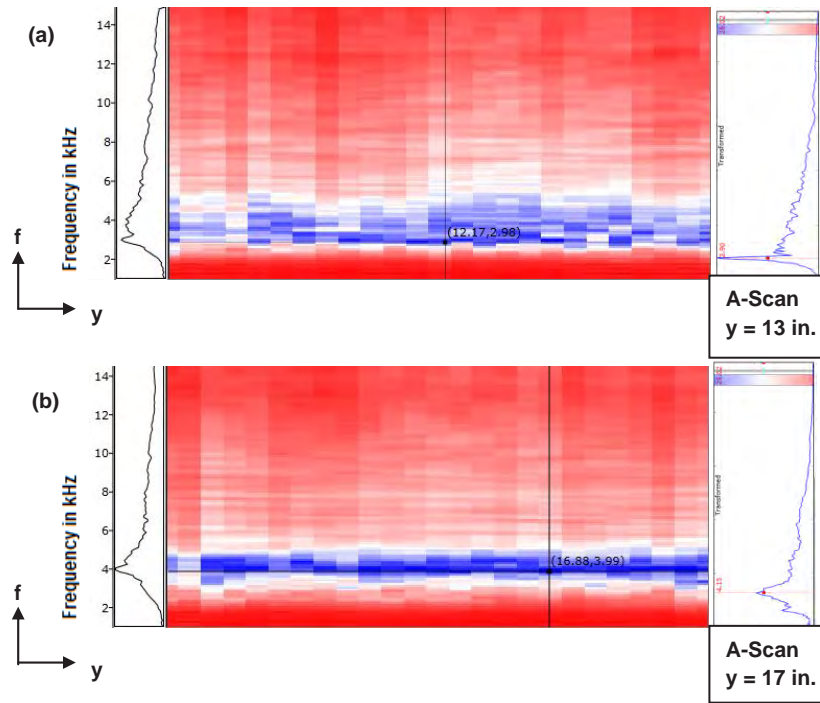


Figure Q.74. CPB2, IE: Spectral A-scans taken at two different locations: (a) through anomaly and (b) through backwall.

nominal thickness of 24 in. This could be a result of errors in the assumed concrete shear wave velocity used in estimating the reflector depths to analyze the US data of CPB2, as the shear wave velocity was assumed to be 2,710 m/s (from CPB1).

The use of the GPR and at least one acoustic NDT method was necessary to analyze CPB2. GPR could reliably detect and identify the reinforcement bars. Both acoustic methods detected the echoes from an anomaly and the backwall. The accurate estimation of the reflector depth was possible only when the wave velocities at test locations were known. Neither ultrasonic echo nor IE could provide the wave velocity of the test medium without having ground

truth information. To measure the velocity profile in situ, other methods such as high frequency spectral analysis of surface waves or multispectral analysis of surface waves could be employed.

Test Area 3

Description of the Test Area

As seen in the sketch in Figure Q.76, a joint near Station 486+67 ran almost through the middle of the test area, hereafter referred to as CPB3. The area was on the east side of the tunnel, opposite the two other test fields (CPB1 and CPB2). The test area was 48 in. long and 24 in. wide,

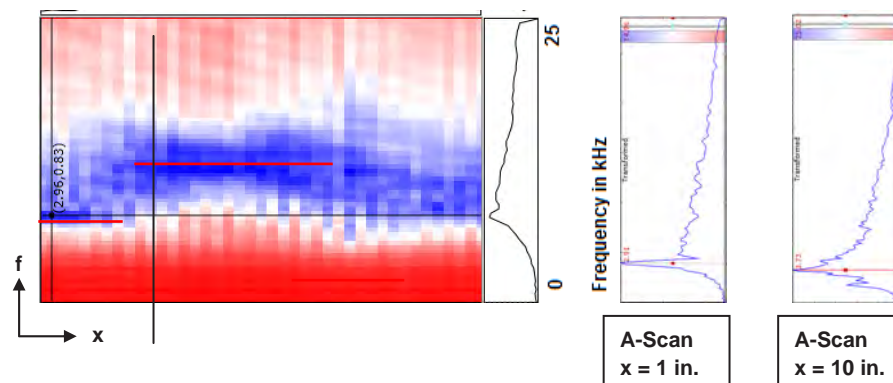


Figure Q.75. CPB2, IE: Spectral D-scan (along x-axis) along with two selected spectral A-scans representing different depths.

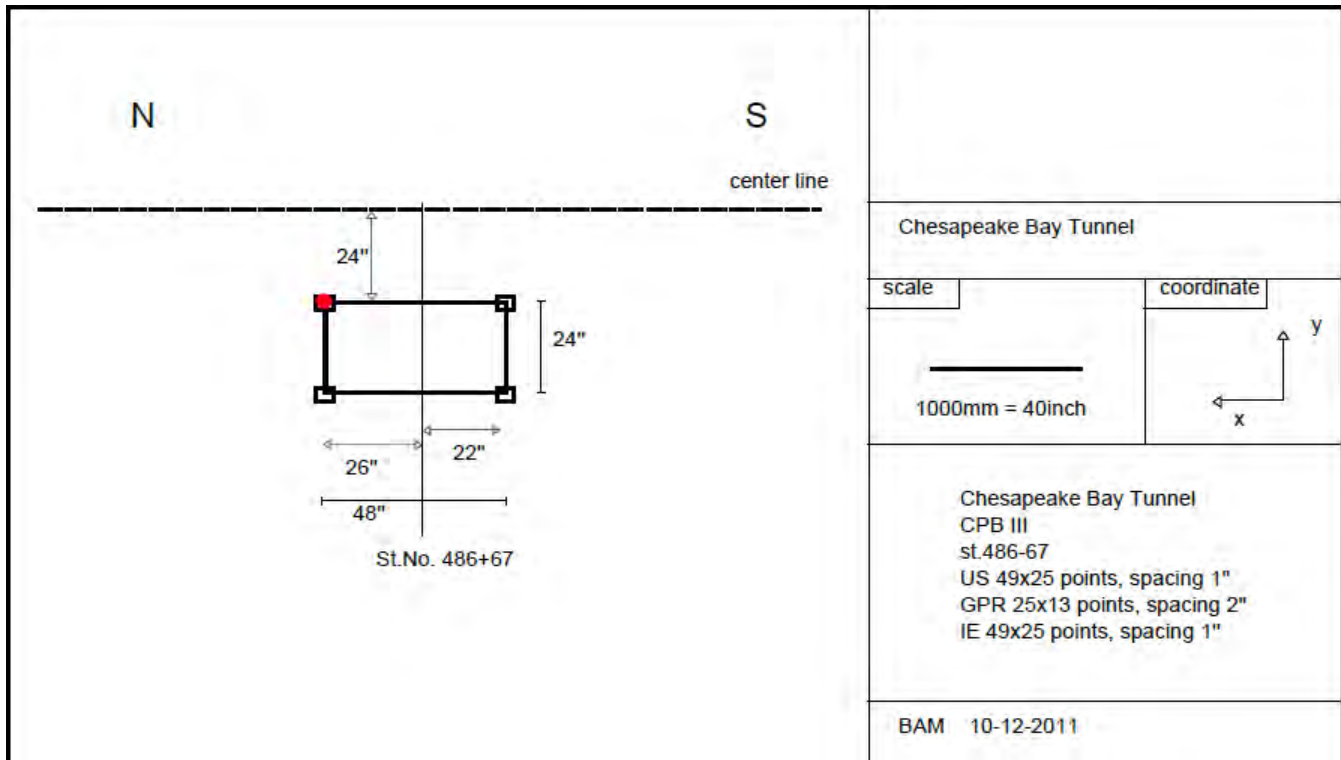


Figure Q.76. Sketch of CPB3, Station 486+67 Chesapeake Channel Tunnel.

extending 22 in. south and 26 in. north of the joint. The test field started at an offset of 24 in. from the centerline of the tunnel.

The grid spacing for ultrasonic echo and IE testing was 1 in. and for GPR testing was 2 in. The length of the GPR, ultrasonic echo, and IE transducers was parallel to the centerline of the tunnel during the scanning.

GPR Results

The reinforcement mesh could be easily seen in GPR C-scans. The transverse rebars in the y -direction were spaced 12 in. from each other and were positioned at $x = 2$ in.,

$x = 14$ in., $x = 26$ in., and $x = 38$ in. at a depth of $z = 1.6$ in., as shown in Figure Q.77. The longitudinal ones in the x -direction were at $y = 0$ in., $y = 18$ in., and $z = 3$ in.-deep (see Figure Q.77).

The D-scans taken at $y = 22$ in. and $y = 18$ in. (Figure Q.78) clearly showed that the rebars in the y -direction ran above those in the x -direction.

The B-scan taken at $x = 26$ in. (Figure Q.79) showed the cross section of one of the transverse rebars (along the y -direction). The one taken at $x = 16$ in. revealed only longitudinal rebars (along the x -direction).

Figure Q.80 is a 3-D image of the volume as a summary of the reinforcing elements.

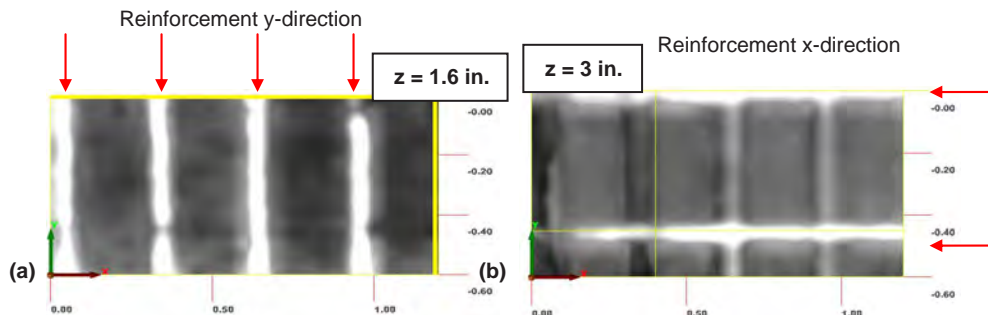


Figure Q.77. CPB2, GPR: C-scans taken at (a) $z = 1.6$ in. showing reinforcement bars in y -direction and (b) $z = 3$ in. showing rebars in x -direction.

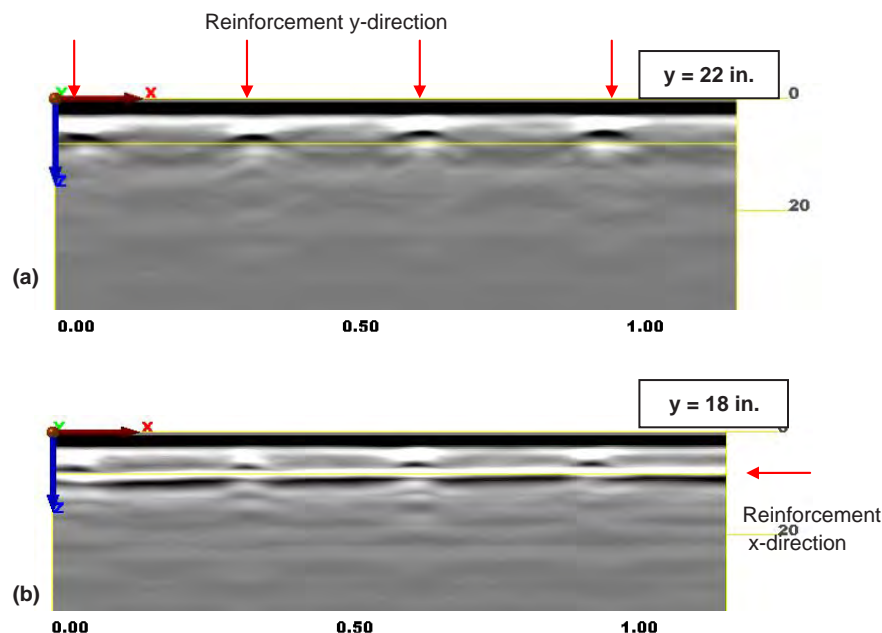


Figure Q.78. CPB3, GPR: D-scans taken at $y = 22$ in. (a) and $y = 18$ in. (b) reveal reinforcement bars in both directions.

Ultrasonic Echo Results

Three of the four transverse reinforcement bars (in the y -direction) could be detected in the ultrasonic echo C-scan at $z = 2$ -in. deep, at $x = 2$ in., $x = 14$ in., and $x = 38$ in. (Figure Q.81). An anomaly was present in the middle of the field starting at a depth of $z = 2$ in. Examining deeper C-scans confirmed the existence of an anomalous reflector (Figure Q.82). At a depth of about $z = 25$ in. (Figure Q.83), the backwall with a positive phase (indicating an impedance higher than the surrounding concrete) could be detected. Between $x = 16$ in. and $x = 38$ in., the backwall echo was missing because of the shadowing effect of the earlier-described anomaly reflector. To analyze the ultrasonic echo data of CPB3, the shear wave velocity 2,710 m/s of CPB1 was assumed.

A D-scan taken at $y = 16$ in. is shown in Figure Q.84. This view reveals multiple reflections from the anomaly at $z = 6$ in., $z = 10$ in., $z = 15$ in., and $z = 20$ in. with changing phase. The backwall echo was missing because the anomaly shadows the deeper reflectors. The multiple reflections with their changing phase gave indications of only one anomaly. However, this could not be verified.

A linear reflector of unknown origin was observed at $x = 26$ in. at the same depth as the backwall (marked with a question mark in both Figure Q.84 and Figure Q.85). Note that at $x = 26$ in., the joint ran across the test field. As the reflector was not seen in the D-scans produced by the raw data, this was likely an artificial feature produced by the SAFT algorithm.

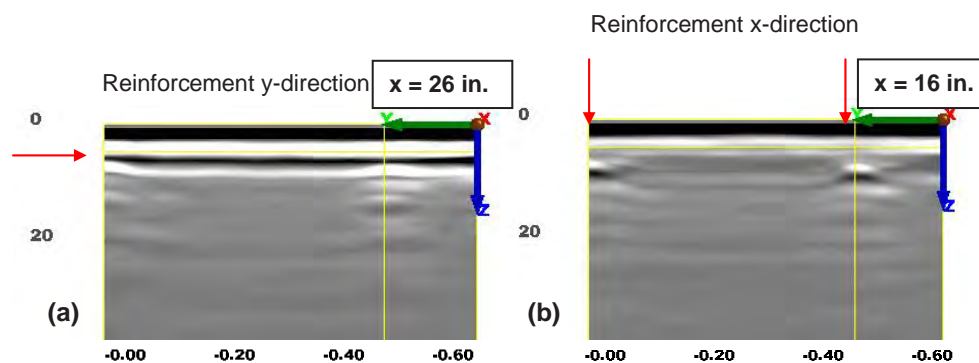


Figure Q.79. CPB3, GPR: B-scans at $x = 26$ in. (a) and $x = 16$ in. (b) reveal reinforcement rebars in both directions.

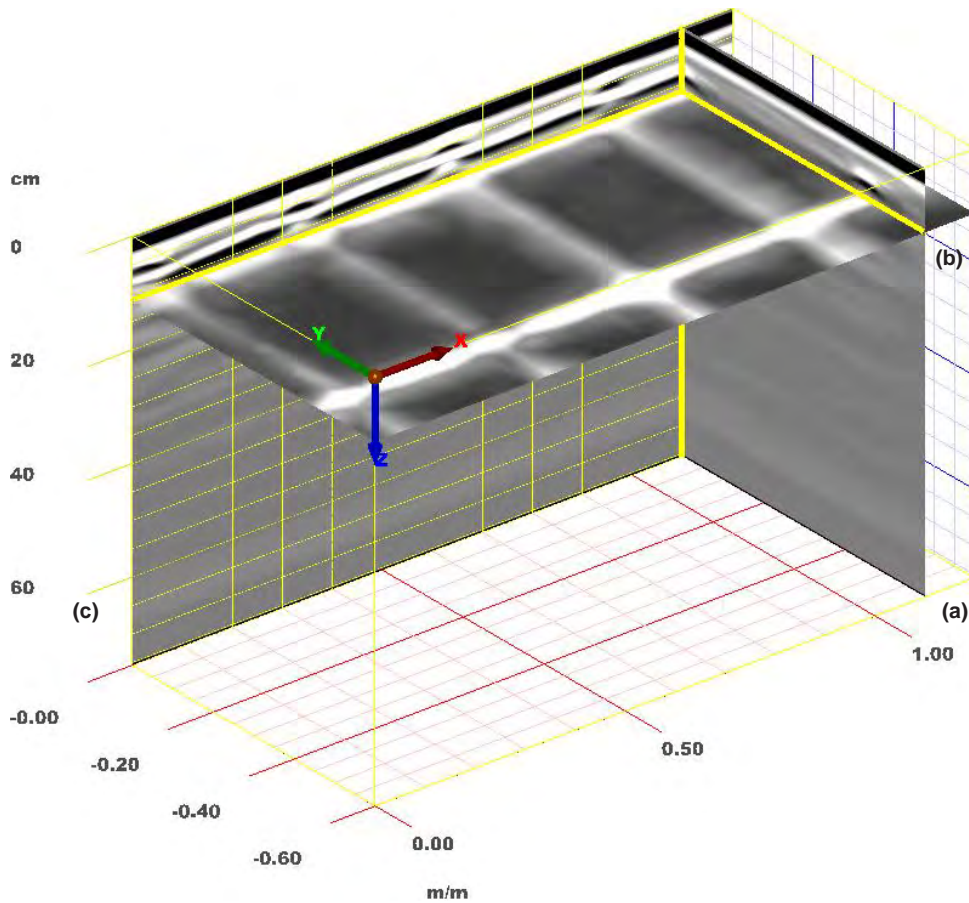


Figure Q.80. CPB3, GPR: 3-D image of volume positioned to reveal reinforcement, with B-scan (a) positioned at $x = 45$ in.; C-scan (b) at $z = 4.5$ in., 4-in. width; and D-scan (c) at $y = 0$ in.

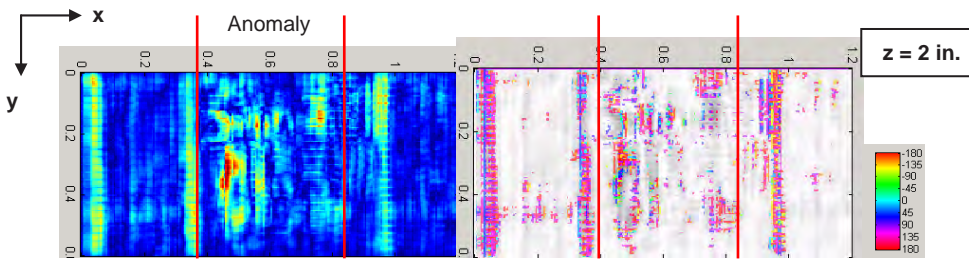


Figure Q.81. CPB3, ultrasonic echo: C-scan at $z = 2$ in., showing reinforcement bars in y -direction as well as anomaly between $x = 16$ in. and $x = 38$ in. (marked). Corresponding phase diagram (right).

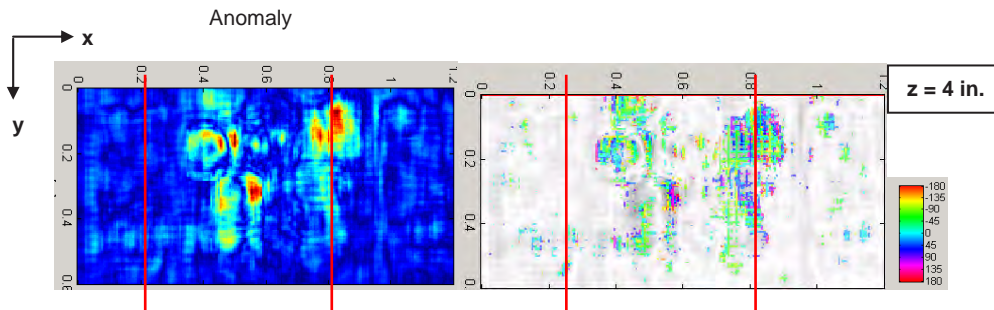


Figure Q.82. CPB3, ultrasonic echo: C-scan obtained at depth of 4 in. Reflector is confined between $x = 14$ in. and $x = 36$ in.

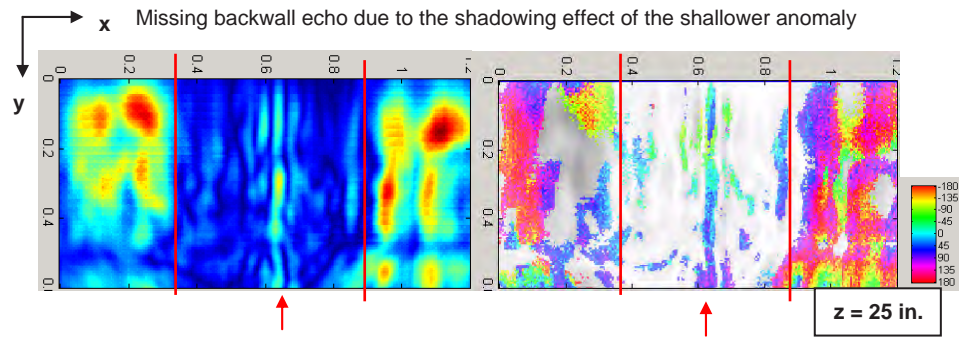


Figure Q.83. CPB3, ultrasonic echo: C-scan at $z = 25$ in. reveals backwall echo. Between $x = 16$ in. and $x = 36$ in., echo is missing due to presence of shallower anomaly.

The B-scans did not provide additional information on the anomaly. As seen in Figure Q.85, the backwall of the tunnel lining could be clearly seen at $z = 25$ in. in the B-scan taken at $x = 1.5$ in. The transverse rebar in the y -direction was also clearly seen. In contrast, the B-scan at $x = 20$ in. contained no backwall echoes, as expected from the D-scan, but no further information about the anomaly itself.

Figure Q.86 shows a 3-D image of the volume focusing on the backwall and its shadowed area, as well as the shallow anomaly.

Impact Echo Results

As seen in Figure Q.87, IE showed tunnel lining thickness resonance frequency except between $x = 13$ in. and $x = 30$ in., where the echo was disturbed. The typical spectral and temporal A-scans from the sound ($x = 5.5$ in.) and disturbed regions ($x = 20$ in.) are compared in the figure. While the sound spectrum contained one clearly dominant frequency,

the disturbed spectrum contained multiple peaks, mostly of frequencies lower than that of the thickness resonance frequency. The thickness resonance frequency appeared at about 3,200 Hz, corresponding to a depth $z = 25$ in.

Comparison of Results

GPR could provide a clear picture of the reinforcement bars in both directions, while ultrasonic echo could only reveal the ones in the y -direction, except the one at $x = 26$ in. This was due to the polarization effects due to the orientation of the ultrasonic echo transducer. The ultrasonic echo could, however, reveal the presence of a localized anomaly. That anomaly could not be detected using GPR. The anomaly appeared between $x = 14$ in. and $x = 30$ in. Ultrasonic echo results indicated multiple reflections with changing phase shifts, suggesting a shallow delamination. The IE frequency spectra were disturbed at the location of the anomaly, containing frequency peaks of lower frequencies than that of the backwall

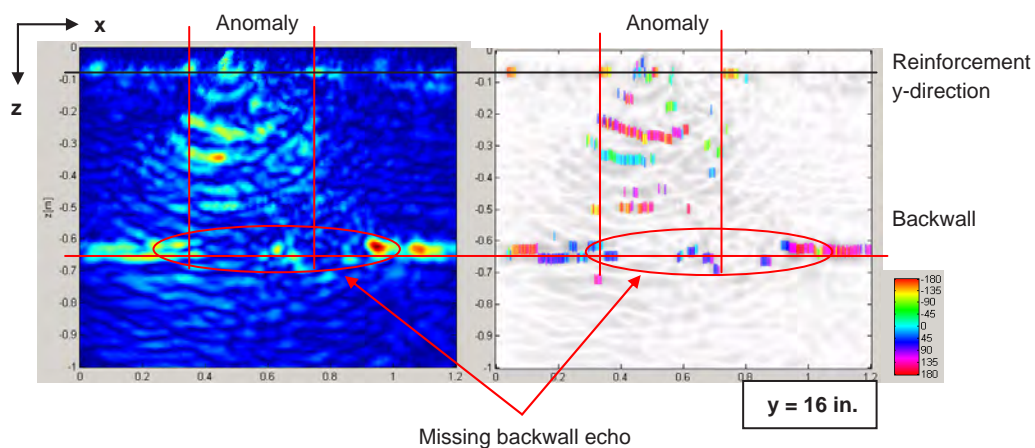


Figure Q.84. CPB3, ultrasonic echo: D-scan at $y = 16$ in. Backwall can be seen where anomaly does not shadow it. Reinforcement in y -direction is seen at $z = 3$ in. Reflector of unknown origin is positioned at $x = 26$ in. at backwall's depth.

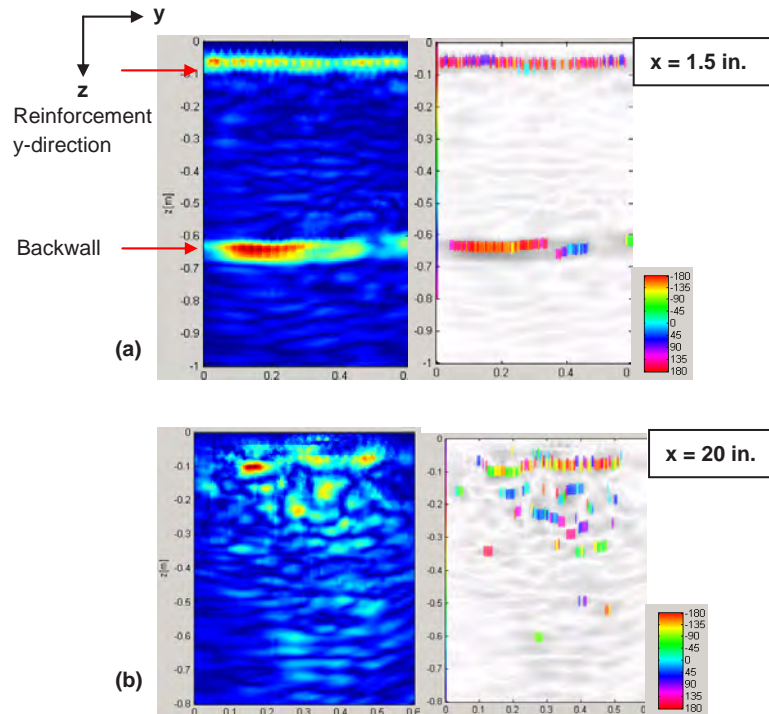


Figure Q.85. CPB3, ultrasonic echo: B-scans showing backwall at $z = 25$ in. and reinforcement in y -direction (a) and through anomaly that caused backwall echo to disappear (b).

echo, also indicating the presence of shallow delamination. However, the nature of the anomaly could not be confirmed. Both acoustic methods detected the backwall at approximately $z = 25$ in.

Shallow reinforcements were best seen using GPR. Defects indicating a change of impedance from concrete to a material

softer than the surrounding tunnel lining could be detected by the acoustic methods: ultrasonic echo and IE. A delamination-like anomaly was indicated. The depth of the anomaly was difficult to estimate, as ultrasonic echo analysis showed multiple reflections of the defect within a cone broadening with depth. IE spectra contained peaks of lower frequencies, indicating a shallow reflector.

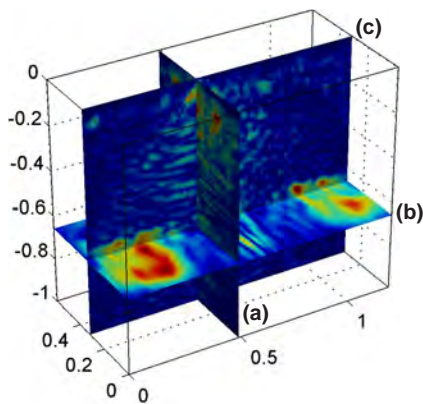


Figure Q.86. CPB3, US: 3-D image of volume positioned to reveal backwall and its shadowed area due to a shallow anomaly. With B-scan (a) positioned at $x = 21$ in., C-scan (b) at $z = 25$ in., and D-scan (c) at $y = 12$ in.

Test Field 4

Description of the Test Area

The last set of measurements at Chesapeake Channel Tunnel was taken inside the tunnel itself. The testing took place overnight, as traffic control measures were needed. Measurements were taken on tile-covered tunnel walls. The tiles were 2 in. by 2 in.

Test area CPB4 was located between Station 486+28 and Station 487, close to the north end of the tunnel, where an anomaly was previously detected in SPACETEC thermal images. As seen in Figure Q.88, the scanner's feet were mounted on the wall near the joint. The test field was larger, covering a 48-in. by 36-in. area. The spacing for ultrasonic echo and IE was set at 1 in., and for GPR at 2 in. During the testing, the GPR, ultrasonic echo, and IE transducers were oriented such that their length was parallel to the centerline of the tunnel. The measurement started in the lower right corner of the test field.

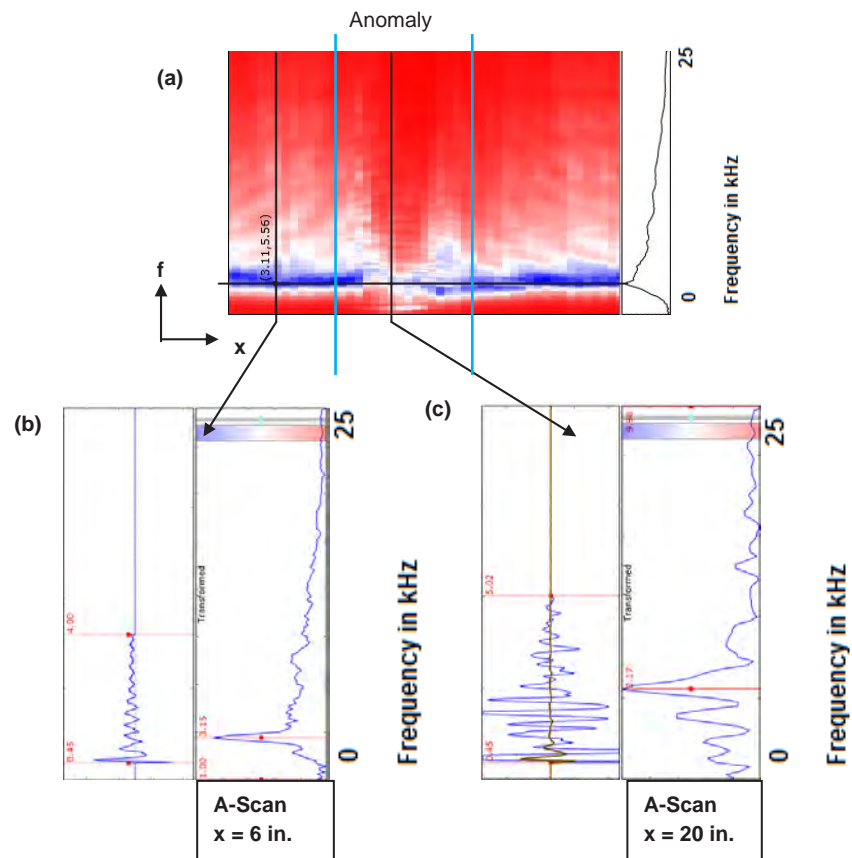


Figure Q.87. CPB3, IE: D-scan of volume (a) and selected A-scans representing echo from sound areas (b) and from areas with anomalies (c).

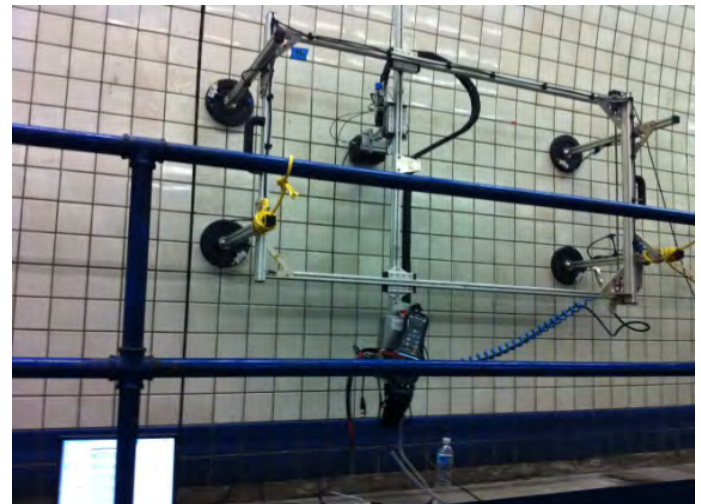


Figure Q.88. Test area CPB4 near Station 486+28.

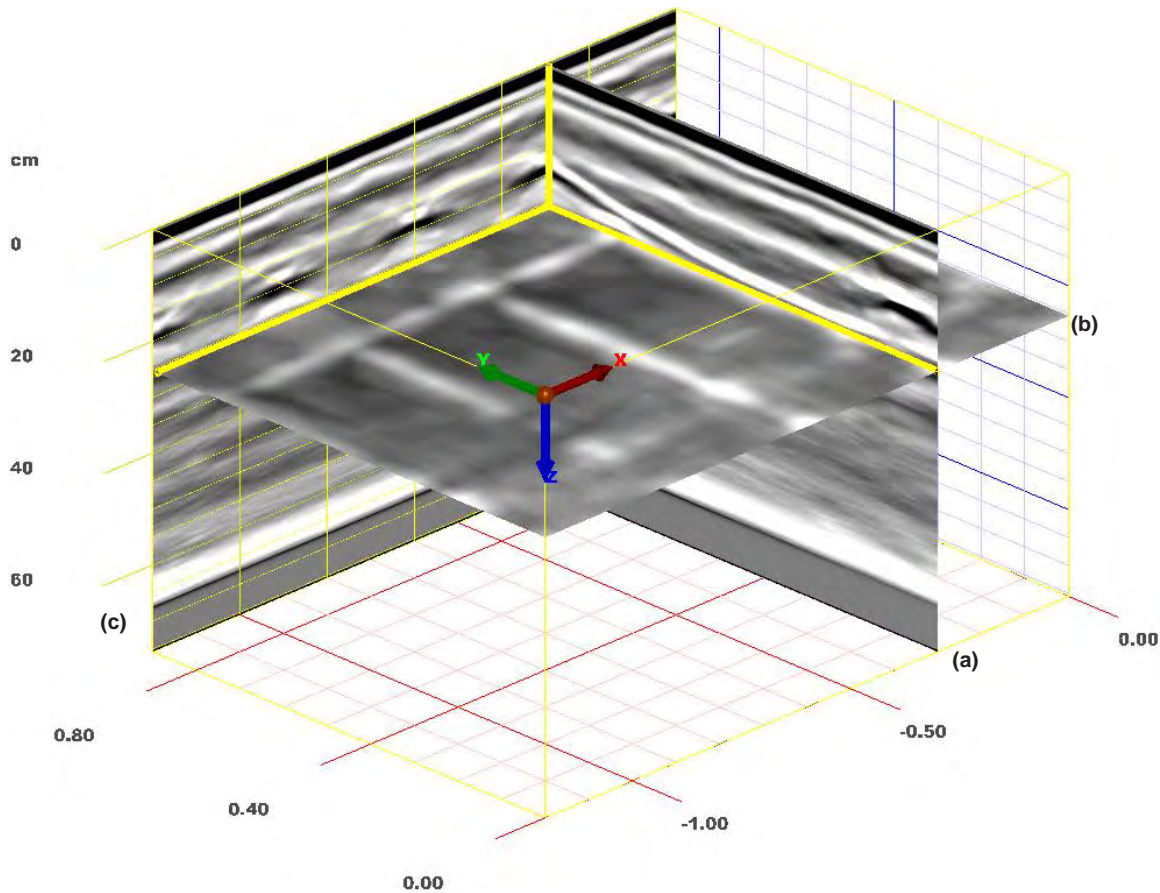


Figure Q.89. CPB4, GPR: 3-D image of volume positioned to reveal reinforcement, with B-scan (a) positioned at $x = 11$ in.; C-scan (b) at $z = 10$ in., 4-in. width, and D-scan (c) at $y = 4$ in.

The scanner moved upward and then left (south). Figure Q.88 shows snapshots of the test area and measurement system.

GPR Results

Figure Q.89, a 3-D image, summarizes the reinforcing elements within the volume.

Steel bars were found in both the x - and y -directions in GPR C-scans. The bars in the y -direction appeared to be spaced 12 in. apart, at $x = 0$ in., $x = 12$ in., $x = 24$ in., $x = 36$ in., and $x = 48$ in., running from 7-in. to 8-in. deep. The bars in the x -direction were at $y = 4$ in., $y = 12$ in., and $y = 30$ in., at $z = 6$ in., $z = 10$ in., and $z = 8$ in., respectively. Figure Q.90 includes several C-scans at various depths.

Two D-scans taken at $y = 2.5$ in. and $y = 12$ in. are shown in Figure Q.91.

Figure Q.92a is a B-scan showing the rebars in the x -direction cut at $x = 18$ in. Three rebars at different depths can be distinguished. Figure Q.92b is a B-scan taken at $x = 12$ in., showing one bar in the y -direction. The rebar does not run parallel to the surface but is curved, which explains why the rebars are seen at different depths in the C-scans. The rebar curves

from $z = 8$ in. at $x = 0$ in. up to $z = 6$ in. at $x = 36$ in. The rebars in the x -direction run above and under those in the y -direction.

Ultrasonic Echo Results

The automatic scanning using ultrasonic echo provided no useful information about the condition of the lining at CPB4. Information about the bonding of the tiles could have been gained by analyzing the individual A-scans. However, the ultrasonic echo transducer was too large (4 in. by 3 in.) compared with the size of the tiles (2 in. by 2 in.). The grid location and spacing had to be adjusted such that meaningful data (one A-scan per tile) could be obtained. However, the measurements were interrupted by an unforeseen weather condition, and no further measurements could be obtained.

Impact Echo Results

Intensifying foggy weather conditions interrupted the testing during IE data collection because the tunnel had to be fully opened to traffic. Therefore, only four scan lines were taken.

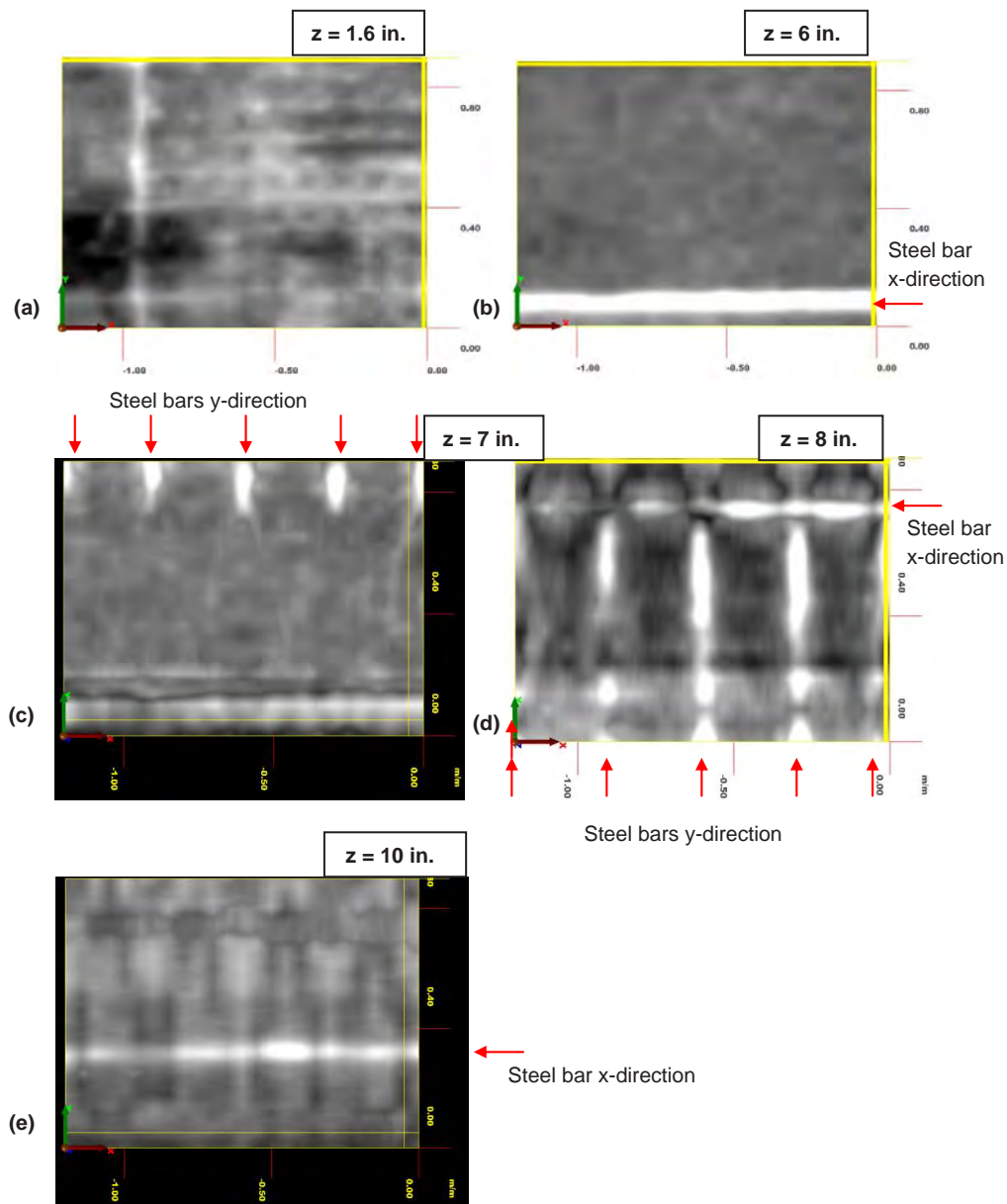


Figure Q.90. CPB4, GPR: C-scans at different depths: (a) $z = 1.6$ in., (b) $z = 6$ in., (c) $z = 7$ in., (d) $z = 8$ in., and (e) $z = 10$ in.

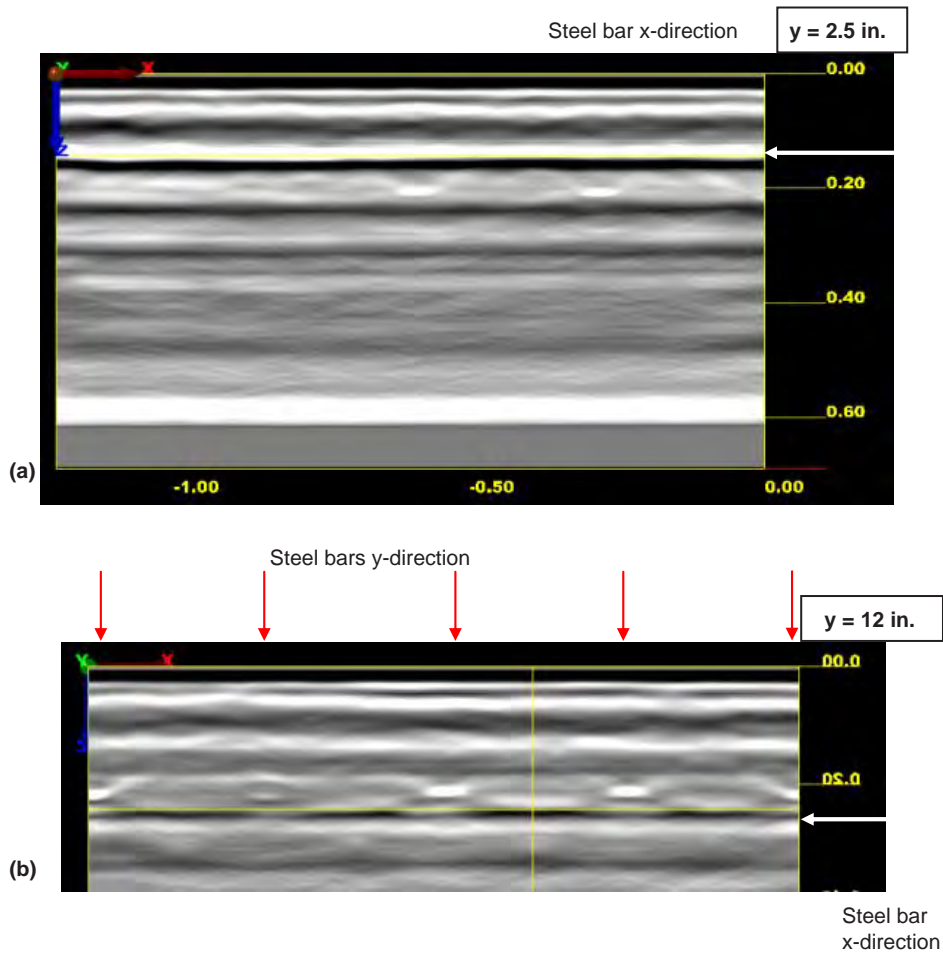


Figure Q.91. CPB4, GPR: D-scans of steel bars along (a) x- and (b) y-directions. Rebars in x-direction run above and under bars in y-direction.

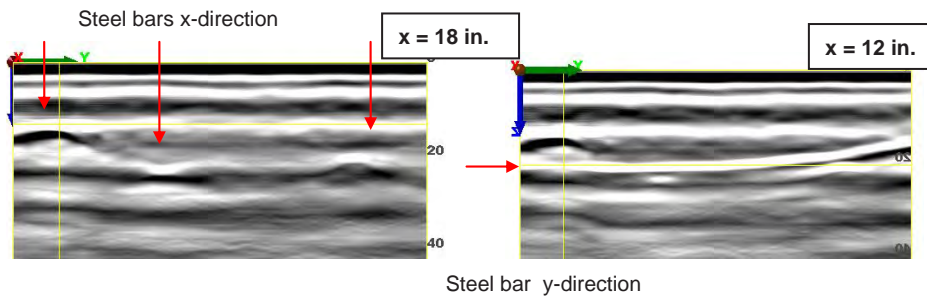


Figure Q.92. CPB4, GPR: B-scans taken at (a) $x = 18$ in. and (b) $x = 12$ in.

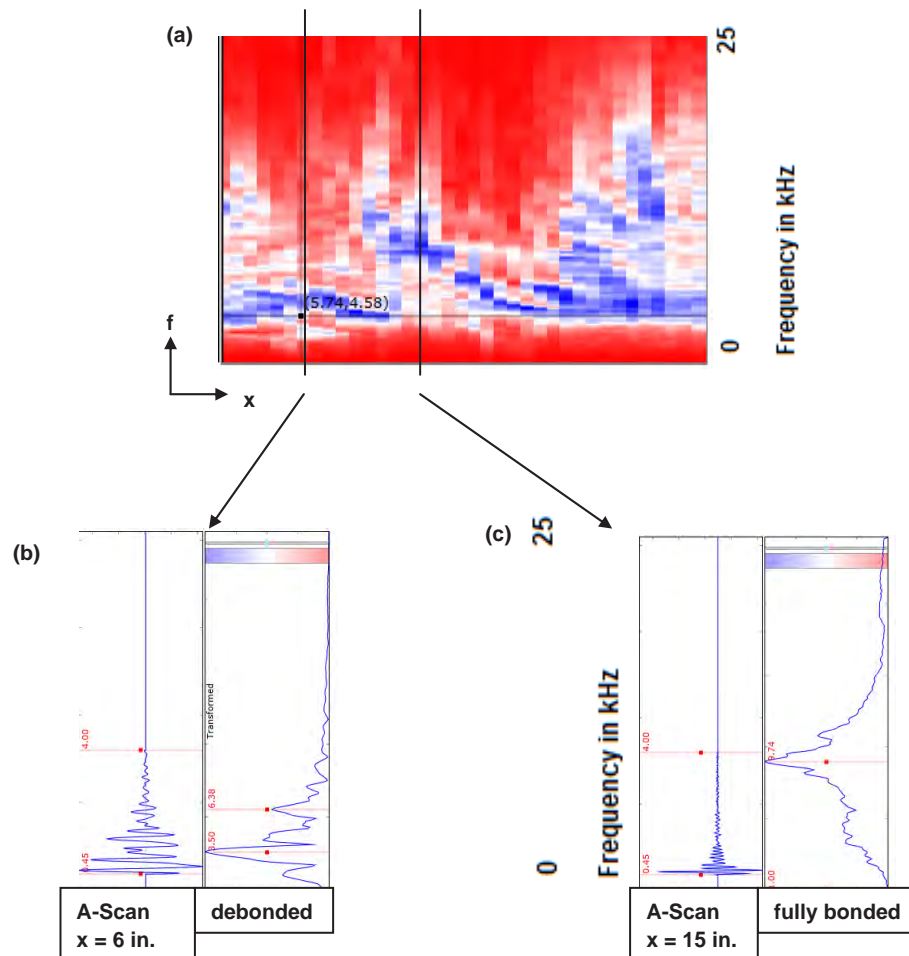


Figure Q.93. CPB4, IE: (a) D-scan, (b) typical A-scans for area with seemingly debonded tiles, and (c) A-scans for area with seemingly bonded tiles.

Earlier manual measurements indicated that IE is able to evaluate the bonding between tiles and walls when A-scans of individual tiles are analyzed. In the case of automated scanning, the analyzed signal is the average of 20 signals recorded close to the source. The dimension of the receiver is 4 in. by 3 in., which covers the area of two tiles. Therefore, evaluating the condition of the bonding of one tile on the basis of automatically collected A-scans is not exact. The grid location and spacing had to be adjusted such that meaningful data (one A-scan per tile) could be obtained. However, because of the interruption of the measurements, this was not possible.

Figure Q.93 illustrates one of the D-scans along with two representative spectral and temporal A-scans, showing signals/spectra from apparently debonded and bonded areas.

Comparison of Results

GPR signals were not disturbed by the presence of the tiles and could capture the reinforcement mesh behind the lining. The IE signals carried useful information about the bonding

condition at tile-concrete interface and occasionally about the lining itself. The grid location and spacing had to be adjusted such that meaningful ultrasonic echo data (one A-scan per tile) could be obtained. However, the measurements had to be suddenly stopped.

References

- Colorado DOT. Eisenhower Tunnel. <http://www.coloradodot.info/travel/eisenhower-tunnel>. Accessed July 2011.
- Salek, M. E. 2002. Glenwood Canyon: An I-70 Odyssey. October. <http://www.mesalek.com/colo/glenwood>.
- Schickert, M., M. Krause, and W. Müller. 2003. Ultrasonic Imaging of Concrete Elements Using Reconstruction by Synthetic Aperture Focusing technique. *ASCE Journal of Materials in Civil Engineering*, Vol. 15, No. 3, pp. 235–246.
- Shokouhi, P. 2005. *Comprehensive Evaluation of Concrete Bridge Decks Using Impact Echo*. PhD dissertation. Rutgers, New Brunswick, N.J.
- Zoega, A., R. Feldmann, and M. Stoppel. 2012. Praktische Anwendungen Zerstörungsfreier Prüfungen und Zukunftsaufgaben February 23–24. *Fachtagung Bauwerksdiagnose*. Berlin: BAM Berlin.

APPENDIX R

Estimated Depths to Defects from Nondestructive Testing

Table R.1. Eisenhower Memorial Tunnel, Colorado (10/3/2011 to 10/4/2011)

	First Layer Reinforcement	Suspected Backwall	Suspected Delamination	Suspected Crack	Other Unknown
Segment 8 +17 ft, Eastbound					
UST measured depth	4.2 in. (to center)	na	na	na	16.2 in.
Segment 8 +22.5 ft, Eastbound					
UST measured depth	3.7 in. to 5.1 in. (to center)	na	na	na	17.2 in.
Segment 10 +6.5 ft, Eastbound					
UST measured depth	4.1 in. (to center)	na	na	na	16.1 in.
Segment 11 +3.4 ft, Eastbound					
BAM's GPR measured depth	2 in. to 3 in.	na	na	na	16 in.
BAM's ultrasonic echo measured depth	2 in. to 3 in.	na	na	na	16 in.
BAM's IE measured depth	na	na	na	na	na

Note: BAM = Federal Institute for Materials Research and Testing; GPR = ground-penetrating radar; IE = impact echo; na = not applicable; UST = ultrasonic tomography.

Table R.2. Hanging Lake Tunnel, Colorado (10/5/2011 to 10/6/2011)

	First Layer Reinforcement	Suspected Backwall	Suspected Delamination	Suspected Crack	Other Unknown
Segment 58 +Unknown Distance, Eastbound					
BAM's GPR measured depth	4 in. to 6 in. to 3 in.	na	na	na	na
BAM's ultrasonic echo measured depth	6 in.	na	na	na	na
BAM's IE measured depth	na	na	na	na	na
Segment 57 +4.2 ft, Eastbound					
BAM's GPR measured depth	5 in. to 8 in.	na	na	<3 in.	na
BAM's ultrasonic echo measured depth	6 in.	na	na	<6 in.	na
BAM's IE measured depth	na	na	na	na	22 in.
Segment 57 +3.4 ft, Eastbound					
UST measured depth	4.6 in. to 6.2 in. (to center)	27.6 in.	12.3 in.	Cracks extending to depth of delamination	na
Segment 57 +2.2 ft, Eastbound					
BAM's GPR measured depth	1 in. to 6 in. to 3 in.	na	na	na	12 in. to 16 in.
BAM's ultrasonic echo measured depth	4 in. to 6 in.	na	na	na	12 in. to 16 in.
BAM's IE measured depth	na	22 in. to 24 in.	na	na	12 in.
Segment 54/55 Joint, Eastbound					
UST measured depth	3.6 in. (to center)	na	na	na	Possible voids 9 in. deep
Segment 49 +11 ft, Eastbound					
UST measured depth	4.3 in. to 5.1 in. (to center)	29.6 in. to 32.4 in.	na	na	na
Segment 49 +6 ft, Eastbound					
UST measured depth	3.7 in. (to center)	24.5 in. to 29.6 in.	na	na	na
Segment 55 +16 ft, Eastbound					
UST measured depth	2.9 in. to 5.1 in. (to center)	na	8 in. to 20 in.	Cracks extending to depth of delamination	na

Note: BAM = Federal Institute for Materials Research and Testing; GPR = ground-penetrating radar; IE = impact echo; na = not applicable; UST = ultrasonic tomography.

Table R.3. Chesapeake Channel Tunnel, Virginia (10/11/2011 to 10/13/2011)

	First Layer Reinforcement	Suspected Backwall	Suspected Delamination	Suspected Crack	Other Unknown
Station 471 +80 ft, Southbound					
UST measured depth	2.4 in. to 4.4 in. (to center)	24.7 in.	na	na	na
Station 473 +56 ft, Southbound					
UST measured depth	2.3 in. (to center)	24.4 in.	na	na	na
Station 474 +27 ft, Southbound					
BAM's GPR measured depth	1.5 in. to 3 in.	na	na	na	na
BAM's ultrasonic echo measured depth	2 in.	24 in.	na	na	15 in.
BAM's IE measured depth	na	22 in. to 24 in.	na	na	Indirectly
Station 474 +27 ft, Southbound					
UST measured depth	2.0 in. to 2.6 in. (to center)	24.1 in.	na	9.0 in.	Possible voids from surface to 9-in. deep in isolated area
Station 481 +76 ft, Southbound					
BAM's GPR measured depth	2.5 in. to 4 in.	na	na	na	na
BAM's ultrasonic echo measured depth	2 in. to 4 in.	28 in.	na	na	20 in.
BAM's IE measured depth	na	27 in.	na	na	20 in.
Station 486 +67 ft, Northbound					
UST measured depth	2.2 in. (to center)	24.1 in. to 26.0 in.	19.2 in. and 2.2 in. in two locations	Cracks extending to depth of deepest delamination	na
BAM's GPR measured depth	1.6 in. to 3 in.	na	na	na	na
BAM's ultrasonic echo measured depth	2 in.	25 in.	na	na	2 in.
BAM's IE measured depth	na	25 in.	na	na	Indirectly
Station 486 +67 ft, Southbound					
UST measured depth	2.0 in. to 3.0 in. (to center)	24.3 in. to 26.0 in.	na	8.6 in.	na
Station 491 +25 ft (Area Extended from Southbound to Northbound)					
UST measured depth	2.7 in. to 3.2 in. (to center)	22.7 in. to 25.9 in.	17.7 in.	9.8 in.	na
Station 488 (Southbound Tile Lining)					
UST measured depth	4.3 in. to 7.7 in. (to center)	25.0 in. to 30.0 in.	15.7 in.	na	na
Station 486 +9 ft (Southbound Tile Lining)					
UST measured depth	4.8 in. to 9.4 in. (to center)	28.1 in. to 31.0 in.	na	8.6 in.	na
Between Station 486 +28 ft and Station 487 (Southbound Tile Lining)					
BAM's GPR measured depth	6 in. to 10 in.	na	na	na	na
BAM's ultrasonic echo measured depth	na	na	na	na	na
BAM's IE measured depth	na	na	na	na	Bonded and debonded tiles
Station 481 +76 ft, Southbound					
UST measured depth	2.0 in. to 3.6 in. (to center)	26.6 in. to 28.4 in.	20.2 in.	na	na

Note: BAM = Federal Institute for Materials Research and Testing; GPR = ground-penetrating radar; IE = impact echo; na = not applicable; UST = ultrasonic tomography.

APPENDIX S

Concrete Permeability Laboratory Study

Introduction

Ground-penetrating radar (GPR) has been widely used for subsurface characterization by geologists, archeologists, and engineers. For civil engineering applications in pavements, GPR has been used to determine pavement and soil layer thickness and moisture content. The use of GPR in cementitious materials such as concrete, however, is still rather limited. Concrete is a widely used construction material made by combining cementitious materials with water, which forms a nanoporous network and binds aggregates together. The porous cementitious matrix contains hydration products and water that exists in the bulk state in the macropores or physically and chemically bound to the pores that fall in the micropore size range. The pore structure of cementitious materials controls mechanical properties, from compressive strength to other time-dependent mechanical behaviors such as creep.

Concrete structures suffer long-term deterioration from various environmental exposures. For example, in cracked concrete tunnel linings surrounded by moisture-bearing materials, moisture may infiltrate through the crack to the tunnel tiles if present and possibly delaminate them. Permeability of concrete directly influences the capability of the concrete to withstand chemical attack internally and is thus of great interest to engineers. The ability to determine the condition of concrete and whether any anomalies exist internally without having to perform destructive testing will allow engineers to conduct inspections at a much lower cost and in a shorter period of time. Engineers have to destructively obtain concrete cores from the field to determine properties such as moisture content and permeability.

The characteristics of electromagnetic wave propagation in materials are dependent on many factors, one of which is the dielectric properties of the material. The interaction of electromagnetic waves in composite materials, such as cementitious materials, is inherently complex, in part because of the difference in electrical properties of constituents within a composite.

The dielectric properties of materials directly affect the propagation of electromagnetic waves. To interpret output from GPR, a thorough understanding of the dielectric properties of the material is required. The solid constituents of porous materials usually have low relative permittivity. However, the porous matrix itself may contain various amounts of water, which greatly influences the dielectric properties in the bulk scale because of water's high relative permittivity.

The microstructure of cementitious materials is complicated, with dimensional scales spanning many orders of magnitudes. This complexity, however, may be exploited to allow engineers to indirectly determine moisture content and pore-size distribution from dielectric response, from which transport properties of cementitious materials may be inferred. Such understanding is required to develop moisture content and permeability correlation to dielectric response, and subsequently, development of nondestructive testing (NDT) using GPR for various types of concrete structures. In this research, the researchers sought to understand fundamental electrical properties of composite cementitious materials for electromagnetic waves at microwave frequencies through experimentation and modeling. The dependence of dielectric response of cementitious materials to pore structure and moisture content is examined in this appendix.

Background and Literature Review

Materials that conduct charges poorly in the presence of an electric field are known as dielectrics. The charges do not move freely under an applied electric field. Instead, the charges polarize; they align with the field polarity, such as is found in the case of a parallel plate capacitor. The ability for the material to polarize is defined as the relative permittivity of the material. Relative permittivity is often referred to as dielectric constant in the literature. The term *complex permittivity* will be used in the rest of this appendix, which quantifies

the relative permittivity ϵ_r , as a function of the dielectric response of the different materials within the cementitious composite that may or may not contain an imaginary part. This will be explored in greater detail in the theory section.

The dielectric response of soils has long been a research interest in fields such as geophysics, geotechnical engineering, archaeology, and so on. Soils are porous mediums containing one or more fluids in their pore space. A model for soil moisture and its associated relative permittivity was developed by Wobschall (1). Applications of GPR in civil engineering applications are well documented see (2–8). Comprehensive reviews on GPR were written by Saarenketo and Scullion on pavements (7) and Huisman et al. on soil moisture content determination (9). Many previous researchers have determined composite dielectric response empirically, e.g., Topp et al. (10). Other methods have also been developed for estimation of moisture content, where the moisture content was determined by solving an inverse problem with GPR data (2, 11, 49). In cementitious materials, the dielectric response was studied by Lee and Zollinger (49) and Miura et al. (12) who examined a range of frequencies to determine degree of hydration. Various mixture laws have been suggested to model the dielectric response of mixtures of sand, gravel, and water with known constituent properties (13) for use in cementitious materials, but the models were not validated with concrete or cement measurements.

For measurement of concrete permeability in the laboratory, rapid chloride ion permeability (ASTM C1202) is widely used, but the results can be significantly affected by differences in the pore-solution chemistry between different concrete samples. Jones and Grasley (14–16) developed dynamic pressurization and radial flow-through techniques for measurement of intrinsic concrete permeability with cylindrical samples. With this technique, however, cores have to be taken from an existing structure, and full saturation may be hard to achieve. Basheer and Nolan (17) developed in situ air permeability measurement techniques. However, permeability obtained from the technique is highly dependent on internal relative humidity (RH), and only the surface permeability can be obtained.

For pavement engineering applications, GPR operates by measuring reflected electromagnetic waves from different layers that result from impedance mismatch between the layers. The GPR has a transmitting antenna operating at a certain frequency and a receiving antenna that records the reflected waves in the time domain. Air-coupled GPR has an antenna that is situated at some distance from the pavement surface separated by air. The layers are assumed to be perfect dielectrics with no losses associated with propagation of the electromagnetic wave through them, which greatly simplifies the analysis of pavement thickness and determination of a composite dielectric constant. Such an assumption cannot be made in concrete materials because concrete has a nonnegligible loss component

in complex permittivity. The measured loss tangent for saturated concretes range from up to 0.5 between frequencies 200 MHz and 6 GHz. The theory section will outline the limitations of time domain reflectometry methods (TDR) in determining the dielectric response of concrete materials.

Dielectric relaxation is the time/frequency dependent dissipation of electromagnetic wave energy in materials that results from effects such as dipolar relaxation at the frequencies of interest in this research. At low frequencies, water molecules polarize almost instantaneously to an alternating electric field without any loss. Dielectric relaxation occurs at higher frequencies (~14 GHz) when the rotation of water molecule dipoles lags behind the alternating electric field, causing dissipation of electrical energy in the applied electric field through heat. Figure S.1 shows the complex permittivity of pure water and water containing conductive ionic species at a concentration commonly found in the pore solution of mature concrete (18).

This literature review is not intended to be a comprehensive review of all of the completed work on the topic of dielectric relaxation. Research on dielectric relaxation on organic materials will likely be of little relevance to cementitious materials. Relevant work done on the dielectric relaxation constituents in cementitious materials, including bulk water and water in confined spaces such as porous glass and soils, will be the focus in this literature review.

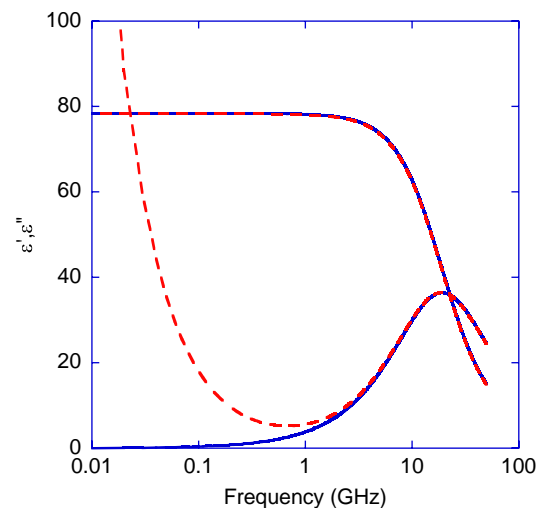


Figure S.1. Complex permittivity of water modeled after empirical equations in work of Meissner and Wentz (19). Abscissa is frequency (GHz) in log scale, and dielectric constants (real and imaginary) are on ordinate. Dashed line indicates effect of minimal salt addition to complex permittivity of water, where at low frequencies a loss resulting from conduction is most apparent. The dashed red and solid blue lines that start at 80 at 0.01 GHz are for ϵ_r' ; the other two lines are for ϵ_r'' .

Dielectric relaxation of materials typically depends on frequency of the applied electric field and temperature, where lower temperature lowers the relaxation frequency. Jonscher (20) has written a thorough review on dielectric relaxation of solids. For more complex materials, a review on the concepts and measurement methods are described in the work of Feldman et al. (21). While the properties of bulk water containing conducting species at various concentrations (i.e., seawater) have been extensively studied over a wide temperature and frequency range (19, 22–27), the behavior of water near interfaces is known to be drastically different (21, 28–32). For confined water such as that found in nanoporous mediums, the physical and electrical properties change dramatically. The dielectric response of water near interfaces can be found in a thorough review by Michot et al. (31). A survey of loss mechanisms (both conduction and polarization) was given in the work of deLoor (33). At current frequency range (>50 MHz) of interest, mechanisms that affect losses include bound water relaxation, bulk water relaxation, and conduction. Clay materials contain structural water, and selected clays' dielectric properties were studied by Ishida et al., where nonbound water, bound water, and interfacial polarization were identified as mechanisms for dielectric relaxation (34).

Other types of porous materials may possess a solid skeleton that resembles porous glass, which is not granular like most soils. Experimental work on dielectric relaxation in saturated porous media has been studied with controlled porous glass. Some of the work done on the characterization of water dynamics with porous glasses, for example, Feldman et al. (28) studied porous sodium borosilicate glass between 20 Hz and 1 MHz at different temperatures. A change in relaxation time resulting from water was observed between different pore sizes. The dynamics of water are hindered by the presence of interfaces. Such a shift in relaxation time was also observed in the work of Feldman et al. (30) on porous glass.

Both early and mature age cement paste dielectric responses at microwave frequencies have been previously studied by the

use of waveguide methods (35–38). Previous studies on cement pastes have focused on the evolution of dielectric response of cement paste due to hydration (37). For determination of moisture content and permeability, the microstructure of the cement paste must be considered. A representative volume element of a hydrated cement paste is shown in Figure S.2.

The solid matrix consists of calcium silica hydrates (CSH), which contain physically bound water in nano-sized pores, and chemically bound water that is a part of the CSH structure. Capillary pores are filled with water containing various ions, and interfaces exist within the boundary between the bulk pore water and solid phases. In addition, interfaces are found within the CSH structure itself, often in very small length scales. Waters contained in these different length scales have different dielectric relaxation times, as demonstrated in previous works on complex permittivity in other types of porous media.

Theory

The interaction between matter and electromagnetic waves is described by Maxwell and Garnett's equations (39). For dielectrics, the constitutive equation of material response under the presence of an electric field is given as Equation S.1:

$$\hat{D} = \epsilon_0 \hat{E} + \hat{P} \quad (\text{S.1})$$

where \hat{D} is the electric displacement field, ϵ_0 is the permittivity of free space, \hat{E} is the electric field, and \hat{P} is the polarization of the material as a function of the applied electric field. In a dielectric material under the presence of an electric field, the molecules in a dielectric material polarize by aligning along the applied field. At small field strengths, material behaves linearly at the presence of an electric field. The polarization \hat{P} for linear materials is defined as Equation S.2:

$$\hat{P} = \chi_e \epsilon_0 \hat{E} \quad (\text{S.2})$$

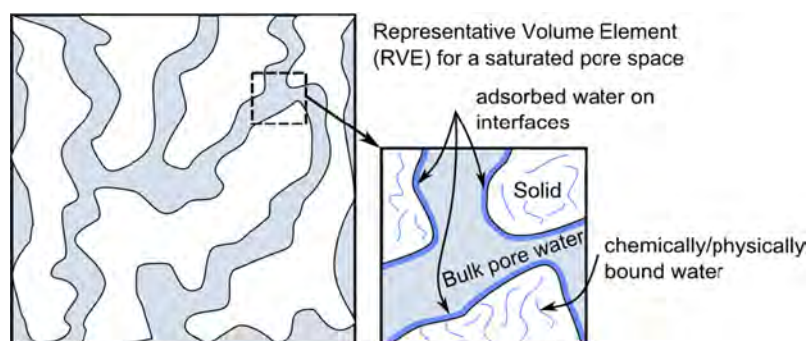


Figure S.2. Schematic of an arbitrary fully saturated pore network. Water near and immediately adjacent to solids has different properties compared with that of bulk water.

where χ_e is the electric susceptibility of the material. Dielectric displacement can thus be written as shown in Equation S.3:

$$\hat{D} = \epsilon_0(1 + \chi_e)\hat{E} = \epsilon_0\epsilon_r\hat{E} \quad (\text{S.3})$$

where ϵ_r is the relative permittivity of the material. In an isotropic, homogeneous material, ϵ_r is a scalar. Cementitious materials are assumed to be isotropic and homogeneous for this investigation because the wavelength is 15 mm at 6 GHz assuming a refractive index of 3.2, which is much longer than any inhomogeneity found in cementitious materials. A perfect dielectric will have no dissipation of electrical energy. Materials experience dielectric dispersion/loss when polarization cannot follow an alternating electric field at certain frequencies. This time dependency of polarization can be written as shown in Equation S.4:

$$\hat{P}(t) = \epsilon_0 \int_{-\infty}^t \chi_e(t-t')\hat{E}(t')dt' \quad (\text{S.4})$$

where $\hat{P}(t)$ is now a convolution of electric susceptibility (time-dependent) integral of a time-dependent electric field with reduced time t' . Dielectric displacement from Equation S.4 can then be written in the frequency domain by applying integral transform as shown in Equation S.5:

$$\tilde{D}(\omega) = \epsilon_r^*(\omega)\epsilon_0\tilde{E}(\omega) = \tilde{\epsilon}(\omega)\tilde{E}(\omega) \quad (\text{S.5})$$

where $\tilde{D}(\omega)$ is the dielectric displacement, $\tilde{\epsilon}(\omega)$ is the absolute permittivity, $\tilde{E}(\omega)$ is the electric field, and $\epsilon_r^*(\omega)$ is the complex permittivity in the frequency domain, respectively. $\epsilon_r^*(\omega)$ has real and imaginary parts and is written as shown in Equation S.6:

$$\epsilon_r^*(\omega) = \epsilon_r'(\omega) + i\epsilon_r''(\omega) \quad (\text{S.6})$$

where $\epsilon_r'(\omega)$ is the real part of the complex permittivity, i is the imaginary number, and $\epsilon_r''(\omega)$ is the imaginary part of the complex permittivity. The real part of complex permittivity indicates the ability for a material to polarize, thus storing charge. The imaginary part of complex permittivity describes losses in the electrical energy resulting from conduction and/or the lag in the polarization of molecules at certain frequencies (dipolar losses). Pure water, for instance, is a good insulator that has a fairly constant complex permittivity (i.e., real) up to the GHz range of frequency.

In a parallel plate capacitor electrical energy is stored on each side of the plates under an applied electric field. When a dielectric material is inserted between the plates, the charges within the material polarize. Charges in a dielectric material require a finite amount of time to reorient to the direction of an applied electric field. At microwave frequencies, molecules such as water cannot align to the externally applied electric

field. This delay causes dissipation in electrical energy. This relaxation time is normally many orders of magnitude larger than that observed in mechanical stress relaxation. For water, the relaxation time is in the order of picoseconds, whereas for viscoelastic materials such as polymeric materials, it is many orders of magnitude above picoseconds. This time-dependent response can be represented with empirical models such as the classical Debye model (40). When discharged, the material returns to the nonpolarized state over time, and the time required for relaxation is governed by the relaxation time. When an alternating field is applied to a material, the rate of polarization cannot follow the field at certain frequencies as a result of different mechanisms, causing dielectric relaxation.

Ground-Penetrating Radar Theory of Operation

A linearly polarized electromagnetic wave sent by a transmitting antenna (incident wave) to the surface layer of a concrete layer is partially transmitted into the concrete from refraction, while the rest is reflected on the surface. The reflection is due to an impedance mismatch between the two layers, meaning they have different refractive indices, which is a function of complex permittivity. Figure S.3 illustrates the propagation of the electromagnetic wave from an air-coupled system into concrete.

As a simplification, several assumptions can be made: the concrete has no steel reinforcement; the electromagnetic wave will entirely dissipate while traveling in the concrete (i.e., no reflection from the second interface or any reflection from the second interface is dissipated); only two layers of air and concrete exist; the concrete has a uniform moisture profile (i.e., constant complex permittivity through depth); and the wave propagates perpendicular to the concrete layer. The electromagnetic wave propagating through a one-dimensional space (z) and time (t) is given as shown in Equation S.7:

$$\hat{E}(z, t) = E_0 e^{-\alpha z} e^{i(\omega t - \beta z)} \quad (\text{S.7})$$

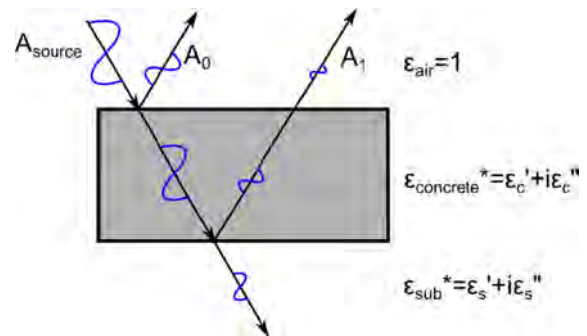


Figure S.3. GPR wave pulse reflection and refraction from concrete slab.

where z is the location from the origin, t is the time, E_0 is half of the magnitude of the wave, α is the attenuation factor, and β is the phase coefficient. In a no-loss propagation medium such as air, α and β are given as shown in Equation S.8:

$$\beta = \omega \sqrt{\mu \epsilon_r} = \omega \sqrt{\mu_r \mu_0 \epsilon_r} = \omega \sqrt{\mu_0} \quad (\text{S.8})$$

where μ_0 is the magnetic permeability of free space in units in Newton Ampere⁻², and μ_r is the relative magnetic permeability of a material. For nonmagnetic materials, $\mu_r = 1$. The ratio of the magnitude of the incident wave and reflected wave is the reflection coefficient given as shown in Equation S.9:

$$\eta_{12} = \frac{n_1 - n_2}{n_1 + n_2} \quad (\text{S.9})$$

where n is the refractive index of a particular layer, and subscripts 1 and 2 denote the air and concrete layers (i.e., air and concrete), respectively. The variable n is defined by Equation S.10:

$$n = \sqrt{\epsilon_r \mu_r} \quad (\text{S.10})$$

Because air and concrete are nonmagnetic and assuming that the bedrock layer is nonmagnetic, the refractive indices are given as shown in Equations S.11 and S.12:

$$n_1 = \sqrt{\epsilon_{r\text{-air}}} = 1 \quad (\text{S.11})$$

$$n_2 = \sqrt{\epsilon_{r\text{-conc}}^*(\omega)} = \sqrt{\epsilon_r(\omega)' + i\epsilon_r(\omega)''} \quad (\text{S.12})$$

The reflection coefficient of a boundary can thus be rewritten as shown in Equation S.13:

$$\eta_{12} = \frac{1 - \sqrt{\epsilon_r(\omega)' + i\epsilon_r(\omega)''}}{1 + \sqrt{\epsilon_r(\omega)' + i\epsilon_r(\omega)''}} \quad (\text{S.13})$$

Note that the reflection coefficient is complex because the concrete layer has an imaginary part in complex permittivity. Because the GPR operates by measuring the time and magnitude of the reflected wave, the time and magnitude of the arriving wave pulse will change as a function of both the real and imaginary part of the complex permittivity. In short, the ratio of the magnitude of the incident and reflected wave represents the complex permittivity in imperfect dielectrics such as concrete. Using the magnitude of the incident and reflected wave to compute a complex permittivity with no-loss parts will lead to an over prediction of the real part of the relative complex permittivity.

In reality, if the electromagnetic wave does not entirely dissipate, the refracted wave through the concrete/air interface can be recorded in the time domain. Two phenomena occur during this time: attenuation of electromagnetic power and

decrease in electromagnetic phase velocity in the reflected wave from the second interface. The assumption of perfect dielectric layers means that no attenuation occurs because the electromagnetic wave energy is stored and released as the electromagnetic wave propagates without losses from conductor or dipolar reorientation. The reflected wave in the concrete/bedrock layer resulting from an imperfect dielectric will therefore have a smaller magnitude. In the case where the waveform is not completely dissipated in the concrete, the ratio of the incident wave within the concrete and from the reflected wave on the concrete/bedrock surface cannot be used to compute the dielectric constant of the bedrock layer. Without calibration, doing so will lead to an erroneous complex permittivity of the bedrock layer, and any determination of thickness will not be valid. In both cases, no information is given about the imaginary part of the concrete with TDR. If a perfect conductor exists behind the concrete where the incident wave is completely reflected at the interface between the concrete and the conductor, the decrease in amplitude of the electromagnetic wave can be used to compute the imaginary part of the complex permittivity in the concrete.

Despite ample evidence of the dielectric relaxation of nanoporous, saturated media being strongly affected by the pore structure, the GPR systems evaluated in this research can only determine the magnitude of complex permittivity on the surface, and not the individual real and imaginary parts.

Modeling of Composite Complex Permittivity

As mentioned in previous sections, composite properties of the cement paste depend on the properties of the individual phases' complex permittivity. The problem of determining effective properties of a medium is the problem of homogenization of partial differential equations, which considers well separated but different length scales to obtain an effective tensor for the constitutive properties of the composite in the bulk scale. Homogenization requires knowledge of the microstructure and can be numerically intensive, and both of the aforementioned limitations are not considered in the scope of this research. The research team instead seeks the bounds and models of the effective tensors with known or inversely determined/backcalculated properties in each of the composite constituent phases, either to validate the experimental results in the case of composite viscoelastic properties of rubber-filled cement paste, or to gain insights into relations between the microstructure of cement paste in relation to complex permittivity. Equations for composite complex permittivity bounds for two-phase and three-phase materials will be presented.

The bounds for real-valued tensors were derived by Hill (41); more restrictive bounds were derived by Hashin and Shtrikman (42) by solving for the composite constitutive property in an assembly of coated spheres, provided the spheres do not disturb

the surrounding field and the constitutive property of the phases are positive and real. The bounds are subsequently derived using Hashin–Shtrikman’s variational principles. All of these derivations assume that the externally applied stimulant/field is static in nature. In the literature, bounds were derived for conductivity tensors and various other constitutive properties, all of which are completely analogous to effective complex permittivity, and as such, the bounds can also be applied to effective complex permittivity problems.

As mentioned in the background section, relative permittivity can be complex. To find the bounds of a composite complex effective tensor, several researchers developed variational principles by transforming the frequency domain \hat{D} and \hat{E} (complex) into real equations. Lossy constituents represented by complex permittivity contain positive values for the imaginary part, and when the imaginary part of the composite is a positive definite, variational principles can be applied (43). This method was used to derive bounds for a two-phase, complex bulk modulus. Analytic methods can also give tight bounds in the complex plane and were used by Bergman to derive complex permittivity for a two-phase material (44). Finally, for a three-phase complex composite material, the field equation recursion method (45) was used to bound the composite complex permittivity.

Composite Constituents

Consider a case of a saturated cement paste. An illustration was shown previously in Figure S.2. The simplest case is a composite containing only water, with no geometrical effect on its dielectric properties, and solid. First, bounds for a two-phase composite with known dielectric properties for its constituents are developed and compared with experimental data. Then one examines the case of a three-phase composite where the geometrical effects on the dielectric properties of water are considered, namely, a distinct separation between confined water and bulk water. The experimental data are compared to the bounds and an effective medium theory model, where the properties of the confined water are determined. Last, the moisture content in a partially saturated case are modeled as a four-phase composite consisting of air, in addition to solid and water subject to various levels of geometric confinement. The complex permittivity of water used in the model is as shown in Figure S.1. The solid is assumed to be the oven-dried complex permittivity of the specimens ($\epsilon_r = 6$), and the air has a relative permittivity of $\epsilon_r = 1$.

Bounds on Complex Permittivity of a Two-Phase Composite

Before considering the more complicated cases, let us assume a completely saturated cementitious matrix with water and a

hydrated cement matrix with relative complex permittivities of $\epsilon_{bw}^*(\omega)$ and $\epsilon_{cem}^*(\omega)$, respectively. Individual phases in the hydrated cement paste are not expected to have drastically different complex permittivities. In fact, most of the solid phases have high resistivity (negligible ohmic losses) and negligible dipolar losses, which give the solid, hydrated cement paste a real relative permittivity only. Water within the pore space is assumed to behave like bulk water. Complex variables in terms of the complex permittivity of composite constituent phases and effective composite complex permittivity are defined by Bergman (44) as shown in Equations S.14 and S.15:

$$s(\omega) \equiv \frac{\epsilon_{cem}^*(\omega)}{\epsilon_{cem}^*(\omega) - \epsilon_{bw}^*(\omega)} \quad (\text{S.14})$$

and

$$F(s(\omega)) \equiv \frac{\epsilon_{cem}^*(\omega) - \epsilon_{eff}^*(\omega)}{\epsilon_{cem}^*(\omega)} \quad (\text{S.15})$$

where $\epsilon_{eff}^*(\omega)$ is the effective complex permittivity of the composite. For a two-phase isotropic composite with known volume fractions (from porosity) and complex permittivities, the bounds in $F(s)$ are derived with the analytic method and are given as shown in Equations S.16 and S.17:

$$F_1(\omega) = \frac{\phi(s(\omega) - s_0)}{s(\omega) \left(s(\omega) - s_0 - \frac{1}{d}(1 - \phi) \right)} \quad (\text{S.16})$$

and

$$F_2(\omega) = \frac{\phi(s(\omega) - s_0)}{(s(\omega) - s_0) \left(s(\omega) - \frac{1}{d}(1 - \phi) \right) - \frac{(d-1)}{d}(1 - \phi)(1 - s_0)} \quad (\text{S.17})$$

where d is the dimension of the system (in this case, $d = 3$ for a three-dimensional system), s_0 is a variable that defines the bound, and ϕ is the porosity. For F_1 , $0 < s_0 < \frac{(d-1)}{d}$, and for

F_2 , $\frac{(d-1)}{d} < s_0 < 1$. Bounds on the effective composite permittivity can be found by solving Equations S.16 and S.17 for $\epsilon_{eff}^*(\omega)$.

Bounds on Complex Permittivity of a Three-Phase Composite

The complication arises when water under geometric confinement in nanoscale pores exhibits more drastically dynamic

properties than bulk water, such that the dynamics of water molecules are hindered, as mentioned in the literature review. This geometrical confinement is well documented in the literature. With this consideration in mind, pore water in the cement paste is separated into two phases, and the research team defined the additional phase as confined water, with an associated complex permittivity $\epsilon_{cw}^*(\omega)$. The bounds are derived with the field recursion method described by Milton (45) and given as shown in Equations S.18 through S.20:

$$\frac{1}{\text{Im}\left[\frac{\epsilon_{cem}}{\epsilon_{cem} - \epsilon_{eff}}\right]} \leq \frac{\phi(1 - p_{bw})}{\text{Im}\left[\frac{\epsilon_{cem}}{\epsilon_{cem} - \epsilon_{cw}(\omega)}\right]} + \frac{\phi p_{bw}}{\text{Im}\left[\frac{\epsilon_{cem}}{\epsilon_{cem} - \epsilon_{bw}(\omega)}\right]} \quad (\text{S.18})$$

$$\frac{1}{\text{Im}\left[\frac{\epsilon_{cw}(\omega)}{\epsilon_{cw}(\omega) - \epsilon_{eff}}\right]} \leq \frac{\phi p_{bw}}{\text{Im}\left[\frac{\epsilon_{cw}(\omega)}{\epsilon_{cw}(\omega) - \epsilon_{bw}(\omega)}\right]} + \frac{\phi}{\text{Im}\left[\frac{\epsilon_{cw}(\omega)}{\epsilon_{cw}(\omega) - \epsilon_{cem}}\right]} \quad (\text{S.19})$$

$$\begin{aligned} \epsilon_{eff}(\omega) &= f_1 \epsilon_{cw}(\omega) + f_2 \epsilon_{bw}(\omega) + f_3 \epsilon_{cem} \\ &= \frac{[f_1 \cos(\theta) + f_2 \sin(\theta) - f_3 (\cos(\theta) + \sin(\theta))]^2}{\frac{\epsilon_{cw}(\omega)}{f_1} \cos^2(\theta) + \frac{\epsilon_{bw}(\omega)}{f_2} \sin^2(\theta)} \\ &\quad + \frac{\epsilon_{cem}}{f_3} (\cos(\theta) + \sin(\theta))^2 \end{aligned} \quad (\text{S.20})$$

where the parameter θ describes the bounds and varies from 0 to 2π , $f_1 = \phi(1 - p_{bw})$, $f_2 = \phi p_{bw}$, $f_3 = \phi$, and p_{bw} is a new dimensionless variable that represents the volume fraction of bulk water within the water in the pore space. All of the relative permittivities of the individual components can be frequency dependent. The reader is directed to (45) for a thorough review of the theory and derivation of the bounds.

To use the derived bounds, cement pastes of different water-to-cement (w/c) ratios are first modeled with known porosities (invariant with frequency) and compared with the measurement results. For a two-phase system, the pore water in the cement paste is assumed to behave like bulk water, without any geometrical confinement effect. Then for a three-phase system, the research team extends the modeling of bounds along with an effective medium theory where the pore water is separated into two phases: bulk water and confined water. With the known complex permittivities of bulk water and cement paste, and the assumption that a certain percentage of confined water exists in the structure (from desorption isotherms), the properties of confined water can

be fitted to the effective medium theory model and compared with the bounds of a three-phase material. An effective medium model of four phases (solid, bound water, confined water, and air) is used to develop collections for predicting moisture content versus complex permittivity and is compared to experimental results.

Effective Medium Model for Three- and Four-Phase Composites

In some cases, the bounds given in the previous sections are not useful for modeling purposes because the bounds themselves are overly broad, such as the bounds given in the three-phase composite case. To model moisture content of hardened cement paste, the Bruggeman formula (46) is used, assuming a three-dimensional space. The assumption is that interfacial polarization occurs at a much lower frequency (~ 1 MHz) and is neglected at this frequency range as shown in Equation S.21:

$$\sum_{i=1}^m f_i \frac{\epsilon_i - \epsilon_{eff}}{\epsilon_i + 2\epsilon_{eff}} = 0 \quad (\text{S.21})$$

where m is the number of phases in the composite. For $m = 3$ (three-phase composite), Equation S.21 is written as shown in Equation S.22:

$$f_1 \frac{\epsilon_{bw} - \epsilon_{eff}}{\epsilon_{bw} + 2\epsilon_{eff}} + f_2 \frac{\epsilon_{cw} - \epsilon_{eff}}{\epsilon_{cw} + 2\epsilon_{eff}} + f_3 \frac{\epsilon_{cem} - \epsilon_{eff}}{\epsilon_{cem} + 2\epsilon_{eff}} = 0 \quad (\text{S.22})$$

For $m = 4$ (four-phase composite), Equation S.21 is written as shown in Equation S.23:

$$\begin{aligned} f_1' \frac{\epsilon_{bw} - \epsilon_{eff}}{\epsilon_{bw} + 2\epsilon_{eff}} + f_2' \frac{\epsilon_{cw} - \epsilon_{eff}}{\epsilon_{cw} + 2\epsilon_{eff}} + f_3' \frac{\epsilon_{cem} - \epsilon_{eff}}{\epsilon_{cem} + 2\epsilon_{eff}} \\ + f_4' \frac{\epsilon_{air} - \epsilon_{eff}}{\epsilon_{air} + 2\epsilon_{eff}} = 0 \end{aligned} \quad (\text{S.23})$$

f_i' is used to denote that the previously given formulations of f_i are different. S denotes the state of saturation of the pore space, where $f_1' = S\phi(1 - p_{bw})$, $f_2' = S\phi p_{bw}$, $f_3' = f_3 = \phi$, and $f_4' = \phi(1 - S)$. ϵ_{eff} in Equations S.22 and S.23 can be solved analytically with different roots, and because the components of a complex ϵ_{eff} have to have positive values for both real and imaginary components, only the positive root is the valid solution. For a three-phase saturated cementitious composite system, the bound water complex permittivity ϵ_{cw} is determined from the saturated case by setting ϵ_{eff} equal to an experimentally determined value at a given frequency. To predict the response ϵ_{eff} as a function of saturation, ϵ_{eff} from Equation S.23 can be solved by using the ϵ_{cw} determined from a three-phase case.

Laboratory Testing

The desorption isotherm of specimens was determined with the mass loss method, where the specimens were placed in an RH-controlled chamber at constant temperature and the mass loss was recorded. Porosity was determined by completely drying the specimen in an oven. For relative and complex permittivity, the effective range of penetration of the percometer was determined. The operating frequency of the percometer was 40 MHz to 50 MHz with the probe selected. The percometer (Figure S.4) operates on the principle of time domain reflectometry for determination of relative permittivity. For the determination of complex permittivity with respect to frequency, a coaxial dielectric probe was used. The method of operation for the coaxial dielectric probe was described in the work of Blackham and Pollard (47). Dielectric measurements at frequencies between 200 MHz and 6 GHz were performed with a coaxial dielectric probe and vector network analyzer manufactured by Hewlett Packard (Agilent), model numbers 85070B and HP8753C, with the S-parameter test set, respectively. This method is hereafter referred to as VNA. Previous testing indicated that the change in complex permittivity ceased after about 7 days with cement pastes from the same type of cement, regardless of the w/c ratio. Nevertheless, all specimens tested were mature (>28 days).

Materials

The following materials were used for fabrication of concrete specimens: ASTM Type 1 portland cement, crushed limestone



Figure S.4. Determination of percometer penetration depth with cement paste cast on stainless steel at different thicknesses. Probe of percometer uses a frequency of 40 MHz to 50 MHz.

Table S.1. Mixture Designs for Concrete Specimens

Mass per Volume (kg/m ³)	Mixture A1	Mixture A2	Mixture A3
Water to cement	0.4	0.5	0.6
Water	210	210	210
Cement	525	420	350
Coarse aggregate	907	907	907
Fine aggregate	692	780	839

as coarse aggregate, and river sand as fine aggregate. The same type of cement was used in cement paste specimens.

Concrete

Specimens were made with embedded RH sensors for measurement of relative complex permittivity at the concrete surface with the percometer, and VNA 0.4-, 0.5-, and 0.6-w/c concrete specimens were fabricated. The specimen dimensions were 12 in. in diameter and approximately 6 in. tall. Plastic tubings were covered with a fibrous filter and inserted into a cylindrical tube normally used in construction, and concrete was cast around the tube. A plastic petri dish cover was placed onto the center of the fresh concrete surface on the top. This ensured that the coaxial dielectric probe had a flat, smooth surface for measurement. These mix designs are shown in Table S.1.

Specimens were covered for curing for 24 hours in a moist curing room before demolding. Specimens were wrapped on the bottom and the sides with tape to allow drying on the top surface of the specimen only. The specimens were then placed in a 100% RH moisture curing room for 28 days before testing. Specimens were placed in an air conditioned laboratory for drying. Wires containing the RH sensors on one end were placed in the plastic tubes and sealed. RH and temperature were measured with a data logger, and data were downloaded from the logger periodically. (See Figure S.5.)

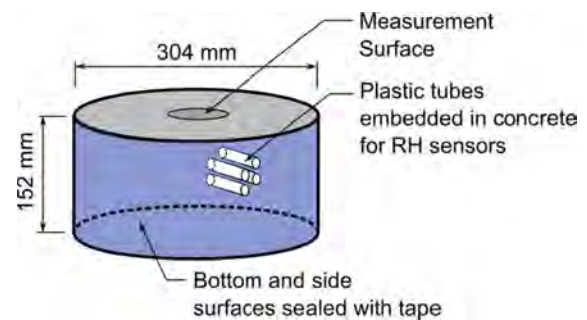


Figure S.5. Concrete specimen illustration. RH sensors on end of wires were placed in plastic tubes and sealed with rubber tape to prevent moisture from escaping.

Measurements were taken with the percometer periodically. The coaxial probe (from VNA) was placed in a holder and calibrated before testing. During testing, the specimen was moved underneath the probe. The probe was then placed in contact with the concrete with minimal movement to the cable to ensure accurate and repeatable measurements. The data were recorded with the software provided by the manufacturer on the computer. A total of four readings were made on the measurement area/surface each time, and the averaged reading was reported.

Cement Paste

For the cement paste specimens, the mixing procedure followed procedures in ASTM C305-06. Two types of specimens were fabricated: one for testing with the VNA and the other for determination of penetration depth of the percometer. Fresh paste was placed into plastic petri dishes after mixing and covered to prevent moisture loss. Specimens with w/c ratios ranging from 0.4 to 0.6 were fabricated at 0.1-w/c increments. Specimens were demolded at the earliest possible time and placed in deionized (DI) water to ensure saturation and to remove as many ions from the pore water as possible to remove effects that result from conducting ionic species. All of the specimens were placed in saturated DI water to cure for at least 28 days. The permeability of the specimens was determined by the dynamic pressurization method (16) with solid cylindrical specimens. Each cement paste specimen was tested three times at the point where the probe made contact on slightly different locations of the specimen surface, as illustrated in Figure S.6. Mass loss for 0.4-, 0.5-, and 0.6-w/c ratios was measured by pulverized, mature specimens for desorption isotherm determination.

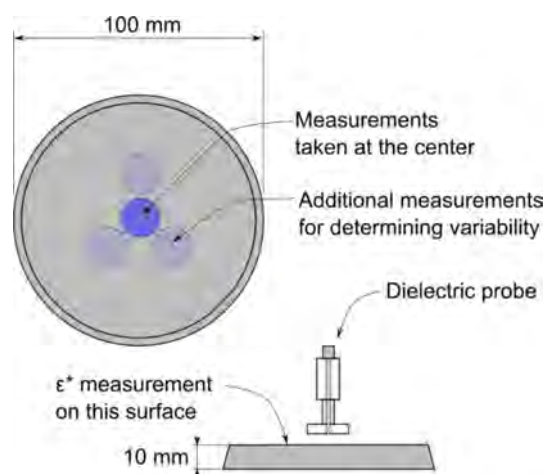


Figure S.6. Complex permittivity determination with dielectric probe. Small-diameter side of specimen (0.4 w/c) is also bottom of casting surface in petri dishes, providing smooth surface for probe.

After calibration, the specimen was placed on the bottom of the probe and the data were recorded. Four areas were tested near the center of the specimen. After testing the cement paste specimens at a saturated state, the specimens were placed in controlled RH chambers (saturated salt solution). Specimens were tested 30 days after being placed in the chambers. For the percometer testing, 0.4-w/c paste was cast on a stainless steel plate. Readings were taken at different time intervals because the specimen was cast. The thickness ranged from 3 mm to 37 mm. The specimen was placed in a bucket partially filled with water for curing.

Porous Ceramics

Porous ceramic specimens were also purchased for testing. Porous ceramics were manufactured from ball clay, and the chemistry is proprietary. Permeability of specimens was provided by the manufacturer. A total of four specimens were purchased from the manufacturer for testing. Two were placed in DI water and vacuum saturated for 24 hours for testing with the VNA. The specimens had a diameter of 25.4 mm and a height of 10.26 mm. For desorption isotherm measurements, two specimens were saturated with DI water, and their mass loss was measured with a precision scale. The specimens had a diameter of 50.8 mm and a height of 7.14 mm.

Test Results

Figure S.7 illustrates the data from the desorption isotherm of 0.4 w/c, 0.5 w/c, and 0.6 w/c. The cement with higher w/c tended to have a lower saturation level as a function of RH. The initial weight of the specimen (saturated surface dry) was obtained by determining the point at which the mass loss

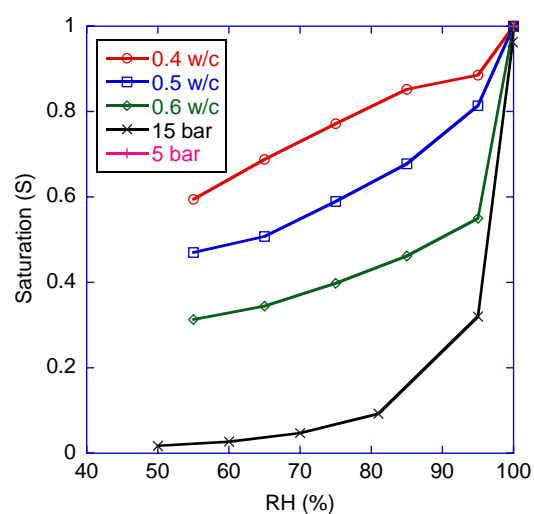


Figure S.7. Desorption isotherms from fabricated cement paste specimens. As expected, larger pores were found in higher-w/c-ratio specimens.

started to equilibrate by diffusion rather than evaporation of water on the specimen holder and specimen surface. Saturation was determined from the amount of free water in the specimens. At full saturation, $S = 1$, and when pores were completely emptied, $S = 0$. Pore sizes can be determined from sorption isotherms (48); and a sharp decrease in mass loss at higher RH levels indicates that more large pores are present, which is an indication of a high w/c ratio. For the concrete blocks, the measured RH is shown in Figure S.8.

RH in Concrete Specimens Versus Time

The measurements of internal RH in the concrete blocks along with the ambient RH are shown in Figure S.8. For the 0.4- and 0.6-w/c specimens, the abnormal fluctuations in the ambient

RH were caused by a malfunctioning air conditioning system in the laboratory.

Even with the top sensors situated only about 9 mm from the surface for all of the specimens tested, the RH level did not significantly decrease until about 100 hours after they were placed in the laboratory. This indicated that the surface moisture content was significantly lower compared with the moisture content within the concrete. A moisture gradient was present in the concrete specimens.

Relative and Complex Permittivity of Concrete Specimens

As the manufacturer noted, the measured ϵ_r is reliable when the material conductivity is under a certain threshold. For the

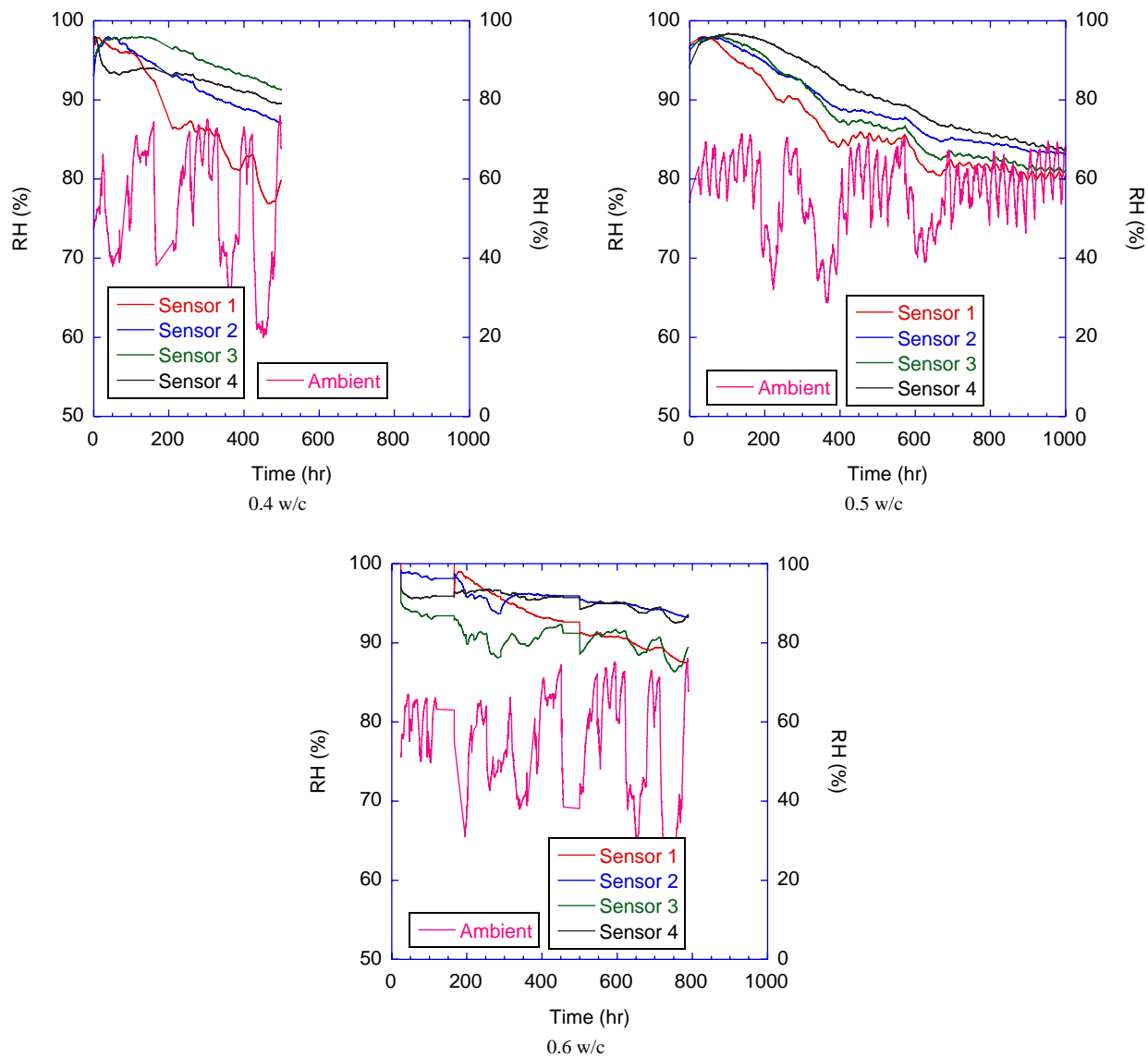


Figure S.8. Concrete RH measurements as a function of time. Note difference in drying rate between 0.4-w/c specimens and 0.5-w/c specimens. The 0.6-w/c specimens had water entrapped in sensor tube, and readings were erroneous.

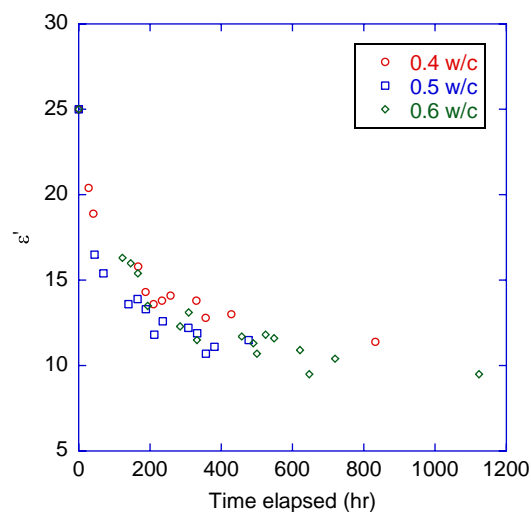


Figure S.9. Percometer readings on concrete specimens as a function of time. Note that despite variation in ambient RH, decrease in relative permittivity (possibly a complex reading) does not vary.

surface probe used in this research, $<2,000 \mu\text{S}/\text{cm}$ is the recommended value. Values beyond that will affect the measurements. Most likely, the measured value from the percometer is actually the magnitude of the complex permittivity when the material is lossy. For the percometer measurements, the measured ϵ_r readings of concrete versus time elapsed since drying are shown in Figure S.9 and the readings of cement paste versus thickness of cement paste are shown in Figure S.10.

The corresponding probe's range of readings for ϵ_r is between 1 and 40. When the range is exceeded, no reading is shown on the percometer, and it is represented by $\epsilon_r = 80$ for

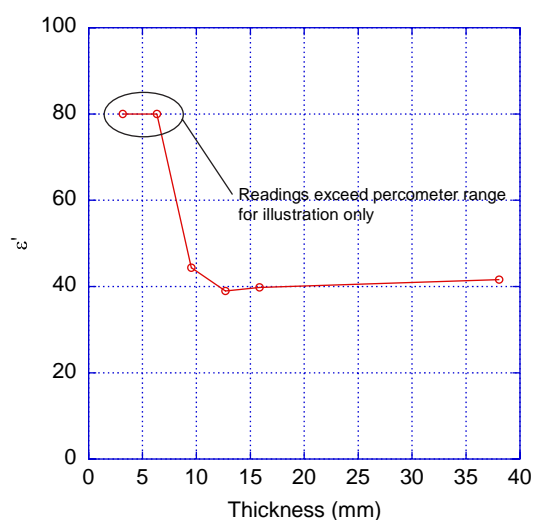


Figure S.10. Real part of permittivity as function of cement paste specimen thickness.

comparison purposes. The range of penetration for a wet cement paste specimen is shown to be about 10 mm to 15 mm for cement paste. The complex permittivity is likely lower than that in the case of concrete, because of the presence of aggregates, and in partially saturated systems. In both of the cases mentioned, the depth of penetration will be higher.

The results from complex permittivity testing of concrete slabs with VNA are shown in Figure S.11 for the real part of complex permittivity and Figure S.12 for the imaginary part of complex permittivity. Very little difference between the magnitude and shape of complex permittivity was observed with respect to frequency. Even with known ambient moisture, the amount of moisture within the tested area (with respect to depth) was not known. The measured complex permittivity from VNA followed the same trend compared to measured relative permittivity from the percometer, which suggested that the w/c and ambient RH fluctuation does not drastically affect the decrease in recorded relative permittivity.

Recall from Figure S.8 that the RH levels on the top sensors (~ 9 mm from the surface) did not drop until after about 100 hours. Yet drastic changes in complex permittivity were recorded for all of the specimens. Because the coaxial dielectric probe had a permittivity-dependent sample size requirement from the manufacturer of the probe (4 mm for $|\epsilon_r^*| = 25$, 9 mm for $|\epsilon_r^*| = 5$), the measured complex permittivity was probably primarily due to the moisture content of the first few millimeters at the surface. The research team hypothesized that after casting of the concrete specimens, the bleed water on the surfaces of the fresh concrete specimens would effectively increase the w/c ratio of the concrete surface layer. The internal RH of the specimens also support this hypothesis, as the top sensors of the specimens stayed at a high RH level for an extended period, even though the top sensor was merely ~ 9 mm away from the surface and drastic drops in magnitude of complex permittivity were recorded. This means that the recorded complex permittivity was most influenced by only the change in RH on the first few millimeters of the surface. The measurements from the concrete specimens thus only gave a qualitative measure of correlation between complex permittivity and moisture content.

Complex Permittivity of Cement Paste Specimens at Room Temperature

Since the measurement of concrete surface complex permittivity cannot be used to correlate RH level, moisture contents of cement paste specimens were conditioned to determine correlations between moisture content and complex permittivity. Figure S.13 and Figure S.14 show the complex permittivity of 0.4-, 0.5-, and 0.6-w/c specimens, respectively, at room temperature.

The differences in magnitude of the dielectric constants were noticed in all of the frequency ranges, which also scaled with the

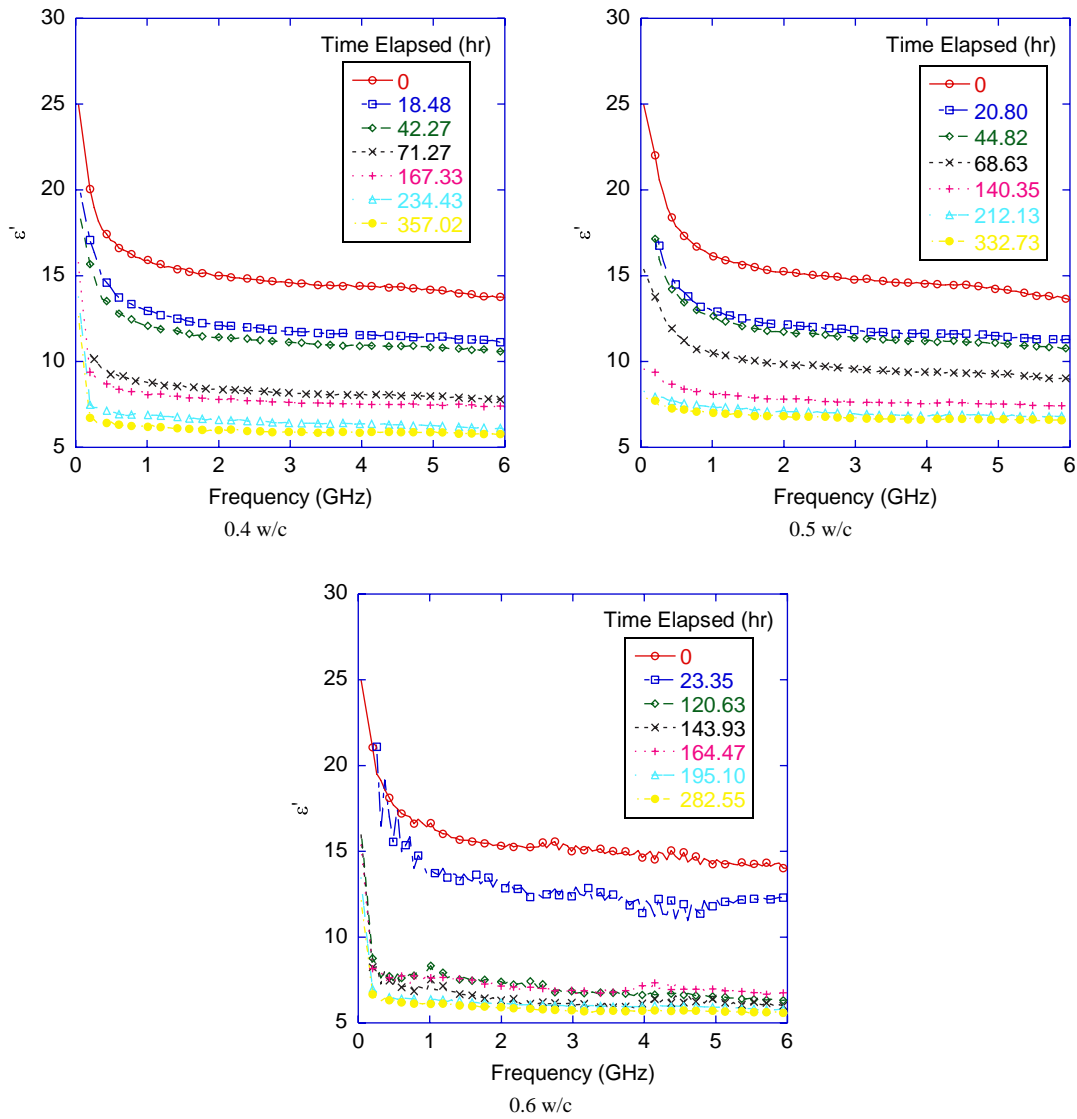


Figure S.11. Real part of complex permittivity from concrete specimens: 0.4 w/c, 0.5 w/c, and 0.6 w/c.

w/c ratio, that is, a higher w/c ratio resulted in a higher ϵ' and ϵ'' . However, the loss part of permittivity appeared to be much less sensitive to change in moisture content, with the 0.6 w/c being the only exception. The real part of complex permittivity should be used to correlate moisture content with complex permittivity because of its high sensitivity to relatively small changes in moisture content. The saturation was obtained from converting RH by desorption isotherms, as shown in Figure S.7.

Complex Permittivity of Saturated Cement Pastes and Porous Ceramics at Different Temperatures

Porous ceramic discs were also tested with VNA to determine dependence of pore size distribution on the complex

permittivity. The pore size distribution for the porous ceramic discs was expected to be narrower than that of cement paste. The research team hypothesized that the narrow pore size distribution found in the ceramic discs would affect the dielectric dispersion in the confined water in the pore space, whereas in cement paste, a range of pore sizes would be found, and therefore a clear indication between water permeability and complex permittivity would not be observed in cement paste. Complex permittivity of porous materials containing water was previously studied; confined water has restricted dipole-dipole movement. This can be observed in the relaxation time of water at different temperatures, where the relaxation occurs at lower frequencies as temperature is lowered. To verify, measurements were made for water-saturated porous ceramics, and results are shown in Figure S.15.

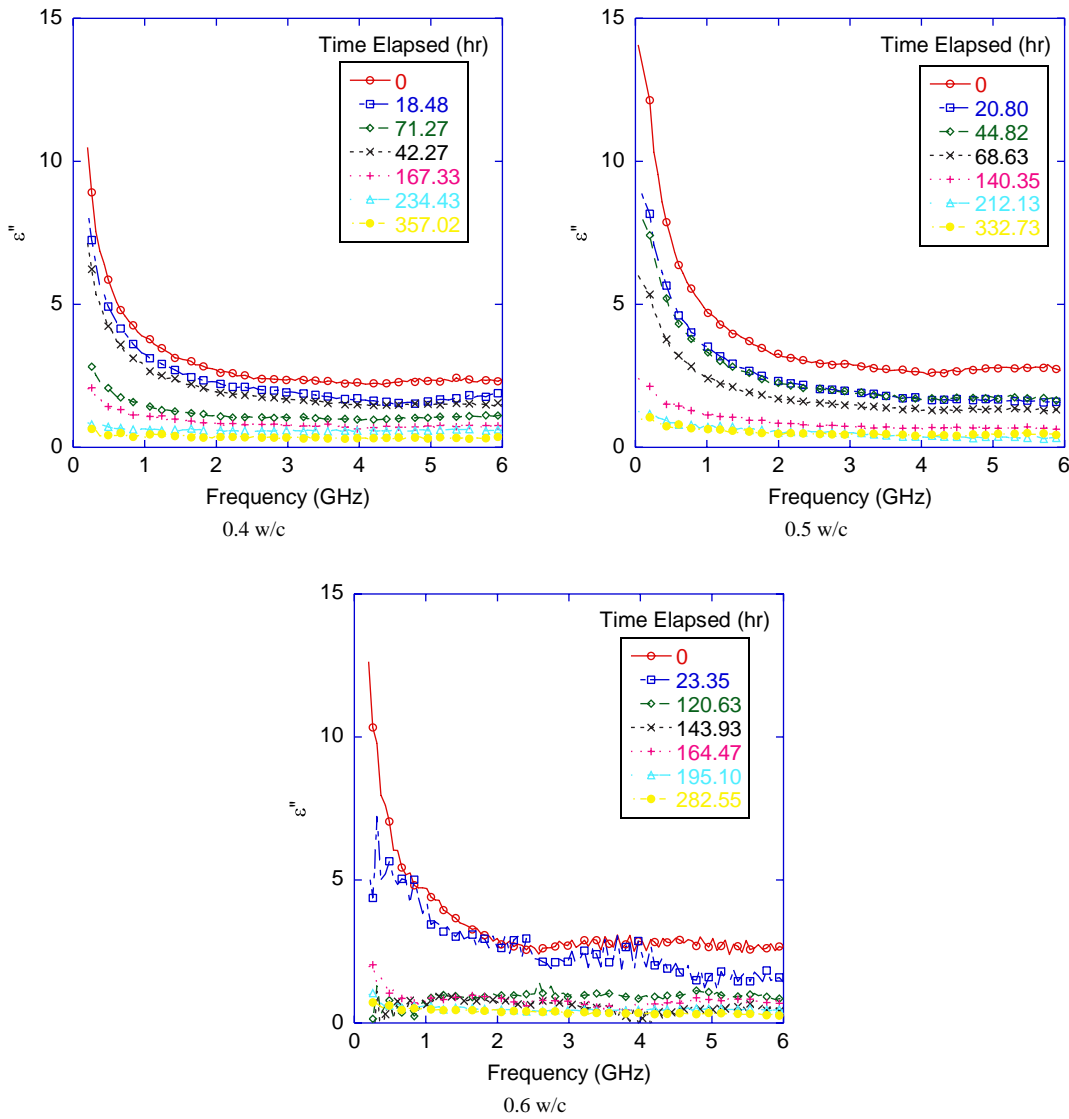


Figure S.12. Imaginary part of complex permittivity from concrete specimens: 0.4 w/c, 0.5 w/c, and 0.6 w/c.

For the imaginary part of complex permittivity, confined water did not seem to play a role in relaxation for the five-bar specimens because of the lack of a peak at the lower frequencies. For 15-bar specimens, a higher loss part was found at lower frequencies. Five-bar specimens had larger pores per volume (see desorption isotherm in Figure S.7). The complex permittivity with respect to frequency of porous ceramics was distinctly different from that observed in cement paste. For cement paste, the complex permittivity appeared to be well represented by an exponential decaying function with no bulk water relaxation component, whereas a distinct change in complex permittivity was observed due to bulk water relaxation in both porous ceramic specimens. For the 15-bar specimen with smaller pores, an exponential decay at the lower frequencies was observed, which is hypothesized to

result from the small amount of confined water in the porous ceramic, similar to that observed in the cement paste.

Modeling of Relevant Material Properties with Experimental Results

Complex Permittivity Bounds and Prediction with Effective Medium Theory

With known values of porosity for each of the materials, complex permittivity of bulk water and a measured value for the complex permittivity of the solid phase, Equations S.16 and S.17 can be used to solve for the bounds of composite relative permittivity, ϵ_{eff}^* . The bounds can then be plotted on

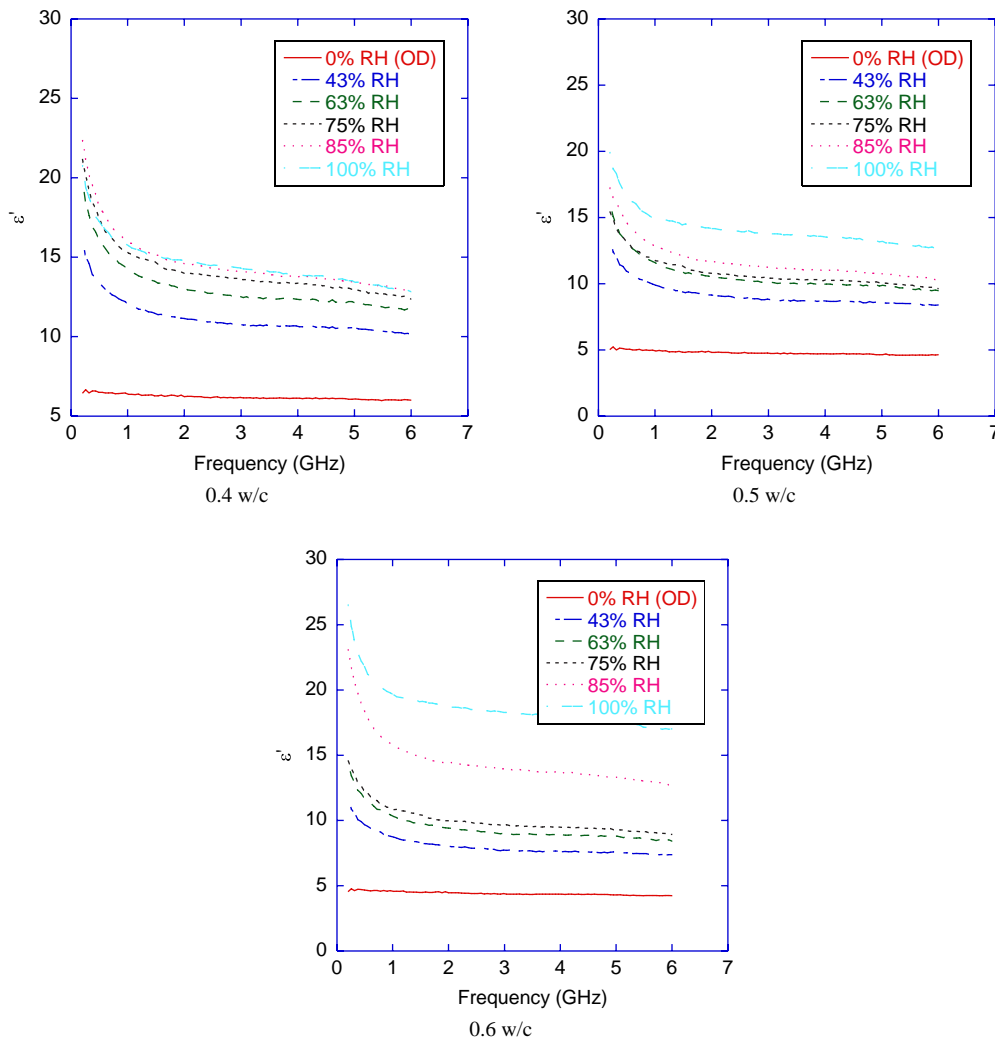


Figure S.13. Real part of complex permittivity for cement paste specimens: 0.4 w/c, 0.5 w/c, and 0.6 w/c. OD = oven dried.

the complex plane for comparison. Figure S.16 shows the difference between measured values at different frequencies versus the complex permittivity predictions from a two-phase composite.

The two-phase composite assumption, while able to produce restrictive bounds on the complex plane, was not able to predict value of the composite complex permittivity. The experimentally measured complex permittivity on the complex plane fell outside of the bounds from the model. Assuming the dielectric response of a saturated hardened cement paste as composite material containing only two phases made up of solids and bulk water was clearly not a valid assumption.

A three-phase composite bound and the effective medium theory (Equation S.22) were used to determine the response of an additional phase of confined water by fitting the complex permittivity of bulk water to the experimentally determined value. The dielectric response of pore water was

assumed to be described by two distinct phases of bulk and confined water, with different complex permittivity. The resulting bounds from Equations S.18, S.19, and S.20 are illustrated in Figure S.19 for a 0.4-w/c specimen at 1 GHz at room temperature.

The bounds were obtained by fitting the experimental data point at each frequency (in the case of Figure S.17, at 1 GHz) by varying the properties of the confined water, which is a complex-valued quantity. The bounds shown in Figure S.17 are much wider than those shown in Figure S.16 because of the different method of derivation. The confined water was assumed to be a discrete phase, and its volume fraction was determined from the desorption isotherm. Water contained in <20 nm pores was assumed to be confined water, and the volume fraction as a function of the total pore volume was used as a model parameter for the confined water. The complex permittivity of the confined water was determined by

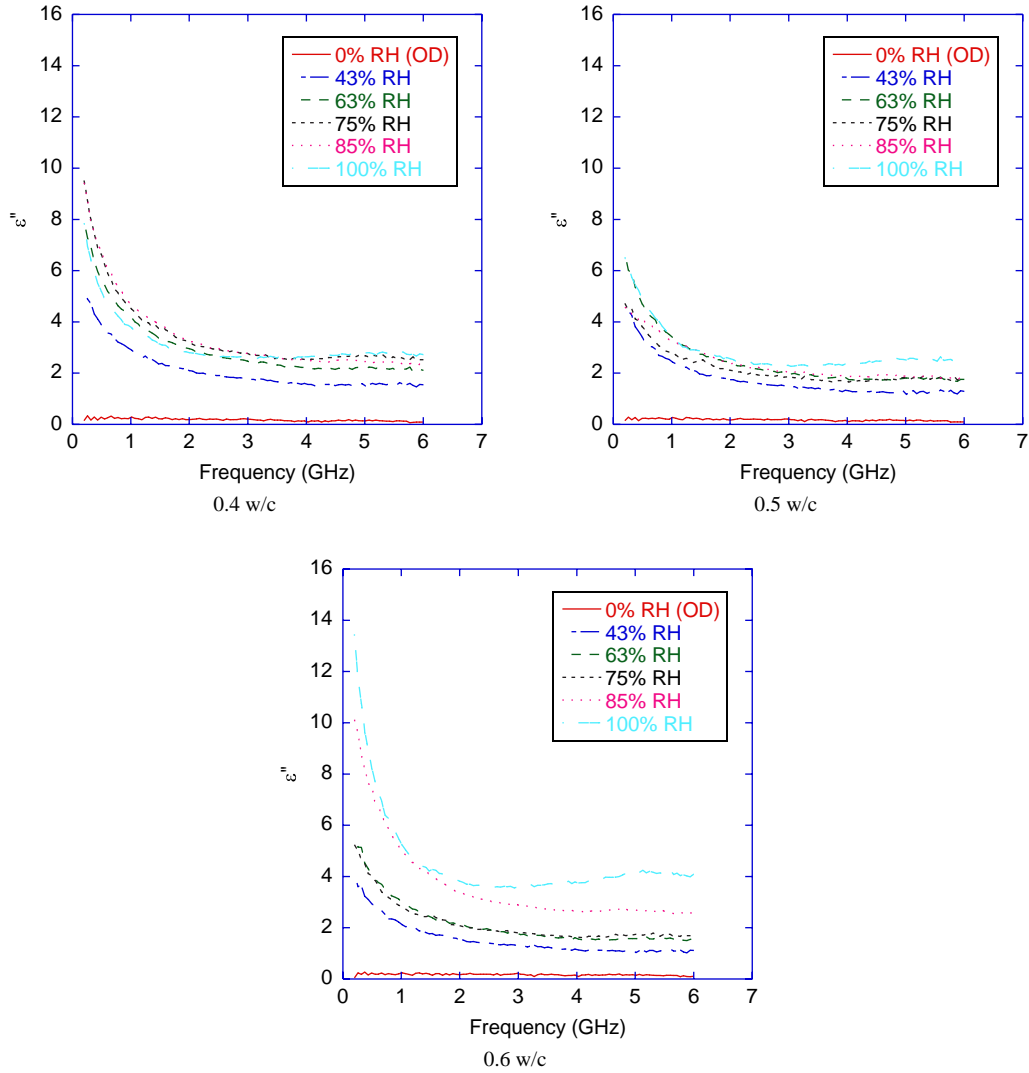


Figure S.14. Imaginary part of complex permittivity for cement paste specimens: 0.4 w/c, 0.5 w/c, and 0.6 w/c. OD = oven dried.

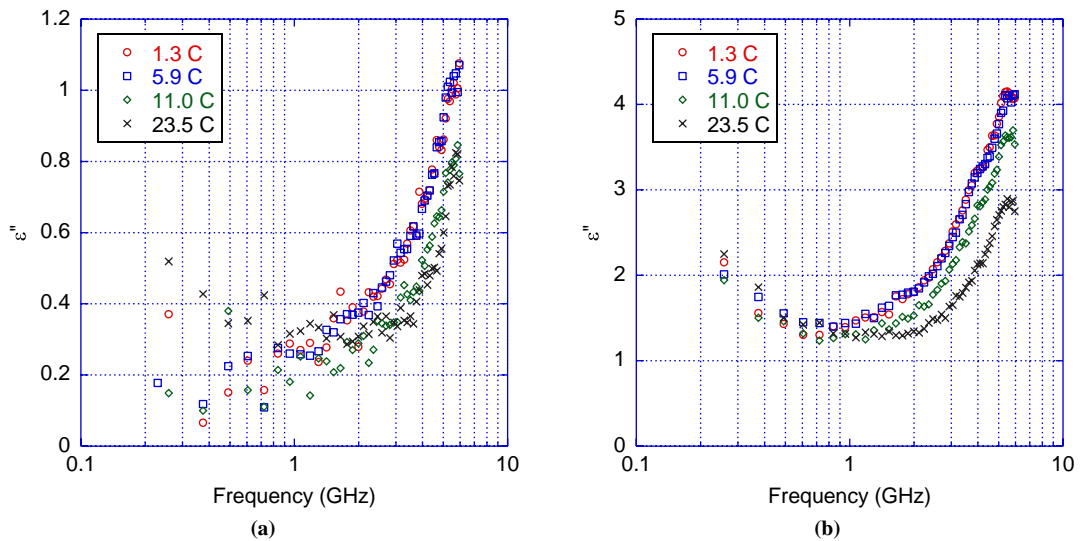


Figure S.15. Examples of porous ceramic loss part of complex permittivity versus temperature. Note that as temperature is lowered, relaxation due to the presence of water in pore space starts to occur at a lower frequency.

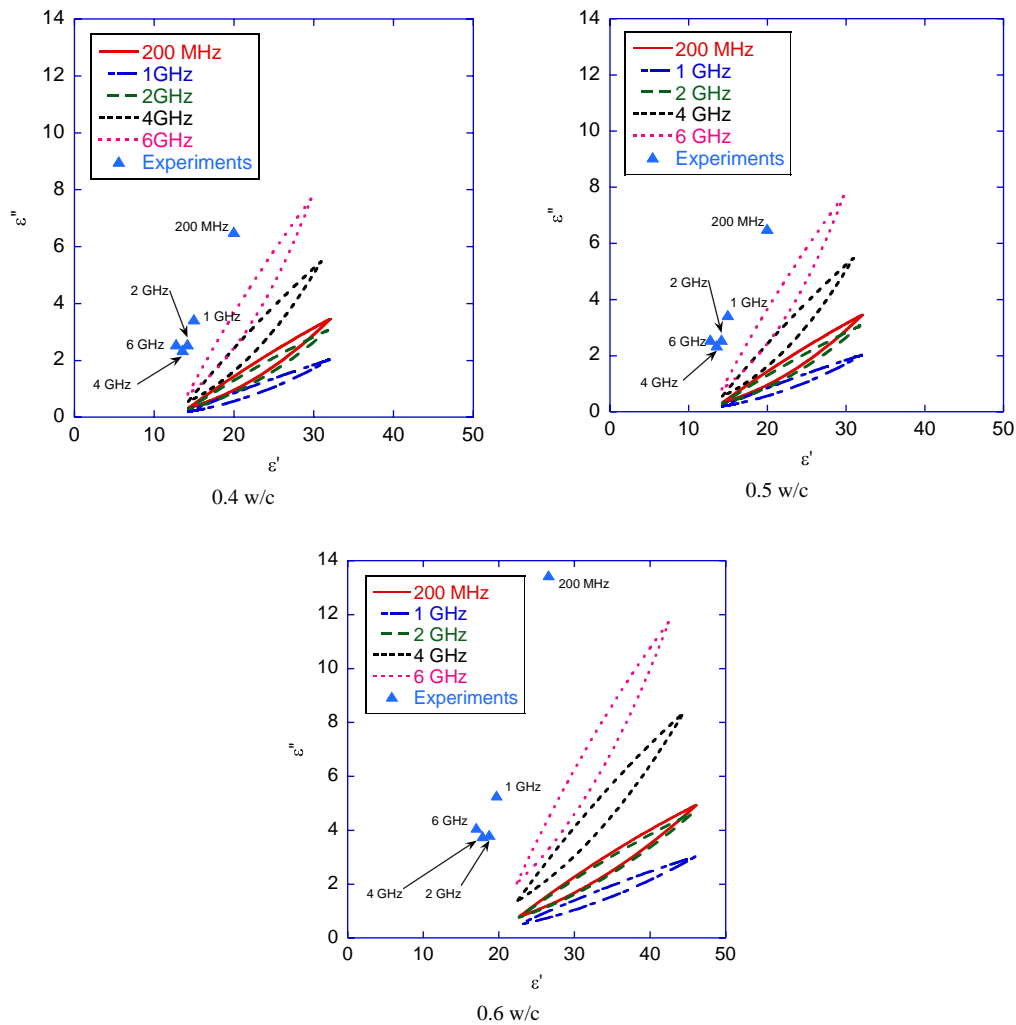


Figure S.16. Two-phase bounds of effective complex permittivity of cement paste versus measured data for 0.4 w/c, 0.5 w/c, and 0.6 w/c.

adjusting the real and imaginary components at each frequency and was fitted to the experimentally measured complex permittivity on the complex plane (i.e., Figure S.17, but at different frequencies). The modeled complex permittivity of the confined water as a function of frequency for each of the materials is shown in Figure S.18.

The modeled real part of complex permittivity of confined water for 0.6-w/c specimens was significantly higher. The research team hypothesized that the additional air bubbles introduced by mixing on a rotating shaft to prevent excessive bleeding of the specimen greatly increased the effective water content of the specimen when tested with the coaxial dielectric probe. Increasing the value of porosity ϕ used in modeling for 0.6 w/c reduced the real part of complex permittivity to a level comparable to 0.4 w/c and 0.5 w/c. The most interesting finding from this three-phase composite model is that the predicted imaginary part of complex permittivity of confined water was significantly higher for a 0.4-w/c specimen

than for a 0.5-w/c or 0.6-w/c specimen. This implies that the confined water cannot be assumed to be a discrete phase being independent from the microstructure and porosity.

Modeling of Cement Paste Moisture Content

Because the surface relative permittivity from GPR used in this research obtains the relative permittivity from reflected wave amplitudes, having the knowledge of complex permittivities at different moisture contents will allow engineers to determine moisture content from GPR readings. Figure S.19 shows the magnitude of complex permittivity of 0.4-w/c through 0.6-w/c cement pastes at different moisture contents. The moisture content was converted from saturation because the porosity of the materials was previously determined. By plotting the associated moisture content for all of the materials (0.4, 0.5, and 0.6 w/c) at the two frequencies near the operating frequency of the air-coupled GPR, a linear relationship between volumetric

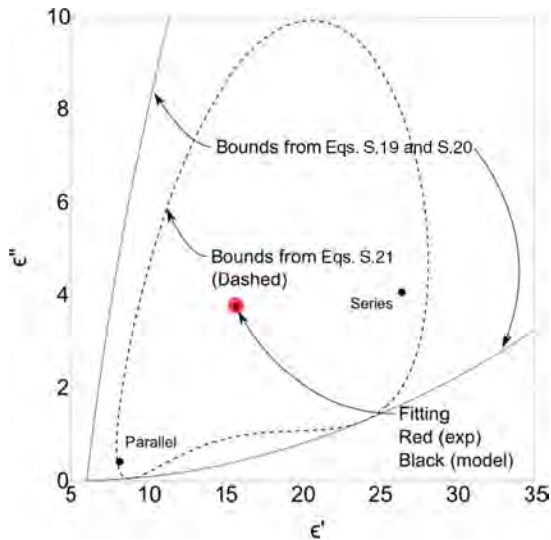


Figure S.17. Three-phase composite bounds of 0.4 w/c at 1 GHz. The red dot represents the experimentally obtained data plotted on the complex plane. The dashed line represents a bound from Equation S.21, whereas the solid lines represent the bounds from Equations S.19 and S.20. The solid black dots represent the parallel and series model, with one of the solid black dots being the predicted composite complex permittivity from Equation S.22.

moisture content and the real part of complex permittivity was observed. Figure S.13 and Figure S.14 show the different w/c versus complex permittivity for specimens conditioned to different RH. Using the values of porosity at each different w/c, degree of saturation, S , can be readily converted to volumetric moisture content, MC . The correlation between laboratory

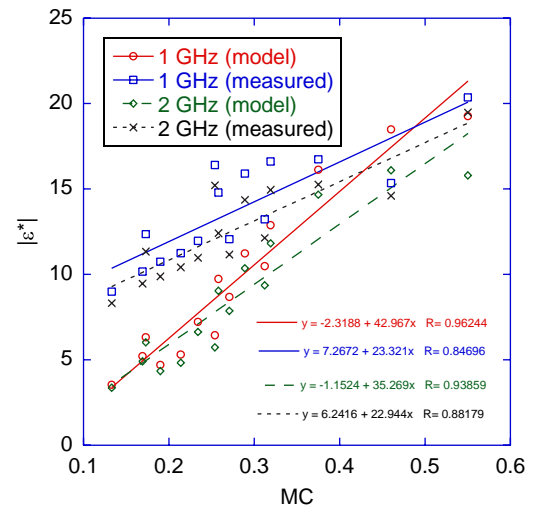


Figure S.19. Empirical fit and modeled magnitude of complex permittivity as a function of moisture content at 1 GHz and 2 GHz. Model used averaged ϵ_{cw} and points from all measurements (0.4 w/c through 0.6 w/c) were plotted on same graph.

measurements and MC and the model prediction from solving for the effective composite complex permittivity ϵ_{eff} with Equation S.23 are shown in Figure S.19.

The modeled response with Equation S.23 also uses an average value of complex permittivity of confined water, which could introduce significant error. The predictions made without using an averaged complex permittivity of confined water can be found in Figure S.20.

The modeled magnitude of complex permittivity slightly improved when the model used the corresponding ϵ_{cw} from

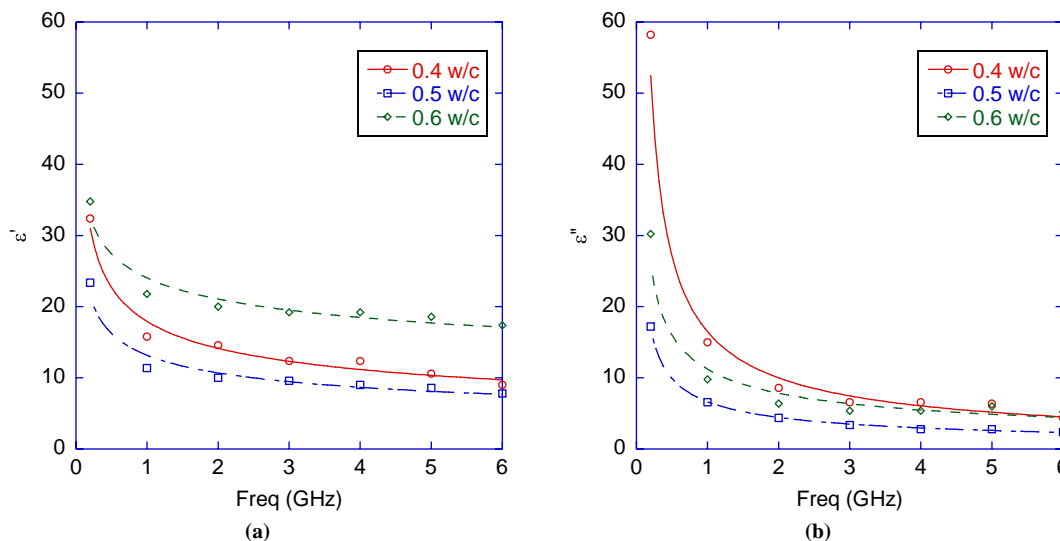


Figure S.18. Modeled confined water complex permittivity versus frequency.

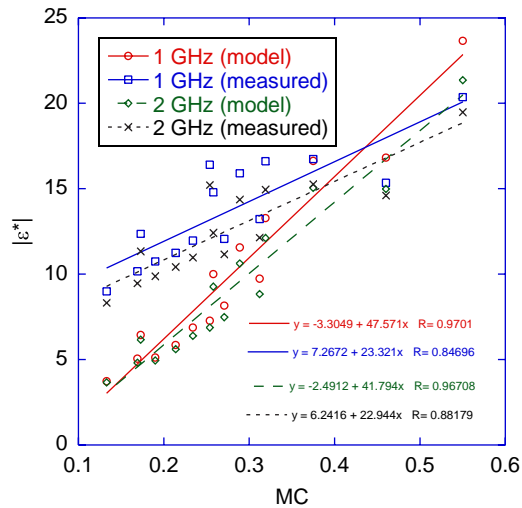


Figure S.20. Empirical fit and modeled magnitude of complex permittivity as a function of moisture content at 1 GHz and 2 GHz. Model used modeled ϵ_{cw} for each w/c-ratio specimen, and magnitude of complex permittivity from all measurements was plotted on same graph.

each of the w/c ratios instead of an averaged value. The complex permittivity from modeling was higher than the experimental values at lower RH. This could be attributed to the fact that even after 2 months of drying, the specimen dimension prevented the specimen from having a fully equilibrated moisture state through depth. It is also possible that the Bruggeman formula does not accurately represent the effective complex permittivity of cementitious materials. Nevertheless, the magnitude of the complex permittivity as a function of moisture content can apparently be represented as a linear relation.

Conclusion

The dependence of complex permittivity on the moisture content of cementitious materials, including concrete and cement paste, was systematically evaluated by microwave dielectric spectroscopy and a percometer. The depth of penetration of the percometer was determined for a saturated cement paste, and the depth of penetration was expected to increase for partially saturated cement paste and concrete. The operator is cautioned that for concrete, the measured value of the real part of relative permittivity from the percometer will likely deviate from the actual value because of the effect of conducting ionic species on electromagnetic wave propagation and reflection. Multiphase composite models were used to validate experimental results on cement paste at various levels of saturation. The model was able to replicate the measured trends between moisture content and magnitude of complex permittivity, with deviations from the

model attributed to the inability to control the internal RH of tested cement paste specimens in a reasonable amount of time.

The properties of the confined water were used to estimate the percentage of confined water by fitting the complex permittivity model to the measured experimental values of a saturated 0.3-w/c paste. The permeability was estimated by considering the Kozeny-Carmen equation.

The frequency dependent dissipation of electromagnetic waves in water in a bulk state and confined spaces, known as dielectric relaxation, has the potential to provide valuable parameters to the pore structure of a material; and transport properties such as permeability can be inferred from pore structures. Dielectric relaxation occurs when the polarization of charge within dielectric materials subjected to a time-dependent alternating electric field cannot follow the electric field because of frictional losses, and the electromagnetic wave energy in the propagating wave is dissipated. Mechanisms associated with dielectric relaxation of the porous medium consisted of bulk water, interfacial, and ionic relaxation components. Bulk water relaxation is due to the rotation of water molecules in the bulk water, presumably not affected by interfaces. Interfacial relaxation occurs when water molecules restrained in confined spaces relax at a different rate than those of bulk water. Ionic relaxation occurs at low frequencies.

References

1. Wobschall, D. 1977. A Theory of the Complex Dielectric Permittivity of Soil Containing Water: The Semidisperse Model. *IEEE Transactions on Geoscience Electronics*, Vol. 15, pp. 49–58.
2. Amico, F. D., C. Guattari, and A. Benedetto. 2010. GPR Signal Processing in Frequency Domain Using Artificial Neural Network for Water Content Prediction in Unsaturated Subgrade. In *13th International Conference on Ground Penetrating Radar (GPR), 2010*, Lecce, Italy, pp. 1–6.
3. Benedetto, A., and F. Benedetto. 2011. Remote Sensing of Soil Moisture Content by GPR Signal Processing in the Frequency Domain. *IEEE Sensors Journal*, Vol. 11, pp. 2432–2441.
4. Charlton, M. 2001. Characterization of Ground-Penetrating Radar (GPR) Response in a Variety of Earth Materials Under Different Moisture Conditions. In *SPIE* (C. Nguyen, ed.), Academic Press, San Diego, Calif., pp. 288–299.
5. Lai, W. L., W. F. Tsang, H. Fang, and D. Xiao. 2006. Experimental Determination of Bulk Dielectric Properties and Porosity of Porous Asphalt and Soils Using GPR and a Cyclic Moisture Variation Technique. *Geophysics*, Vol. 71, pp. K93–K102.
6. Laurens, S., J. P. Balaýssac, J. Rhazi, G. Klysz, and G. Arliguie. 2005. Non-Destructive Evaluation of Concrete Moisture by GPR: Experimental Study and Direct Modeling. *Materials and Structures*, Vol. 38, pp. 827–832.
7. Saarenketo, T., and T. Scullion. 2000. Road Evaluation with Ground Penetrating Radar. *Journal of Applied Geophysics*, Vol. 43, pp. 119–138.
8. Soutsos, M. N., J. H. Bungey, S. G. Millard, M. R. Shaw, and A. Patterson. 2001. Dielectric Properties of Concrete and Their Influence on Radar Testing. *NDT & E International*, Vol. 34, pp. 419–425.

9. Huisman, J. A., S. S. Hubbard, J. D. Redman, and A. P. Annan. 2003. Measuring Soil Water Content with Ground Penetrating Radar: A Review. *Vadose Zone Journal*, Vol. 2, pp. 476–491.
10. Topp, G. C., J. L. Davis, and A. P. Annan. 1980. Electromagnetic Determination of Soil-Water Content—Measurements in Coaxial Transmission Lines. *Water Resources Research*, Vol. 16, pp. 574–582.
11. Grote, K., S. Hubbard, and Y. Rubin. 2003. Field-Scale Estimation of Volumetric Water Content Using Ground-Penetrating Radar Ground Wave Techniques. *Water Resources Research*, Vol. 39, No. 11.
12. Miura, N., N. Shinyashiki, S. Yagihara, and M. Shiotsubo. 1998. Microwave Dielectric Study of Water Structure in the Hydration Process of Cement Paste. *Journal of the American Ceramic Society*, Vol. 81, pp. 213–216.
13. Halabe, U. B., A. Sotoodehnia, K. R. Maser, and E. A. Kausel. 1993. Modeling the Electromagnetic Properties of Concrete. *ACI Materials Journal*, Vol. 90, pp. 552–563.
14. Jones, C. A., and Z. C. Grasley. 2009. Correlation of Radial Flow-Through and Hollow Cylinder Dynamic Pressurization Test for Measuring Permeability. *Journal of Materials in Civil Engineering*, Vol. 21, pp. 594–600.
15. Jones, C. A., and Z. C. Grasley. 2009. Correlation of Hollow and Solid Cylinder Dynamic Pressurization Tests for Measuring Permeability. *Cement and Concrete Research*, Vol. 39, pp. 345–352.
16. Jones, C. A., and Z. C. Grasley. 2009. Novel and Flexible Dual Permeability Measurement Device for Cementitious Materials. *ACI Materials Journal*, Vol. 106, pp. 192–197.
17. Basheer, P. A. M., and E. Nolan. 2001. Near-Surface Moisture Gradients and In Situ Permeation Tests. *Construction Building Materials*, Vol. 15, pp. 105–114.
18. Snyder, K. A., X. Feng, B. D. Keen, and T. O. Mason. 2003. Estimating the Electrical Conductivity of Cement Paste Pore Solutions from OH⁻, K⁺ and Na⁺ Concentrations. *Cement and Concrete Research*, Vol. 33, pp. 793–798.
19. Meissner, T., and F. J. Wentz. 2004. The Complex Dielectric Constant of Pure and Sea Water from Microwave Satellite Observations. *IEEE Transactions on Geoscience and Remote Sensing*, Vol. 42, pp. 1836–1849.
20. Jonscher, A. K. 1999. Dielectric Relaxation in Solids. *Journal of Physics D: Applied Physics*, Vol. 32, pp. R57–R70.
21. Feldman, Y., A. Puzenko, and Y. Ryabov. 2005. Dielectric Relaxation Phenomena in Complex Materials. In *Fractals, Diffusion, and Relaxation in Disordered Complex Systems*, John Wiley & Sons, Inc., Hoboken, N.J., pp. 1–125.
22. Lane, J. A., and J. A. Saxton. 1952. Dielectric Dispersion in Pure Polar Liquids at Very High Radio Frequencies. III. The Effect of Electrolytes in Solution. *Proceedings of the Royal Society of London Series A: Mathematical and Physical Sciences*, Vol. 214, pp. 531–545.
23. Ho, W., and W. F. Hall. 1973. Measurements of the Dielectric Properties of Seawater and NaCl Solutions at 2.65 GHz. *Journal of Geophysical Research*, Vol. 78, pp. 6301–6315.
24. Liebe, H. J., G. A. Hufford, and T. Manabe. 1991. A Model for the Complex Permittivity of Water at Frequencies Below 1 THz. *International Journal of Infrared and Millimeter Waves*, Vol. 12, pp. 659–675.
25. Ellison, W., A. Balana, G. Delbos, K. Lamkaouchi, L. Eymard, C. Guillou, and C. Prigent. 1998. New Permittivity Measurements of Seawater. *Radio Science*, Vol. 33, pp. 639–648.
26. Guillou, C., W. Ellison, L. Eymard, K. Lamkaouchi, C. Prigent, G. Delbos, G. Balana, and S. A. Boukabara. 1998. Impact of New Permittivity Measurements on Sea Surface Emissivity Modeling in Microwaves. *Radio Science*, Vol. 33, pp. 649–667.
27. Wang, J. R. 2002. A Comparison of the MIR-Estimated and Model-Calculated Fresh Water Surface Emissivities at 89, 150, and 220 GHz. *IEEE Transactions on Geoscience and Remote Sensing*, Vol. 40, pp. 1356–1365.
28. Feldman, Y., A. Gutina, E. Axelrod, A. Puzenko, E. Rysiakiewicz-Pasek, and N. Kozlovich. 1998. Dielectric Relaxation of Porous Glasses. *Journal of Non-Crystalline Solids*, Vol. 235, pp. 302–307.
29. Kremer, F., A. Huwe, P. Behrens, and W. Schwieger. 2001. Molecular Dynamics in Confining Space: From the Single Molecule to the Liquid State. *Physical Review Letters*, Vol. 82, pp. 2338–2341.
30. Feldman, Y., Y. Ryabov, A. Gutina, and V. Arkhipov. 2001. Dielectric Relaxation of Water Absorbed in Porous Glass. *The Journal of Physical Chemistry B*, Vol. 105, pp. 1845–1850.
31. Michot, L. J., F. Villieras, M. Francois, I. Bihannic, M. Pelletier, and J. M. Cases. 2002. Water Organisation at the Solid-Aqueous Solution Interface. *Comptes Rendus Geoscience*, Vol. 334, pp. 611–631.
32. Spanoudaki, A., B. Albel, L. Bonneviot, and M. Peyrard. 2005. The Dynamics of Water in Nanoporous Silica Studied by Dielectric Spectroscopy. *European Physical Journal E*, Vol. 17, pp. 21–27.
33. deLoor, G. P. 1983. The Dielectric-Properties of Wet Materials. *IEEE Transactions on Geoscience and Remote Sensing*, Vol. 21, pp. 364–369.
34. Ishida, T., T. Makino, and C. J. Wang. 1000. Dielectric-Relaxation Spectroscopy of Kaolinite, Montmorillonite, Allophane, and Imogolite Under Moist Conditions. *Clays and Clay Minerals*, Vol. 48, pp. 75–84.
35. Gorur, K., M. K. Smit, and F. H. Wittmann. 1982. Microwave Study of Hydrating Cement Paste at Early Age. *Cement and Concrete Research*, Vol. 12, pp. 447–454.
36. Gu, P., and J. J. Beaudoin. 1996. Dielectric Behaviour of Hardened Cement Paste Systems. *Journal of Materials Science Letters*, Vol. 15, pp. 182–184.
37. Hager, N. E., and R. C. Domszy. 2004. Monitoring of Cement Hydration by Broadband Time-Domain-Reflectometry Dielectric Spectroscopy. *Journal of Applied Physics*, Vol. 96, pp. 5117–5128.
38. Wittmann, F. H., and F. Schlude. 1975. Microwave Absorption of Hardened Cement Paste. *Cement and Concrete Research*, Vol. 5, pp. 63–71.
39. Maxwell, J. C., and W. Garnett. 1881. *An Elementary Treatise on Electricity*. At the Clarendon Press, Oxford, United Kingdom.
40. Debye, P. J. W. 1954. *The Collected Papers of Peter J. W. Debye*. Interscience Publishers, New York.
41. Hill, R. 1952. The Elastic Behaviour of a Crystalline Aggregate. *Proceedings of the Physical Society Section A*, Vol. 65, pp. 349–354.
42. Hashin, Z., and S. Shtrikman. 1963. Variational Approach to Theory of Elastic Behaviour of Multiphase Materials. *Journal of Mechanics and Physics of Solids*, Vol. 11, pp. 127–140.
43. Gibiansky, L. V., and G. W. Milton. 1993. On the Effective Viscoelastic Moduli of 2-Phase Media. I. Rigorous Bounds on the Complex Bulk Modulus. *Proceeding of the Royal Society of London Series A: Mathematical Physical and Engineering Sciences*, Vol. 440, pp. 163–188.
44. Bergman, D. J. 1982. Rigorous Bounds for the Complex Dielectric-Constant of a 2-Component Composite. *Annals of Physics (New York)*, Vol. 138, pp. 78–114.
45. Milton, G. W. 2002. *The Theory of Composites*. Cambridge University Press, Cambridge, New York.
46. Bruggeman, D. A. G. 1935. Berechnung verschiedener physikalischer Konstanten von heterogenen Substanzen. I. Dielektrizitätskonstanten und Leitfähigkeiten der Mischkörper aus isotropen Substanzen, *Annalen der Physik*, Vol. 416, pp. 636–664.
47. Blackham, D. V., and R. D. Pollard. 1997. An Improved Technique for Permittivity Measurements Using a Coaxial Probe. *IEEE Transactions on Instrumentation and Measurement*, Vol. 46, pp. 1093–1099.
48. Lowell, S., and J. E. Shields. 1991. *Powder Surface Area and Porosity*, 3rd ed., Chapman & Hall, London, New York.
49. Lee, S. I., and Dan G. Zollinger. 2012. Estimating Volume Fraction of Free Water in Hardening Concrete by Interpretation of Dielectric Constant. *Journal of Materials in Civil Engineering*, Vol. 24, No. 2, pp. 159–67, [http://dx.doi.org/10.1061/\(ASCE\)MT.1943-5533.0000371](http://dx.doi.org/10.1061/(ASCE)MT.1943-5533.0000371).

APPENDIX T

Radar Specifications for Air-Coupled Ground-Penetrating Radar Antennae

These specifications are based on the ground-penetrating radar (GPR) reflection from a large metal plate. A typical metal plate reflection (MPR) is shown in the upper part of Figure T.1. The amplitude of reflection (i.e., volts) is measured from the maximum positive peak to the preceding negative. No filtering, averaging, or signal clean up, such as sky wave removal (and reflection subtraction), is allowed.

Performance specifications are as follows:

1. **Noise-to-Signal Ratio Test.** The antenna will be positioned at its recommended operating height (between 12 in. and 18 in.) above a minimum square foot (4 ft by 4 ft) metal plate. The radar unit shall be turned on and allowed to operate for a 15-min warm-up period. After warm up, the unit shall be operated at maximum pulse rate, and fifty (50) radar waveform pulses shall be recorded. The recorded waveforms shall then be evaluated for noise-to-signal ratio. The noise-to-signal ratio is described by the following equation:

$$\frac{\text{Noise Level } (A_n)}{\text{Signal Level } (A_{mp})} \leq 0.05 \text{ (5\%)}$$

The signal level, A_{mp} , is defined as the average metal plate reflection amplitude as measured from the peak to the preceding minimum. The noise level, A_n , is defined as the worst-case maximum amplitude occurring between 1 and 10 ns after the surface echo. The noise level is measured from any positive peak to either the preceding or trailing negative, whichever is greater. The noise-to-signal ratio shall be less than or equal to 0.05 (5%).

2. **Signal Stability Test.** The same test configuration shall be used as described in the noise-to-signal ratio test. Fifty (50) traces shall be recorded at the minimum data rate of 25 traces per second. The signal stability shall be evaluated using the following equation:

$$\frac{A_{\max} - A_{\min}}{A_{\text{AVG}}} \leq 0.01 \text{ (1\%)}$$

where A_{\max} is defined as the maximum amplitude for all 50 traces, A_{\min} is defined as the minimum amplitude for all 50 traces, and A_{AVG} is defined as the average trace amplitude of all 50 traces.

The signal stability test results for the GPR shall be less than or equal to 1%.

3. **Long-Term Signal Stability.** The same test configuration shall be used as described in the noise-to-signal ratio test. The radar shall be switched on with no warm up and allowed to operate for 2 hours continuously. At a minimum, a single waveform shall be captured every 2 min, 60 in total. The amplitude of reflection shall be calculated and plotted against time. To check for signal drift, the time at which the metal plate reflection occurs shall be captured and plotted against time. For the system to be performing adequately, the amplitude should remain constant after a short warm-up period, and the system should have little or no drift.

The stability criterion is as follows:

$$\frac{A_{\text{any}} - A_{20}}{A_{20}} \leq 0.03 \text{ (3\%)}$$

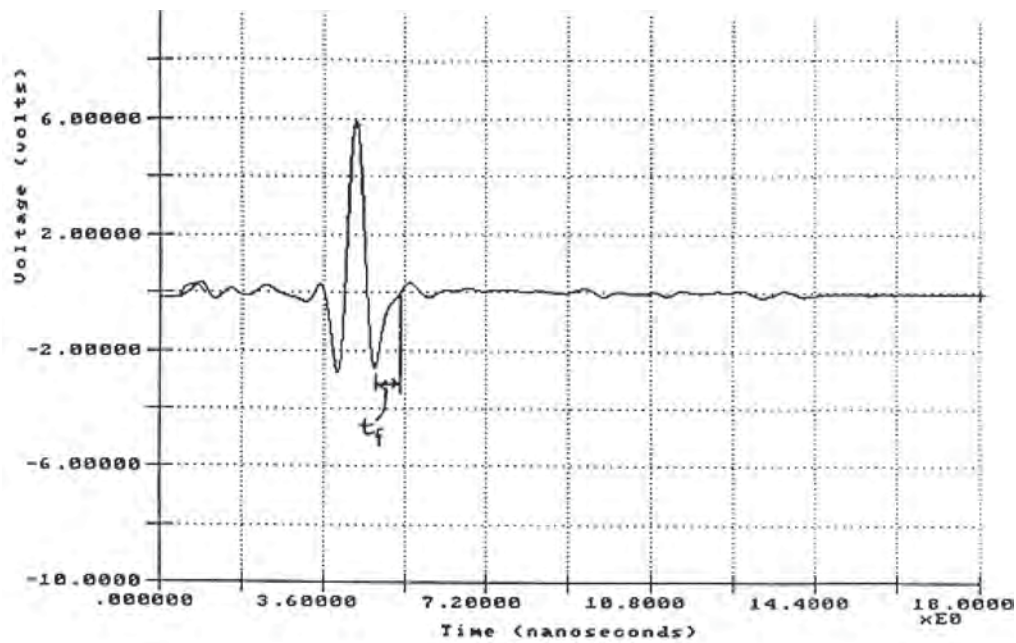
where A_{20} is the amplitude measured at 20 min, and A_{any} is any amplitude measured after 20 min.

The drift criterion is as follows:

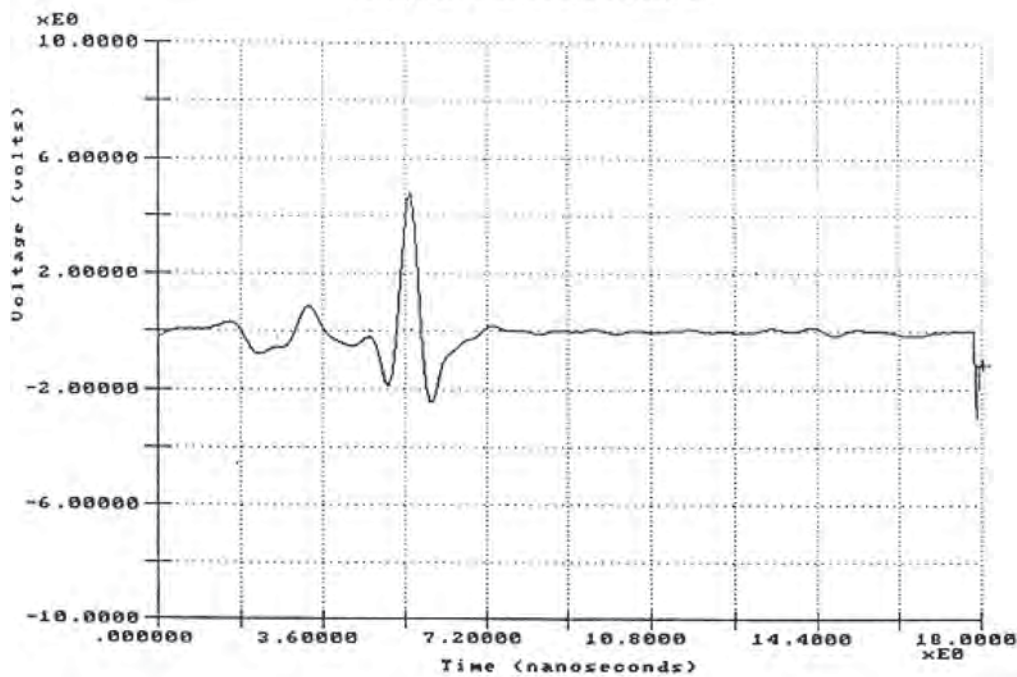
$$\frac{t_{\text{any}} - t_{20}}{t_{20}} \leq 0.05 \text{ (5\%)}$$

where t_{20} is the time when the peak metal plate reflection occurs at 20 min, and t_{any} is the time when the MPR occurs in any trace after 20 min.

4. **Variations in Time Calibration Factor.** The same test configuration shall be used as described in the noise-to-signal ratio test. Fifty (50) traces shall be collected, and the height of the antenna shall be measured. The test shall be repeated at two other heights. Typically, heights of approximately 12 in., 16 in., and 20 in. are used. The time delay from the



Acceptable Metal Plate Reflection



Unacceptable Metal Plate Reflection Fails Specification Tests 5 and 6.1

Figure T.1. Examples of acceptable and unacceptable metal plate reflections.

end reflection at the tip of the antenna to the metal plate reflection shall be measured for each trace, and their mean is time t_i (where the subscript represents height position at i). The difference between t_2 and t_1 represents the time to travel a fixed distance in air. For bistatic antennae, the travel distance must be calculated on the basis of the system geometry. The factor C_1 is calculated by dividing the distance by the time difference (e.g., in. per nanosecond). The factor C_2 represents the same between heights 2 and 3. The variation in time calibration factor is as shown below:

$$\frac{C_1 - C_2}{\text{Mean of } C_1 \text{ and } C_2} \leq 0.02 \text{ (2\%)}$$

The variation in time calibration factor shall be less than or equal to 2%.

5. End Reflection Test. The same test configuration and results from the noise-to-signal ratio test shall be used. The amplitude of the end reflection directly preceding the metal plate reflection shall be measured. This is a measure of the adequacy of system tuning. The size of the end reflection shall be

$$\frac{A_E}{A_{mp}} < 0.15 \text{ (15\%)}$$

where A_E is the mean of the amplitude of end reflection defined as any peak occurring from 1 ns to 5 ns before the metal plate reflection, and A_{mp} is the mean of the amplitude of reflection from the metal plate.

The end reflection in the metal plate test shall be less than 15% of the amplitude of the metal plate reflection.

6. Symmetry of Metal Plate Reflection. The same test configuration as used in the noise-to-signal ratio test shall be used. Two different criteria have been established for symmetry, as described below:

- 6.1. The first criterion is that the time from the maximum negative peak following the surface reflection to the

zero crossing point shall be measured. This time (t_f) is shown in Figure T.1. The required specification is

$$t_f \leq 0.7 \text{ ns}$$

An example of metal plate reflections that pass and fail this specification are shown in Figure T.1.

- 6.2. The second criterion is based on the symmetry of the legs of the metal plate reflection. The amplitude is measured from the positive peak to both the preceding and trailing negative. The specification is

$$A_{\min} / A_{\max} > 0.95 \text{ (95\%)}$$

where A_{\min} and A_{\max} are the minimum and maximum metal plate reflections measured using the preceding or trailing negatives. The ratio should be at least 95%.

7. Concrete Penetration Test. The antenna shall be placed at its recommended operating height above a 6-in.-thick concrete block. The concrete block shall be nonreinforced, have a minimum age of 28 days, and have a minimum 3,000 psi compressive strength. The block shall be 3 ft (36 in.) by 3 ft (36 in.) or greater to ensure that all the GPR energy enters the concrete. The concrete block shall be placed on top of a metal plate. Two hundred (200) traces shall be recorded. The reflection amplitude from the top and bottom of the concrete block shall be measured. The concrete penetration test is defined by the following equation:

$$\frac{A_{\text{bottom}}}{A_{\text{top}}} \geq 0.25 \text{ (25\%)}$$

where A_{top} is the mean of the measured return amplitude from the top of the concrete slab, and A_{bottom} is the mean of the measured return amplitude from the metal plate.

The concrete penetration test results for the GPR should be greater than or equal to 25%.

APPENDIX U

Portable Seismic Property Analyzer Slab Tests

Introduction

A survey of several concrete slabs constructed by the Texas A&M Transportation Institute (TTI) was carried out with a portable seismic property analyzer (PSPA) within the framework of the second Strategic Highway Research Program (SHRP 2) Renewal Project R06G. Eleven concrete slabs and 13 shotcrete slabs were involved in this study. The dimensions of the slabs and defects are more optimized toward the application of ground-penetrating radar (GPR). The concrete slabs were evaluated on November 9 and 10, 2011, and the shotcrete slabs were assessed on November 10 and 11, 2011. The scope of this University of Texas at El Paso study was to evaluate the performance of the PSPA in locating defects inside concrete.

The PSPA used in the study was developed primarily for testing pavement sections. As part of this study, the PSPA was modified to be more user-friendly for implementation in tunnels. A second set of tests were carried out on January 28 through 31, 2013, to test the viability of the new version on some of the slabs tested previously with the traditional PSPA.

Given the desire of SHRP 2 to develop user-friendly devices, the results presented here are as reported by the PSPA in the current state without further advanced analyses using an experienced expert analyst. The lessons learned are being incorporated in the new version of the PSPA under development.

Description of PSPA and Testing Methods

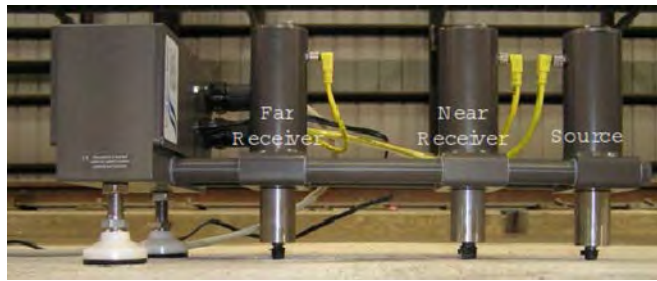
The PSPA is a portable device that can perform two simultaneous tests: impact echo (IE) and ultrasonic surface wave (USW). The traditional PSPA is a box containing a solenoid-type impact hammer and two high frequency accelerometers (Figure U.1a). All controls and data acquisition are in a computer connected to the box. The two receivers allow the calculation of the V_p using the USW method. The test at a single point

is simple and takes less than 30 s. The impact duration (contact time) is about 60 μ s and the data acquisition system has a sampling frequency of 390 kHz. The advantage of combining the two methods in a single device is that once the test is performed, the variations in the modulus (an indication of the quality of concrete) and return resonance frequency (an indication of the full thickness or depth of delamination) of a slab can be assessed concurrently.

As shown in Figure U.1b, the PSPA has been redesigned to make it more user-friendly and compact for tunnel work. The new PSPA is self-contained as it does not need an external personal computer to collect data. The waveforms collected in the field are stored in a removable flash memory. The new PSPA is also lighter compared with the traditional PSPA (8 lb versus 16 lb). Data collection with the new PSPA is a two-hand operation, which can accommodate the curvature within the tunnel more easily. Data acquisition with the new PSPA is on average two to three times faster than the traditional one. The new PSPA is also equipped with three receivers to better optimize the data collection for the combined IE/USW methods. The receivers are spaced at -3 in., 3 in., and 9 in. from the source. The power source for the device is six AAA batteries in a container that can be carried on the operator's belt.

Impact Echo Method

The IE method is one of the most commonly used non-destructive testing (NDT) methods in detecting delamination in concrete (Carino et al. 1986). This method is based on striking a plate-like object such as a tunnel lining with an impactor that generates stress waves at frequencies up to 20 kHz to 30 kHz and collecting signals with a receiver (Figure U.2a). By using a fast Fourier transform (FFT) algorithm, the recorded time domain signal is converted into a frequency domain function (amplitude spectrum), and the peak frequency is monitored. For an intact point on a slab or an intact portion of a slab, the thickness (h) is then determined



(a)



(b)

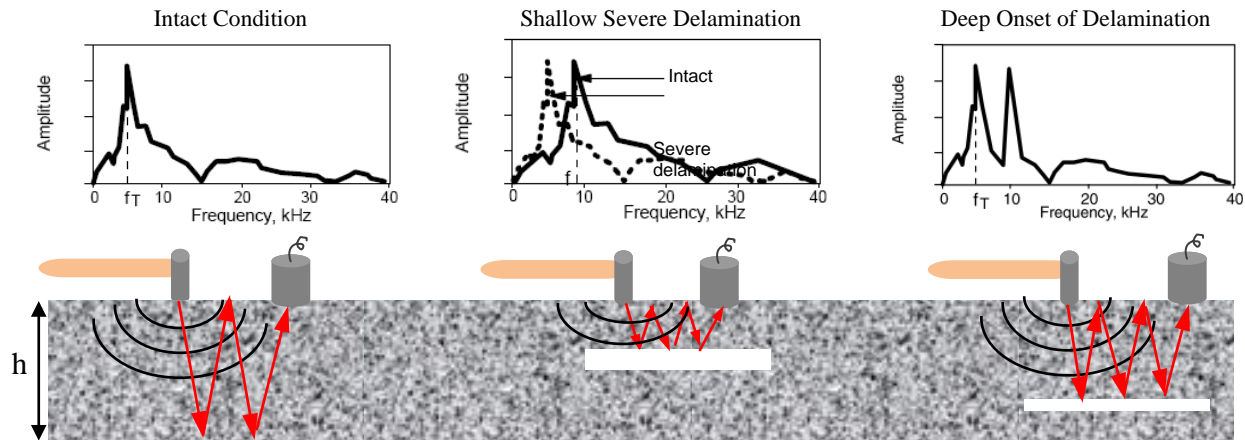
Figure U.1. Portable seismic property analyzer.

from the compression wave velocity (V_p) and the return frequency (f) as shown in Equation U.1:

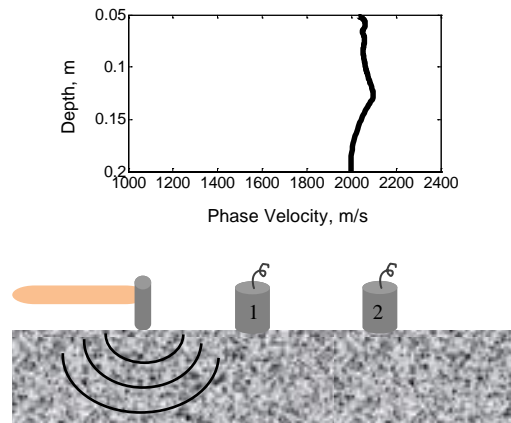
$$h = \alpha \frac{V_p}{2f} \quad (U.1)$$

where α is about 0.96 for concrete slabs.

For a deep and relatively small delaminated location in a concrete slab, the return frequency may shift to a higher frequency corresponding to the depth of the delamination. As shown in Figure U.2a, a shallow or a deep but extensive and severe delaminated area is usually manifested by a low peak frequency, indicating that little or no energy propagates toward



(a) IE method



(b) USW method

Source: Gucunski and Maher 1998.

Figure U.2. Schematic illustration of test methods.

the bottom of the deck and a flexural mode dominates the frequency response. In this case, Equation U.1 is not applicable to measure the depth of delamination because it is influenced by several factors.

Ultrasonic Surface Waves Method

The USW method is used to estimate the average velocity of propagation of surface waves in a medium on the basis of the time at which different types of energy arrive at each sensor (Figure U.2b). The velocity of propagation, V_R , is typically determined by dividing the distance between two receivers, ΔX , by the difference in the arrival time of a specific wave, Δt . Knowing the wave velocity, the modulus can be determined from shear modulus, G , through Poisson's ratio (ν) by using Equation U.2:

$$E = 2(1 + \nu)G \quad (\text{U.2})$$

Shear modulus can be determined from shear wave velocity, V_S , by using Equation U.3:

$$G = \frac{\gamma}{g} V_S^2 \quad (\text{U.3})$$

The modulus from surface wave velocity, V_R , first converted to shear wave velocity can be determined by Equation U.4:

$$V_S = V_R(1.13 - 0.16\nu) \quad (\text{U.4})$$

In the USW method, the variation in velocity with wavelength is measured to generate a so-called dispersion curve. For a uniform or intact concrete slab, the dispersion curve shows more or less a constant velocity within the wavelengths not greater than the thickness of the slab. When a delamination or void is present in a concrete slab or the concrete has deteriorated, the average surface wave velocity (or modulus) becomes less than the actual one because of interference caused by the defect. In this case, the velocity or modulus obtained may be called an apparent velocity or modulus.

Description of Slabs

An overall view of the test slabs is shown in Figure U.3, and their characteristics are summarized in Table U.1. Two sets of slabs were tested in this study. Each slab was 6 ft by 6 ft. The first set of specimens included six intact concrete slabs with thicknesses of 12 in., 15 in., 18 in., and 24 in., and three defective 15-in.-thick slabs with embedded 1-ft by 1-ft delaminated zones in the center of the slabs. The last three slabs contained defects at depths of 1 in., 2 in., and 3 in. from the top surface. Two other concrete



Figure U.3. Overall view of TTI slabs.

slabs in this set were 15 in. thick with embedded air voids and water voids at a depth of 8 in.

The second set of slabs was shotcrete slabs that included four intact slabs with thicknesses of 4 in., 6 in., 8 in., and 12 in. and five 12-in.-thick delaminated slabs. The 1-ft by 1-ft delaminated areas were embedded at the center of each slab at depths of 1 in., 2 in., 3 in., 4 in., and 8 in. from the top surface. Four other shotcrete slabs contained air voids and water voids with different sizes at different depths.

Data Collection Process

The testing schemes of different slabs are shown in Figure U.4. Every intact slab was assessed through 11 testing lines equally spaced at 4-in. intervals. On each line, 11 points were tested at every 4 in. Therefore, 121 data points were collected for each intact slab (Figure U.4a). A similar scheme was used for the defective slabs except that data were collected at 143 points, as shown in Figure U.4b. Each test slab took about 1 h to test and about 30 min to interpret and develop the contour maps.

All slabs were investigated using the traditional PSPA in 2011. At each point, the PSPA source was placed on the grid point. The near and far receiver spacing from the source were 4 in. and 10 in., respectively. For reporting the USW results, the coordinate was shifted 7 in. (half the distance between the two receivers and the source). For the IE results, the coordinate was shifted 2 in. (half the distance between the source and Receiver 1). Some of the slabs, as indicated in Table U.1, were assessed again in 2013 with the new PSPA. Similarly, the PSPA source was placed on the test point. Based on the source and receivers spacing, the coordinate was shifted 6 in. for reporting USW results and 1.5 in. for IE results.

Table U.1. Characteristics of TTI Slabs

Slab Information		Thickness (in.)	Type of Defect	Size of Defect (ft by ft)	Depth of Defect (in.)	Tested with Traditional PSPA (2011)	Tested with New PSPA (2013)
Concrete	Slab 1	12	Intact	NA	NA	Yes	Yes
	Slab 2	18	Intact	NA	NA	Yes	Yes
	Slab 3	12	Intact	NA	NA	Yes	Yes
	Slab 4	24	Intact	NA	NA	Yes	Yes
	Slab 5	24	Intact	NA	NA	Yes	No
	Slab 6	15	Intact	NA	NA	Yes	Yes
	Slab 7	15	Delamination	12 by 12	2	Yes	Yes
	Slab 8	15	Delamination	12 by 12	3	Yes	Yes
	Slab 9	15	Delamination	12 by 12	1	Yes	No
	Slab 10	15	Air void	12 by 12	8	Yes	Yes
	Slab 11	15	Water void	12 by 12	8	Yes	Yes
Shotcrete	Slab 1	4	Intact	NA	NA	Yes	No
	Slab 2	6	Intact	NA	NA	Yes	Yes
	Slab 3	8	Intact	NA	NA	Yes	Yes
	Slab 4	12	Air void	12 $\frac{1}{8}$ by 9 $\frac{3}{4}$, 17 $\frac{1}{4}$ by 14 $\frac{3}{4}$ ^a	7.5	Yes	No
	Slab 5	12	Water void	11 by 10 $\frac{1}{2}$, 15 $\frac{3}{4}$ by 14 $\frac{1}{2}$ ^a	7.5	Yes	No
	Slab 6	12	Air void	12 $\frac{1}{4}$ by 12, 14 $\frac{3}{4}$ by 17 $\frac{1}{8}$ ^a	3	Yes	Yes
	Slab 7	12	Water void	10 $\frac{1}{2}$ by 10 $\frac{1}{2}$, 15 $\frac{1}{2}$ by 14 $\frac{1}{4}$ ^a	3	Yes	No
	Slab 8	12	Delamination	12 by 12	8	Yes	Yes
	Slab 9	12	Delamination	12 by 12	4	Yes	Yes
	Slab 10	12	Delamination	12 by 12	3	Yes	No
	Slab 11	12	Delamination	12 by 12	2	Yes	Yes
	Slab 12	12	Delamination	12 by 12	1	Yes	No
	Slab 13	12	Intact	NA	NA	Yes	Yes

Note: NA = not available.

^aThe first set of numbers indicates the void, and the second set indicates the bag that encapsulates the void.

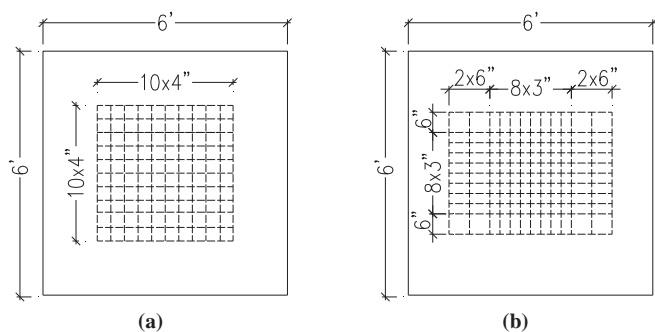


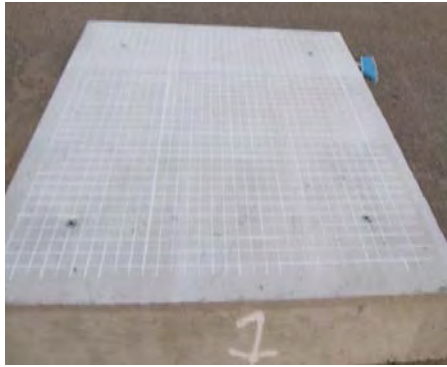
Figure U.4. Testing schemes of different slabs.

Test Results

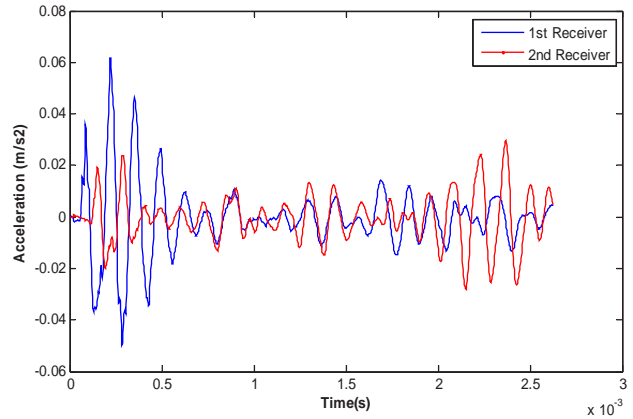
The USW and IE results from different concrete and shotcrete slabs are presented and compared in this section. A detailed description of the data reduction process was provided in a companion report related to testing in actual tunnels in Colorado and Virginia (see Appendix P). As such, they are not repeated here.

Intact Concrete Slabs

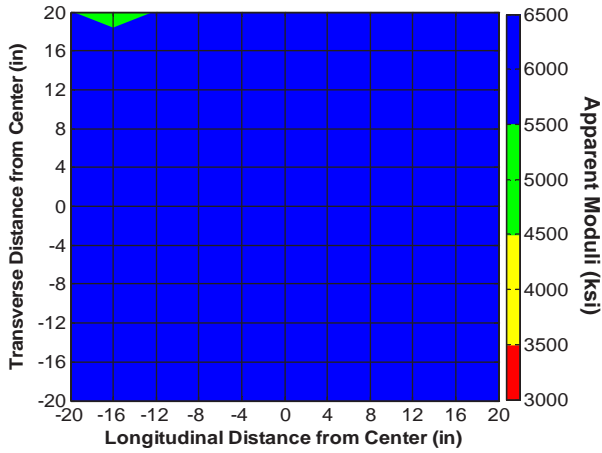
Figure U.5 contains the traditional PSPA results from Slab 1. Figure U.5a is a picture of the slab on the day of testing. The slab was visually uniform with a smooth finish. The acquired waveforms from the two PSPA receivers at the center point of the slabs are shown in Figure U.5b. Because of the size of the



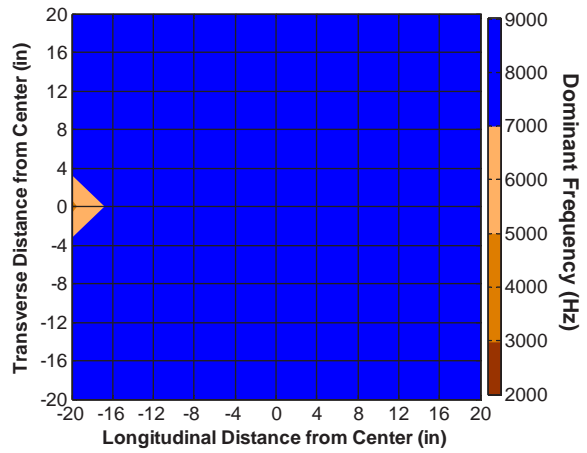
(a) Slab 1



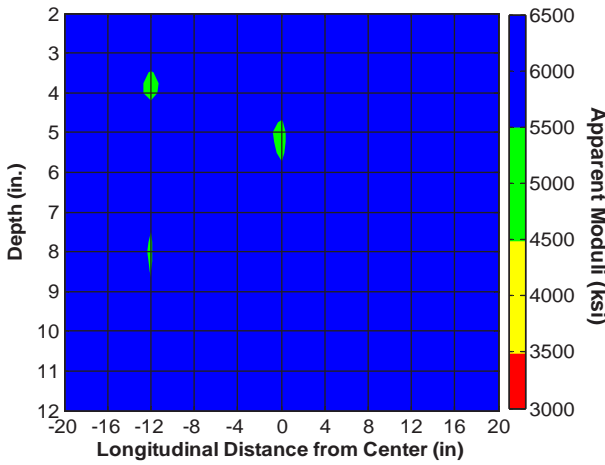
(b) Waveform obtained from PSPA at center point



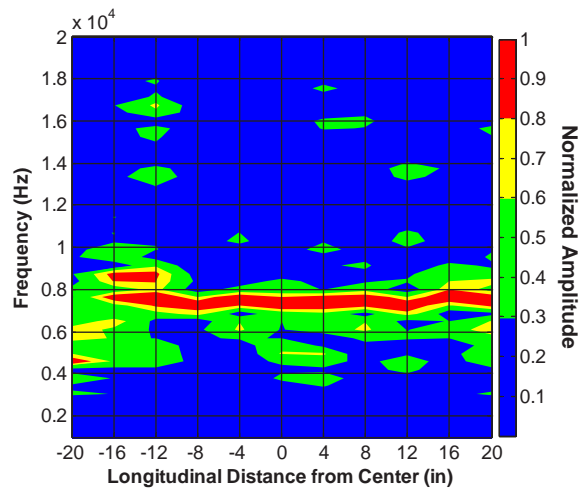
(c) Average modulus from USW



(d) Dominant frequency from IE



(e) USW B-Scan along centerline



(f) IE Spectral B-Scan along centerline

Figure U.5. Contour maps of acquired results from traditional PSPA for concrete Slab 1 (12-in.-thick intact slab).

specimens, reflections from the vertical boundaries are apparent in the later portions of the signals. The PSPA software contains appropriate filters to minimize the effect of these reflections as long as the PSPA is located an adequate distance from the boundary.

Because the IE and USW methods used in this study are point inspection methods, contour maps are more useful for visualizing the results than individual evaluations. The contour map of the variations in the average modulus (from a depth of 2 in. to nominal thickness of the slab) from the USW tests is shown in Figure U.5c. The slab exhibited a fairly uniform modulus. The mean average modulus of the slab was 6,400 ksi with a standard deviation of about 375 ksi. Similarly, the contour map of the dominant return frequency from the IE method, as shown in Figure U.5d, was also uniform. In addition to the planar contour maps, the USW and IE line scans (B-scans) along the centerline are also shown in Figure U.5. The USW B-scan (Figure U.5e) is in the form of variation in modulus with wavelength, which can qualitatively be viewed as a scaled variation of modulus with depth. In this case, the variation in modulus with depth is small. The spectral B-scan of the IE results (Figure U.5f) is in the form of variation of normalized amplitude with frequency. Throughout the width of the slab, a frequency of about 7.7 kHz (manifested as a red band) corresponds to the 12-in. thickness of the slab. The thickness reported from IE tests was 11.9 in. with a standard deviation of 0.8 in.

Figure U.6 shows the same results from the new PSPA on Slab 1. Unlike in 2011, the slab contained some micro cracks. Figure U.6a again shows the slab on test day. The time records from the new PSPA are similar or slightly higher quality than those from the traditional PSPA (Figure U.6b). The planar contour maps of the variations in the average modulus from the USW method and the dominant return frequency from the IE method are shown in Figures U.6c and U.6d, respectively. The mean average modulus of the slab was 4,590 ksi with a standard deviation of about 560 ksi. The average modulus from 2011 is greater than that from 2013. Aside from material degradation manifested as micro cracks, the reasons for such differences are under investigation. The higher standard deviation can be attributed to the new micro cracks observed in the slab. The average dominant return frequency is around 7.3 kHz through the entire slab, which is similar to the dominant frequency observed in 2011. A minor defect in the slab manifested in the IE planar contour map in Figure U.5d between -2 in. and $+2$ in. of the centerline manifests itself more prominently in the USW and IE B-scans of Figures U.6e and U.6f, respectively.

Slab 2 was an 18-in.-thick intact slab and contained two cracks. Figure U.7 compares the severity of the cracks in two years of testing. Compared with 2011, the cracks had progressed significantly by 2013. The traditional and new PSPA results from Slab 2 are shown in Figures U.8 and U.9, respectively. The interaction between the cracks and seismic wave

propagation is rather complex. When the source–receiver array is parallel to the crack, the USW modulus variation and the IE response spectrum are marginally affected in the current software. When the crack is between the source and the first receiver, the USW modulus is typically greater than normal because of the travel path of the wave. Similarly, when the crack is between the two sensors, the reported USW modulus is lower than normal. To maintain the regularity of the testing program, we chose to carry out the tests on a rigid grid and not adjust the location of the sensors to avoid the cracks. As reflected in Figure U.8c, the PSPA sensors crossed the cracks at only a few points. For example, at a coordinate of -4 in. in Figure U.8e, the crack is propagating deep within the slab. The mean of the obtained average modulus with the traditional PSPA of this slab was about 5,980 ksi with a standard deviation of about 533 ksi. The IE thickness was about 16.3 in.; but as shown in Figure U.8f, the return frequency was very consistent, and with one core, the thickness could be readily calibrated to the actual thickness.

The mean average modulus from the new PSPA (Figure U.9a) is around 5,130 ksi with a standard deviation of about 586 ksi. The dominant frequency peak is uniform in Figure U.9b. The average dominant frequency is around 4.9 kHz; therefore, the slab thickness estimates were similar to the previous results.

Slab 3 (Figure U.10) was supposed to be similar to Slab 1. The average modulus was about 5,997 ksi with a standard deviation of about 750 ksi. The average thickness was about 11.4 in. Slab 3 was placed on a steel plate with a 1-ft by 1-ft hole in 2012 (Figure U.11a). The objective was to identify the NDT methods that could detect the hole. The USW and IE results in Figures U.11b and U.11c demonstrate an intact slab, and the hole in the steel plate could not be detected as anticipated. The mean average modulus of 5,500 ksi with a standard deviation of 622 ksi was obtained. The average IE dominant frequency of around 7.6 kHz is quite similar to those measured by the traditional PSPA.

Slabs 4 and 5 were each 24-in. thick. The IE method as configured in the traditional PSPA cannot detect thickness in excess of 18 in. Thus, detection of slab thickness was not possible for these two slabs, as reflected in Figures U.12 and U.13. However, the quality of the concrete, except in isolated points, was high with mean average moduli of 5,900 ksi. Slab 4 was also tested with the new PSPA and the results are shown in Figure U.14. The mean average modulus dropped to 4,560 ksi. Similar to the traditional PSPA, with the source–receiver configuration of the new PSPA the detection of the bottom of the slab was not feasible.

Finally, with the traditional PSPA, the 15-in.-thick intact slab 6 yielded an average modulus of 6,220 ksi (Figure U.15c) with a thickness of 14.2 in. (Figure U.15). The new PSPA gave an average modulus of 5,230 ksi for Slab 6 (Figure U.16a). The average dominant frequency measured with the new

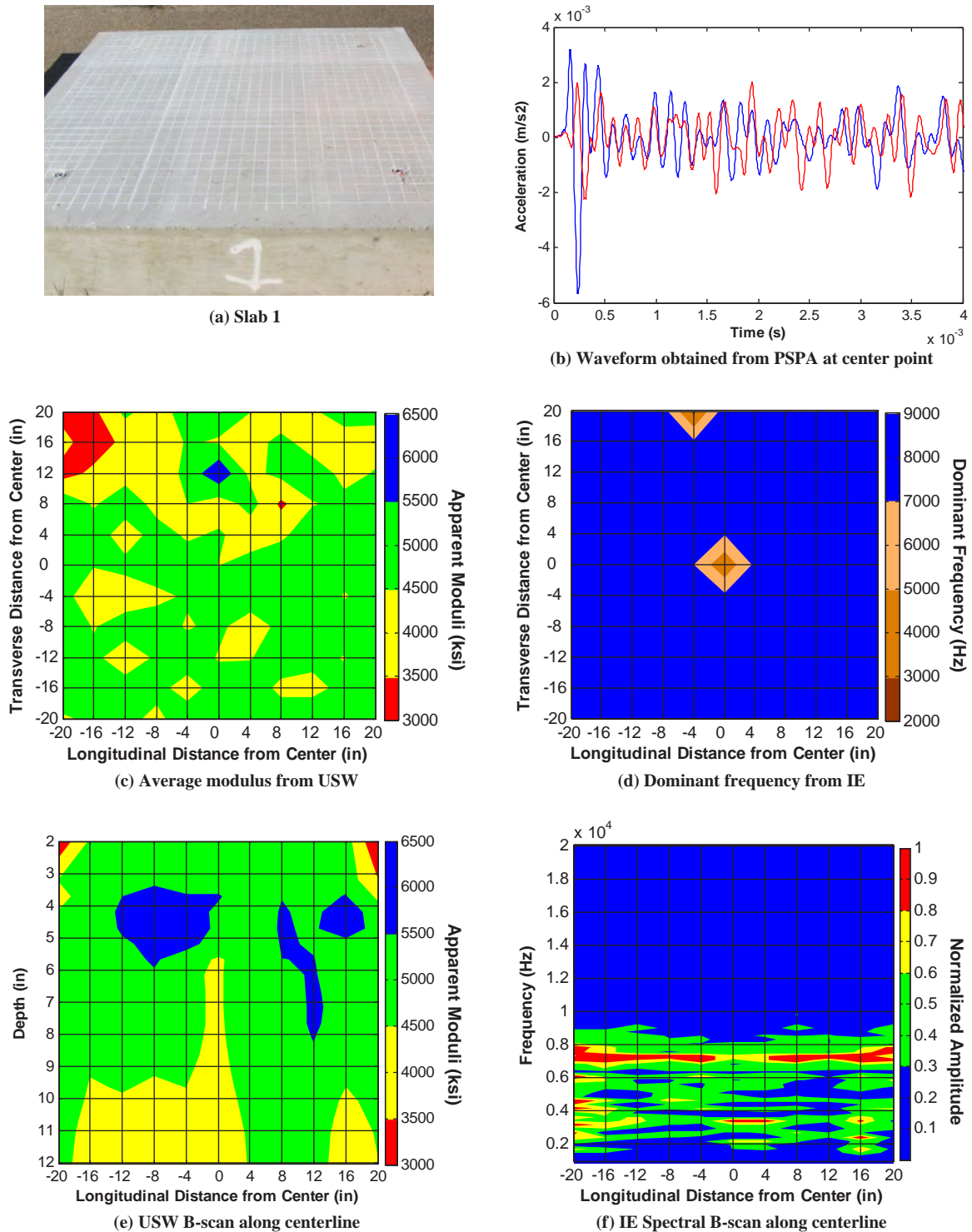
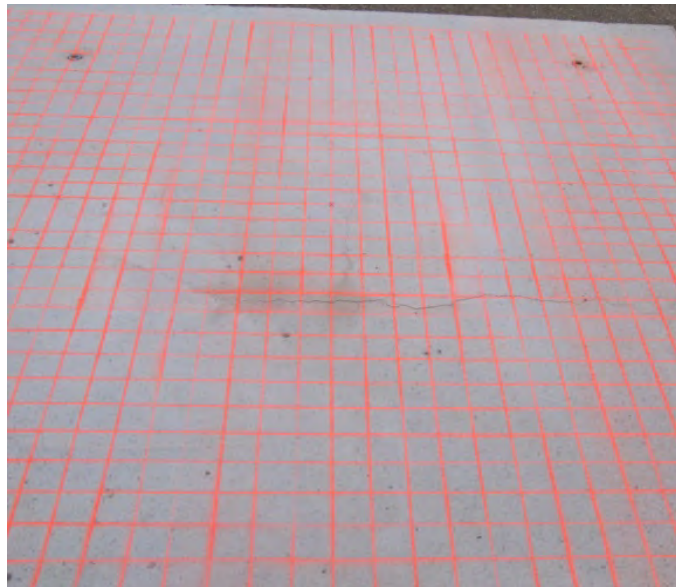


Figure U.6. Contour maps of acquired results from new PSPA for concrete Slab 1 (12-in.-thick intact slab).



(a) Slab view in 2011



(b) Slab view in 2013

Figure U.7. Crack progression on Slab 2 in a two-year period: (a) in 2011 and (b) in 2013.

PSPA was close to that measured with the traditional PSPA (Figure U.16b).

Delaminated Concrete Slabs

Slab 7 (Figure U.17a) was similar to Slab 6, with a delamination embedded at a depth of 2 in. from the top surface. A comparison of the time records in Figures U.15b and U.17b clearly demonstrates the differences in the time records from an intact area and a delaminated area. With a few days of experience, the operator can readily detect the delamination by simply looking at the time signals. The delaminated area is clearly detectable in both the USW and IE results from the traditional PSPA in Figures U.17c through U.17f. The USW and IE results acquired with the new PSPA (Figure U.18) provide similar delamination maps. However, the IE results from the new PSPA in Figure U.18b provide a clearer indication of the delaminated area.

The same statements can be made for the traditional PSPA results from Slab 8 (Figure U.19) with delaminated zones at nominal depths of 3 in. By comparing the amplitudes of the waveforms in Figures U.17b and U.19b, one can roughly estimate that the delamination in Slab 7 is shallower than the one in Slab 8. The delamination in Slab 8 is readily approximated in both the USW results and IE results from the traditional PSPA in Figures U.19c and U.19d. Slab 8 was also investigated with the new PSPA. Similar to the traditional PSPA results, the new PSPA is able to detect the delamination through USW and IE contour maps (Figure U.20).

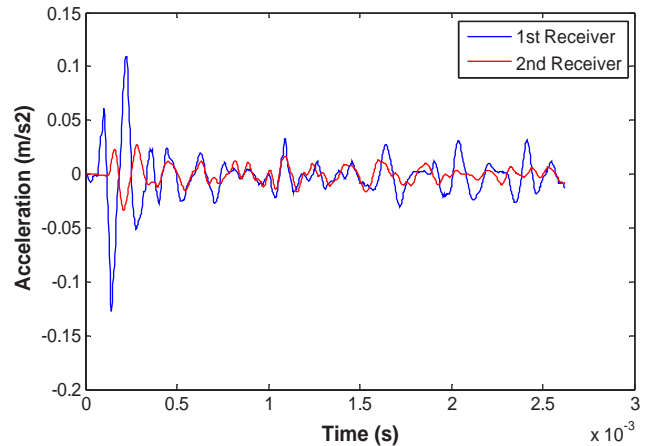
In the design of the PSPA, the assumption has been that a 1-in.-deep delamination can be readily detected by tapping, and a device may not be needed during field testing. Slab 9 (Figure U.21a) was only tested by the traditional PSPA. One unexpected result was observed: the presence of the 1-in.-deep delamination was obvious from the amplitude of time records in Figure U.21b and the USW results in Figure U.21c but was not reflected in the IE interpretation in Figure U.21d. This simply occurred because of the high-pass filters applied to the IE results. The vibration frequency was so low that it was eliminated from the signal.

Concrete Slabs with Voids

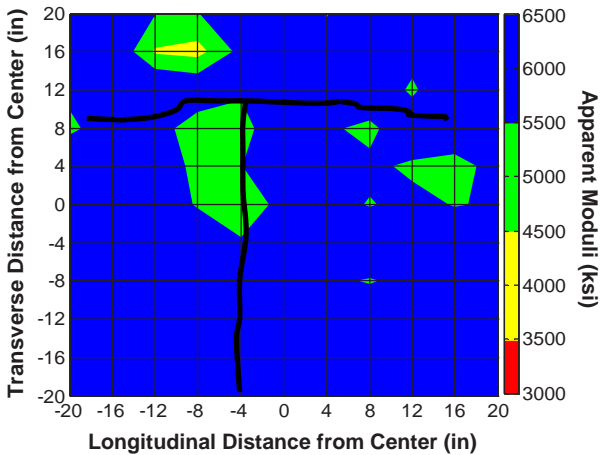
Slabs 10 and 11 (Figures U.22 through U.26) contained voids at a depth of 8 in. from the surface of the specimens. As reflected in Figure U.22, slab 10 contained several surficial cracks. Comparing Figures U.22a and U.22b, these cracks progressed between 2011 and 2013. The cracks are reflected in the USW results from the traditional and new PSPAs (Figures U.23c and U.24a). The progression of the vertical crack during the 2-year period can be observed in the USW map in



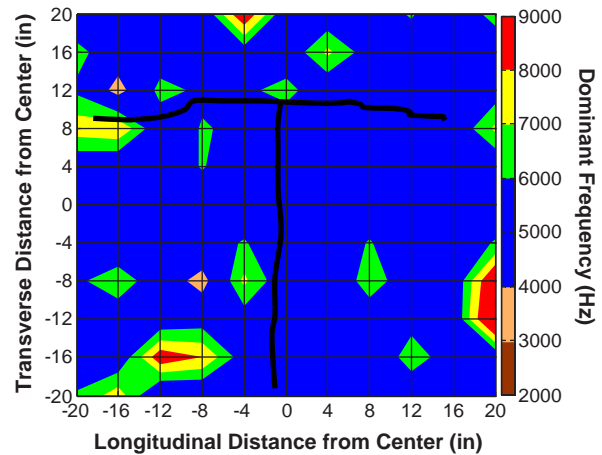
(a) Slab 2



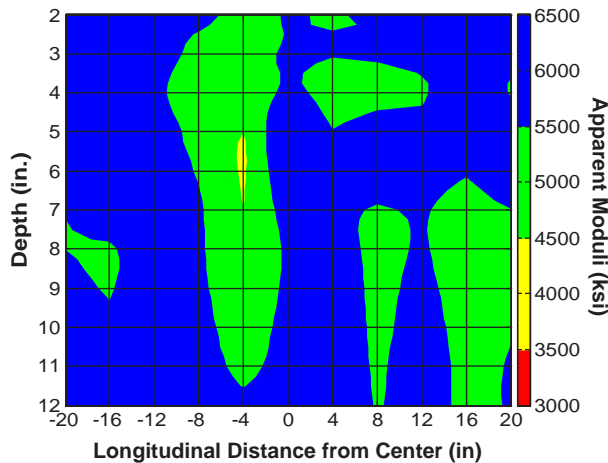
(b) Waveform obtained from PSPA at center point



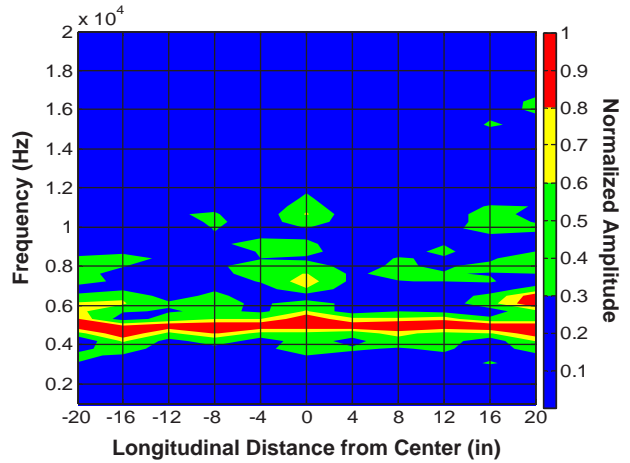
(c) Average modulus from USW



(d) Dominant frequency from IE



(e) USW B-scan along centerline



(f) IE Spectral B-scan along centerline

Figure U.8. Contour maps of acquired results from traditional PSPA for concrete Slab 2 (18-in.-thick intact slab).

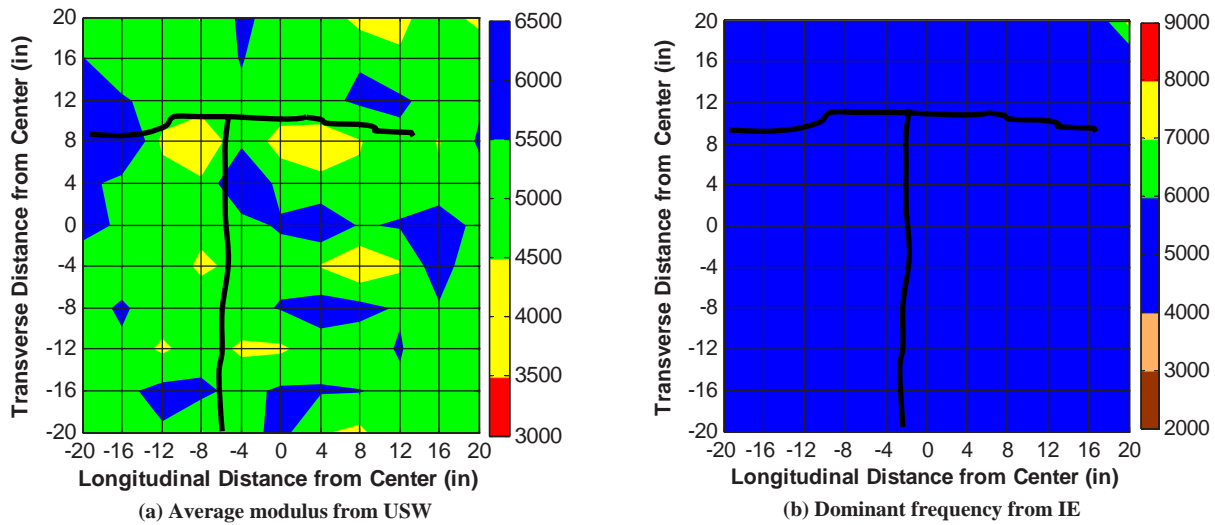
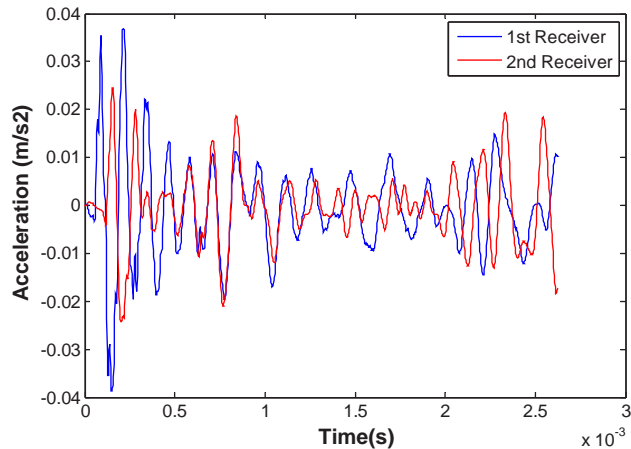


Figure U.9. Contour maps of acquired results from new PSPA for concrete Slab 2 (18-in.-thick intact slab).



(a) Slab 3



(b) Waveform obtained from PSPA at center point

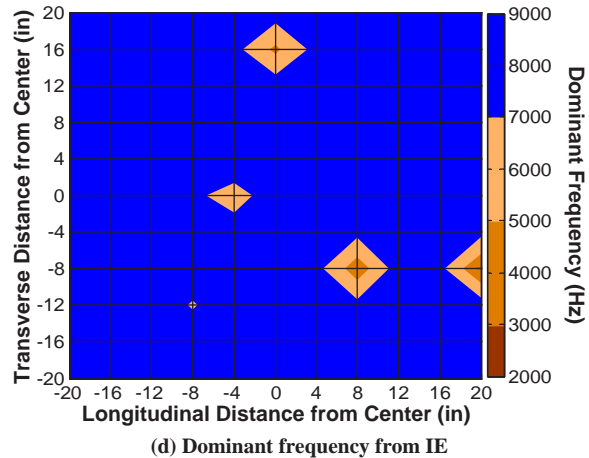
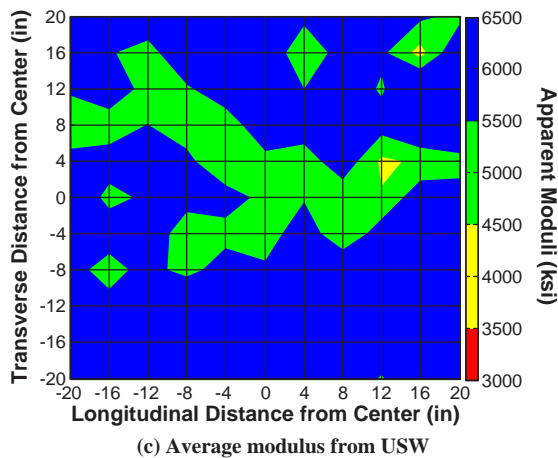


Figure U.10. Contour maps of acquired results from traditional PSPA for concrete Slab 3 (12-in.-thick intact slab). (Continued on next page.)

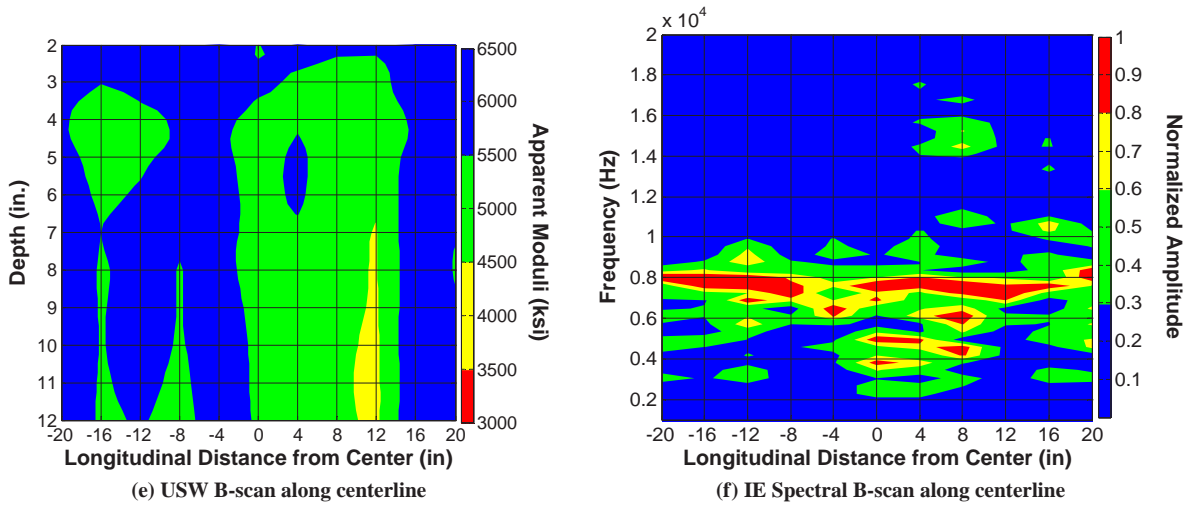


Figure U.10. (Continued.)



(a) Slab 3 on steel plate

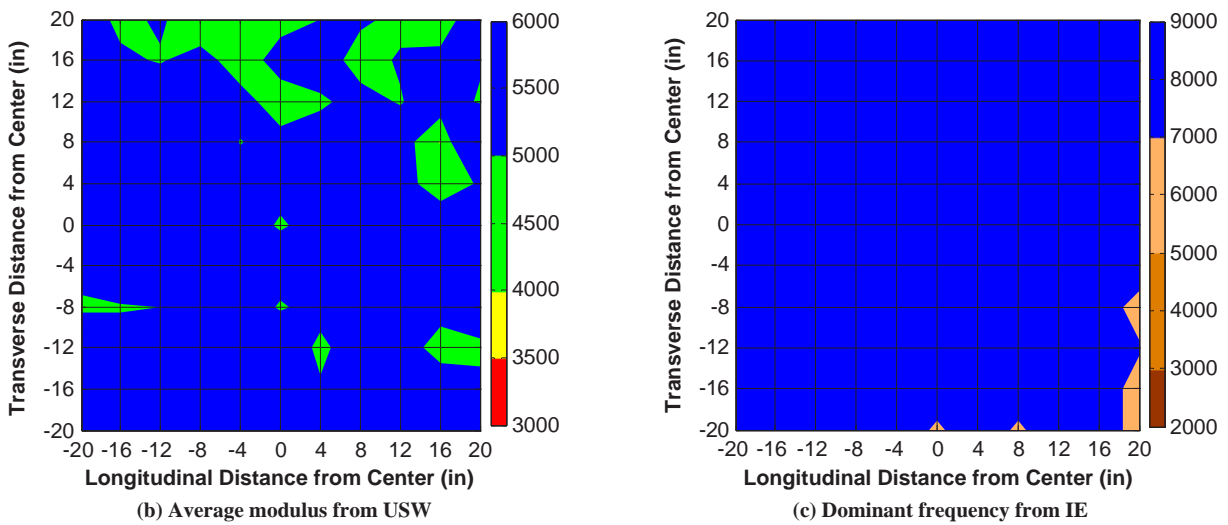
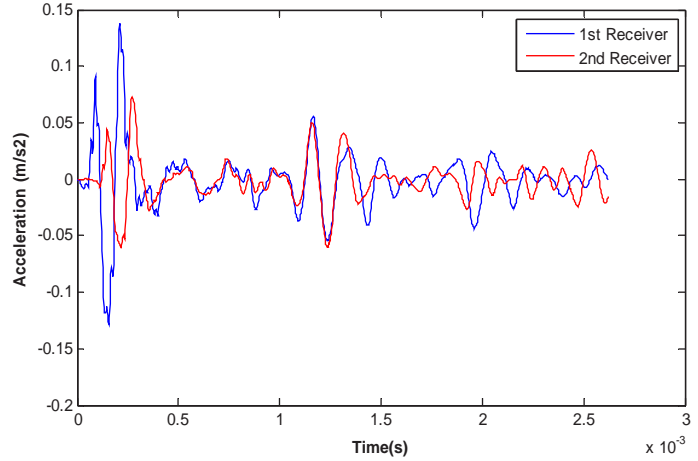


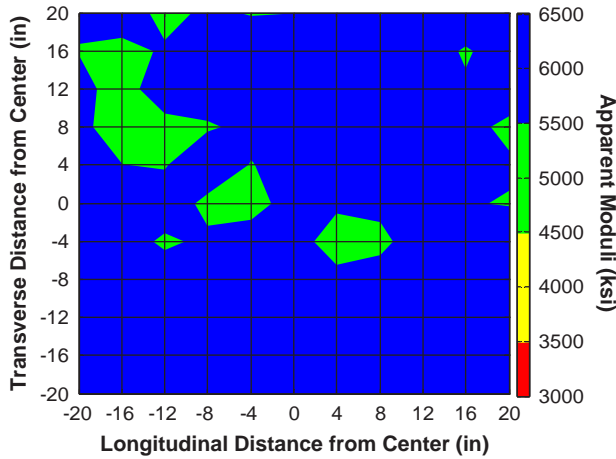
Figure U.11. Contour maps of acquired results from new PSPA for concrete Slab 3 (12-in.-thick intact slab).



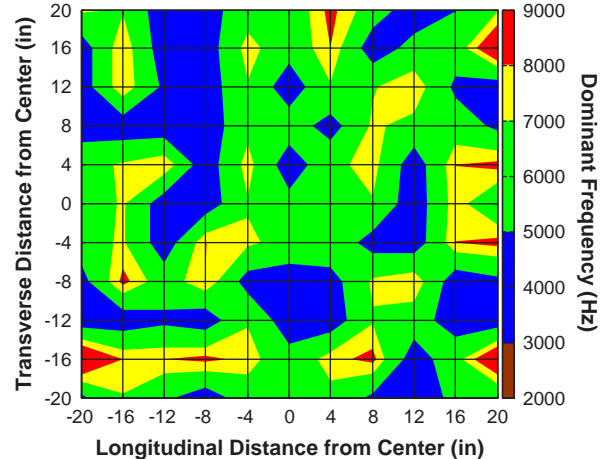
(a) Slab 4



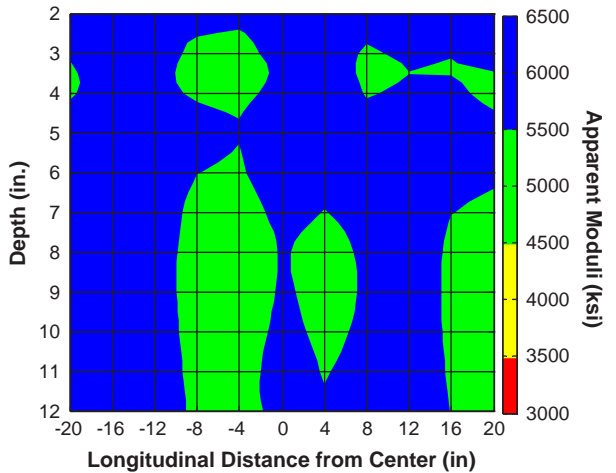
(b) Waveform obtained from PSPA at center point



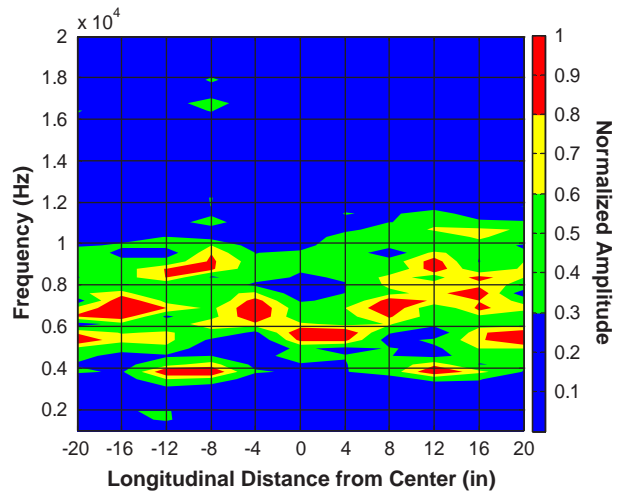
(c) Average modulus from USW



(d) Dominant frequency from IE



(e) USW B-scan along centerline

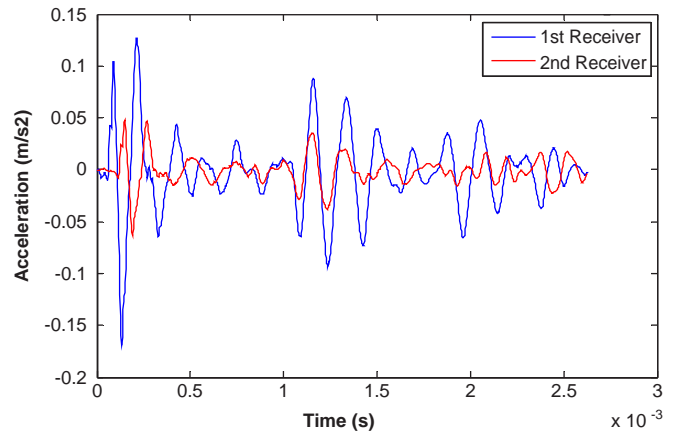


(f) IE Spectral B-scan along centerline

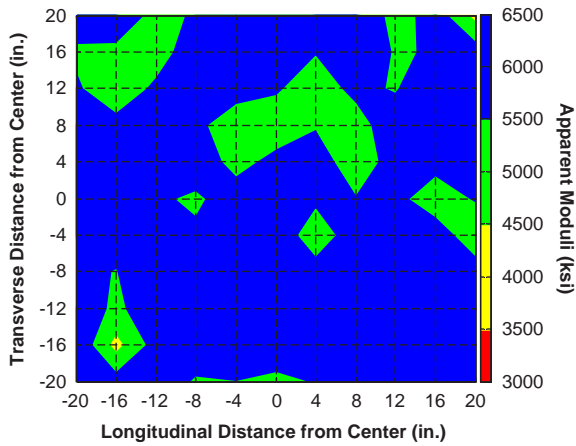
Figure U.12. Contour maps of acquired results from traditional PSPA for concrete Slab 4 (24-in.-thick intact slab).



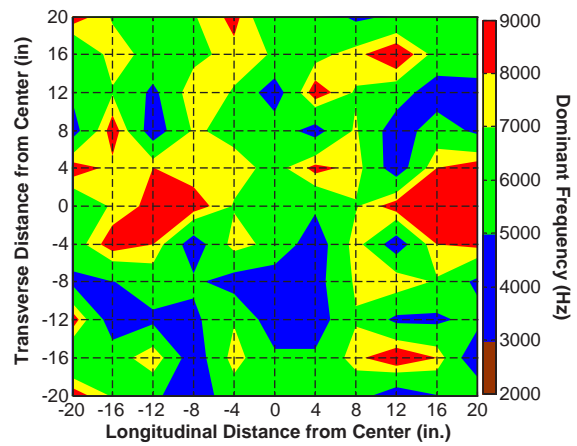
(a) Slab 5



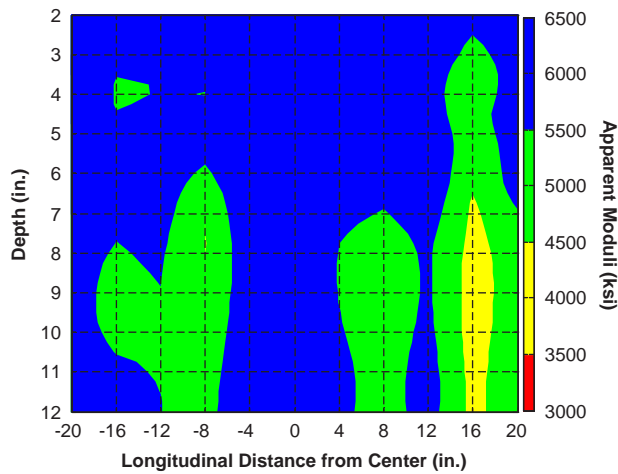
(b) Waveform obtained from PSPA at center point



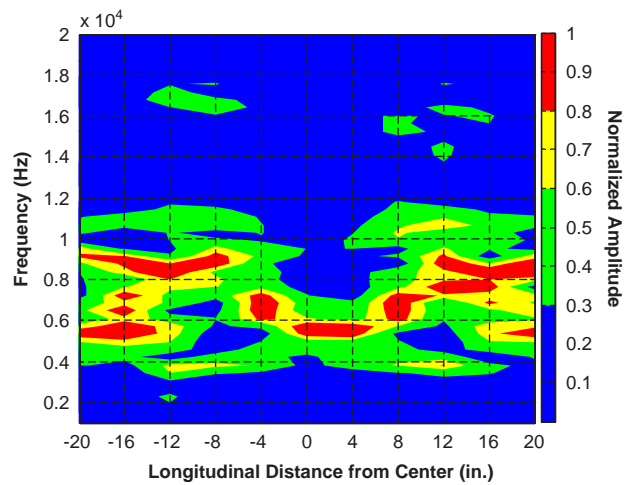
(c) Average modulus from USW



(d) Dominant frequency from IE



(e) USW B-scan along centerline



(f) IE Spectral B-scan along centerline

Figure U.13. Contour maps of acquired results from traditional PSPA for concrete Slab 5 (24-in.-thick intact slab).

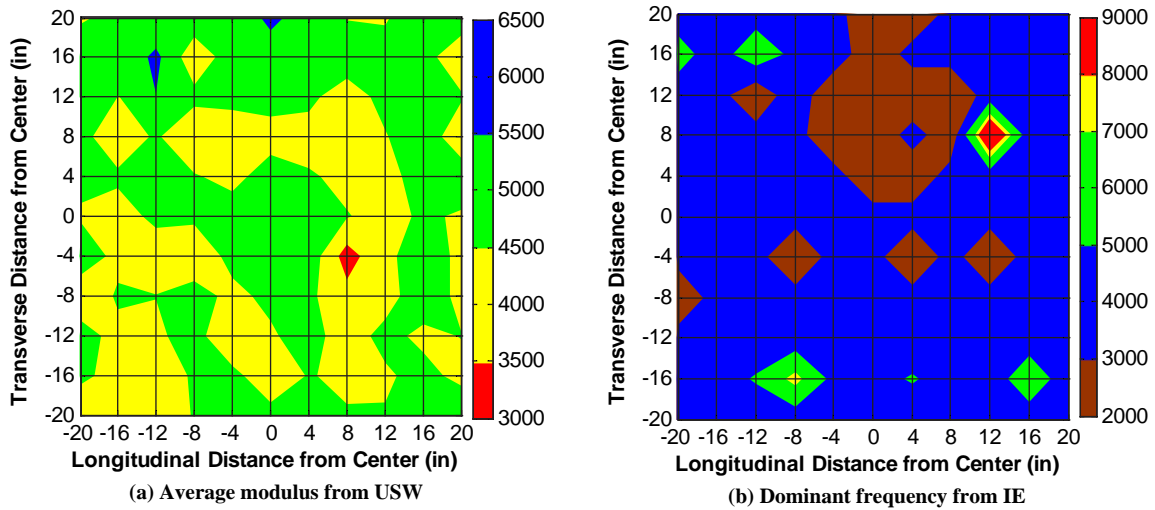
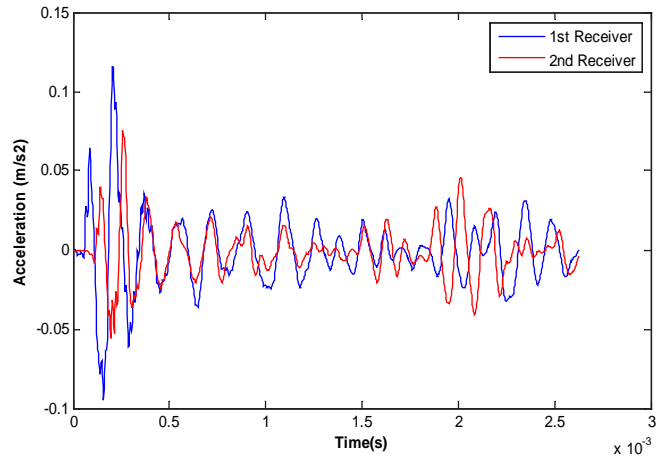


Figure U.14. Contour maps of acquired results from new PSPA for concrete Slab 4 (24-in.-thick intact slab).



(a) Slab 6



(b) Waveform obtained from PSPA at center point

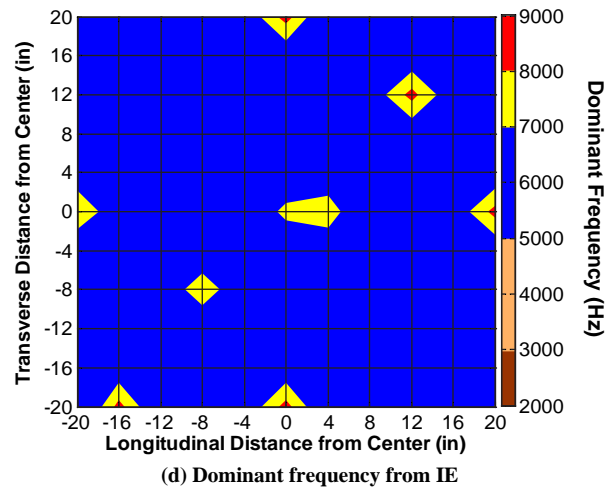
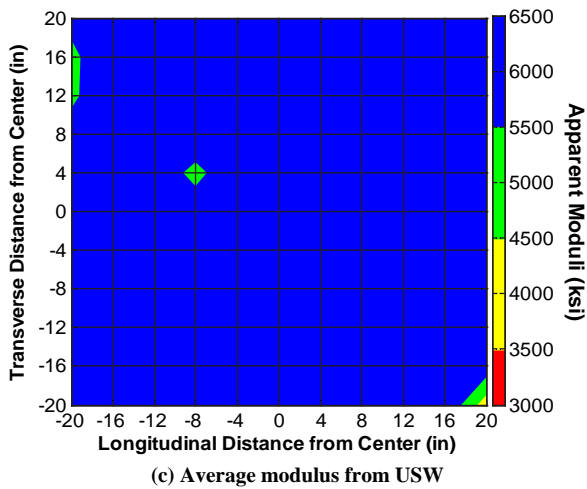


Figure U.15. Contour maps of acquired results from traditional PSPA for concrete Slab 6 (15-in.-thick intact slab). (Continued on next page.)

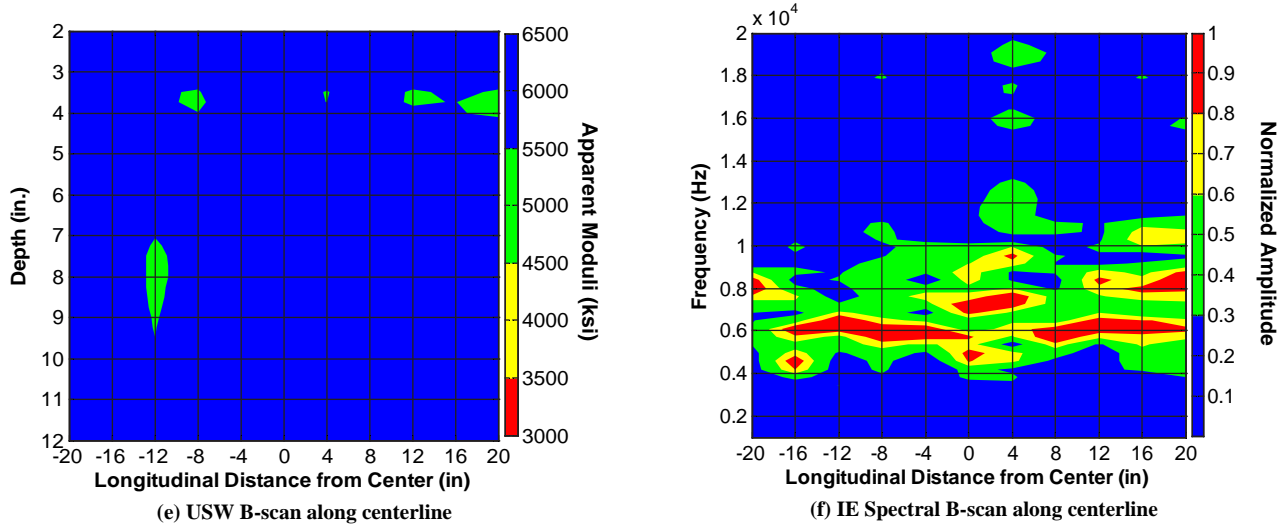


Figure U.15. (Continued.)

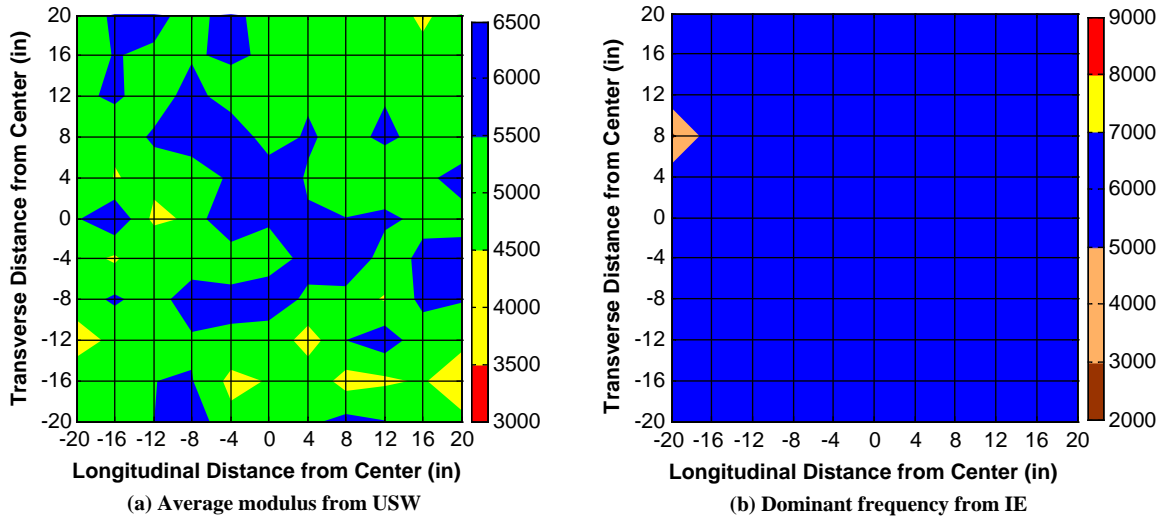
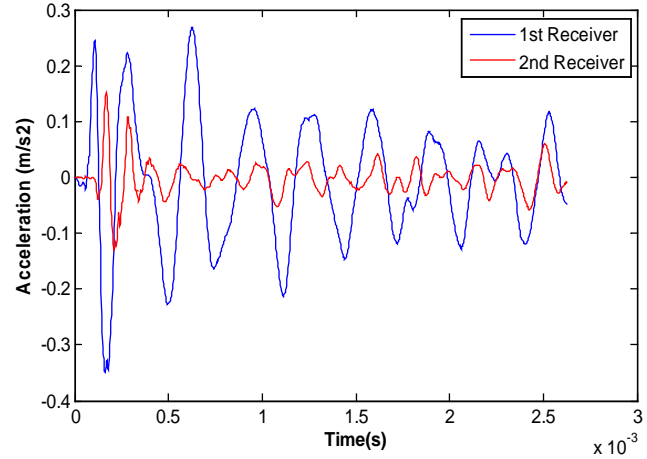


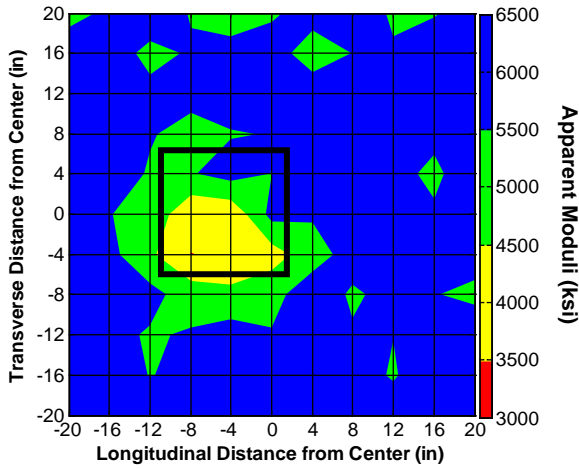
Figure U.16. Contour maps of acquired results from new PSPA for concrete Slab 6 (15-in.-thick intact slab).



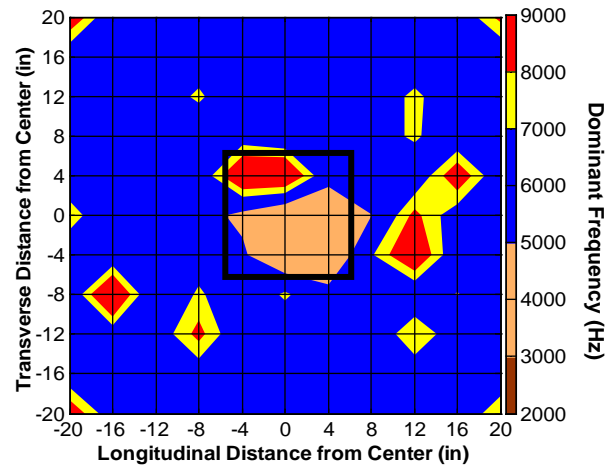
(a) Slab 7



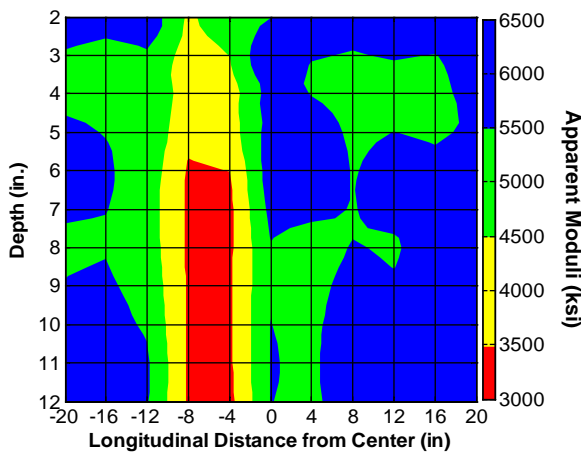
(b) Waveform obtained from PSPA at center point



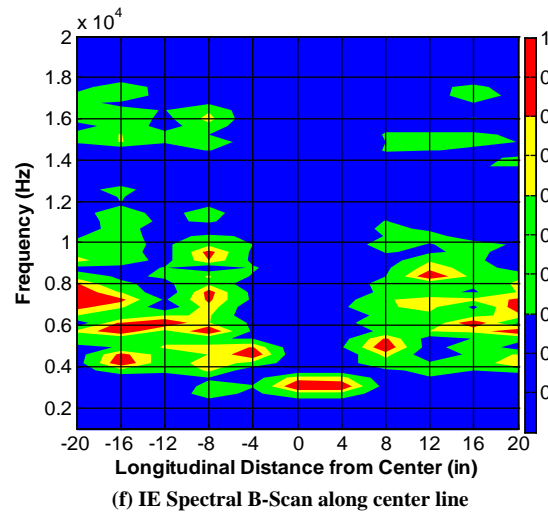
(c) Average modulus from USW



(d) Dominant frequency from IE



(e) USW B-Scan along center line



(f) IE Spectral B-Scan along center line

Figure U.17. Contour maps of acquired results from traditional PSPA for concrete Slab 7 (15 in. thick, delaminated at 2 in.).

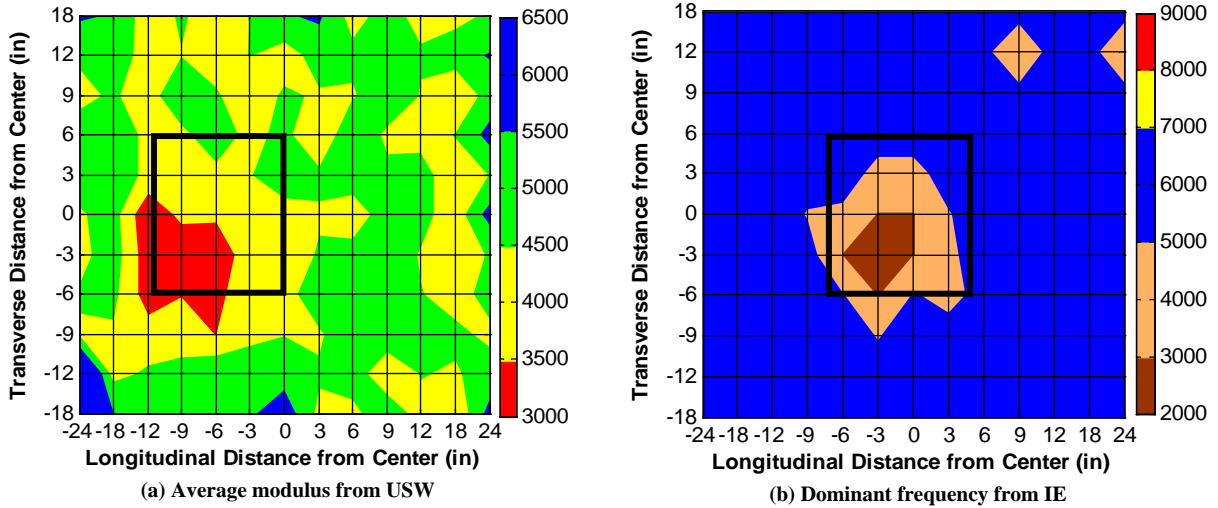
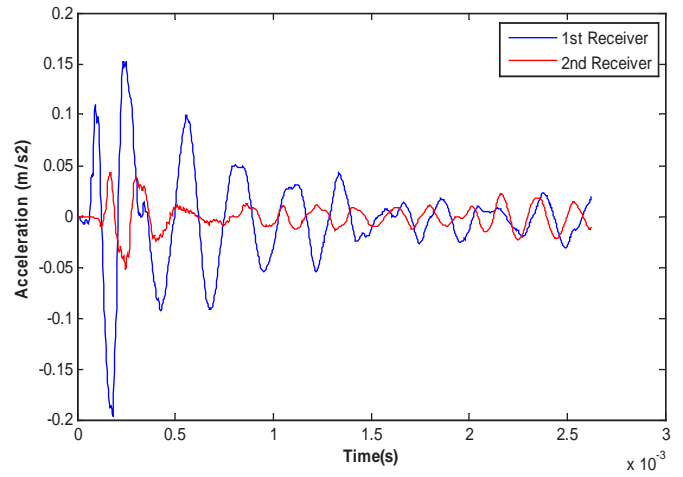


Figure U.18. Contour maps of acquired results from new PSPA for concrete Slab 7 (15 in. thick, delaminated at 2 in.).



(a) Slab 8



(b) Waveform obtained from PSPA at center point

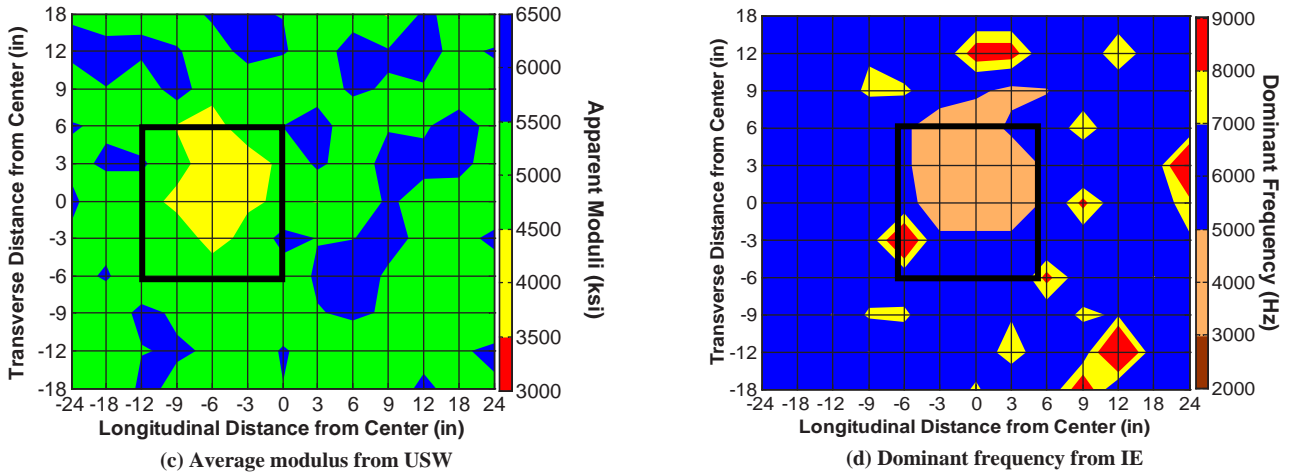


Figure U.19. Contour maps of acquired results from traditional PSPA for concrete Slab 8 (15 in. thick, delaminated at 3 in.). (Continued on next page.)

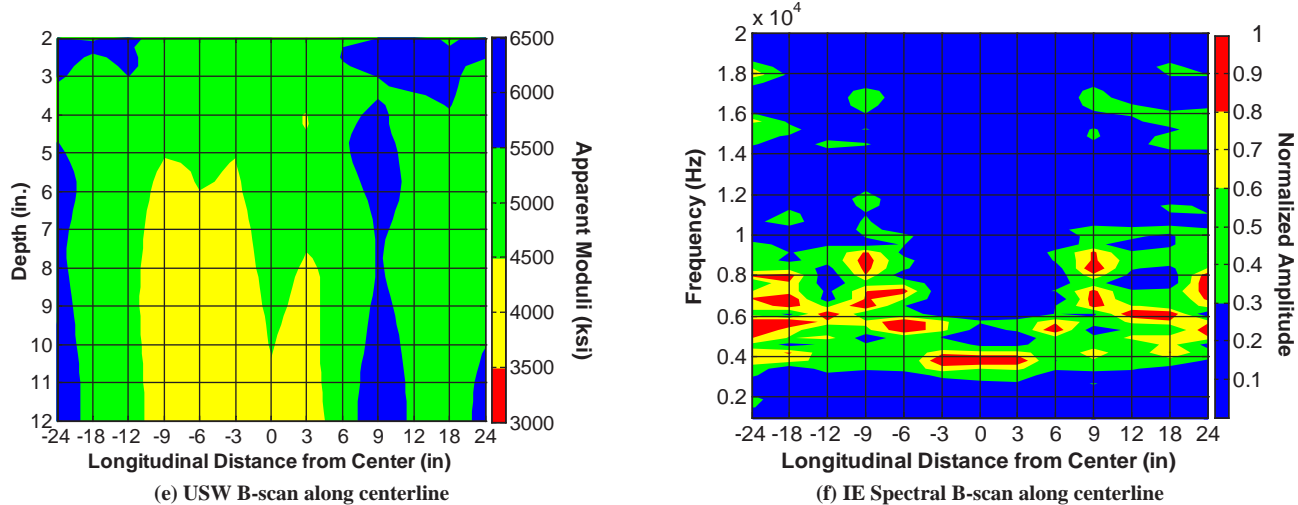


Figure U.19. (Continued.)

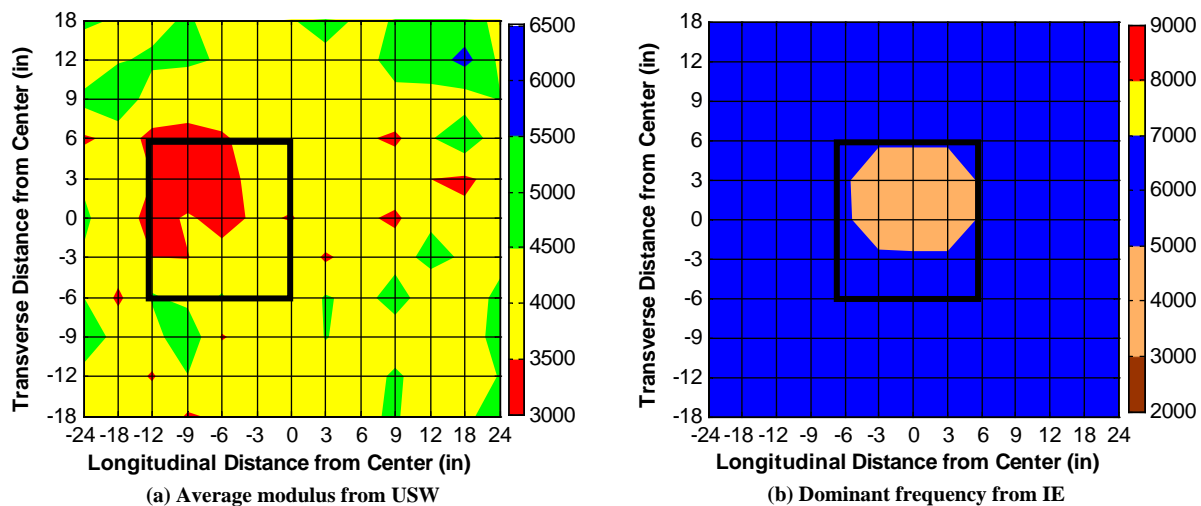
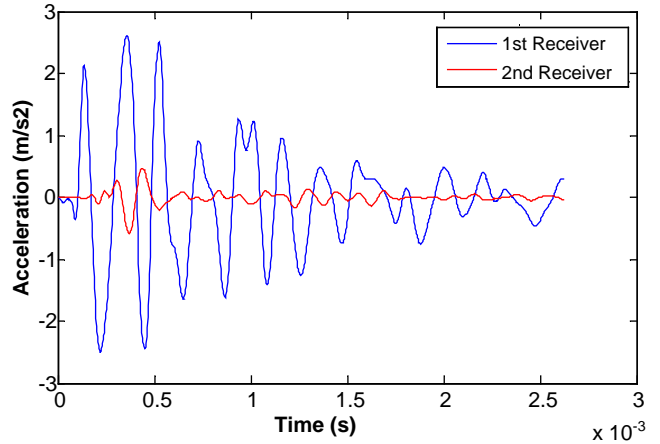


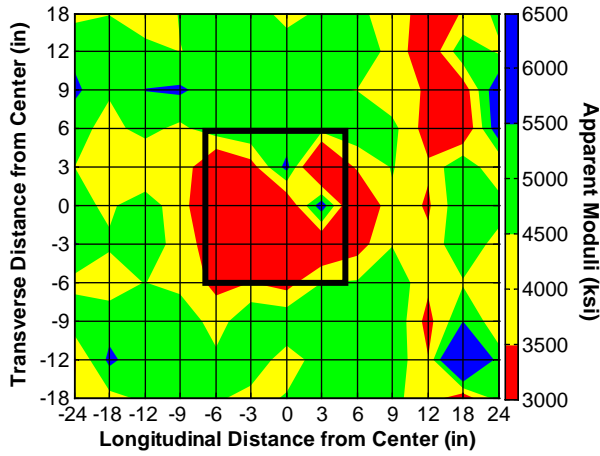
Figure U.20. Contour maps of acquired results from new PSPA for concrete Slab 8 (15 in. thick, delaminated at 3 in.).



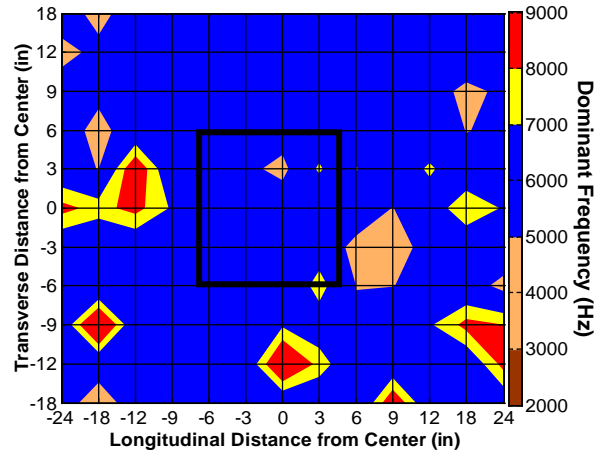
(a) Slab 9



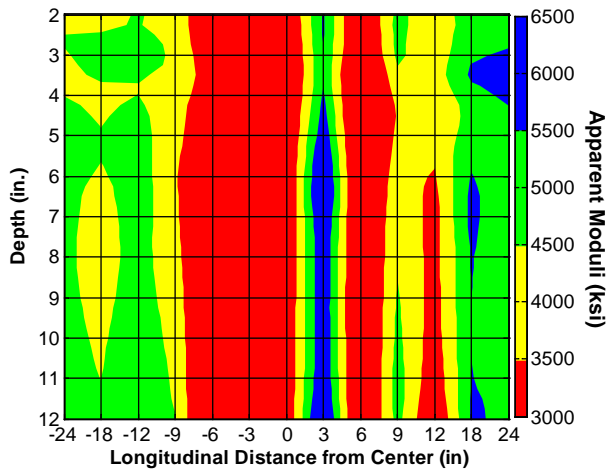
(b) Waveform obtained from PSPA at center point



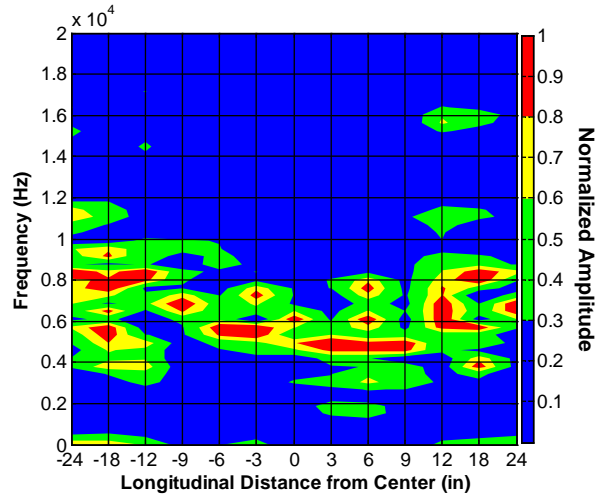
(c) Average modulus from USW



(d) Dominant frequency from IE

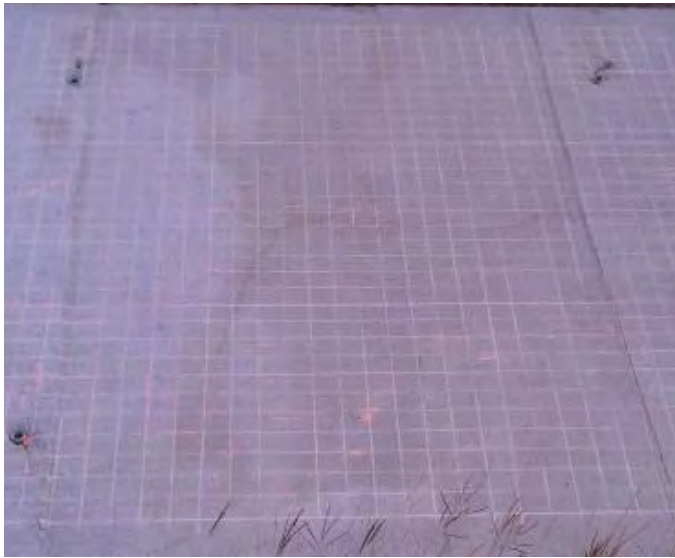


(e) USW B-scan along centerline



(f) IE Spectral B-scan along centerline

Figure U.21. Contour maps of acquired results from traditional PSPA for concrete Slab 9 (15 in. thick, delaminated at 1 in.).



(a) Slab view in 2011

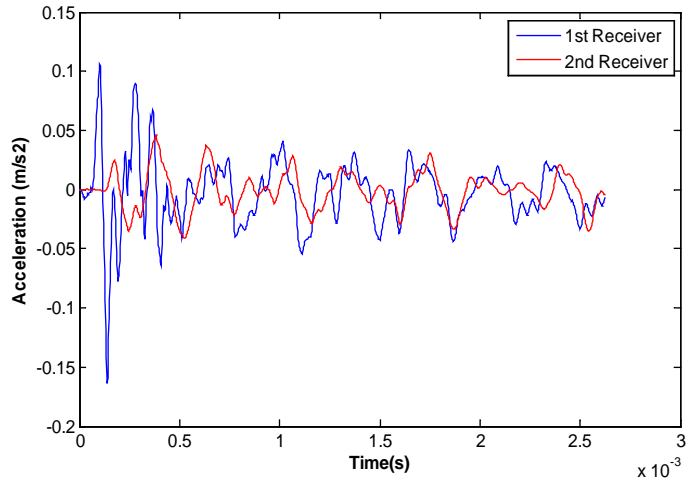


(b) Slab view in 2013

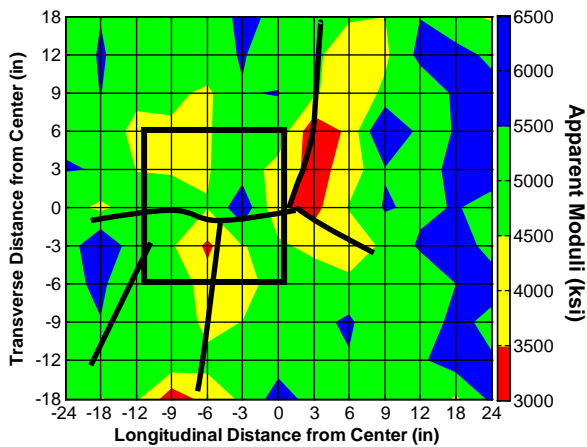
Figure U.22. Crack progression on Slab 10 in a 2-year period of testing.



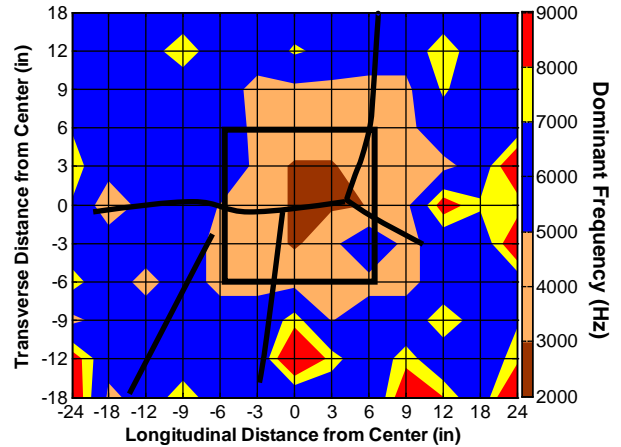
(a) Slab 10



(b) Waveform obtained from PSPA at center point



(c) Average modulus from USW



(d) Dominant frequency from IE

Figure U.23. Contour maps of acquired results from traditional PSPA for concrete Slab 10 (15 in. thick with air void at 8 in. deep). (Continued on next page.)

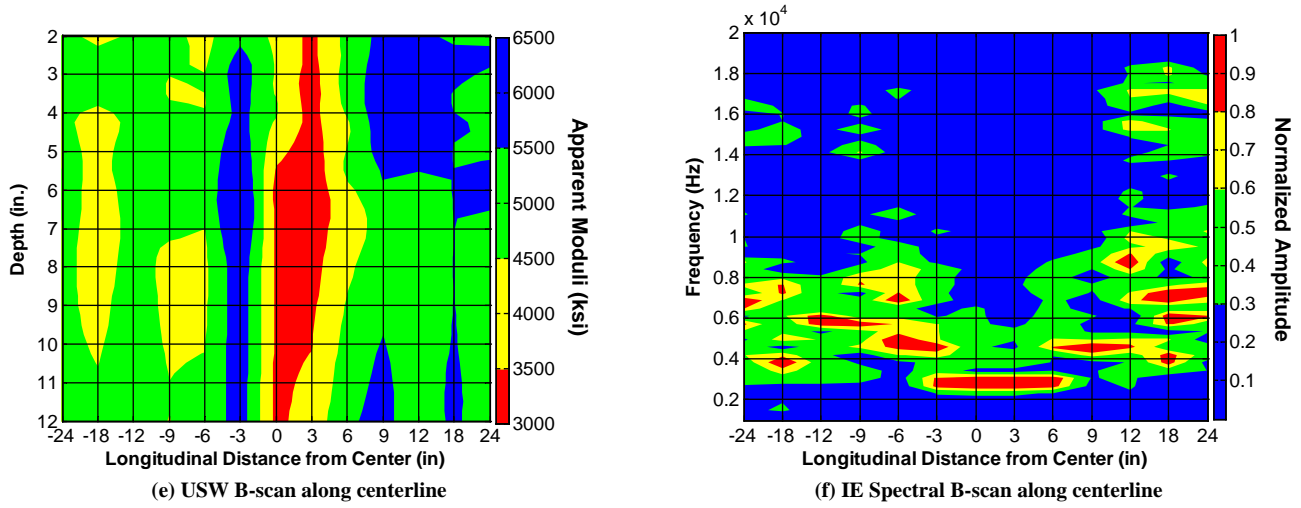


Figure U.23. (Continued.)

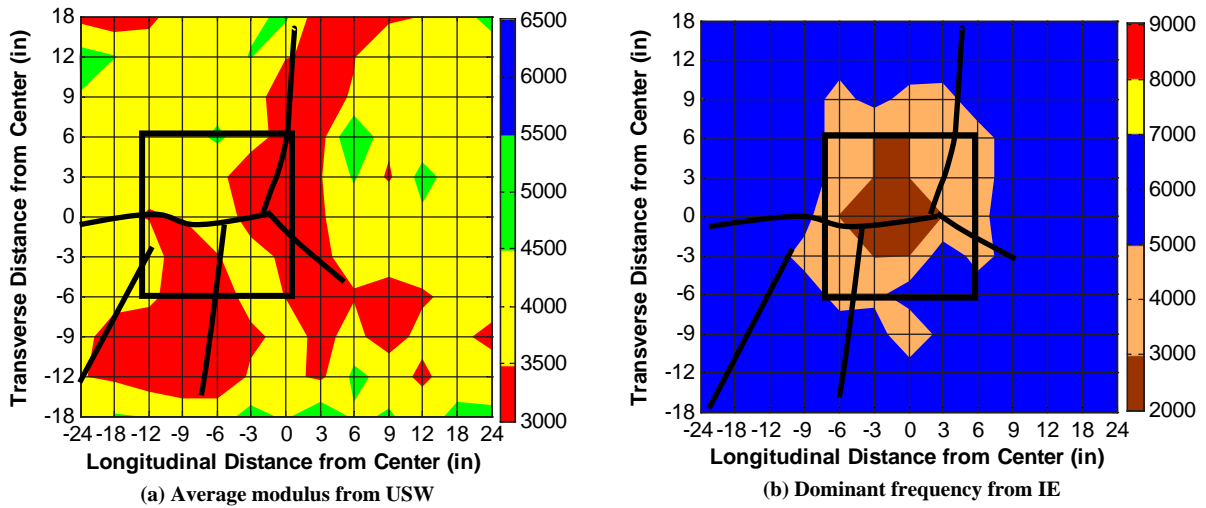
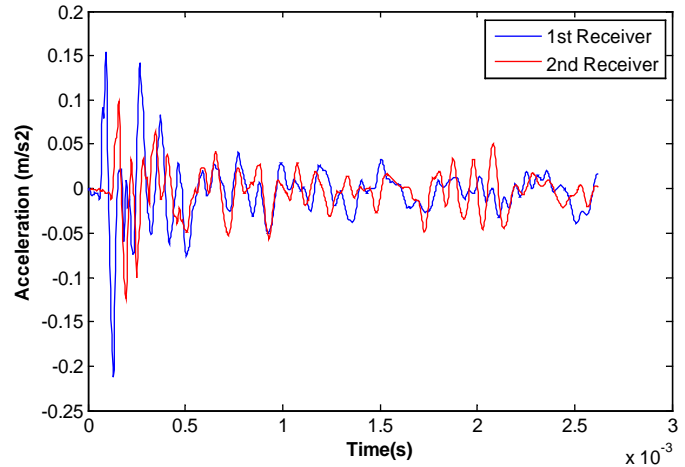


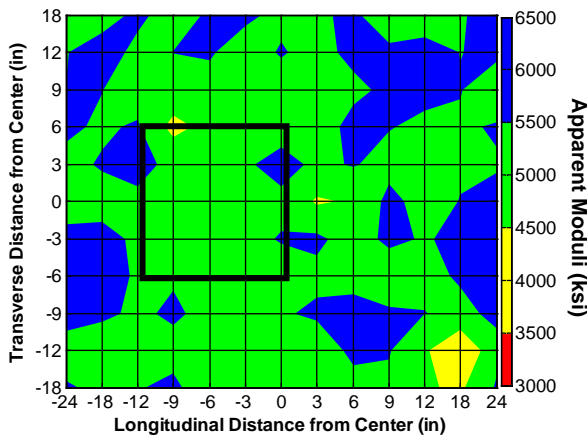
Figure U.24. Contour maps of acquired results from new PSPA for concrete Slab 10 (15 in. thick with air void at 8 in. deep).



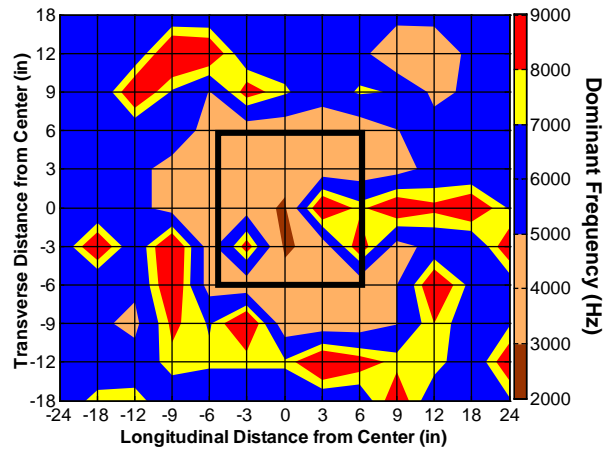
(a) Slab 11



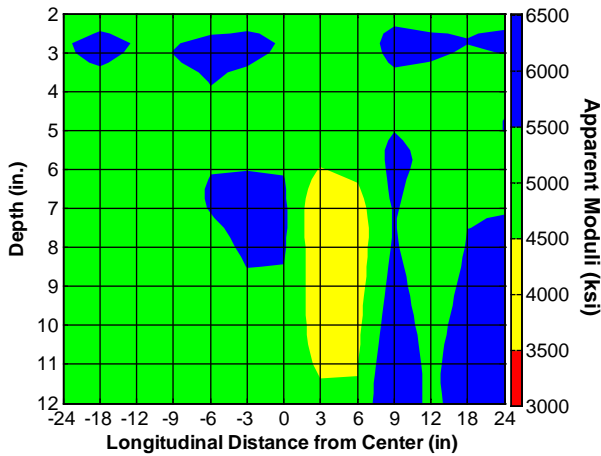
(b) Waveform obtained from PSPA at center point



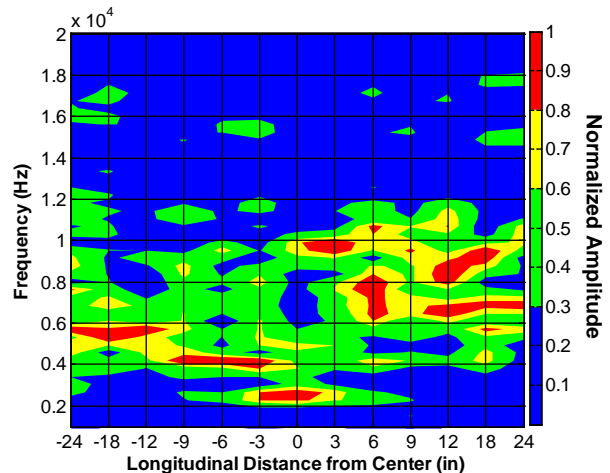
(c) Average modulus from USW



(d) Dominant frequency from IE



(e) USW B-scan along centerline



(f) IE Spectral B-scan along centerline

Figure U.25. Contour maps of acquired results from traditional PSPA for concrete Slab 11 (15 in. thick with water void at 8 in. deep).

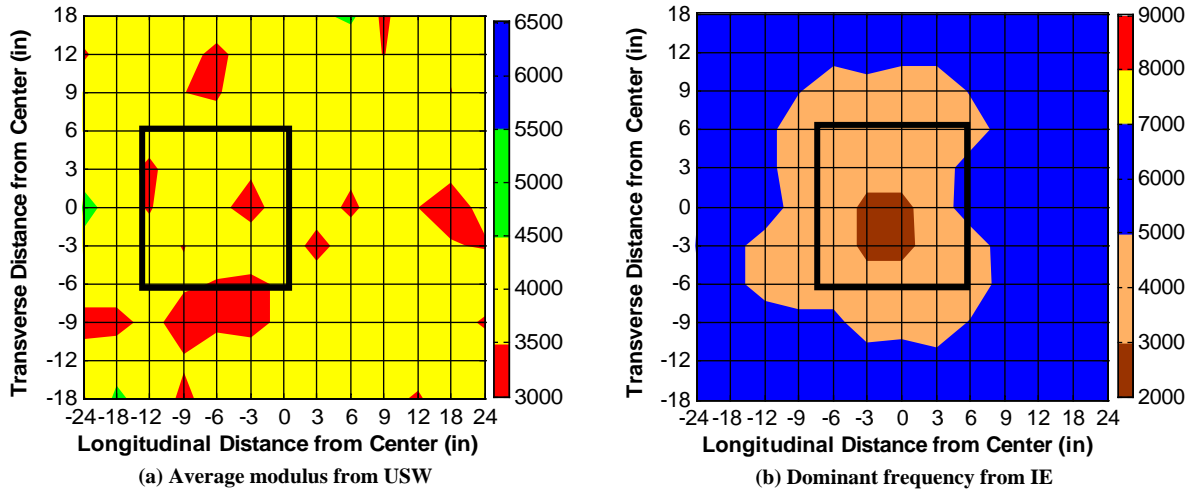


Figure U.26. Contour maps of acquired results from new PSPA for concrete Slab 11 (15 in. thick with water void at 8 in. deep).

Figure U.24a. The manifestation of the deep void was not readily detectable from the USW results with the traditional or new PSPA (Figures U.23c and U.24a). According to the principles of wave propagation, the detection of voids with USW becomes less effective as the depth of the defect increases. In this case, surface waves propagated along a cylindrical front, and as such, they became less sensitive to horizontal discontinuities with depth.

However, the air void was clearly mapped in contour maps of dominant frequency from the IE method with both the traditional and new PSPAs (Figures U.23d and U.24b). The void seems to have propagated beyond the boundaries intended. Similar results can be observed for Slab 11 with the water-filled void in Figures U.25 and U.26 from the traditional and new PSPAs, respectively.

Intact Shotcrete Slabs

By nature, shotcrete is quite variable in its properties. The traditional and new PSPA results from four intact shotcrete slabs with thicknesses of 4 in., 6 in., 8 in., and 12 in. are shown in Figures U.27 through U.33. The thicknesses of the 4-in. and 6-in. slabs could not be ascertained with the IE results from the traditional and new PSPAs because of the source–receiver configurations in both PSPAs. The thickness of Slab 3 and Slab 13 (thicknesses of 8 in. and 12 in.) was estimated as 9.8 in. and 13.1 in., respectively, with the traditional PSPA using the properties of concrete and dominant frequency. The new PSPA seems to be more promising in detecting the bottom of Slab 13; the IE method gives an average thickness of 11.5 in. for Slab 13 with the thickness of 12 in. However, the new PSPA could not estimate the thickness of 8 in. for Slab 3 accurately. Unlike the concrete slabs, the reported thicknesses from the traditional and new PSPAs resulted in high standard deviations, making

the IE method suitable for only a rough estimation of the thickness of shotcrete. The reason is the rough surface of shotcrete slab that makes a poor contact between the sensors and the surface.

The average and standard deviation of the modulus from the traditional and new PSPAs of each intact shotcrete slab are shown in Table U.2. The average moduli varied significantly among the slabs, and the standard deviation increased (uniformity of construction decreased) as the shotcrete slab became thicker. Generally, the mean average modulus for each slab decreased from 2011 to 2013.

Delaminated Shotcrete Slabs

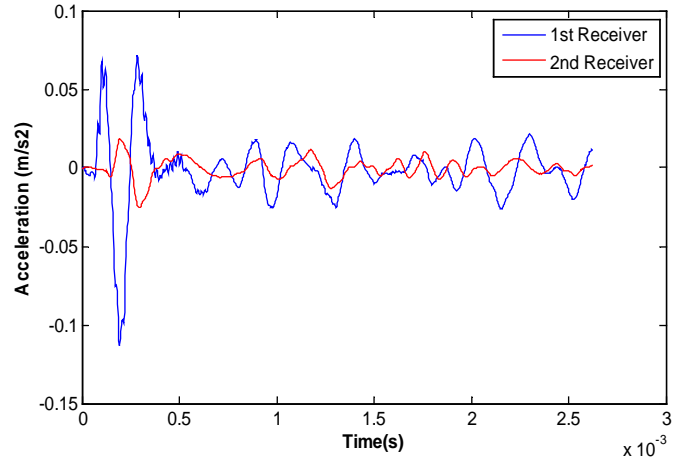
Five 12-in.-thick slabs (Slabs 8 through 12) were similar to Slab 13, except that they contained 1-ft-square delaminated zones at depths varying from 8 in. to 1 in. from the top surface. Some of the delaminated slabs were selected for investigation with the new PSPA. The results from the tested slabs are shown in Figures U.34 through U.41. These slabs exhibited nonuniform finishes and contained microcracks (often) and macrocracks in a few cases.

By simply comparing the waveforms in Figures U.34b, U.36, U.38, U.39, and U.41 with the time record in Figure U.32b (intact Slab 13), one can conclude that Slabs 8 through 12 were delaminated. The higher amplitude in time records in Figures U.39b and U.41b indicate very shallow delamination. Therefore, the operator could roughly interpret time signals at the time of testing.

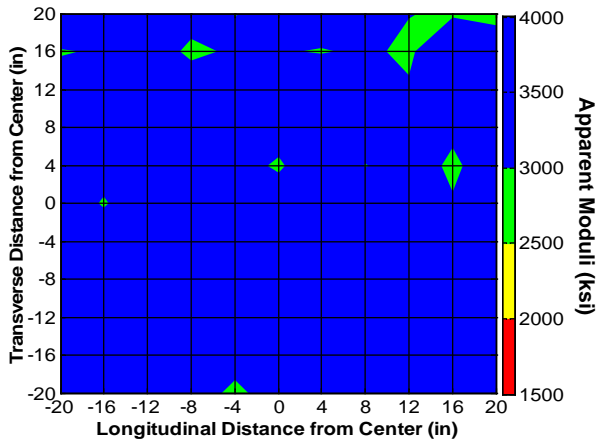
As reflected in Figures U.34c, U.35a, U.36c, and U.37a, USW results from the traditional and new PSPAs were not as promising in estimating deep delamination as they were in locating shallower ones (Figures U.38 through U.41). However, the 8-in.-deep and 4-in.-deep delaminated zones were clearly detectable



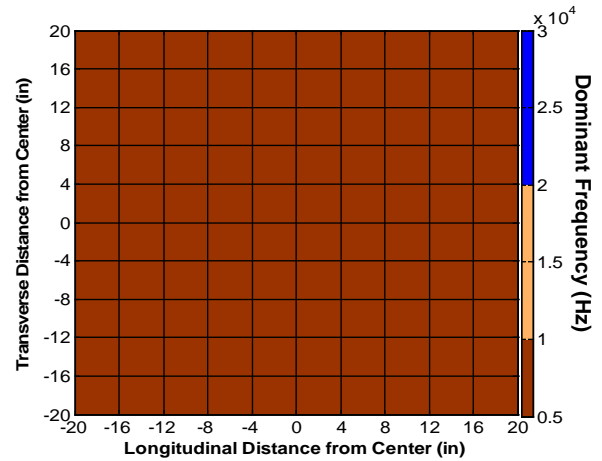
(a) Slab 1



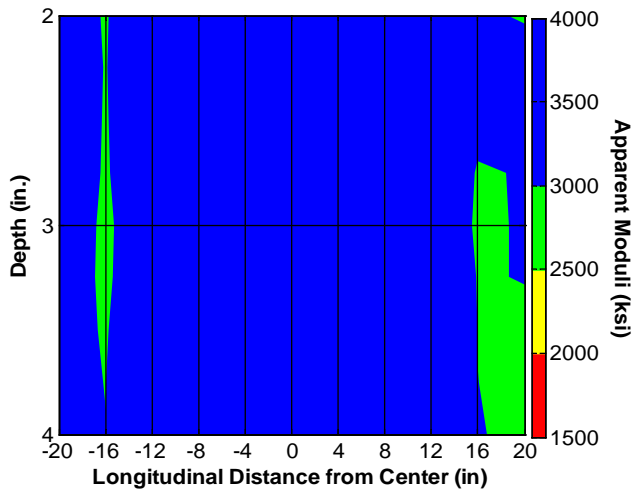
(b) Waveform obtained from PSPA at center point



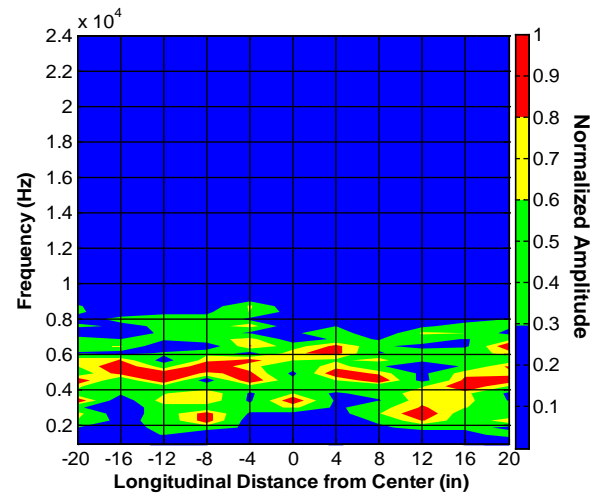
(c) Average modulus from USW



(d) Dominant frequency from IE



(e) USW B-scan along centerline

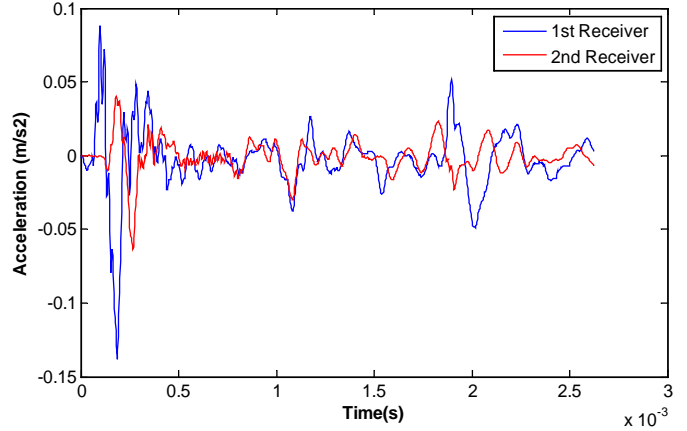


(f) IE Spectral B-scan along centerline

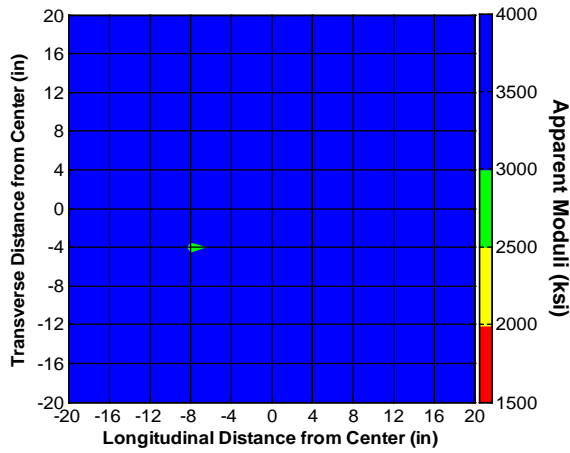
Figure U.27. Contour maps of acquired results from traditional PSPA for shotcrete Slab 1 (4-in.-thick intact slab).



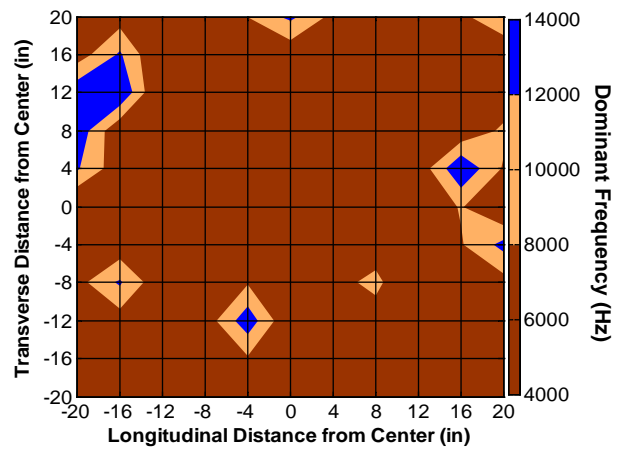
(a) Slab 2



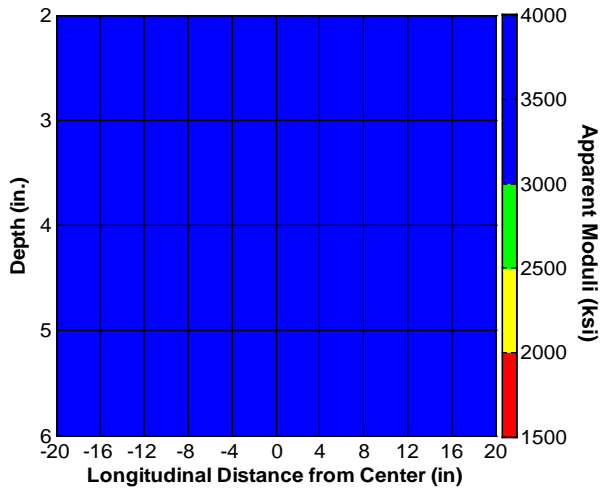
(b) Waveform obtained from PSPA at center point



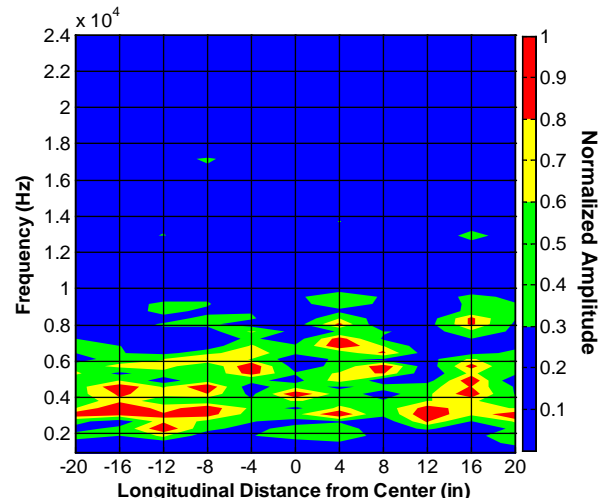
(c) Average modulus from USW



(d) Dominant frequency from IE



(e) USW B-scan along centerline



(f) IE Spectral B-scan along centerline

Figure U.28. Contour maps of acquired results from traditional PSPA for shotcrete Slab 2 (6-in.-thick intact slab).

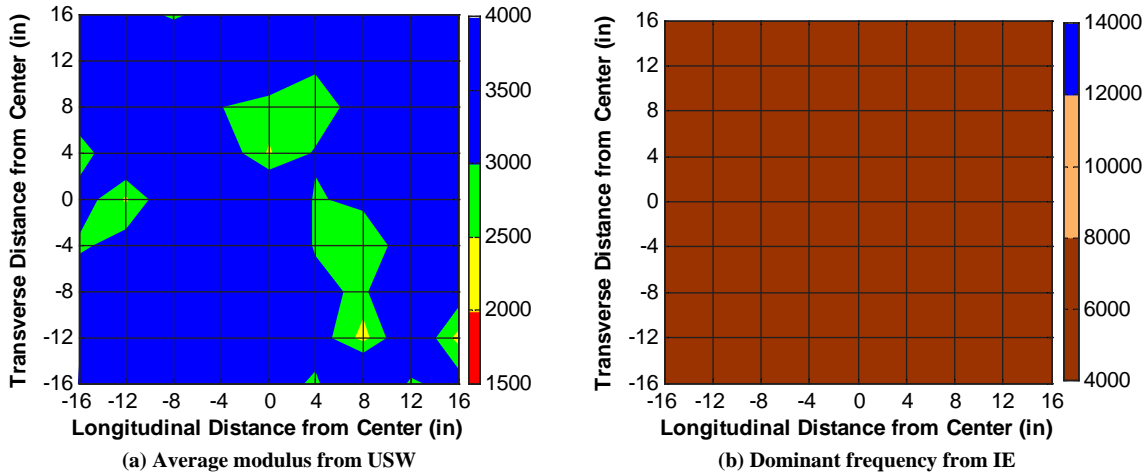
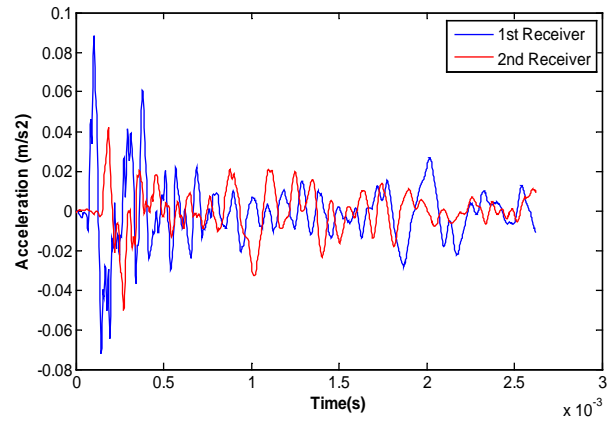


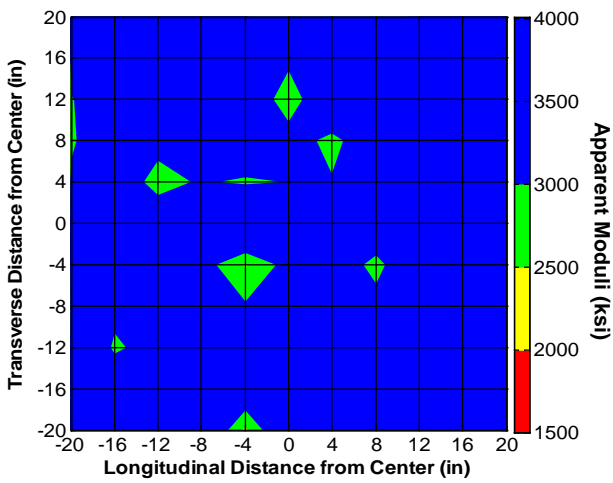
Figure U.29. Contour maps of acquired results from new PSPA for shotcrete Slab 2 (6-in.-thick intact slab).



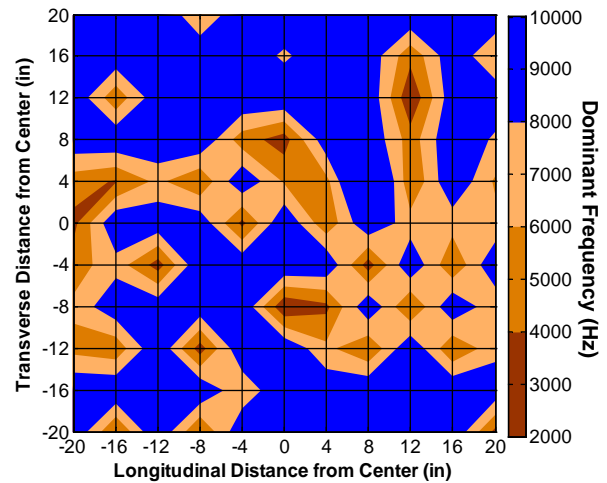
(a) Slab 3



(b) Waveform obtained from PSPA at center point



(c) Average modulus from USW



(d) Dominant frequency from IE

Figure U.30. Contour maps of acquired results from traditional PSPA for shotcrete Slab 3 (8-in.-thick intact slab). (Continued on next page.)

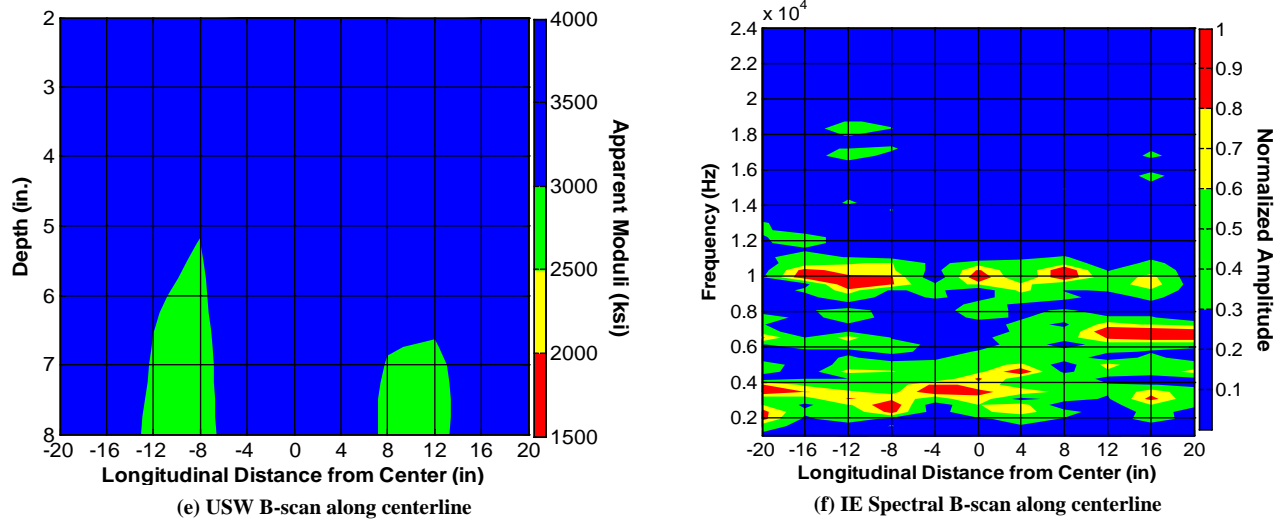


Figure U.30. (Continued.)

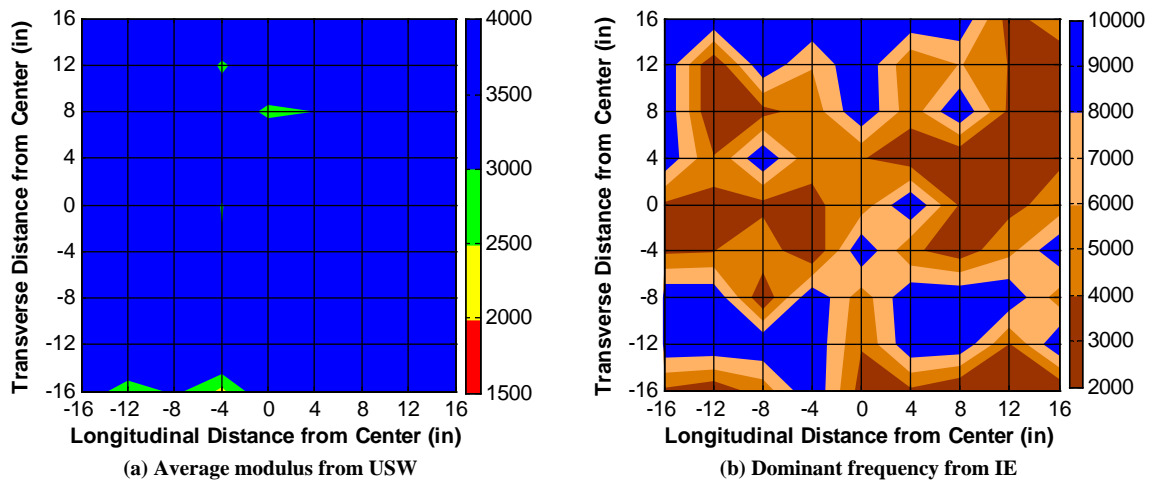
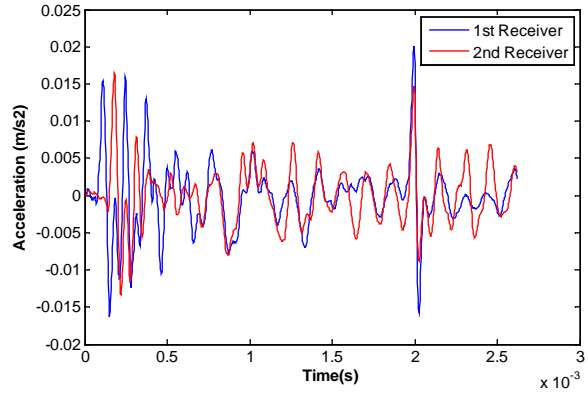


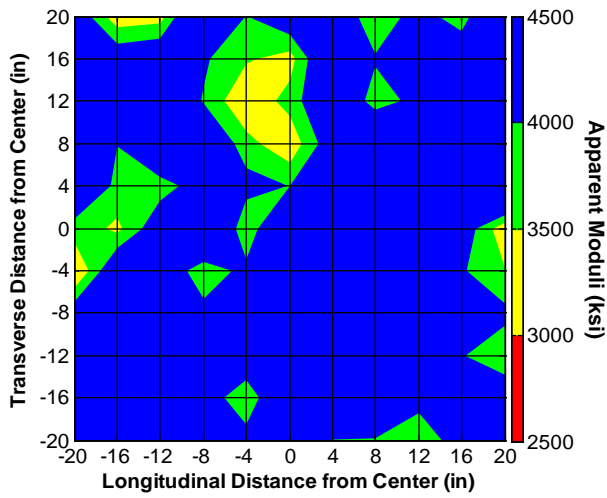
Figure U.31. Contour maps of acquired results from new PSPA for shotcrete Slab 3 (8-in.-thick intact slab).



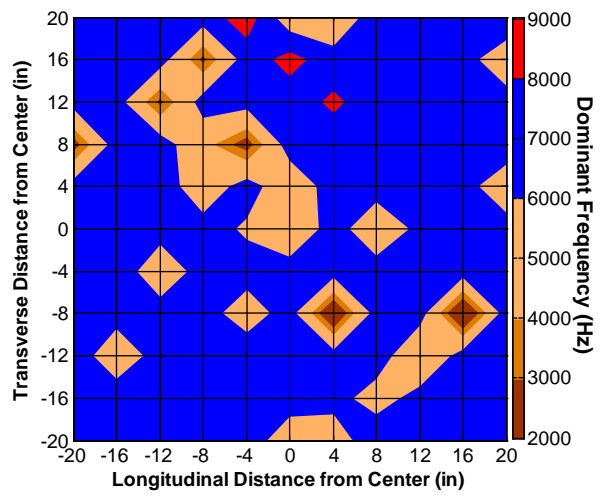
(a) Slab 13



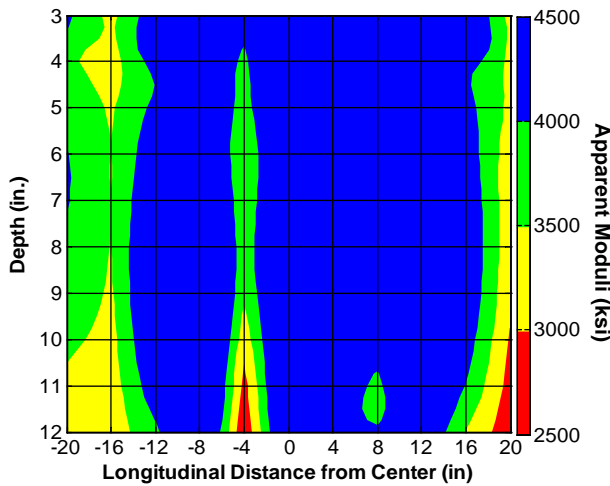
(b) Waveform obtained from PSPA at center point



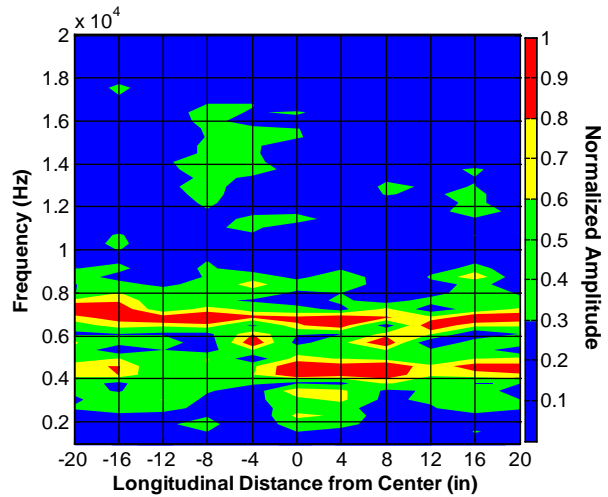
(c) Average modulus from USW



(d) Dominant frequency from IE



(e) USW B-scan along centerline



(f) IE Spectral B-scan along centerline

Figure U.32. Contour maps of acquired results from traditional PSPA for shotcrete Slab 13 (12-in.-thick intact slab).

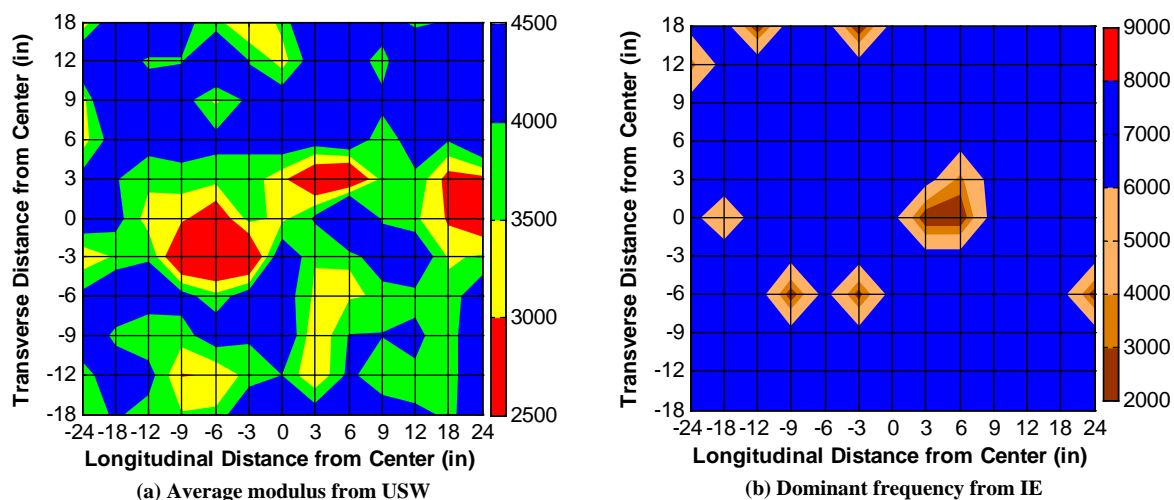


Figure U-33. Contour maps of acquired results from new PSPA for shotcrete Slab 13 (12-in.-thick intact slab).

in the contour maps of the dominant return frequency from the IE method with both the traditional and new PSPAs (Figures U.34d, U.35b, U.36d, and U.37b). The IE results from the new PSPA indicate a more confined area for the 2-in.-deep delamination in Slab 11. The size of detected delamination in Slab 11 with the traditional PSPA was bigger than it was expected to be.

Shotcrete Slabs with Voids

Slabs 4 through 7 contained different sizes of bags that simulated air-filled voids and water-filled voids at different depths. In Slabs 4 and 5, the voids were embedded at a depth of 7.5 in. from the surface and in Slabs 6 and 7 at a depth of 3 in. Slab 6 was tested with the new PSPA. Again, the time signals in Figures U.42b through U.44b are significantly different from the time records of a similar intact slab (Slab 13) in Figure U.33b.

As in the case of concrete slabs, the USW method lost its resolving power as the defects were placed deeper. As shown

in Figures U.42c and U.43c, the deep voids were not as readily detectable from the USW results as were the shallower ones with the traditional and new PSPAs, shown in Figures U.44c, U.45b, and U.46c. The deep and shallow voids were mapped in contour maps of the dominant frequency from the IE method with the traditional and new PSPAs (Figures U.42d, U.43d, U.44d, U.45b, and U.46d). The voids in Slabs 6 and 7 were apparently bigger than intended, and they shifted when the slabs were constructed.

Estimation of Depth of Defects

One of the goals of this study was to estimate the depth of defects, especially the shallow ones (less than 4 in.). For severe defects like the ones installed in the TTI slabs, the flexural mode of vibration controls the responses obtained from the IE method. However, as demonstrated in two concurrent SHRP 2 Renewal projects (R06A for concrete and R06C for hot-mix asphalt) the depth-to-defect can be estimated from the USW B-scans. To demonstrate this concept, the USW B-scans from the traditional PSPA for the defective concrete and shotcrete slabs were recontoured, as seen in Figures U.47 through U.48. The recontouring process was needed because, as reflected in Azari et al. (2012), the previous contour maps were optimized to accentuate the existence of the defects. The reported depths of defects are shown with a black solid line in Figures U.47 and U.48.

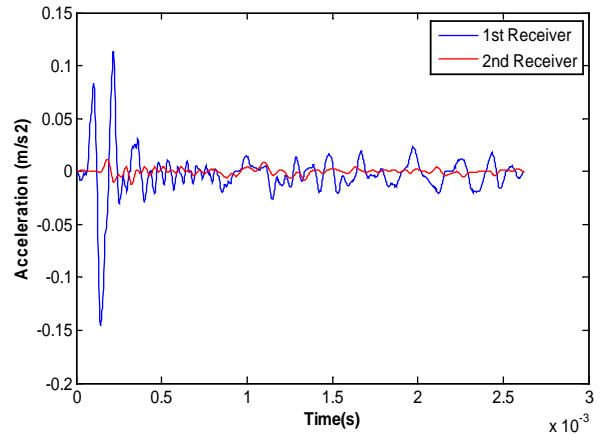
Given the limitation of the minimum depth of investigation of the PSPA (2 in.), the depths of delamination were fairly accurate for Slabs 7, 8, and 9. Figures U.47b and U.47c indicate that the delaminated zone extended beyond the intended areas. As was previously discussed, the predictive power of the USW method diminished with depth. As reflected in Figure U.47d, the quality of the concrete above the 8-in.-deep air

Table U.2. Average and Standard Deviation of Moduli of Intact Shotcrete Slabs

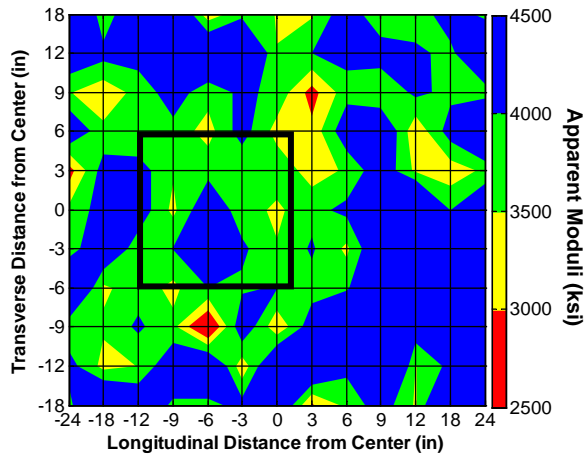
Slab	USW Modulus (ksi)			
	Traditional PSPA		New PSPA	
	Average	SD	Average	SD
1	3,460	386	Not tested	Not tested
2	4,178	549	3,440	506
3	3,607	506	3,610	464
13	4,401	684	3,990	777



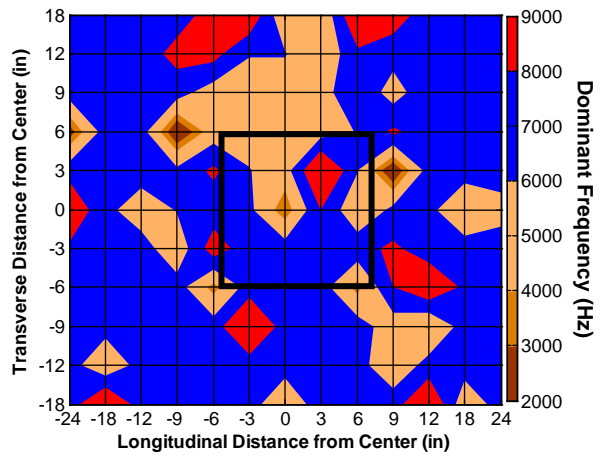
(a) Slab 8



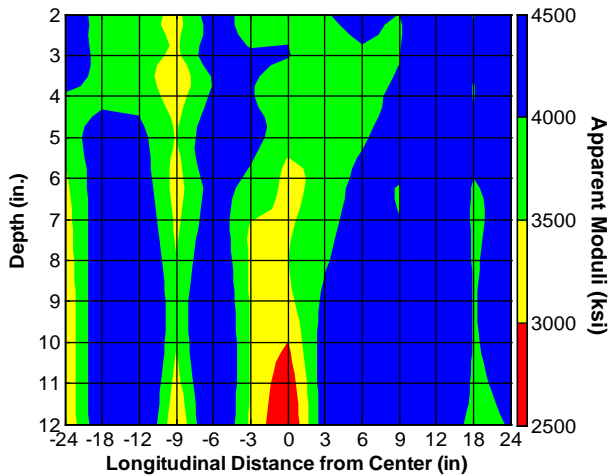
(b) Waveform obtained from PSPA at center point



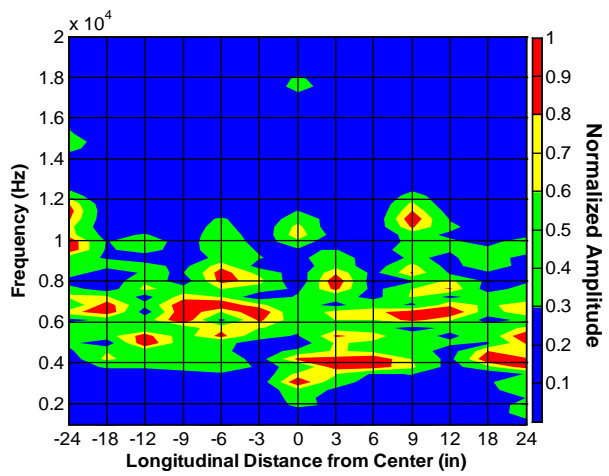
(c) Average modulus from USW



(d) Dominant frequency from IE



(e) USW B-scan along centerline



(f) IE Spectral B-scan along centerline

Figure U.34. Contour maps of acquired results from traditional PSPA for shotcrete Slab 8 (12 in. thick, delaminated at 8-in. depth).

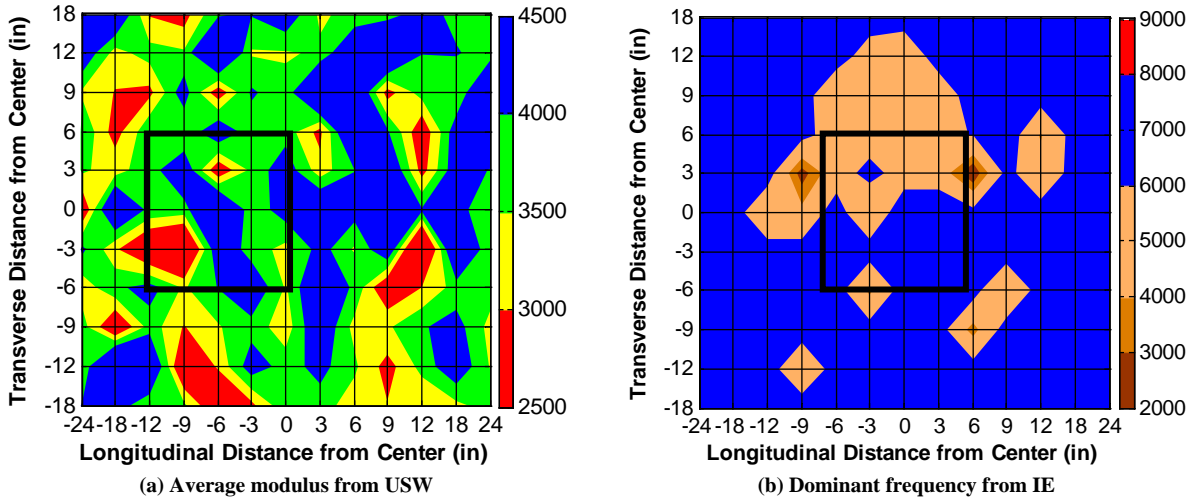
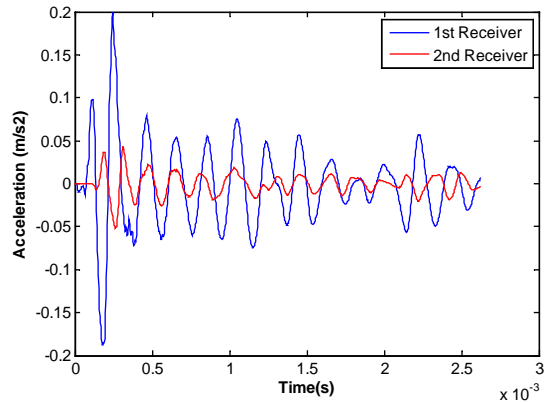


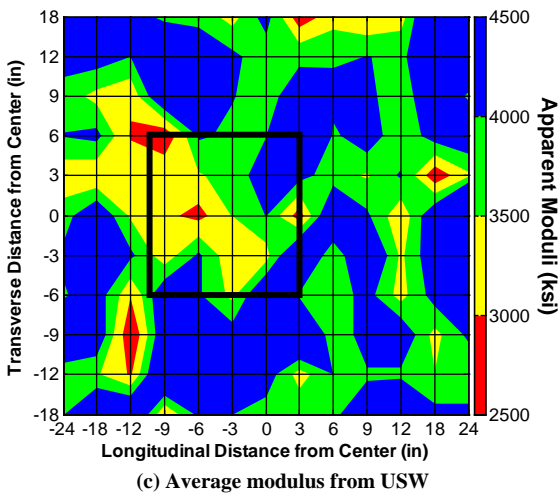
Figure U.35. Contour maps of acquired results from new PSPA for shotcrete Slab 8 (12 in. thick, delaminated at 8-in. depth).



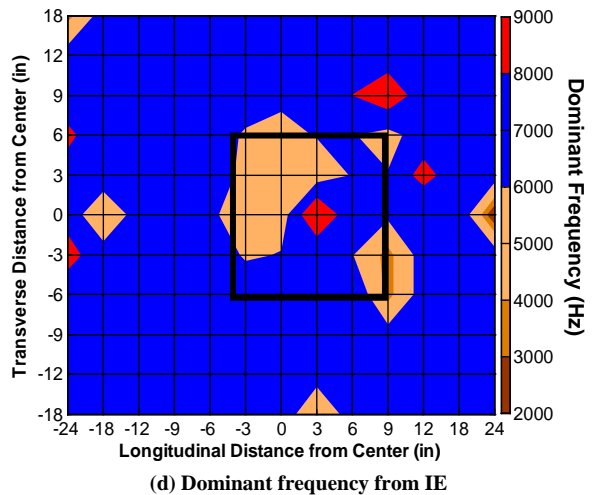
(a) Slab 9



(b) Waveform obtained from PSPA at center point



(c) Average modulus from USW



(d) Dominant frequency from IE

Figure U.36. Contour maps of acquired results from traditional PSPA for shotcrete Slab 9 (12 in. thick, delaminated at 4-in. depth). (Continued on next page.)

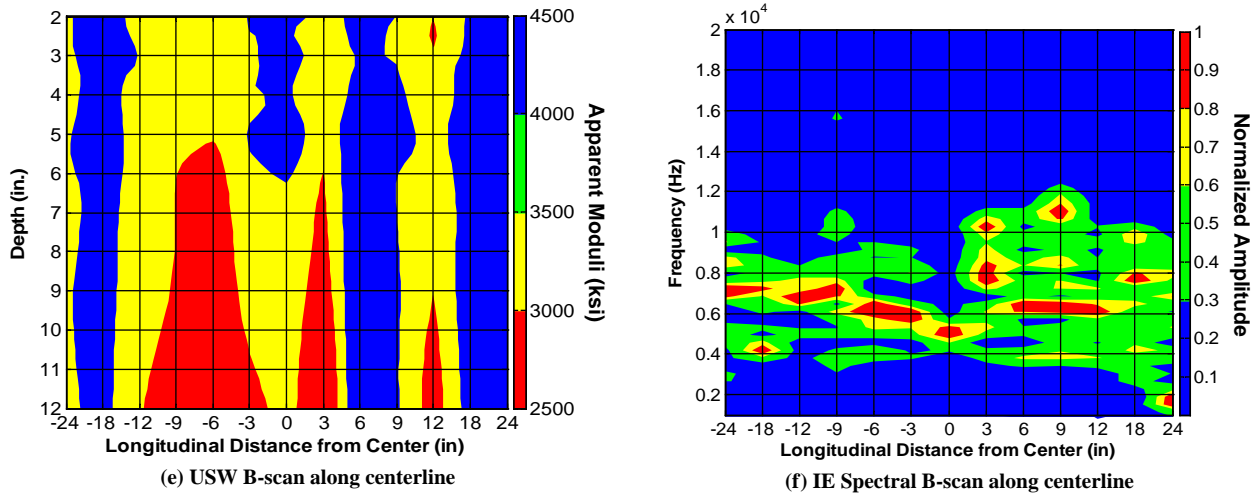


Figure U.36. (Continued.)

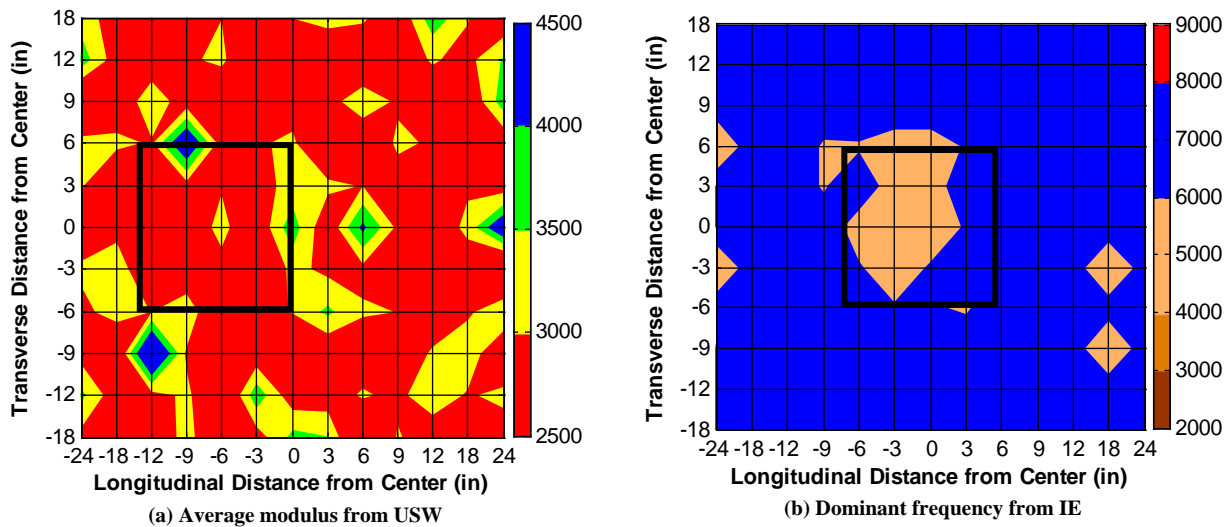
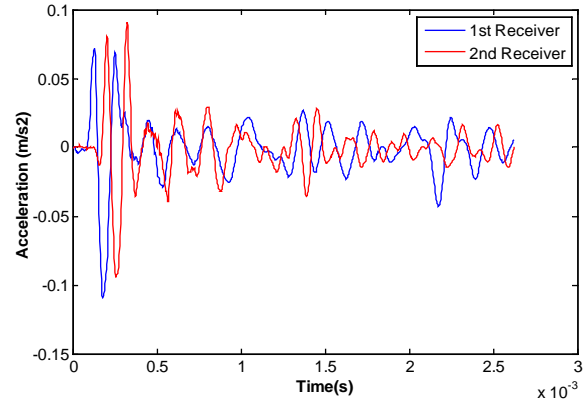


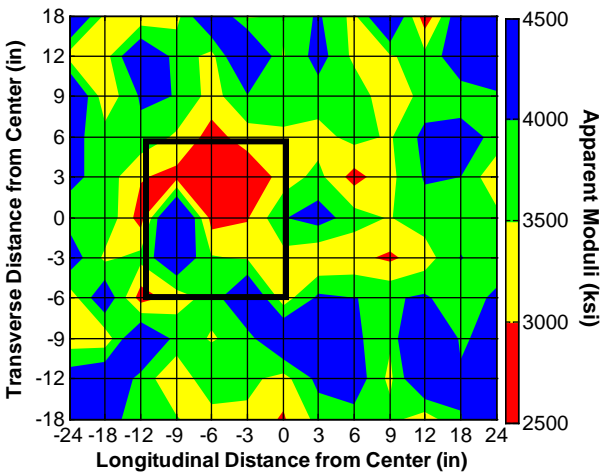
Figure U.37. Contour maps of acquired results from new PSPA for shotcrete Slab 9 (12 in. thick, delaminated at 4-in. depth).



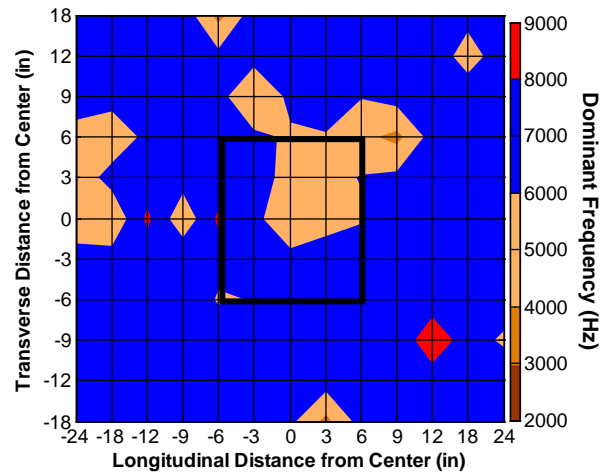
(a) Slab 10



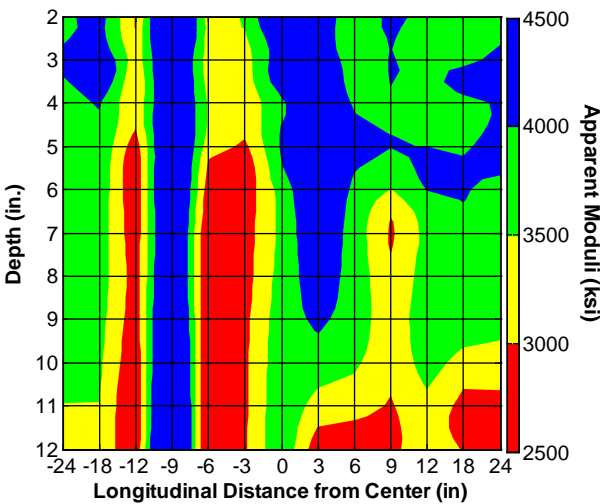
(b) Waveform obtained from PSPA at center point



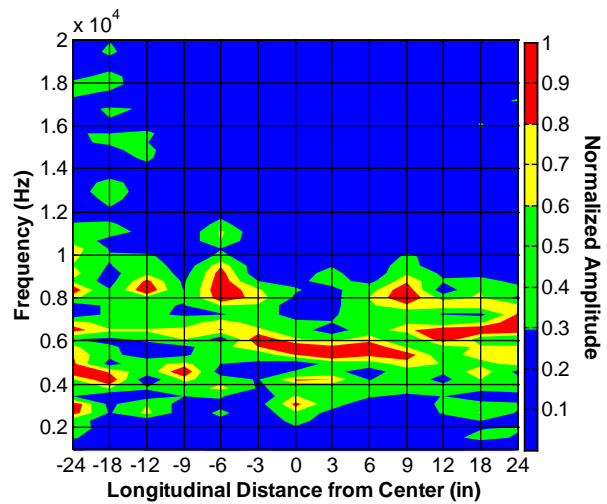
(c) Average modulus from USW



(d) Dominant frequency from IE



(e) USW B-scan along centerline

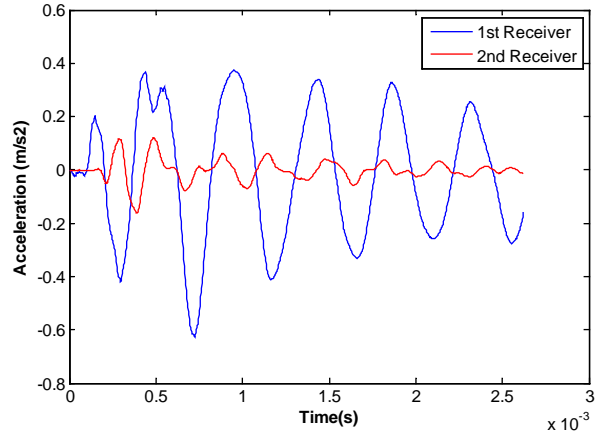


(f) IE Spectral B-scan along centerline

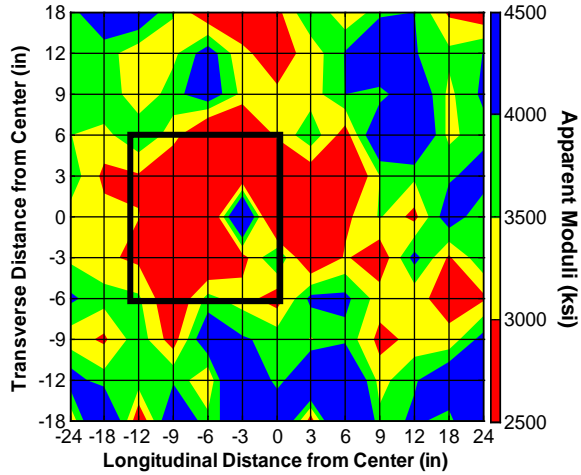
Figure U.38. Contour maps of acquired results from traditional PSPA for shotcrete Slab 10 (12 in. thick, delaminated at 3-in. depth).



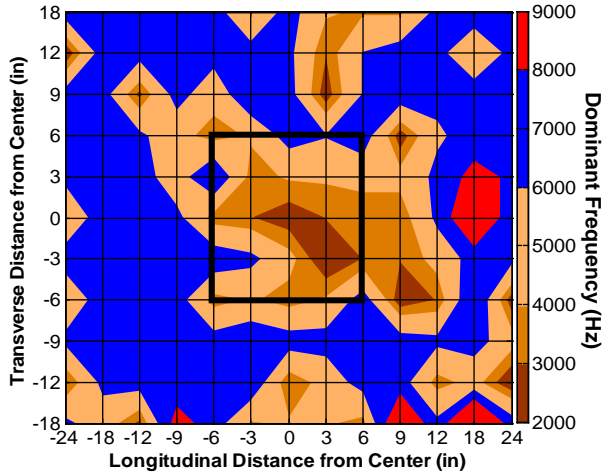
(a) Slab 11



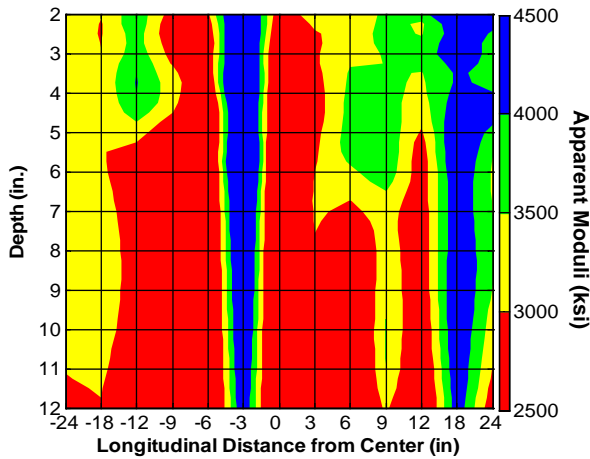
(b) Waveform obtained from PSPA at center point



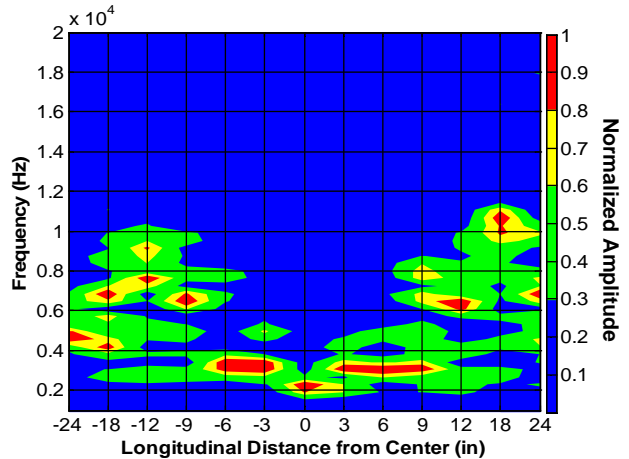
(c) Average modulus from USW



(d) Dominant frequency from IE



(e) USW B-Scan along center line



(f) IE Spectral B-Scan along center line

Figure U.39. Contour maps of acquired results from traditional PSPA for shotcrete Slab 11 (12 in. thick, delaminated at 2-in. depth).

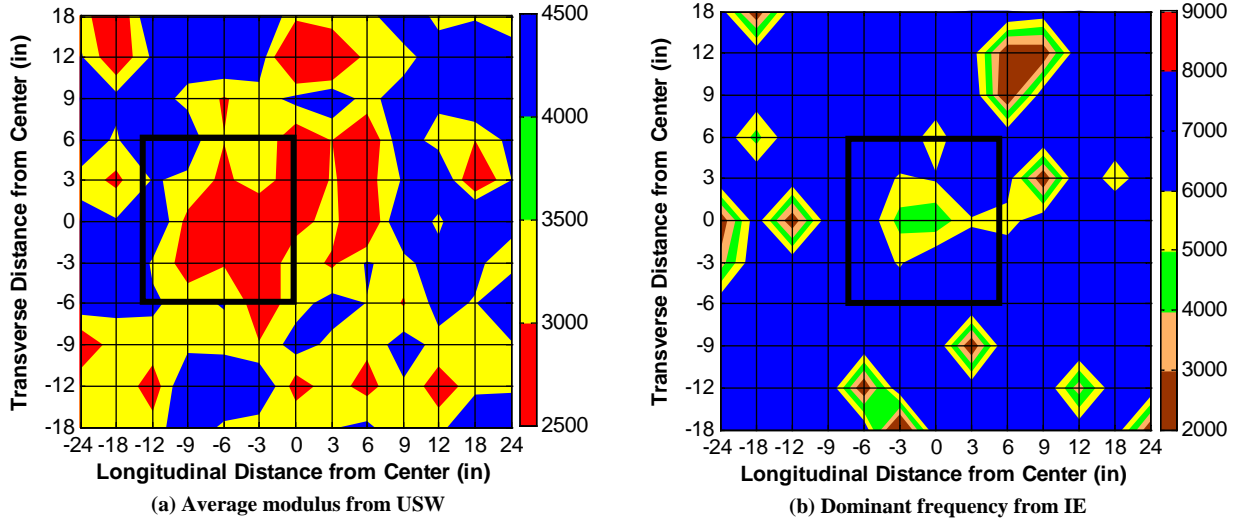
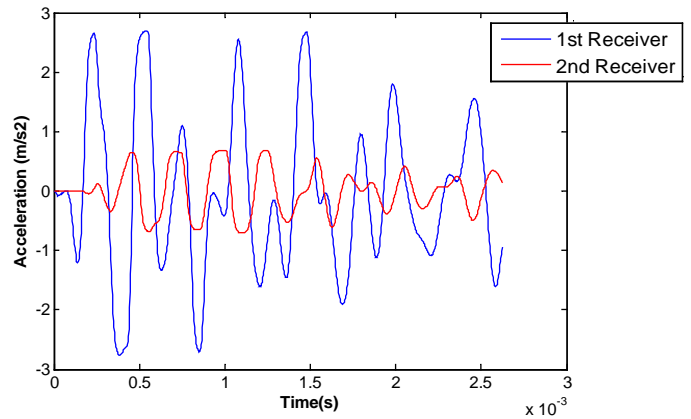


Figure U.40. Contour maps of acquired results from new PSPA for shotcrete Slab 11 (12 in. thick, delaminated at 2-in. depth).



(a) Slab 12



(b) Waveform obtained from PSPA at center point

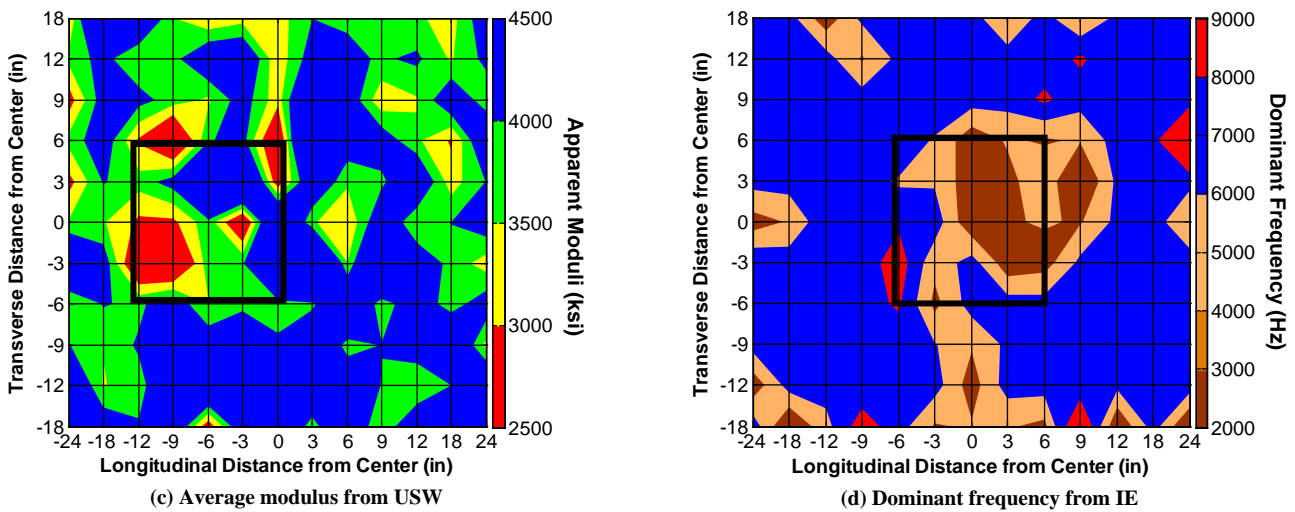


Figure U.41. Contour maps of acquired results from traditional PSPA for shotcrete Slab 12 (12 in. thick, delaminated at 1-in. depth). (Continued on next page.)

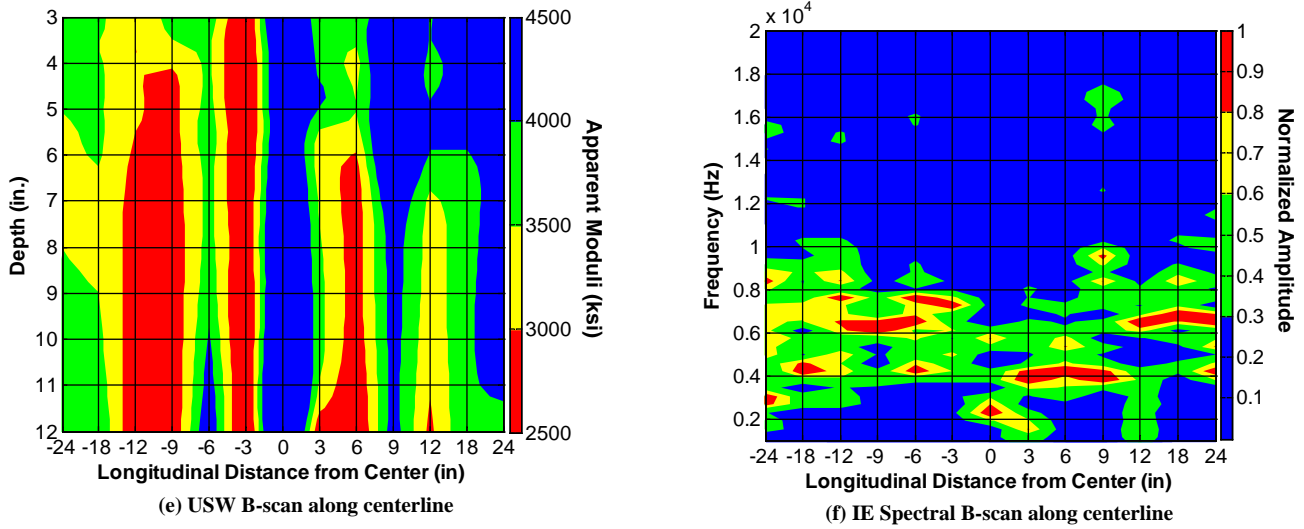
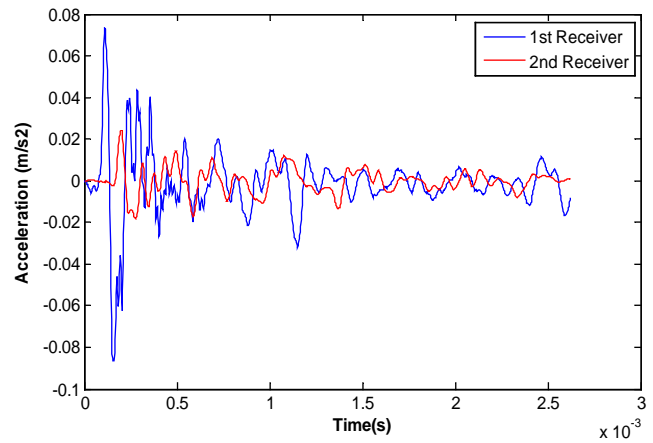


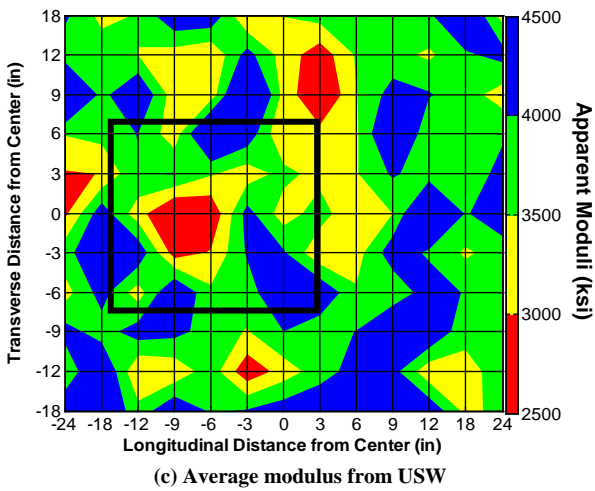
Figure U.41. (Continued.)



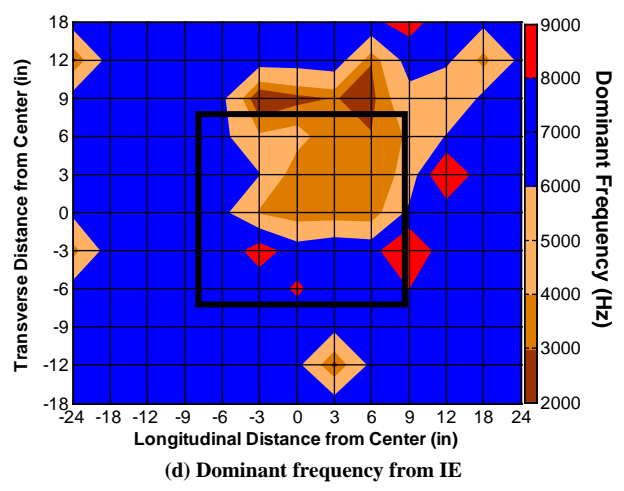
(a) Slab 4



(b) Waveform obtained from PSPA at center point



(c) Average modulus from USW



(d) Dominant frequency from IE

Figure U.42. Contour maps of acquired results from traditional PSPA for shotcrete Slab 4 (12 in. thick, with air void at 7.5-in. depth). (Continued on next page.)

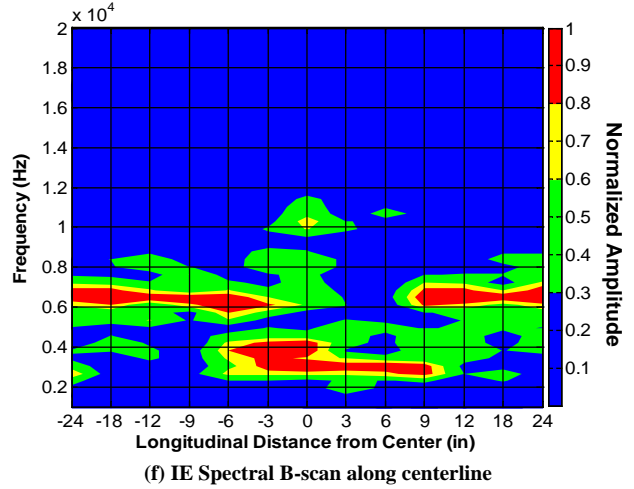
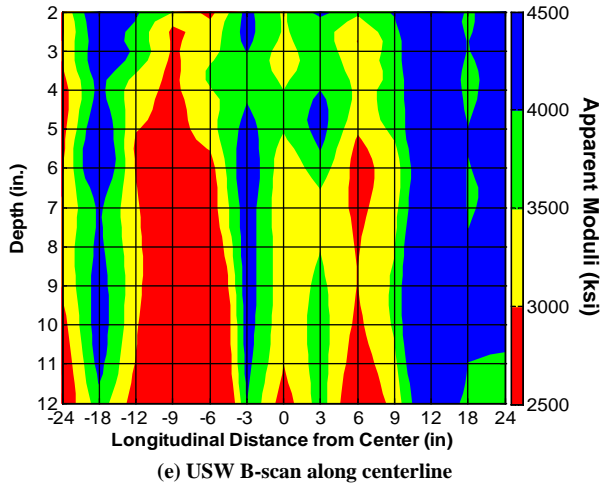
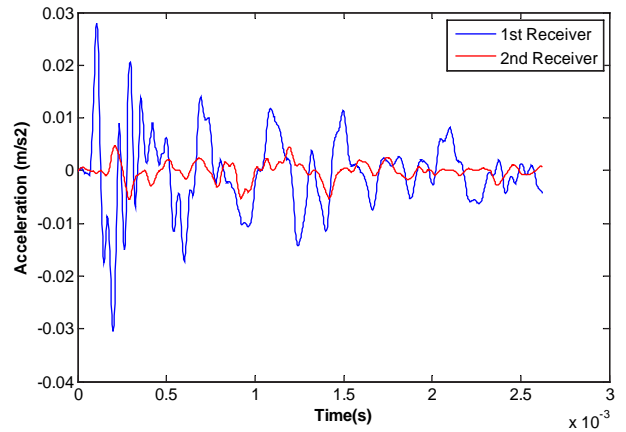


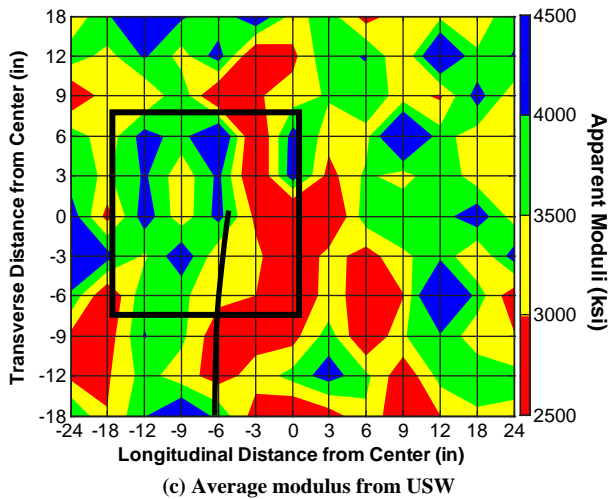
Figure U.42. (Continued.)



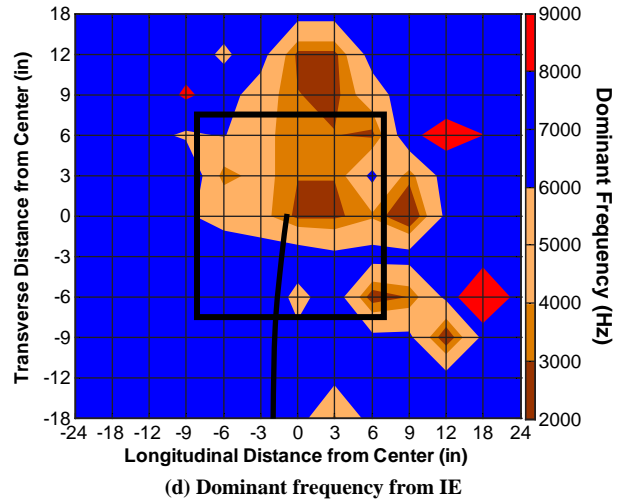
(a) Slab 5



(b) Waveform obtained from PSPA at center point



(c) Average modulus from USW



(d) Dominant frequency from IE

Figure U.43. Contour maps of acquired results from traditional PSPA for shotcrete Slab 5 (12 in. thick, with water void at 7.5-in. depth). (Continued on next page.)

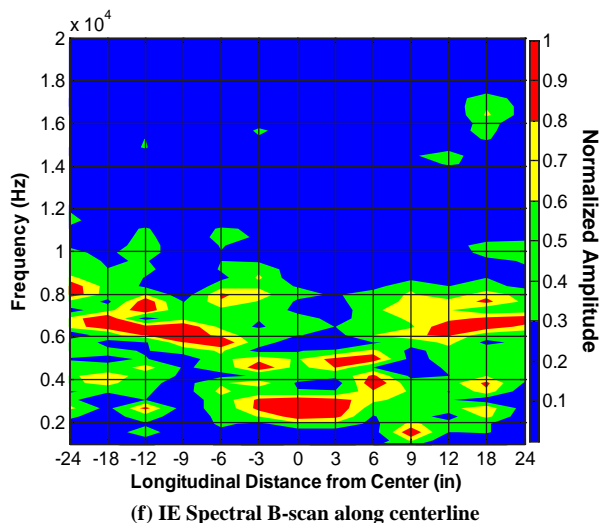
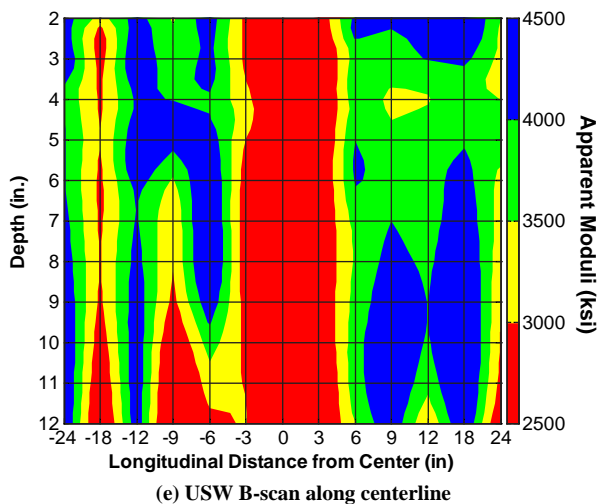


Figure U.43. (Continued.)

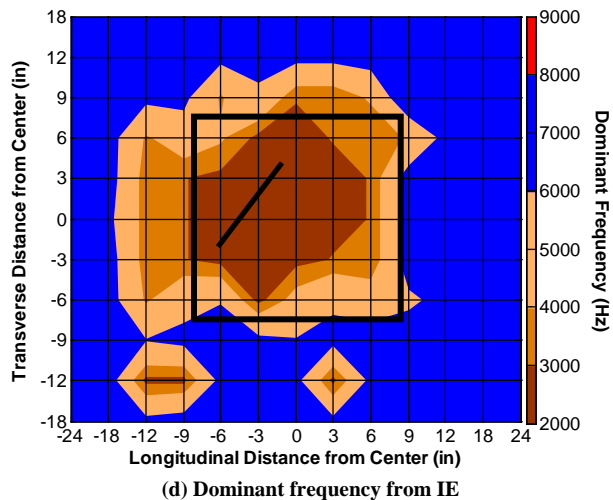
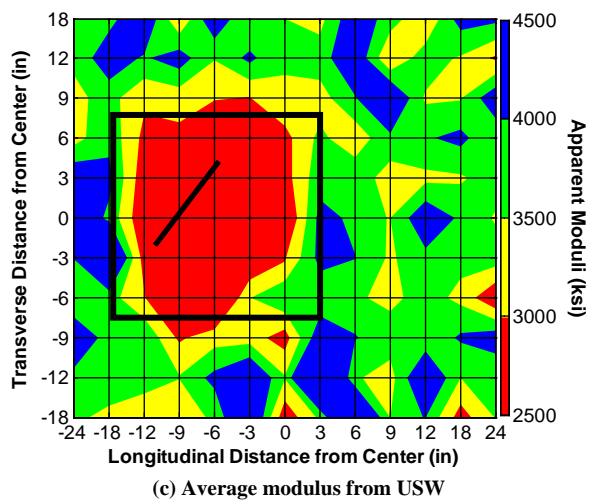
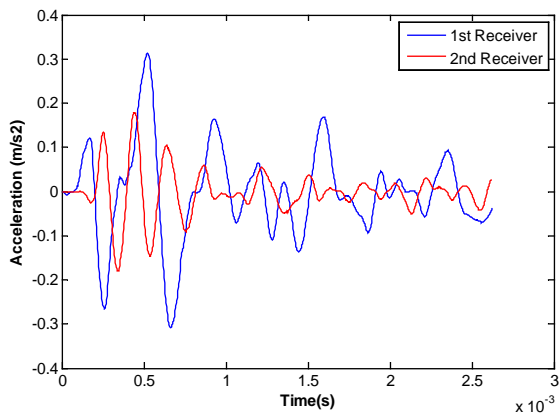


Figure U.44. Contour maps of acquired results from traditional PSPA for shotcrete Slab 6 (12 in. thick, with air void at 3-in. depth). (Continued on next page.)

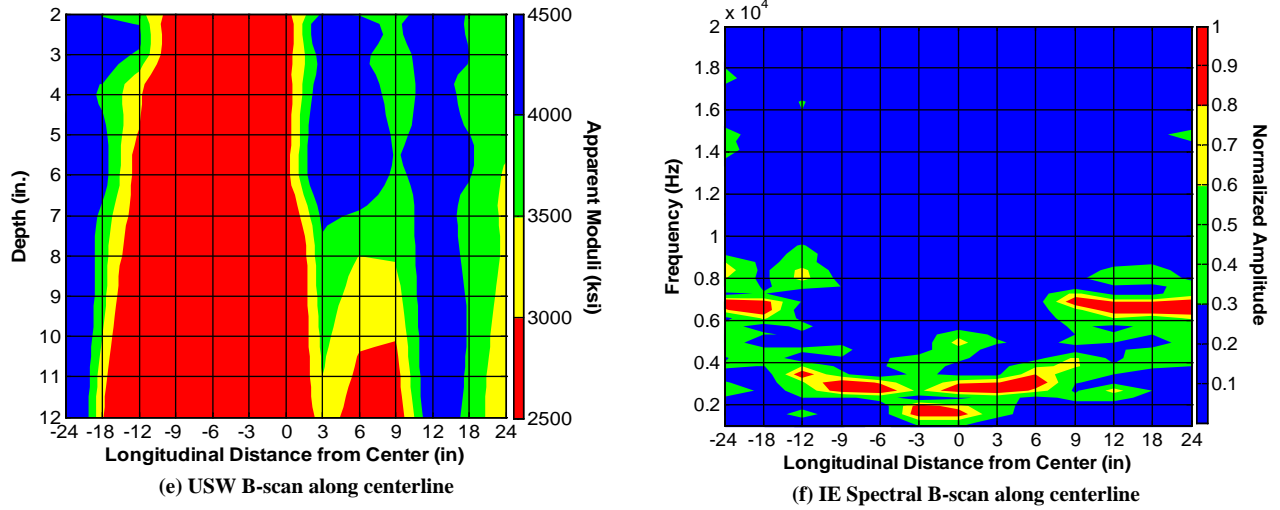


Figure U.44. (Continued.)

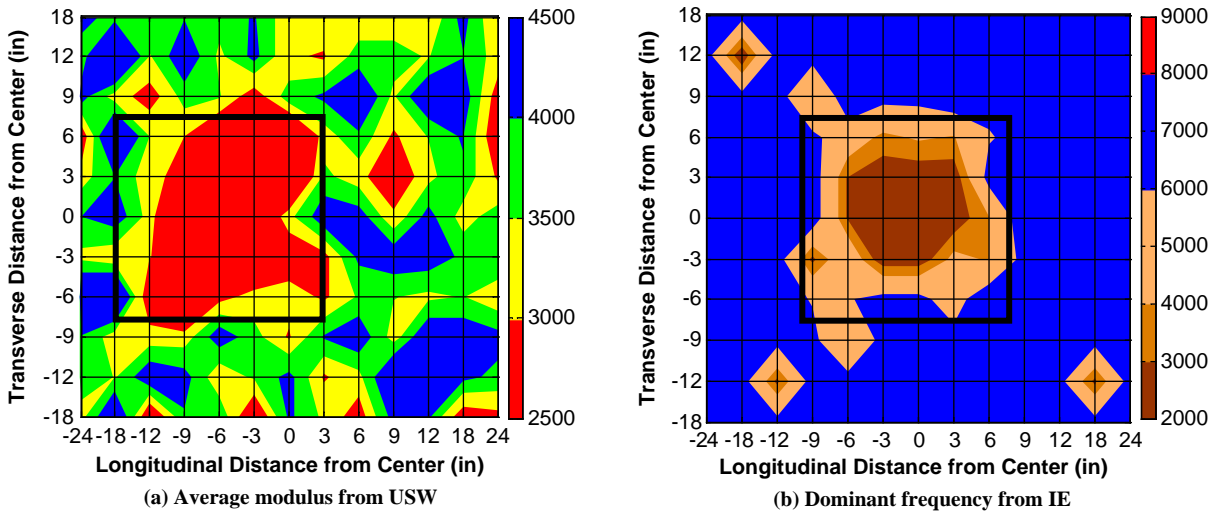
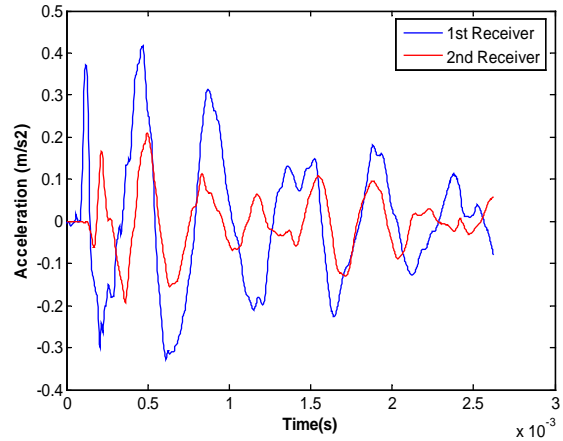


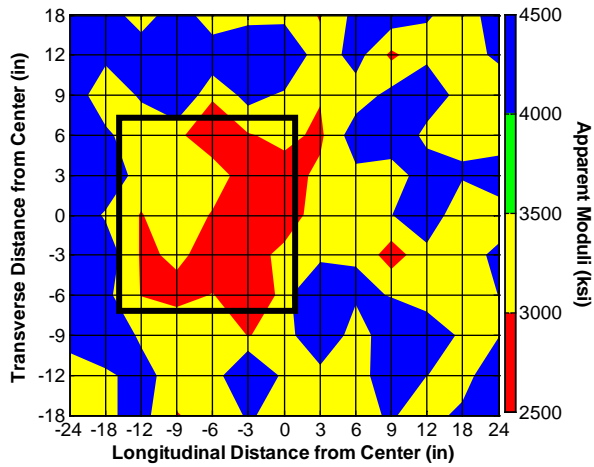
Figure U.45. Contour maps of acquired results from new PSPA for shotcrete Slab 6 (12 in. thick, with air void at 3-in. depth).



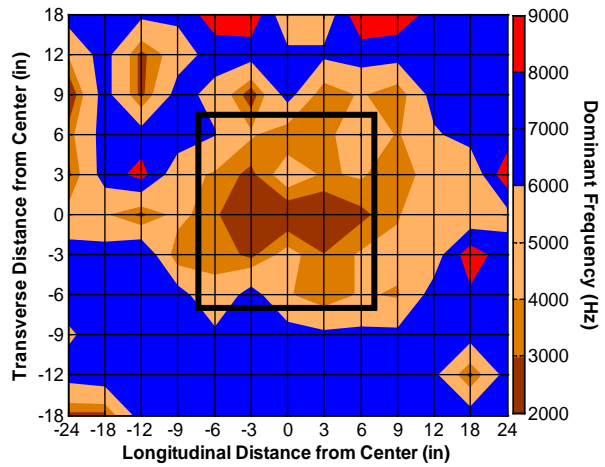
(a) Slab 7



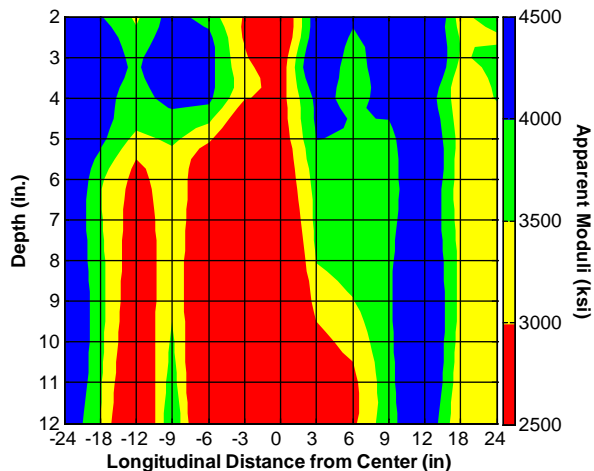
(b) Waveform obtained from PSPA at center point



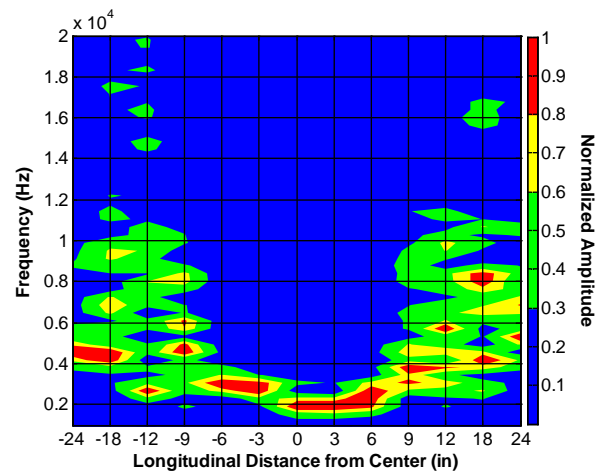
(c) Average modulus from USW



(d) Dominant frequency from IE



(e) USW B-scan along centerline



(f) IE Spectral B-scan along centerline

Figure U.46. Contour maps of acquired results from traditional PSPA for shotcrete Slab 7 (12 in. thick, with water void at 3-in. depth).

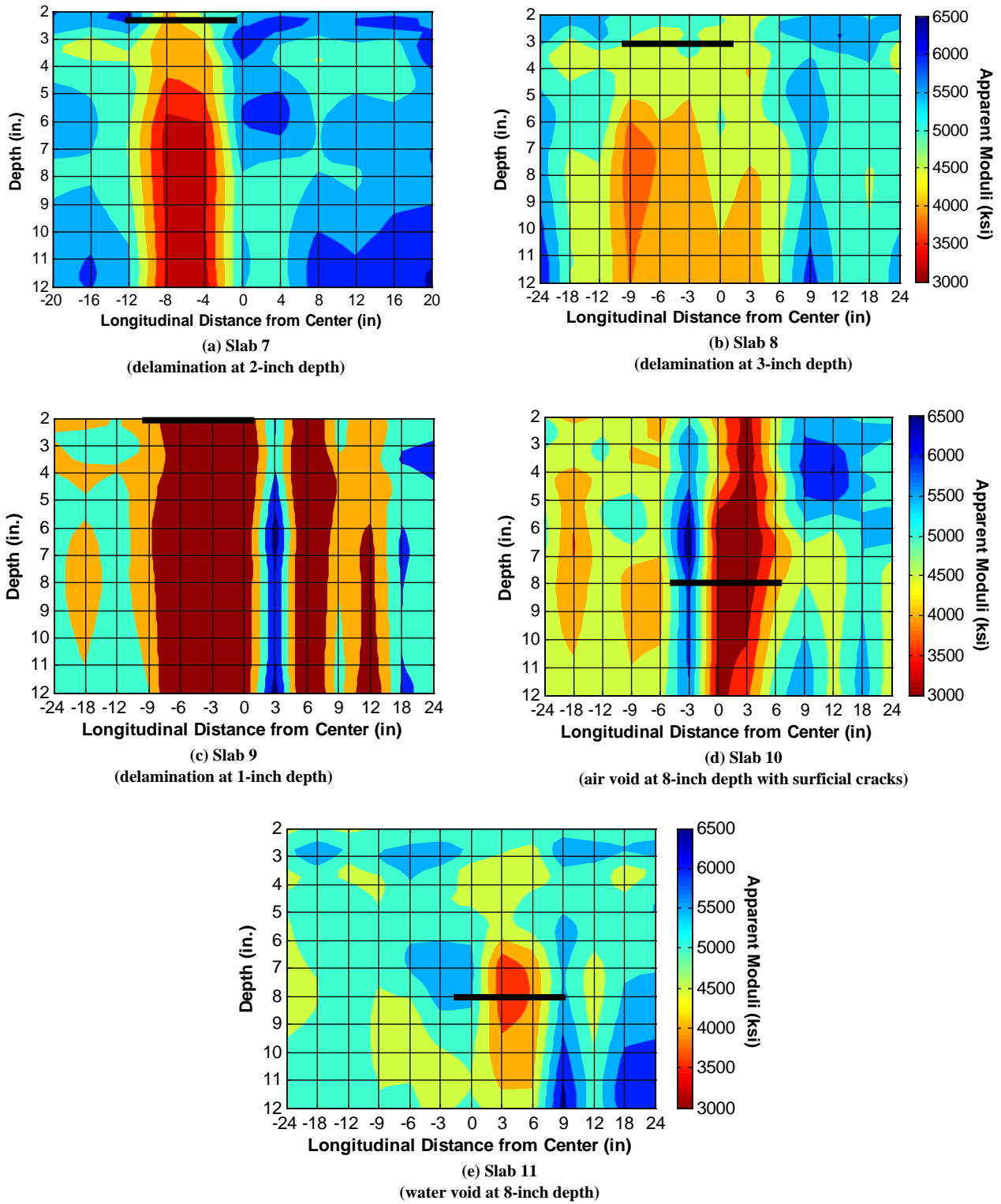
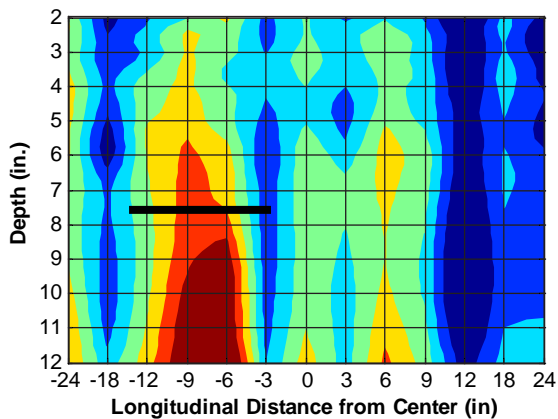
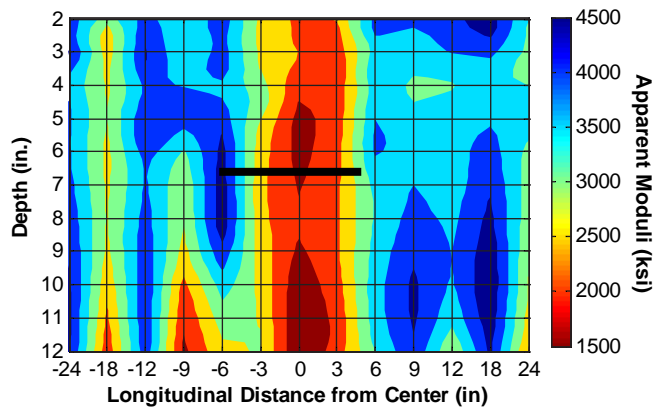


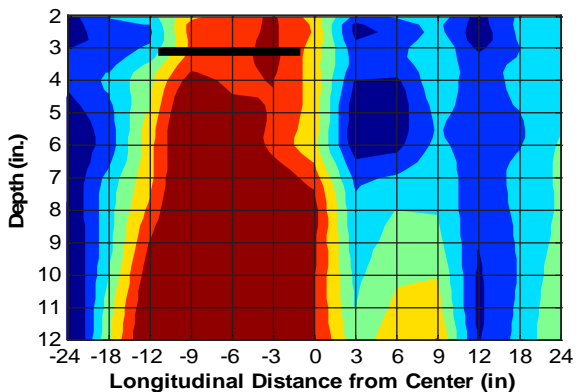
Figure U.47. USW B-scan along centerline for concrete slabs.



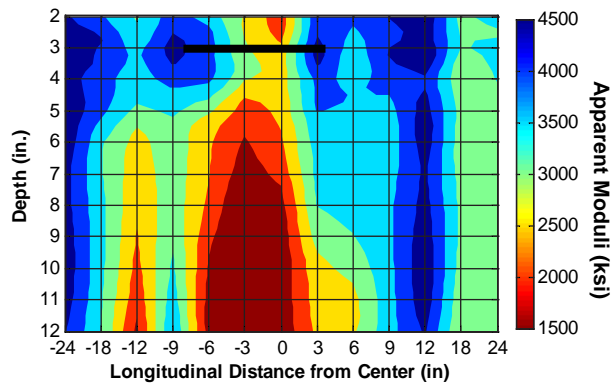
(a) Slab 4
(air void at 7.5-inch depth)



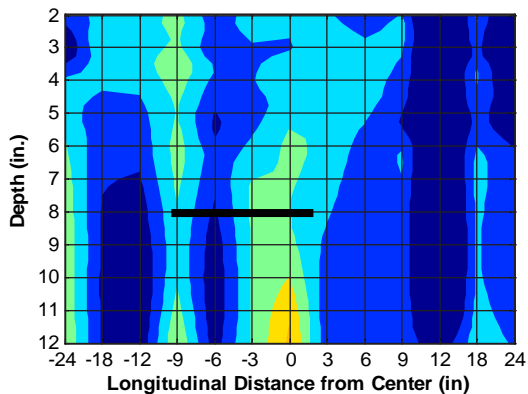
(b) Slab 5
(water void at 7.5-inch depth with surficial cracks)



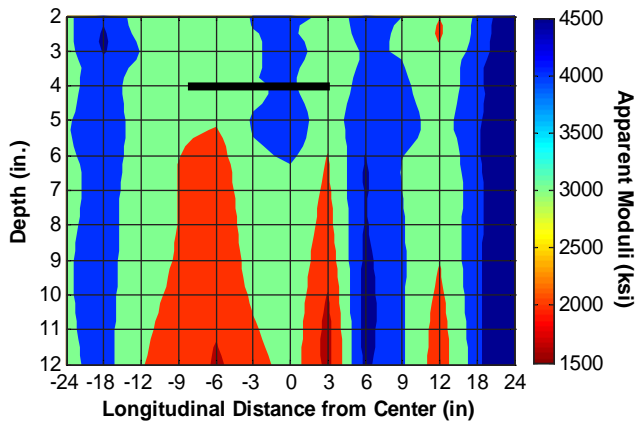
(c) Slab 6
(air void at 3-inch depth with surficial cracks)



(d) Slab 7
(water void at 3-inch depth)



(e) Slab 8
(delamination at 8-inch depth)



(f) Slab 9
(delamination at 4-inch depth)

Figure U.48. USW B-scan along centerline for shotcrete slabs. (Continued on next page.)

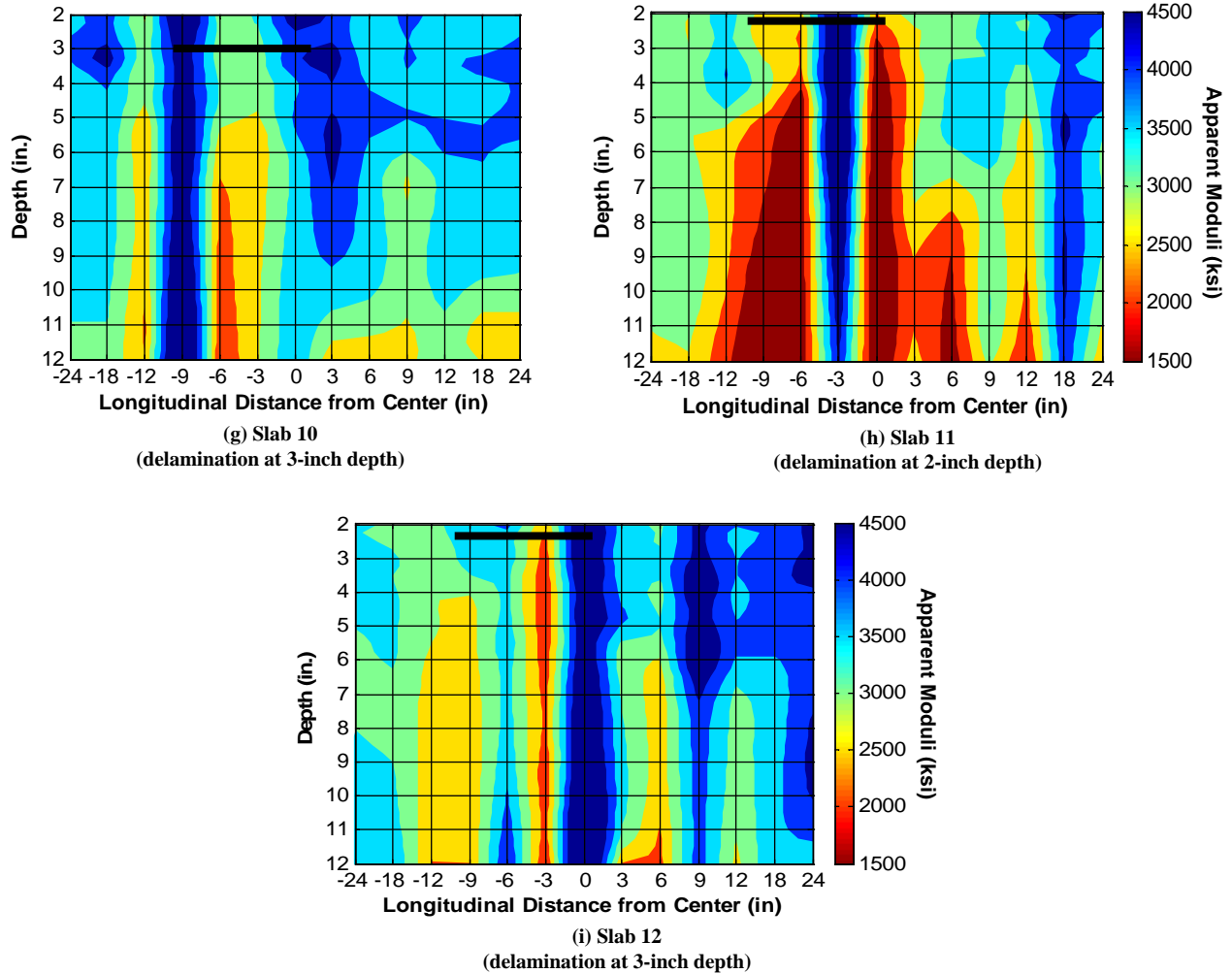


Figure U.48. (Continued.)

void was quite low, manifesting as severe cracking on the slab surface (see Figure U.23). The manifestation of the water-filled void at the same depth in Slab 11 could be detected; however, once again the quality of the concrete above that void was lower than the intact areas. Similar results were obtained in the defective shotcrete slabs in Figure U.48. The depths of the defects could be quantitatively estimated from the new B-scans only in an approximate fashion. However, the USW B-scans provided information about the change in quality of concrete placed after the installation of the defects. That is why the indication of defect (lower modulus) in some of the slabs started a few inches above the top of the defects.

References

- Azari, H., D. Yuan, S. Nazarian, and N. Gucunski. 2012. Impact of Testing Configuration and Data Analysis Approach on Detection of Delamination in Concrete Bridge Deck with Sonic Methods. In *Transportation Research Record: Journal of Transportation Research Board*, No. 22292, Transportation Research Board of the National Academies, Washington, D.C., pp. 113–124.
- Carino, N. J., M. Sansalone, and N. N. Hsu. 1986. A Point Source–Point Receiver, Pulse-Echo Technique for Flaw Detection in Concrete. *ACI Material Journal*, Vol. 83, No. 2, pp. 199–208.
- Gucunski, N., and A. Maher. 1998. Bridge Deck Condition Monitoring by Impact Echo Method. *Proc., International Conference MATEST '98—Life Extension*, Brijuni, Croatia, pp. 39–45.

APPENDIX V

Analysis of SPACETEC Data

Broken tiles on the interior of a tunnel (especially on the roof) are hazardous to vehicles passing through the tunnel at 55 mph. Routine tunnel maintenance measures include examination of tiles and detection and repair of loose tiles. The current state of the practice is visual inspection and hammer tapping of the tiles. Before this field investigation, the Chesapeake Bay Bridge-Tunnel (CBBT) owners had employed one engineer for 1 month to evaluate the bonding of roof tiles in the Chesapeake Channel Tunnel with the hammer sounding method. Broken and loose tiles were found and marked as such.

During the first round of field evaluation using the SPACETEC scanner in April 2011, a thermal anomaly (an isolated hot spot) around Station 483 that did not correspond to any known or marked loose tiles was detected. Manual measurements using impact echo (IE) and ultrasonic echo were carried out to investigate the bonding of tiles at the location of the thermal anomaly.

Both IE and ultrasonic echo tests were conducted on the selected eight-tile by eight-tile grid covering the location of the detected anomaly. IE was carried out on an adjacent four-tile by four-tile grid. Measurements were taken on individual tiles and repeated three times. Data analysis was done in time domains, examining the time histories of the signal recorded on each tile. Frequency spectra as well as the short-time Fourier transform-based spectrograms were calculated and examined. The envelopes of the US signals depicting their attenuation rates were also calculated.

To showcase the data corresponding to the areas of good bonding and possible debonding, two rows of the eight-tile by eight-tile grid were selected for presentation here. Figures V.1 to V.3 provide the IE test results corresponding to the tiles on the sixth row (from the top) of the eight-tile by eight-tile grid, illustrating the time histories, spectra, and short-time Fourier transform (STFT) spectrograms. The time signals in Figure V.1 attenuate rapidly (the impact energy propagates in the

lining); and the frequency spectra in Figure V.2 are broadband with spectral energy centered on 50 kHz. Four records (one on the top left and three at the bottom left) depict additional frequency peaks of lower frequencies as well. Time and frequency features can be seen simultaneously in the spectrograms of Figure V.3. These characteristics in time and frequency domains are indications of good bonding between the tested tiles and the underlying lining.

Figures V.4 through V.6 provide the IE test results corresponding to the tiles on the third row (from the top) of the eight-tile by eight-tile grid, including the time histories, spectra, and spectrograms. In contrast to those shown in Figure V.1, the time signals of Figure V.4 show little or no attenuation. The frequency spectra in Figure V.5 contain multiple equally spaced frequency peaks. Both measured time and frequency features are expected for loose tiles, as the debonding from the tunnel lining leads to multiple reflections of the acoustic energy between the tile and the underlying lining.

The individual records obtained on each tile were analyzed in both time and frequency domains, and their assessed bonding conditions were color coded and superimposed on the thermal image in Figure V.7. In this figure, green indicates well-bonded tiles, while loose tiles are marked with orange-to-red spots. A comparison of the obtained results reveals that the tiles at the thermal anomaly detected by SPACETEC as a noticeable warm spot were diagnosed as debonded by IE measurements.

Ultrasonic echo measurements were taken on the same eight-tile by eight-tile grid (the eight-tile by eight-tile grid *only*) as described for IE testing. The ultrasonic echo time histories and spectra obtained on the sixth row of the tiles (from top) are shown in Figures V.8 and V.9, respectively. The ultrasonic echo time histories and spectra obtained on the third row of the tiles (from top) are shown in Figures V.10 and V.11, respectively.

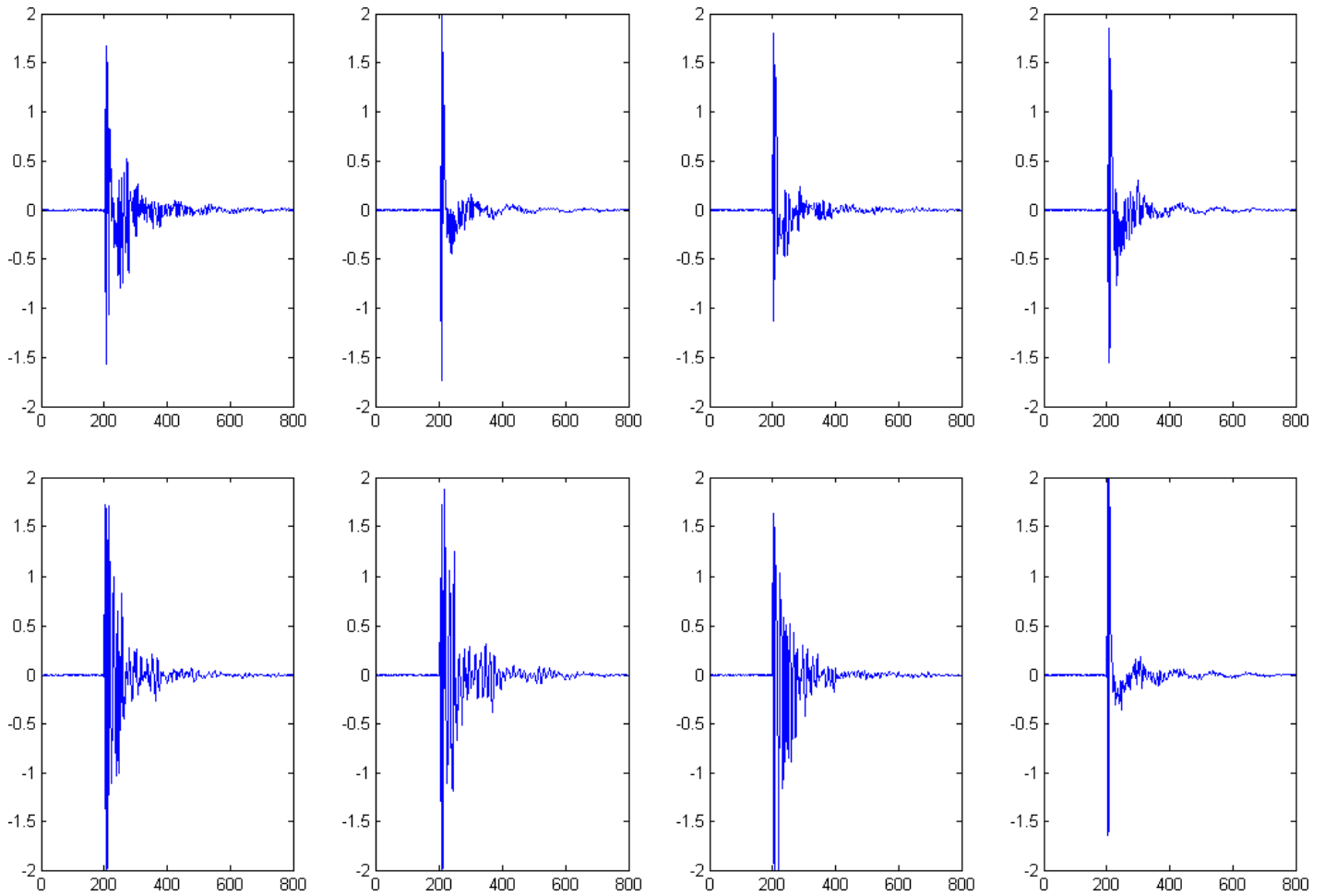


Figure V.1. Time histories of IE signals along the sixth row of the eight-tile by eight-tile grid at about Station 483 of the Chesapeake Channel Tunnel, where the thermal anomaly in SPACETEC data was detected.

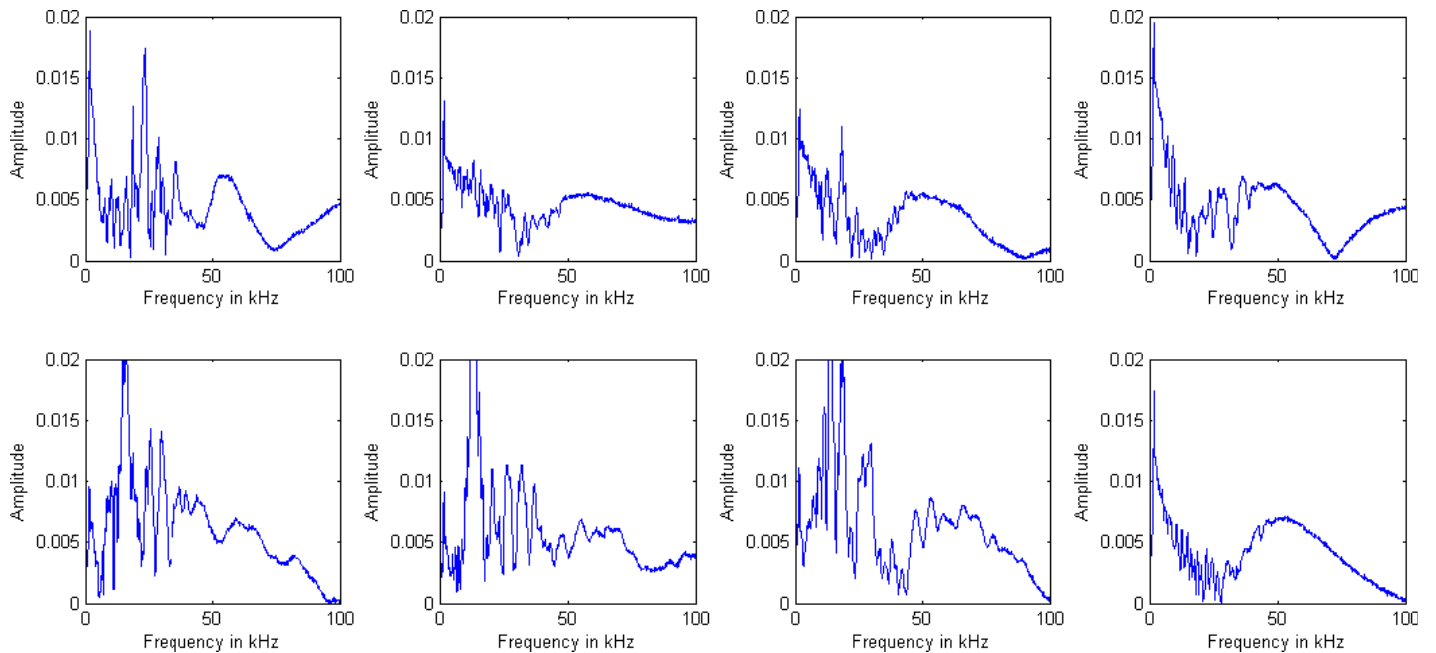


Figure V.2. Frequency spectra of IE signals along the sixth row of the eight-tile by eight-tile grid at about Station 483 of the Chesapeake Channel Tunnel, where the thermal anomaly in SPACETEC data was detected.

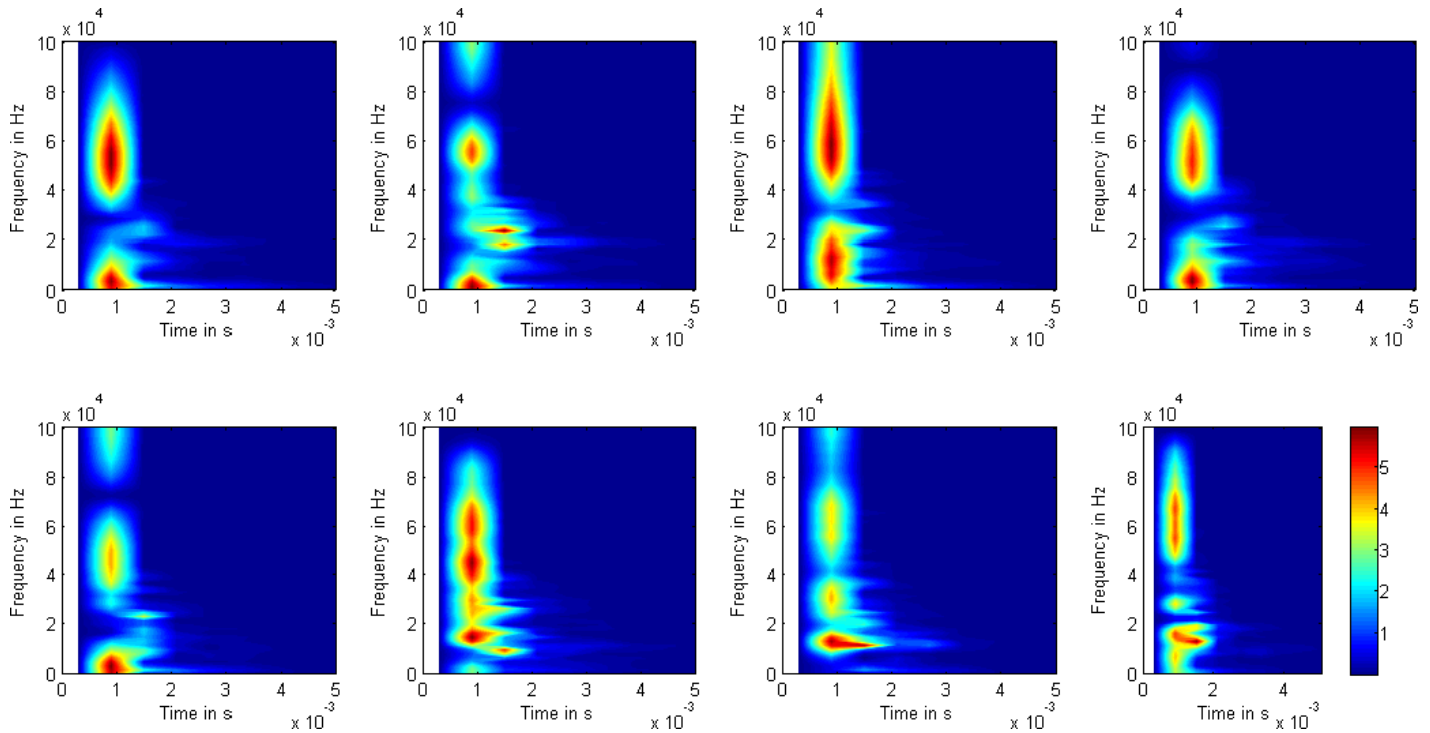


Figure V.3. STFT spectrograms of IE signals along the sixth row of the eight-tile by eight-tile grid at about Station 483 of the Chesapeake Channel Tunnel, where the thermal anomaly in SPACETEC data was detected.

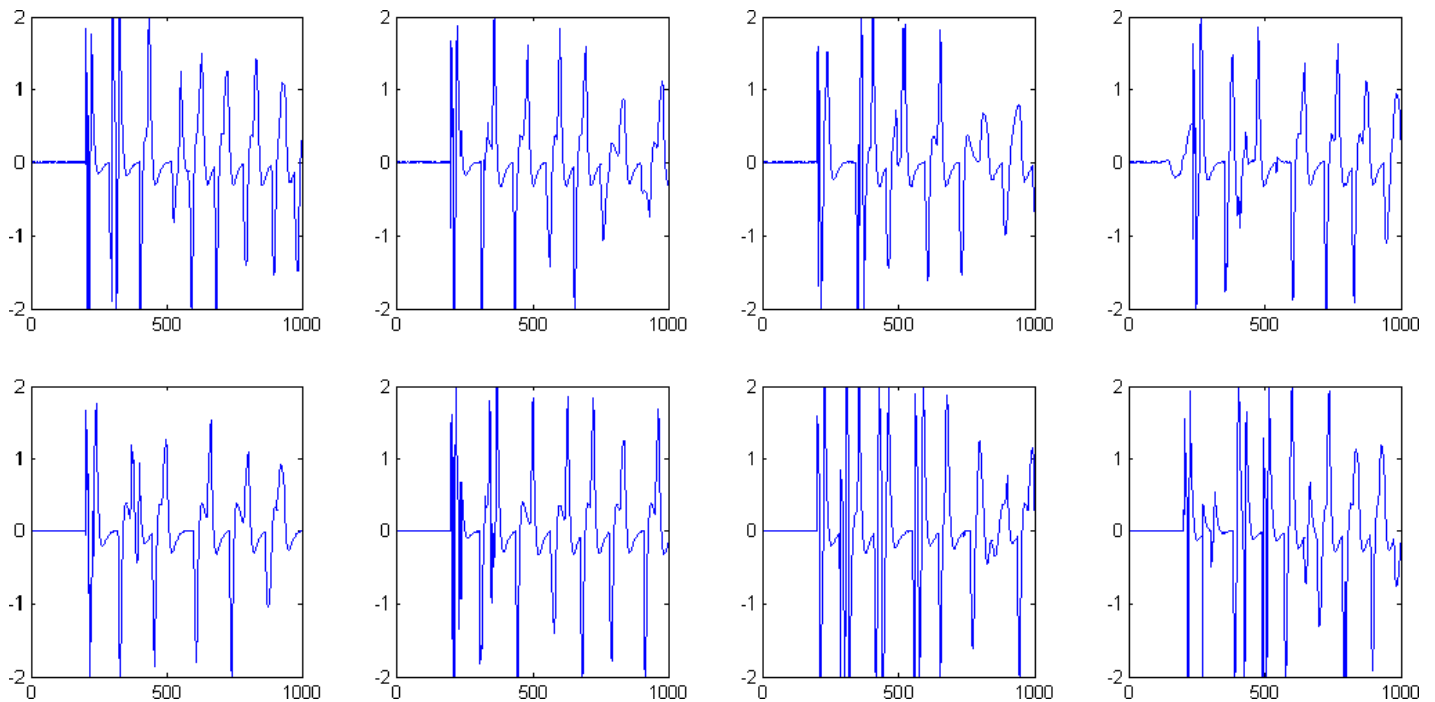


Figure V.4. Time histories of IE signals along the third row of the eight-tile by eight-tile grid at about Station 483 of the Chesapeake Channel Tunnel, where the thermal anomaly in SPACETEC data was detected.

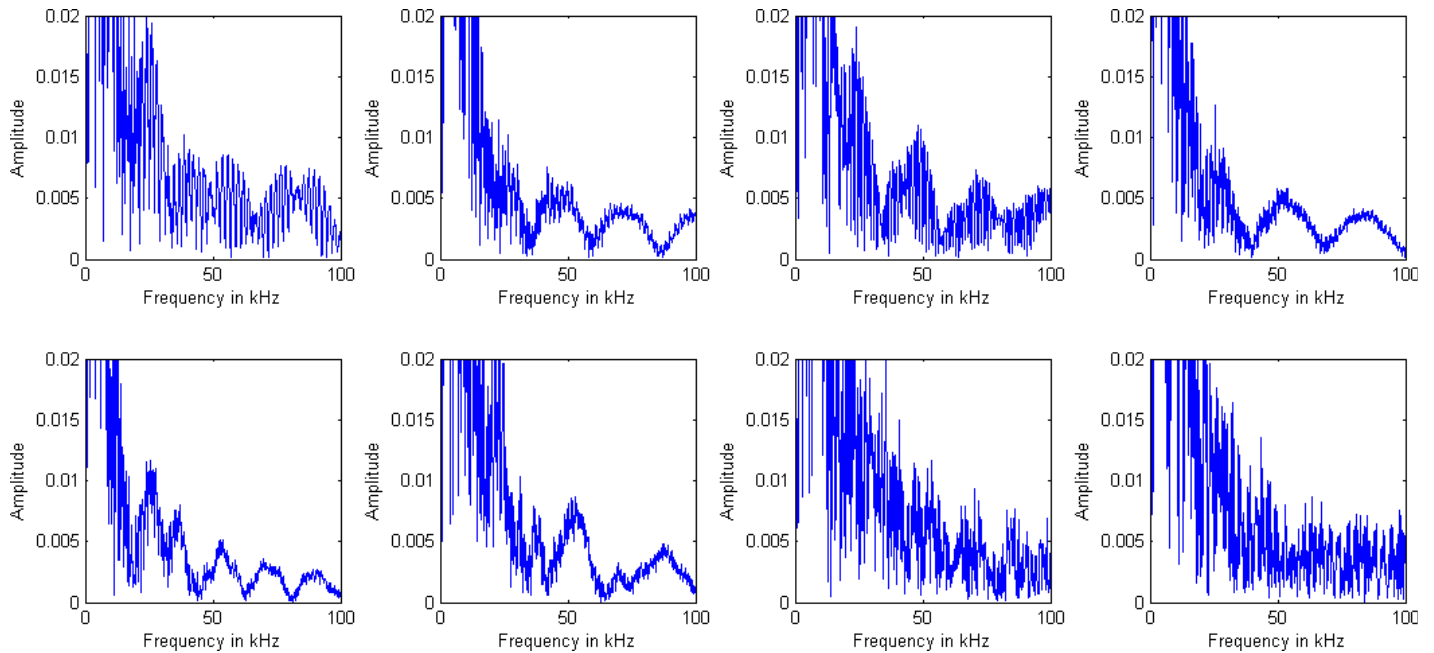


Figure V.5. Frequency spectra of IE signals along the third row of the eight-tile by eight-tile grid at about Station 483 of the Chesapeake Channel Tunnel, where the thermal anomaly in SPACETEC data was detected.

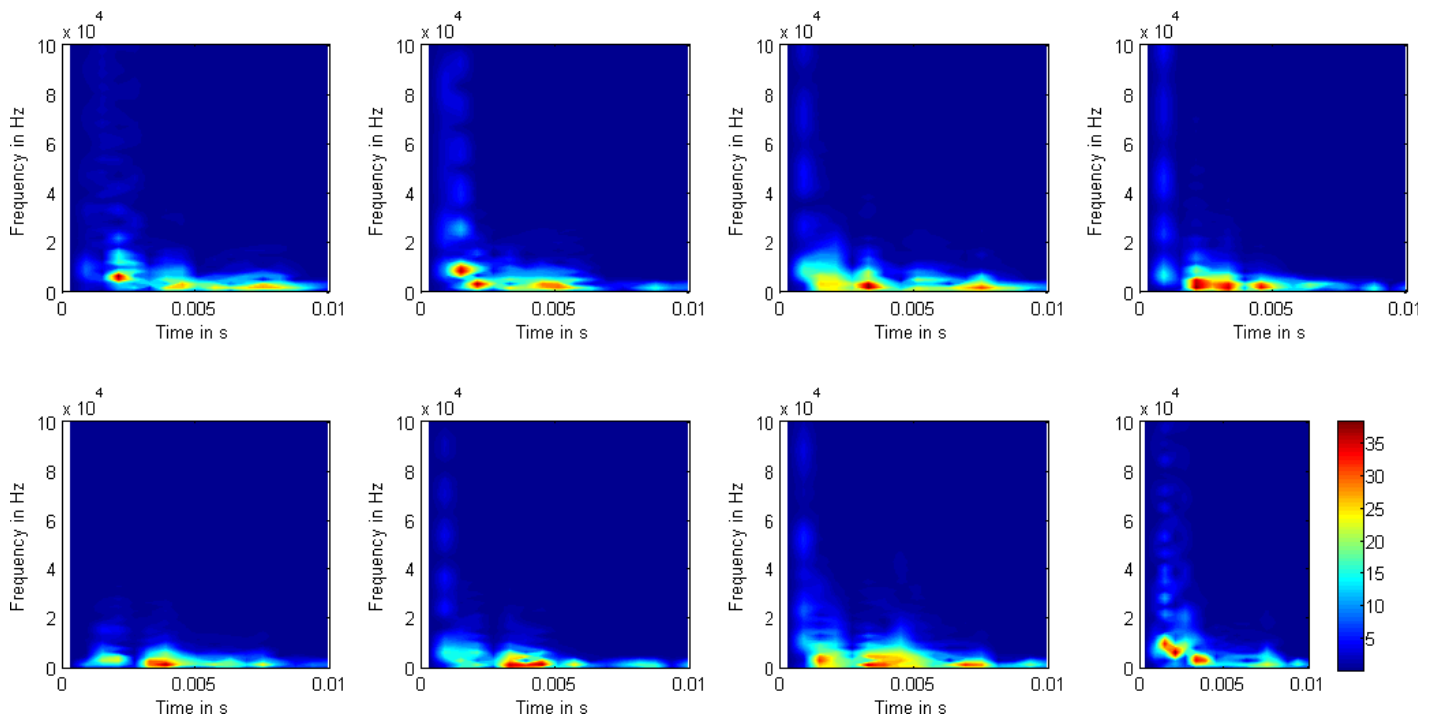


Figure V.6. STFT spectrograms of IE signals along the third row of the eight-tile by eight-tile grid at about Station 483 of the Chesapeake Channel Tunnel, where the thermal anomaly in SPACETEC data was detected.

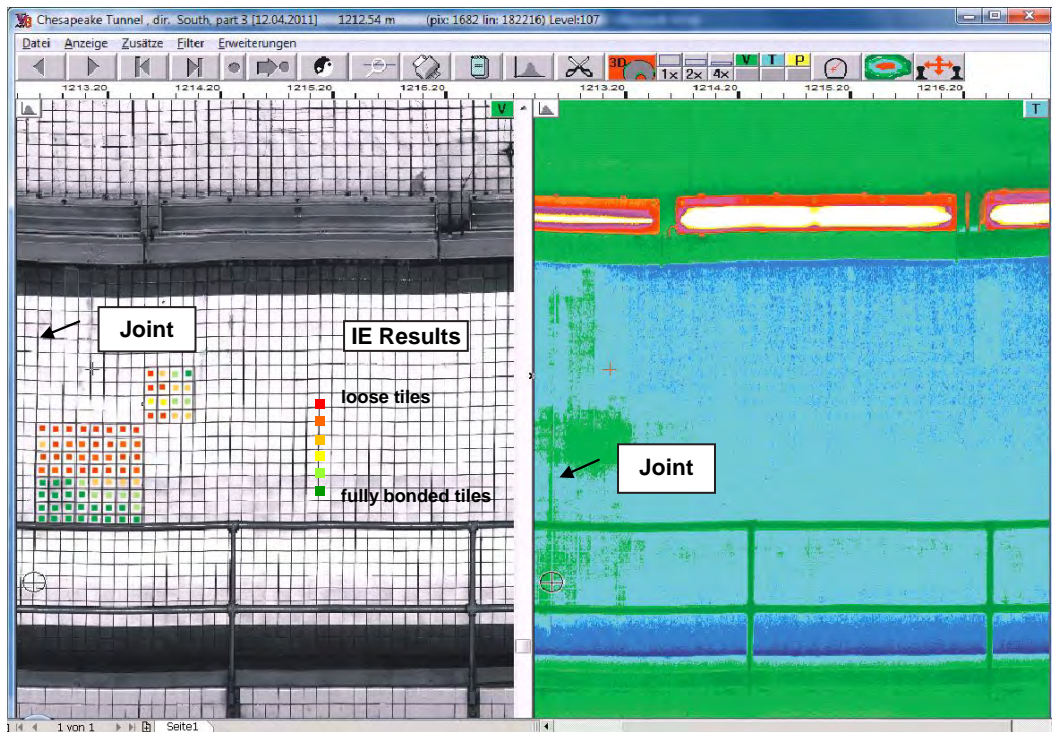


Figure V.7. Visual image (left) and thermal image (right) at about Station 483 of the Chesapeake Channel Tunnel. Bonding conditions of tiles around the location of the thermal anomaly (warm spot) evaluated on the basis of IE measurements are color coded and superimposed on the thermal image.

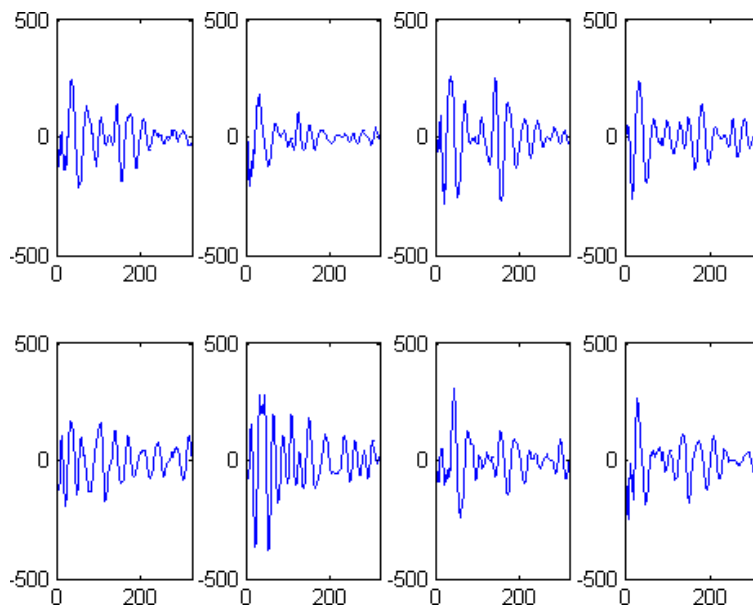


Figure V.8. Ultrasonic echo time histories along the sixth row of the eight-tile by eight-tile grid at about Station 483 of the Chesapeake Channel Tunnel, where the thermal anomaly in SPACETEC data was detected.

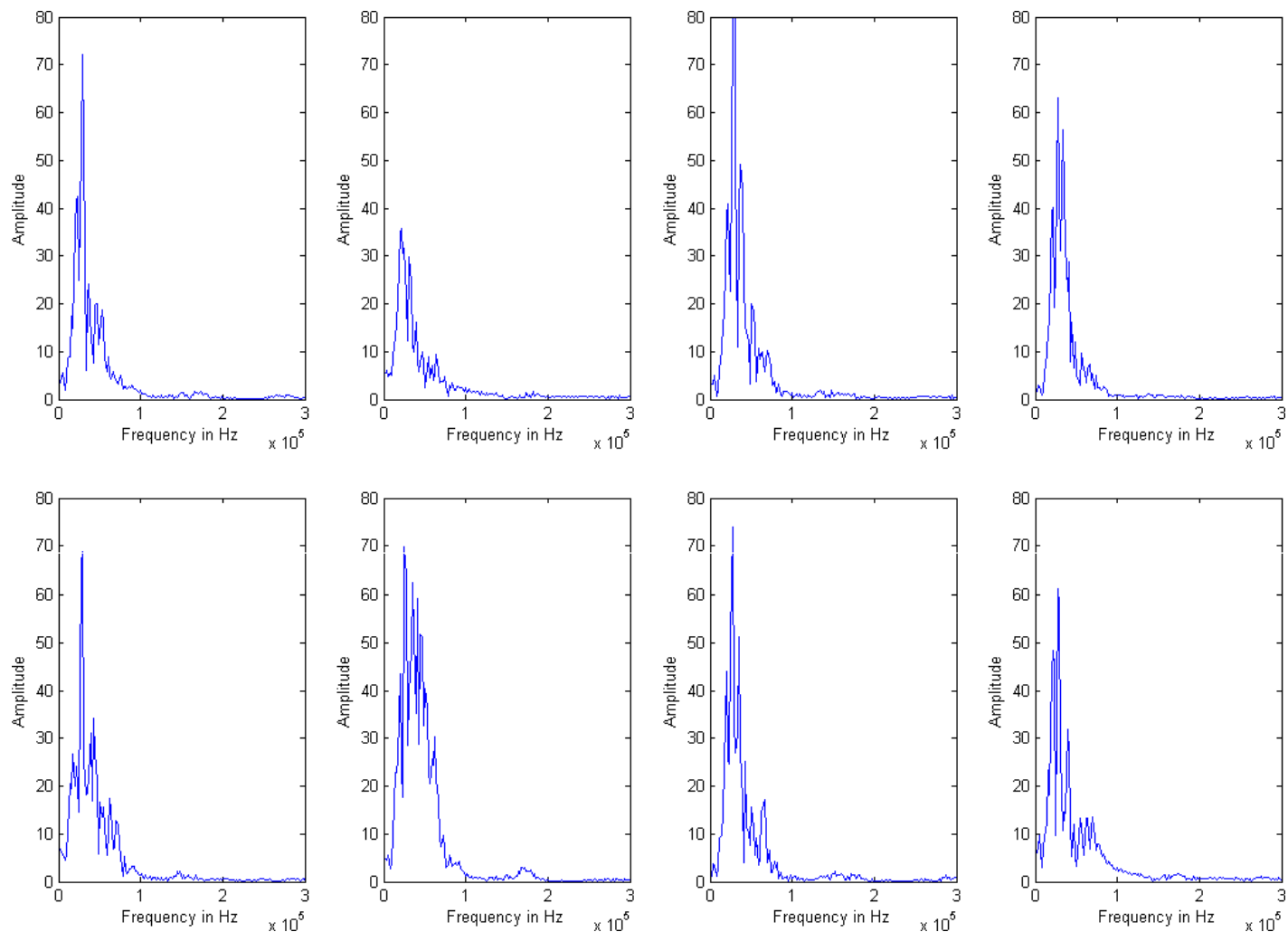


Figure V.9. Frequency spectra of ultrasonic echo signals along the sixth row of the eight-tile by eight-tile grid at about Station 483 of the Chesapeake Channel Tunnel, where the thermal anomaly in SPACETEC data was detected.

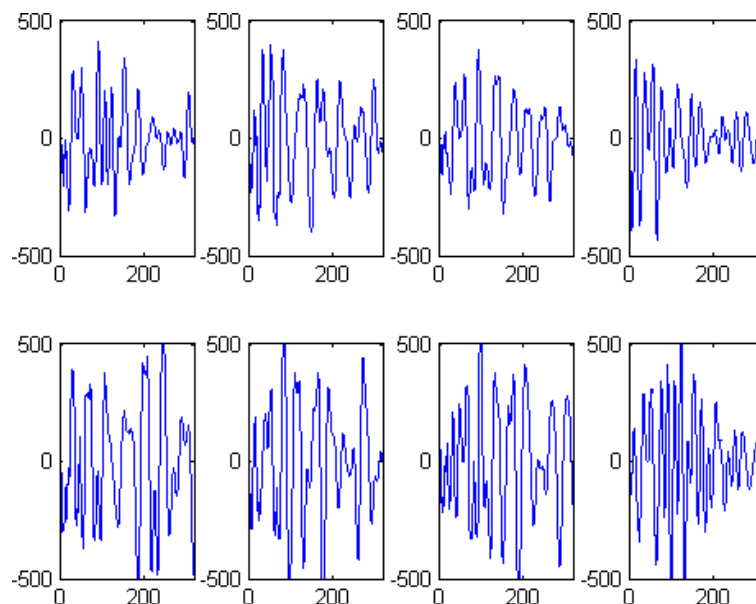


Figure V.10. Ultrasonic echo time histories along the third row of the eight-tile by eight-tile grid at about Station 483 of the Chesapeake Channel Tunnel, where the thermal anomaly in SPACETEC data was detected.

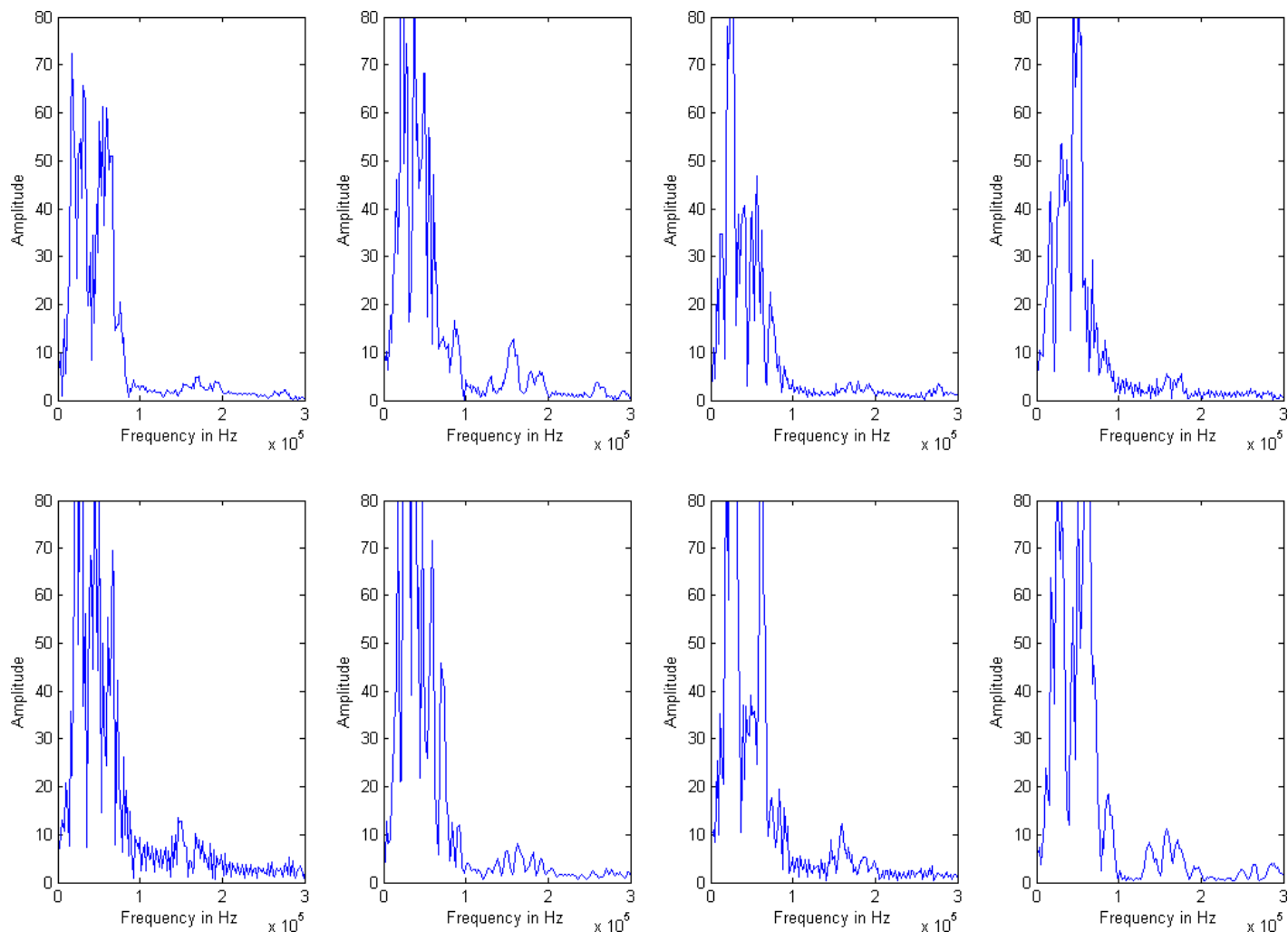


Figure V.11. Frequency spectra of ultrasonic echo signals along the third row of the eight-tile by eight-tile grid at about Station 483 of the Chesapeake Channel Tunnel, where the thermal anomaly in SPACETEC data was detected.

The characteristics of the ultrasonic echo signals were similar to those of the IE signals: when the tiles were loose, the time signals were less attenuated. The spectral energy in the frequency spectra on bonded tiles were centered on 50 kHz (which is about the center frequency of the transducer). The spectra obtained on presumably debonded tiles were broader, showing multiple peaks. Ultrasonic echo amplitudes were generally higher on debonded tiles. However, given the variability of the pressing pressure during hand measurements, no reliable correlation between the ultrasonic echo amplitude and debonding condition could be concluded.

The individual ultrasonic echo signals were analyzed, and their bonding conditions were color coded and superimposed on the thermal image of Figure V.12. Similar to the IE results, the manual ultrasonic echo measurements indicated the presence of loose tiles where a thermal anomaly

(warm spot) by SPACETEC was registered. It appears that loose tiles can be detected as thermal anomalies in SPACETEC thermal images.

To further investigate this hypothesis, the thermal and visual images obtained from the SPACETEC scanner along one direction were compared with the manual hammer sounding maps provided to the research team by CBBT owners. An example of such comparisons obtained at about Station 475 is given in Figure V.13. Thermal anomalies (marked green) seemed to correspond well to the tiles deemed as loose (or debonded) during the hammer sounding survey.

A statistical analysis was performed to establish the sensitivity of thermal and visual imaging to the debonding of tiles on the tunnel ceiling, as detected by hammer sounding. Both thermal and visual images were used to find anomalies in SPACETEC survey results. Data collected along one direction

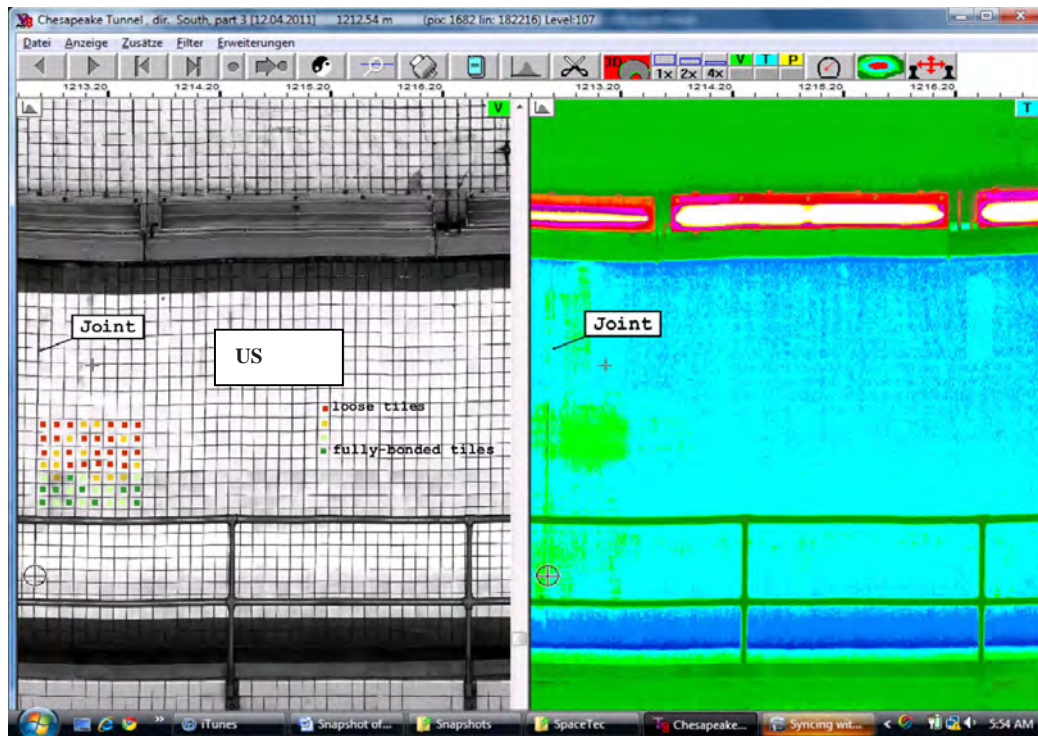


Figure V.12. Visual image (left) and thermal image (right) at about Station 483 of the Chesapeake Channel Tunnel. Bonding conditions of tiles around the location of the thermal anomaly (warm spot) evaluated based on ultrasonic echo (US) measurements are color coded and superimposed on the thermal image.

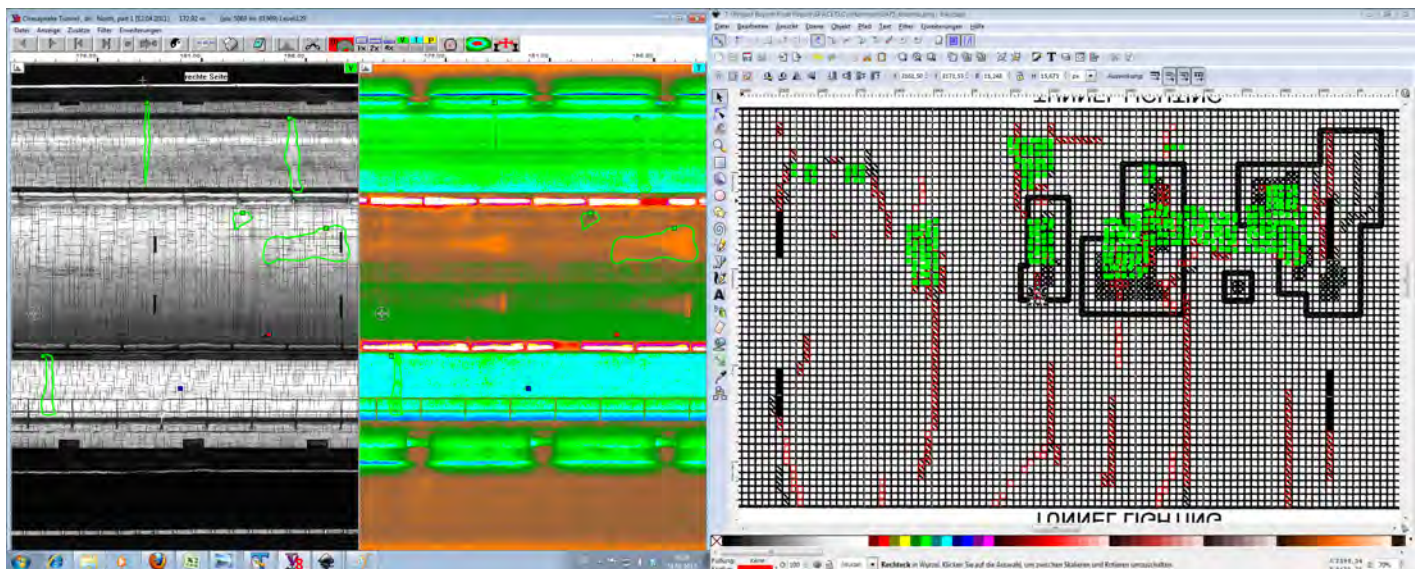


Figure V.13. Comparison of anomalies detected in SPACETEC visual and thermal images (left) against results of manual hammer sounding survey conducted by tunnel owners (right) at about Station 475. Thermal anomalies are superimposed on the hammer sounding map as green-colored tiles, while broken tiles seen on visual images are shown as red-hatched areas. The hammer sounding data and the SPACETEC data were collected in opposite directions; to compare the data sets, the plan sheet images had to be reversed.

(southbound) was used for this analysis. The sensitivity was calculated according to Equation V.1:

$$\text{Sensitivity} = TP / (TP + FN) \quad (\text{V.1})$$

where TP and FN stand for true positives and false negatives, respectively. Given the nature of the available data, only the sensitivity could be estimated here. The hammer sounding results were assumed to give the true number and location of debonded tiles. That means anomalies detected by SPACETEC, where no delaminated tiles were marked, were considered false alarms.

Sensitivity was calculated separately for defect groups of various sizes (tile counts) as shown in Figure V.14. The overall sensitivity (independent of the defect size) was obtained as 0.71, or 71%. Ninety-seven percent of areas including more than 50 tiles could be detected, compared with 55% for areas covering less than 50 tiles. A visual comparison of thermal and visual anomalies versus the delaminated tiles is provided in Figures V.15 through V.37. In these figures, thermal anomalies

are superimposed on hammer sounding maps at various locations along the tunnel. The hammer sounding maps were flipped because the hammer sounding data and the thermal anomaly data were collected in opposite directions.

An additional analysis was performed to investigate why some of the debonded areas were not detected in SPACETEC data. Very small debonded areas covering less than 20 tiles seem not to be always detectable in thermal images obtained during this particular survey. Reflection of light from the surface of tiles (at certain scanning angles) and the interference with the temperature gradient in front of the air vents were found to be the top two factors why larger debonded areas were not detected.

This analysis suggests that a combination of thermal and visual imaging offers a reliable alternative to the tedious practice of hammer sounding on individual tiles. The great advantage of such scanning operations becomes obvious considering the speed of the SPACETEC survey (about 1 h at 1.5 km/h, or 1 mph) compared with that of hammer sounding (one man-month).

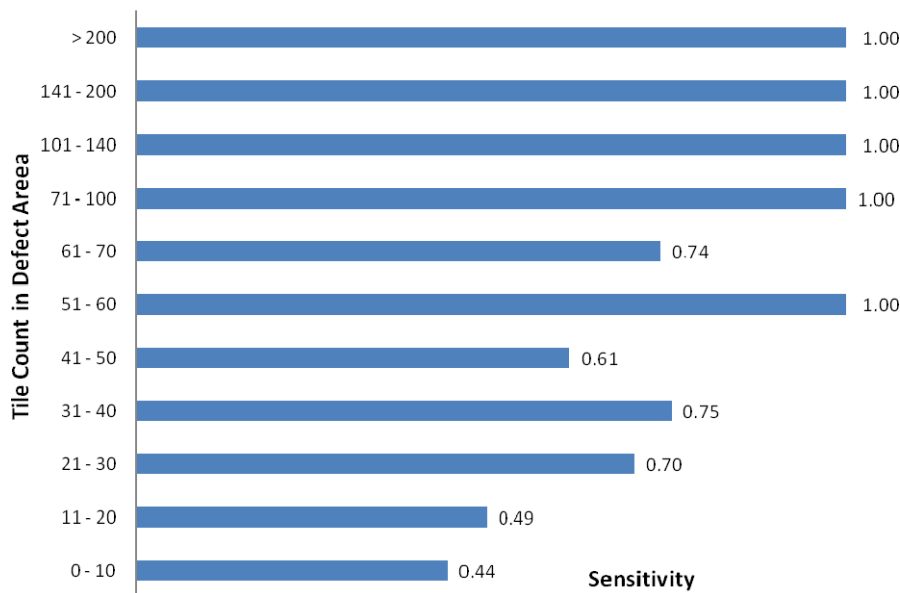


Figure V.14. Sensitivity of SPACETEC thermal and visual imaging to debonded tiles as detected by manual hammer sounding. Sensitivity is calculated for defect areas of various sizes (tile count).

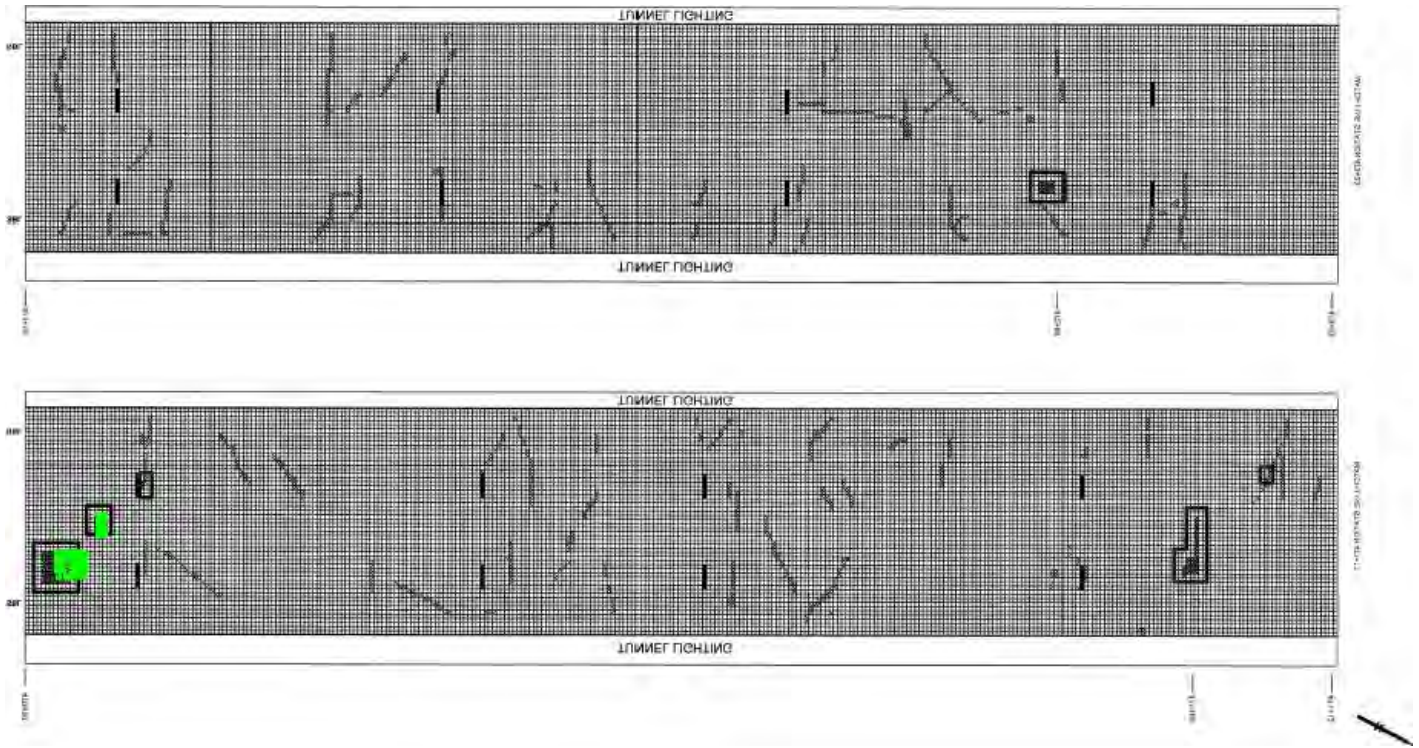


Figure V.15. Visual comparison of thermal anomalies and delaminated tiles (as detected by hammer sounding) between Stations 470+00 and 472+23.

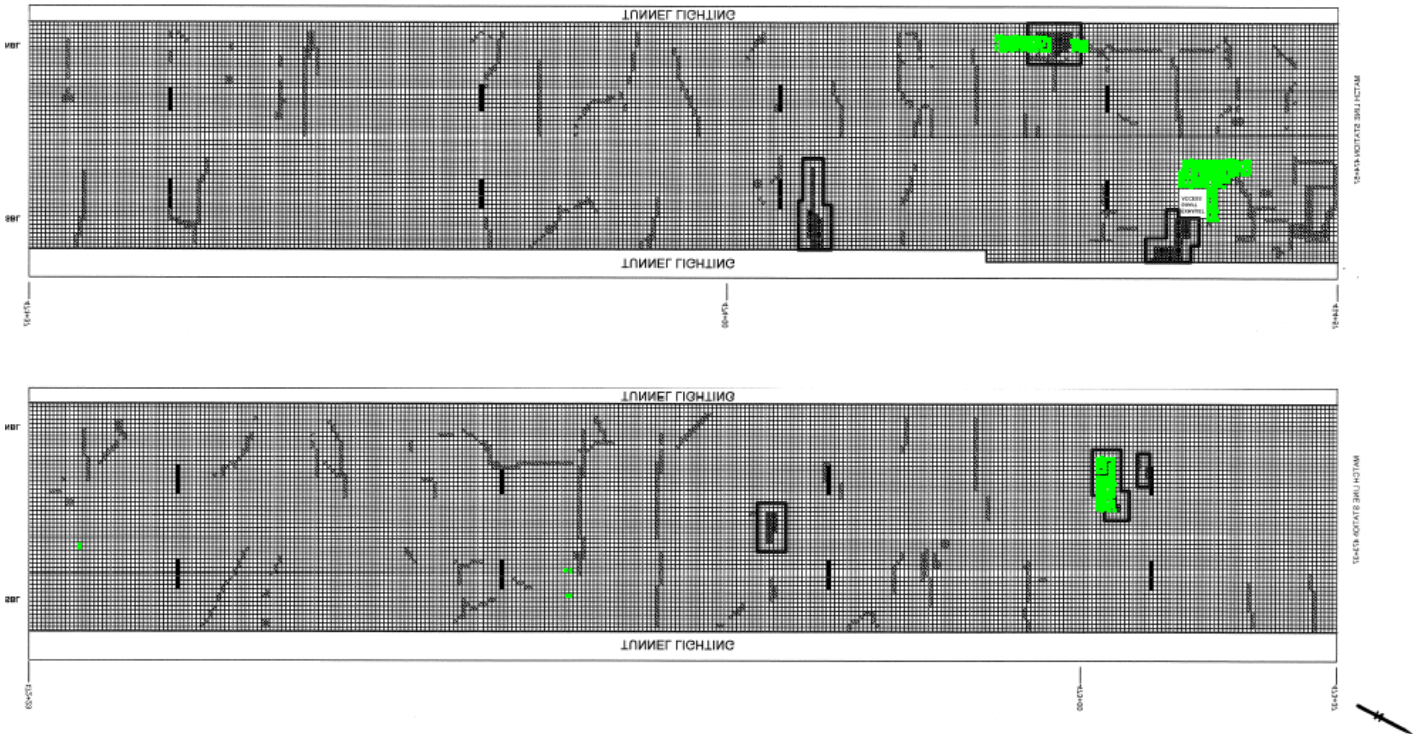


Figure V.16. Visual comparison of thermal anomalies and delaminated tiles (as detected by hammer sounding) between Stations 472+23 and 474+57.

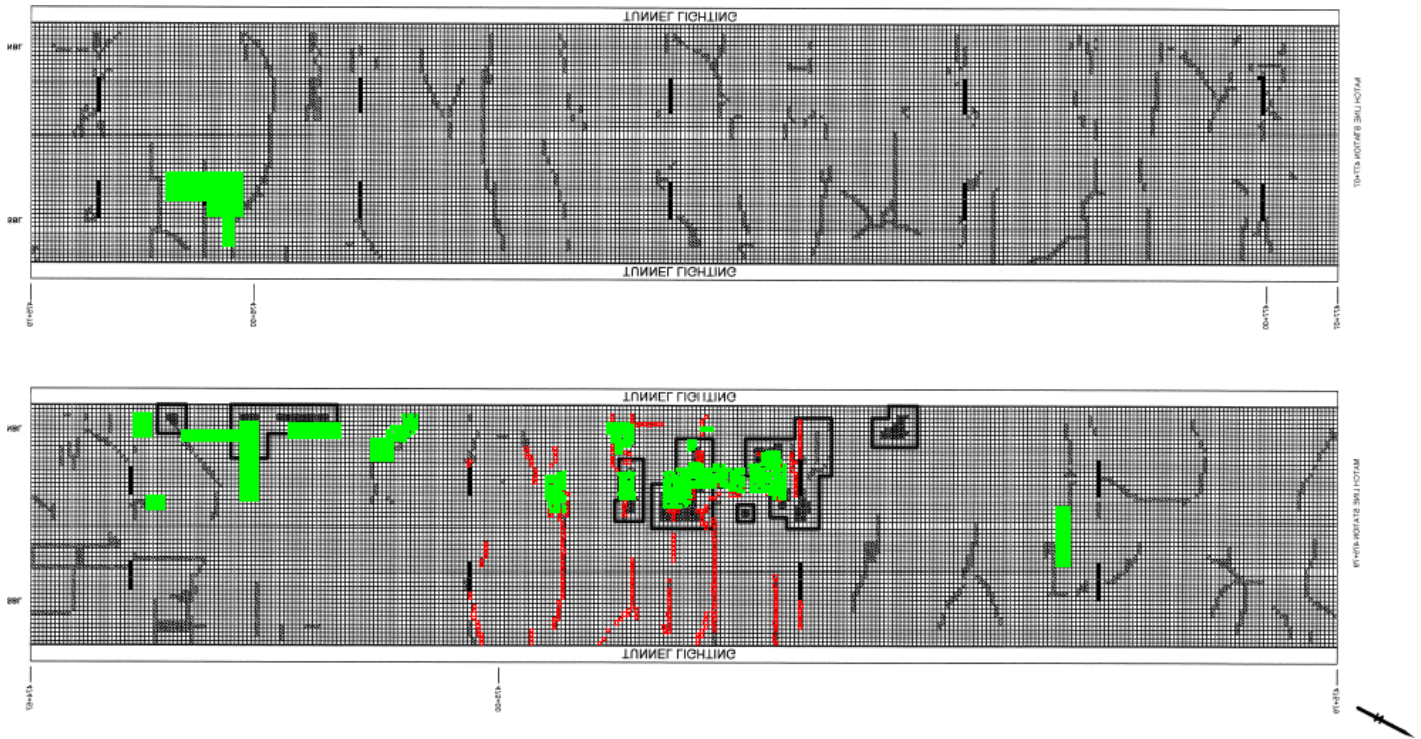


Figure V.17. Visual comparison of thermal anomalies and delaminated tiles (as detected by hammer sounding) between Stations 474+57 and 477+07.

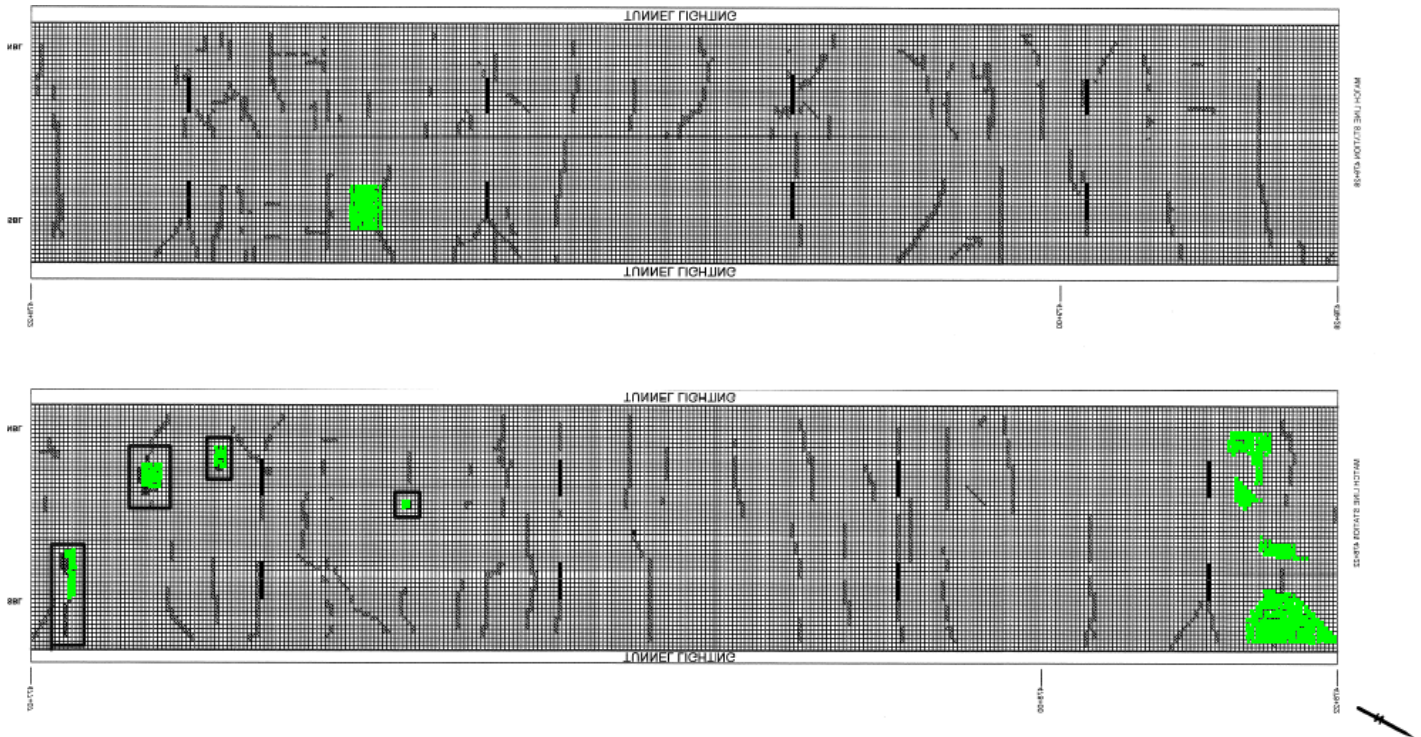


Figure V.18. Visual comparison of thermal anomalies and delaminated tiles (as detected by hammer sounding) between Stations 477+07 and 479+28.

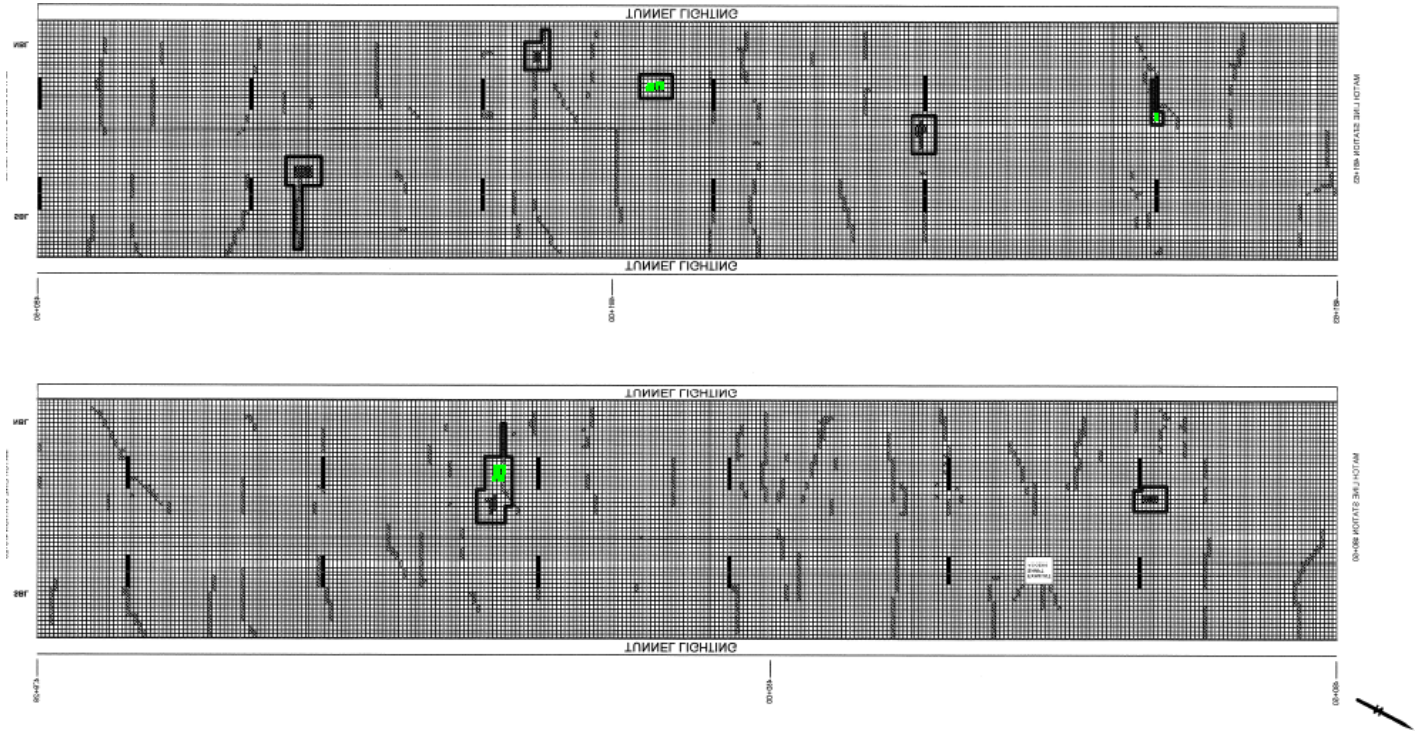


Figure V.19. Visual comparison of thermal anomalies and delaminated tiles (as detected by hammer sounding) between Stations 479+28 and 481+63.

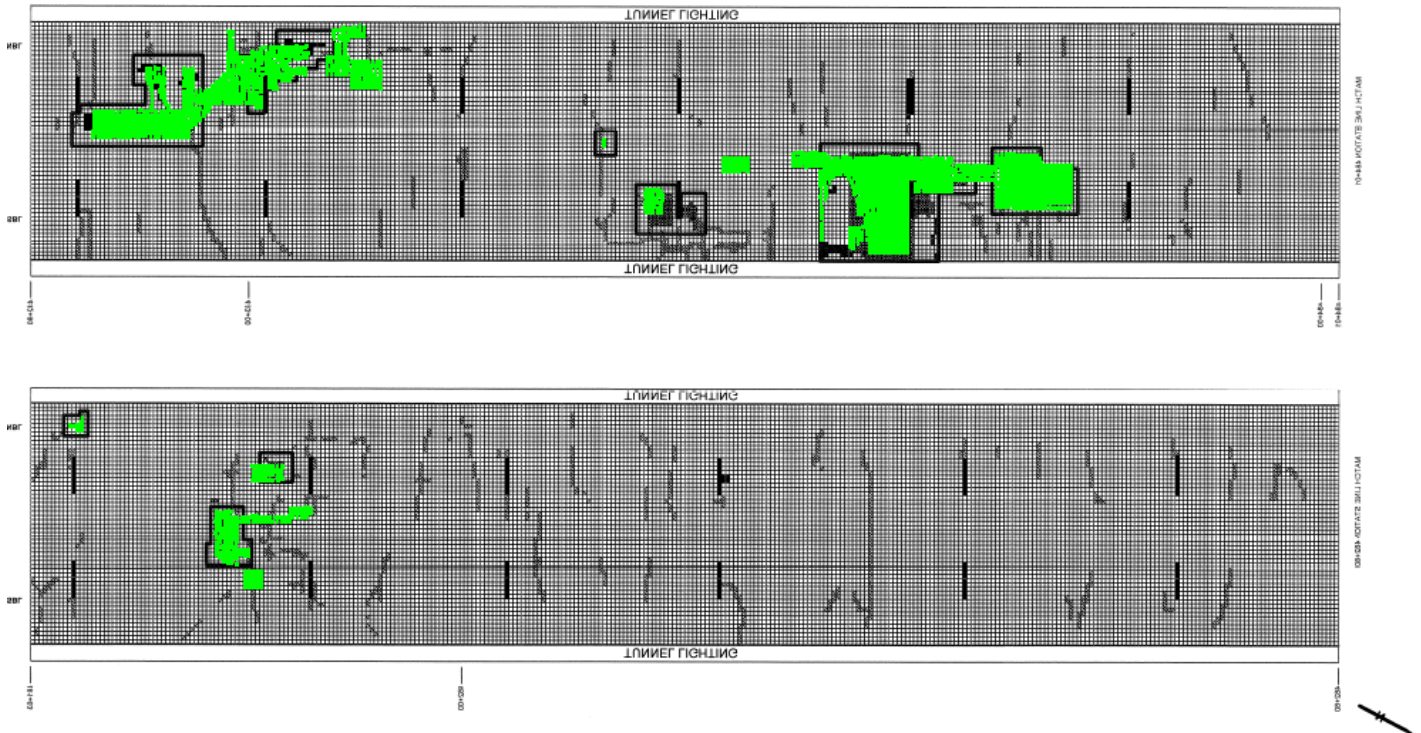


Figure V.20. Visual comparison of thermal anomalies and delaminated tiles (as detected by hammer sounding) between Stations 481+63 and 484+01.

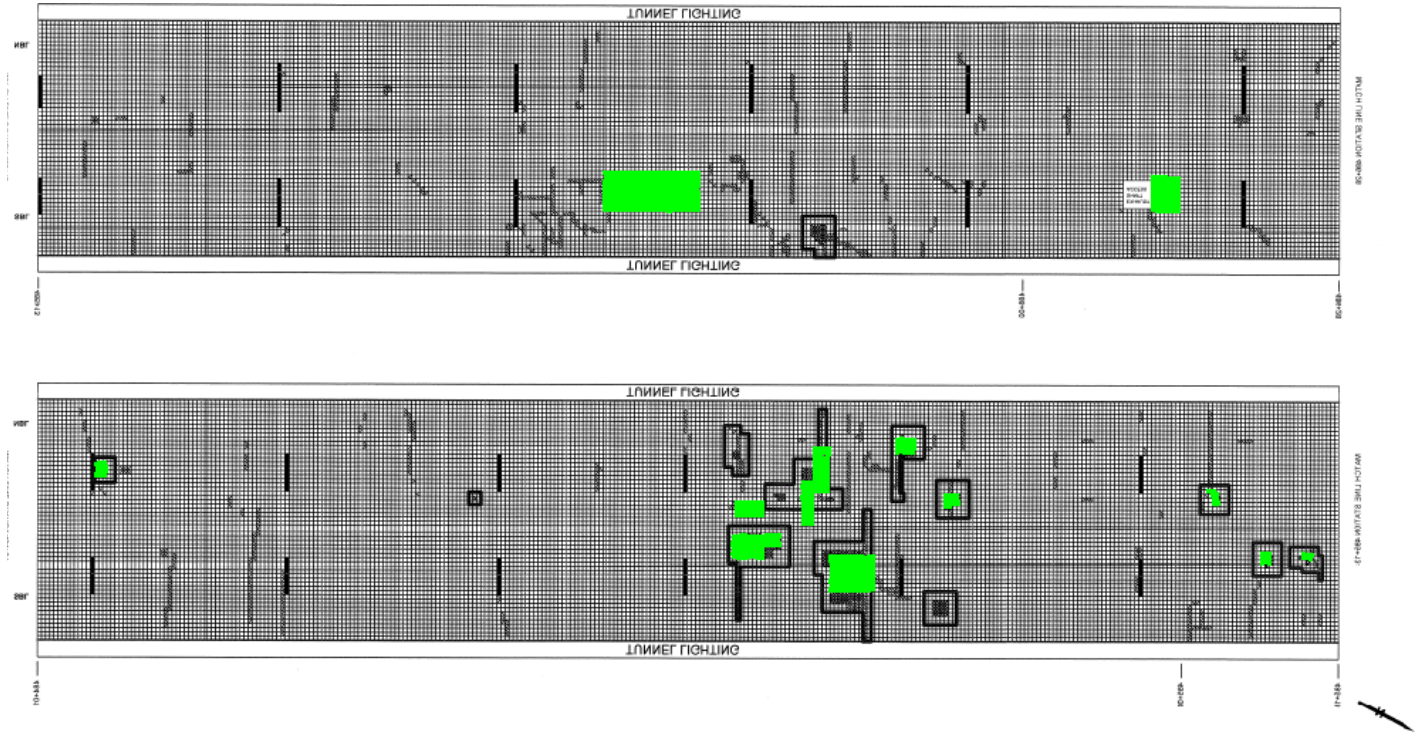


Figure V.21. Visual comparison of thermal anomalies and delaminated tiles (as detected by hammer sounding) between Stations 484+01 and 486+28.

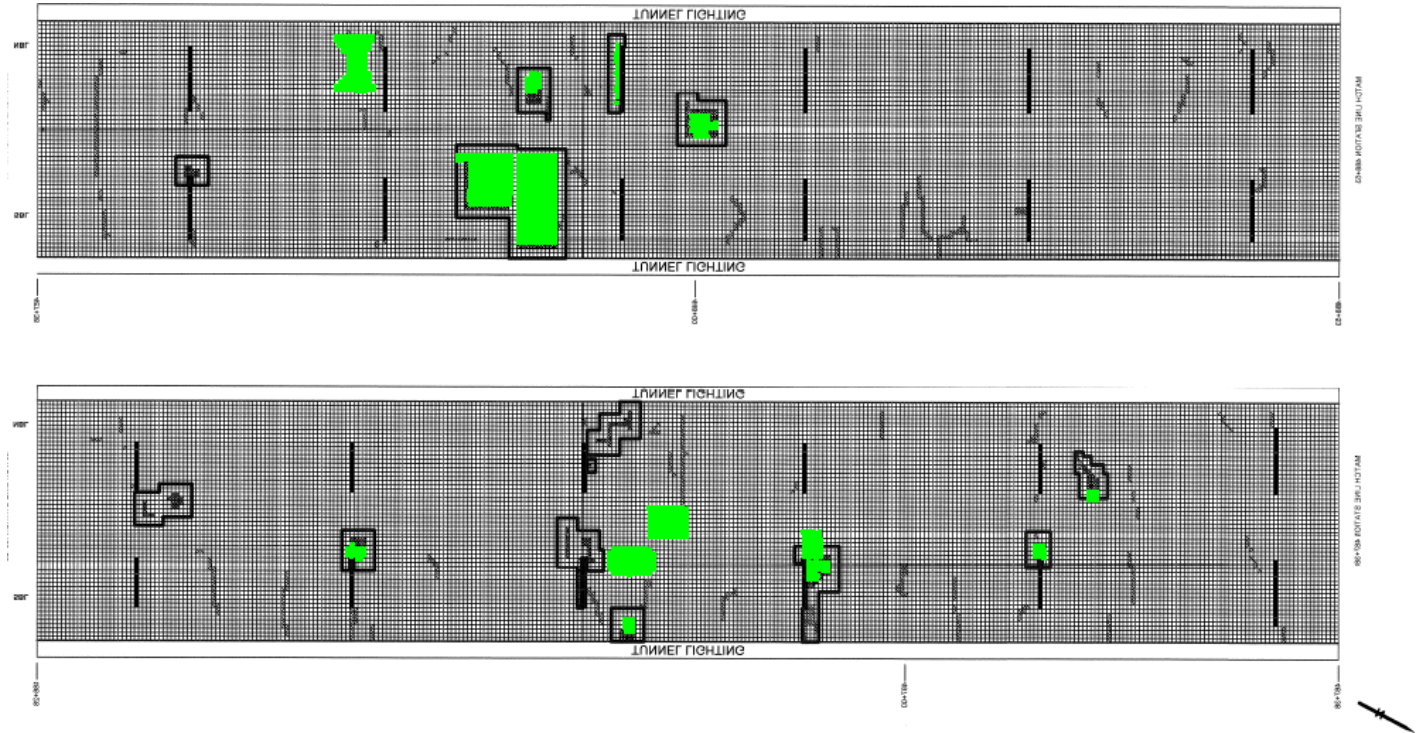


Figure V.22. Visual comparison of thermal anomalies and delaminated tiles (as detected by hammer sounding) between Stations 486+28 and 488+53.

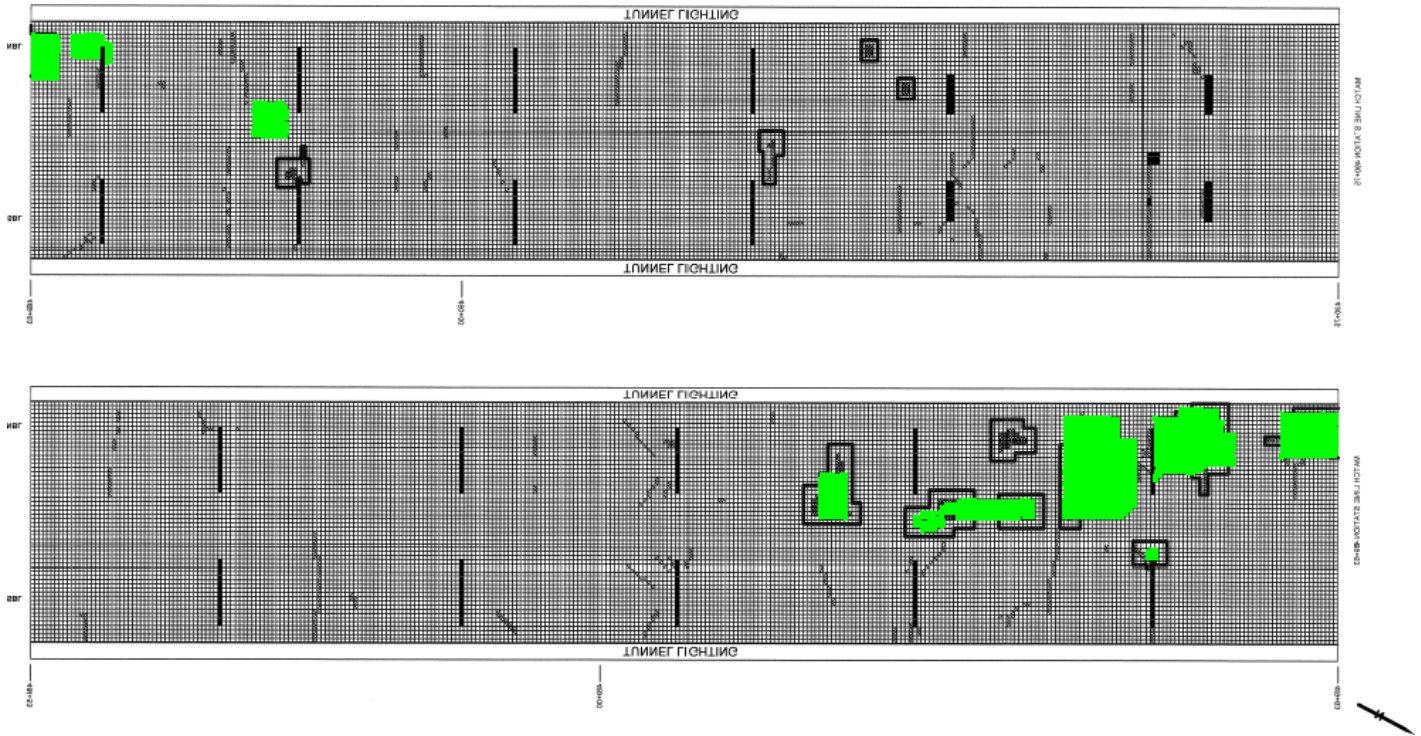


Figure V.23. Visual comparison of thermal anomalies and delaminated tiles (as detected by hammer sounding) between Stations 488+53 and 490+75.

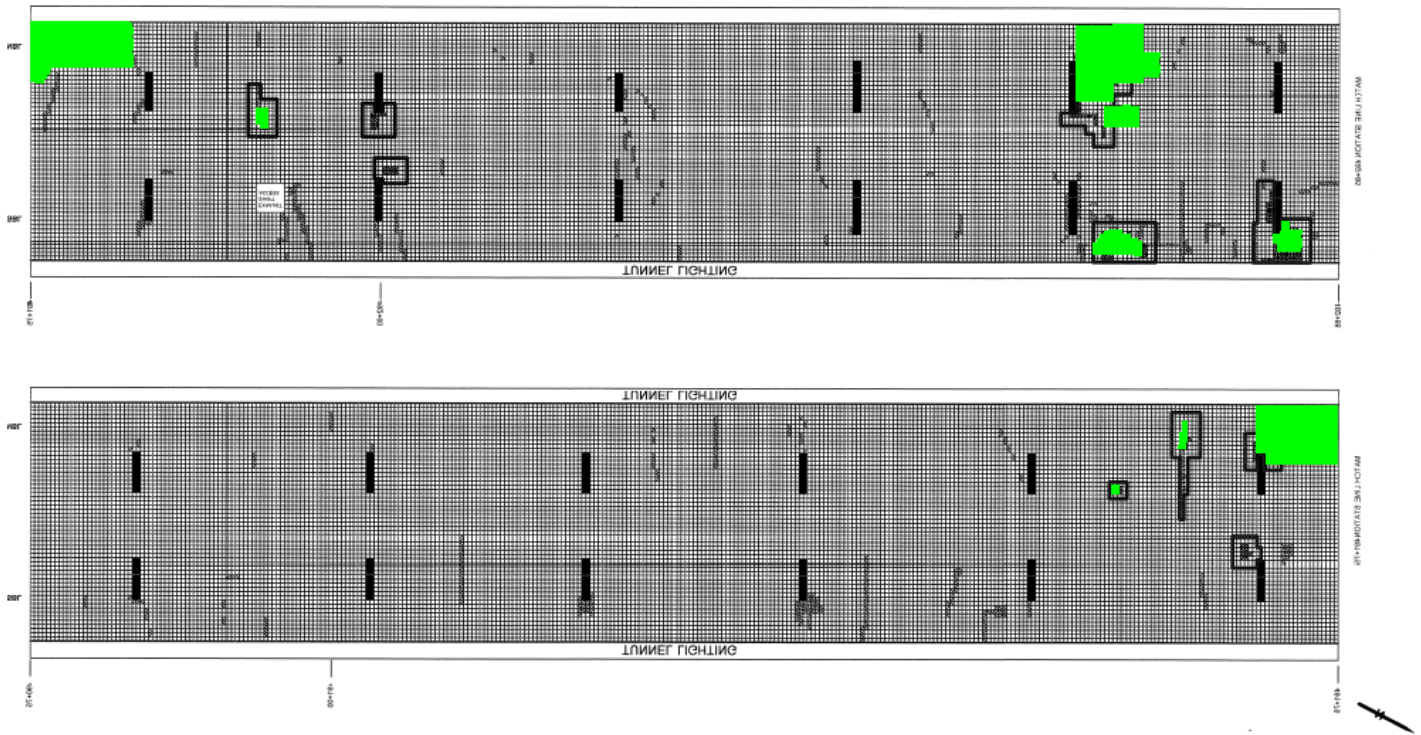


Figure V.24. Visual comparison of thermal anomalies and delaminated tiles (as detected by hammer sounding) between Stations 490+75 and 492+85.

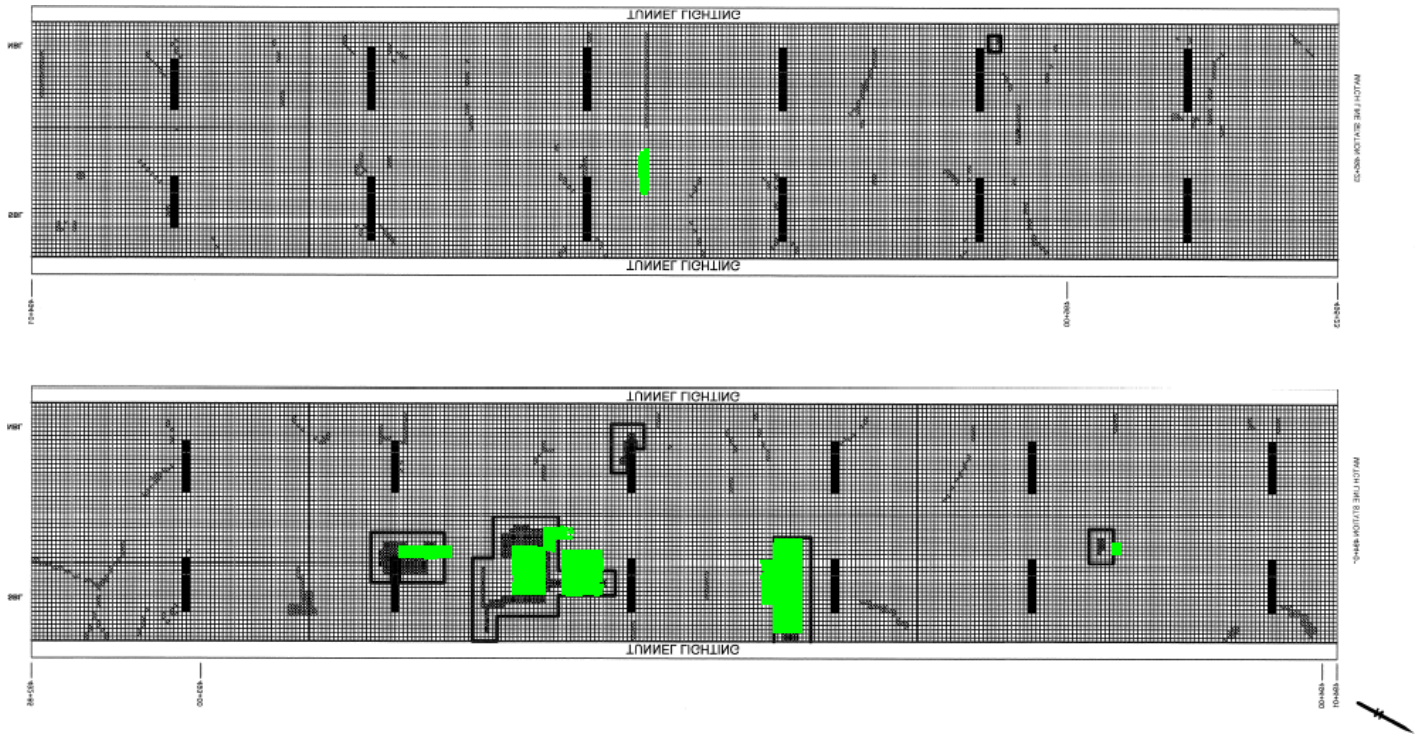


Figure V.25. Visual comparison of thermal anomalies and delaminated tiles (as detected by hammer sounding) between Stations 492+85 and 495+23.

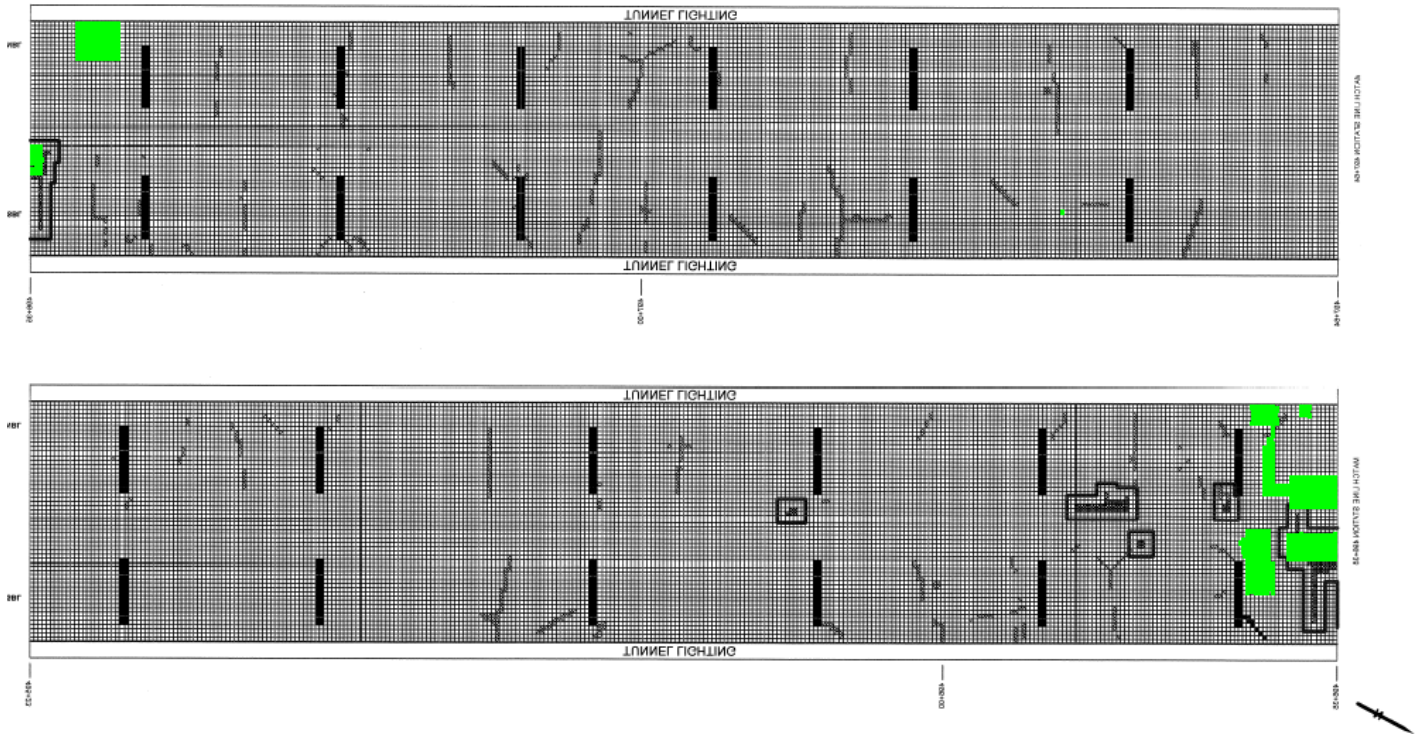


Figure V.26. Visual comparison of thermal anomalies and delaminated tiles (as detected by hammer sounding) between Stations 495+23 and 497+64.

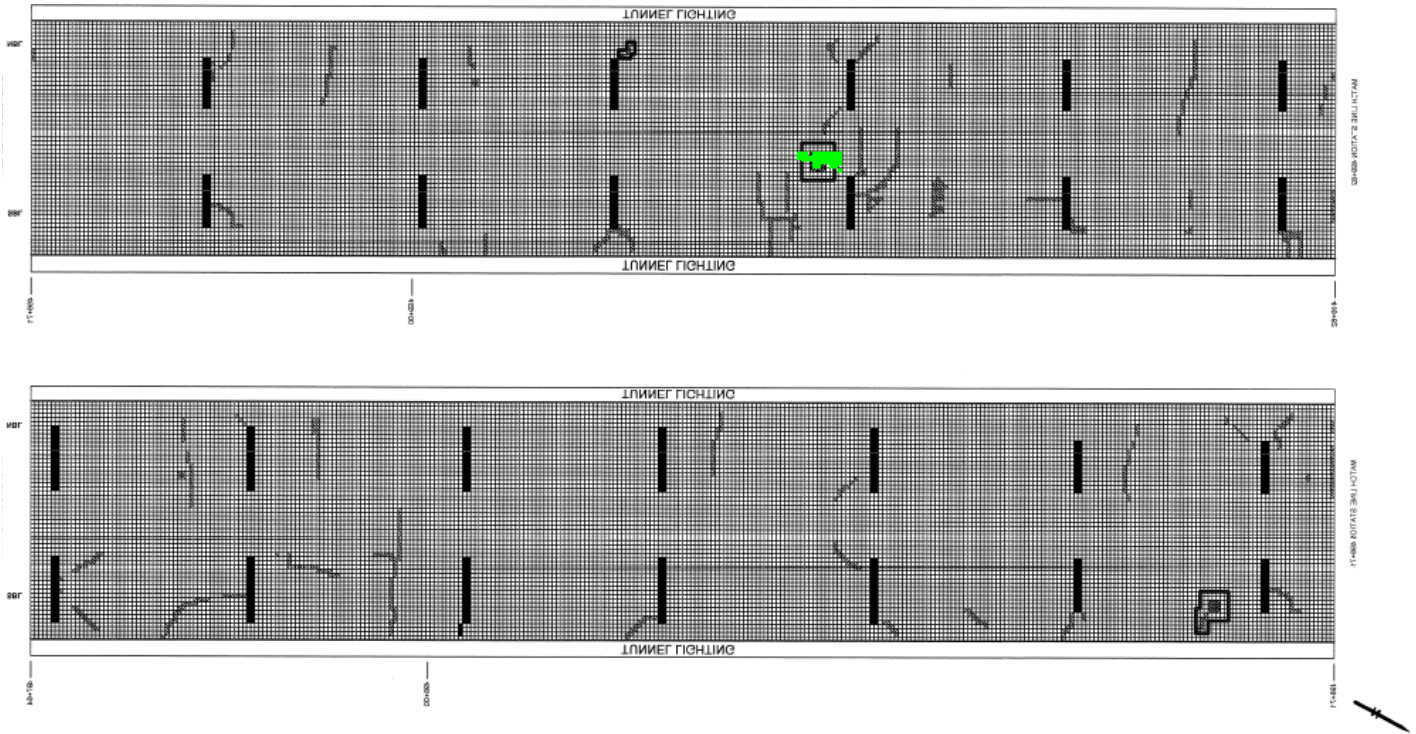


Figure V.27. Visual comparison of thermal anomalies and delaminated tiles (as detected by hammer sounding) between Stations 497+64 and 499+82.

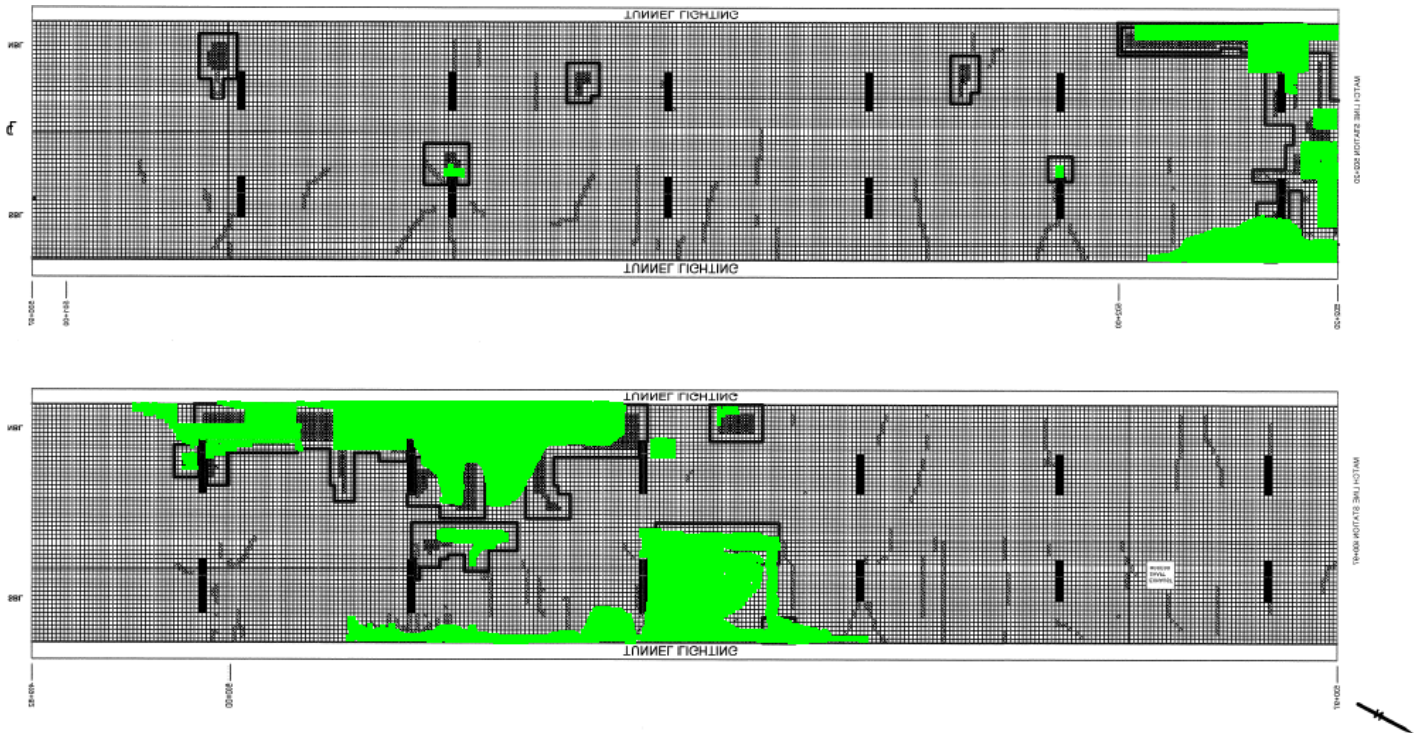


Figure V.28. Visual comparison of thermal anomalies and delaminated tiles (as detected by hammer sounding) between Stations 499+82 and 502+20.

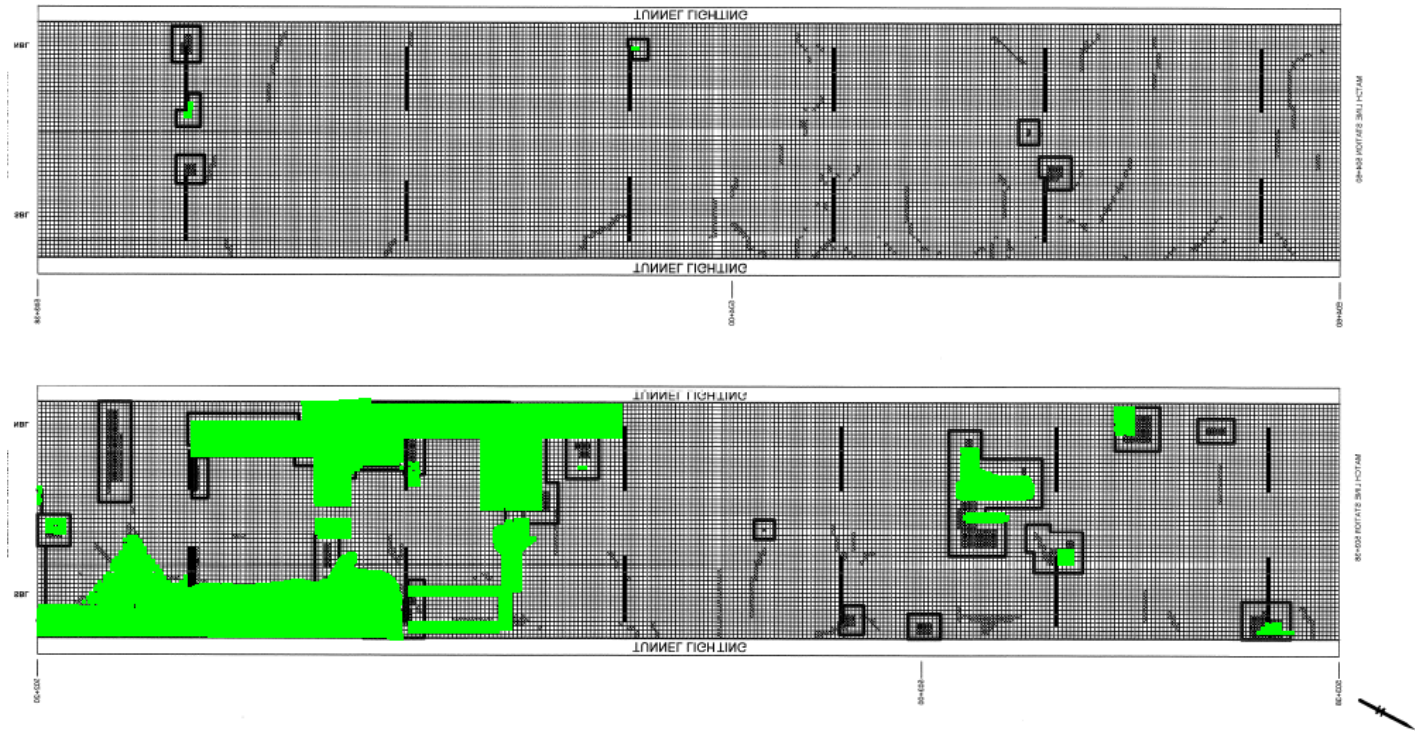


Figure V.29. Visual comparison of thermal anomalies and delaminated tiles (as detected by hammer sounding) between Stations 502+20 and 504+60.

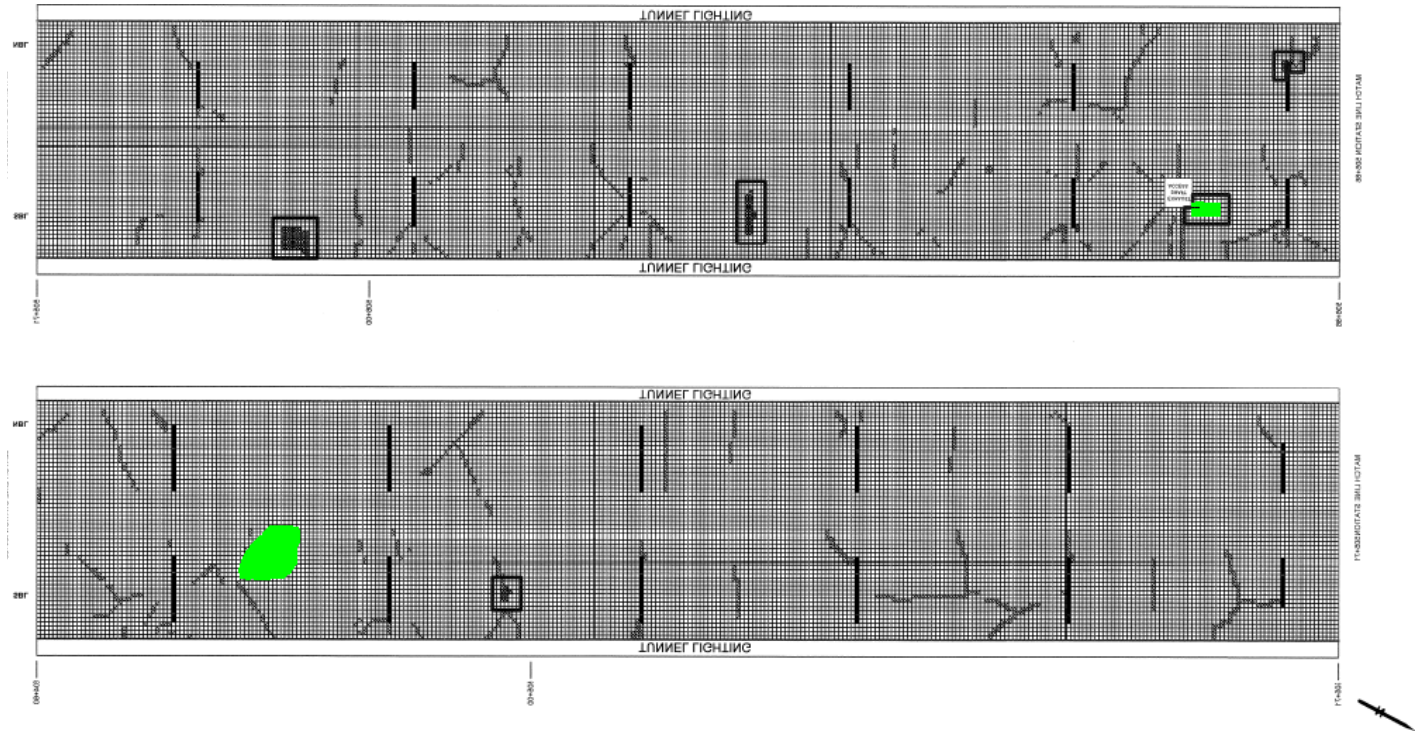


Figure V.30. Visual comparison of thermal anomalies and delaminated tiles (as detected by hammer sounding) between Stations 504+60 and 506+86.

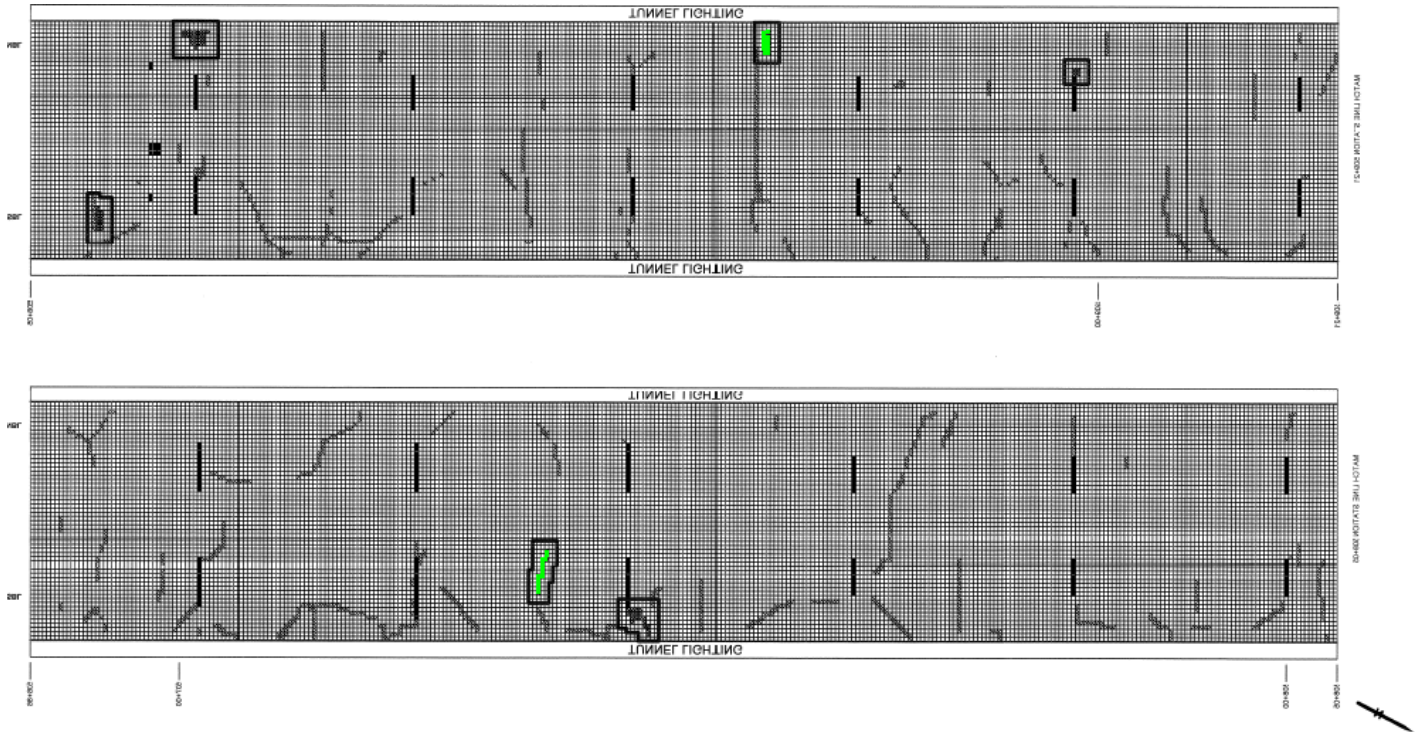


Figure V.31. Visual comparison of thermal anomalies and delaminated tiles (as detected by hammer sounding) between Stations 506+86 and 509+21.

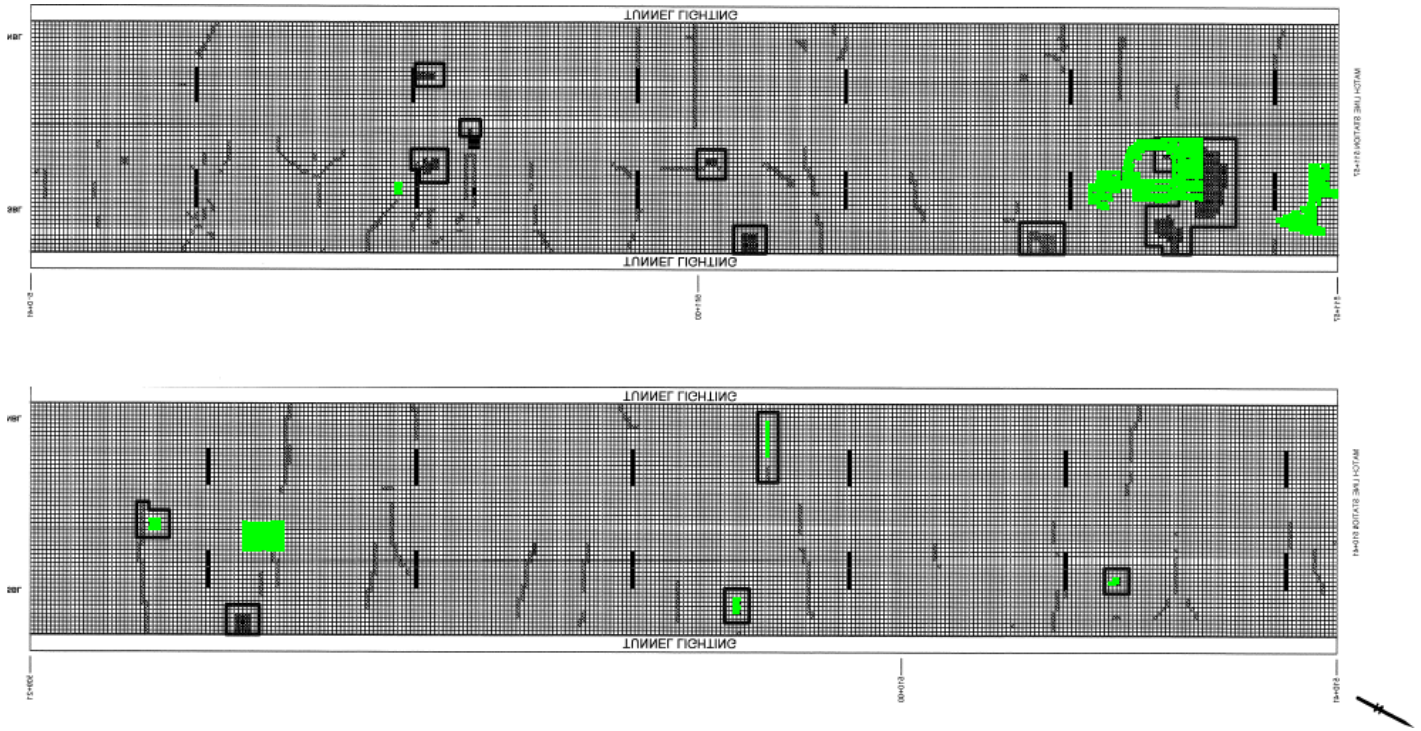


Figure V.32. Visual comparison of thermal anomalies and delaminated tiles (as detected by hammer sounding) between Stations 509+21 and 511+57.

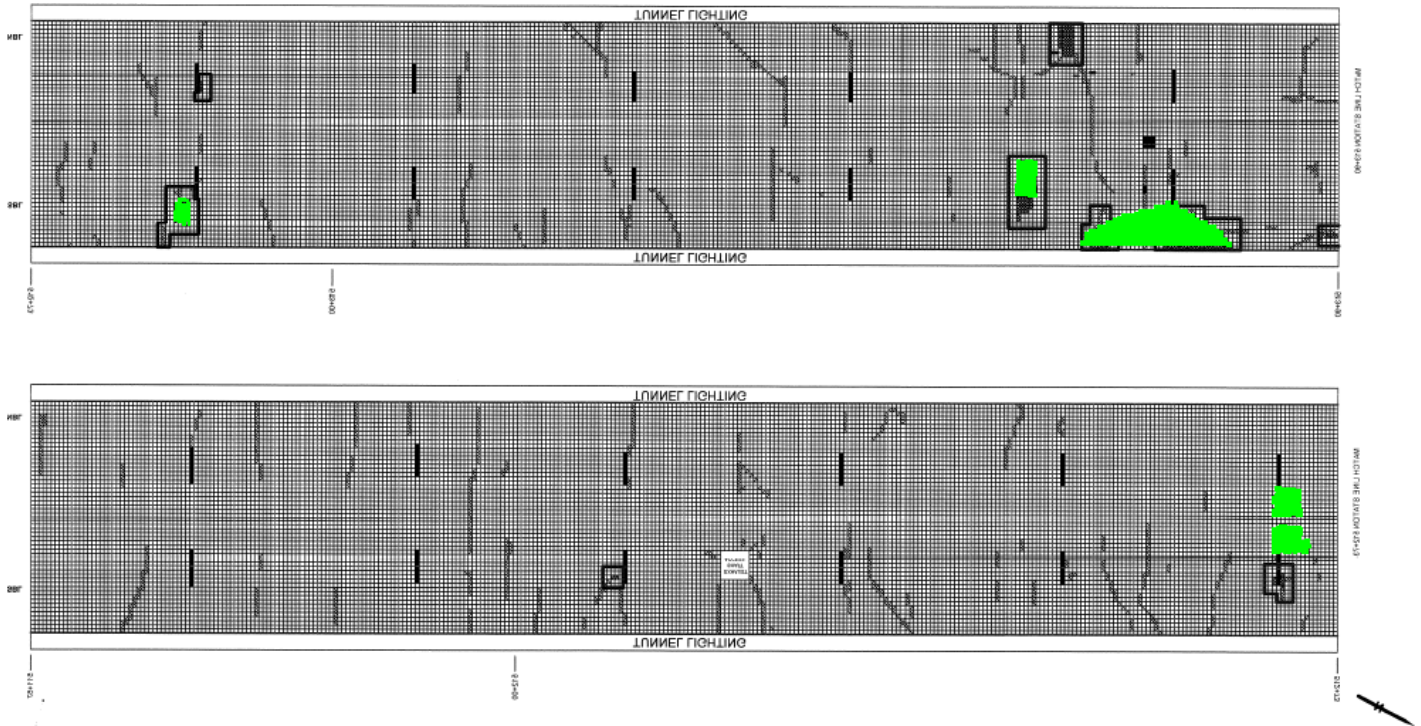


Figure V.33. Visual comparison of thermal anomalies and delaminated tiles (as detected by hammer sounding) between Stations 511+57 and 513+90.

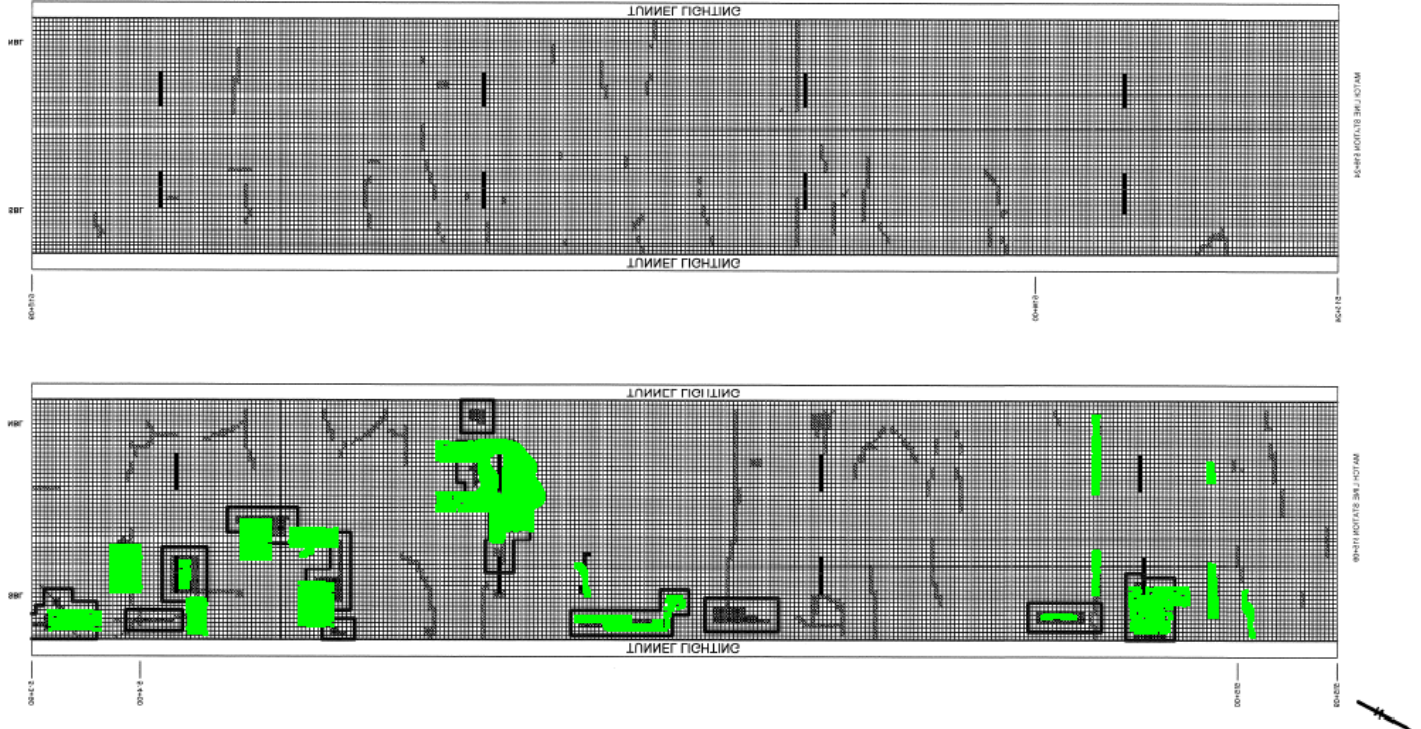


Figure V.34. Visual comparison of thermal anomalies and delaminated tiles (as detected by hammer sounding) between Stations 513+90 and 516+24.

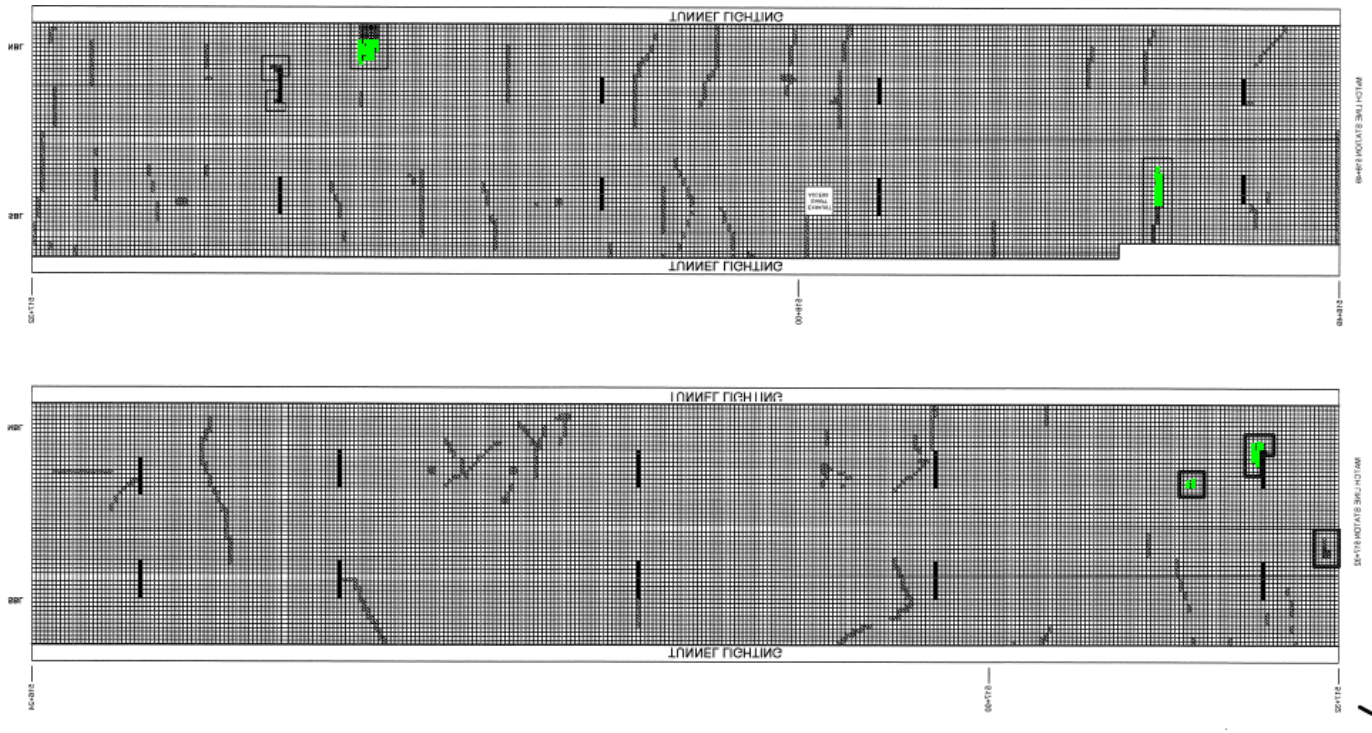


Figure V.35. Visual comparison of thermal anomalies and delaminated tiles (as detected by hammer sounding) between Stations 516+24 and 518+49.

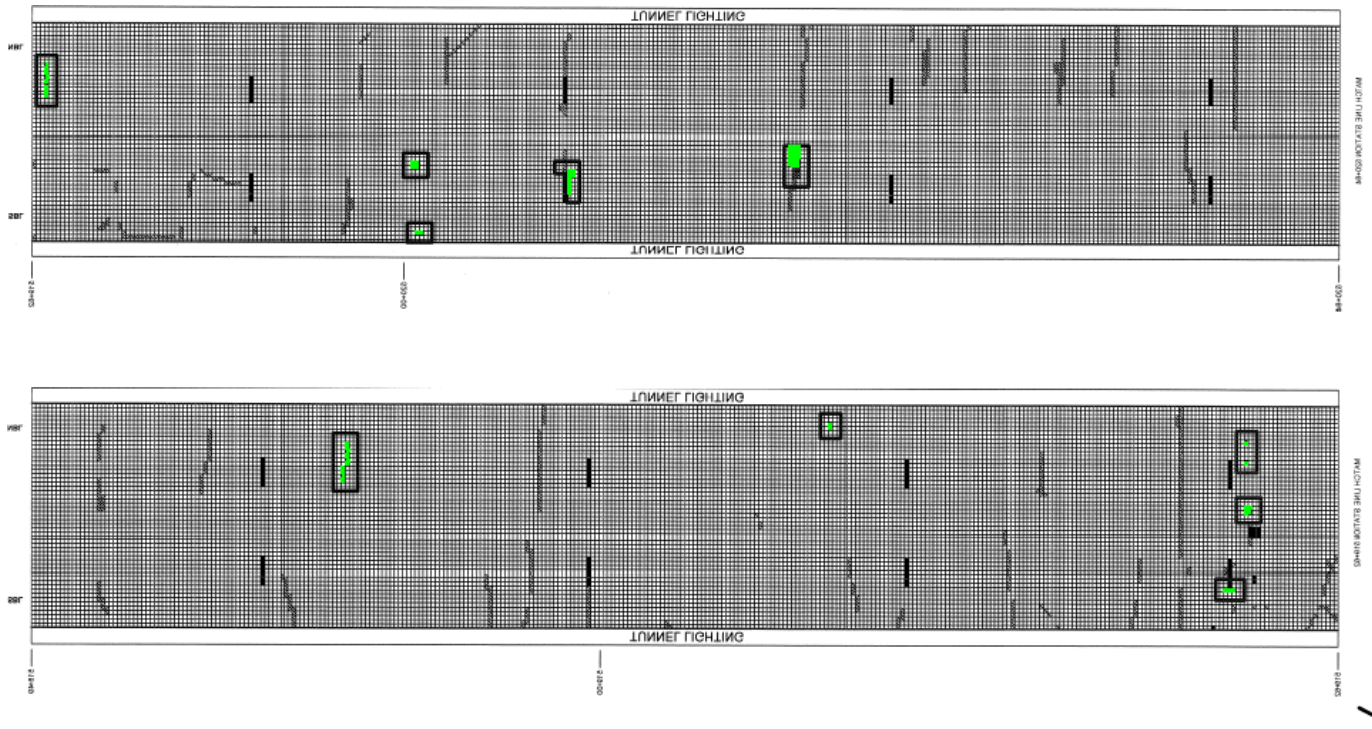


Figure V.36. Visual comparison of thermal anomalies and delaminated tiles (as detected by hammer sounding) between Stations 518+49 and 520+84.

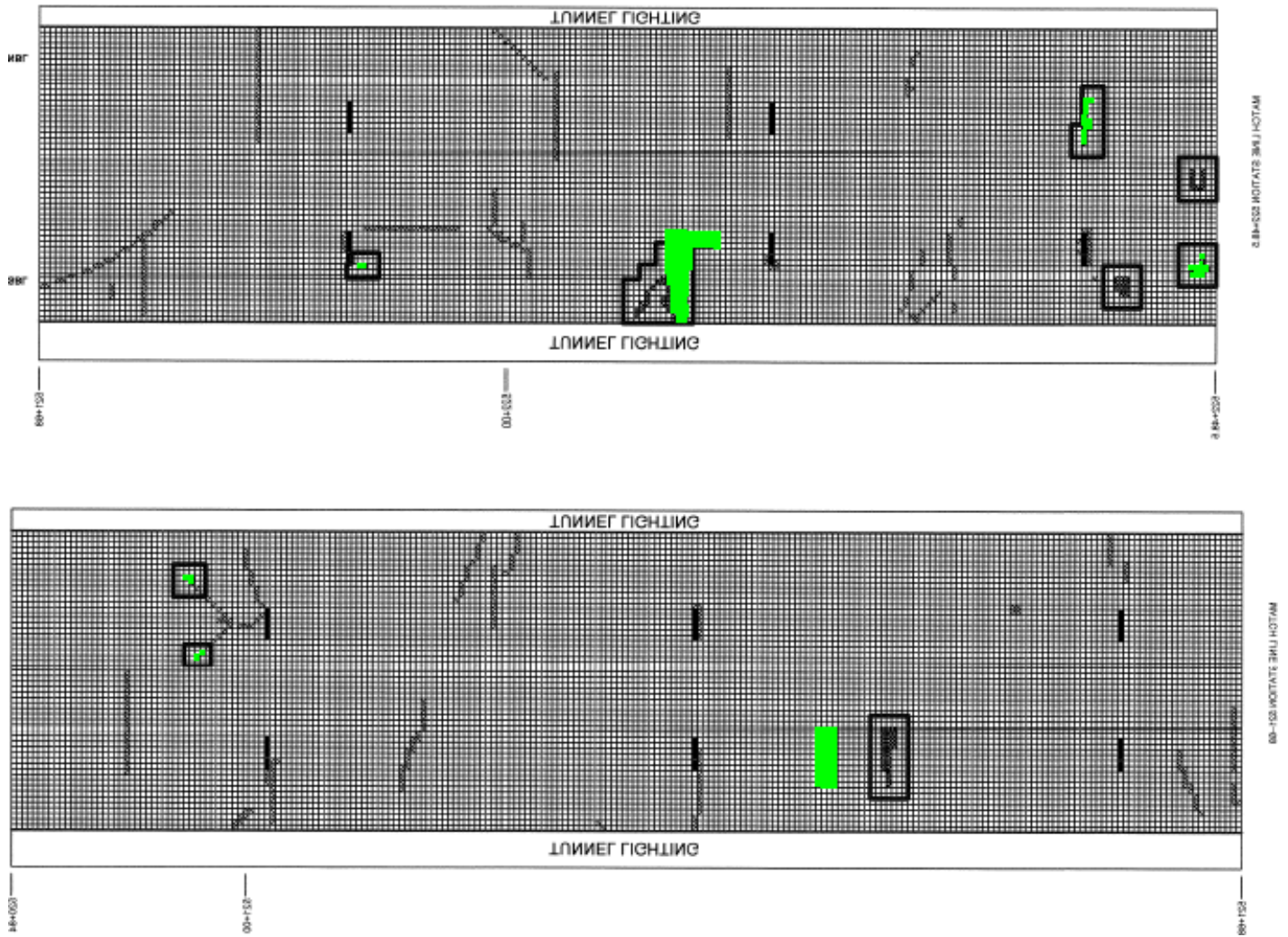


Figure V.37. Visual comparison of thermal anomalies and delaminated tiles (as detected by hammer sounding) between Stations 520+84 and 522+48.5.

APPENDIX W

Findings and Applications of the BAM

Detecting Delaminations and Voids

Delamination-like anomalies were detected by the Federal Institute for Materials Research and Testing (BAM) at three test sites in two different tunnels. At Hanging Lake Tunnel, Segment 56 (BAM-HL1), ground-penetrating radar (GPR) detected an anomaly at a depth of 12 in. The GPR C-scan (at a depth of 12 in.) and D-scan are shown in Figures W.1 and W.2, respectively. The anomaly size was at its largest (24 in. by 20 in.), as shown in Figure W.1.

The same anomaly was detected in the ultrasonic echo records, as shown in Figure W.3, D-scan taken at $y = 5$ in., and Figure W.4, B-scans at $x = 6$ in. and $x = 23$ in. Figure W.3 shows the anomalous reflector at a depth between $z = 12$ in. and $z = 16$ in. The phase evaluation of the anomalous reflector pointed to an acoustic impedance lower than that of concrete (similar to air-concrete interfaces). A three-dimensional (3-D) view of ultrasonic data, including the anomaly, is shown in Figure W.5.

Two other anomalies were found within the test areas of the Chesapeake Channel Tunnel. The first one at Station 474+27 (BAM-CPB1) was only detected with ultrasonic echo. This anomaly was detected directly at $z = 15$ in., spreading over about 20 in., from $x = 20$ in. to $x = 40$ in. (Figure W.6a), and indirectly because of the suddenly weakened backwall reflection (Figure W.6b). The D- and B-scans shown in Figure W.7 depict the location of the anomaly within the lining. The phase evaluation at detected reflections was not conclusive. Therefore, no reliable conclusions could be made about the nature of the anomaly.

The 3-D image in Figure W.8 illustrates the location of the anomaly within the test volume.

Another anomaly at Station 486+67 (BAM-CPB3) was detected by both the ultrasonic echo and impact echo (IE) techniques.

In the ultrasonic echo data, the anomaly manifested itself directly as an anomalous reflector at depths from $z = 2$ in. to

$z = 4$ in. and indirectly as the missing backwall echo between $x = 16$ in. and $x = 38$ in., as seen in Figure W.9. The phase evaluation indicated an acoustic impedance lower than that of the surrounding concrete.

D-scans cutting through the length of the test area showed multiple reflectors in the volume above the missing backwall echoes at $z = 6$ in., $z = 10$ in., $z = 15$ in., and $z = 20$ in., with changing phases (Figure W.10). Multiple reflections with their phase jumping between negative and positive are typically indications of shallow delamination (Shokouhi et al. 2005).

The 3-D image of Figure W.11 illustrates the missing backwall echo and the anomalous reflections above it.

Figure W.12 presents a spectral D-scan and two selected IE A-scans (spectra). The tunnel lining thickness resonance frequency can be seen throughout the D-scan, except between $x = 13$ in. and $x = 30$ in., where the echo is disturbed. Two typical spectral and temporal A-scans from the sound ($x = 5.5$ in.) and disturbed ($x = 20$ in.) regions are compared in this figure. While the sound spectrum contains one clearly dominant frequency, the disturbed spectrum contains multiple peaks, mostly of frequencies lower than that of thickness resonance frequency, indicating shallow delamination (2). The thickness resonance frequency appears at about 3.2 kHz, corresponding to a depth of about $z = 25$ in.

The three data sets discussed above were combined as shown in Figure W.13. Data combination was achieved by weighing and adding the three different data sets. Depth-varying weights were assigned to each data set to account for the different resolution and penetration depths associated with each method. A combined image of IE, ultrasonic echo, and GPR data at $y = 15$ in. is shown in Figure W.14. The image provides a concise combined presentation of all the useful information provided by each method: the reinforcement from GPR and ultrasonic echo, a reflector at $z = 4$ in. at $x = 32$ in. from ultrasonic echo, and the backwall from ultrasonic echo and IE. In the area of missing ultrasonic echo backwall echoes, the disturbed IE spectra are seen.

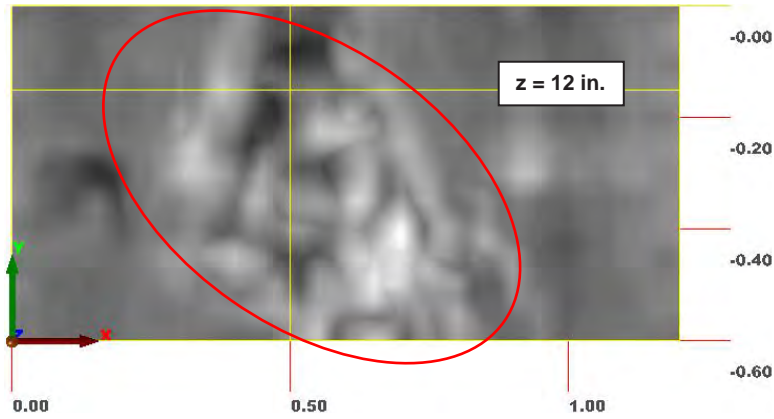


Figure W.1. BAM-HL1, GPR: C-scan showing anomaly at depth, $z = 12$ in. Encircled area is about 24 in. by 20 in. HL = Hanging Lake.

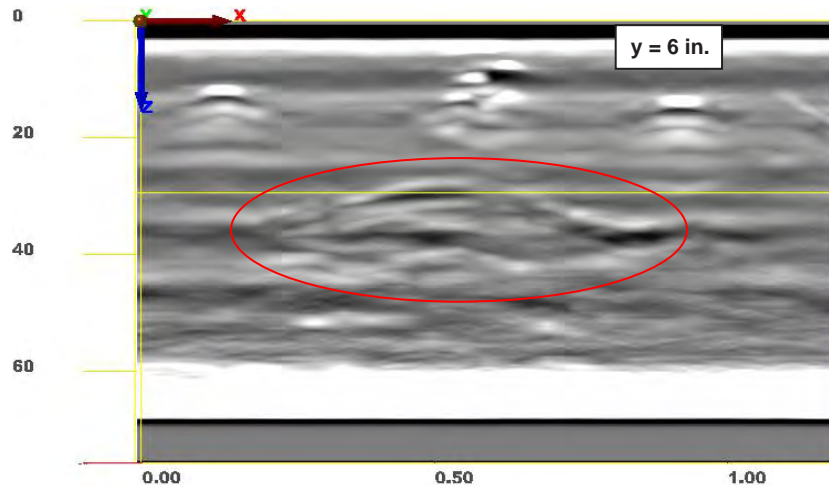


Figure W.2. BAM-HL1, GPR: D-scan showing extension of anomaly from $z = 12$ in. to $z = 16$ in. Slice was taken at $y = 6$ in. HL = Hanging Lake.

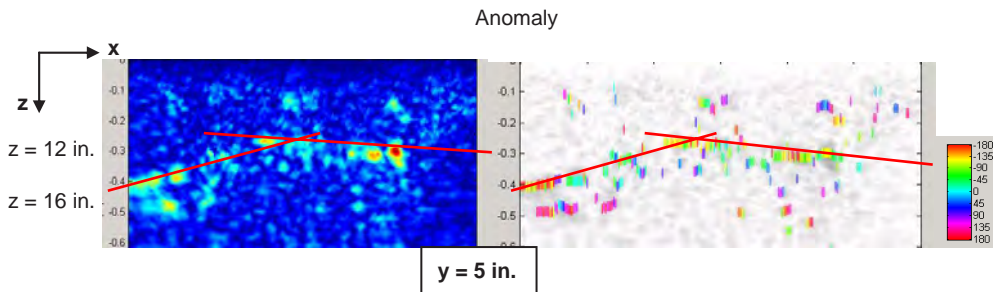


Figure W.3. BAM-HL1 ultrasonic echo: D-scan taken at $y = 5$ in. Curved anomalous reflector of mostly negative phase was detected between $z = 12$ in. and $z = 16$ in. HL = Hanging Lake.

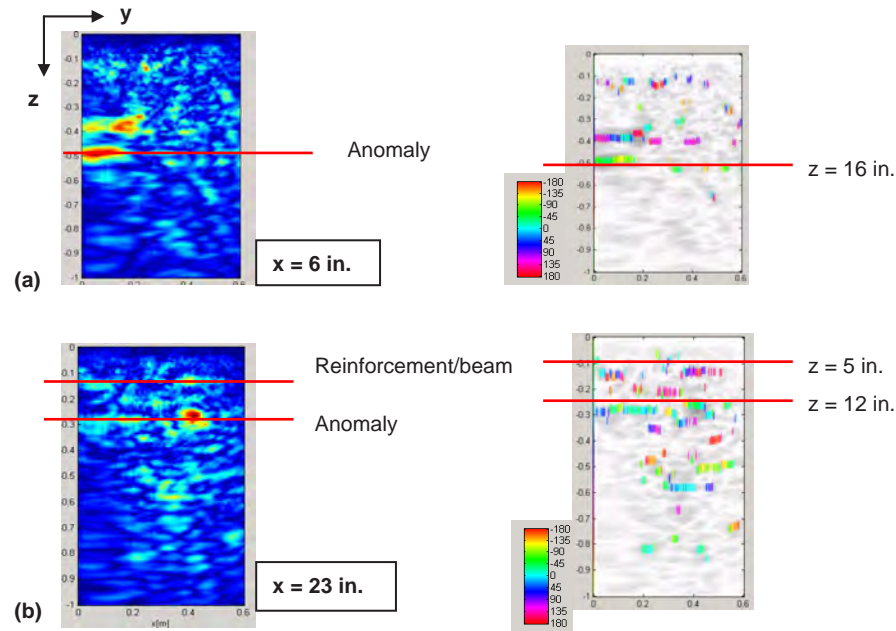


Figure W.4. BAM-HL1, ultrasonic echo: B-scans to evaluate extent of anomaly within tunnel lining: (a) B-scan crossing through deeper part of reflector, and (b) B-scan crossing through shallower part of reflector. HL = Hanging Lake.

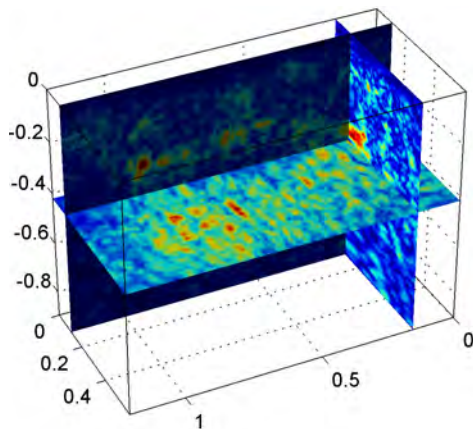


Figure W.5. BAM-HL1, ultrasonic echo: 3-D image of volume positioned to reveal anomaly, with B-scan positioned at $x = 6$ in., C-scan at $z = 21$ in. (4 in. thick), and D-scan at $y = 6$ in. HL = Hanging Lake.

A surface crack was detected at one of the test fields at Hanging Lake Tunnel (Segment 57). In the GPR results, the crack manifested itself as a change in electromagnetic impedance, most likely because of the intrusion of moisture into the lining. Figure W.15 presents a collection of GPR B-, C-, and D-scans with the cracked zone marked on each scan.

The circled areas mark the reflections at the location of the surface crack. The reason for the seeming mismatch of the first 6 in. in the C-scan was a missing profile line caused by a failure during the measurement process, which resulted in artifacts in the reconstructed images. Figure W.15c shows the reflector at a depth of $z = 3$ in. The B-scan at $x = 19$ in. (Figure W.15a) shows that the reflector extended down to a depth of 3.4 in.

In the ultrasonic echo data, the crack was indirectly detected, where a part of the longitudinal reinforcement was missing (Figure W.16). As the ultrasonic echo only detected the anomaly indirectly, the technique could not specify the depth of the crack or the dimension of the possible moisture intrusion.

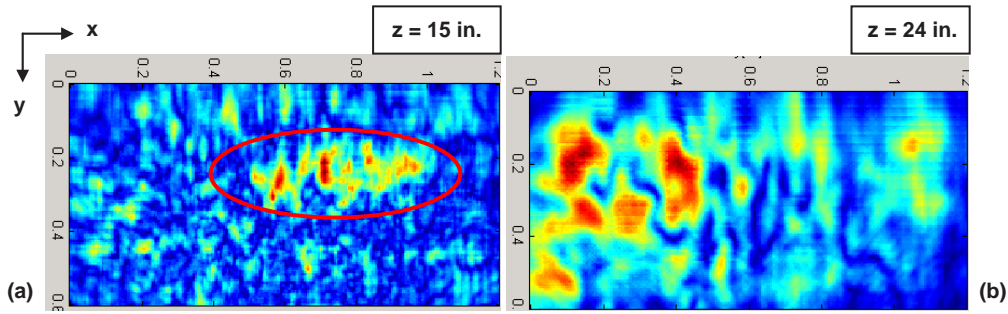


Figure W.6. BAM-CPB1, ultrasonic echo: (a) C-scans showing anomaly directly at a depth of 15 in., and (b) indirectly as a weakened backwall reflection.

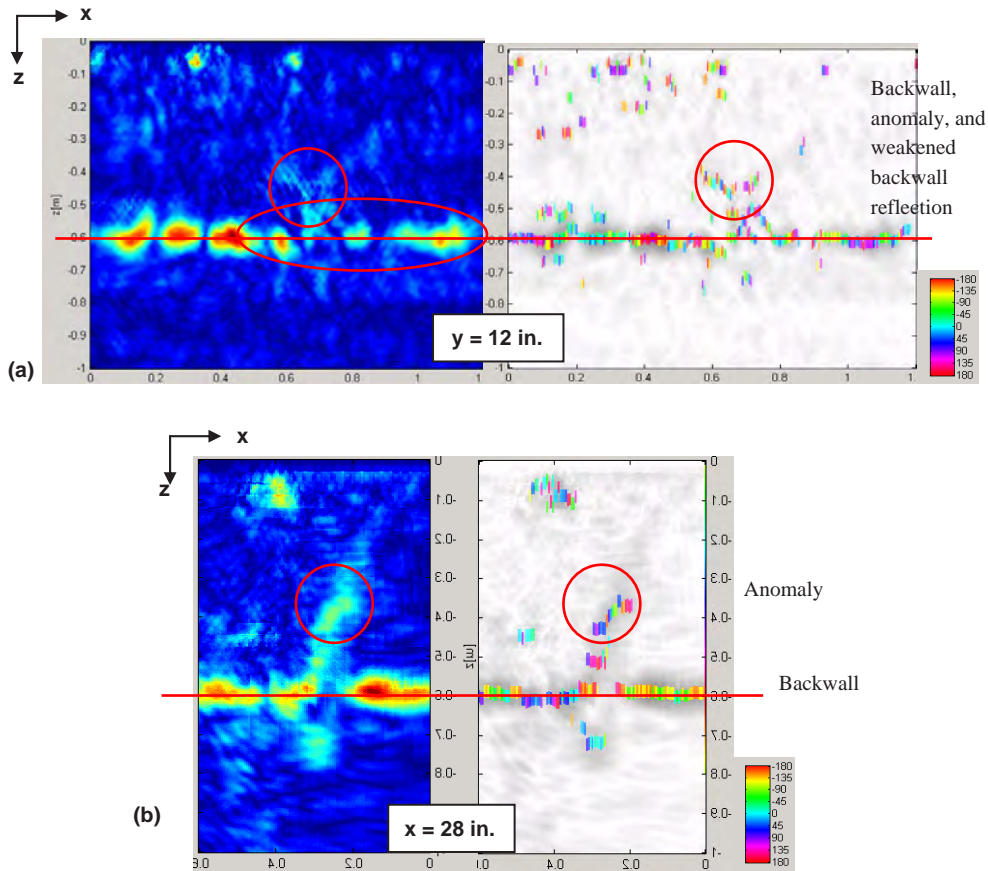


Figure W.7. BAM-CPB1, ultrasonic echo: (a) D-scan at $y = 12$ in., and (b) B-scan at $x = 28$ in. depicting anomaly and weakened backwall reflection. No conclusive information could be drawn from phase diagram. (Image reversed to compare data collected in opposite directions.)

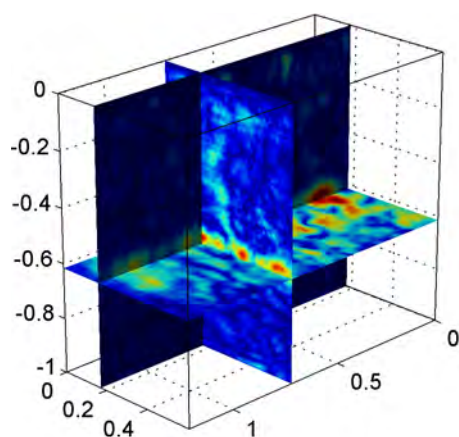


Figure W.8. BAM-CPB1, ultrasonic echo: 3-D image of volume positioned to reveal backwall and anomaly, with B-scan positioned at $x = 29$ in., C-scan at $z = 24$ in., and D-scan at $y = 7$ in.

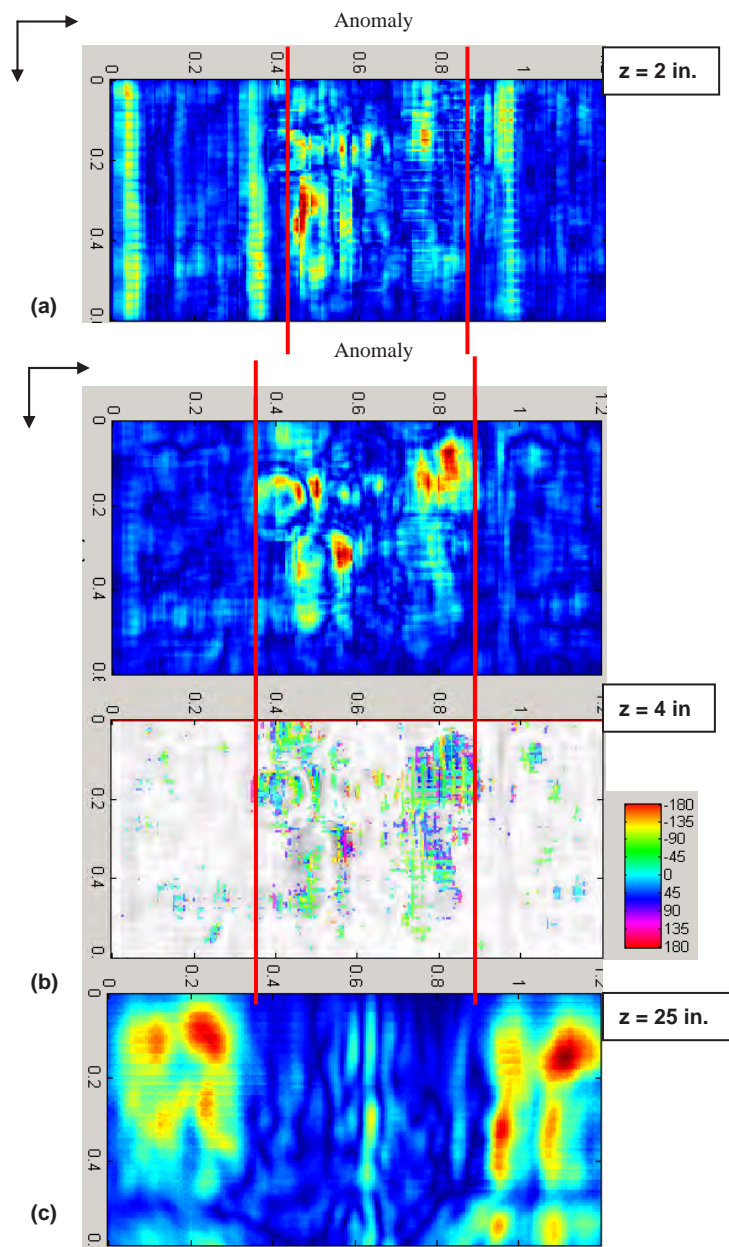


Figure W.9. BAM-CPB3, ultrasonic echo: C-scans showing anomaly at (a) $z = 2$ in., (b) $z = 4$ in., and (c) missing backwall echo at $z = 25$ in.

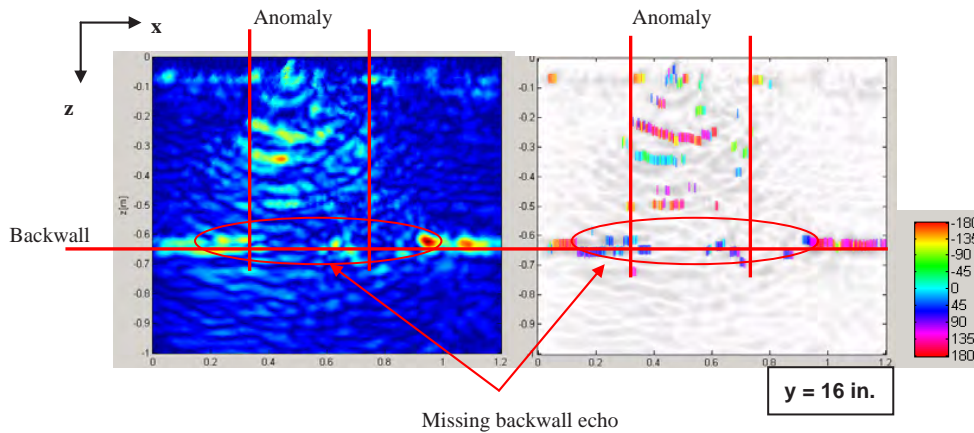


Figure W.10. BAM-CPB3, ultrasonic echo: D-scan at $y = 16$ in. showing multiple anomalous reflections with depth as well as missing backwall echo. Phase values jumped between positive and negative, from reflection to reflection.

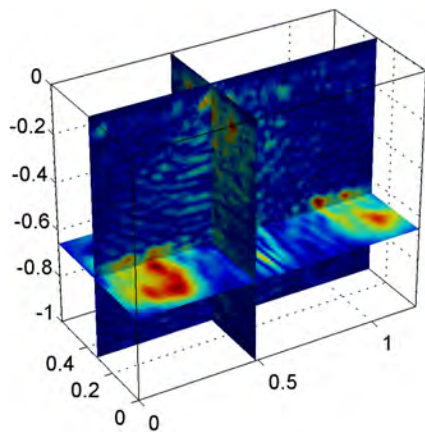


Figure W.11. BAM-CPB3, ultrasonic echo: 3-D image of volume positioned to reveal backwall and its shadowed area resulting from apparent shallow anomaly. B-scan is positioned at $x = 21$ in., C-scan at $z = 25$ in., and D-scan at $y = 12$ in.

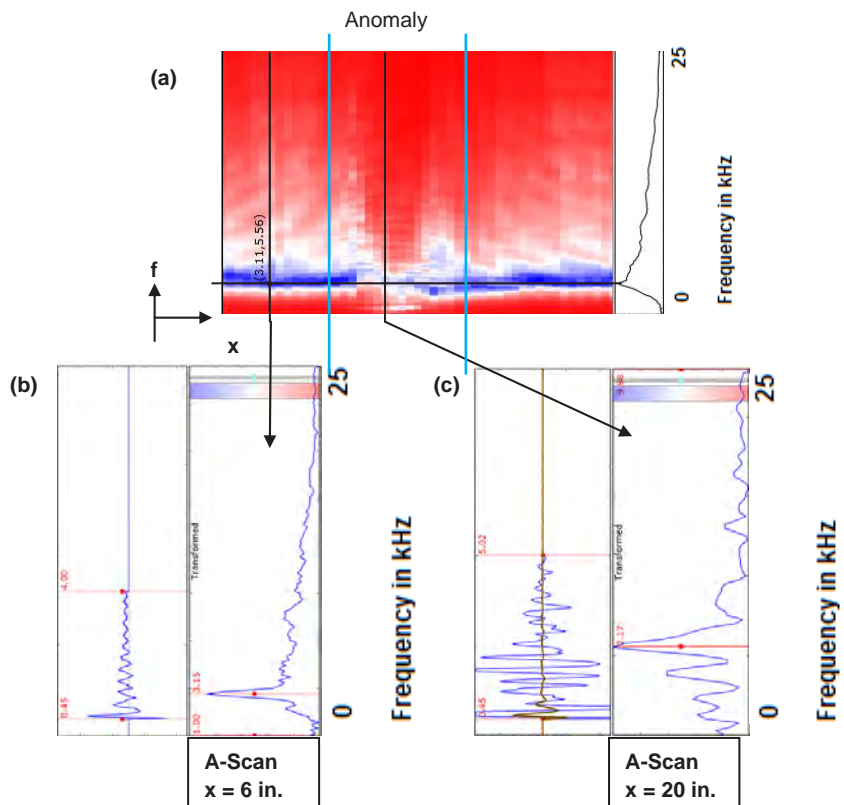


Figure W.12. BAM-CPB3, IE: D-scan (a) and selected A-scans representing echo from sound section (b) and from area with anomaly (c).

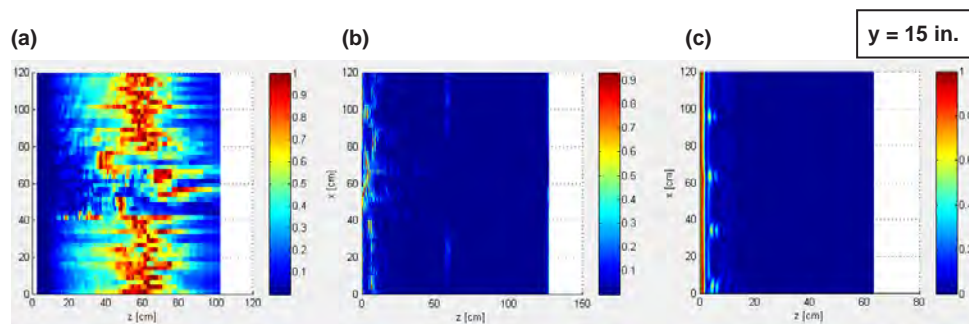


Figure W.13. BAM-CPB3: Individual D-scans at $y = 15$ in. for each nondestructive testing (NDT) method: (a) IE, (b) ultrasonic echo, and (c) GPR.

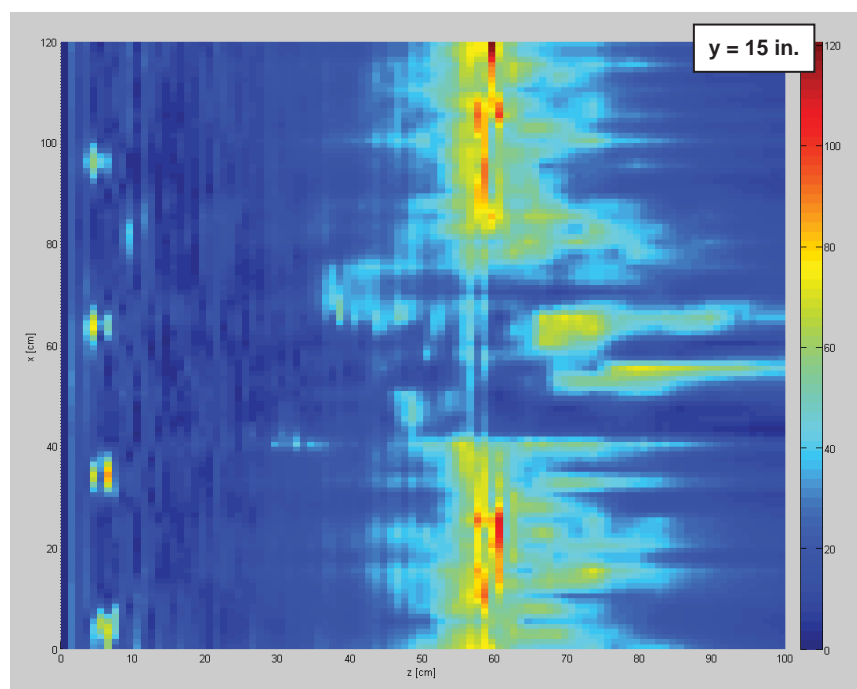


Figure W.14. BAM-CPB3: Combined IE-ultrasonic echo-GPR D-scan at $y = 15$ in.

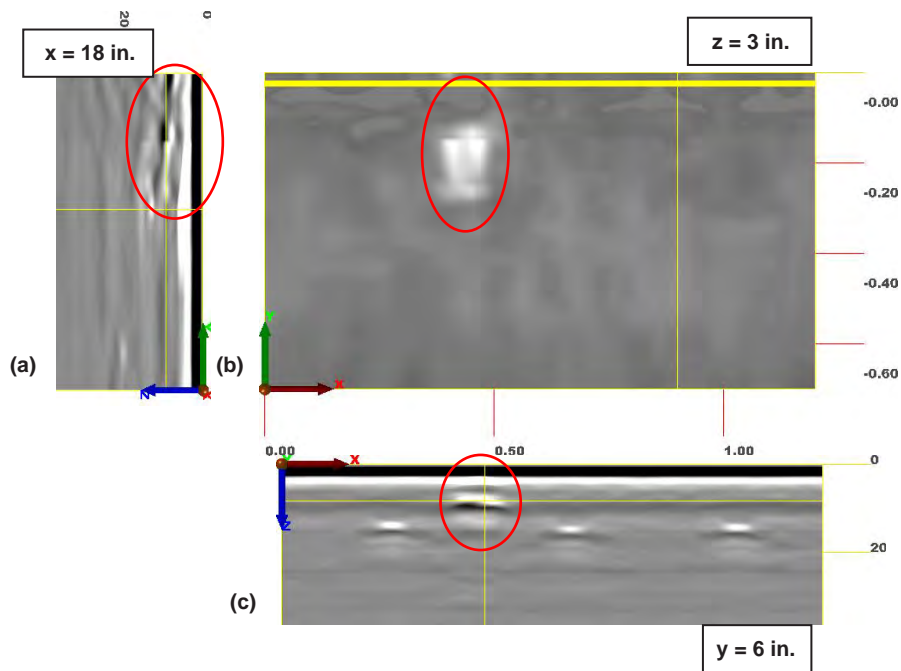


Figure W.15. BAM-HL2, GPR: C-, D-, and B-scans showing reflections caused by presence of a surface crack. HL = Hanging Lake.

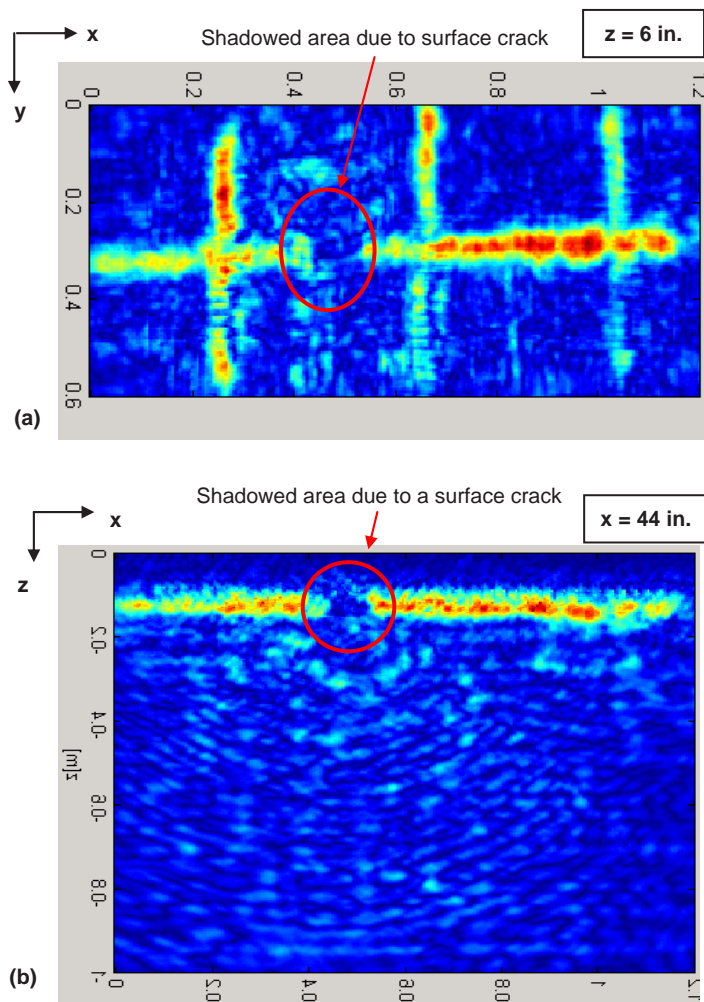


Figure W.16. BAM-HL2, ultrasonic echo: (a) C-scan at $z = 6$ in. and (b) D-scan at $x = 44$ in., showing missing echoes of longitudinal reinforcement resulting from surface crack. HL = Hanging Lake. (Image reversed to compare data collected in opposite directions.)

APPENDIX X

Digital Photogrammetry

Data Acquisition

The basic principles of photogrammetry are illustrated in Figure X.1: once a pair of photographs is acquired, the same point, P , is identified on each photograph, and the spatial coordinates of point P on the object (the ground in this case) are calculated by tracing two rays from the focal points O_l and O_r of each photograph, respectively, through the pixels that represent point P on each photograph. A patch of an object's surface is therefore reconstructed from each pair of photographs: it is the patch portrayed by both photographs. The reconstructed surface can then be either scaled or scaled and georeferenced in a reference system of interest.

Because each point on the reconstructed surface comes from a known pixel, each pixel can be exactly attributed to the relevant point of the reconstructed surface. Thus, the reconstructed surface is exactly textured with high-definition photos, allowing for a reliable and realistic virtualization of the object under consideration. This means that when the trace of a lining crack is digitized by following the trace pixels on the textured surface, the correct trace geometry on the underlying surface can be identified with certainty; this is not the case with laser scanner applications.

Once a three-dimensional (3-D) model has been reconstructed, it can be scaled, or it can be scaled and georeferenced. A scaled model allows for crack, spalling, and visible moisture detection and measurement: crack length, aperture, location (relative to an arbitrary point); spalling area, depth, volume, and location; and moist area and location. Additionally, a scaled and georeferenced model allows for the following:

- Change detection, that is, determining changes in crack lengths and aperture, spalling extent (area and depth), and moist area;
- Determination of
 - Crack orientation, which is very useful for ensuring that the grouting holes actually intersect the crack;

- Wall displacements such as convergence, tile delamination, concrete delamination, and ceiling or floor sagging; and
- Overall tunnel displacement, for example, in immersed tube tunnels, lifting caused by loss of ballast or sinking caused by debris discharge over the tunnel.

The speed of photograph acquisition depends on the accuracy required, the minimum distance between the cameras and the tunnel lining, and whether the tunnel is accessible to vehicles. As part of this research, special technology has been developed to achieve the performance detailed in Table X.1.

Accuracy of the 3-D Model and Information Provided to Client

An additional advantage of digital photogrammetry with respect to the laser scanner is that the bundle adjustment residual is provided at each common point P (see Figure X.1), and then the root mean square (RMS) of the residuals is provided for each photograph, and for the entire model. These data provide detailed local and global information on the accuracy of the model, which is not available in laser scanner applications.

The pixel size on the lining is chosen before entering the tunnel on the basis of the desired accuracy. For example, Table X.2 refers to the two-lane Liberty Tunnel in Pennsylvania, which is about 20 ft wide. In this tunnel, photographs were taken from the left lane, and the maximum distance from cameras to the opposite wall was about 12 ft. The a priori calculated accuracy of the photogrammetric model was 0.8 mm; the chosen pixel size on the lining (farthest distance to the camera) was about 1 mm by 1 mm. For each picture actually taken in the field, Table X.2 provides the RMS of the residuals, which is always less than 0.3 pixels, that is, 0.3 mm on the lining. The Active Points column refers to the number of common points between a given picture and all overlapping pictures.

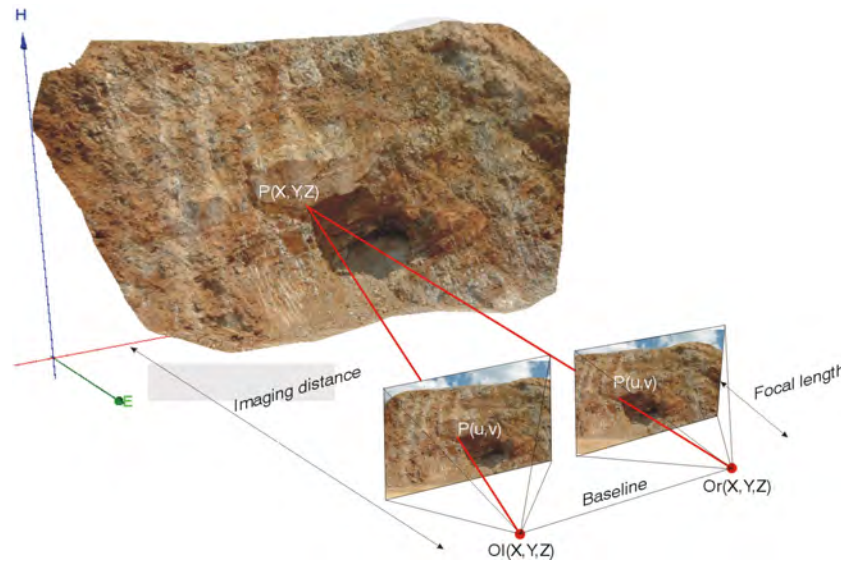


Figure X.1. Photogrammetry principles.

Residuals are also calculated on:

- *Scale bars (scaled models)*: Table X.3 gives the residuals at the scale bars used at the Liberty Tunnel. The scale bar dimensions are provided with a National Institute of Standards and Technology–traceable certificate of calibration. The residuals are better than 50 microns (0.002 in.).
- *Surveyed targets applied to the final lining (scaled and georeferenced models)*: Table X.4 gives the residuals obtained on surveyed targets in the road enclosure of the Eisenhower Memorial Tunnel in Colorado. The residuals in each direction are equal to about 0.5 mm (0.02 in.), and the overall, spatial residual is equal to 0.8 mm (0.03 in.). The overall accuracy (target survey and photogrammetric model) obtained in the divider wall at the Eisenhower Memorial Tunnel was equal to 1 mm.

These results indicate that the following may be identified with confidence:

- Bulging caused by incipient spalling and tile delaminations;
- Subtle ceiling/floor movements that may indicate progressive failure of the support (e.g., roof collapse at the Central Artery/Tunnel in Boston);
- Convergence of the tunnel walls; and
- Overall tunnel displacement (e.g., in immersed tube tunnels, lifting caused by loss of ballast or sinking caused by debris discharge over the tunnel).

Figures X.2 through X.13 provide an example of a 3-D model of a tunnel lining—Liberty Tunnel in Pennsylvania—and its use in identifying lining defects. (Figures X.3 through X.8 show close-up views of the circled spalling event.) Figure X.14,

Table X.1. Speed of Photograph Acquisition

Tunnel Type	Taking Pictures from	Taking Pictures of	Lane Closure Required	Accuracy Required ^a	Speed
2-lane road enclosure	1 lane	Entire tunnel	1 lane from which pictures are taken	0.8 mm	1,200 ft/hr (360 m/hr)
2-lane road enclosure	1 lane	Entire tunnel	1 lane from which pictures are taken	1 mm	2,400 ft/hr (720 m/hr)
2-lane road enclosure	1 lane	Single wall (e.g., only tile panels)	1 lane from which pictures are taken	0.8 mm	2,000 ft/hr (600 m/hr)
2-lane road enclosure	1 lane	Single wall (e.g., only tile panels)	1 lane from which pictures are taken	1 mm	3,300 ft/hr (1,000 m/hr)
Air duct (20 ft [6 m] wide)	Center	Entire duct	No	0.6 mm	660 ft/hr (200 m/hr)
Air duct (20 ft [6 m] wide)	Center	Entire duct	No	0.7 mm	1,000 ft/hr (300 m/hr)

^a Accuracy refers to photogrammetric model only.

Table X.2. Residuals and Active Points for Pictures Taken at Liberty Tunnel

Name	RMS Error (pixels)			Active Points	Name	RMS Error (pixels)			Active Points
	X	Y	Total			X	Y	Total	
IMG_2272.JPG	0.116403	0.153484	0.192632	195	IMG_2287.JPG	0.164044	0.212679	0.268594	211
IMG_2273.JPG	0.117043	0.179321	0.214138	277	IMG_2288.JPG	0.117306	0.184640	0.218753	228
IMG_2274.JPG	0.131904	0.214972	0.252214	337	IMG_2289.JPG	0.097516	0.177364	0.202404	355
IMG_2275.JPG	0.145841	0.182533	0.233640	226	IMG_2290.JPG	0.097395	0.143055	0.173062	333
IMG_2276.JPG	0.119270	0.228402	0.257668	281	IMG_2291.JPG	0.114015	0.175516	0.209297	472
IMG_2277.JPG	0.082480	0.207591	0.223376	283	IMG_2292.JPG	0.113118	0.204120	0.233368	473
IMG_2278.JPG	0.098254	0.161682	0.189195	298	IMG_2293.JPG	0.133337	0.195348	0.236515	353
IMG_2279.JPG	0.114083	0.212339	0.241046	383	IMG_2294.JPG	0.110535	0.183812	0.214488	388
IMG_2280.JPG	0.135485	0.190771	0.233987	343	IMG_2295.JPG	0.112492	0.179191	0.211574	342
IMG_2281.JPG	0.123500	0.181342	0.219401	244	IMG_2296.JPG	0.109538	0.122035	0.163985	268
IMG_2282.JPG	0.132664	0.236927	0.271540	236	IMG_2297.JPG	0.111083	0.189163	0.219367	407
IMG_2283.JPG	0.107341	0.179687	0.209307	330	IMG_2298.JPG	0.122423	0.203170	0.237203	446
IMG_2284.JPG	0.109541	0.168065	0.200612	289	IMG_2299.JPG	0.114291	0.180656	0.213773	365
IMG_2285.JPG	0.153775	0.200796	0.252914	252	IMG_2300.JPG	0.117907	0.184573	0.219019	352
IMG_2286.JPG	0.176630	0.198991	0.266075	210	IMG_2301.JPG	0.119525	0.167282	0.205595	235

Figure X.15, Table X.5, and Table X.6 exemplify the results provided to the client at the end of the photogrammetric survey to document existing cracks and spalling events.

Figures X.16 through X.21 illustrate the 3-D model of the clean air supply duct at the Eisenhower Memorial Tunnel. In this research, special lighting systems have been devised to evenly illuminate the lining even in dark situations, such as air ducts, and to ensure that the colors of the lining are reliably reproduced. The pipes attached to the divider wall have not been reproduced satisfactorily in three dimensions because pattern is needed in photogrammetry to find relative-only points, and steel pipes have very little, if any, pattern. Regardless, one of the objectives of this application was to check the use of photogrammetry in surveying a divider wall with embedded steel hangers that cannot be examined by any non-destructive technique. Details of the divider walls are given in

Figures X.17 and X.18, and a global accuracy of 1 mm was achieved, which ensures that progressive yielding of a hanger (or hangers) may be detected if surveys of this kind are carried out systematically. Figures X.19 and X.20 depict the model of the south wall as seen from the inside of the tunnel, where several cracks are evident. Some of the cracks have been digitized in Figure X.20: one is a typical construction (pour) joint, but the others are not, and their orientation allows one to infer the causes of distress in a specific area of the lining. Such inferences are difficult to make while inspecting the tunnel and mapping cracks by hand. Finally, Figure X.21 provides a detail of a cracked area of the lining.

The provided model and the quantities obtained are completely objective and defensible, and may be used at any time during the operational phases of the underground infrastructures.

Table X.3. Residuals at Scale Bars Used at Liberty Tunnel

Scale Bar Name	First Point ID	Second Point ID	Distance (m)	Accuracy (m)	Residual (m)
Scale bar 1	Point 1	Point 2	1.095956	0.000010	-0.000044
Scale bar 2	Point 3	Point 4	1.096029	0.000010	0.000029

Table X.4. Residuals at Scale Bars Used at Eisenhower Memorial Tunnel (Road Enclosure)

Control Point Names	Number of Observations	Image Point Residuals		Control Point Residuals (m)		
		X (pixels)	Y (pixels)	X	Y	Z
1	2	0.0067	0.0407	-0.0000	0.0004	-0.0006
2	2	0.0846	0.1426	0.0001	-0.0004	0.0006
3	2	0.1233	0.0489	0.0002	-0.0003	-0.0006
4	2	0.0458	0.1339	-0.0003	0.0003	0.0005
Control point RMS				0.0002	0.0004	0.0006
Total				0.0008		



Figure X.2. Three-dimensional model of Liberty Tunnel inbound tube by the ventilation shaft.



Figure X.4. Foreshortened view of spalling by ventilation shaft.



Figure X.3. Liberty Tunnel: Detail of spalling by ventilation shaft.



Figure X.5. Detail of exposed aggregate and rebar by ventilation shaft.



Figure X.6. Backside view of spalling by ventilation shaft to better appreciate depth and extent of spalling.

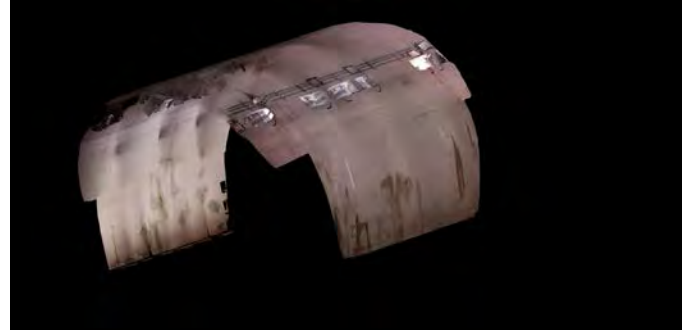


Figure X.9. Overall view of a tunnel stretch by southern portal.

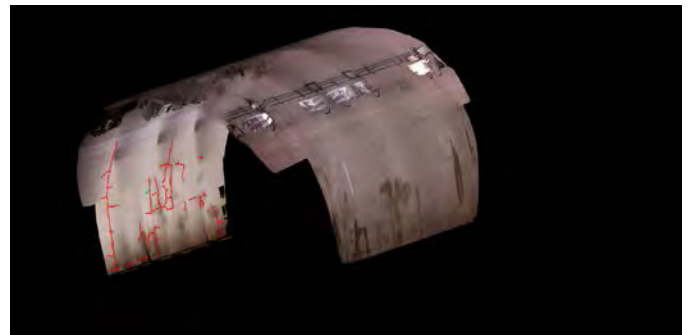


Figure X.10. Overall view of tunnel stretch by southern portal with digitized cracks on left wall.



Figure X.7. Closed polyline to determine area of spalling by ventilation shaft.

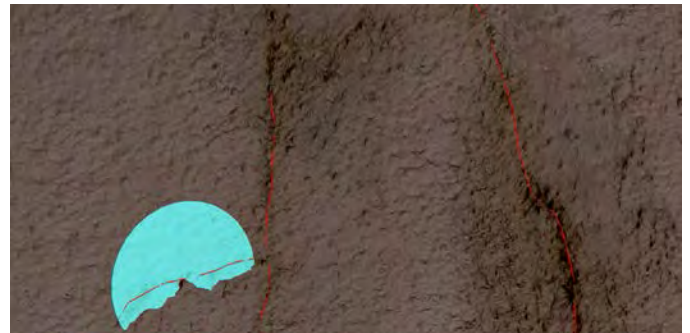


Figure X.11. Detail of digitized shotcrete cracks on left wall by southern portal; also visible is a plane interpolated through crack trace.

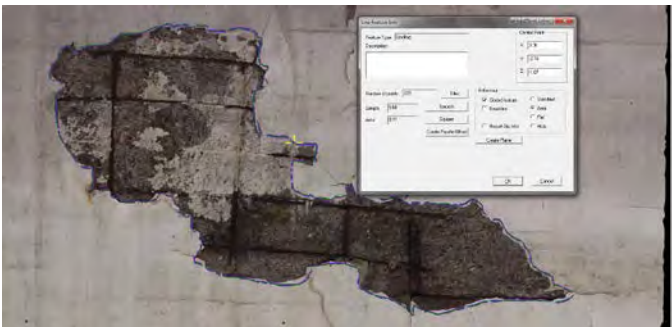


Figure X.8. Information on spalling by ventilation shaft—coordinates of center point and area.



Figure X.12. Detail of shotcrete cracks on left wall by southern portal with digitized cracks toggled off.

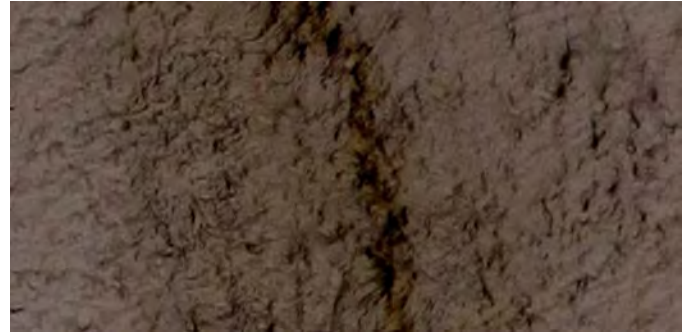


Figure X.13. Close-up view of shotcrete crack on left wall by southern portal: detail of surface roughness.

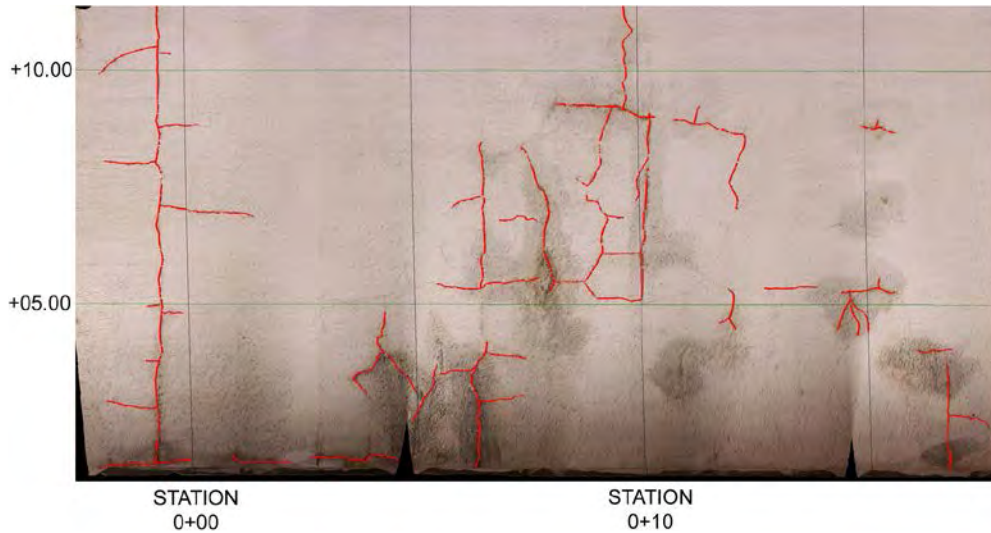


Figure X.14. Typical survey of existing cracks in a final lining.

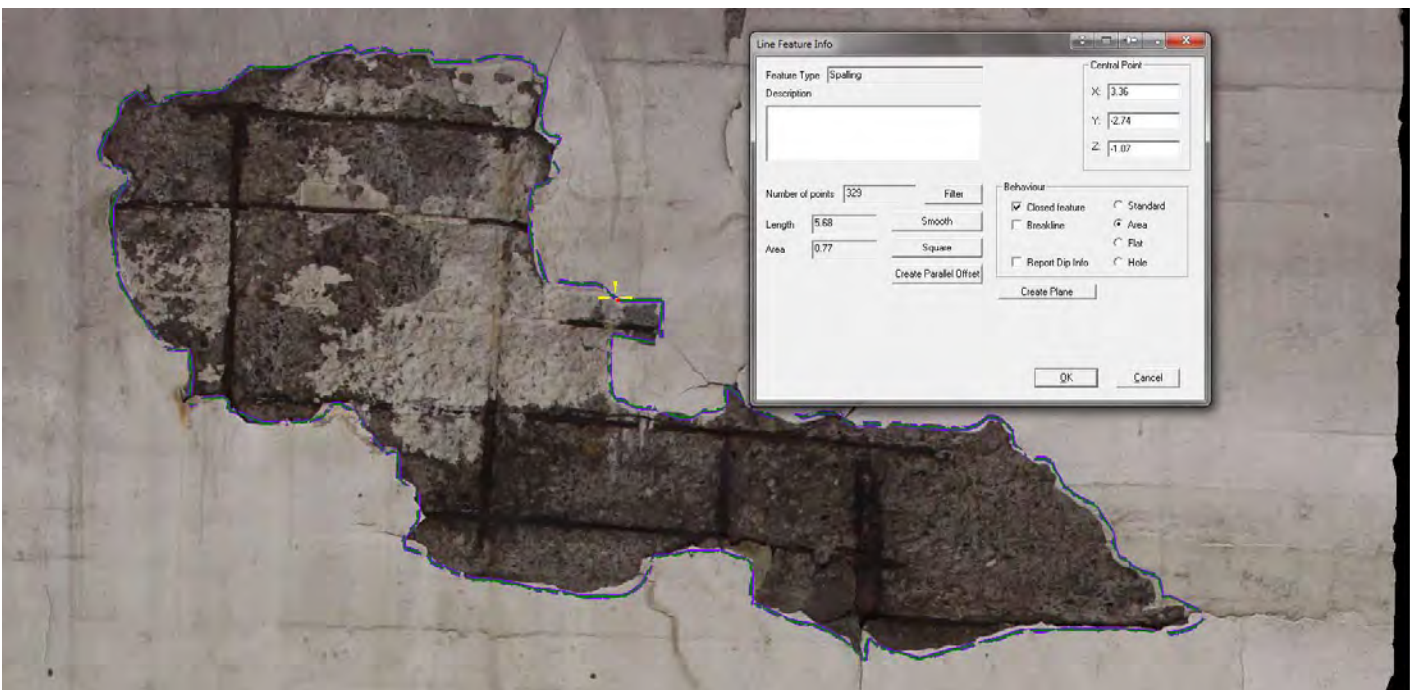


Figure X.15. Typical survey of spalling event in a final lining.

Table X.5. Example of Surveyed Crack Report for a Final Lining

Center X (ft)	Center Y (ft)	Center Z (ft)	Dip ^o	Direction ^o	Diameter (ft)	Trace Length (ft)
7.218	34.186	0.098	90.0	0.0	11.188	10.925
9.383	13.944	-0.886	89.9	176.0	12.238	12.041
9.974	13.222	-3.839	88.0	84.0	1.444	1.411

Table X.6. Example of Surveyed Spalling Report for a Final Lining

Center X (ft)	Center Y (ft)	Center Z (ft)	Area	Depth (in.)	Volume (sq ft)	Exposed Rebars?
23.845	151.513	3.515	3.51	2.4	0.702	Yes

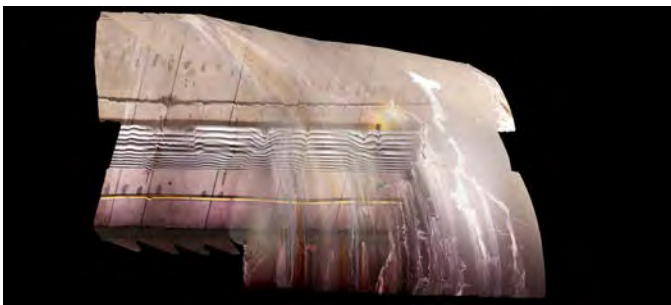


Figure X.16. Eisenhower Memorial Tunnel: Clean air supply duct, south-west ventilation building.

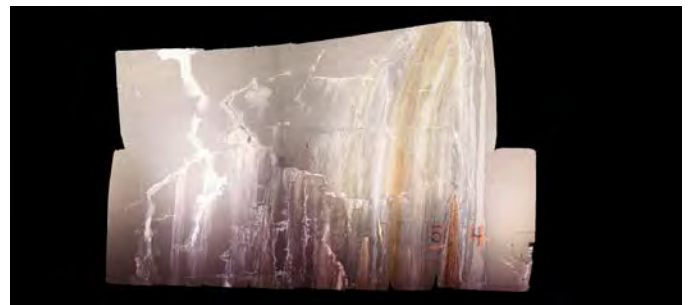


Figure X.19. Clean air supply duct, south-west ventilation building, view of south lining wall from within duct.

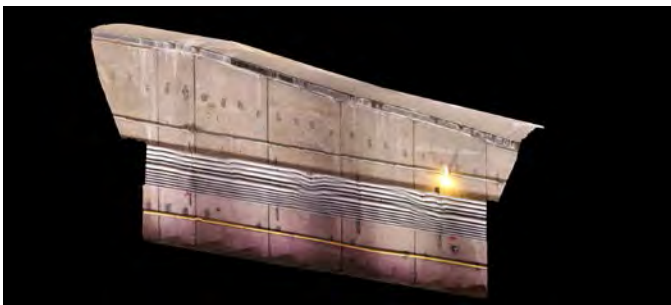


Figure X.17. Eisenhower Memorial Tunnel: Clean air supply duct, south-west ventilation building, divider wall.

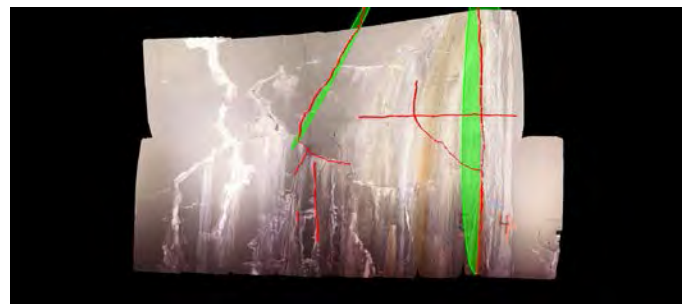


Figure X.20. Clean air supply duct, south-west ventilation building, view of south lining wall from within duct with digitized features.

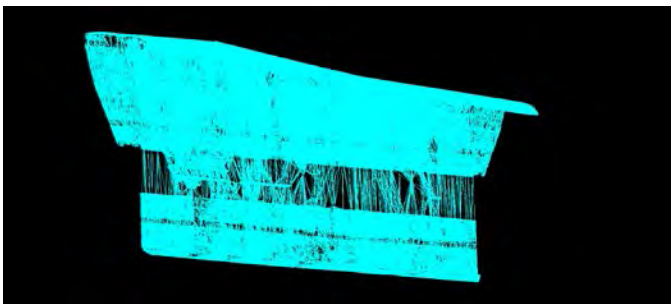


Figure X.18. Clean air supply duct, south-west ventilation building, triangulated mesh of divider wall.



Figure X.21. Clean air supply duct, south-west ventilation building, detail of south lining wall from within duct.

TRB OVERSIGHT COMMITTEE FOR THE STRATEGIC HIGHWAY RESEARCH PROGRAM 2*

CHAIR: **Kirk T. Steudle**, *Director, Michigan Department of Transportation*

MEMBERS

H. Norman Abramson, *Executive Vice President (retired), Southwest Research Institute*
Alan C. Clark, *MPO Director, Houston–Galveston Area Council*
Frank L. Danchetz, *Vice President, ARCADIS-US, Inc.*
Malcolm Dougherty, *Director, California Department of Transportation*
Stanley Gee, *Executive Deputy Commissioner, New York State Department of Transportation*
Mary L. Klein, *President and CEO, NatureServe*
Michael P. Lewis, *Director, Rhode Island Department of Transportation*
John R. Njord, *Executive Director (retired), Utah Department of Transportation*
Charles F. Potts, *Chief Executive Officer, Heritage Construction and Materials*
Ananth K. Prasad, *Secretary, Florida Department of Transportation*
Gerald M. Ross, *Chief Engineer (retired), Georgia Department of Transportation*
George E. Schoener, *Executive Director, I-95 Corridor Coalition*
Kumares C. Sinha, *Olson Distinguished Professor of Civil Engineering, Purdue University*
Paul Trombino III, *Director, Iowa Department of Transportation*

EX OFFICIO MEMBERS

Victor M. Mendez, *Administrator, Federal Highway Administration*
David L. Strickland, *Administrator, National Highway Transportation Safety Administration*
Frederick “Bud” Wright, *Executive Director, American Association of State Highway and Transportation Officials*

LIAISONS

Ken Jacoby, *Communications and Outreach Team Director, Office of Corporate Research, Technology, and Innovation Management, Federal Highway Administration*
Tony Kane, *Director, Engineering and Technical Services, American Association of State Highway and Transportation Officials*
Jeffrey F. Paniati, *Executive Director, Federal Highway Administration*
John Pearson, *Program Director, Council of Deputy Ministers Responsible for Transportation and Highway Safety, Canada*
Michael F. Trentacoste, *Associate Administrator, Research, Development, and Technology, Federal Highway Administration*

*Membership as of July 2014.

RENEWAL TECHNICAL COORDINATING COMMITTEE*

CHAIR: **Daniel D’Angelo**, *Recovery Acting Manager, Director and Deputy Chief Engineer, Office of Design, New York State Department of Transportation*

MEMBERS

Rachel Arulraj, *President, InfoInnovation*
Michael E. Ayers, *Consultant, Technology Services, American Concrete Pavement Association*
Thomas E. Baker, *State Materials Engineer, Washington State Department of Transportation*
John E. Breen, *Al-Rashid Chair in Civil Engineering Emeritus, University of Texas at Austin*
Steven D. DeWitt, *Chief Engineer (retired), North Carolina Turnpike Authority*
Tom W. Donovan, *Senior Right of Way Agent (retired), California Department of Transportation*
Alan D. Fisher, *Manager, Construction Structures Group, Cianbro Corporation*
Michael Hemmingsen, *Davison Transportation Service Center Manager (retired), Michigan Department of Transportation*
Bruce Johnson, *State Bridge Engineer, Oregon Department of Transportation, Bridge Engineering Section*
Leonnie Kavanagh, *PhD Candidate, Seasonal Lecturer, Civil Engineering Department, University of Manitoba*
Cathy Nelson, *Technical Services Manager/Chief Engineer (retired), Oregon Department of Transportation*
John J. Robinson, Jr., *Assistant Chief Counsel, Pennsylvania Department of Transportation, Governor’s Office of General Counsel*
Ted M. Scott II, *Director, Engineering, American Trucking Associations, Inc.*
Gary D. Taylor, *Professional Engineer*
Gary C. Whited, *Program Manager, Construction and Materials Support Center, University of Wisconsin–Madison*

AASHTO LIAISON

James T. McDonnell, *Program Director for Engineering, American Association of State Highway and Transportation Officials*

FHWA LIAISONS

Steve Gaj, *Leader, System Management and Monitoring Team, Office of Asset Management, Federal Highway Administration*
Cheryl Allen Richter, *Assistant Director, Pavement Research and Development, Office of Infrastructure Research and Development, Federal Highway Administration*
J. B. “Butch” Wlaschin, *Director, Office of Asset Management, Federal Highway Administration*

CANADA LIAISON

Lance Vigfusson, *Assistant Deputy Minister of Engineering & Operations, Manitoba Infrastructure and Transportation*

*Membership as of July 2014.

Related SHRP 2 Research

Nondestructive Testing to Identify Concrete Bridge Deck Deterioration (R06A)

Evaluating Applications of Field Spectroscopy Devices to Fingerprint Commonly Used Construction Materials (R06B)

Using Both Infrared and High-Speed Ground Penetrating Radar for Uniformity Measurements on New HMA Layers (R06C)

Nondestructive Testing to Identify Delaminations between HMA Layers (R06D)

Real-Time Smoothness Measurements on Portland Cement Concrete Pavements During Construction (R06E)

Assessment of Continuous Pavement Deflection Measuring Technologies (R06F)